



HAL
open science

Boson de Higgs: du simple au double

Jessica Levêque

► **To cite this version:**

Jessica Levêque. Boson de Higgs: du simple au double. Physique des Hautes Energies - Expérience [hep-ex]. Université Grenoble Alpes, 2018. tel-02381784v2

HAL Id: tel-02381784

<https://theses.hal.science/tel-02381784v2>

Submitted on 27 Nov 2019

HAL is a multi-disciplinary open access archive for the deposit and dissemination of scientific research documents, whether they are published or not. The documents may come from teaching and research institutions in France or abroad, or from public or private research centers.

L'archive ouverte pluridisciplinaire **HAL**, est destinée au dépôt et à la diffusion de documents scientifiques de niveau recherche, publiés ou non, émanant des établissements d'enseignement et de recherche français ou étrangers, des laboratoires publics ou privés.

UNIVERSITÉ GRENOBLE ALPES

Mémoire présenté par

Jessica Levêque

pour obtenir le diplôme de

Habilitation à Diriger des Recherches

Spécialité: Physique des Particules

Boson de Higgs: du simple au double

Soutenu le 15/11/2018 devant le Jury composé de :

Patrizia AZZI	(INFN, Padova)	<i>Rapporteur</i>
Lucia DI CIACCIO	(UGA/LAPP, Annecy)	<i>Examineur</i>
Giovanni LAMANNA	(UGA/LAPP, Annecy)	<i>President du Jury</i>
Bruno MANSOULIÉ	(CEA, Saclay)	<i>Rapporteur</i>
Laurent SERIN	(LAL, Orsay)	<i>Rapporteur</i>

Table des matières

Introduction	2
1 Calorimètre électromagnétique : mise en route et préparation des données	5
1.1 Opérations, monitoring et qualité des données	7
1.2 Analyse des premières données du LHC	9
2 Physique des processus diphoton	14
2.1 Section efficace différentielle des processus diphoton	14
2.2 Mesure des couplages du boson de Higgs et mise en évidence du mode VBF	17
2.3 Recherche de nouvelles résonances au-delà du Modèle Standard	23
3 R&D pour le HL-LHC	26
3.1 Physique du Higgs au HL-LHC	26
3.2 Détecteur à pixels ITk : de la conception à la réalisation	28
3.2.1 Optimisation de la géométrie	28
3.2.2 Contraintes techniques	30
3.2.3 Le design Alpin	32
3.3 Simulation ITk	36
3.3.1 FastGeoModel et XML	37
3.3.2 Simulation des services	45
3.4 Programme démonstrateur	47
3.5 Etudes thermiques	51
4 Perspectives	58
4.1 Programme pour le HL-LHC	58
4.2 Au-delà des Alpes : l'EVEReST	60
Remerciements	65
Bibliographie	66
Publications	70
Annexes : publications choisies	72
A The monitoring and data quality assessment of the ATLAS liquid argon calorimeter . .	73
B Readiness of the ATLAS liquid argon calorimeter for LHC collisions	113
C Measurement of the isolated diphoton cross-section in pp collisions at $\sqrt{s} = 7$ TeV with the ATLAS detector	132
D Observation of a new particle in the search for the Standard Model Higgs boson with the ATLAS detector at the LHC	157
E Measurements of Higgs boson production and couplings in diboson final states with the ATLAS detector at the LHC	181
F Search for Scalar Diphoton Resonances in the Mass Range 65-600 GeV with the ATLAS Detector in pp Collision Data at $\sqrt{s} = 8$ TeV	205

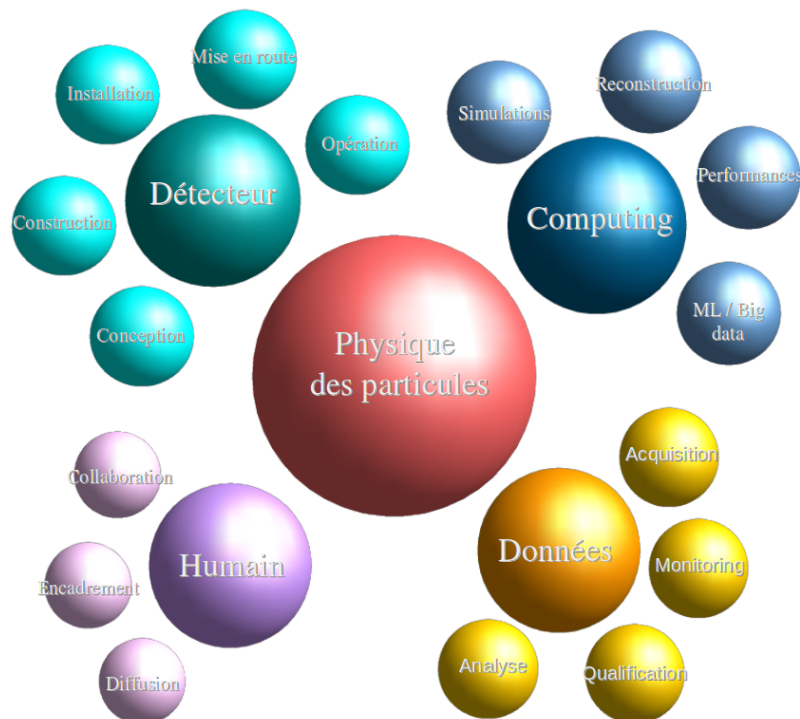
Introduction

La physique des particules, discipline qui vise à étendre notre compréhension de la structure fondamentale de la matière et de ses interactions, est évidemment un sujet fascinant en soi. Elle touche aux tout premiers instants de l'Univers, nous interroge sur son futur, et nous rattache à toutes les composantes de la nature, ici et maintenant.

Mais elle est plus encore. Plus que toute autre, cette discipline scientifique fédère des milliers de chercheurs, techniciens et ingénieurs des quatre coins du globe, qui unissent leurs efforts pour construire des machines inégalées, des équipements scientifiques colossaux, déploient une ingéniosité sans limite pour répondre aux grandes questions fondamentales de l'Univers : le boson de Higgs existe-t-il ? Qu'y a-t-il au-delà du modèle Standard ?

Au cours des 10 années passées au sein de la collaboration ATLAS, ma fascination pour la composante humaine du projet est devenue prédominante. Au-delà des réponses scientifiques, j'ai cherché à comprendre les rouages qui régissent cette fourmilière improbable qu'est la communauté scientifique d'ATLAS, et l'imbrication des compétences techniques, scientifiques et humaines nécessaires à sa réussite. Depuis la conception mécanique et électronique des détecteurs, leur installation et maintenance, le développement d'outils de simulations numériques, d'analyses de données, jusqu'à la formation des étudiants, l'organisation internationale des sous-projets, les processus de communication intra-collaboration et la diffusion scientifique auprès du grand public... Chaque facette de notre discipline, bien qu'indispensable au projet global et d'une complexité extrême, ne représente qu'une infime partie du Grand Tout. Il faudrait 10 vies pour tout apprendre.

Le plus incompréhensible, c'est que le monde soit compréhensible, avait dit Einstein. Il aurait peut-être révisé son jugement au vu du fonctionnement de la collaboration ATLAS. Dans ce cas précis, le plus incompréhensible, c'est que ça marche.



Pouvoir aborder tous les aspects de la physique expérimentale des hautes énergies au sein d'un même grand projet est une chance. Je n'ai pas la prétention de pouvoir couvrir tous les sujets au cours de ma carrière, ni même d'avoir suffisamment creusé chacun de ceux auxquels je me suis attelée depuis 10 ans. Mais je me suis attachée à diversifier au maximum mes activités au gré des opportunités, des rencontres et des circonstances, toujours en phase avec l'avancement du programme du LHC.

Ce rapport d'habilitation présente succinctement l'ensemble des travaux que j'ai réalisés au sein de la collaboration ATLAS depuis mon embauche au CNRS en 2007. Les détails techniques sont documentés dans une sélection de publications personnelles proposées en annexe.

Mes travaux sont structurés en trois grands axes, qui suivent logiquement l'historique de l'expérience et la chronologie du programme LHC : la mise en route du détecteur et la préparation des données [2007-2012], l'analyse des données du Run 1, couronnée par la découverte du célèbre et élitif boson de Higgs [2011-2014], et enfin la préparation des upgrades de la phase à haute luminosité du LHC [2013-2024]. La chronologie est résumée sur la Figure 1.

Le fil directeur de ce rapport est aussi le boson de Higgs. Graal du Modèle Standard, sa recherche représentait une motivation majeure pour la construction du LHC et la conception des sous-détecteurs d'ATLAS. Le calorimètre électromagnétique en particulier, a été optimisé pour maximiser l'acceptance et la précision de reconstruction des photons et électrons pour la recherche du boson de Higgs dans les canaux $H \rightarrow \gamma\gamma$ et $H \rightarrow ZZ^* \rightarrow 4e$. Pour chacun des physiciens de la collaboration, les années 2010 à 2012 représentent une période d'indicible excitation, avec la découverte du boson prédit et recherché depuis plus de 60 ans. Après la découverte, les mesures de ses propriétés fondamentales et la recherche de bosons scalaires additionnels à haute et basse masse ont occupé une grande place au sein de la collaboration.

La suite logique de ces travaux est la préparation des mesures de précision et de l'observation de la dernière prédiction du Modèle Standard pour la phase à haute luminosité du LHC : la très rare production d'une paire de bosons de Higgs. Ce programme nécessite une augmentation significative de la luminosité de la machine, et un remplacement des détecteurs les plus sensibles, en particulier le détecteur à pixels, qui devra s'accommoder d'un bruit d'empilement 5 fois supérieur au niveau actuel et s'équiper d'une électronique de lecture 10 fois plus rapide qu'aujourd'hui. Le programme HL-LHC est une opportunité majeure de participer à la conception et à la construction d'un nouveau détecteur pour collisionneur hadronique. Opportunité qui, compte-tenu de l'allongement du temps d'exploitation des grands collisionneurs, risque de ne plus se présenter avant 15 ou 20 ans.

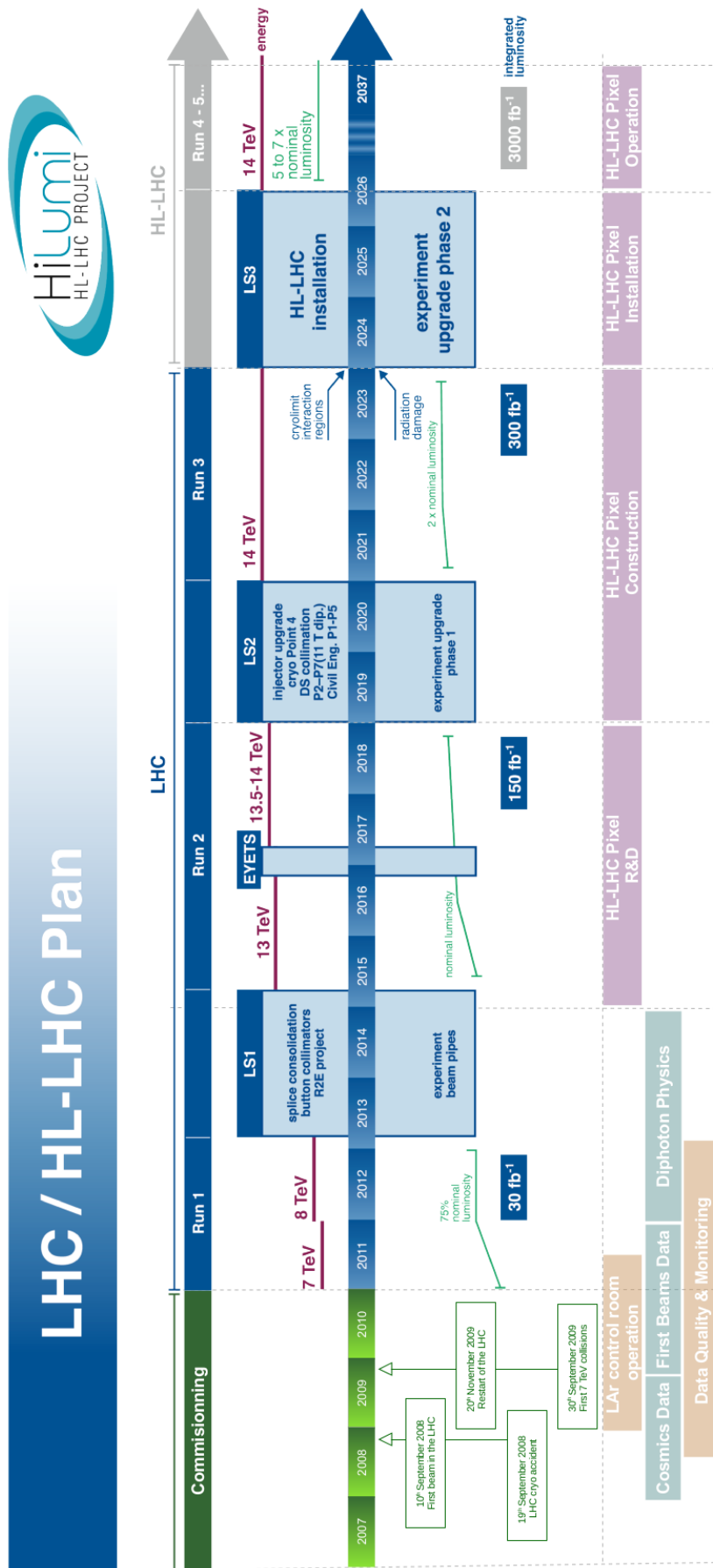


FIGURE 1 – Planning du LHC, du HL-LHC et chronologie des travaux présentés dans ce rapport d’habilitation.

1 Calorimètre électromagnétique : mise en route et préparation des données

Le détecteur ATLAS [ref1] a été conçu pour la recherche du boson de Higgs et de nouvelle physique auprès du collisionneur hadronique LHC [ref2], dans un environnement extrêmement difficile contenant de multiples événements d'empilement et une énergie dans le centre de masse inégalée de 14 TeV.

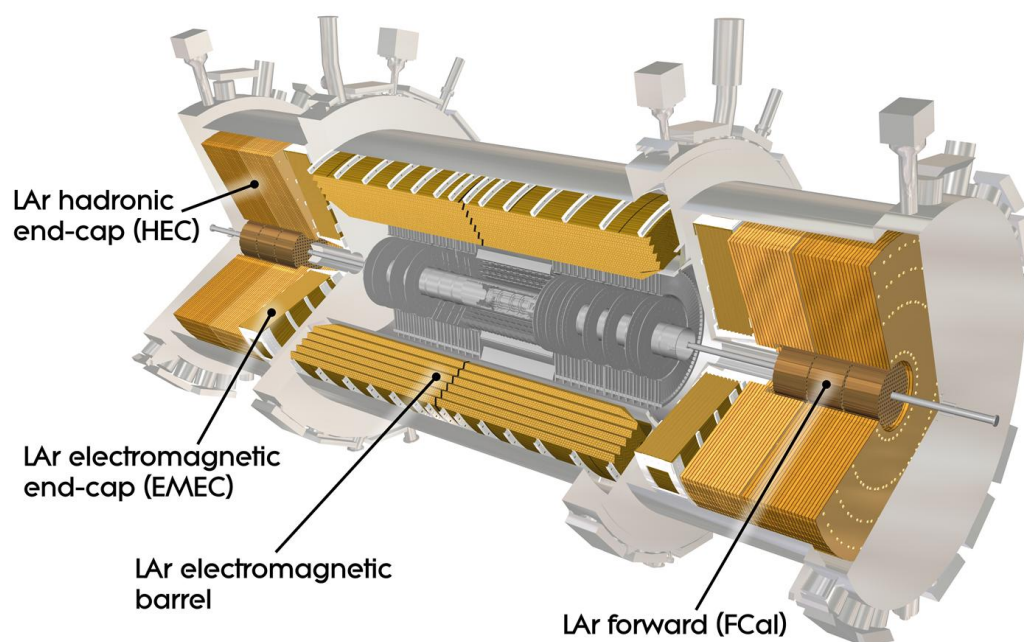


FIGURE 2 – Vue en coupe du calorimètre à argon liquide d'ATLAS.

Le calorimètre à argon liquide, optimisé pour la reconstruction précise des électrons et photons dans un large domaine de pseudo-rapidité ($\eta < 2.5$), est un élément clé pour la recherche du boson de Higgs dans les canaux diboson $H \rightarrow ZZ^* \rightarrow e^+e^-e^+e^-$ et $H \rightarrow \gamma\gamma$. Il s'agit d'un calorimètre à échantillonnage, dont le milieu actif est l'argon liquide. Il est séparé en quatre sections distinctes illustrées sur la Figure 2 : le tonneau et les bouchons électromagnétiques (EMB et EMEC), les bouchons hadroniques (HEC) et le calorimètre avant (FCAL). La section électromagnétique présente une géométrie en accordéon pour minimiser la perte d'acceptance due aux services, et comprend un pré-échantillonneur dans la région $\eta < 1.8$ pour permettre l'estimation des pertes d'énergie en amont du détecteur. Les quatre calorimètres sont segmentés longitudinalement (Figure 3) et correspondent à un total de 182 468 cellules de lecture. L'énergie déposée par les particules dans les cellules du calorimètre est reconstruite à partir du signal électronique échantillonné à 40 MHz et de constantes de calibration en utilisant la méthode des coefficients d'*optimal filtering* [ref3] (Figure 4).

La reconstruction précise de l'énergie des électrons et des photons ainsi que la maximisation de la quantité de données de bonne qualité disponibles pour les analyses requière une logistique faramineuse : opération et maintenance du détecteur, monitoring en temps réel des 182 000 cellules, prise quotidienne

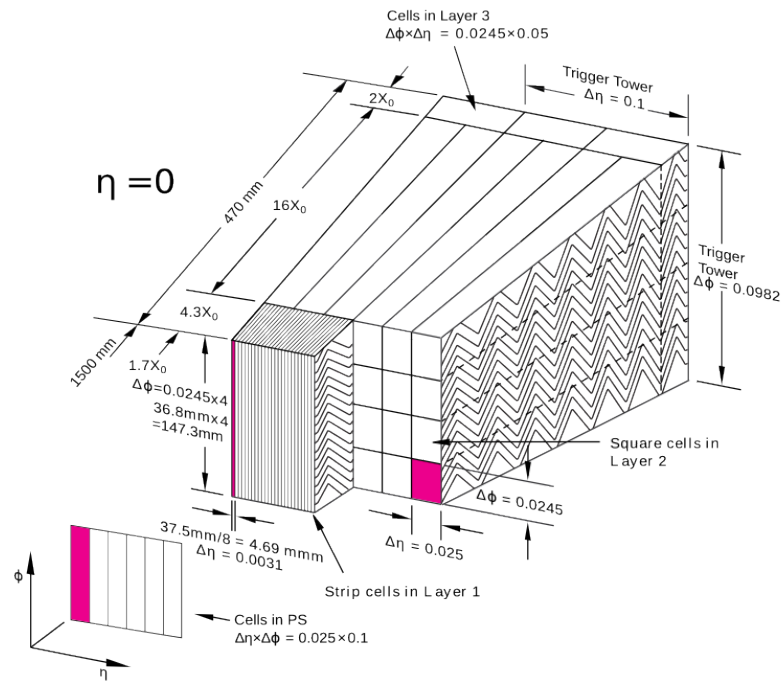


FIGURE 3 – Géométrie en accordéon des électrodes du calorimètre électromagnétique et segmentation longitudinale des cellules de lecture.

de données de calibration entre les runs de collisions suivies de mises à jour des bases de données des conditions du détecteur (haute-tension d’opération des électrodes, constantes de calibration, liste des cellules bruyantes...). Conditions qui seront ensuite utilisées pour nettoyer, corriger et calibrer les données de physique pendant leur reconstruction au Tier 0.

Comprendre le cheminement des données dans les méandres du système d’acquisition et développer les outils nécessaires à cette première étape cruciale de préparation des données de physique m’ont occupée pendant plus de 4 ans.

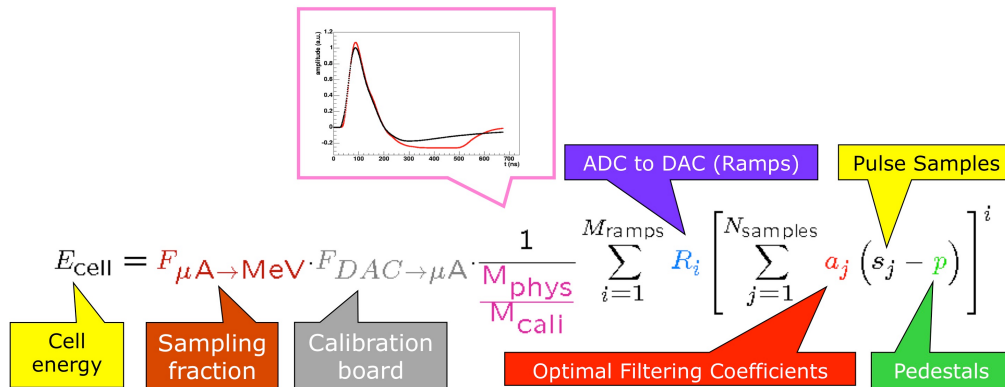


FIGURE 4 – Reconstruction de l’énergie des cellules du calorimètre à partir de la méthode des coefficients d’*Optimal Filtering* [ref3].

1.1 Opérations, monitoring et qualité des données

L'opération partielle du calorimètre à argon liquide a commencé en 2006, bien avant la circulation des premiers faisceaux de protons du LHC. Entre 2006 et 2008, les cellules du calorimètre ont été progressivement connectées pour aboutir à la lecture complète du détecteur en 2008. Pendant cette période, des semaines de runs de muons cosmiques combinés ont été planifiées pour intégrer progressivement les différents sous-détecteurs d'ATLAS dans le système d'acquisition global. En effet, ces particules électriquement chargées et très énergétiques sont capables de pénétrer dans la cavité ATLAS et de déposer un signal détectable dans tous les sous-détecteurs : trajectographes, calorimètres, et évidemment, chambres à muons. Le premier run de cosmiques intégrant le calorimètre à argon liquide a été enregistré en 2007.

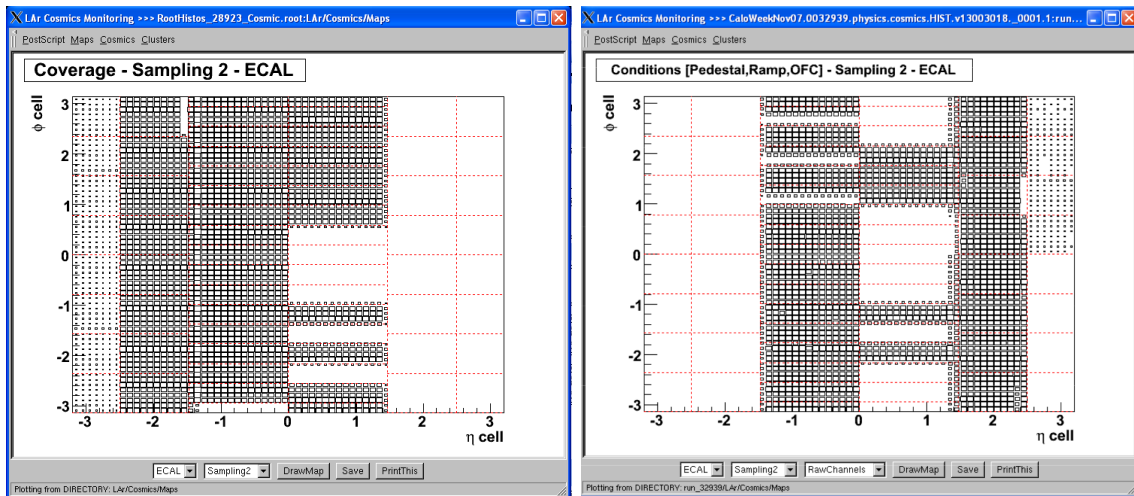


FIGURE 5 – Exemple de l'état de connexion et de lecture des cellules du calorimètre électromagnétique dans la couche 2, novembre 2007.

Lors de mon arrivée dans la salle de contrôle en 2007, c'est-à-dire durant la dernière année d'installation du calorimètre électromagnétique, mon intention première était simplement de tenter de comprendre le chemin parcouru par le signal d'ionisation laissé par un muon cosmique dans le calorimètre électromagnétique au travers des méandres de l'électronique de lecture et du système d'acquisition, de comprendre le fonctionnement d'un run de calibration, puis de tenter de faire apparaître, en temps réel, un joli "pulse" de calorimètre sur un écran de la salle de contrôle.

Le chemin fut long et difficile. Le système d'acquisition était en cours d'installation et de validation, les outils de monitoring étaient en développement, et surtout, il n'existait aucune procédure documentée sur l'opération du calorimètre à argon liquide dans la salle de contrôle, le système *online* étant exclusivement opéré par les experts du détecteur, qui s'accommodaient parfaitement de travailler quotidiennement sur une base de commandes shell indéchiffrables pour un profane et de fichiers ASCII codés en hexadécimal. Ma mission s'est donc petit à petit transformée en l'élaboration d'une "Pierre de Rosette" du calorimètre à argon liquide, pour faire la jonction entre le monde des experts du calorimètre et celui des futurs shifters sans aucune expertise qui seraient affectés à la surveillance du calorimètre à argon liquide 24h/24h à partir de 2008, dès les premières collisions.

Ce travail consistait à inventer des procédés de visualisation simples traduisant les dysfonctionnements parfois complexes du détecteur, mettre au point des procédures de diagnostics rapides et fiables en combinant plusieurs sources d'information (DCS, trigger, erreurs provenant des cartes front-end,...),

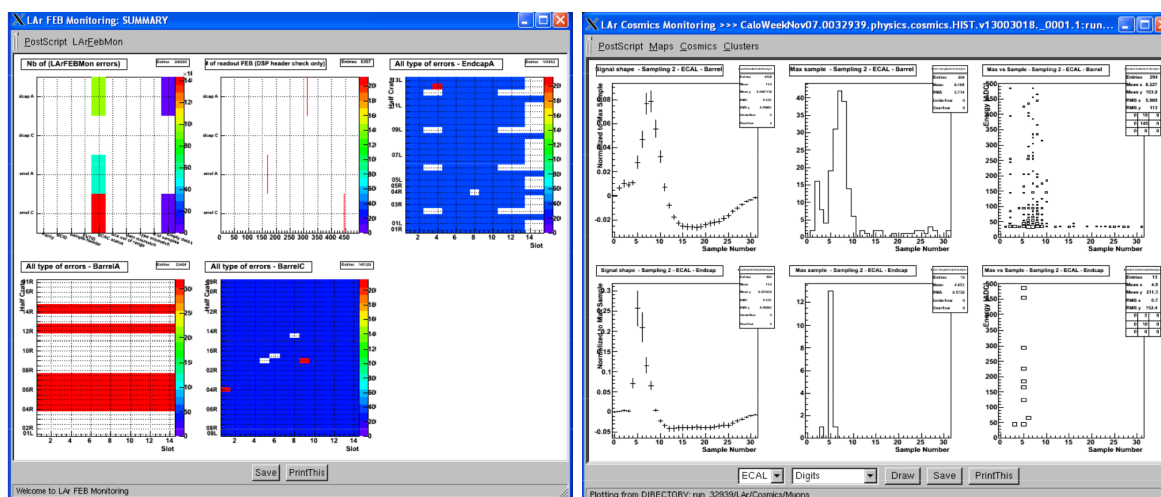


FIGURE 6 – Monitoring du calorimètre en cours de développement, novembre 2007. A gauche, tests d'intégrité des données envoyées par les cartes front-end. A droite, visualisation en temps-réel des premiers signaux de physique laissés par des muons cosmiques dans l'argon liquide.

établir une série d'instructions pour que le shifter puisse "réparer" les erreurs les plus courantes ou sache quand décider d'appeler un expert au milieu de la nuit. Ce travail impliquait également de jouer les cobayes pour tous les outils de diagnostic mis en place dans la salle de contrôle, et de participer ainsi à leur amélioration en suggérant l'ajout de nouvelles fonctionnalités au fur et à mesure de l'expérience gagnée dans les opérations du détecteur, pour simplifier et optimiser la prise de données et les diagnostics.

De 2008 à 2010, j'ai demandé à être basée au CERN en tant que Project Associate pour l'expérience ATLAS, ce qui m'a permis de passer suffisamment de temps dans la salle de contrôle pour mener à bien ce projet : mettre au point les procédures de shifts lors du démarrage du détecteur requière une présence assidue et constante dans la salle de contrôle. Les procédures d'opération devaient être corrigées quasi-quotidiennement en fonction des difficultés rencontrées par les shifters, des conditions de runs ou du comportement parfois erratique du calorimètre, avec des ajustement fréquents des seuils de déclenchement des erreurs ou l'ajout de nouveaux outils de monitoring pour détecter des dysfonctionnements inattendus. La Figure 6 présente un exemple des premiers tests d'intégrité des données mis en place dans la salle de contrôle, ainsi que les premiers vrais pulses de physique observés en temps réel dans le calorimètre à argon liquide lors du passage de muons cosmiques.

J'ai pendant cette période rempli la fonction d'experte *on-call* pour le monitoring online de l'argon liquide et celle de responsable de l'encadrement et de la formation des shifters pour l'opération du détecteur. J'ai formé des dizaines d'étudiants, chercheurs et postdocs aux opérations et au monitoring, et encadré plusieurs étudiants pour développer de nouveaux histogrammes de diagnostic spécifiques au calorimètre (Louis Helary, timing [ref4]; Mathieu Arousseau, DSP [ref5]; Samir Arfaoui, haute-tension [ref6], Maud Schwoerer, cellules bruyantes [ref13]). J'ai également motivé et encadré le développement de nombreux outils online, comme par exemple le *LArIdTranslator*, interface web utilisée pour convertir les différents systèmes d'indexation des cellules du calorimètre (numéros de cellule, numéros de front-end board, identifiants des crates, coordonnées physiques...), ou le *LArWebDisplay* qui permet de visualiser de façon synthétique pour chaque run le résultat des tests automatisés de centaines d'histogrammes de monitoring : liste précise des cellules problématiques avec pré-diagnostic (bruit, problème de calibration), liste des canaux par front-end présentant des erreurs d'intégrité, liste des canaux avec haute-tension non-nominale, etc... Ces outils sont toujours en service aujourd'hui et disponibles depuis

la page d'instruction des shifters^{1 2}

Un autre aspect intéressant du monitoring est de déterminer dans quelle mesure un problème trop récurrent ne devrait plus être systématiquement géré par les shifters mais réglé en amont par les experts : lorsque les interruptions deviennent trop fréquentes et perturbent la prise de donnée pour l'ensemble des sous-détecteurs d'ATLAS, ou lorsqu'un problème *a priori* considéré comme mineur rend une quantité non-négligeable de données inutilisables (combien ?) pour la physique. Ce dernier point m'a progressivement amenée à m'interroger sur l'étape qui suit la prise de données : une fois sorties du détecteur, que deviennent-elles ? Comment sont suivis les problèmes reportés par les shifters dans les logbooks de la salle de contrôle ? Qui se charge de vérifier que les corrections de haute tension sont bien appliquées, ou que les cellules bruyantes sont bien masquées ? Qui contrôle en bout de chaîne que les données sont véritablement utilisables pour la physique, ou que des problèmes de détecteur ne sont pas passés inaperçus dans la salle de contrôle ?

En 2010, peu de procédures de contrôle qualité étaient en place dans la chaîne de reconstruction. J'ai ainsi commencé une collaboration de plusieurs années avec Benjamin Trocmé (LPSC) pour mettre en place la procédure complète de qualité des données de l'argon liquide, depuis l'opération du détecteur dans la salle de contrôle en passant par la gestion des informations enregistrées dans les bases de données de conditions jusqu'à la validation finale après reconstruction au Tier 0. Le résultat de ces quatre années de travail est décrit dans un article technique de quarante pages publié dans *JINST* [pub1] et présenté dans l'annexe A.

En 2012, grâce à l'expertise de monitoring et de qualité des données développées pour l'argon liquide, j'ai été nommée coordinatrice Data Quality pour l'ensemble des sous-détecteurs d'ATLAS. Les diagnostics établis par les différents sous-systèmes manquaient de cohérence, en particulier les seuils déclencheurs d'actions immédiates à réaliser dans la salle de contrôle pour éviter la perte irréversible de données. La qualité des méta-données attachées aux dysfonctionnements mineurs des détecteurs ainsi que le contenu informatif des compte-rendus hebdomadaires variaient significativement en fonction du sous-système et/ou du shifter en charge de la validation des données. Il était également très difficile d'obtenir une vue globale de la quantité de données utilisables pour la physique, et d'obtenir un bilan cohérent sur une période définie des principales sources de pertes de données.

J'ai réorganisé le groupe Data Quality en réduisant drastiquement le nombre de réunions, en instaurant un système de rapports quotidiens online pour les shifters en charge du contrôle des données pour chaque sous-système et en développant des outils capables de fournir des bilans de pertes globales automatisés. On peut par exemple mentionner un module python spécifique à la qualité de données ajouté dans l'outil *Run Query*³ d'ATLAS, qui permet de visualiser les sources de pertes par sous-système et par run, et d'obtenir des graphiques combinés pour de longues périodes de prise de données (Figure 7). Cette coordination d'une année s'est achevée avec la rédaction d'un rapport résumant la qualité des données du Run 1, l'organisation des opérations de contrôle de qualité des données dans ATLAS et une série de recommandations pour les futures campagnes de prise de données [pub2].

1.2 Analyse des premières données du LHC

Les premiers faisceaux de protons ont circulé dans le LHC en septembre 2008 (Figure 8). Mais suite à l'incident qui a détruit un important secteur d'aimants du LHC [ref7], les collisions n'ont réellement pu démarrer qu'en septembre 2009 [ref8].

Cependant, une autre source de particules était disponible pour occuper les chercheurs : les muons

1. *LArIdTranslator* : <https://atlas-larmon.cern.ch/LArIdtranslator/>

2. *LArWebDisplay* : <https://atlas-larmon.cern.ch/WebDisplayExtractor/>

3. *Run Query* : <https://atlas-runquery.cern.ch/query.py?q=find+run+350310+%2F+show+dqsum>

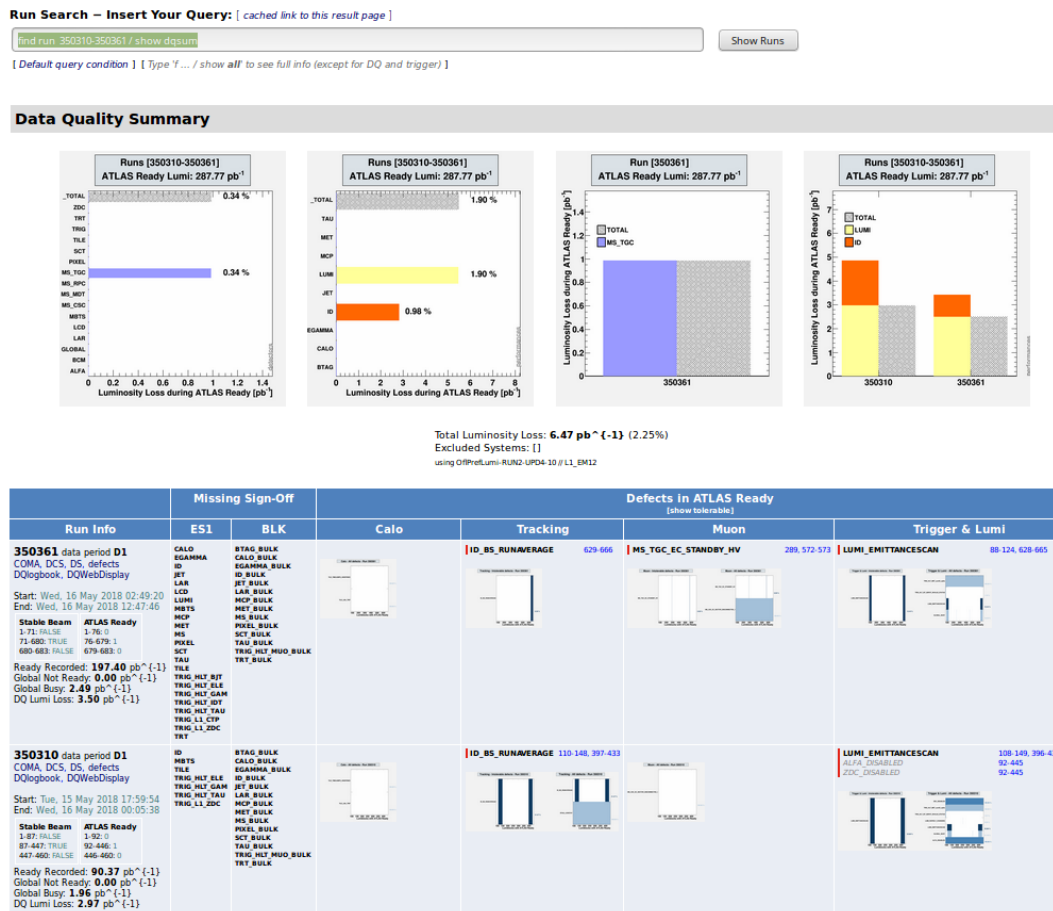


FIGURE 7 – Exemple de bilan de la qualité des données généré en ligne via l’interface web *Run Query* d’ATLAS : <https://atlas-runquery.cern.ch/query.py?q=find+run+350310+%2F+show+dqsum>

cosmiques. Plusieurs millions de muons cosmiques ont été enregistrés par ATLAS lors de runs combinés planifiés entre 2007 et 2009. Ces données ont été utilisées pour s’exercer à la calibration et à l’alignement des détecteurs, pour tester le système de déclenchement et le monitoring, et même pour réaliser les premières études de performances : tracking combiné, identification des électrons et des photons, reconstruction des jets et de l’énergie transverse manquante.

Un travail minutieux réalisé par toute la communauté de l’argon liquide a permis de démarrer la prise de données de collisions avec un calorimètre parfaitement maîtrisé : linéarité de la réponse, système de déclenchement, stabilité des constantes de calibration, reconstruction, performances. Les résultats des études préparatoires réalisées entre 2007 et 2009 à partir des données cosmiques sont présentés dans l’annexe B [pub3]). Dans ce cadre, je me suis concentrée avec plusieurs étudiants successifs sur la reconstruction des objets physiques (électrons, photons et énergie transverse manquante) dans les données du calorimètre électromagnétique collectées dans des événements "vides", c’est-à-dire déclenchés avec un trigger aléatoire et ne comportant donc aucune trace de particule physique, seulement du bruit électronique. On peut mentionner en particulier le travail réalisé avec Elisabeth Petit pendant son stage de M2 et le début de sa thèse [ref9] sur la compréhension de l’énergie transverse manquante (Figure 9 [pub4]), qui a nécessité la mise en place d’une base de données des cellules bruyantes du calorimètre, et à terme, a servi à valider toute la chaîne de qualification des données, en particulier la détection et le masquage automatisés des cellules bruyantes.

Avec le véritable démarrage du LHC (Figure 10), les analyses des premières données de collisions ont

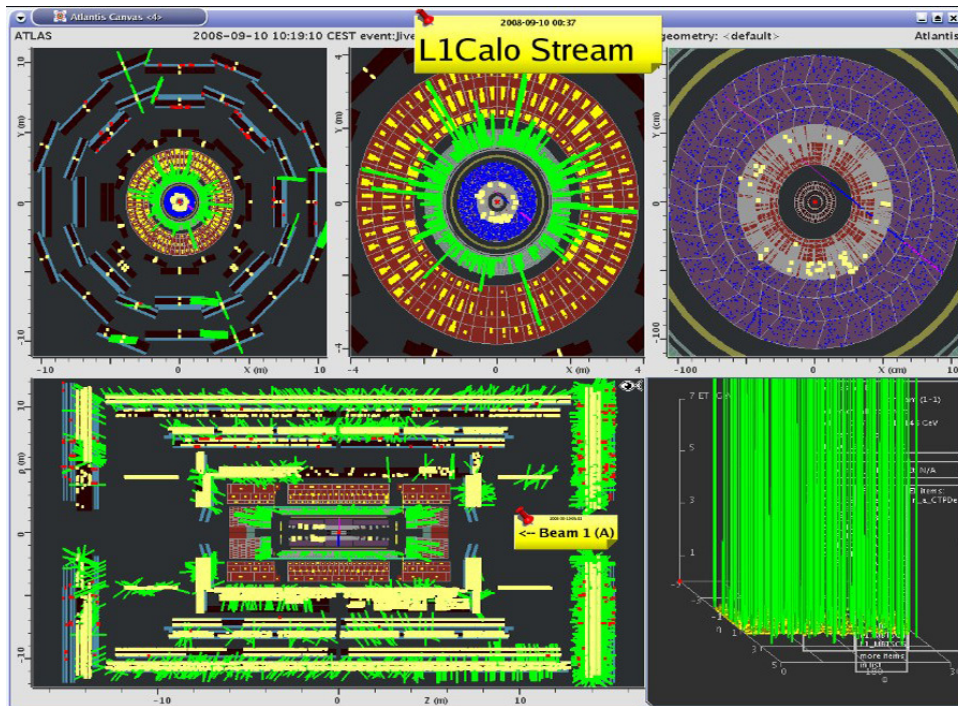


FIGURE 8 – L'un des premiers événements *Beam Splash* enregistrés par l'expérience ATLAS le 10 Septembre 2008.

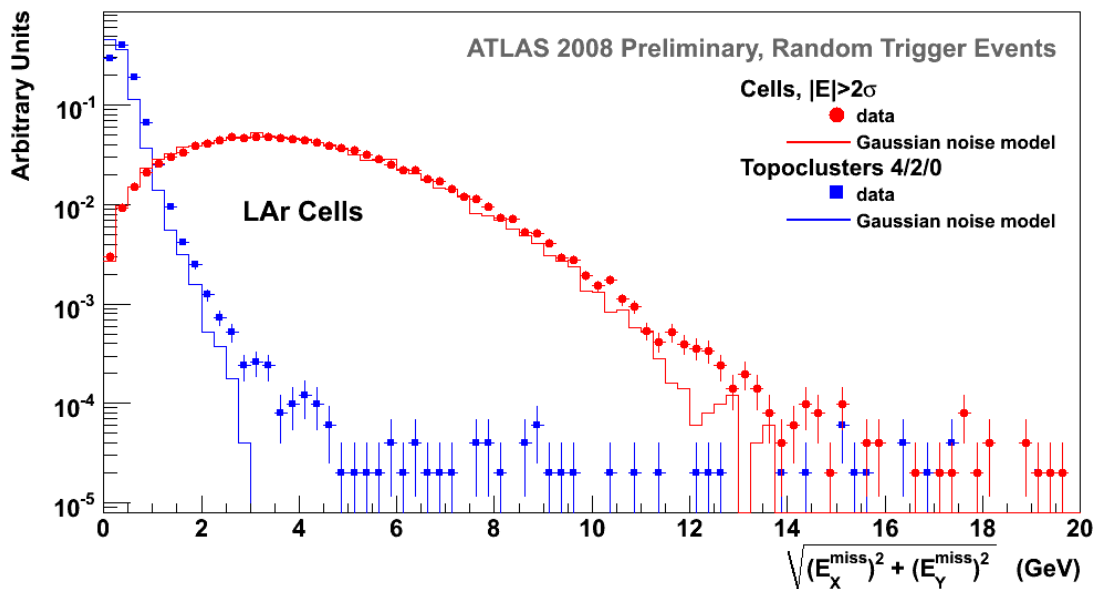


FIGURE 9 – Premières mesures de l'énergie transverse manquante dans le calorimètre électromagnétique d'ATLAS, réalisées à partir de données cosmiques "vides". Elisabeth Petit [pub12]

enfin pu commencer. Les premières mesures ont surtout servi à redécouvrir le Modèle Standard (Figure 11[pub5]), ajuster les simulations Monte-Carlo, parfaire la calibration des détecteurs et comprendre les bruits de fond du LHC pour préparer la recherche du boson de Higgs et de nouvelle physique. Ces



FIGURE 10 – Explosion de joie sur (presque) tous les visages lors du redémarrage du LHC. Salle de contrôle ATLAS, Septembre 2009.

sujets seront abordés dans le chapitre suivant.

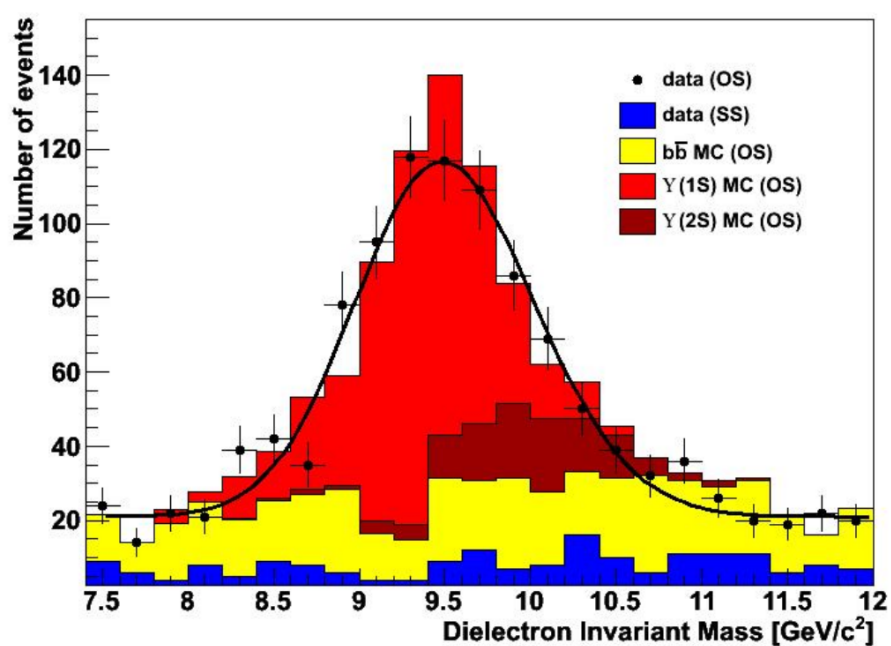


FIGURE 11 – Première mise en évidence du Upsilon dans 11.4 pb^{-1} de données à 7 TeV. Maud Shwoerer [pub4]

2 Physique des processus diphoton

Le boson de Higgs, désormais célèbre jusqu'au grand public, fut pendant longtemps la pièce manquante du Grand Puzzle des particules élémentaires. Cet ingrédient *ad-hoc*, ajouté en 1964 pour expliquer la masse des bosons de jauge W et Z et celle des fermions [ref10][ref11], a tenu en haleine plusieurs générations de physiciens expérimentateurs qui l'ont recherché sans relâche et sans succès pendant près de 60 ans. Mais le 4 juillet 2012, après à peine plus de deux ans d'exploitation du LHC, le CERN annonçait l'observation simultanée par les expériences ATLAS et CMS d'une nouvelle particule compatible avec le boson de Higgs prédit par le Modèle Standard [pub6], dans les canaux $H \rightarrow \gamma\gamma$ et $H \rightarrow ZZ^* \rightarrow e^+e^-e^+e^-$.



FIGURE 12 – Annonce de l'observation d'une nouvelle résonance compatible avec le boson de Higgs par les collaborations ATLAS et CMS. Auditorium du CERN, 4 juillet 2012.

La désintégration du boson de Higgs en deux photons présente l'un des taux de branchement les plus faibles (0.2% à 125 GeV [ref12]). Cependant, l'excellente résolution fournie par le calorimètre électromagnétique sur la mesure des paramètres cinématiques des deux photons offre à ce canal une signature expérimentale très claire : un pic de masse étroit dans le spectre de masse diphoton, au-dessus d'un bruit de fond continu (Figure 13). Le canal diphoton a joué un rôle essentiel dans la recherche, la découverte et la mesure des propriétés du boson de Higgs. L'étude de ce canal constitue l'essentiel du travail de thèse de Maud Schwoerer [ref13], que j'ai eu la chance de co-encadrer de 2010 à 2013, durant la période excitante et historique de la découverte du boson de Higgs au LHC.

Cette section présente les études réalisées avec Maud pendant sa thèse : mesure du taux de production d'événements diphotons au LHC, première mise en évidence du boson de Higgs dans le mode de production VBF, et mesure des couplages du boson nouvellement découvert. La fin du chapitre présente une étude plus récente, entièrement réalisée par le groupe photon du LAPP, dans le prolongement naturel de la recherche du boson de Higgs : la recherche de résonances additionnelles au-delà du Modèle Standard dans le spectre de masse diphoton.

2.1 Section efficace différentielle des processus diphoton

Le bruit de fond $\gamma\gamma$ non-résonant, dominant dans la recherche du boson de Higgs, est un sujet d'étude à part entière. La mesure de section efficace différentielle de production de paires de photons

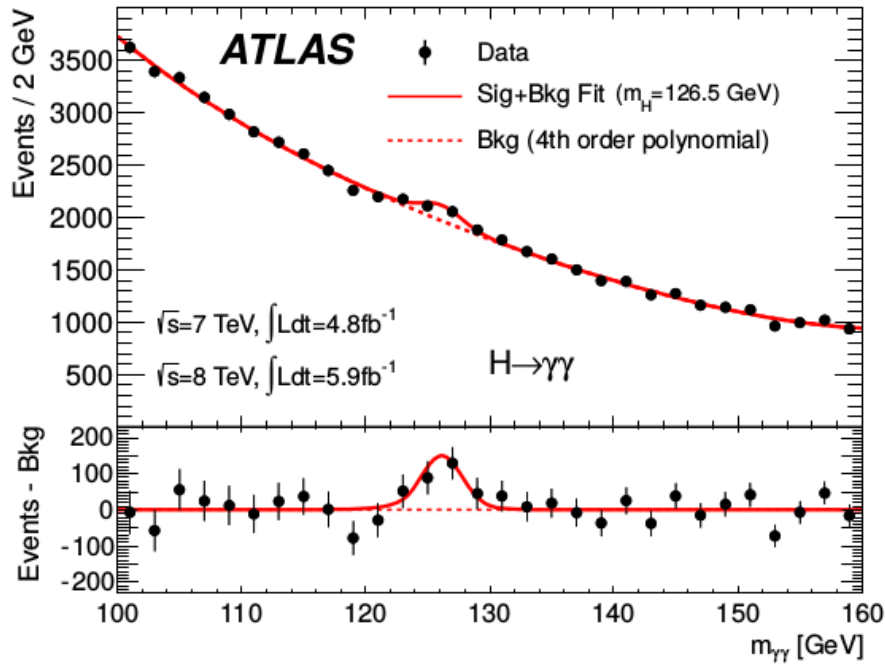


FIGURE 13 – Apparition d’un pic autour de 125 GeV dans la distribution de masse invariante diphoton.

directs avec une statistique conséquente permet de tester les prédictions de QCD perturbative et de raffiner les générateurs Monte-Carlo dans des régions de l’espace des phases où les données sont aujourd’hui encore mal comprises.

En outre, la mesure de sections efficaces différentielle des processus diphoton requiert une compréhension fine de l’efficacité de reconstruction des photons, de l’énergie déposée dans le cône d’isolation de ces derniers, et la maîtrise du bruit de fond réductible provenant de jets mal identifiés dans les processus QCD γ -jet et jet-jet. L’analyse des processus diphotons procure ainsi des bases solides pour la construction d’une analyse rigoureuse de recherche du boson de Higgs dans le canal $H \rightarrow \gamma\gamma$.

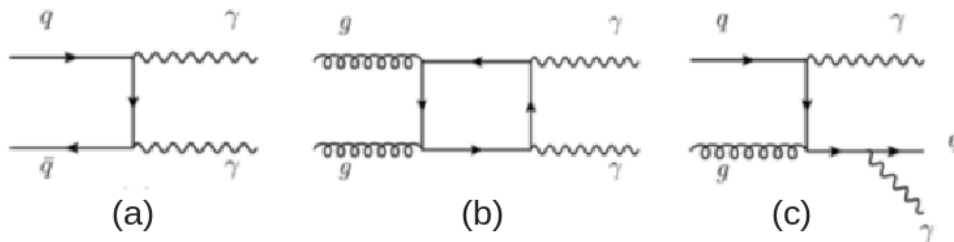


FIGURE 14 – Processus à l’ordre dominants de production directe de paires de photons au LHC : processus de Born (a), boîte (b) et bremsstrahlung (c).

Il existe deux modes principaux de production de paires de photons au LHC : la production directe (Figure 14) et la fragmentation d’un parton (Figure 15). Dans le cas de la production directe à l’ordre dominant, on distingue trois processus principaux :

- Le processus de Born : annihilation $qq \rightarrow \gamma\gamma$, d’ordre α_{QED}^2
- Le processus de boîte (box) : $gg \rightarrow \gamma\gamma$, d’ordre $\alpha_S^2 \cdot \alpha_{QED}^2$. Ce processus est d’ordre supérieur au

processus de Born, mais la très forte densité de gluons au LHC génère une section efficace du même ordre de grandeur [ref14].

- Le processus de rayonnement (bremsstrahlung) : $qg \rightarrow q\gamma$, d'ordre $\alpha_S \cdot \alpha_{QED}^2$. Ce processus est également d'ordre supérieur mais compensé par l'importante densité de gluons.

Dans le cas du processus de bremsstrahlung, quand l'angle de séparation entre le parton et le photon émis tend vers 0, une singularité apparaît dans le calcul du processus $qg \rightarrow q\gamma\gamma$. Les divergences sont factorisées et absorbées dans une fonction de fragmentation [ref14]. L'échelle arbitraire de fragmentation qui détermine artificiellement la distinction entre les deux processus (bremsstrahlung ou fragmentation) n'est pas un paramètre physique. Les deux contributions, directe et fragmentation, doivent être donc être combinées pour obtenir une description physique complète de l'émission d'un photon par un parton. Seule la somme des deux contributions est une observable physique [ref14].

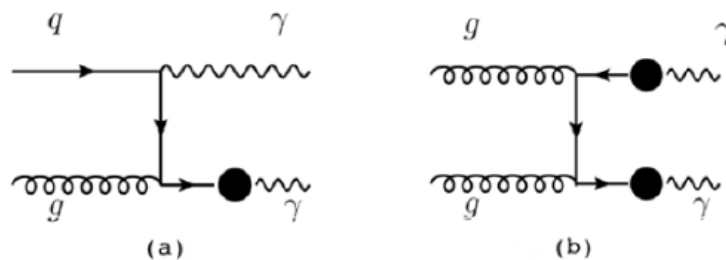


FIGURE 15 – Diagrammes de Feynman à l'ordre dominant pour la simple (a), et double (b) fragmentation.

Des mesures de sections efficaces différentielles de production de paires de photons au LHC à $\sqrt{s} = 7$ TeV ont déjà été publiées par les collaborations ATLAS [ref15] et CMS [ref16] en 2011. Ces mesures ont montré des désaccords importants entre les données et les prédictions théoriques NLO, en particulier dans les régions où l'angle entre les deux photons ($\Delta\phi_{\gamma\gamma}$) est très petit et la masse invariante diphoton ($m_{\gamma\gamma}$) très faible, qui correspondent à une zone où les corrections NNLO sont sous-estimées. Dans la région à haut $\Delta\phi_{\gamma\gamma}$, les prédictions théoriques à ordre fixe semblent à l'inverse très supérieures aux mesures. Une amélioration des erreurs statistiques et la comparaison avec plusieurs générateurs permettrait de mieux restreindre et de mieux comprendre les zones de désaccords.

Expérimentalement, la composante de photons issus de la fragmentation d'un parton présente dans les données diphoton sélectionnées est intimement liée au critère d'isolation appliqué aux photons. L'isolation des photons est absolument nécessaire pour réduire le bruit de fond provenant des processus γ -jet et jet-jet, dont les taux de production au LHC sont plus de 100 fois supérieurs à celui des processus $\gamma\gamma$. Contrairement aux photons directs, le bruit de fond provenant de jets comprend une intense activité hadronique autour des cellules calorimétriques les plus énergétiques. Pour séparer les jets des photons directs produits par le processus de Born ou de boîte, une coupure est appliquée sur l'énergie d'isolation transverse E_T^{iso} , définie comme la somme de l'énergie transverse déposée autour du candidat photon dans un cône de rayon fini R. Dans le cas des photons issus de la fragmentation d'un parton, lorsque l'angle entre le parton et le photon émis est petit, E_T^{iso} augmente. La coupure sur E_T^{iso} soustrait ainsi du signal une partie importante de la composante de fragmentation. Entre 2 et 5% de la fragmentation simple subsiste, tandis que la fragmentation double est presque totalement supprimée [ref14]. La comparaison entre sections efficaces mesurées et prédites n'a donc de sens que si la coupure sur l'énergie d'isolation est appliquée également au niveau des générateurs.

Deux principaux critères d'isolation sont utilisés dans les prédictions théoriques : l'isolation avec un cône, équivalente à l'isolation expérimentale, et l'isolation *Frixione* [ref17] qui supprime complètement les composantes de fragmentation. Pendant sa thèse, Maud a étudié dans le cadre d'un groupe de travail de l'école des Houches 2011 l'impact de l'utilisation du critère d'isolation *Frixione* sur la composante de fragmentation [ref18](pages 165-178).

La Figure 16 illustre la comparaison des sections efficaces différentielles diphoton mesurées avec les générateurs DIPHOX et 2γ NNLO. Un résultat très intéressant obtenu à l'issue de cette analyse est la confirmation de la présence de la *Guillet Shoulder* [ref14] autour de 50-60 GeV dans le spectre $P_T^{\gamma\gamma}$. Cette observation a été confirmée par l'analyse équivalente de CMS [ref19] en 2014. Ce pic, prédit par les calculs mais à peine visible dans les analyses plus anciennes par manque de statistique, est un effet cinématique indirect entièrement dû aux composantes de fragmentation [ref14].

La description complète de notre analyse des événements diphoton et les comparaisons des sections efficaces différentielles diphoton avec les générateurs ont été publiées [ref15] et sont présentées dans l'annexe C.

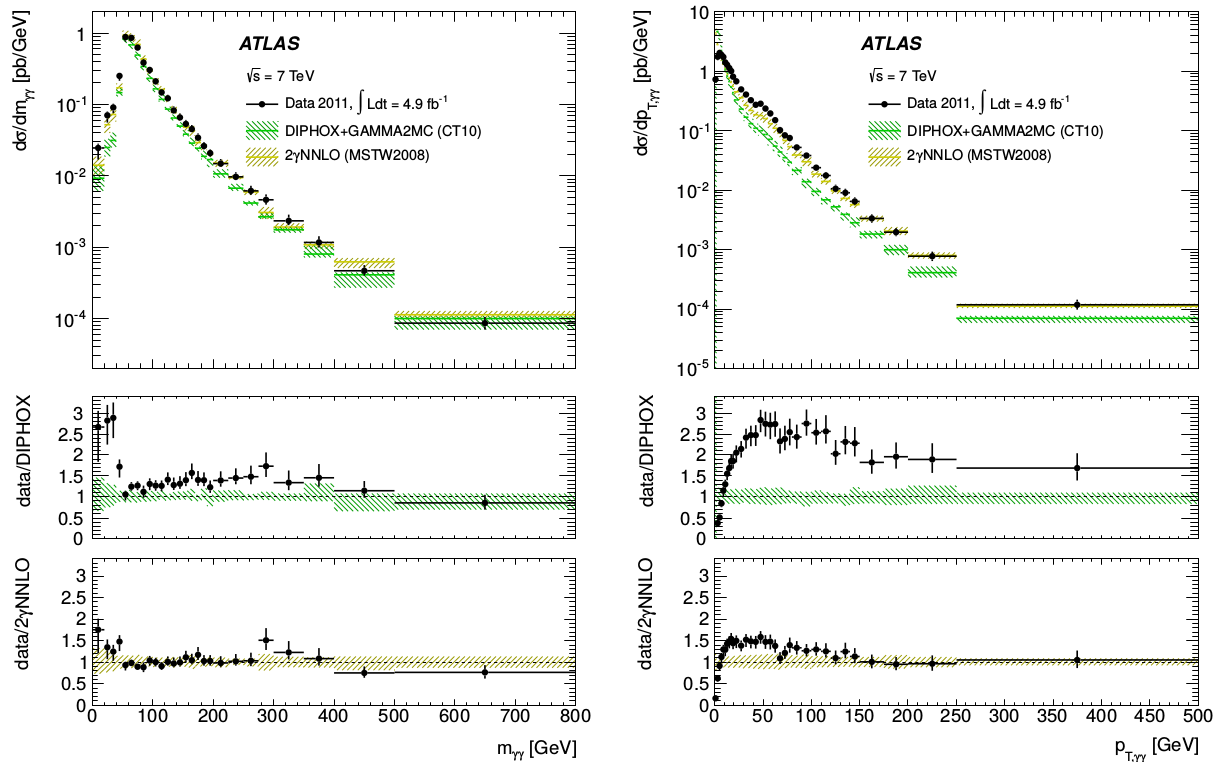


FIGURE 16 – Mesure de la section efficace différentielle diphoton et comparaison avec les générateurs DIPHOX et 2γ NNLO.

2.2 Mesure des couplages du boson de Higgs et mise en évidence du mode VBF

Passée l'excitation de découverte d'une nouvelle résonance au LHC[pub6], présentée en annexe D, la question de la confirmation de la nature standard de cette nouvelle particule s'est rapidement posée. De nombreuses études ont été entreprises pour mesurer l'ensemble des caractéristiques de ce nouveau boson : largeur de désintégration, spin, mesure précise de sa masse, mise en évidence de tous les modes de production (Figure 17) et mesure des couplages du boson de Higgs aux particules du

modèle Standard. Pendant la thèse de Maud, nous nous sommes attelées à deux sujets : la mise en évidence de la production du boson de Higgs dans le mode VBF, et l'extraction de ses couplages [pub7]. La publication correspondante est proposée en annexe E.

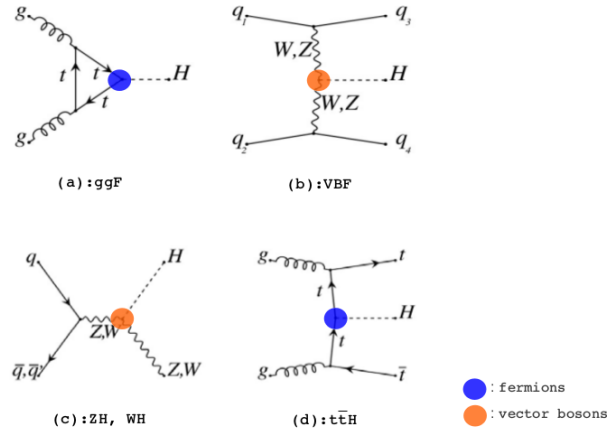


FIGURE 17 – Processus de production du boson de Higgs au LHC.

Les quatre modes de production dominants au LHC d'un boson de Higgs de 125 GeV sont la fusion de gluons ($ggF \approx 87\%$), la fusion de bosons vecteurs ($VBF \approx 7\%$), la production associée aux bosons W et Z ($VH \approx 5\%$) et la production associée à des quarks top ($ttH \approx 1\%$) (Figure 17). Dans le cas du processus de production VBF, le boson de Higgs est produit à partir de la fusion de bosons W ou Z, en association avec deux jets de grande énergie présentant une large séparation en pseudo-rapidité et un très petit angle de diffusion, ce qui rend ce canal facilement identifiable.

Pour maximiser la signification statistique et augmenter ainsi les chances de découverte du boson de Higgs, l'analyse initiale D sépare les événements diphoton en 9 catégories, selon la cinématique des photons (impulsion transverse, pseudo-rapidité) et la qualité des photons reconstruits (convertis, non convertis). Ceci permet de donner davantage de poids aux catégories les moins affectées par le bruit de fond et pour lesquelles la résolution sur la masse invariante diphoton reconstruite est la meilleure.

Après la découverte de la nouvelle résonance, l'objectif de l'analyse a changé. Il s'agissait désormais de mettre en évidence les différents modes de production de ce boson, et de tester ainsi sa compatibilité avec le boson de Higgs prédit par le Modèle Standard. De nouvelles catégories d'événements basées sur l'état final ont été ajoutées (jets additionnels, leptons, énergie manquante, Figure 18), et le canal VBF a été ré-optimisé pour minimiser les incertitudes statistiques et systématiques sur la mesure de la force du signal μ_{VBF} , défini comme le rapport entre le nombre de bosons de Higgs mesuré dans un canal de production donné et celui prédit par le Modèle Standard. La mesure du rapport μ_{VBF} présente la mesure sous forme d'une déviation par rapport aux prédictions du Modèle Standard, et nécessite de faire des hypothèses sur les sections efficaces et les rapports de branchement. Cette observable présente une forte sensibilité aux erreurs théoriques.

Minimiser l'erreur statistique sur μ_{VBF} impose de conserver une grande pureté de signal dans la catégorie associée. Pour réduire les incertitudes systématiques, le bras de levier principal est de limiter l'utilisation de variables basées sur l'énergie des jets. En effet, l'échelle de calibration des jets est en soi une source majeure d'incertitude systématique au LHC, et d'autre part, la description du spectre en P_T des jets issus de radiation dans les événements ggF simulés (qui constituent le bruit de fond principal de la catégorie VBF) est trop peu contrainte, ce qui génère d'importantes incertitudes sur la composition réelle du bruit de fond dans la catégorie VBF. Deux optimisations de l'analyse ont été menées en parallèle : l'une basée sur la définition de coupures simples, et l'autre basée sur l'utilisation

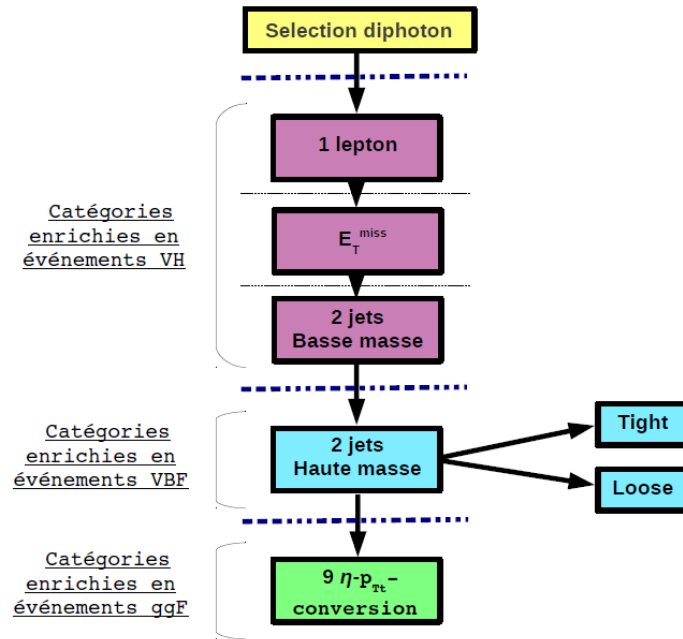


FIGURE 18 – Séquence des critères de sélections appliqués aux événements diphotons pour catégoriser les modes de production du boson de Higgs, en évitant le double-comptage.

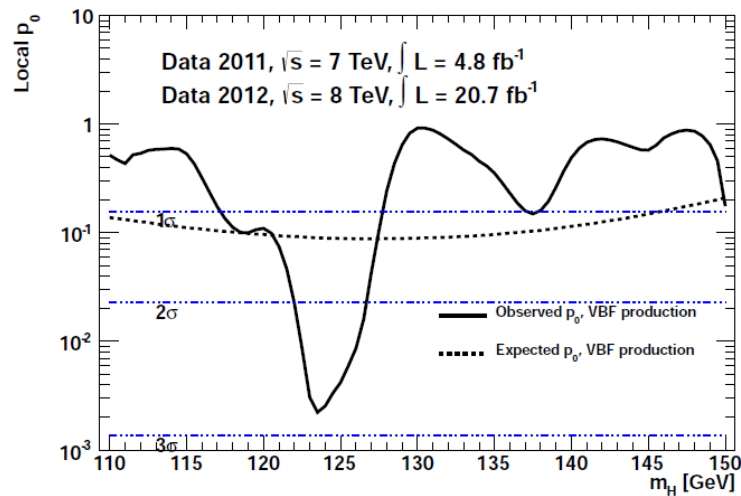


FIGURE 19 – p_0^{VBF} observée et attendue pour le mode de production VBF en fonction de la masse hypothétique du boson de Higgs pour 4.8 fb^{-1} de données à 7 TeV et 20.7 fb^{-1} de données à 8 TeV.

d’outils d’analyse multivariée. La Figure 19 montre la valeur p du paramètre μ_{VBF} extrait par Maud en 2014. La plus grande valeur p_0^{VBF} , soit 2.9σ pour $m_H = 123.5 \text{ GeV}$, s’interprète comme une probabilité inférieure à 99.6% pour que le nombre d’événements observé soit compatible avec l’absence du mode de production VBF. La Figure 20 présente l’ensemble des forces de signal extraites par Maud en 2014 en combinant l’information de l’ensemble des catégories simultanément. La “découverte” officielle du canal VBF à 6.5σ par une seule expérience a été annoncée durant la conférence ICHEP de juillet 2018 [ref20].

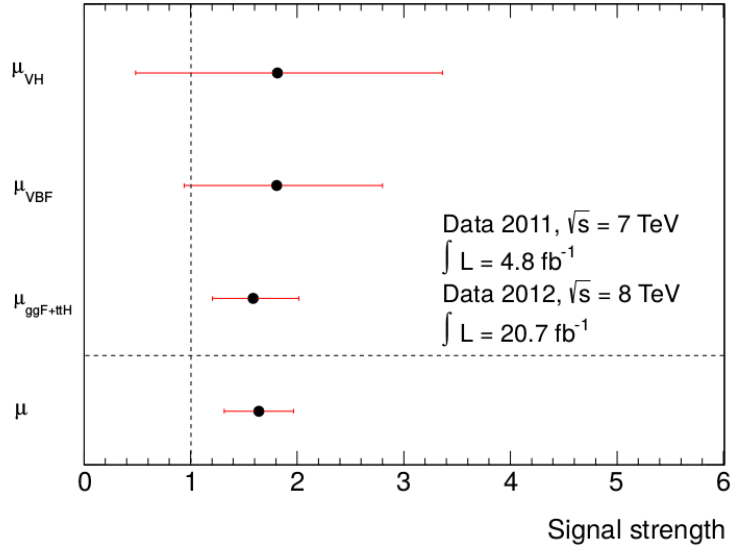


FIGURE 20 – Force du signal mesurée pour les modes de production, $\mu_{ggF+ttH}$, μ_{VBF} , μ_{VH} , et force du signal global μ pour 4.8 fb^{-1} de données à 7 TeV et 20.7 fb^{-1} de données à 8 TeV.

La première comparaison des taux de production du boson de Higgs par mode de production a pu fournir une première image relativement “standard” du boson nouvellement découvert au LHC, même si les incertitudes, largement dominées par la statistique, limitent grandement l’observation de potentielles déviations. La Figure 21 présente les mesures les plus récentes (ICHEP 2018, [ref20]) des sections efficaces multipliées par le rapport de branchement pour tous les les processus de production du boson de Higgs au LHC, dans tous les modes de désintégration accessibles dans ATLAS, et normalisés aux prédictions du Modèle Standard. L’ensemble des canaux restent compatibles avec l’hypothèse du Modèle Standard dans la limite des incertitudes systématiques et statistiques, déjà réduites d’un facteur 4 pour les modes dominants.

A partir des mesures de sections efficaces fois le rapport de branchement, il est possible de rechercher des déviations des couplages du boson de Higgs aux bosons et fermions du Modèle Standard en interprétant les résultats dans le cadre du κ framework [ref21]. Dans ce cadre, on introduit des corrections multiplicatives κ appliquées aux couplages du boson de Higgs :

$$\sigma_i.B_f = \kappa_i \sigma_i^{SM} \frac{\kappa_f^2 \Gamma_F^{SM}}{\kappa_H^2 \Gamma_H^{SM}}$$

Dans l’équation ci-dessus, i est le mode de production, f le mode de désintégration, σ_i^{SM} sont les sections efficaces prédites par le Modèle Standard et Γ_H^{SM} et Γ_f^{SM} sont respectivement les largeurs totale et partielle du boson de Higgs dans l’état final f . En supposant que le boson de Higgs ne se désintègre pas en particules non-standard et en l’absence de nouvelle physique dans les processus de boucles, il est possible d’extraire les facteurs correctifs κ appliqués aux couplages, présentés sur la Figure 22 [ref20] en fonction de la masse des particules du Modèle Standard.

La Figure 23 [ref22] montre les perspectives d’amélioration de la précision sur la mesure des couplages du boson de Higgs pour la future phase à haute-luminosité du LHC, qui sera discutée plus en détails dans le chapitre suivant. On peut constater que les performances déjà atteintes au Run 2 sont quasi-compétitives avec les projections pour les trois canaux principaux $\gamma\gamma$, ZZ et WW .

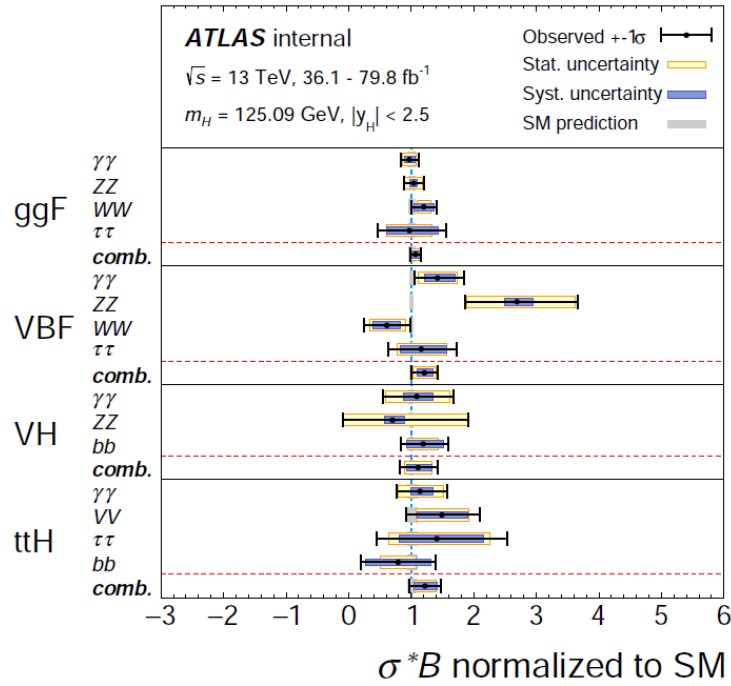


FIGURE 21 – Sections efficaces multipliées par le rapport de branchement pour les processus ggF, VBF, VH et ttH dans chaque mode de désintégration accessibles au LHC, normalisés aux prédictions du Modèle Standard. Les résultats combinés par mode de production sont également montrés, en supposant les valeurs du Modèle Standard pour les rapports de branchement. Source : ICHEP 2018 [ref20]

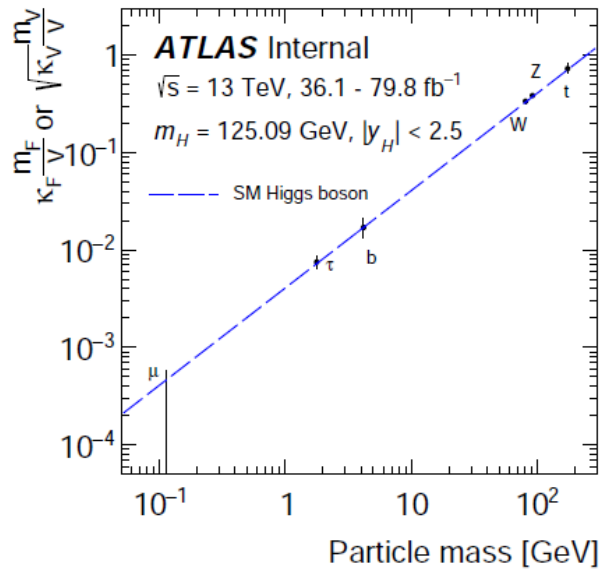


FIGURE 22 – Facteurs correctifs des couplages en fonction de la masse des particules, pour les bosons W, Z, les quarks t et b quarks et les leptons τ et muons.

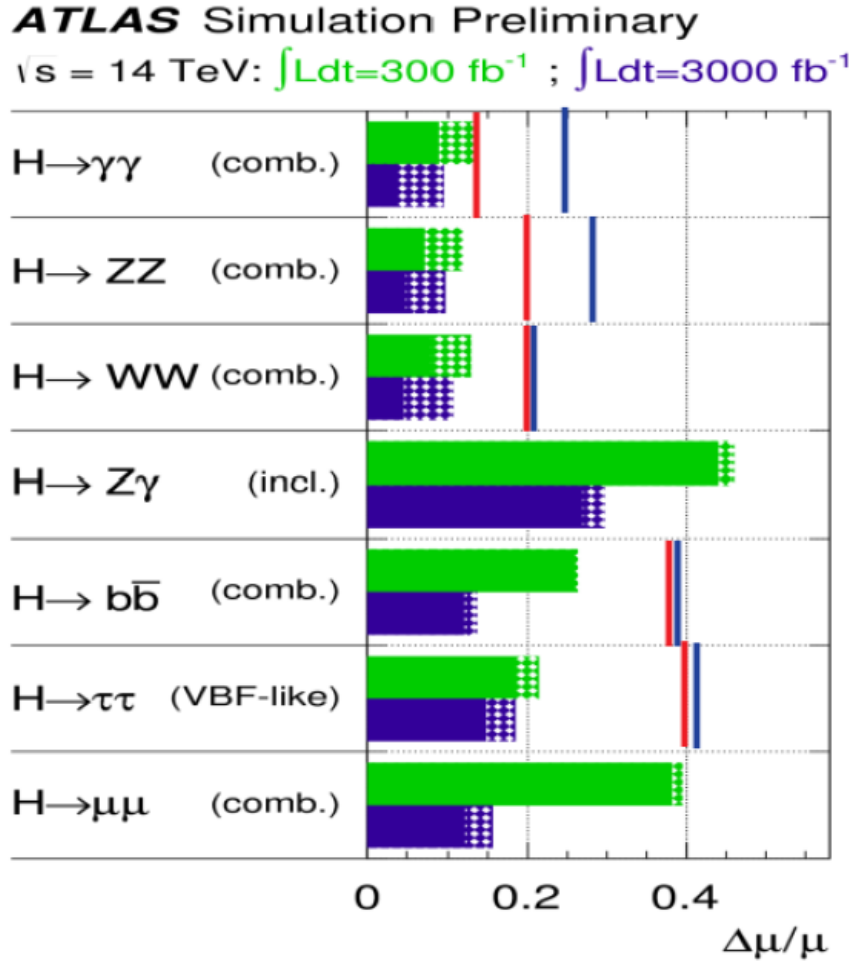


FIGURE 23 – Incertitudes relatives sur les forces de signal μ_i attendues au HL-LHC, basées sur les extrapolations des analyses du Run1 pour 300 fb^{-1} (vert) et 3000 fb^{-1} (bleu) de données à 14 TeV. La zone pleine correspond aux incertitudes statistiques, et les zones hachurées ajoutent la contribution dues aux incertitudes théoriques. Les lignes verticales bleu/rouge correspondent aux précisions publiées avec les données Run 1/Run 2. Pour les états finals $Z\gamma$ et $\mu\mu$, les valeurs Run1/Run2 sont en dehors des limites de l’histogramme.

2.3 Recherche de nouvelles résonances au-delà du Modèle Standard

Pour achever ce parcours au cœur de la physique des processus diphoton, et pour conjurer la désespérante absence de manifestations non-standards dans la mesure des caractéristiques du boson nouvellement découvert, il restait à réaliser une recherche directe de nouvelle physique dans le canal diphoton.

En 2013, avec le groupe photon du LAPP⁴, nous avons choisi de développer une toute nouvelle analyse du spectre inclusif $m_{\gamma\gamma}$, dans l'intervalle [65-600] GeV. La limite basse était en partie motivée par les recherches du LEP, qui suggéraient une possible accumulation d'événements compatibles avec un boson de Higgs de 98 GeV [ref23][ref24]. La limite haute est tout simplement imposée par la statistique disponible dans les données : au-delà de 600 GeV, le nombre d'événements diphoton n'est plus suffisant pour autoriser un ajustement des fonctions qui décrivent le bruit de fond avec une incertitude statistique acceptable. Le point amusant de cette analyse est que le boson de Higgs de 125 GeV nouvellement découvert est, peut-être pour la première fois, considéré non pas comme un signal, mais comme un bruit de fond (Figure 24).

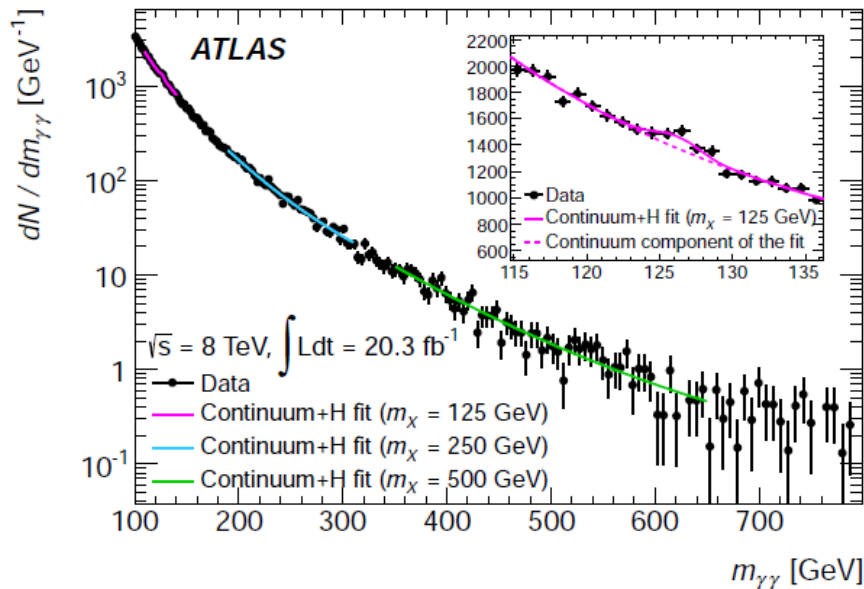


FIGURE 24 – Ajustement au spectre de masse $m_{\gamma\gamma}$ des fonctions décrivant le bruit de fond $\gamma\gamma$. Les lignes pleines montrent la somme des contributions du boson de Higgs et du bruit de fond continu. La ligne pointillée montre uniquement la composante continue.

De nombreux modèles au-delà du Modèle Standard prédisent des résonances diphoton additionnelles au-dessus ou en dessous de la masse du boson de Higgs (NMSSM, 2HDM,...). Nous avons cependant choisi de réaliser une analyse totalement indépendante des modèles théoriques, en définissant un espace de phase fiduciel le moins dépendant possible du mode de production de la particule se désintégrant en deux photons.

La Figure 25 [ref25] montre l'efficacité des coupures d'acceptance d'un boson scalaire, pour plusieurs points de masse et pour un ensemble de modes de production supposés couvrir toutes les configurations : production simple, production associée, avec énergie manquante, avec de nombreux jets dans l'état final. La seule dépendance dont il est difficile de s'affranchir est celle liée au boost des particules de faible masse dans le cas de productions associées. Les différences d'acceptance entre modes de production

4. Nicolas Berger, Rémi Lafaye, Elisabeth Petit, Marco Delmastro, Zuzana Barnovska

dans la région [60-110] GeV sont incluses dans la limite sur les sections efficaces observées sous forme d'incertitude systématique.

L'une des difficultés les plus intéressantes de l'analyse fût de réussir à comprendre la cinématique des événements issus de la désintégration du boson Z, lorsque la paire électron/positron est reconstruite comme des photons. Ces événements proviennent de processus de Bremsstrahlung extrêmes, dans lesquels la trace du lepton initial, de très faible impulsion, n'est pas reconstruite tandis que le photon emporte la quasi-totalité de l'énergie. Après correction angulaire, il est possible de décrire très précisément le pic de masse de ce bruit de fond dans le spectre de masse $m_{\gamma\gamma}$ (Figure 26).

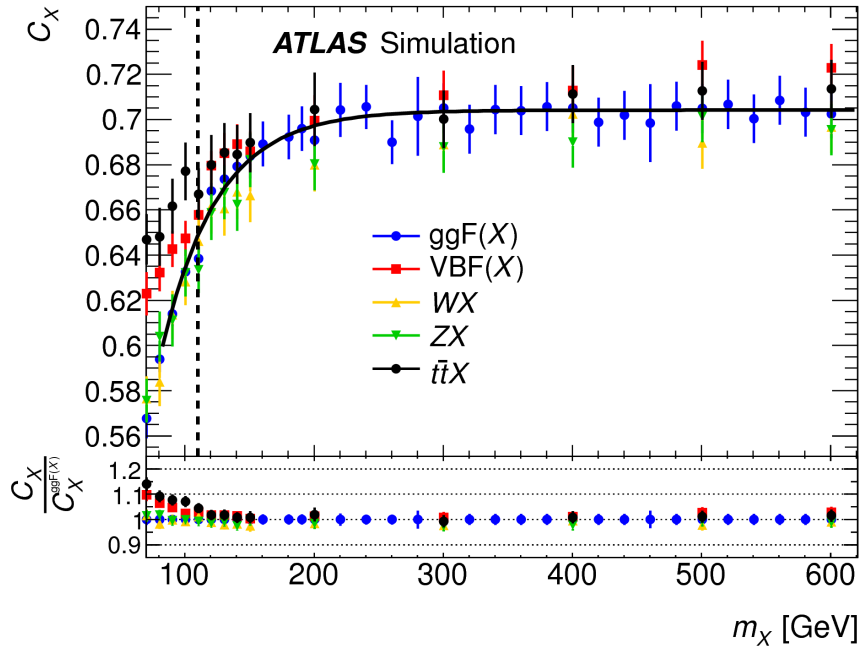


FIGURE 25 – Efficacité des coupures fiducielles C_X pour 5 modes de production d'une résonance scalaire de type "Higgs", en fonction de la masse m_X .

La description complète de l'analyse et la limite obtenue sur la section efficace fiducielle diphoton dans l'intervalle de masse [65-600] GeV sont présentées dans une publication jointe dans l'annexe F. Une routine RIVET⁵ a également été fournie aux théoriciens. A ce jour, la page *arxiv* de notre analyse⁶ recense plus d'une cinquantaine de publications utilisant nos mesures pour contraindre des modèles de nouvelle physique (Figure 27).

Les mises à jour les plus récentes de notre analyse ont permis d'étendre significativement la recherche dans le spectre à haute masse, au-delà du TeV, mais n'ont pas mis en évidence d'excès significatif [ref26]. Une mise à jour de l'analyse à basse masse est en cours de publication [ref27].

5. http://rivet.hepforge.org/analyses/ATLAS_2014_I1307756.html

6. <https://arxiv.org/abs/1407.6583>

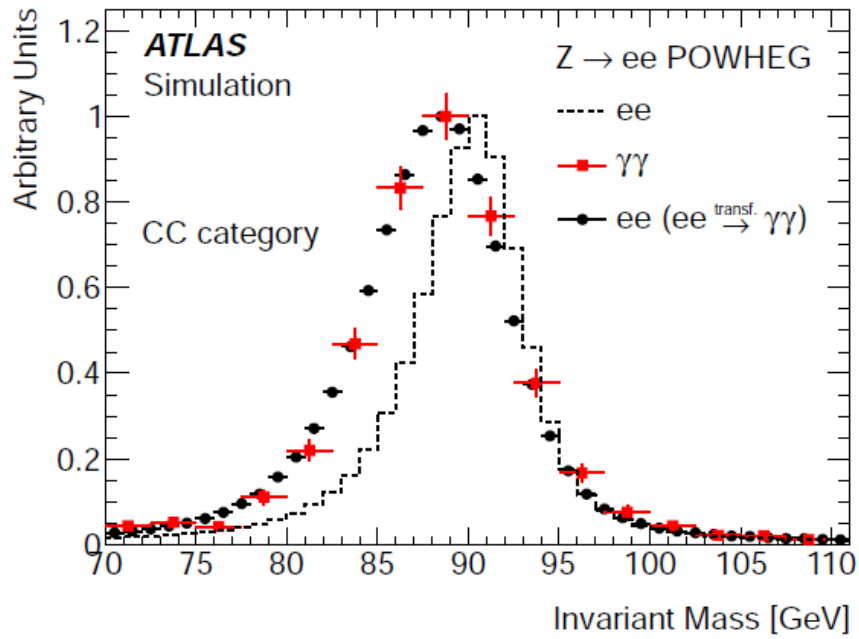


FIGURE 26 – Distribution de masse invariante d'événements Z générés en simulation complète, reconstruits comme une paire d'électrons (ligne pointillée), reconstruits comme une paire de photons (carrés) et reconstruits comme électrons mais après application d'une correction cinématique transformant les électrons en photons de Bremsstrahlung (cercles).



FIGURE 27 – SUSY ressurgissant d'une zone reculée de l'espace de phase $(m_{\tilde{g}}, m_{\tilde{\chi}_0})$.

3 R&D pour le HL-LHC

"Ils ne savaient pas que c'était impossible, alors ils l'ont fait" (Mark Twain).

3.1 Physique du Higgs au HL-LHC

La luminosité instantanée au HL-LHC sera augmentée d'un facteur 5 à 7 par rapport à la luminosité actuelle du LHC. L'une des motivations principales de cette augmentation de luminosité est l'exploration précise du mécanisme de brisure de la symétrie électrofaible dans le Modèle Standard au travers de processus rares.

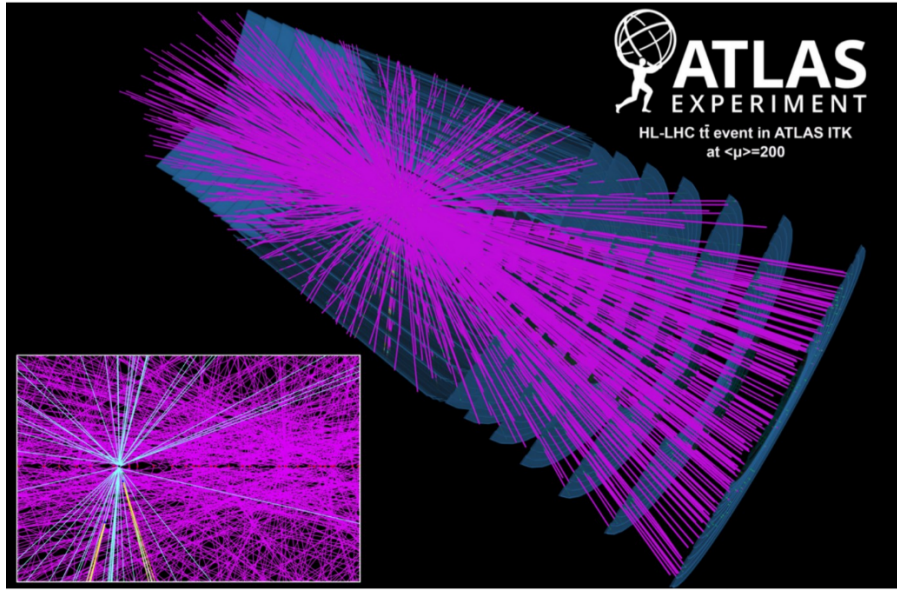


FIGURE 28 – Simulation d'une collision au HL-LHC reconstruite dans le détecteur ATLAS, avec 200 vertex provenant du bruit d'empilement.

Une première indication indirecte de déviation peut être recherchée au travers de la mesure de la section efficace des processus de diffusion de bosons vecteurs à haute masse ($m_{VV} > 1$ TeV [ref28]). Ces processus, sans la contribution virtuelle du boson de Higgs, ne vérifieraient pas la condition d'unitarité (Figure 29).

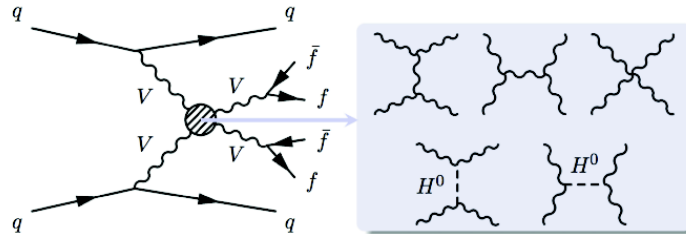


FIGURE 29 – Diagrammes de Feynman de diffusion de bosons vecteurs au HL-LHC.

Outre la mesure précise des couplages du boson de Higgs déjà évoqués au chapitre précédent, un autre objectif du programme HL-LHC est la mise en évidence du couplage direct aux leptons de

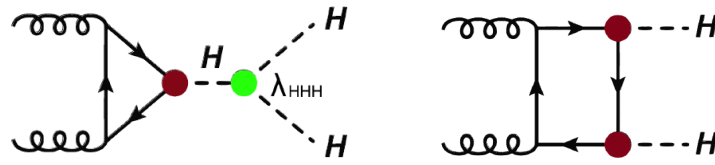


FIGURE 30 – Production des paires de boson de Higgs au HL-LHC. Les deux diagrammes interfèrent de manière destructive.

deuxième génération, accessible au HL-LHC via le canal $H \rightarrow \mu\mu$ [ref28]. Enfin, il reste encore à observer la très rare production d'une paire de boson de Higgs prédite par le Modèle Standard. Ce dernier processus donne accès à l'auto-couplage trilinéaire λ_{HHH} du boson de Higgs [ref29]. Les deux diagrammes présentés sur la Figure 30 [ref30] interfèrent de façon destructive. La valeur de λ_{HHH} peut s'extraire à partir de la mesure de la section efficace totale du processus HH et la forme de la distribution m_{HH} .

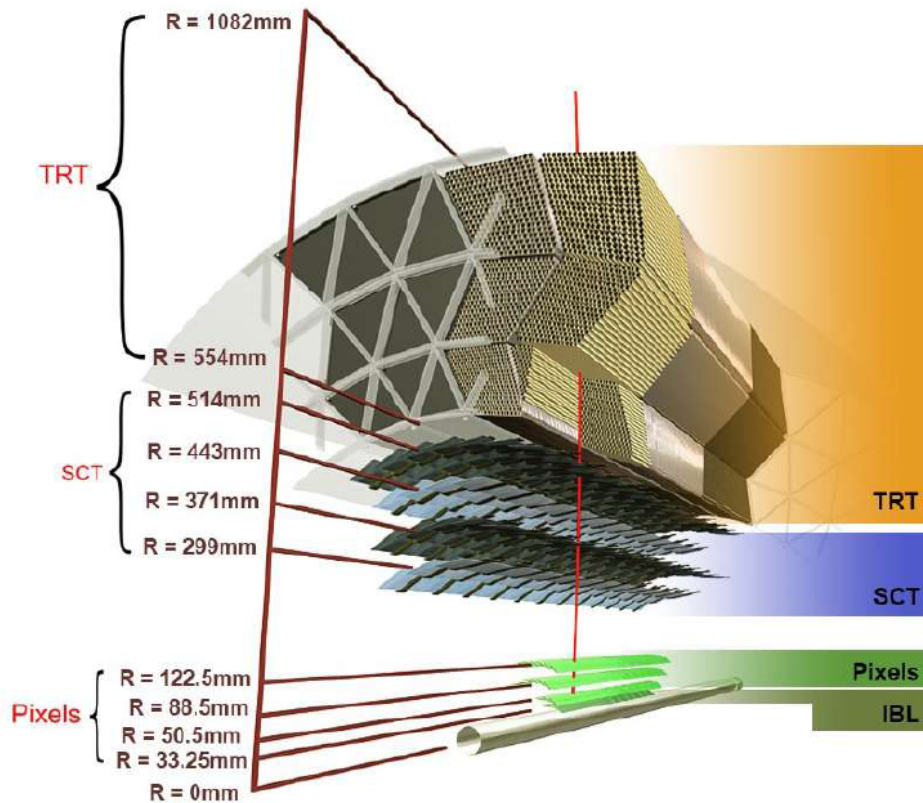


FIGURE 31 – Vue en coupe du trajectographe actuel d'ATLAS.

Dans les conditions de bruit d'empilement attendues au HL-LHC, la réalisation de ce programme de physique ambitieux nécessitera la construction d'un trajectographe de très haute performance pour reconstruire les vertex primaires, identifier les jets de saveur lourde, et atteindre une résolution suffisante sur l'impulsion des traces de haute énergie pour reconstruire précisément le pic de masse du boson de Higgs se désintégrant en deux muons.

Le trajectographe actuel d'ATLAS (Figure 31 [ref31]) se compose de deux sous-détecteurs en silicium (pixels et microstrips), et d'un trajectographe à radiation de transition (TRT) dans sa partie la

plus externe. Ce détecteur a été conçu pour fonctionner 10 ans avec un pic de luminosité instantanée de $10^{34} \text{ cm}^2\text{s}^{-1}$, un bruit d'empilement moyen supposé de 23 événements de pile-up toutes les 25 ns et un taux d'acquisition de 100 kHz. Même s'il fonctionne aujourd'hui dans des conditions bien plus difficiles que prévues initialement, les modules de silicium ne survivront pas au-delà de 2024, date à laquelle il devrait avoir atteint la dose de radiation maximale⁷, qui correspond à environ 400 fb^{-1} de luminosité intégrée. La couche de pixels la plus interne (*Insertable B-Layer* [ref32]), ajoutée en 2014, devrait théoriquement pouvoir supporter jusqu'à 850 fb^{-1} , mais la granularité des pixels et l'électronique de lecture ne seront de toute façon plus suffisantes face aux taux d'acquisition de données et aux taux d'occupation attendus au HL-LHC.

Le détecteur ATLAS sera donc équipé d'un nouveau trajectographe (ITk) pour la phase à haute luminosité, utilisant la totalité du volume du tracker actuel mais entièrement composé de modules de silicium : pixels dans la partie internes et strips à grand rayon. Ce nouveau trajectographe sera installé pendant le dernier long arrêt technique du LHC, de 2024 à 2026.

Dans le chapitre suivant, nous allons nous intéresser plus particulièrement à la conception détecteur à pixels ITk, le plus critique pour la trajectographie de haute précision au HL-LHC. Les détails concernant les strips peuvent être consultés dans le TDR ITk Strip publié en 2017 [pub8].

3.2 Détecteur à pixels ITk : de la conception à la réalisation

Pour optimiser la géométrie du détecteur à pixels, il faut garder en ligne de mire les objectifs du tracking : mesurer le plus précisément possible l'impulsion transverse des particules chargées, reconstruire efficacement les vertex primaires et secondaires, et séparer sans ambiguïté des traces proches pour identifier les conversions de photon ou supprimer le bruit d'empilement. Dans cette section, les notions de base utiles à l'optimisation d'un détecteur de traces seront rappelées, et un design novateur s'approchant au mieux d'un détecteur idéal sera présenté.

3.2.1 Optimisation de la géométrie

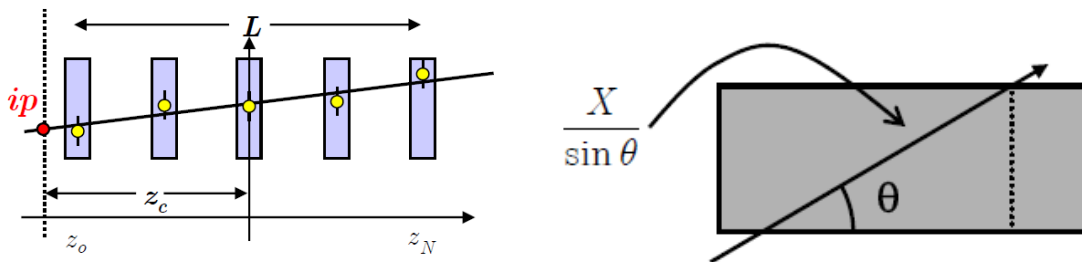


FIGURE 32 – Illustration des paramètres déterminant la précision sur la mesure de l'impulsion et du paramètre d'impact longitudinal des traces chargées dans le détecteur à pixels.

L'impulsion d'une particule chargée est estimée à partir de la courbure de sa trajectoire dans le champ magnétique [ref33]. A bas P_T , la résolution sur l'impulsion transverse est dominée par un terme de diffusion élastique constant, proportionnel à la quantité de matière traversée par les particules. Ce terme de diffusion élastique dépend de la longueur de radiation (X_0) du matériau traversé et de l'angle d'incidence de la particule. Pour les grandes impulsions, la résolution est inversement proportionnelle au bras de levier L et au nombre de points de mesures (Figure 32). On peut montrer [ref33] que l'optimal

7. $1015 \text{ neq.cm}^2 - 1 \text{ MeV}$ neutron équivalent par centimètre carré

de résolution est obtenu pour des points de mesures équidistants, groupés au début, au milieu et à la fin de la trace (communément appelés *tracklets*).

Le second paramètre critique est le paramètre d'impact de la trajectoire. Pour des particules de grande impulsion [ref34], la résolution sur le paramètre d'impact transverse dépend de la résolution intrinsèque du détecteur à pixels, soit $p/\sqrt{12}$ où p est la taille des pixels dans le plan $r-\phi$, ainsi que de la distance entre deux points de mesure successifs (Figure 32). Pour les particules de faible impulsion, la résolution est dominée par le terme de diffusion élastique.

Le détecteur à pixels idéal doit donc proposer des points de mesures multiples, si possibles équidistants et proches les uns des autres. Le premier point de mesure doit se trouver le plus près possible du point d'interaction, et le dernier point de la trajectoire devra se trouver au plus grand rayon accessible pour maximiser le trajet de la particule dans le champ magnétique. La granularité des pixels doit être la plus petite possible, en particulier pour les deux premiers points de mesure. Enfin, la quantité de matière traversée par les particules doit être minimisée, en particulier à l'avant du détecteur, zone la plus sensible aux traces de faible impulsion issues du bruit d'empilement.

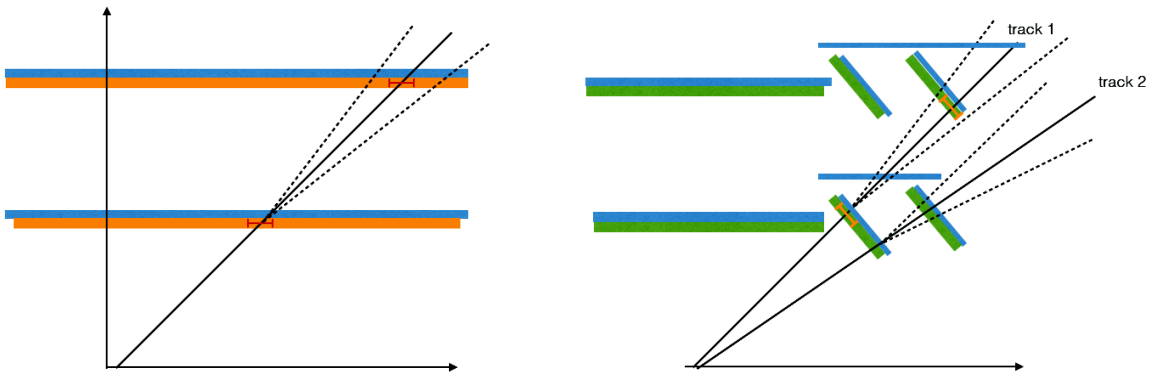


FIGURE 33 – Optimisation du détecteur à pixels basée sur l'utilisation de modules inclinés à la place d'un design classique de type tonneau/bouchon : réduction de la surface totale de silicium pour une même couverture angulaire, réduction de la distance d'extrapolation entre les points de mesures, multiples points de mesure par couche, réduction de la quantité de matière traversée grâce à l'angle d'incidence plus proche de la normale à la direction incidente des particules.

La Figure 33 compare la géométrie classique d'un détecteur à pixel avec un design idéal dans lequel les modules de silicium sont progressivement inclinés en fonction de la pseudo-rapacité. L'idée directrice du concept incliné est de minimiser la quantité de matière vue par les particules provenant du point d'interaction en s'approchant le plus possible de l'angle d'incidence normal. Autour de $|\eta|=2.5$, la quantité de matière vue par une particule est 2 fois plus faible dans la configuration inclinée par rapport à un détecteur classique. Le détecteur incliné présente de nombreux autres avantages :

- la surface totale de silicium requise pour une couverture angulaire similaire est jusqu'à 40% inférieure à celle d'un détecteur classique. Un module incliné couvre un angle solide plus important qu'un module horizontal, pour une même surface de silicium.
- le concept incliné fournit plusieurs points de mesures par couche, ce qui autorise la reconstruction de *tracklets* indépendantes qui peuvent ensuite être associées pour limiter la statistique combinatoire et le taux de fausses traces.
- la distance entre les points de mesure des différentes couches est réduite par rapport à un détecteur classique.
- le nombre moyen de pixels touchés est plus faible pour les modules inclinés que pour le design

classique, en particulier à grand pseudo-rapacité, ce qui améliore la résolution spatiale des points de mesure et la capacité de séparation des traces proches dans la région avant où le bruit d'empilement devient problématique pour l'identification des jets.

Dans les sections suivantes, nous allons voir comment passer du concept de détecteur idéal à la réalisation technique d'un détecteur ITk réaliste.

3.2.2 Contraintes techniques

Le cahier des charges complet du détecteur à pixels ITk peut être consulté dans le Technical Design Report publié en 2017 [pub9]. Nous ne discuterons ici que les paramètres les plus pertinents pour la conception du support mécanique du détecteur à pixels et des services électriques associés. Ces deux axes de développements techniques ont bénéficié d'un apport crucial du groupe ITk du LAPP, fondé par Teodore Teodorov au LAPP en 2011 et dont j'ai repris la coordination en Novembre 2014⁸.

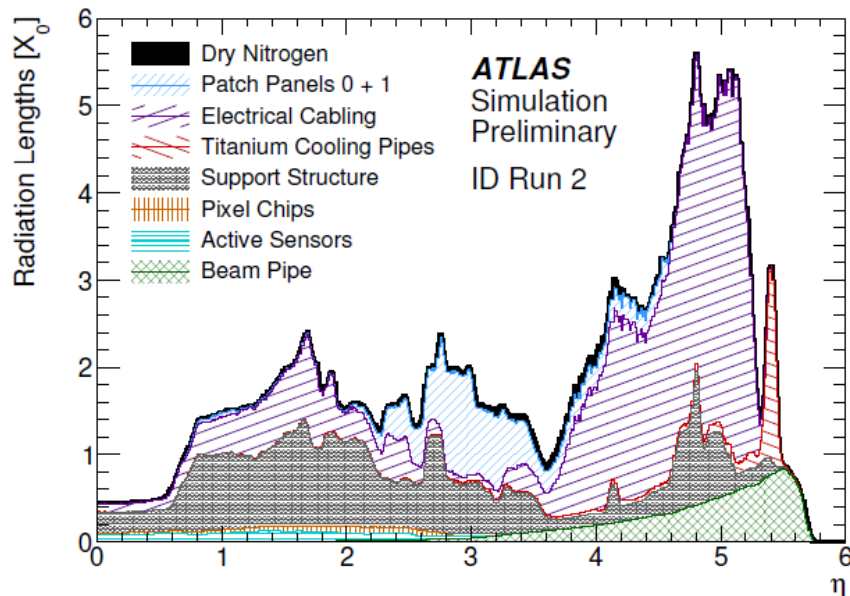


FIGURE 34 – Longueur de radiation totale dans le détecteur à pixels actuel d'ATLAS (Run 2).

Les services représentent la composante dominante de la matière inerte dans le détecteur à pixels, comme illustré sur la Figure 34. Parvenir aux performances requises pour le détecteur ITk implique de réduire le budget matière d'un facteur 2 par rapport au détecteur actuel. Pour y parvenir, il faut pouvoir construire des structures mécaniques légères sans compromettre la rigidité mécanique, réduire la quantité de services électriques, et minimiser la quantité de matière nécessaire au refroidissement des modules (tubes de refroidissement et liquide réfrigérant).

Structure mécanique : plusieurs structures ont été développées pour le détecteur ITk et sont présentées sur la Figure 35. Le point commun de toutes ces propositions est une base de fibre et/ou de mousse carbone. Ce matériau déjà utilisé pour la conception de l'IBL présente trois caractéristiques idéales pour la construction du détecteur à pixels : c'est un matériau peu dense, qui permet la réalisa-

8. <https://forum.camptocamp.org/t/chute-tragique-dimanche-18-octobre-dans-lascension-du-gouter-temoignage/148026>

tion de structure mécaniques complexes et très rigides, avec une conduction thermique suffisante pour évacuer la puissance dissipée par les modules.

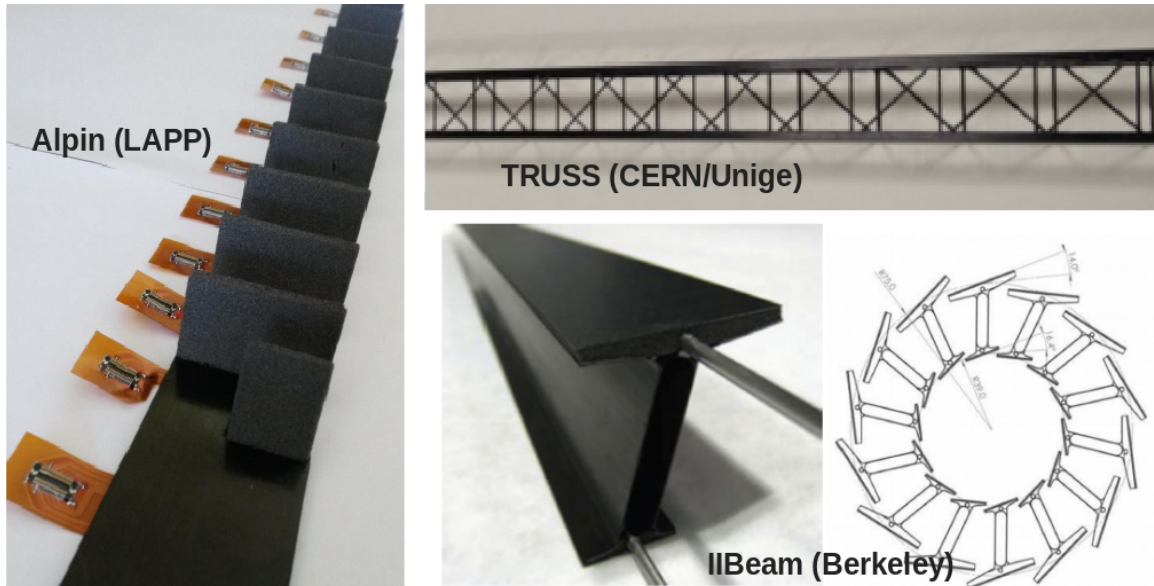


FIGURE 35 – Exemples de structures mécaniques en carbone proposées pour le détecteur à pixels ITk : Ibeam, Truss, et Alpin.

Alimentation des modules : un effort important est fourni aujourd’hui par la communauté ITk pour réduire le nombre de câbles nécessaires à l’alimentation du détecteur et améliorer la modularité de ces câbles pour autoriser une répartition plus uniforme et moins dense des services. Plusieurs pistes sont suivies, comme l’utilisation d’alimentations haute-tension plus puissantes, le développement d’une électronique front-end consommant le moins de courant possible et une alimentation des modules en série, qui a l’avantage de limiter le nombre de lignes mais implique l’ajout de composants spécifiques sur chaque module pour éviter une rupture de la chaîne d’alimentation.

Transmission des données : la totalité du détecteur à pixels ITk devra être lue au niveau L0 du système de déclenchement, à une fréquence de 500 kHz. Le taux de transmission de données attendu pour des modules de 4 chips est de 5 Gb.s^{-1} dans les couches les plus internes, et de 1.25 Gb.s^{-1} pour les couches externes. Plusieurs solutions concurrentes sont à l’étude pour la transmission des données : des câbles micro-twinaxes, dont l’efficacité de transmission sans atténuation majeure est très élevée, mais dont le budget matière est relativement pénalisant pour la physique, et des circuits flexibles qui ont un coût en matière plus acceptable mais dont les performances de transmission sur de longues distances restent à démontrer.

Refroidissement des modules : la réduction de la matière liée aux services concerne aussi la contrainte de refroidissement des modules. En plus de la dissipation de chaleur normale de l’électronique de lecture, les radiations endommagent progressivement les senseurs, provoquant ainsi une augmentation du courant de fuite dans l’électronique front-end. A terme, ce processus amène un phénomène d’emballement appelé “thermal runaway” [ref35], qui rend l’électronique inutilisable. Pour garantir la stabilité de l’électronique de lecture ITk en fin de vie, il faut refroidir la surface des modules pixels à une température inférieure à -20°C . Le choix d’un système de refroidissement utilisant du CO_2 dipha-

sique, déjà validé pour le détecteur IBL [], permet d'atteindre des températures très basses avec une quantité de fluide bien moindre que pour les réfrigérants classiques et une perte de charge le long des tubes significativement plus faible (Figure 36).

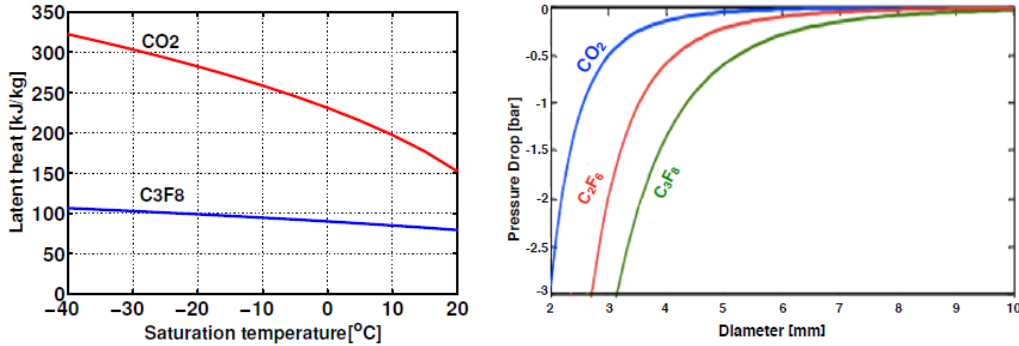


FIGURE 36 – Comparaison de la chaleur latente (gauche) et de la perte de pression le long du tube de refroidissement (droite) pour du CO2 diphasique, utilisés dans IBL, et le C3F8, utilisé dans les pixels d'ATLAS.

3.2.3 Le design Alpin

Pour réaliser une combinaison optimale des performance de tracking et des contraintes techniques, Teodore Todorov a proposé en 2012 un concept de détecteur novateur, comprenant des modules inclinés disposés sur des petites montagnes en mousse carbone, baptisé design *alpin* en hommage aux montagnes qu'il affectionnait tant. La structure globale du détecteur alpin dans sa version initiale, comprenant 3 couches de modules pixels pour une couverture angulaire $\eta < 2.5$.

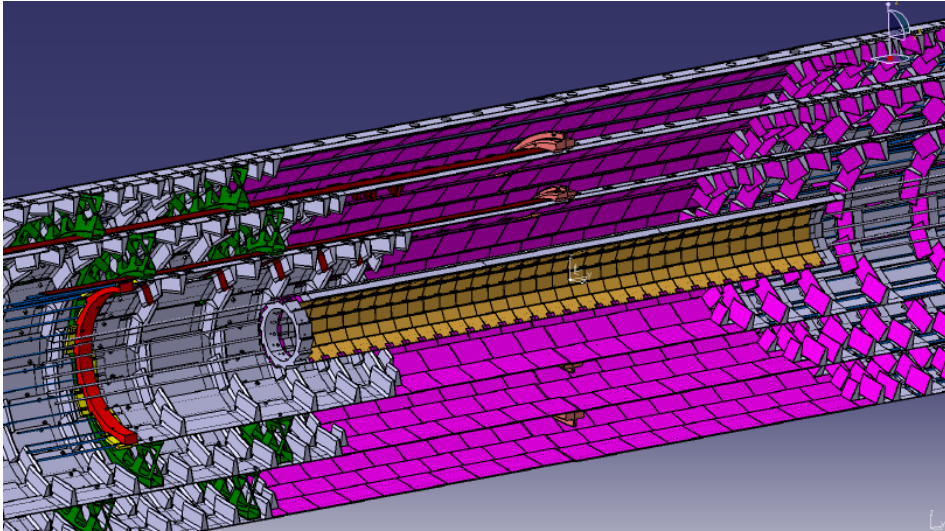


FIGURE 37 – Géométrie du détecteur alpin dans sa version $|\eta| < 2.5$

Le détecteur alpin est conçu à partir de cylindres d'échelles en mousse carbone, comportant à la fois des modules horizontaux sur la partie la plus centrale et des modules inclinés au-delà de $|\eta| > 1.1$. L'avantage d'une structure composée uniquement de supports horizontaux au lieu de l'agencement

classique des modules en cylindres et disques est de permettre de faire passer la totalité des services électriques en dehors de la zone d'acceptance du tracking (Figure 38).

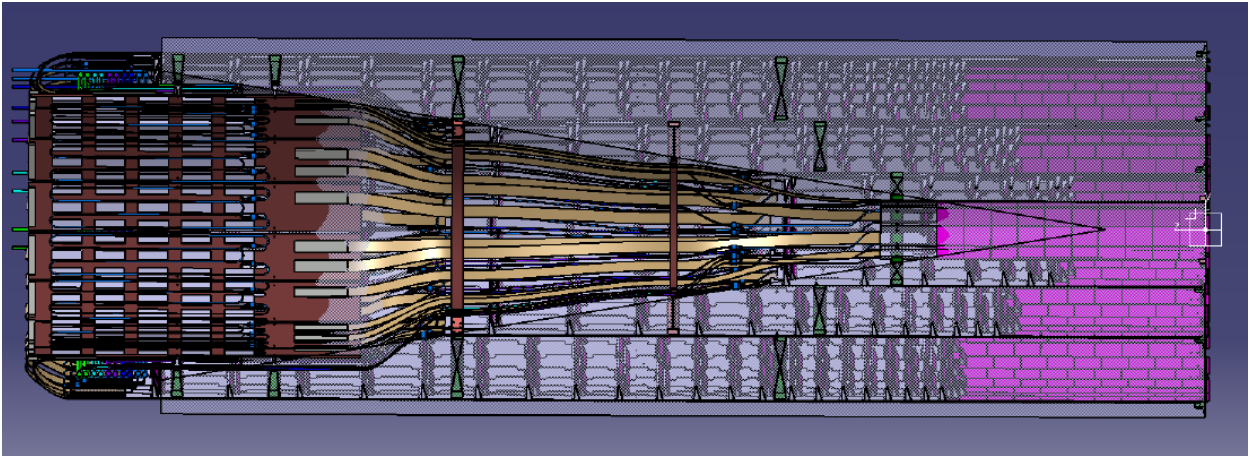


FIGURE 38 – Routage des services électriques dans le détecteur Alpin. Aucun câble ne se trouve dans l'acceptance du tracking $|\eta| < 2.5$

Les équipes techniques du LAPP ont conçu, optimisé, construit et qualifié pendant plus de 5 ans des prototypes mécaniques et électriques pour le détecteur alpin. Le LAPP a ainsi pu démontrer très tôt à la collaboration ITk la faisabilité du concept incliné. La rigidité mécanique obtenue avec des brides et des échelles carbone (Figure 41) satisfait aux spécifications, et les services électriques ont été qualifiés pour l'alimentation en série des modules et la transmission des données jusqu'à 5 Gb.s^{-1} [ref36]. Le LAPP a également démontré que le refroidissement des modules inclinés au travers de la structure carbone [ref37] est suffisant pour permettre leur fonctionnement dans les conditions du HL-LHC. Les études thermiques des structures inclinées seront abordées plus en détails dans la section 3.5.

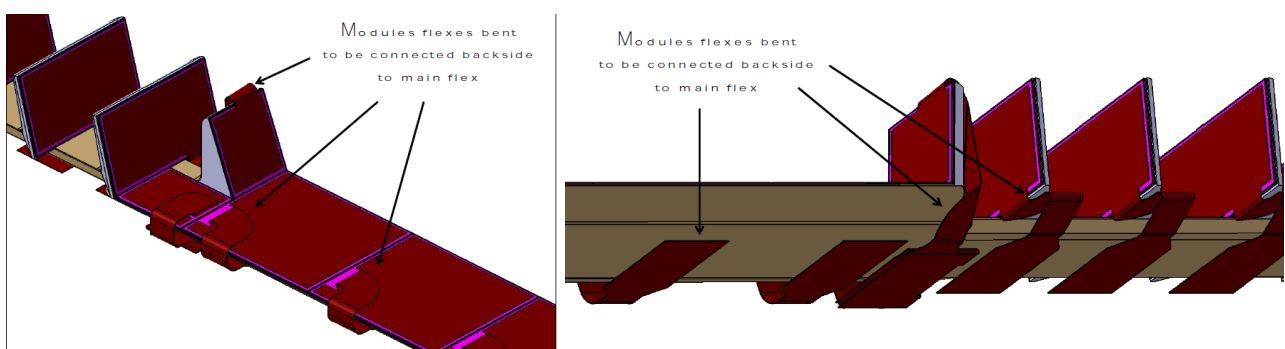


FIGURE 39 – Design des pigtaills pour la lecture des modules pixels sur l'échelle Alpine. Les pigtaills sont équipées de connecteurs miniaturisés, connectables sur les circuits flexes situé à l'arrière de la structure.

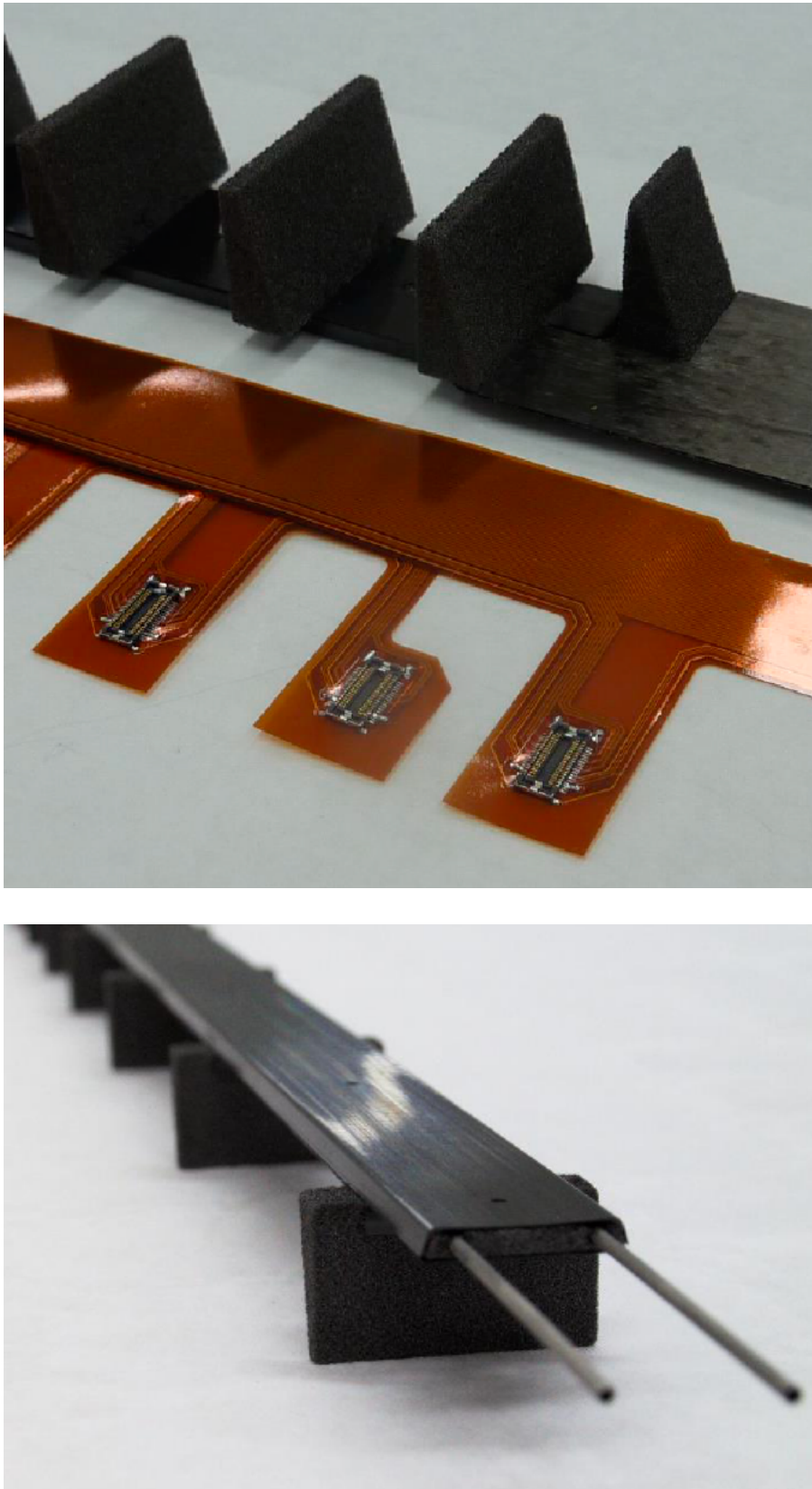


FIGURE 40 – Le détecteur alpin, de la conception à la réalisation : structure en mousse carbone incluant les tubes de refroidissement en titane, et services électriques sur circuits flexes équipés de connecteurs.

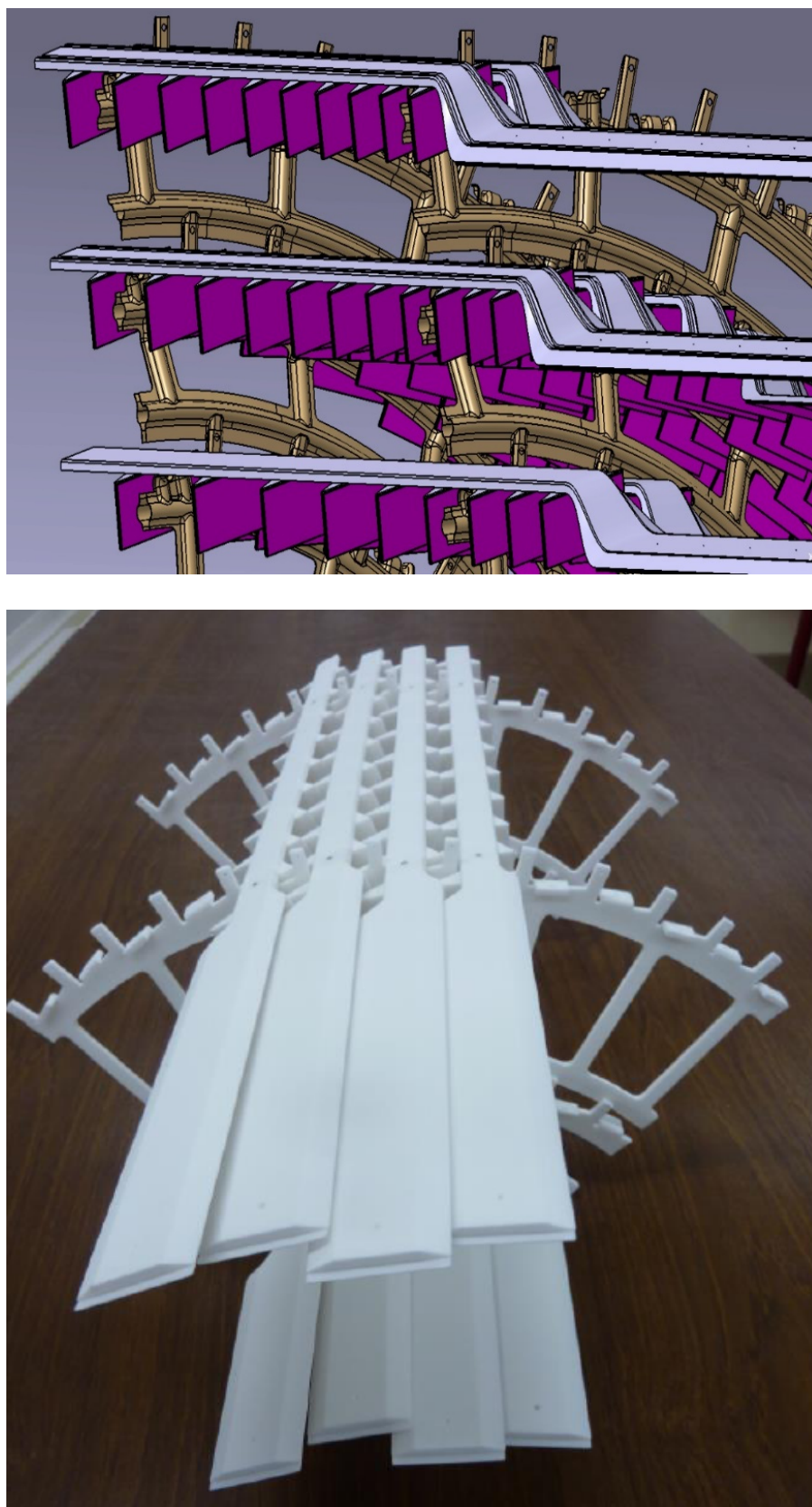


FIGURE 41 – Modèle CATIA des brides de support des échelles alpines et modèle d'intégration des échelles réalisé en impression 3D

3.3 Simulation ITk

La première version officielle du détecteur à pixel ITk est présentée dans la *Letter Of Intent (LoI)* d'ATLAS [ref38] publiée en 2012. La base de référence est une géométrie classique composée de cylindres dans la région centrale ($|\eta| < 1.5$) et de disques dans la région avant ($1.5 < |\eta| < 2.5$). Ce détecteur comprend 4 couches de pixels de rayon maximal $R < 250$ mm et 5 couches de strips qui couvrent les rayons supérieurs jusqu'à $R = 1200$ mm. L'ajout d'une cinquième couche de pixels est envisagée et il y est fait mention du concept alpin proposé par Teodore Teodorov.

Lors du workshop ECFA de 2013 [ref39], une étude présentée par la collaboration CMS fait grand bruit en proposant d'étendre la couverture du tracker au HL-LHC jusqu'à $|\eta| = 4$. Cette proposition est motivée par l'étude des processus de fusion de bosons vecteurs (VBF) et de diffusion de bosons vecteurs (VBS). Leur signature caractéristique est la présence de deux jets très à l'avant ($|\eta| \sim 3$) présentant une large séparation angulaire. Pour extraire du bruit de fond de pile-up ces jets produits en dehors de l'acceptance classique du tracker, et en l'absence d'une granularité calorimétrique suffisante, il faut augmenter les seuils de coupure sur l'impulsion transverse, ce qui a pour effet une dégradation rapide de l'efficacité de sélection du signal.

La Figure 42 présente les résultats de deux études réalisées par la collaboration CMS, qui montrent que l'extension de l'acceptance du détecteur de traces jusqu'à $|\eta| = 4$ pour les canaux VBS/VBF permettrait de supprimer la quasi-totalité de la contribution des jets de pile-up tout en conservant des seuils en P_T similaires à ceux appliqués au LHC. Pour le canal $H \rightarrow 4\mu$, l'acceptance du signal pourrait être améliorée de près de 50% [ref40].

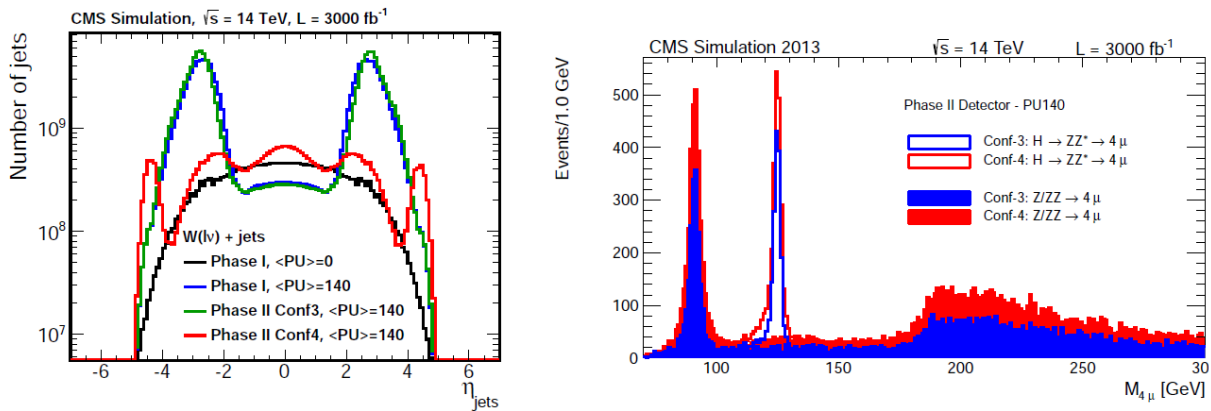


FIGURE 42 – Gauche : distribution de la pseudo-rapidité des jets de $p_T > 30$ GeV dans des événements W +jets simulés, pour différents scénarios de pile-up. L'extension de l'acceptance du trajectrographe au HL-LHC (scenario 4) diminue presque complètement la contribution du pile-up. Droite : distribution de masse invariante de 4 muons dans les canaux $H \rightarrow ZZ^* \rightarrow 4\mu$ et pour le bruit de fond irréductible $ZZ^* \rightarrow 4\mu$. Les deux processus sont simulés avec (scenario 4) et sans (scenario 3) l'extension du tracker jusqu'à $|\eta| < 4$.

Conséquemment, une *Large Eta Task Force* est créée dans ATLAS en 2014 pour déterminer la pertinence de la proposition d'extension du programme de physique du HL-LHC dans la région $2.5 < |\eta| < 4$. La conclusion principale de ces études [pub10] est que l'augmentation d'acceptance du tracking semble justifiée, mais les performances doivent être réévaluées en simulations complètes avec une implémentation plus réaliste des services pour déterminer la couverture angulaire optimale

L'*Initial Design Report* [ref41] et le *Scoping Document* [ref42] publiés en 2014 et 2015 mentionnent plusieurs nouvelles options pour le détecteur à pixels⁹ : une possibilité d'extension de la couverture du tracker jusqu'à $|\eta| = 3.2$ ou $|\eta| = 4.0$, une géométrie classique de type tonneau + disques (*LoI layout*), une géométrie inclinée (*Inclined layout*) et une géométrie basée sur un très long tonneau (*Extended layout*), dont le concept est illustré sur la figure 43.

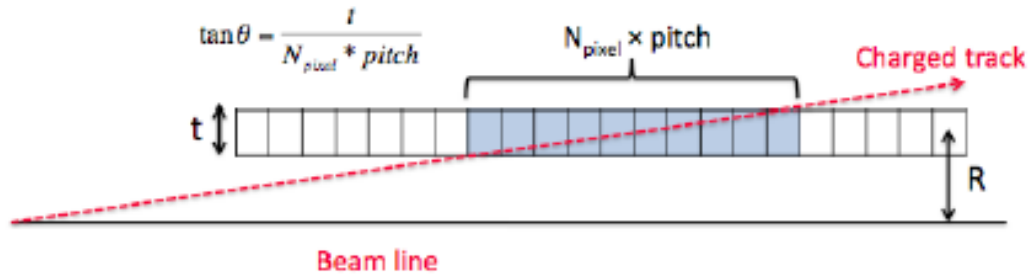


FIGURE 43 – Principe de fonctionnement du tracking *Extended* dans la région très à l'avant. L'angle d'incidence, reconstruit suffisamment précisément, pourrait permettre d'améliorer la résolution sur la position du vertex primaire et ainsi limiter l'effet du pile-up.

3.3.1 FastGeoModel et XML

Pendant la phase de prototypage et de développement des géométries ITk, le programme paramétrique IDRes [ref43] a servi de base pour l'évaluation rapide des résolutions sur les paramètres des traces, de l'herméticité du détecteur et du nombre de points de mesure en fonction de la pseudo-rapidité.

Ce programme est cependant insuffisant pour évaluer véritablement les performances du détecteur final. Il ne tient pas compte de la redondance des points de mesure due à la superposition des modules dans certaines régions, considère un effet moyenné de diffusion élastique avec une localisation approximative de la matière inerte du détecteur, la création de particules secondaires est inexistante et les dépôts d'énergie issus du pile-up ne peuvent pas être simulés. Ces effets ne peuvent être intégrés que dans le framework de simulation complète du détecteur.

Le programme de simulation complète d'ATLAS utilise une description géométrique basée sur des bibliothèques `GeoModel` [ref44]. Cette géométrie est ensuite convertie dans une géométrie `Geant4` [ref45] ou une géométrie de reconstruction, la `TrackingGeometry` [ref46] dans notre cas. En 2014, deux difficultés majeures empêchaient la collaboration ATLAS de réaliser les études en simulation complète qui auraient permis de choisir le meilleur détecteur ITk rapidement, et sans ambiguïté :

1. L'expertise technique nécessaire à l'implémentation d'un `GeoModel` pixel se trouvait dans les mains d'une seule et unique personne pour toute la collaboration ATLAS : Sabine Elles, ingénieure en informatique au LAPP. Son implication déjà très importante sur la simulation du détecteur IBL ne lui permettait pas de dégager suffisamment de temps pour développer et assurer le suivi d'un (ou plusieurs) `GeoModel` ITk.

2. Même en supposant que le `GeoModel` ITk soit disponible, les classes de `TrackingGeometry` existantes ne permettaient pas d'extrapoler les trajectoires dans les structures contenant des modules

9. <https://twiki.cern.ch/twiki/bin/view/Main/ITkGeometries>

inclinés. La Figure 44 montre que pour naviguer dans une couche pixel contenant des modules inclinés et extraire la liste des surface de tracking, il faut pouvoir déterminer à la fois le point d’entrée et le point de sortie, ce qui n’est pas prévu pour les classes de tracking classiques basées sur des cylindres ne contenant que des modules horizontaux. De nouvelles classes étaient en cours d’implémentation dans le framework Athena, mais toute la validation du tracking restait à faire.

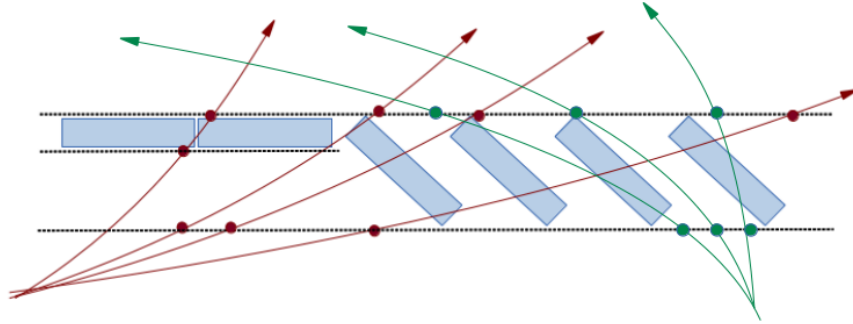


FIGURE 44 – Représentation schématique de la navigation dans une couche de pixels. Pour des modules horizontaux, le point d’entrée dans la couche de tracking est suffisamment proche du point de sortie pour permettre d’identifier de manière unique un module et son plus proche voisin. Dans le cas de modules inclinés, le nombre de surfaces actives touchées dépend de la distance parcourue et de l’angle de la trajectoire à l’entrée du volume de tracking.

Pour tenter de faire avancer les choses, le LAPP a proposé en 2014 que Sabine Elles réorganise entièrement le code C++ du `GeoModel` ITk Pixel en packages indépendants¹⁰. L’idée était de parvenir à encapsuler toutes les connaissances techniques de Sabine dans des “boîtes noires”, et de rendre ces boîtes configurables de façon suffisamment intuitive pour qu’un collaborateur non expert puisse facilement construire un `FastGeoModel` à partir de paramètres simples : nombre de couches, nombre de disques, rayons des cylindres, taille des modules pixels, pitch, inclinaison des modules, angle de tilt des échelles, matériaux (tubes de refroidissement, câbles, structure mécanique, etc..). L’objectif était de fournir à la collaboration un outil permettant de réaliser “rapidement” des études en simulation complète de plusieurs géométries en parallèle, et de pouvoir choisir ainsi objectivement la meilleure solution pour optimiser les performances de physique.

Rémi Lafaye et moi-même avons pris en charge l’écriture du package d’interface “physicien”, basé sur l’utilisation de fichiers XML¹¹ qui permettait deux choses : en premier lieu, construire la `TrackingGeometry` en s’affranchissant du `GeoModel`, et dans un second temps, utiliser ce même package pour configurer la construction du `FastGeoModel` associé, indispensable pour produire les cartes de matière précises utilisées par le tracking. L’imbrication de ces différents éléments est illustrée sur la Figure 45.

Concernant la validation, nous avons interfacé ces nouvelles géométries de tracking avec FATRAS [ref47], en étroite collaboration avec Andreas Salzburger (CERN) et Noemi Calace (Unige). La reconstruction des hits a été validée pour toutes les configurations de détecteurs possibles : LoI, Inclined, Extended, avec rings, avec disques, et même hybrides, comprenant à la fois des couches de modules inclinés et des couches cylindriques standard. La Figure 46 montre la reconstruction des hits dans FATRAS pour une configuration de détecteur incliné. La Figure 47 montre les visualisations de la `TrackingGeometry` avec le logiciel VP1 [ref48], et la Figure 48 présente des vues 3D des `FastGeoModel` configurables de Sabine Elles.

10. <https://twiki.cern.ch/twiki/bin/view/Sandbox/FastGeoModelGeometryImplementationGuide>

11. <https://twiki.cern.ch/twiki/bin/view/Sandbox/CustomGeometryImplementationGuide>

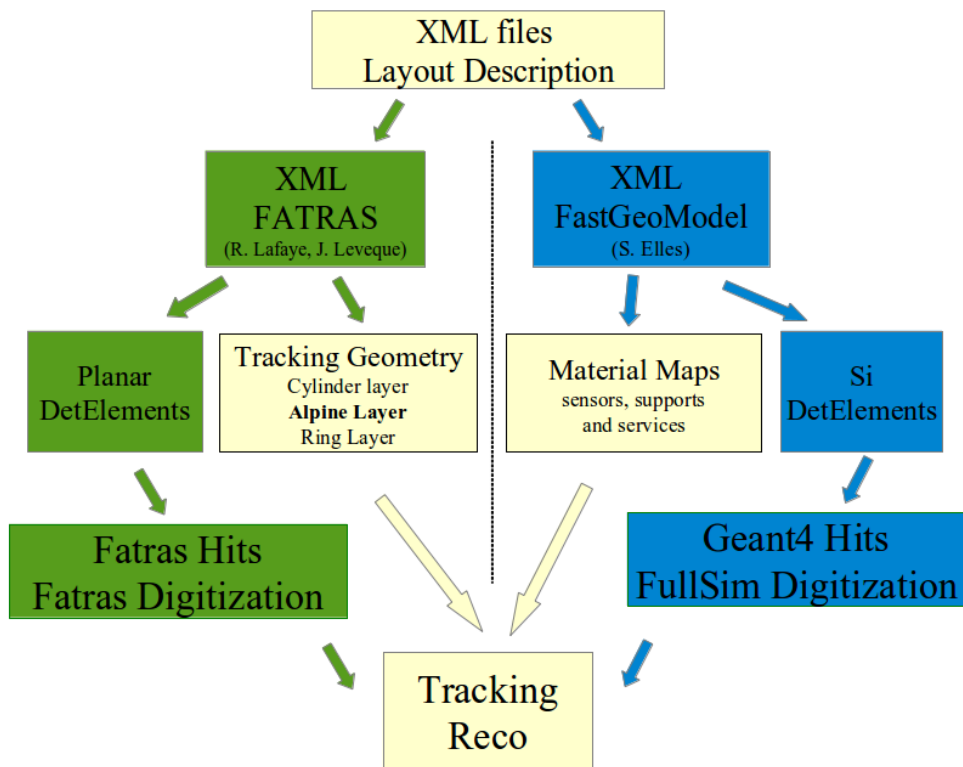


FIGURE 45 – Contributions du LAPP pour permettre une construction rapide de géométries ITk configurables via des fichiers XML.

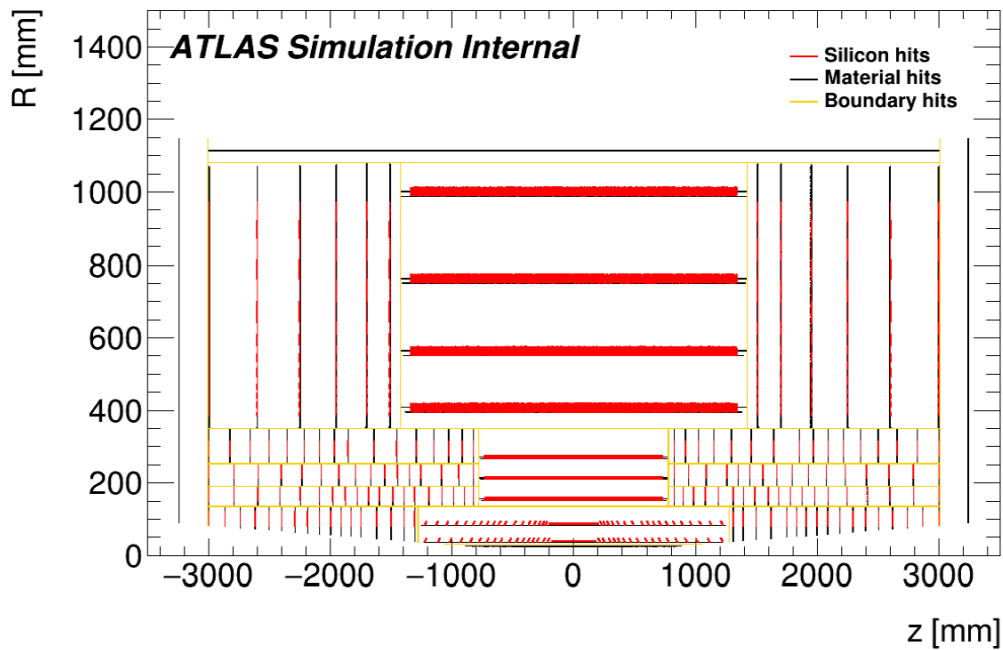


FIGURE 46 – Simulation des hits et validation de la géométrie de tracking dans FATRAS.

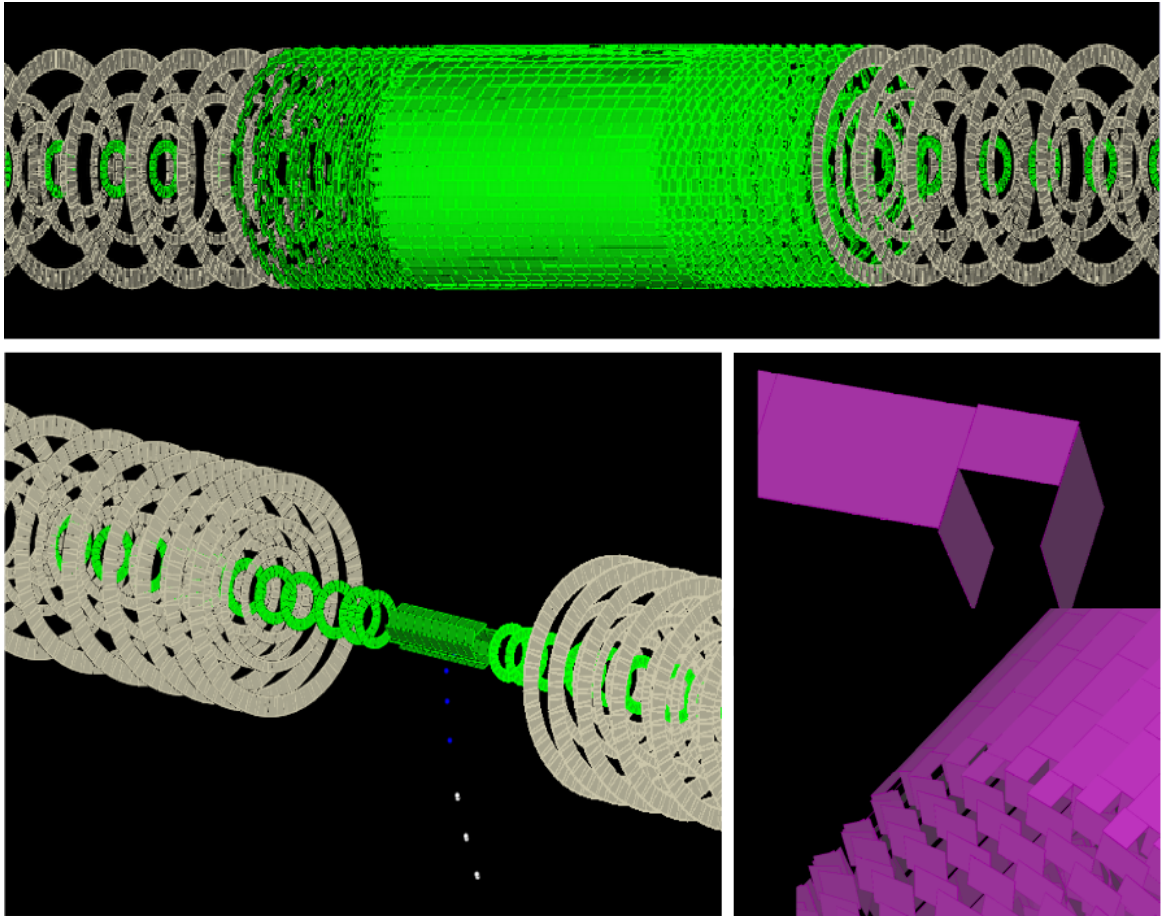


FIGURE 47 – Visualisation 3D avec le logiciel VP1 des surfaces de tracking et des hits simulés dans FATRAS pour plusieurs géométries de détecteurs ITk

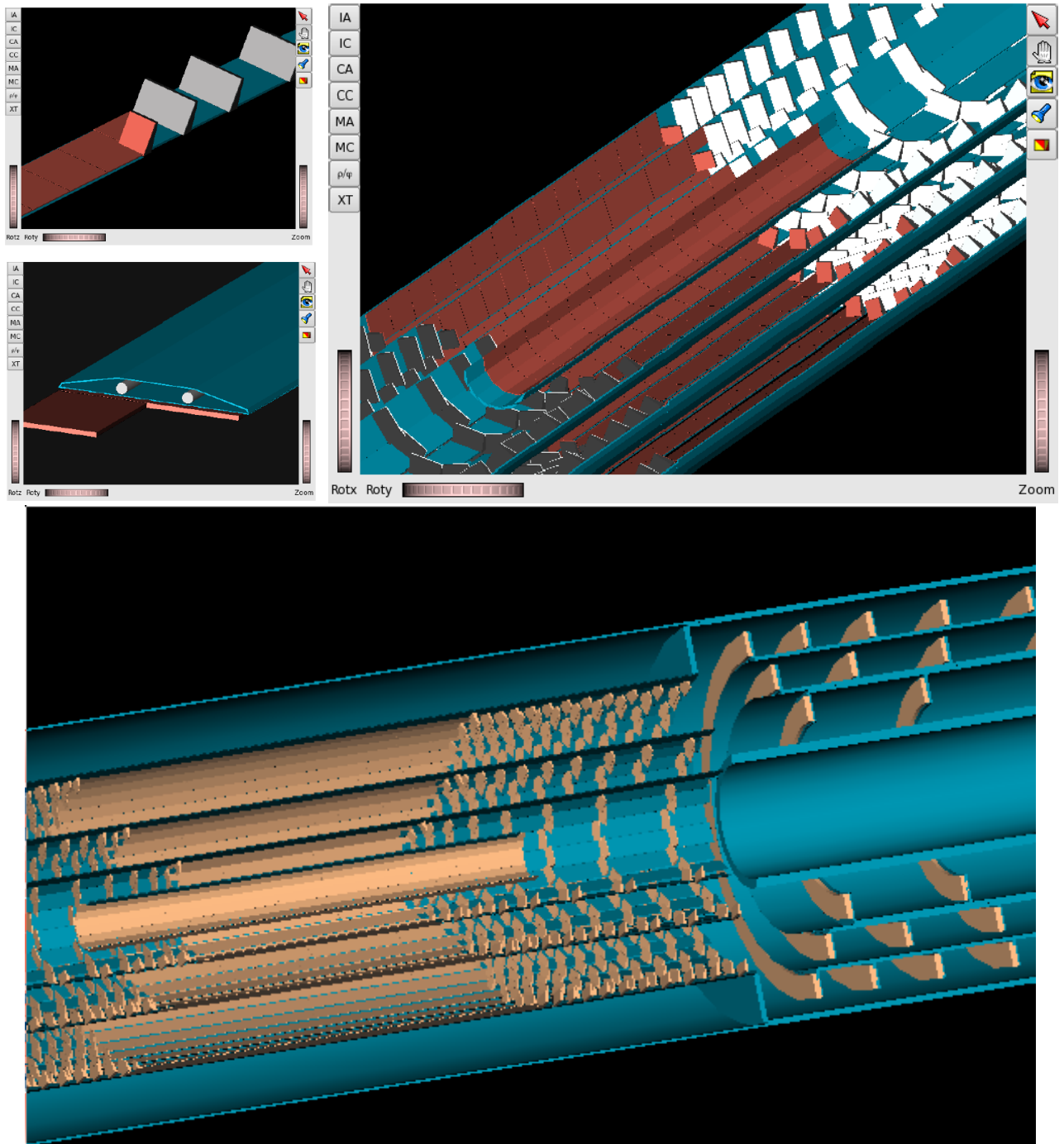


FIGURE 48 – Visualisation des FastGeoModels ITk avec le logiciel VP1.

Il aura fallu plus de deux ans pour que ce travail aboutisse et soit entièrement intégré et validé dans le framework de simulation complète d'ATLAS. Deux packages `FastGeoModel` contenant les bases nécessaires au développement de deux concepts de détecteurs concurrents ont été fournis par Sabine Elles à la communauté ITk : le package `Extended` pour l'équipe de Berkeley, et le package `Inclined` pour l'Université de Genève. Ces deux détecteurs sont présentés sur la Figure 49.

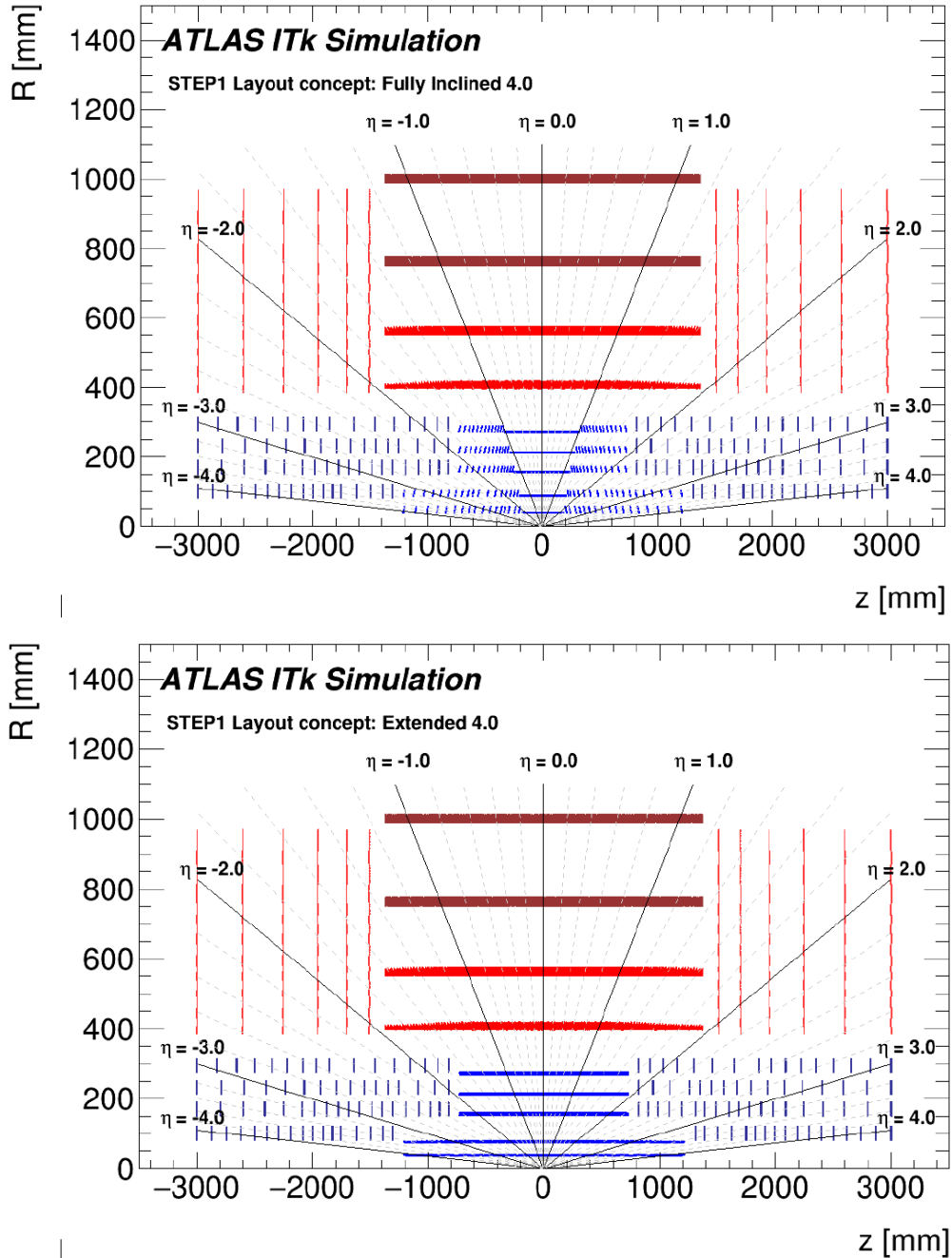


FIGURE 49 – Vue longitudinale des deux géométries concurrentes pour le détecteur ITk étendu jusqu'à $|\eta| < 4$: *Inclined* layout (haut) et *Extended* layout (bas).

Les premiers lots de données en simulation complète ont pu être produits à partir de l'été 2016, autorisant enfin une comparaison objective des deux propositions de détecteurs. En janvier 2017, la

Layout Task Force rend son rapport définitif [pub11], qui prône la construction d’un détecteur à pixels “embrassant les propriétés du concept incliné”. La Figure 50 montre la comparaison des performances des deux géométries concurrentes pour la reconstruction du paramètre d’impact transverse de muons isolés de faible impulsion. La Figure 51 montre les résolutions sur les paramètres des traces dans des événements $t\bar{t}$ superposés avec 200 événements de pile-up, plus représentatives des processus de physique attendus au HL-LHC.

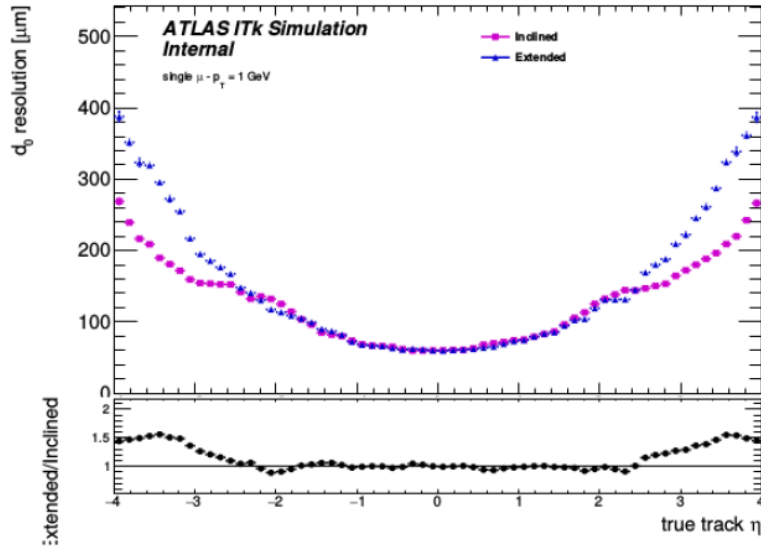


FIGURE 50 – Résolution sur le paramètre d’impact transverse pour des muons isolés de $P_T=1$ GeV, en fonction de la pseudo-rapidité, pour les géométries “Inclined” et “Extended”

L’ensemble des comparaisons de performance entre les deux géométries peut être consulté dans le rapport de la *Layout Task Force*, et de nombreux résultats annexes sont discutés dans l’excellent manuscrit de thèse de Noemi Calace [ref49].

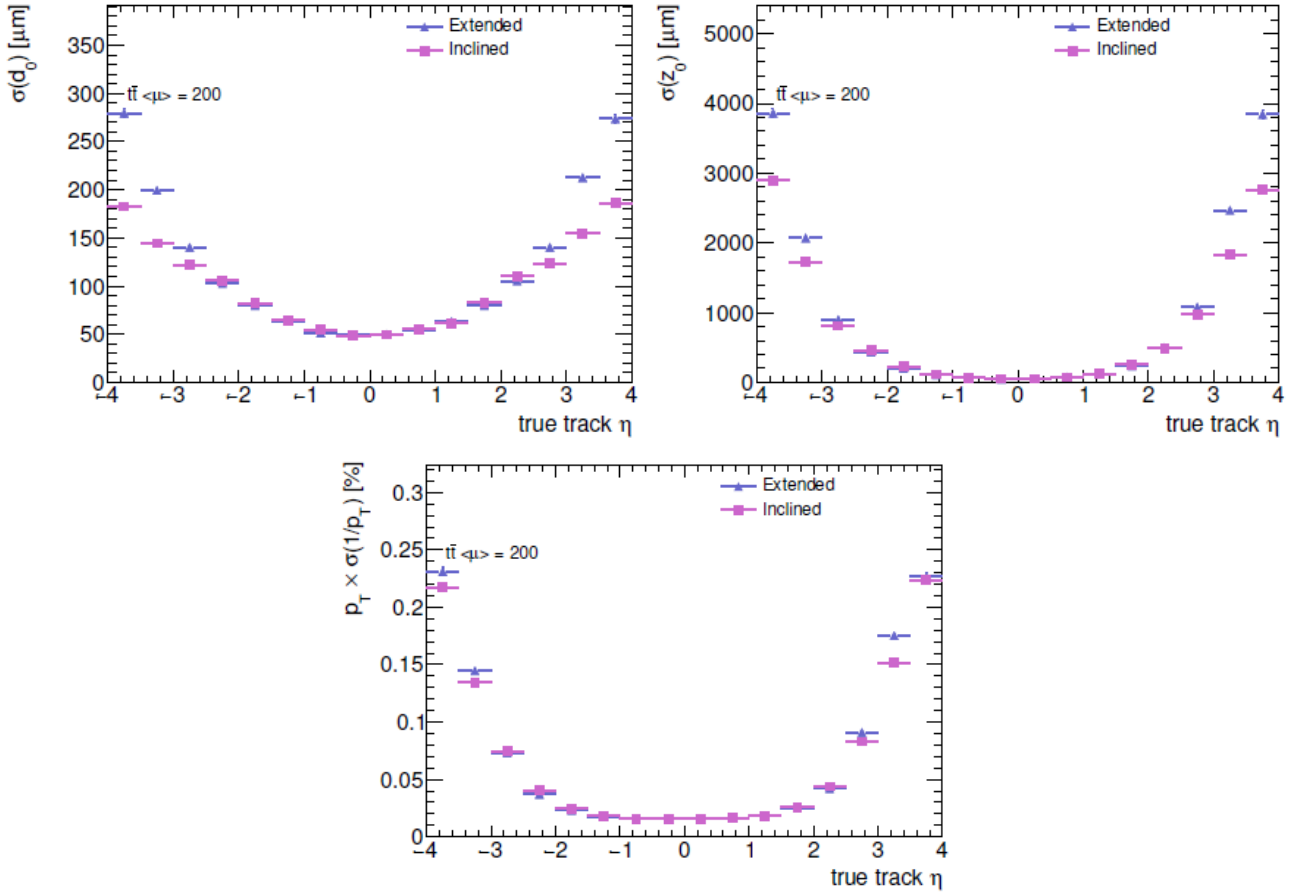


FIGURE 51 – Résolution sur les paramètres d’impact transverse d_0 , longitudinal z_0 et impulsion transverse relative pour des traces provenant des paires de quarks top, générées avec 200 événements d’empilement, pour les géométries “Inclined” et “Extended”. La géométrie inclinée montre des performances significativement meilleures, en particulier dans la région à très grande pseudo-rapacité où le bruit d’empilement est le plus dense.

3.3.2 Simulation des services

Même si la construction des géométries ITk a été grandement simplifiée, la modélisation des services et leur routage dans le détecteur nécessitent toujours d'ouvrir les "boîtes noires" du GeoModel. Dans le groupe de simulation ITk, plusieurs collaborateurs ont gagné en expertise technique grâce à la démocratisation des FastGeoModels, mais pas suffisamment de permanents. Le LAPP a conservé l'essentiel de l'expertise de fond pour la mise à jour rigoureuse des GeoModel ITk.

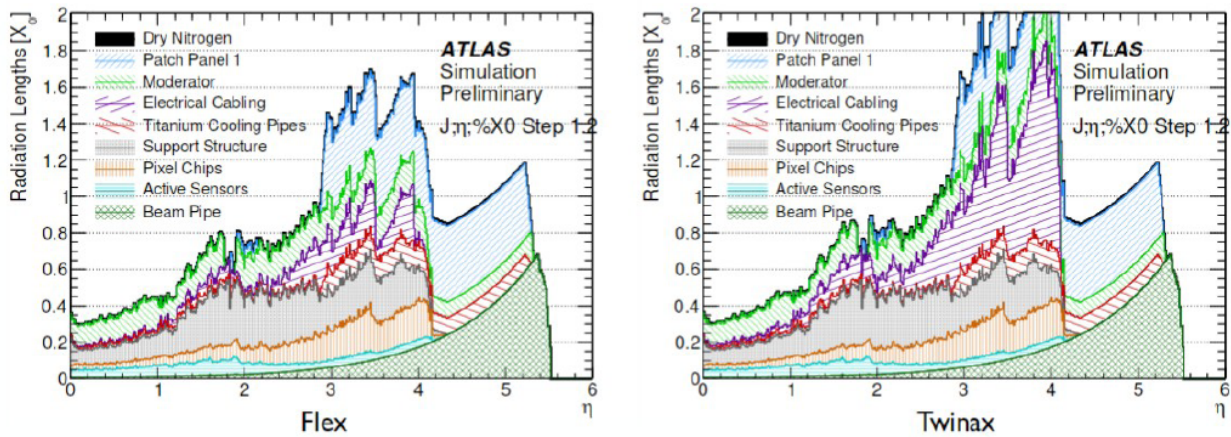


FIGURE 52 – Simulation Geant4 montrant la quantité de matière dans le détecteur à pixels ITk Inclined, dans l'hypothèse de l'utilisation de câbles de type flexes (gauche) ou twinaxes (droite) pour la transmission des données.

Dans les sections précédentes, nous avons vu que les services jouent un rôle prédominant dans les performances du détecteur à pixels. Depuis 2016, j'ai mis un point d'honneur à continuer de suivre l'évolution des simulations ITk en impliquant le LAPP sur la maintenance et le développement du GeoModel ITk pixel. L'objectif pour la fin de la phase de R&D est de conserver un modèle aussi proche que possible des développements techniques, parfois très rapides, pour confronter régulièrement les modifications imposées par les contraintes d'ingénierie avec leur impact sur les performances de physique, de la façon la plus réactive et la plus constructive possible.

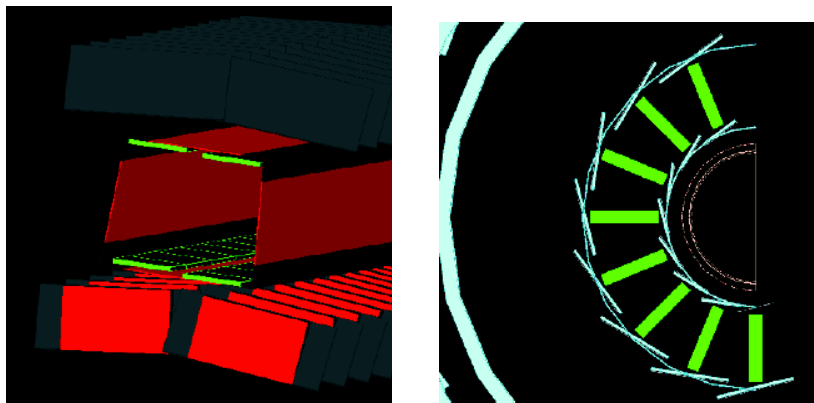


FIGURE 53 – Simulation Geant4 de la structure mécanique TRUSS supportant deux couches de modules pixels inclinés qui constitue la baseline du TDR pixel (gauche), et détails de la structure mécanique IBeam (droite).

Depuis 2016, Ben Smart, Francesco Costanza, Sarka Todorova (LAPP) et Nathan Readioff (LPSC) ont fourni des contributions majeures pour l'amélioration de la simulation ITk. On peut mentionner une étude comparant l'utilisation de flexes en lieu et place des câbles twinaxes utilisés comme baseline dans la simulation (Figure 52), et l'implémentation détaillée de la géométrie des structure IBeam et TRUSS (Figure 53). La Figure 54 montre que le compactage des services électriques de type twinaxes à l'intérieur de la structure carbone IBeam induit des pics en ϕ pouvant atteindre jusqu'à 5% X_0 .

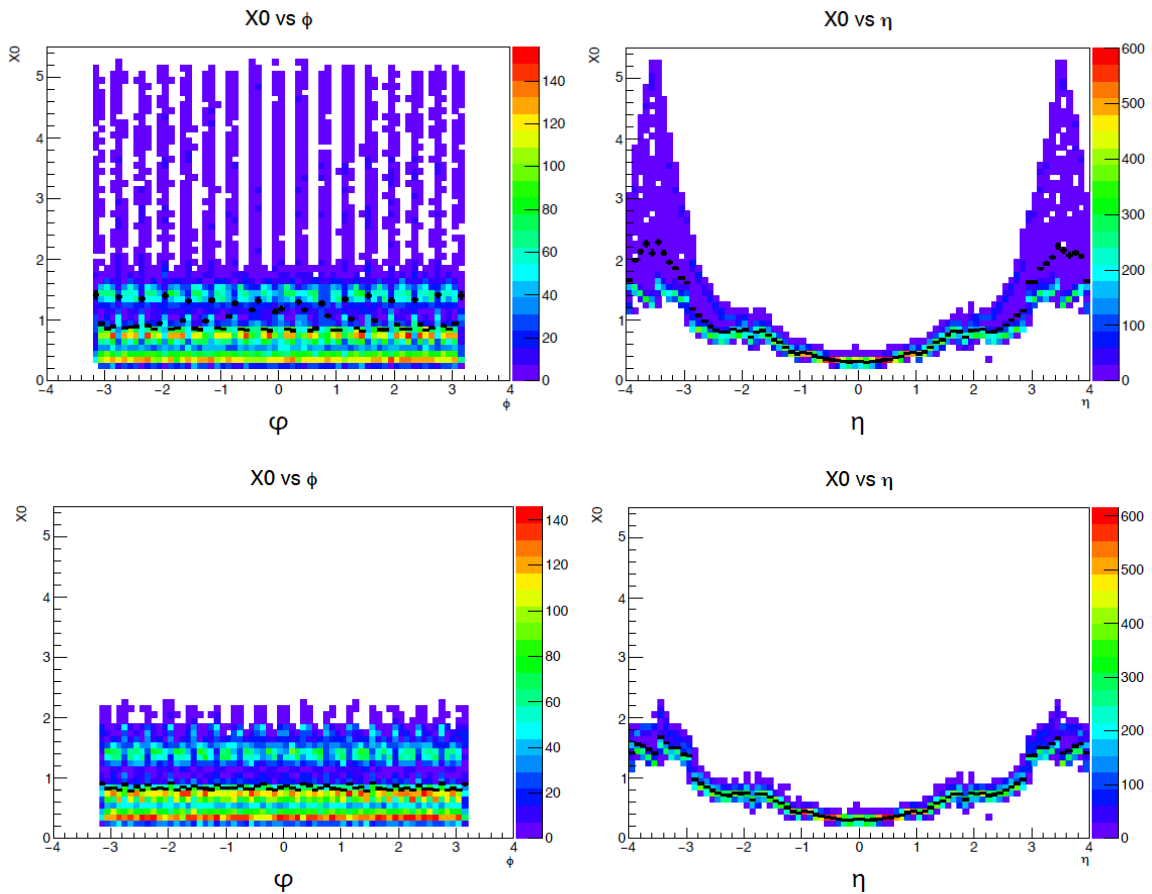


FIGURE 54 – Simulation Geant4 de la quantité de matière inerte liée aux services pour le détecteur à pixels ITk *Extended*, dans l'hypothèse de l'utilisation d'une structure de type IBeam et des câbles de type flexes (bas) ou twinaxes (haut) pour la transmission des données.

Le groupe du LAPP travaille activement sur la mise à jour des simulations, et compare régulièrement la quantité de matière avec les estimations fournies par les ingénieurs en mécanique. Dans les prochains mois, le modèle sera de nouveau adapté pour refléter le raccourcissement des structures mécaniques dans les couches pixels externes, remplacées par des rings inclinés pour simplifier la construction et l'intégration du détecteur (Figure 55). Une nouvelle étude sera également démarrée très prochainement pour optimiser la position du *Patch Panel 0*, carte électronique dont le rôle est d'assurer la transition entre les câbles de type 0 et les câbles de type 1 (Figure 56).

Inclined Section: Corrugated Shells

- Study possible solution to gain additional radial space to implement powering in phi

Corrugated shells to take advantage of the gaps between rings

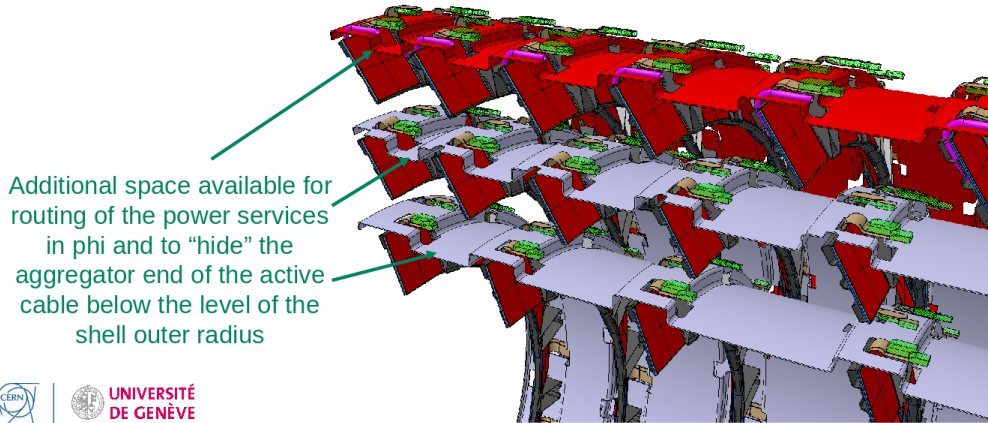


FIGURE 55 – Nouveau design (mai 2018) proposées pour les couches de pixels externes : structure mécanique centrale raccourcie, rings inclinés, et coque carbone ondulée pour l'intégration des services.

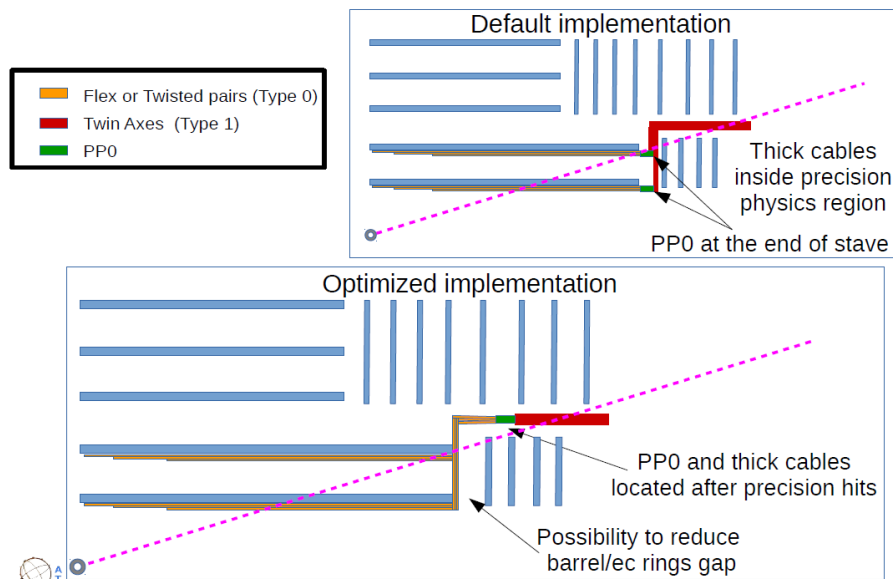


FIGURE 56 – Exemple de positionnements du *Patch Panel 0* et alternatives de routage des câbles dans le détecteur ITk pixel pour minimiser l'impact des services sur les performances de tracking.

3.4 Programme démonstrateur

Concomitamment à la décision d'ATLAS de construire un détecteur pixel de type incliné, les responsabilités de construction ont été clairement établies : les Etats-Unis seront responsables de la conception et de la fabrication des deux couches de pixels les plus proches du faisceau, le *Inner Barrel*, tandis que les trois couches externes *Outer Barrel* seront conçues et construites par une communauté constituée de l'Allemagne, la France, la Suisse, la Norvège et le Japon.

En janvier 2017, la communauté *Outer Barrel* s'est organisée pour mettre en place un programme de démonstrateur, et construire plusieurs prototypes d'échelles inclinées en vue de valider toutes les étapes de conception, production, assemblage et test des différents composants destinés à équiper le futur détecteur à pixels. J'ai engagé le groupe ITk du LAPP dans ce programme pour contribuer aux développements suivants :

- Conception, production, test et intégration des services électriques (alimentation et transmission de données)
- Etudes thermofluidiques et mesures des performances thermiques
- Conception et construction d'une enceinte de test pour le CERN, destinée à la qualification des prototypes en environnement contrôlé.



FIGURE 57 – Tests d'intégration des circuits flexes conçus au LAPP dans la structure mécanique de type TRUSS développée par l'Université de Genève et le CERN.

L'objectif du démonstrateur pour l'équipe du LAPP, outre de valoriser et de partager l'expertise acquise depuis 5 ans sur la conception d'un détecteur incliné, est de se préparer pour la construction. Le LAPP s'est engagé à produire l'ensemble des services de type 0 pour les couches externes à partir de 2020, à intégrer et connecter les modules pixels sur 20% des structures mécaniques inclinées, et à qualifier entièrement ces structures avant leur transport au CERN. De plus, suite aux tests de qualification et d'intégration des flexes réalisés dans le cadre du programme démonstrateur, le LAPP est désormais officiellement en charge de la conception des services de type 0 pour le *Outer Barrel*.



FIGURE 58 – Enceinte de test conçue par le LAPP, en cours d'assemblage au CERN (juin 2018)

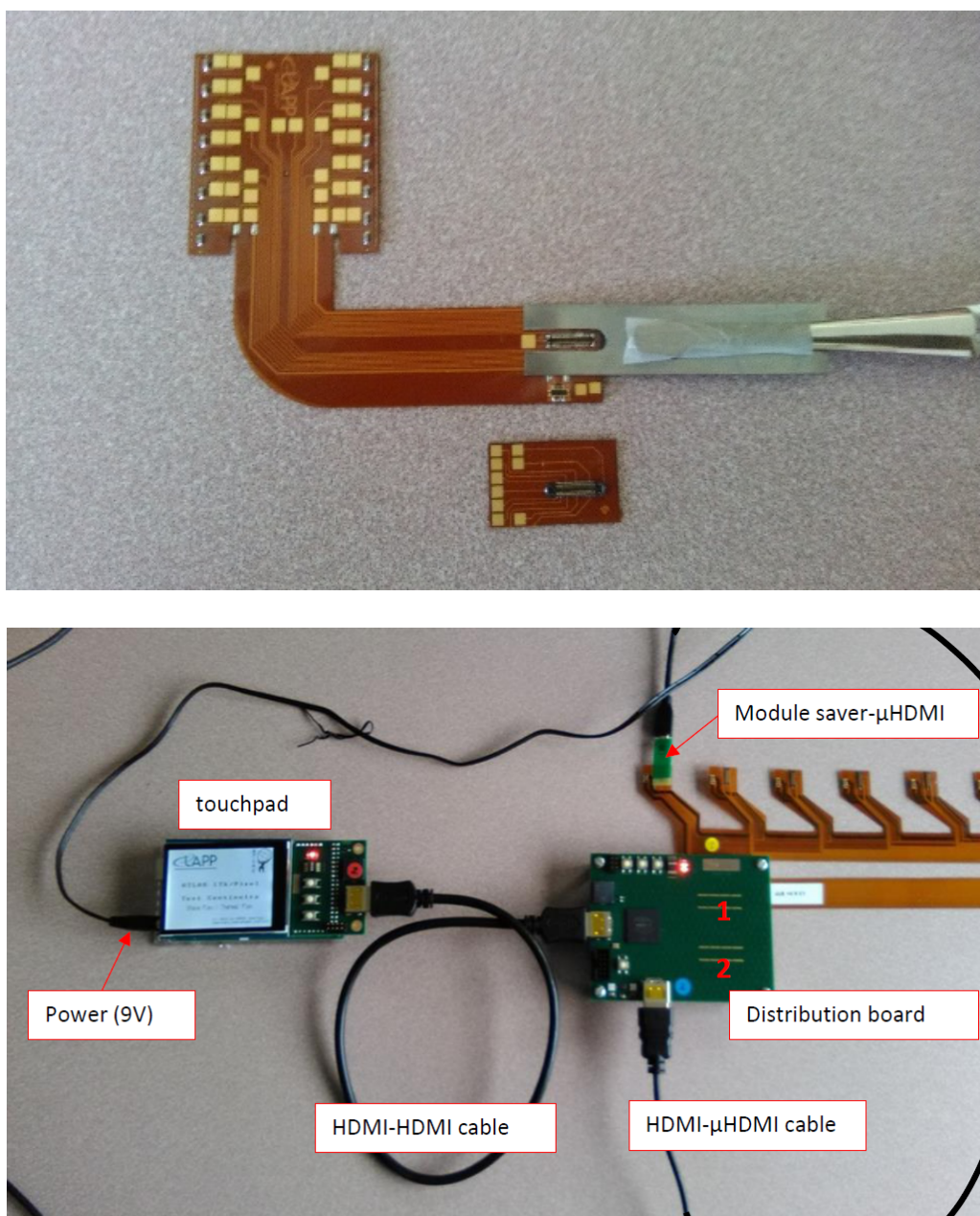


FIGURE 59 – Contributions du LAPP au programme démonstrateur : design mécanique des circuits flexes utilisés pour la lecture des modules, conception d'un outillage pour les connecteurs, design et production des services électriques de type circuits flexibles, design et production des cartes de tests de continuité de ces circuits flexibles.

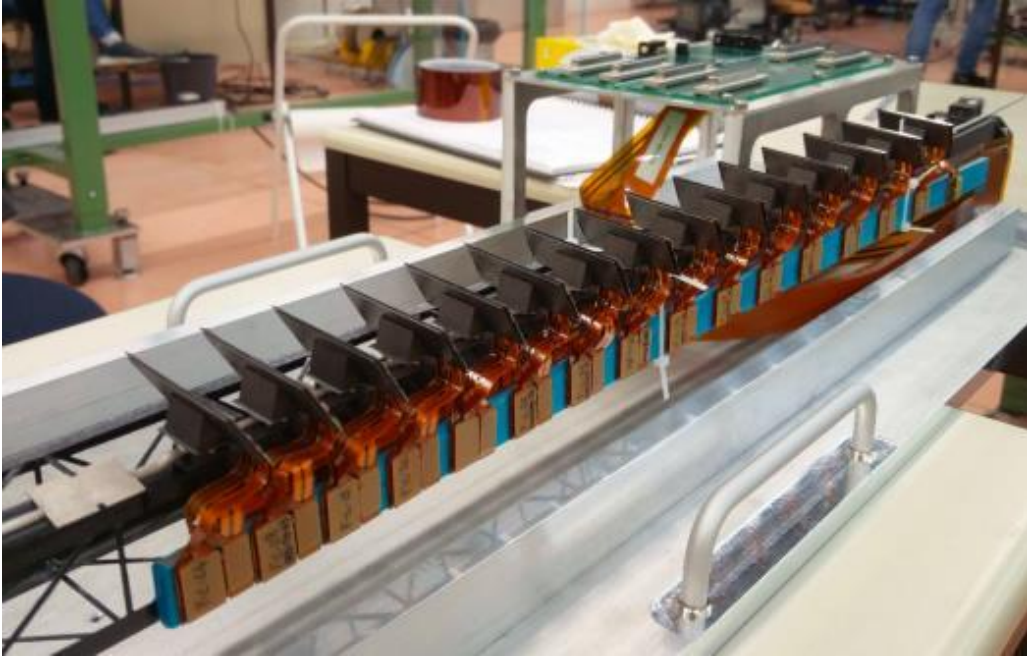


FIGURE 60 – Prototype thermique en cours d'assemblage, réalisé au CERN dans le cadre du programme démonstrateur *Outer Barrel*.

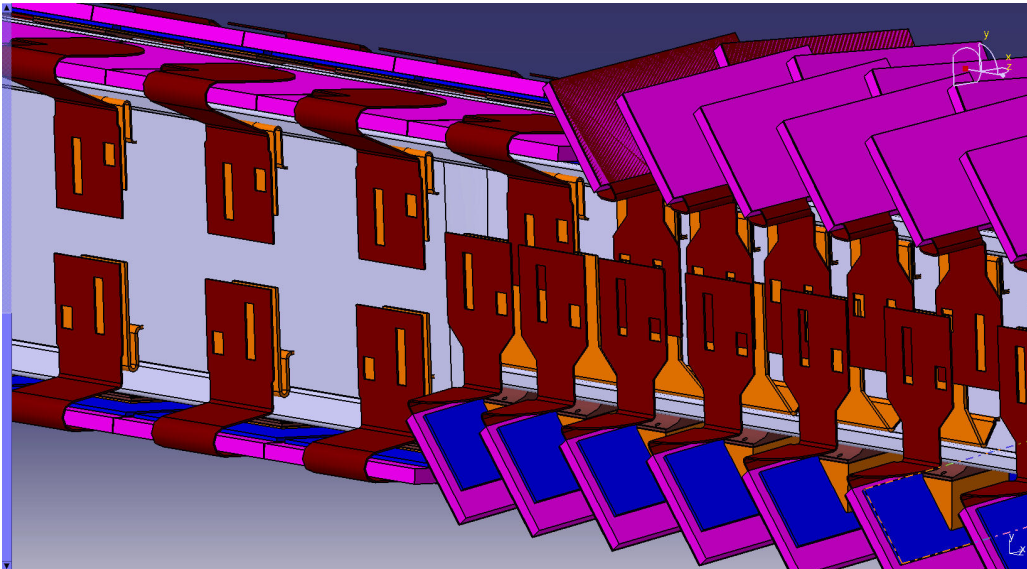


FIGURE 61 – Design et routage des services électriques réalisés par le LAPP dans le cadre du programme démonstrateur *Outer Barrel*.

3.5 Etudes thermiques

L'un des aspects les plus critiques pour la validation du design du détecteur à pixels incliné est de démontrer que les transferts thermiques au travers du support mécanique sont suffisants pour évacuer la chaleur dissipée par l'électronique de lecture. Contrairement au détecteur IBL, le chemin thermique entre les modules inclinés et les tubes de refroidissement est relativement grand (Figure 62).

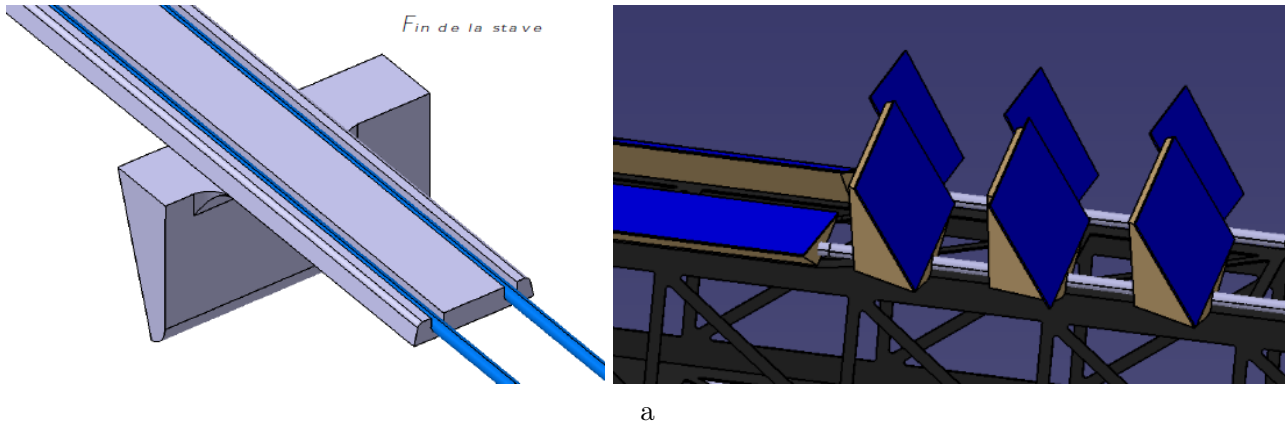


FIGURE 62 – Positionnement des tubes de refroidissement dans la structure en mousse carbone pour le détecteur alpin du LAPP (gauche) et le détecteur SLIM de l'Universités de Genève (droite).

Les études de performances thermiques du détecteur alpin ont été démarrées au LAPP avec la thèse de Zhan Zhang [ref37], de 2012 à 2015. Son travail, que j'ai encadré à partir de 2015, a permis au laboratoire de s'équiper d'une station de refroidissement au CO₂ diphasique et d'acquérir une expertise solide pour l'opération des dispositifs expérimentaux dédiés aux mesures thermiques. Zhan a pu démontrer grâce à des prototypes en mousse carbone réalisés par le LPSC (Figure 63) et testés au LAPP que le refroidissement de modules pixels inclinés sur la structure alpine était compatible avec les spécifications requises. Elle a également pu valider une partie des prédictions du modèle CoBra (CO₂ BRAnch Calculator) développé par Bart Verlaat [ref50] sur le comportement du CO₂ diphasique le long des tube en titane. Cependant, à l'issue de la thèse de Zhan, les mesures thermiques réalisées sur les prototypes alpins montraient d'importants désaccords avec les simulations. Les prototypes semblaient présenter des performances thermiques bien meilleures que celles prédites par les simulations.

L'observable considérée pour l'estimation des performances thermiques est la température du point le plus chaud à la surface du module. Pour prédire cette température, il faut estimer deux composantes. La première composante est la variation de température entre le fluide et la paroi du tube titane, déterminée par le coefficient de transfert thermique (HTC) du CO₂ diphasique. La deuxième composante est le gradient de température dans le support mécanique, entre la paroi du tube et la surface du module. Ces deux composantes sont illustrées sur la Figure 64. La Figure 65 présente un modèle de montagne alpine modélisée dans ABAQUS ainsi que les prédictions de gradient de température obtenues en modifiant certains matériaux du support.

Le HTC du CO₂ est prédit par le logiciel CoBra en fonction de paramètres tels que le débit, la température du fluide, la pression, la longueur du tube et la densité de flux de chaleur à évacuer. Le gradient dans le support mécanique est estimé avec le logiciel de calculs par éléments finis ABAQUS¹², qui prend en compte les épaisseurs des matériaux utilisés pour la structure des montagnes, leurs conductivités thermiques, le flux de chaleur total et sa distribution dans le support.

12. <https://www.3ds.com/fr/produits-et-services/simulia/produits/abaqus/>

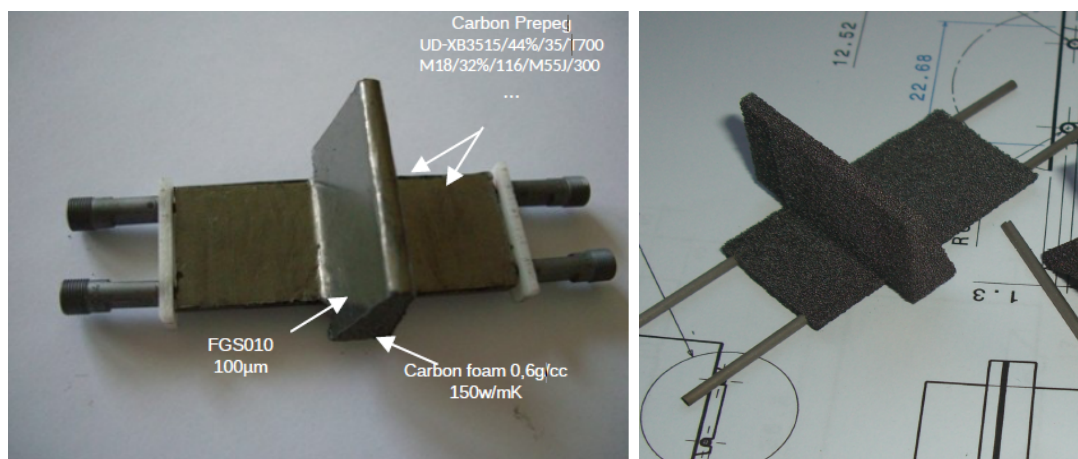


FIGURE 63 – Prototypes alpins fabriqués au LPSC et testés au LAPP pour l'évaluation des performances thermiques.

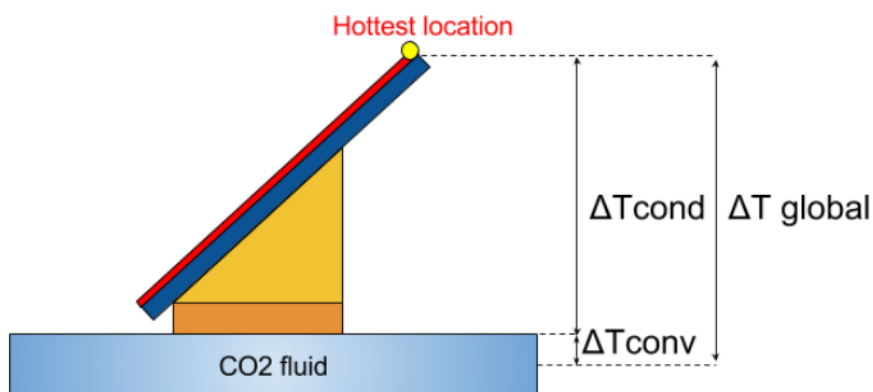


FIGURE 64 – Schéma descriptif des deux composantes influençant la température maximale à la surface du module : la composante convective (ΔT_{conv}) entre le fluide et la paroi du tube, déterminée à partir du logiciel CoBRA, et la composante conductive (ΔT_{cond}) entre la paroi du tube et la surface du module, simulée avec ABAQUS.

Pour essayer de comprendre et d'expliquer les désaccords observés entre mesures et prédictions, plusieurs effets devaient être étudiés et quantifiés. La difficulté principale de l'exercice étant de parvenir à mettre au point un dispositif expérimental pertinent pour tester chaque hypothèse indépendamment :

- Les mesures thermiques n'étaient pas réalisées dans une enceinte à vide, mais à l'air libre. De fait, les apports de chaleur extérieure par convection pouvaient faire varier les résultats des mesures de plusieurs degrés selon le moment de la journée. Ces effets convectifs étant difficiles à modéliser dans ABAQUS, ils étaient tout simplement ignorés pour les comparaisons.
- Les valeurs de conductivités thermiques des matériaux utilisées dans ABAQUS sont extraites de publications ou de fiches techniques de fabricants, assez peu précises et souvent mesurées à une température ambiante de 20 degrés. La plupart du temps, aucune dépendance en température n'est fournie pour ces conductivités thermiques, qui sont appliquées telles quelles à -30 degrés, la température d'opération du détecteur ITk. De plus, une modification mineure dans la composition de certains alliages ou la présence d'impuretés peuvent changer drastiquement les valeurs de conductivités thermiques.

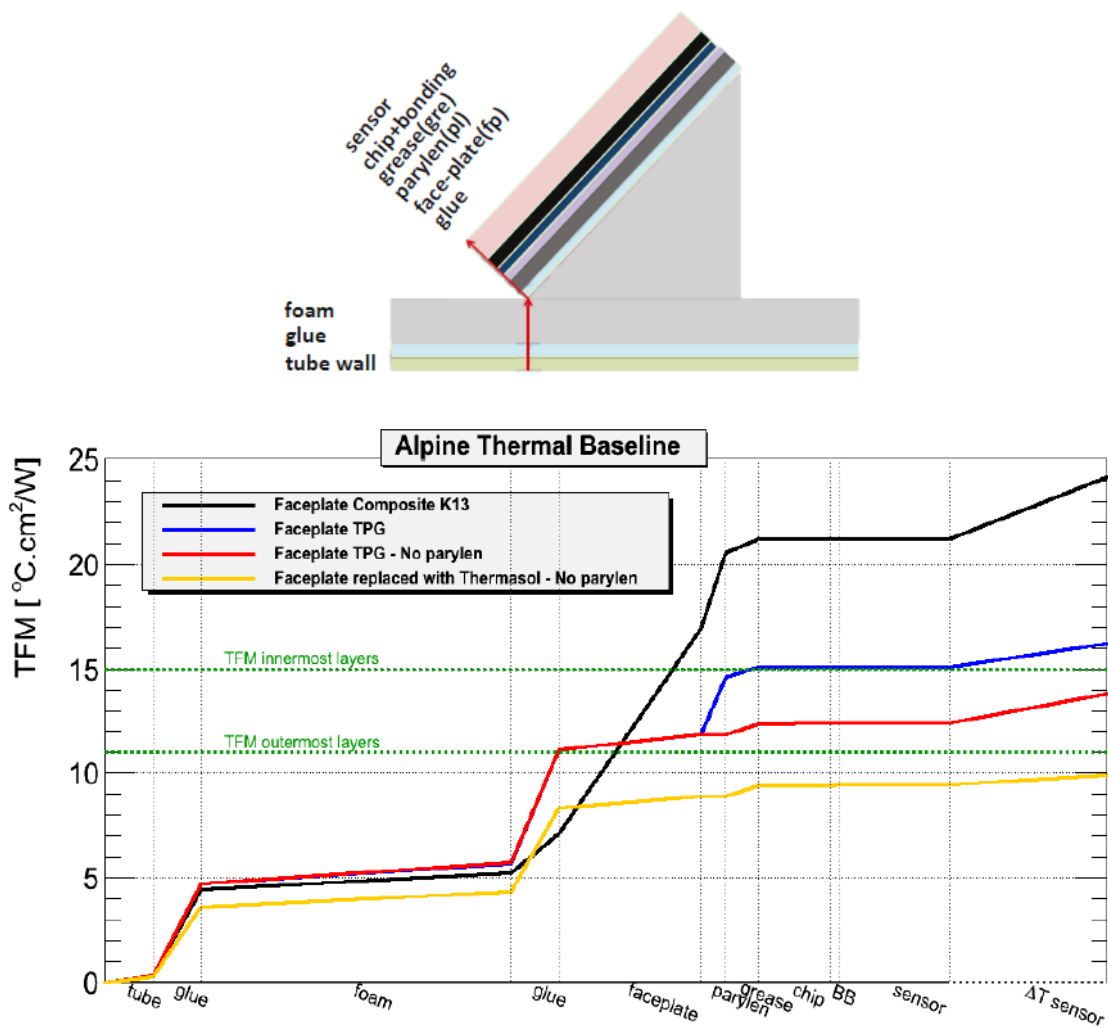


FIGURE 65 – Modèle ABAQUS utilisé pour la simulation du gradient thermique dans le support mécanique alpin (haut) et performances attendues en faisant varier certains paramètres critiques du modèle (bas).

- Certains matériaux et certaines interfaces sont difficilement modélisables dans ABAQUS et génèrent des incertitudes importantes sur les conductivités thermiques effectives : diffusion de la colle dans les alvéoles de la mousse carbone, maîtrise imparfaite de l'épaisseur des dépôts pour les colles ou les pâtes thermiques...
- Le modèle théorique utilisé dans CoBRA pour décrire le comportement du CO₂ diphasique est un modèle semi-empirique [ref51], ajusté sur des mesures thermiques correspondant approximativement à la zone de fonctionnement du détecteur IBL. Les prédictions de CoBRA ont par ailleurs été validées par Zhan et Bart Verlaart pour le détecteur IBL. Mais dans le cas du détecteur ITk comportant des modules inclinés, les flux de chaleurs mis en jeu sont 5 à 10 fois plus importants que pour l'IBL, du fait d'une surface de contact plus faible entre le module et la zone de refroidissement. La Figure 66 compare l'espace de phase des données utilisées pour ajuster le modèle décrivant le comportement du CO₂ diphasique avec les zones d'opération des détecteurs IBL et ITk. Ce graphique suggère fortement de vérifier que le modèle de CoBRA est réellement extrapolable dans la zone de fonctionnement de l'ITk.

En septembre 2016, Pierre Barroca a démarré une thèse sur le sujet, sous supervision conjointe de Stéphane Jézéquel et moi-même. Durant la première année, nous avons mis au point une enceinte de test sous vide pour s'affranchir d'une partie des apports de chaleurs parasites et travaillé longuement sur toutes les procédures expérimentales (préparation des prototypes, collage des chauffettes kaptons et des sondes de température sur les échantillons, traitement des données, installation et calibration de capteurs environnementaux...). Au terme de cette première année, nous étions enfin parvenus à obtenir des résultats reproductibles.

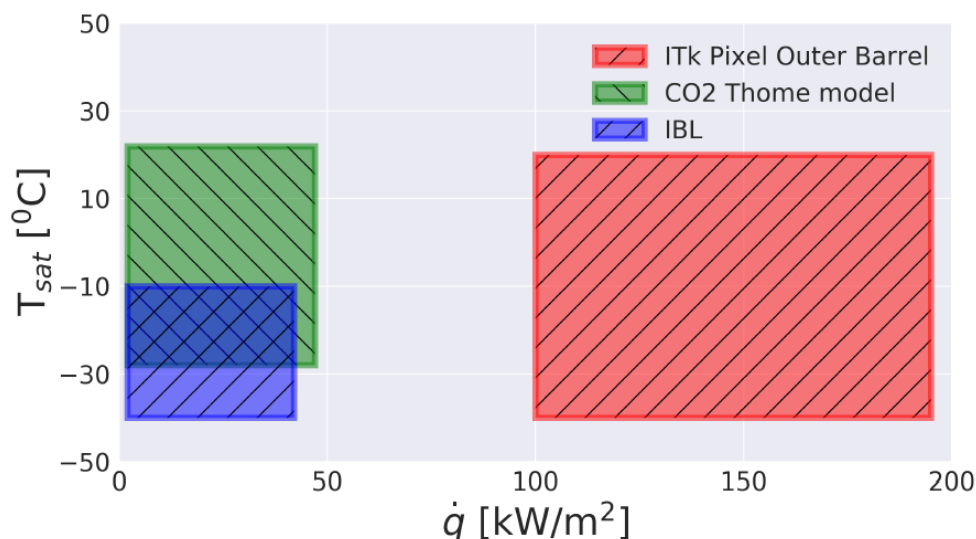


FIGURE 66 – Comparaison de l'espace de phase (Température du fluide T_{sat} ; Flux de chaleur \dot{q}) correspondant aux données utilisées pour ajuster le modèle CoBRA (vert) avec les zones d'opération des détecteurs IBL (bleu) et ITk (rouge).

En 2017, le CERN et l'Université de Genève ont réalisé des mesures thermiques dans des conditions approximativement similaires à celles réalisées au LAPP, sur un prototype de support pixels incliné concurrent, et ils ont observé des désaccords semblables : les prototypes testés semblent avoir des performances meilleures que celles prédites par le modèles CoBRA + éléments finis combinés (Figure 67).

Suite à ces observations, nous avons demandé à l'Université de Genève de nous fournir un prototype thermique simplifié, constitué de simples blocs de cuivre brasés sur un tube en inox et équipés de chauffettes kapton (Figure 68). Ce prototype permet de minimiser le nombre de paramètres nécessaires à la modélisation des gradients de température dans le support mécanique.

Nous avons réalisé 18 séries de mesures sur ce prototype, en variant les conditions expérimentales liées au CO2 (débit, température, fraction gaz/liquide) ainsi que la charge thermique appliquée (de 1 à 8 Watts). Chaque série a été réalisée indépendamment pour chacun des 5 blocs de cuivre.

En utilisant un modèle paramétrique pour décrire le terme conductif (commun pour tous les blocs de cuivre) et le terme convectif affecté d'un paramètre de correction α pour chaque série de mesures, et en ajustant ce modèle avec des paramètres de nuisance adaptés¹³, il devient possible de mesurer le comportement du CO2 en s'affranchissant des incertitudes sur la modélisation du support mécanique. Grâce à ce travail, Pierre a pu extraire de ses données les conductivités thermiques *in situ* des matériaux

13. et avec l'aide précieuse de Nicolas Berger

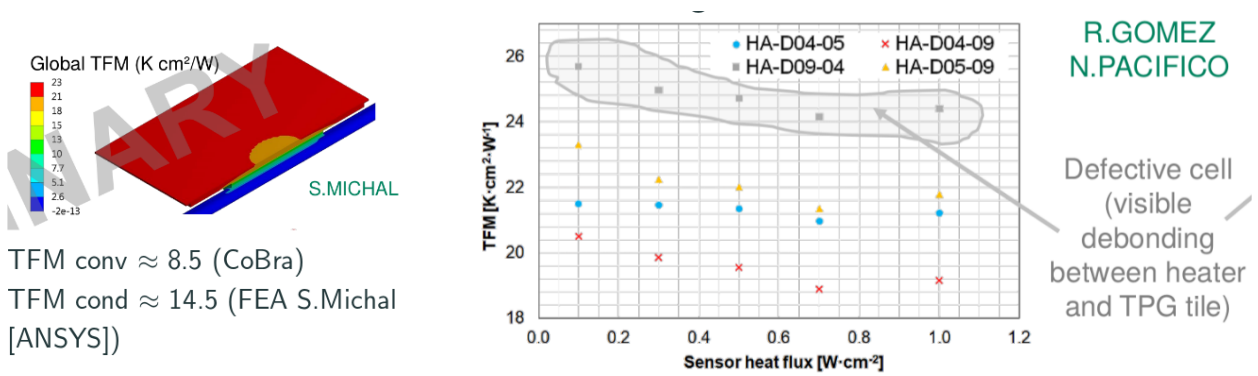


FIGURE 67 – Comparaison des performances thermiques prédites (gauche) et mesurées au CERN (droite) pour le prototype de détecteur pixels incliné CERN/Université de Genève. Les modèles prédisent une augmentation de température de $23 \text{ K}\cdot\text{m}^{-2}/\text{W}$, tandis qu'une valeur de $18 \text{ K}\cdot\text{m}^{-2}/\text{W}$ est observée dans les mesures effectuées sur le banc de test thermique du CERN.

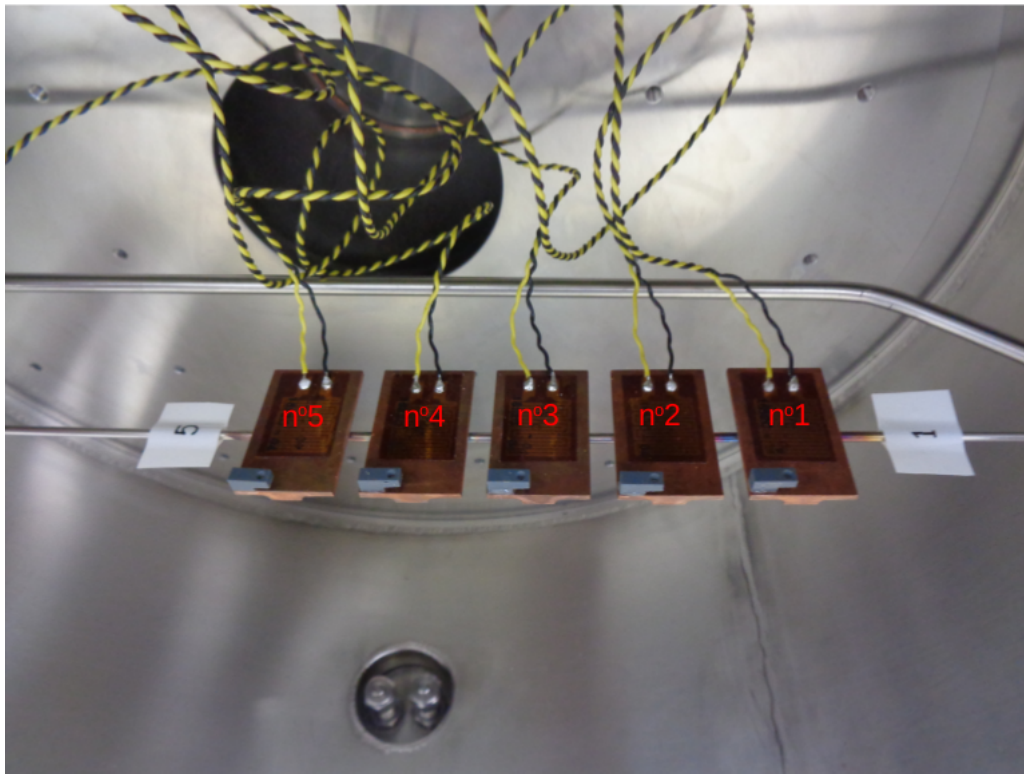


FIGURE 68 – Prototype thermique simplifié fabriqué par le CERN/Unige et installé pour des tests thermiques dans l'enceinte à vide du LAPP.

avec une précision de l'ordre de 5%, mesurer la variabilité et la qualité des soudures entre les blocs de cuivre, et surtout, démontrer que le modèle utilisé dans CoBRA dérive significativement des mesures pour des densités de flux de chaleurs de l'ordre de ceux mis en œuvre dans le détecteur ITk incliné (Figures 69 et 70).

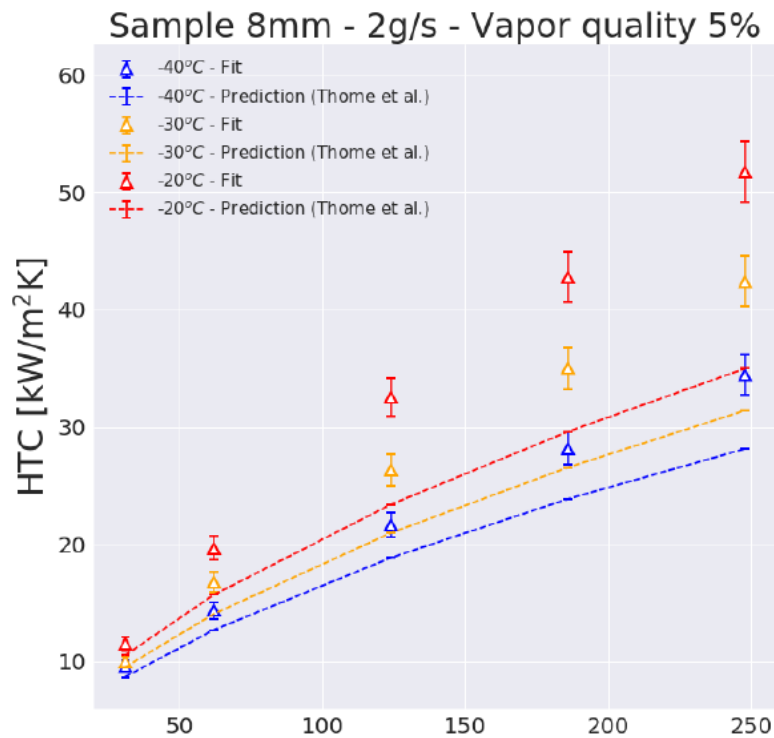


FIGURE 69 – Valeurs de HTC extraites des ajustements contraints réalisés sur les mesures du prototype thermique simplifié (markers), comparés avec les prédictions de CoBRA (lignes pointillées) en fonction de la densité de flux de chaleur \dot{q} . Les déviations s’observent pour les flux de chaleur importants, dans une zone de l’espace de phase (T_{CO_2}, \dot{q}) très éloignée de celle des données qui ont été utilisées pour ajuster le modèle de Thome.

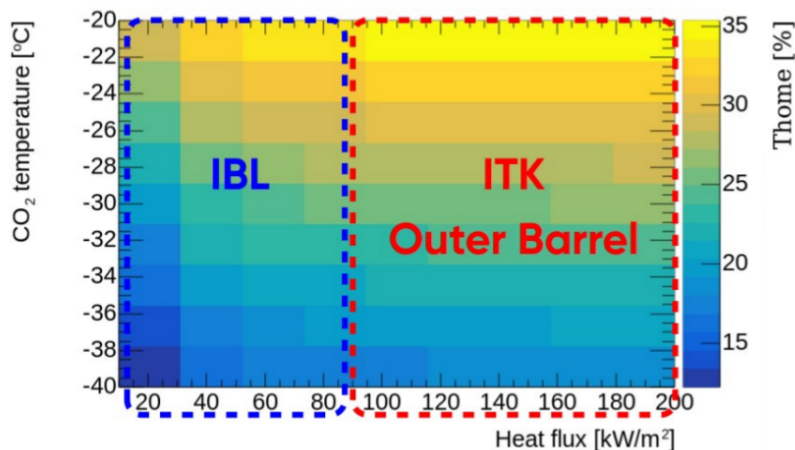


FIGURE 70 – Facteur de correction α sur les prédictions HTC de CoBRA, extrait des ajustements contraints réalisés sur les mesures du prototype thermique simplifié. Dans la zone à très grand flux de chaleur, qui correspond à la région de fonctionnement du détecteur ITk, le modèle de Thome sous-estime la valeur du coefficient de transfert thermique du CO₂ de 30 à 35%.

L'ensemble de ces résultats thermiques et la mise au point du banc de test associé sont documentés dans la thèse de Pierre Barroca [ref52], et les outils d'analyse développés par Pierre vont être exploités intensivement durant les dernières années de R&D du détecteur à pixels ITk, pour qualifier le procédé de fabrication des prototypes, optimiser la forme des supports inclinés et tester les interfaces thermiques (soudure, collage, plaquette thermique...) avant de figer le design définitif.

4 Perspectives

4.1 Programme pour le HL-LHC

Le programme des dix années à venir est relativement bien tracé. Les trois prochaines années seront consacrées à la fin de la R&D du détecteur ITk, la qualification des prototypes définitifs et la production des services de type 0. L'intégration des modules pixels sur les structures mécaniques au laboratoire et leur qualification doit démarrer en 2020, et s'achever au plus tard en 2023. Durant cette période, l'équipe ITk du LAPP participera à l'intégration au CERN du détecteur *Outer Barrel*, à son installation et au câblage en caverne. Et la boucle sera bouclée : commissioning du nouveau détecteur, participation aux opérations, monitoring, analyse des premières données... Nouvelles découvertes ?

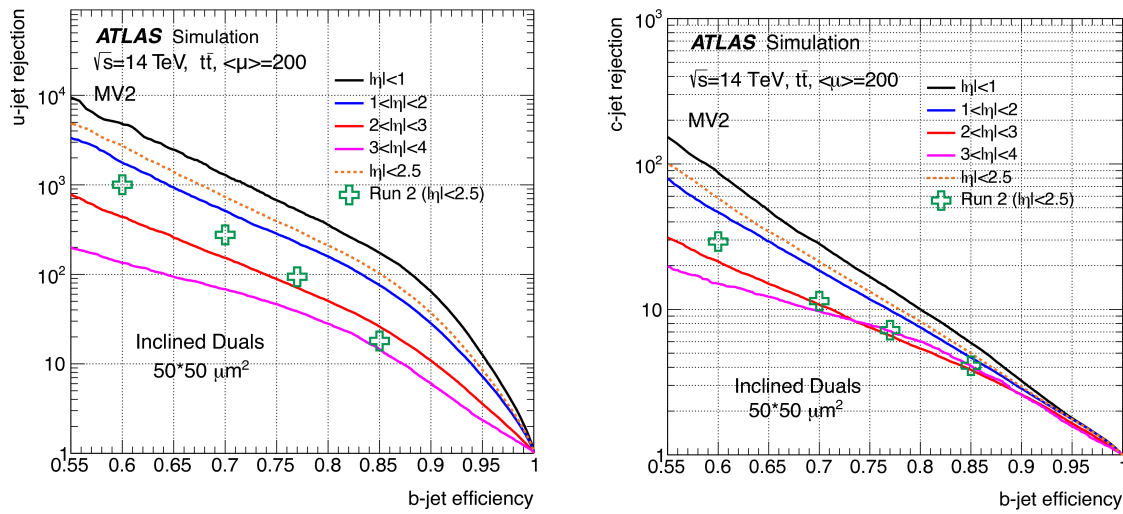


FIGURE 71 – Réjection des jets légers et des jets c en fonction de l'efficacité d'identification des jets b pour le détecteur ITk dans des conditions $\mu=200$ et comparaison avec les performances du Run 2 dans les conditions $\mu=60$.

Durant cette période, il sera intéressant de tirer profit des améliorations apportées par le détecteur ITk (Figures 71 et 72) pour développer les analyses de mise en évidence des processus HH et de mesure du couplage trilinéaire du boson de Higgs. La Figure 73 suggère que des progrès significatifs sont certainement encore à attendre dans ce domaine dans les années à venir. Une piste de développement pour les performances est la combinaison des informations du tracking à l'avant avec les informations temporelles fournies par le détecteur HGTD [ref53]. Une extension de l'acceptance des électrons au-delà de $\eta = 3.2$ et l'amélioration de la mesure de l'énergie d'isolation des photons pourraient contribuer à l'amélioration de la signification des canaux $HH \rightarrow ZZ^* \rightarrow 4e$ et $HH \rightarrow \gamma\gamma b\bar{b}$ respectivement.

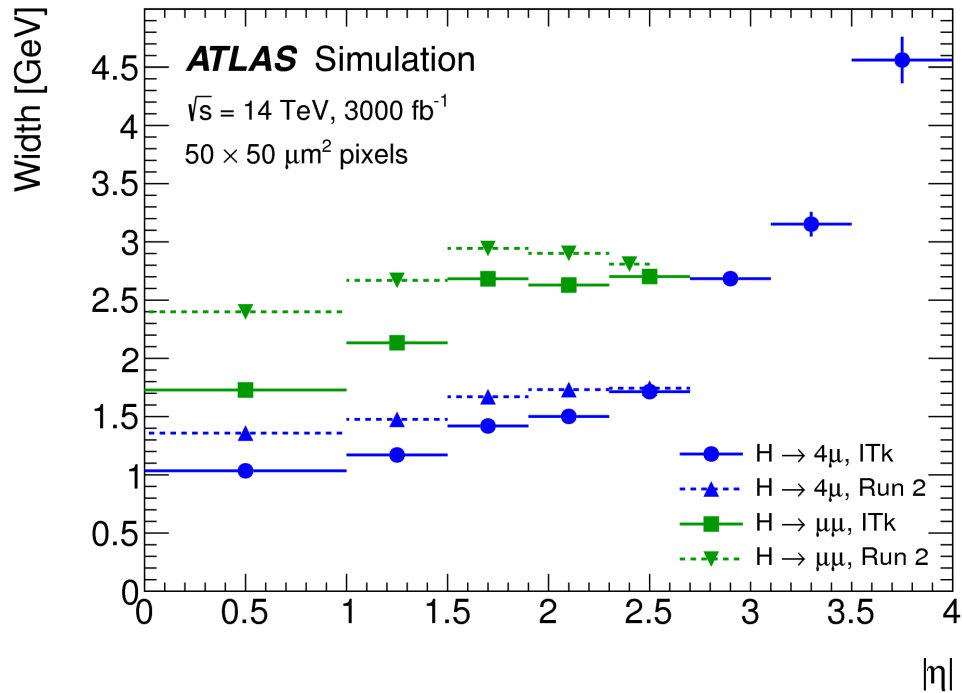


FIGURE 72 – Largeur de masse invariante reconstruite dans les canaux $H \rightarrow ZZ^* \rightarrow 4\mu$ (bleu) et $H \rightarrow \mu\mu$ (vert) en fonction de la plus grande pseudo-rapidité $|\eta|$ des muons produits. La largeur attendue au HL-LHC avec le détecteur ITk est comparée à la valeur du Run 2, basée sur les performances du tracker actuel.

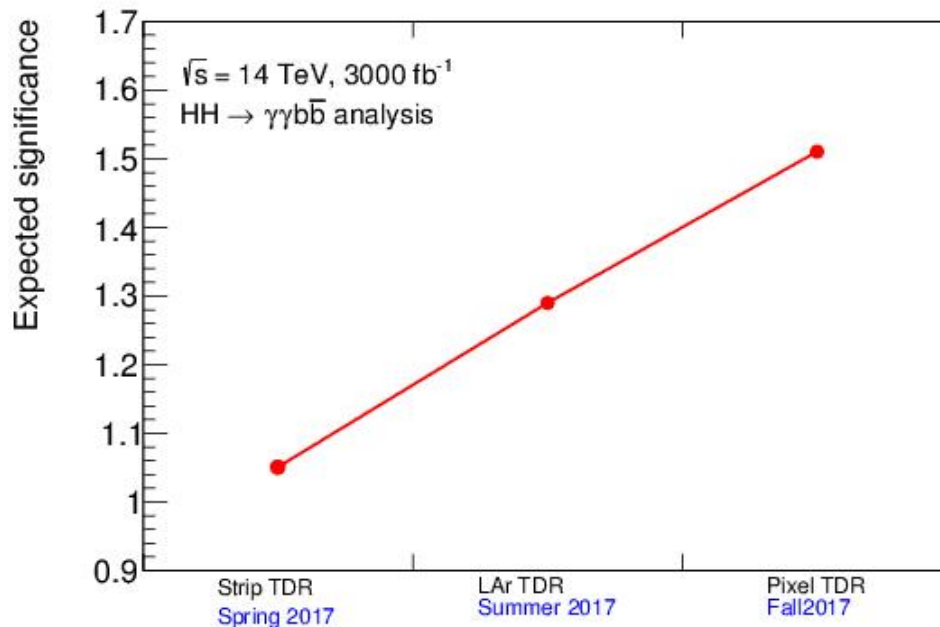


FIGURE 73 – Amélioration de la signification du canal $HH \rightarrow \gamma\gamma b\bar{b}$ après chaque publication de Technical Design Report pour les upgrades HL-LHC. Crédit : Elisabeth Petit.

4.2 Au-delà des Alpes : l'EVEReST

Il semble difficile de clore ce chapitre sans regarder en direction des projets de futurs collisionneurs FCC [ref54] (Figures 75 et 74).

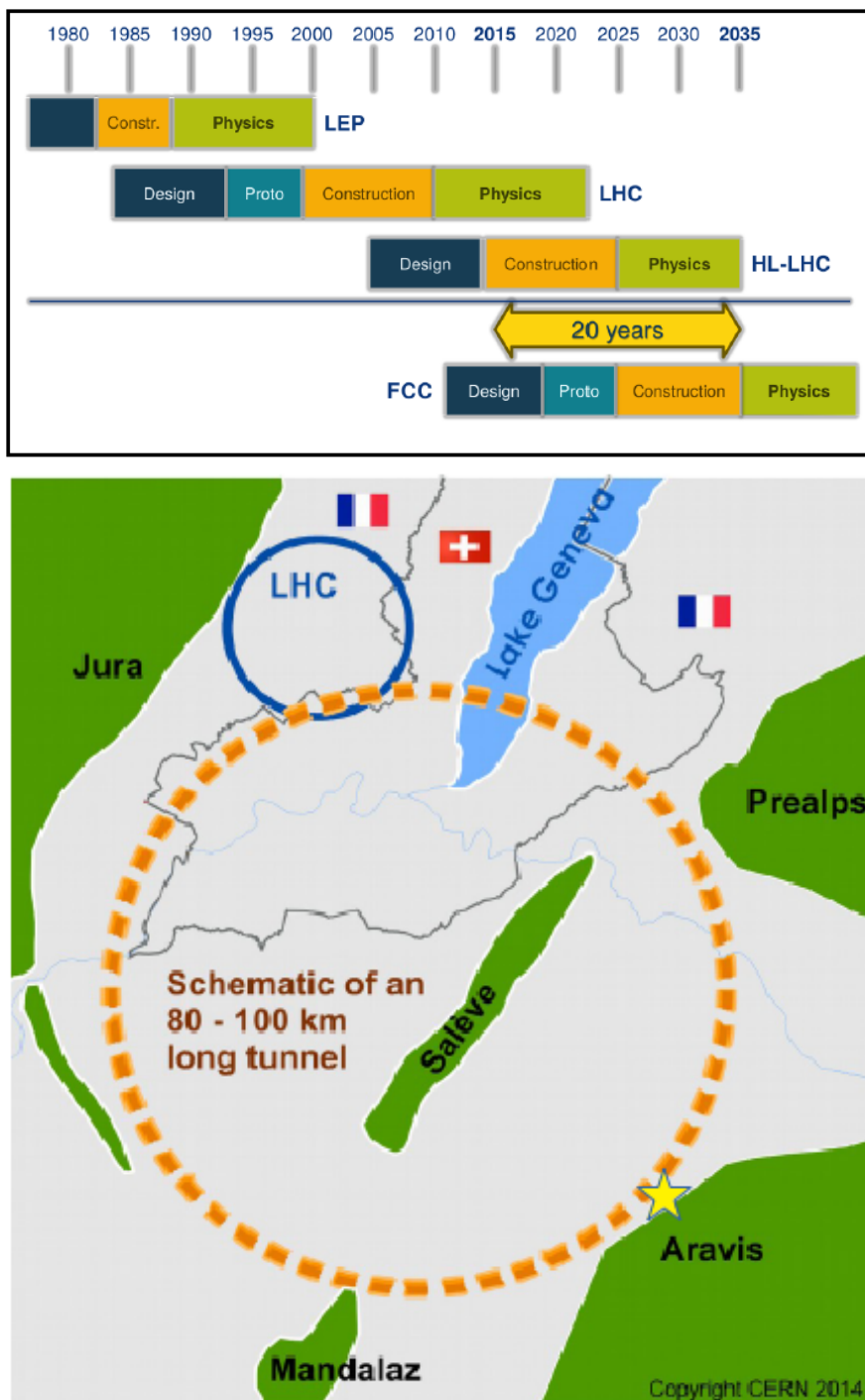


FIGURE 74 – Planning du projet de collisionneur FCC (haut) et localisation du futur tunnel (bas). L'étoile sur la carte localise ma maison.

parameter		FCC-hh	HE-LHC	HL-LHC	LHC
collision energy cms [TeV]		100	27	14	14
dipole field [T]		16	16	8.33	8.33
circumference [km]		97.75	26.7	26.7	26.7
beam current [A]		0.5	1.12	1.12	0.58
bunch intensity [10^{11}]		1	1 (0.2)	2.2 (0.44)	1.15
bunch spacing [ns]		25	25 (5)	25	25
synchr. rad. power / ring [kW]		2400	101	7.3	3.6
SR power / length [W/m/ap.]		28.4	4.6	0.33	0.17
long. emit. damping time [h]		0.54	1.8	12.9	12.9
beta* [m]		1.1	0.3	0.25	0.20
normalized emittance [μm]		2.2 (0.4)	2.5 (0.5)	2.5	3.75
peak luminosity [$10^{34} \text{ cm}^{-2}\text{s}^{-1}$]		5	30	25	1
events/bunch crossing		170	1k (200)	~800 (160)	27
stored energy/beam [GJ]		8.4	1.3	0.7	0.36

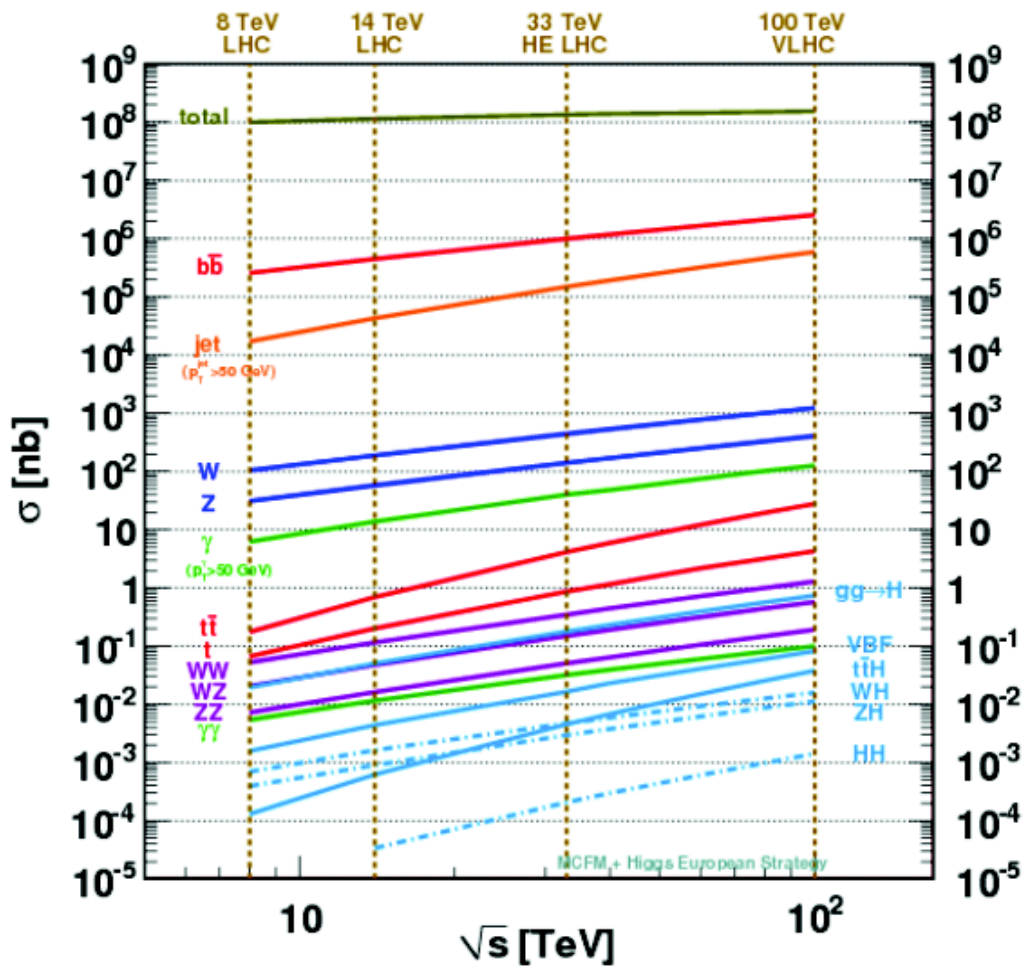


FIGURE 75 – Paramètres caractéristiques des futurs collisionneurs (haut), et section efficace des processus de physique les plus intéressants en fonction de l'énergie dans le centre de masse (bas).

Aujourd'hui, le projet le plus inspirant pour poursuivre des développements de trackers ambitieux est celui du FCC-hh, où un bruit d'empilement pouvant aller jusqu'à 1000 événements simultanés est attendu. La base de référence pour le tracker du FCC-hh [ref54] est un détecteur à modules inclinés dont la couverture en pseudo-rapacité est étendue jusqu'à $|\eta|=4$. La Figure 76 montre que les performances ne seront pas suffisantes, même en ajoutant un détecteur à haute résolution temporelle à l'avant, pour garantir des capacités de tracking raisonnables au-delà de $|\eta| = 3$. Dans cette région, en présence d'un bruit d'empilement d'une telle ampleur, la matière traversée dans le tube à vide et le très long bras de levier entre le point d'interaction et le premier point de mesure sont les principaux facteurs limitants. Une possibilité d'amélioration serait d'utiliser une paroi de tube à vide avec une surface ondulée [ref55], qui permettrait d'atténuer les effets de matière. Mais les matériaux et la technique de production restent encore à développer.

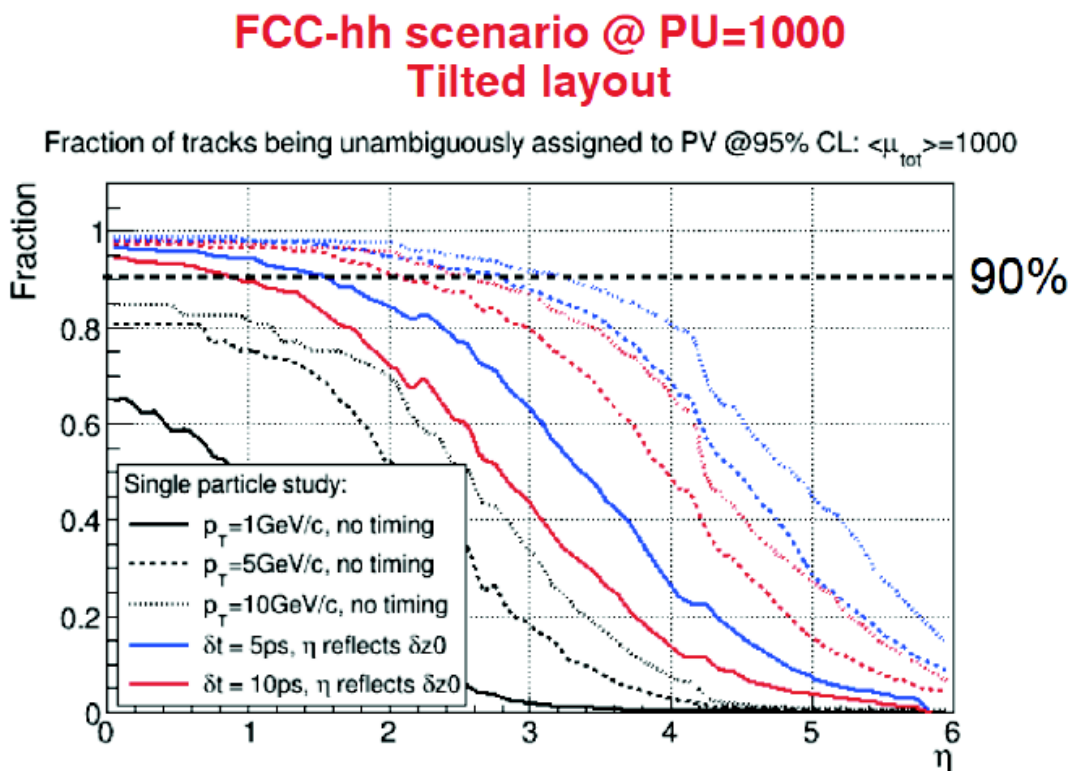


FIGURE 76 – Performances de tracking attendues au FCC-hh avec un bruit d'empilement moyen de 1000 événements. La limitation à grande pseudo-rapacité provient de la quantité de matière traversée par les particules dans la paroi du tube du faisceau, et de la trop grande distance d'extrapolation entre le point d'interaction et le premier point de mesure.

Une autre option serait de réduire le bras de levier. Lors des développements du détecteur alpin, Teodore Todorov avait proposé un concept de détecteur (un peu trop novateur) dans lequel trois couches de pixels sont placées dans le tube à vide [ref56]. A l'image du tracker VELO de l'expérience LHCb [ref57], le premier point de mesure pixel est situé à un rayon de 10mm du point d'interaction, ce qui réduit la distance d'extrapolation et mitige les effets de diffusion multiple dus à la matière du tube à vide pour les traces de grande pseudo-rapacité. Ce détecteur permet d'atteindre d'excellentes résolutions sur les paramètres des traces jusqu'à $|\eta| < 4$ (Figure 77).

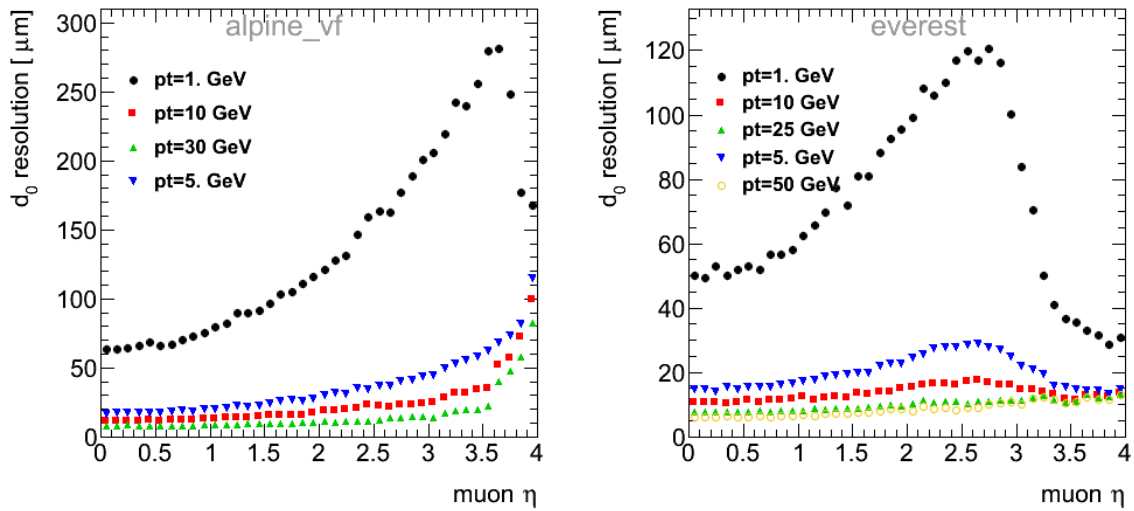


FIGURE 77 – Comparaison de la résolution sur le paramètre d'impact transverse obtenue avec le détecteur alpin développé pour le HL-LHC (gauche) et le projet de détecteur EVEReST (droite). Les 3 couches de pixels situées dans le tube à vide permettent de conserver une résolution de l'ordre de $20 \mu\text{m}$ sur tout le spectre en pseudo-rapidité, jusqu'à $\eta=4$ (Résultats obtenus en simulations paramétriques et sans bruit d'empilement).

Techniquement, ce concept nécessite de lever un certain nombre de verrous technologiques. En premier lieu, il impose de développer une électronique de lecture capable de tenir un niveau de radiation au moins 600 fois supérieur à celui du LHC [ref58]. Mécaniquement, ces trois couches de pixels devront être rétractables pour ne pas être endommagées lors de la préparation du faisceau (scrubbing). Le refroidissement de l'électronique devra être réalisé par un système de *micro-channels* [ref59] pour des raisons évidentes de limitation de l'espace et de la quantité de matière. Enfin, le détecteur devra être encapsulé dans une enceinte à vide secondaire pour ne pas risquer de compromettre le vide poussé nécessaire à une durée de vie suffisante des faisceaux. Cette paroi pourrait en revanche être bien plus fine que celle du vrai tube à vide pour limiter l'effet de diffusion multiple. Une ébauche d'un tel détecteur, baptisé EVEReST¹⁴, est présentée sur la Figure 78. Peut-être que cette idée, la dernière de Theodore Todorov, servira un jour pour concevoir les détecteurs de traces auprès des accélérateurs du futur.

14. Extended Vacuum-Embedded Retractable Silicon Tracker

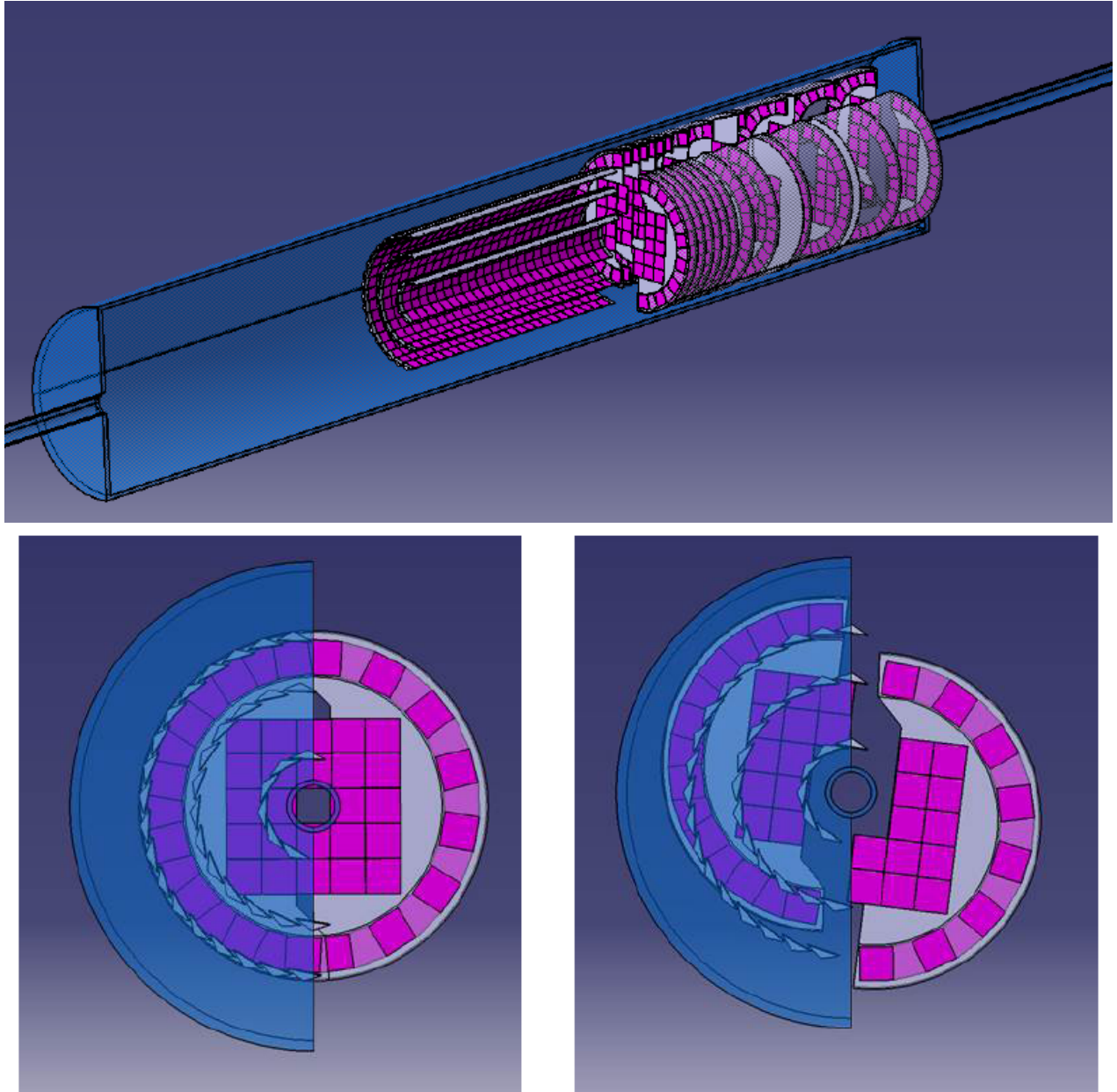


FIGURE 78 – Premières études en CAO CATIA du projet de détecteur à pixels EVEReST, proposé par le LAPP en 2014 pour le HL-LHC. Crédit : Nicolas Geffroy.

Remerciements

Le travail présenté dans ce mémoire n'aurait jamais vu le jour sans les contributions techniques et l'enthousiasme de mes nombreux collègues et des étudiants que j'ai eu la chance d'encadrer. Au sein d'une collaboration de plus de 3000 personnes, il n'est évidemment pas possible de citer tous les noms. Je vais donc me contenter de décerner quelques mentions spéciales.

- Jean-Baptiste de Vivie, sans lequel je n'aurais probablement jamais pu finir ma thèse. Thèse qui avait pour objet, rappelons-le, d'évaluer la probabilité d'observation d'une particule hypothétique dans un canal impensable à l'aide d'un détecteur pas encore construit. La motivation et la combativité n'étaient pas tous les jours au rendez-vous. Mais grâce à Jean-Baptiste et son optimisme indéfectible, j'ai pu surmonter cette difficile épreuve, la première dans le long parcours du chercheur : "Non mais regarde, c'est beaucoup mieux, on a progressé. Il ne reste plus qu'à réduire le bruit de fond d'un facteur 600."
- Emmanuel Monnier, qui a su déceler dans la salle de contrôle d'ATLAS l'un de mes talents cachés, le plantage systématique de la DAQ, et mettre à profit ce talent pour le développement du système de monitoring online le plus robuste de toute l'expérience ATLAS.
- Benjamin Trocmé, mon binôme de 4 années fantastiques entièrement vouées au monitoring et au contrôle qualité du calorimètre à argon liquide, alors que l'intitulé de la tâche ne laissait a priori que moyennement rêveur. Et merci pour l'écriture (en quasi-totalité) du papier [pub1]
- Elisabeth Petit, ma première étudiante de M2, dont l'esprit critique et affûté m'a permis très tôt d'affirmer mes choix d'orientations scientifiques. On notera cependant que mon tout premier sujet de stage, certes un peu austère (Mesurer zéro dans un calorimètre vide...), a quand même servi dans 3 publications [pub3][pub4] [pub12], puis de base pour une thèse sur la première observation du boson W dans l'expérience ATLAS [ref9], et représente surtout le point de départ d'une amitié et d'une collaboration scientifique de plus de 10 ans.
- Theodore Todorov, physicien et alpiniste, avec qui j'avais prévu de tout apprendre sur la conception et la construction des détecteurs de traces, parti beaucoup trop tôt. Teddy a quand même eu le temps de me transmettre son enthousiasme pour le projet Alpin. Un projet peu dingue, complètement outsider, et a priori désespéré à défendre dans une collaboration relativement hostile. Mais on a gagné Teddy : ton détecteur est bien meilleur que celui des américains.
- Sabine Elles et Rémi Lafaye, l'équipe de combat de choc avec armes de simulation massive, précurseuse du power-coding au LAPP, et sans laquelle le détecteur à modules pixels inclinés n'aurait jamais pu être choisi par la collaboration ATLAS [pub9].
- Nicolas Berger, pour me rappeler régulièrement à la physique, et nous concocter une "petite analyse maison" entièrement réalisée en famille [pub13].
- Toute l'équipe ITk du LAPP, ITAs, thésards, postdocs et physiciens, dans laquelle je puise une large part de mon énergie et de ma motivation pour faire avancer le projet quotidiennement.
- Et enfin, la Team des "Physiciens Montagnards" du CERN : Florian Bauer, Julien Morel, David d'Enterria et Henri Bachacou, pour mes plus belles ascensions alpines, mes plus beaux souvenirs de ski de rando, de pique-nique aux sommets et de galères en cordées.

Bibliographie

- [ref1] ATLAS Collaboration, *The ATLAS Experiment at the CERN Large Hadron Collider*, JINST **3** no. 08, (2008) S08003. <http://stacks.iop.org/1748-0221/3/i=08/a=S08003>.
- [ref2] L. Evans and P. Bryant, *LHC Machine*, JINST **3** (2008) S08001.
- [ref3] W. E. Cleland and E. G. Stern, *Signal processing considerations for liquid ionization calorimeters in a high rate environment*, Nucl. Instrum. Meth. **A338** no. 2-3, (1994) 467–497.
- [ref4] L. Helary, *Looking for Technicolor using ATLAS. Tools development and performances study of the Liquid Argon Calorimeter*. Theses, Université de Grenoble, Dec., 2011. <https://tel.archives-ouvertes.fr/tel-00673341>.
- [ref5] M. Aurousseau, *In-situ measurement of the electromagnetic calorimeter uniformity and search for the first di-photon events in ATLAS*. Theses, Université de Savoie, Sept., 2010. <https://tel.archives-ouvertes.fr/tel-00546713>.
- [ref6] S. Arfaoui, *Système haute-tension du calorimètre à argon liquide du détecteur ATLAS : mise en oeuvre, optimisation, et mesure de luminosité du LHC*. PhD thesis, 2011. <http://www.theses.fr/2011AIX22081/document>. Thèse de doctorat dirigé par Monnier, Emmanuel Instrumentation Aix-Marseille 2 2011.
- [ref7] C. press release, *CERN releases analysis of LHC incident*, <https://press.cern/press-releases/2008/10/cern-releases-analysis-lhc-incident>.
- [ref8] C. press release, *Two circulating beams bring first collisions in the LHC*, <https://press.cern/press-releases/2009/11/two-circulating-beams-bring-first-collisions-lhc>.
- [ref9] E. Petit, *Première mesure de section efficace de production du boson W et de son asymétrie de charge avec l'expérience ATLAS*. PhD thesis, 2011. <http://www.theses.fr/2011AIX22066/document>. Thèse de doctorat dirigée par Pralavorio, Pascal Physique des particules et astroparticules Aix- Marseille 2 2011.
- [ref10] F. Englert and R. Brout, *Broken Symmetry and the Mass of Gauge Vector Mesons*, Phys. Rev. Lett. **13** (1964) 321–323. [,157(1964)].
- [ref11] P. W. Higgs, *Broken Symmetries and the Masses of Gauge Bosons*, Phys. Rev. Lett. **13** (1964) 508–509. [,160(1964)].
- [ref12] A. Denner, S. Heinemeyer, I. Puljak, D. Rebuszi, and M. Spira, *Standard Model Higgs-Boson Branching Ratios with Uncertainties*, Eur. Phys. J. **C71** (2011) 1753, [arXiv:1107.5909](https://arxiv.org/abs/1107.5909) [hep-ph].
- [ref13] M. Schwoerer, *Etudes des états finals diphoton dans l'expérience ATLAS au LHC : mesure de section efficace différentielle, découverte d'une nouvelle résonance dans la recherche du boson de Higgs et étude de ses propriétés*. PhD thesis, 2013. <http://www.theses.fr/2013GRENY053>. Thèse de doctorat dirigé par Isabelle Wingerter Seez, Marco Delmastro et Jessica Levêque, Physique Subatomique et Astroparticules Grenoble 2013.
- [ref14] T. Binoth, J. P. Guillet, E. Pilon, and M. Werlen, *A Full next-to-leading order study of direct photon pair production in hadronic collisions*, Eur. Phys. J. **C16** (2000) 311–330, [arXiv:hep-ph/9911340](https://arxiv.org/abs/hep-ph/9911340) [hep-ph].
- [ref15] ATLAS Collaboration, G. Aad et al., *Measurement of the isolated di-photon cross-section in pp collisions at $\sqrt{s} = 7$ TeV with the ATLAS detector*, Phys. Rev. **D85** (2012) 012003, [arXiv:1107.0581](https://arxiv.org/abs/1107.0581) [hep-ex].
- [ref16] CMS Collaboration, S. Chatrchyan et al., *Measurement of the Production Cross Section for Pairs of Isolated Photons in pp collisions at $\sqrt{s} = 7$ TeV*, JHEP **01** (2012) 133, [arXiv:1110.6461](https://arxiv.org/abs/1110.6461) [hep-ex].

- [ref17] J. P. Guillet, *Photon production at hadronic colliders*,
<https://indico.cern.ch/event/91353/timetable/?print=1&view=standard>.
- [ref18] SM MC Working Group, SM and NLO MULTILEG Working Group Collaboration, J. Alcaraz Maestre et al., *The SM and NLO Multileg and SM MC Working Groups : Summary Report*, pp. , 165–178. 2012. arXiv:1203.6803 [hep-ph].
<https://inspirehep.net/record/1095506/files/arXiv:1203.6803.pdf>.
- [ref19] CMS Collaboration, S. Chatrchyan et al., *Measurement of differential cross sections for the production of a pair of isolated photons in pp collisions at $\sqrt{s} = 7$ TeV*, Eur. Phys. J. **C74** no. 11, (2014) 3129, arXiv:1405.7225 [hep-ex].
- [ref20] A. Collaboration, S. Gadatsch, and J. Wang, *Combined measurements of Higgs boson production and decay using up to 79.8 fb^{-1} of proton—proton collision data at $\sqrt{s} = 13$ TeV collected with the ATLAS experiment*, Tech. Rep. ATLAS-COM-CONF-2018-029, CERN, Geneva, Jun, 2018. <https://cds.cern.ch/record/2625365>.
- [ref21] LHC Higgs Cross Section Working Group Collaboration, J. R. Andersen et al., *Handbook of LHC Higgs Cross Sections : 3. Higgs Properties*, arXiv:1307.1347 [hep-ph].
- [ref22] M. Testa, A. Calandri, V. M. Walbrecht, S. Gadatsch, and S. Jezequel, *Impact of theory uncertainties related to Higgs boson production in the $H \rightarrow ZZ^* \rightarrow 4l$ and the $t\bar{t}H$ channels with the ATLAS detector at the HL-LHC*, Tech. Rep. ATL-COM-PHYS-2018-768, CERN, Geneva, Jun, 2018. <https://cds.cern.ch/record/2623685>.
- [ref23] DELPHI, OPAL, ALEPH, LEP Working Group for Higgs Boson Searches, L3 Collaboration, S. Schael et al., *Search for neutral MSSM Higgs bosons at LEP*, Eur. Phys. J. **C47** (2006) 547–587, arXiv:hep-ex/0602042 [hep-ex].
- [ref24] OPAL, DELPHI, LEP Working Group for Higgs boson searches, ALEPH, L3 Collaboration, R. Barate et al., *Search for the standard model Higgs boson at LEP*, Phys. Lett. **B565** (2003) 61–75, arXiv:hep-ex/0306033 [hep-ex].
- [ref25] ATLAS Collaboration, *Search for Scalar Diphoton Resonances in the Mass Range 65 – 600 GeV with the ATLAS Detector in pp Collision Data at $\sqrt{s} = 8$ TeV*, tech. rep.
<http://atlas.web.cern.ch/Atlas/GROUPS/PHYSICS/PAPERS/HIGG-2014-04/>. Analysis supporting material.
- [ref26] ATLAS Collaboration Collaboration, *Search for scalar diphoton resonances with 15.4 fb^{-1} of data collected at $\sqrt{s}=13$ TeV in 2015 and 2016 with the ATLAS detector*, Tech. Rep. ATLAS-CONF-2016-059, CERN, Geneva, Aug, 2016. <https://cds.cern.ch/record/2206154>.
- [ref27] A. Collaboration, *Search for resonances in the 65 to 110 GeV diphoton invariant mass range using 80 fb^{-1} of pp collisions collected at $\sqrt{s} = 13$ TeV with the ATLAS detector*, Tech. Rep. ATL-COM-PHYS-2018-504, CERN, Geneva, May, 2018.
<https://cds.cern.ch/record/2316944>.
- [ref28] ATLAS Collaboration Collaboration, A. Liss and J. Nielsen, *Physics at a High-Luminosity LHC with ATLAS*, Tech. Rep. ATL-PHYS-PUB-2013-007, CERN, Geneva, Jul, 2013.
<http://cds.cern.ch/record/1564937>.
- [ref29] T. Plehn, M. Spira, and P. M. Zerwas, *Pair production of neutral Higgs particles in gluon-gluon collisions*, Nucl. Phys. **B479** (1996) 46–64, arXiv:hep-ph/9603205 [hep-ph]. [Erratum : Nucl. Phys.B531,655(1998)].
- [ref30] A. K. Duncan, *Physics prospects at the HL-LHC with ATLAS*, PoS **FPCP2017** (2017) 044.
- [ref31] ATLAS Collaboration, M. S. Alam et al., *ATLAS pixel detector : Technical design report*,.

- [ref32] ATLAS Collaboration, M. Capeans, G. Darbo, K. Einsweiler, M. Elsing, T. Flick, M. Garcia-Sciveres, C. Gemme, H. Pernegger, O. Rohne, and R. Vuillermet, *ATLAS Insertable B-Layer Technical Design Report*,.
- [ref33] R. L. Gluckstern, *Uncertainties in track momentum and direction, due to multiple scattering and measurement errors*, Nucl. Instrum. Meth. **24** (1963) 381–389.
- [ref34] S. Haywood, *Impact Parameter Resolution in the Presence of Multiple- Scattering*,.
- [ref35] G. Beck and G. Viehhauser, *Analytic model of thermal runaway in silicon detectors*, Nuclear Instruments and Methods in Physics Research Section A: Accelerators, Spectrometers, Detectors and Associated Equipment **618** no. 1, (2010) 131 – 138.
<http://www.sciencedirect.com/science/article/pii/S0168900210005498>.
- [ref36] S. Vilalte, *MULTI-FLEX PROTOTYPE FOR THE LAYER 2 ATLAS ALPINE STAVES LAYOUT*, Research Report LAPP-TECH-2016-01, LAPP, June, 2016.
<http://hal.in2p3.fr/in2p3-01377767>.
- [ref37] Z. Zhang, *Optimisation de la performance thermique du détecteur Pixel Alpine*. PhD thesis, 2015. <http://www.theses.fr/2015GREAY071>. Thèse de doctorat dirigée par Lucia Di Ciaccio, Physique appliquée Grenoble Alpes 2015.
- [ref38] A. Clark et al., *ATLAS Phase II Letter of Intent : Backup Document*,.
- [ref39] *ECFA High Luminosity LHC Experiments Workshop : Physics and Technology Challenges. 94th Plenary ECFA meeting*,. <https://cds.cern.ch/record/1631032>.
- [ref40] CMS Collaboration Collaboration, *H to ZZ to 4l*, Tech. Rep. CMS-PAS-FTR-13-003, CERN, Geneva, 2013. <https://cds.cern.ch/record/1607076>.
- [ref41] S. McMahon, P. Allport, H. Hayward, and B. Di Girolamo, *Initial Design Report of the ITk : Initial Design Report of the ITk*, Tech. Rep. ATL-COM-UPGRADE-2014-029, CERN, Geneva, Oct, 2014. <https://cds.cern.ch/record/1952548>.
- [ref42] ATLAS Collaboration Collaboration, *ATLAS Phase-II Upgrade Scoping Document*, Tech. Rep. CERN-LHCC-2015-020. LHCC-G-166, CERN, Geneva, Sep, 2015.
<https://cds.cern.ch/record/2055248>.
- [ref43] N. Hessel, “Idres program.”.
- [ref44] J. Boudreau and V. Tsulaia, *The GeoModel Toolkit for Detector Description*,.
<https://cds.cern.ch/record/865601>.
- [ref45] GEANT4 Collaboration, S. Agostinelli et al., *GEANT4 : A Simulation toolkit*, Nucl. Instrum. Meth. **A506** (2003) 250–303.
- [ref46] A. Salzburger, S. Todorova, and M. Wolter, *The ATLAS Tracking Geometry Description*, Tech. Rep. ATL-SOFT-PUB-2007-004. ATL-COM-SOFT-2007-009, CERN, Geneva, Jun, 2007.
<https://cds.cern.ch/record/1038098>.
- [ref47] N. Calace and A. Salzburger, *ATLAS Tracking Detector Upgrade studies using the Fast Simulation Engine*, Journal of Physics : Conference Series **664** no. 7, (2015) 072005.
<http://stacks.iop.org/1742-6596/664/i=7/a=072005>.
- [ref48] “The virtual point 1 website.” <https://atlas-vp1.web.cern.ch/atlas-vp1/home/>.
- [ref49] N. Calace, G. Iacobucci, and A. Salzburger, *Jet Substructure Techniques for the Search of Diboson Resonances at the LHC and Performance Evaluation of the ATLAS Phase-II Inner Tracker Layouts*, May, 2018. <https://cds.cern.ch/record/2628351>.
- [ref50] *Design Considerations of Long Length Evaporative CO2 Cooling Lines.*, 2012.

- [ref51] L. Cheng, G. Ribatski, and J. Thome, *New prediction methods for CO₂ evaporation inside tubes : Part II - An updated general flow boiling heat transfer model based on flow patterns*, International Journal of Heat and Mass Transfer **51** (2008) 125–135.
- [ref52] *Modelling CO₂ cooling of the ATLAS ITk Pixel Detector*. PhD thesis.
- [ref53] A. Collaboration, *Technical Proposal : A High-Granularity Timing Detector for the ATLAS Phase-II Upgrade*, Tech. Rep. ATL-COM-LARG-2018-008, CERN, Geneva, Mar, 2018. <https://cds.cern.ch/record/2310228>. Draft of Technical Proposal for circulation to ATLAS.
- [ref54] W. Riegler, *Physics Perspectives for a Future Circular Collider : FCC-hh - Accelerator and Detectors*. ,. <https://cds.cern.ch/record/2288391>.
- [ref55] Z. Drasal, *CERN Detector Seminar : Status and Challenges of the Tracker Design for FCC-hh*, September, 2017. <https://indico.cern.ch/event/666204/>.
- [ref56] T. Todorov, *ATLAS Upgrade Week In Freiburg*, April, 2014. <https://indico.cern.ch/event/310352/>.
- [ref57] L. Collaboration, *LHCb VELO Upgrade Technical Design Report*, Tech. Rep. CERN-LHCC-2013-021. LHCB-TDR-013, Nov, 2013. <https://cds.cern.ch/record/1624070>.
- [ref58] M. C. Vignali, *Development of Silicon Detectors for Tracking and Timing within the RD50 Collaboratio*, April, 2018. <https://indico.cern.ch/event/656491/contributions/2918521/>.
- [ref59] S. T. Kadam and R. Kumar, *Twenty first century cooling solution : Microchannel heat sinks*, International Journal of Thermal Sciences **85** (2014) 73 – 92. <http://www.sciencedirect.com/science/article/pii/S129007291400163X>.
- [ref60] D. Aloni, K. Blum, A. Dery, A. Efrati, and Y. Nir, *On a possible large width 750 GeV diphoton resonance at ATLAS and CMS*, JHEP **08** (2016) 017, arXiv:1512.05778 [hep-ph].
- [ref61] C. ATLAS, *Letter of Intent for the Phase-II Upgrade of the ATLAS Experiment*, Tech. Rep. CERN-LHCC-2012-022. LHCC-I-023, CERN, Geneva, Dec, 2012. <https://cds.cern.ch/record/1502664>. Draft version for comments.
- [ref62] K. Edmonds, S. Fleischmann, T. Lenz, C. Magass, J. Mechnich, and A. Salzburger, *The Fast ATLAS Track Simulation (FATRAS)*, Tech. Rep. ATL-SOFT-PUB-2008-001. ATL-COM-SOFT-2008-002, CERN, Geneva, Mar, 2008. <http://cds.cern.ch/record/1091969>.

Publications

- [pub1] ATLAS Collaboration, *Monitoring and data quality assessment of the ATLAS liquid argon calorimeter*, JINST **9** (2014) P07024, arXiv:1405.3768 [hep-ex].
- [pub2] ATLAS Collaboration, *ATLAS Data Quality Operations in 2012*, Tech. Rep. ATL-COM-DAPR-2013-009, CERN, Geneva, Dec, 2013. Editors : J. Frost, J. Leveque, P. Onyisi.
- [pub3] ATLAS Collaboration, *Readiness of the ATLAS Liquid Argon Calorimeter for LHC Collisions*, Eur. Phys. J. **C70** (2010) 723–753, arXiv:0912.2642 [physics.ins-det].
- [pub4] ATLAS Collaboration, *Studies of the performance of the ATLAS detector using cosmic-ray muons*, Eur.Phys.J. **C71** (2011) 1593, arXiv:1011.6665 [physics.ins-det].
- [pub5] M. Delmastro, P. Iengo, J. Lévêque, and M. Schwoerer, $\Upsilon \rightarrow e^+e^-$ decays in the ATLAS experiment, Tech. Rep. ATL-PHYS-INT-2011-054, CERN, Geneva, Jun, 2011.
- [pub6] ATLAS Collaboration, *Observation of a new particle in the search for the Standard Model Higgs boson with the ATLAS detector at the LHC*, Phys.Lett. **B716** (2012) 1–29, arXiv:1207.7214 [hep-ex].
- [pub7] ATLAS Collaboration, *Measurements of Higgs boson production and couplings in diboson final states with the ATLAS detector at the LHC*, Phys.Lett. **B726** (2013) 88–119, arXiv:1307.1427 [hep-ex].
- [pub8] A. Collaboration, *Technical Design Report for the ATLAS Inner Tracker Strip Detector*, Tech. Rep. CERN-LHCC-2017-005. ATLAS-TDR-025, CERN, Geneva, Apr, 2017. <http://cds.cern.ch/record/2257755>.
- [pub9] A. Collaboration, *Technical Design Report for the ATLAS ITk Pixel Detector : Pixel TDR*, Tech. Rep. ATL-COM-UPGRADE-2017-020, CERN, Geneva, Nov, 2017. <https://cds.cern.ch/record/2293299>.
- [pub10] ATLAS Collaboration, *ATLAS Large eta task force report*, Tech. Rep. ATL-UPGRADE-INT-2015-001, CERN, Geneva, May, 2015. <https://cds.cern.ch/record/2020591>.
- [pub11] A. Salzburger et al., *Final Report of the ITk Layout Task Force*, Tech. Rep. ATL-COM-UPGRADE-2016-042, CERN, Geneva, Dec, 2016. <https://cds.cern.ch/record/2239573>.
- [pub12] M. Cooke, P. S. Mangear, M. Plamondon, M. Aleksa, M. Delmastro, L. Fayard, S. Henrot-Versillé, F. Hubaut, R. Lafaye, W. Lampl, J. Levêque, H. Ma, E. Monnier, J. Parsons, P. Pralavorio, P. Schwemling, L. Serin, B. Trocmé, G. Unal, M. Vinciter, and H. Wilkens, *In situ commissioning of the ATLAS electromagnetic calorimeter with cosmic muons*, tech. rep., 2007.
- [pub13] ATLAS Collaboration, *Search for Scalar Diphoton Resonances in the Mass Range 65 – 600 GeV with the ATLAS Detector in pp Collision Data at $\sqrt{s} = 8$ TeV*, Phys.Rev.Lett. **113** no. 17, (2014) 171801, arXiv:1407.6583 [hep-ex].
- [pub14] ATLAS Collaboration, *Expected Performance of the ATLAS Inner Tracker at the High-Luminosity LHC*, Tech. Rep. ATL-PHYS-PUB-2016-025, CERN, Geneva, Oct, 2016. <https://cds.cern.ch/record/2222304>.
- [pub15] ATLAS Collaboration, *Measurement of isolated-photon pair production in pp collisions at $\sqrt{s}=7$ TeV with the ATLAS detector*, Journal of High Energy Physics **2013** no. 1, (2013) 86. [https://doi.org/10.1007/JHEP01\(2013\)086](https://doi.org/10.1007/JHEP01(2013)086).

- [pub16] ATLAS Collaboration, *Performance of the ATLAS Detector using First Collision Data*, JHEP **09** (2010) 056, [arXiv:1005.5254](#) [[hep-ex](#)].
- [pub17] DØ Collaboration, *Model-independent measurement of the W boson helicity in top quark decays at $D0$* , Phys.Rev.Lett. **100** (2008) 062004, [arXiv:0711.0032](#) [[hep-ex](#)].
- [pub18] DØ Collaboration, V. Abazov et al., *Measurement of the $t\bar{t}$ production cross-section in $p\bar{p}$ collisions using dilepton events*, Phys.Rev. **D76** (2007) 052006, [arXiv:0706.0458](#) [[hep-ex](#)].
- [pub19] CDF and D0 Collaboration, J. Leveque, *Measurement of top quark properties at the Tevatron*, [arXiv:hep-ex/0607005](#) [[hep-ex](#)].

Annexes : publications choisies

Monitoring and data quality assessment of the ATLAS liquid argon calorimeter

The ATLAS Collaboration

ABSTRACT: The liquid argon calorimeter is a key component of the ATLAS detector installed at the CERN Large Hadron Collider. The primary purpose of this calorimeter is the measurement of electron and photon kinematic properties. It also provides a crucial input for measuring jets and missing transverse momentum. An advanced data monitoring procedure was designed to quickly identify issues that would affect detector performance and ensure that only the best quality data are used for physics analysis. This article presents the validation procedure developed during the 2011 and 2012 LHC data-taking periods, in which more than 98% of the proton–proton luminosity recorded by ATLAS at a centre-of-mass energy of 7–8 TeV had calorimeter data quality suitable for physics analysis.

KEYWORDS: Calorimeters, Performance of High Energy Physics Detectors, Data processing methods.

Contents

1. Introduction	2
2. Data quality assessment operations and infrastructure	4
2.1 Online monitoring	4
2.2 Relevant aspects of LHC and ATLAS trigger operations	4
2.3 Practical implementation of the data quality assessment	6
2.4 Data quality logging	7
3. Detector conditions	8
3.1 Detector control system infrastructure	8
3.2 Monitoring of high-voltage conditions	9
3.3 Validation of data taken during the ramp-up procedure	10
3.4 Monitoring of coverage	11
3.5 Associated data rejection in 2012	12
4. Data integrity and online processing	13
4.1 Basic data integrity	14
4.2 Online computation accuracy	15
4.3 Missing condition data	16
4.4 Associated data rejection in 2012	17
5. Calorimeter synchronization	18
5.1 Global synchronization	18
5.2 Synchronization at front-end board level	19
6. Treatment of large-scale coherent noise	21
6.1 Description of the pathology	21
6.2 Use of the quality factor for noise identification	23
6.3 Time duration of the pathology	23
6.4 Time-window veto procedure	24
6.5 Luminosity dependence	26
6.6 Associated data rejection in 2012	26
7. Treatment of per-channel noise	28
7.1 Regular calibration procedure	28
7.2 Monitoring of Gaussian noise during collision runs	29
7.3 Monitoring of non-Gaussian noise during collision runs	29
7.4 Proportion of masked cells	33
7.5 Associated data rejection in 2012	34

8. Achieved performance and outlook	34
8.1 Performance in proton–proton collision run (2011–2012)	34
8.2 Performance in lead–lead and lead–proton collision run (2011–2013)	36
8.3 Outlook	36

1. Introduction

The ATLAS liquid argon calorimeter (LAr calorimeter) was designed to measure accurately electron and photon properties in a wide pseudorapidity (η) region,¹ $|\eta| < 2.5$. It also significantly contributes to the performance of jet and missing transverse momentum measurements (E_T^{miss}) in the extended pseudorapidity range $|\eta| < 4.9$. This detector played a key role in the discovery of the Higgs boson [1].

Figure 1(a) shows the LAr calorimeter, which consists of four distinct sampling calorimeters [2, 3], all using liquid argon as the active medium. The electromagnetic barrel (EMB) and endcaps (EMEC) use lead as the passive material, arranged in an accordion geometry. This detector geometry allows a fast and azimuthally uniform response as well as a coverage without instrumentation gap. The electromagnetic calorimeters cover the pseudorapidity region $|\eta| < 3.2$ and are segmented into layers (three in the range $|\eta| < 2.5$, two elsewhere) to observe the longitudinal development of the shower and determine its direction. Furthermore, in the region $|\eta| < 1.8$ the electromagnetic calorimeters are complemented by a presampler, an instrumented argon layer that provides information on the energy lost in front of the electromagnetic calorimeters. For the hadronic endcaps (HEC) covering the pseudorapidity range $1.5 < |\eta| < 3.2$, copper was chosen as the passive material and a parallel plate geometry was adopted. For the forward calorimeter (FCal), located at small polar angles where the particle flux is much higher and the radiation damage can be significant, a geometry based on cylindrical electrodes with thin liquid argon gaps was adopted. Copper and tungsten are used as passive material. The hadronic and forward calorimeters are also segmented in depth into four and three layers respectively. The four detectors are housed inside three cryostats (one barrel and two endcaps) filled with liquid argon and kept at a temperature of approximately 88 K. Each detector part is referred to as a *partition* named EMB, EMEC, HEC and FCal with an additional letter, C or A, to distinguish the negative and positive pseudorapidity regions respectively.² Hence, there are eight different partitions.

Although each detector has its own characteristics in terms of passive material and geometry, a special effort was made to design uniform readout, calibration and monitoring systems across the eight partitions. The 182468 calorimeter channels are read out by 1524 front-end boards (FEBs) [4, 5] hosted in electronics crates located on the three cryostats. These FEBs shape the signal and

¹ATLAS uses a right-handed coordinate system with its origin at the nominal interaction point (IP) in the centre of the detector and the z -axis along the beam pipe. The x -axis points from the IP to the centre of the LHC ring, and the y -axis points upward. Cylindrical coordinates (r, ϕ) are used in the transverse plane, ϕ being the azimuthal angle around the beam pipe. The pseudorapidity is defined in terms of the polar angle θ as $\eta = -\text{Ln} \tan(\theta/2)$.

²The barrel is made of two halves housed in the same cryostat.

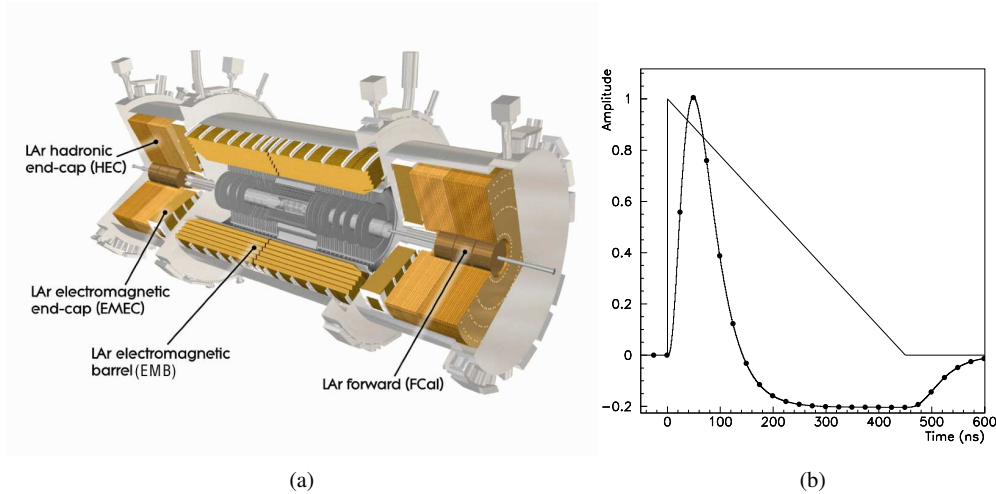


Figure 1: (a) Cut-away view of the liquid argon calorimeter. (b) Signal shape as produced in the electromagnetic barrel (triangle), and after shaping (curve with dots). The dots represent the time and amplitude of the digitized samples.

send the digitized samples via optical links to 192 processing boards (named “RODs” for read-out drivers) [6] that compute the deposited energies before passing them to the central data-acquisition system. The signal shapes before and after the FEB shaping are shown in Figure 1(b).

This article describes the data quality assessment procedure applied to ensure optimal calorimeter performance together with low data rejection, emphasizing the performance achieved in 2012, when 21.3 fb^{-1} of proton–proton collisions were recorded by the ATLAS experiment. The integrated luminosity is derived, following the same methodology as that detailed in reference [7], from a preliminary calibration of the luminosity scale derived from beam-separation scans performed in November 2012. This dataset is divided into ten time periods within which data-taking conditions were approximately uniform: the characteristics of these periods are summarized in table 1. The dataset is also divided into *runs* that correspond to a period of a few hours of data taking (up to 24 hours depending on the LHC beam lifetime and the ATLAS data-taking performance). Each run is divided into one-minute blocks (periods known as luminosity blocks).

The article is organized as follows: the ATLAS data processing organization and data quality assessment infrastructure are described in section 2. Sections 3–7 detail the specific LAr calorimeter procedures developed to assess the data quality in all aspects: detector conditions (section 3), data integrity (section 4), synchronization (section 5), large-scale coherent noise (section 6) and isolated pathological cells (section 7). For each aspect of the data quality assessment, the amount of rejected data is presented chronologically as a function of data-taking period. For illustration purposes, the ATLAS run 205071 from June 2012 is often used. With 226 pb^{-1} accumulated in 18 hours of the LHC collisions period (“fill”) number 2736, it is the ATLAS run with the highest integrated luminosity. Finally, section 8 recaps the data quality performance achieved in 2011 and 2012, and provides a projection towards the higher energy and luminosity conditions scheduled for the LHC restart in 2015.

Table 1: Characteristics of the ten data-taking periods defined in 2012. The F and K periods not considered in this article correspond to data taking without LHC collisions, and are hence not relevant for data quality assessment.

2012 data-taking periods	A	B	C	D	E	G	H	I	J	L
Start date (day/month)	4/4	1/5	1/7	24/7	23/8	26/9	13/10	26/10	2/11	30/11
Integrated luminosity recorded (fb^{-1})	0.84	5.30	1.54	3.37	2.70	1.30	1.56	1.06	2.72	0.89
Peak luminosity ($10^{33}\text{cm}^{-2}\text{s}^{-1}$)	5.5	6.7	6.2	7.3	7.6	7.3	7.5	7.3	7.4	7.5
Mean instantaneous luminosity ($10^{33}\text{cm}^{-2}\text{s}^{-1}$)	2.0	3.6	2.9	3.8	4.2	4.0	4.3	4.4	4.2	4.3

2. Data quality assessment operations and infrastructure

The ATLAS data are monitored at several stages of the acquisition and processing chain to detect as early as possible any problem that could compromise their quality. Most of the monitoring infrastructure is common to both the online and offline environments, but the levels of details in the monitoring procedure evolve with the refinement of the analysis (from online to offline).

2.1 Online monitoring

During data taking, a first and very crude quality assessment is performed in real time on a limited data sample by detector personnel called *shifters* in the ATLAS control room. The shifters focus on problems that would compromise the data quality without any hope of improving it later, such as serious data corruption or a significant desynchronization. During data taking, tracking the calorimeter noise is not considered a priority as long as the trigger rates remain under control. The trigger rates are checked by a dedicated trigger shifter who can decide, if needed, to take appropriate action. This may consist of either simply ignoring the information from a noisy region of typical size $\Delta\phi \times \Delta\eta = 0.1 \times 0.1$ or setting an appropriate prescale factor for the trigger item saturating the bandwidth (see next section for more details of the trigger system).

To assess the data quality of the ongoing run, the ATLAS control room shifters run simple algorithms to check the content of selected histograms, and the results are displayed using appropriate tools [8]. Even though the running conditions are constantly logged in a dedicated electronic logbook [9], no firm data quality information is logged at this point by the shifters.

2.2 Relevant aspects of LHC and ATLAS trigger operations

The LHC is designed to contain trains of proton bunches separated by 25 ns [10]. The corresponding 25 ns time window, centred at the passage time of the centre of the proton bunch at the interaction point, defines a bunch crossing. The nominal LHC configuration for proton–proton collisions contains 3564 bunch crossings per revolution, each of which is given a unique bunch crossing identifier (BCID). However, not all BCIDs correspond to bunches filled with protons. The

filling is done in bunch trains, containing a number of equally spaced bunches. Between the trains, short gaps are left for the injection kicker and a longer gap occurs for the abort kicker. A configuration frequently used in 2012 consists of a mixture of 72- and 144-bunch trains (typically a dozen) with a bunch spacing of 50 ns for a total of 1368 bunches. Each train therefore lasts 3.6–7.2 μ s, and two trains are spaced in time by between 600 ns and 1 μ s. The BCIDs are classified into bunch groups by the ATLAS data-acquisition system [11]. The bunch groups of interest for this article are

- *filled bunch group*: a bunch in both LHC beams;
- *empty bunch group*: no proton bunch.

In the configuration widely used in 2012, the empty bunch group consisted of 390 BCIDs, roughly three times less than the filled bunch group (1368 BCIDs). As the average electron drift time in the liquid argon (of the order of several hundreds nanoseconds) is longer than the time between two filled bunches, the calorimeter response is sensitive to collision activity in bunch crossings before and after the BCID of interest. These unwanted effects are known as out-of-time pile-up. To limit its impact, the BCIDs near a filled BCID (within six BCIDs) are excluded from the empty bunch group.

The ATLAS trigger system consists of three successive levels of decision [12–14]. A *trigger chain* describes the three successive trigger items which trigger the writing of an event on disk storage. The ATLAS data are organized in *streams*, defined by a trigger menu that is a collection of trigger chains. The streams are divided into two categories: calibration streams and physics streams. The calibration streams are designed to provide detailed information about the run conditions (luminosity, pile-up, electronics noise, vertex position, etc.) and are also used to monitor all the detector components while the physics streams contain events that are potentially interesting for physics analysis.

In the case of the LAr calorimeter, four main calibration streams are considered for the data quality assessment.

- The *Express* stream contains a fraction of the data (around 2–3% of the total in 2012) representative of the most common trigger chains used during collision runs; almost all of these trigger chains are confined to the filled bunch group.
- The *CosmicCalo* stream contains events triggered in the empty bunch group, where no collisions are expected.
- The *LArCells* stream contains partially built collision events [15], where only a fraction of the LAr data are stored (the cells belonging to a high-energy deposit as identified by the second level of the trigger system). The reduced event size allows looser trigger conditions and significantly more events in the data sample.
- The *LArCellsEmpty* stream benefits from the same “partial event building” facility as the *LArCells* stream, and the trigger is restricted to the empty bunch group.

The *CosmicCalo*, *LArCellsEmpty* and *LArCells* streams mainly contain trigger chains requesting a large energy deposit in the calorimeters.

Several physics streams are also mentioned in this article. The *JetTauEtmis* stream is defined

to contain collision events with jets of large transverse momentum, τ lepton candidates or large missing transverse momentum. The *EGamma* stream is defined to contain collision events with electron or photon candidates.

The LAr calorimeter data quality assessment procedure is meant to identify several sources of potential problems and to address solutions. The calibration streams containing collision events (Express and LArCells streams) are used to identify data corruption issues, timing misalignments and large coherent noise. The CosmicCalo and LArCellsEmpty streams, filled with events triggered in the empty bunch group, are used to identify isolated noisy cells.

The LAr calorimeter data quality assessment procedure is not meant to monitor higher-level objects (such as electron/photon, J/ψ candidates, etc.) and their characteristics (uniformity, calibration, mass, etc.): this task is performed in a different context and is beyond the scope of this article.

2.3 Practical implementation of the data quality assessment

A graphical view of the ATLAS data processing organization is shown in figure 2. Since the information provided by the calibration streams is necessary to reconstruct the physics data, the calibration streams are promptly processed during the *express processing* which is launched shortly after the beginning of a run. The data are processed with the ATLAS Athena software on the

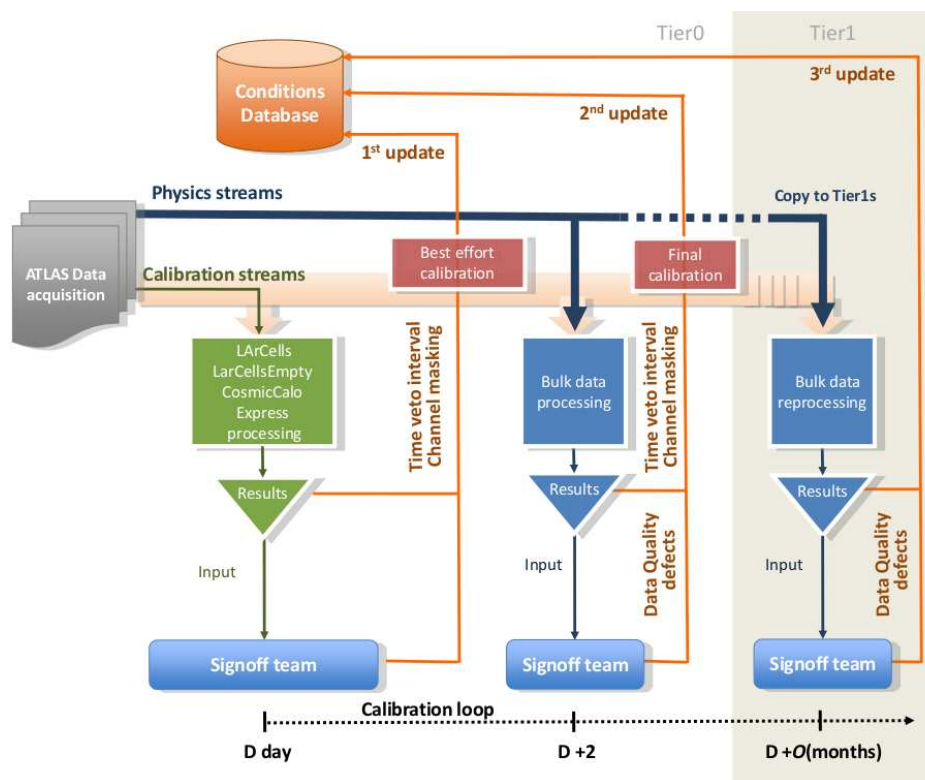


Figure 2: ATLAS data processing and monitoring organization and calibration loop scheme (with focus on the LAr calorimeter case).

CERN computing farms [16], either the Grid Tier 0 farm or the Calibration and Alignment Facility (CAF) farm [17]. The monitoring histograms are produced at the same time within the Athena monitoring framework and then post-processed with dedicated algorithms to extract data quality information. The data quality results are available through a central ATLAS web site [18] for all the ATLAS subdetectors. A first data quality assessment is performed at this stage. The conditions databases [19] which store the complete picture of the detector status and the calibration constants as a function of time are also updated. These tasks are completed within 48 hours after the end of the run, before the start of the physics stream reconstruction. The 48-hour period for this primary data quality review is called the *calibration loop*.

Given the complexity of the checks to be completed over the 182468 calorimeter cells, a dedicated web infrastructure was designed. It enables quick extraction and summarization of meaningful information and optimization of data quality actions such as the automated production of database updates. Despite the high level of automation of the LAr calorimeter data quality procedure, additional supervision by trained people remains mandatory. In 2011 and 2012, people were assigned during daytime hours, seven days per week, to assess the relevance of the automatically proposed actions. These one or two people are referred to as the *signoff team*.

Once the database conditions are up-to-date and the 48-hour period completes, the processing of all the physics streams (also called *the bulk*) is launched. Typically, the complete dataset is available after a couple of days, and a final data quality assessment is performed to check if the problems first observed during the calibration loop were properly fixed by the conditions updates. If the result of the bulk processing is found to be imperfect, further database updates may be needed. However, such new conditions data are not taken into account until the next data reprocessing, which may happen several months later. The final data quality assessment for the bulk processing is done using exactly the same web infrastructure as for the primary data quality assessment with the express processing.

2.4 Data quality logging

At each stage, any problem affecting the data quality is logged in a dedicated database. The most convenient and flexible way to document the data losses consists of assigning a *defect* [20] to a luminosity block. Approximately 150 types of defects were defined to cover all the problems observed in the LAr calorimeter during the 2011 and 2012 data taking. These defects can be either global (i.e. affecting the whole calorimeter) or limited to one of the eight partitions. A defect can either be *intolerable*, implying a systematic rejection of the affected luminosity block, or *tolerable*, and mainly set for bookkeeping while the data are still suitable for physics analysis.

The defects are used to produce a list of luminosity blocks and runs that are declared as “good” for further analysis. This infrastructure is powerful, as it permits precise description and easy monitoring of the sources of data loss; it is also flexible, since a new list of good luminosity blocks and runs can be produced immediately after a defect is changed. However, since the smallest time granularity available to reject a sequence of data is the luminosity block, the infrastructure is not optimized to deal with problems much shorter than the average luminosity block length (i.e. one minute).

To reduce the data losses due to problems lasting much less than a minute, a complementary method that stores a status word in each event’s header block allows event-by-event data rejection.

In order not to bias the luminosity computation, small time periods are rejected rather than isolated events. This *time-window veto* procedure allows the vetoed interval to be treated like another source of data loss: the corresponding luminosity loss can be accurately estimated and accounted for in physics analyses. The time periods to be vetoed are defined in a standard ATLAS database before the start of the bulk processing. The database information is read back during the Tier 0 processing, and the status word is filled for all events falling inside the faulty time window. Since this information must be embedded in all the derived analysis files, the database conditions required to fill this status word must be defined prior to the start of bulk reconstruction, i.e. during the calibration loop. In that sense, the status word is less flexible than the defect approach, but it can reject very small periods of data.

3. Detector conditions

Stable operation in terms of detector safety, powering and readout is essential for ensuring high quality of data. Information about the detector conditions is provided by both the ATLAS Detector Control System (DCS) [21] and the Tier 0 processing output.

3.1 Detector control system infrastructure

The ATLAS DCS system provides a *state* and a *status* word per partition: the state reflects the present conditions of a partition (“Ready”, “Not_Ready”, “Unknown”, “Dead”), while the status is used to flag errors (“OK”, “Warning”, “Error”, “Fatal”). The state/status words are stored in a database and used by the ATLAS DCS data quality calculator [22] to derive an overall DCS data quality flag that is specific to the LAr calorimeter for each luminosity block and is represented by a colour. The condition assigned to each luminosity block is based on the worst problem affecting the data during the corresponding time interval, even if the problem lasted for a very short time. Table 2 summarises the policy used to derive the LAr calorimeter DCS data quality flags. The colour hierarchy is the following with increasing severity: green – amber – grey – red.

The DCS system allows the masking of known problems to avoid continuous state/status errors, as this would prevent the shifter from spotting new problems during data taking. Therefore, a *green* flag does not always mean that the LAr calorimeter is in an optimal state. A green flag ensures that the detector conditions from the DCS point of view remain uniform during a run, since no new problem masking is expected during data taking.

Table 2: Assignment policy for LAr calorimeter DCS data quality flag.

State	Status	DCS flag	Possible source of problem
Ready	OK	Green	-
Unknown Dead	Warning, Error	Amber	Loss of communication
Not_Ready	Warning, Error, Fatal	Red	Power supply trip
Anything else	Anything else	Grey	Corrupted/missing data in DCS database

There is no defect automatically derived from the DCS flag. However, the signoff team is expected to understand any DCS flag differing from green and cross-check with other sources, such as the monitoring algorithm and operation reports. For the period 2010–2012, the main source of abnormal DCS flags was high-voltage power supply trips.

3.2 Monitoring of high-voltage conditions

The high voltage (HV) – applied for charge collection on the active liquid argon gaps of the calorimeter – is distributed among 3520 sectors of typical size $\Delta\eta \times \Delta\phi = 0.2 \times 0.2$ (in the three layers of the electromagnetic calorimeters) [3]. Each sector is supplied by two or four independent HV lines in a redundant scheme. Because the HV conditions impact the amount of signal collected by the electrodes, and therefore are a crucial input for the energy computation, they are constantly monitored online, and stored in a dedicated conditions database. The HV values are written every minute or every time a sizeable variation (greater than 5 V) is observed.

The most common issue encountered during data taking is a trip of one HV line, i.e. a sudden drop of voltage due to a current spike. When a current spike occurs, the HV module automatically reduces the voltage in that sector. The HV line is usually ramped up automatically directly afterwards. If the automatic ramp-up procedure fails (or before automatic ramping was used, e.g. early 2011), the HV line can either be ramped up manually or left at zero voltage until the end of the run; in the latter case, thanks to the redundant HV supply, the affected regions remain functional although with a worse signal/noise ratio. During data acquisition, the calibration factors associated with the HV settings are stored in registers of the ROD boards [6] and cannot be changed without a run stop; therefore they remain constant during a run, even if the effective HV value changes. As reduced HV settings induce a reduced electron drift speed, the energy computed online is underestimated and impacts the trigger efficiency near the trigger threshold. Given the limited size of a sector and the rare occurrence of such a configuration, this had a negligible impact. As previously described, the HV trips are recorded by the DCS data quality flag, but a dedicated HV database including all the trip characteristics is also filled daily by an automated procedure.

During the offline Tier 0 reconstruction, a correction factor is automatically applied by the reconstruction software based on the HV reading. A variation of HV conditions also requires an update of the expected noise per cell, which has to be corrected in the same way as the energy in order not to bias the clustering mechanism. Due to the data reconstruction model, this update cannot be automated and requires human intervention within the 48-hour calibration loop delay.

The data quality assessment makes use of the three different sources of information (DCS flags, HV database and offline HV correction monitoring) to get a consistent picture of the HV conditions during a run. During a trip, the HV, and therefore the energy scale, vary too quickly to be accurately assessed. In addition, the luminosity block in which the trip happened is usually affected by a large burst of coherent noise (see section 6) and is hence unusable for physics. Therefore, the luminosity blocks where a HV drop occurred are systematically rejected by marking an intolerable defect. The policy regarding luminosity blocks with HV ramp-up has evolved over time. Initially rejected, these periods are now corrected offline with the proper HV values and marked with a tolerable defect, after a careful check of the noise behaviour. The studies performed on data with HV ramping are detailed in section 3.3.

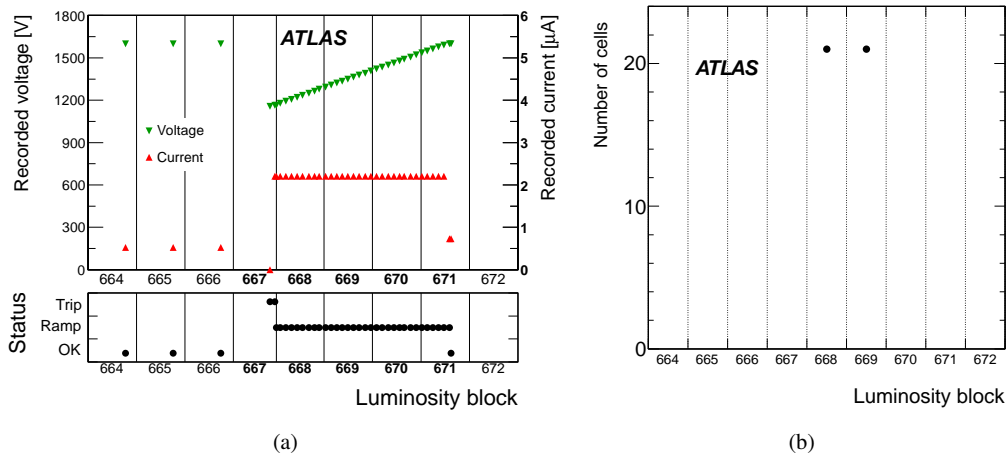


Figure 3: Example of a typical trip of a HV line supplying one HEC sector. (a) Recorded voltage, current and status evolution. The luminosity block numbers shown in bold indicate a red DCS flag. (b) Number of readout cells with a HV correction greater than 5% (with respect to the start of run) as a function of the luminosity block number.

The DCS information about a typical trip of a HV line supplying one hadronic calorimeter sector is shown in figure 3(a). A voltage drop of 500 V (from 1600 V down to 1100 V) is observed in luminosity block 667. The high-voltage was then automatically ramped up at a rate of 2 V/s, lasting approximately four minutes. The nominal HV value was recovered during luminosity block 671. The DCS flag is red for five luminosity blocks 667–671, which is consistent with the error status bit also displayed in figure 3(a) for this interval. Figure 3(b) shows the corresponding offline monitoring plot for the same HV trip, displaying how many calorimeter cells have a HV correction factor greater than 5% at the beginning of the luminosity block. Only two luminosity blocks are identified: 668 and 669.³ Based on this consistent information, the luminosity block 667 was marked with an intolerable defect. The luminosity block range 668–671 when the ramping voltage occurred was marked with a tolerable defect.

3.3 Validation of data taken during the ramp-up procedure

As already mentioned, the offline software takes into account the effective HV settings to correct the energy. The electronics noise correction is estimated at the beginning of the ramp-up period, and considered constant until the voltage is stable again. As the noise correction factor is maximal at the start of the ramp-up period, this means that during this short time, the electronics noise is slightly overestimated, inducing a negligible bias in the clustering algorithm. The reconstruction software therefore appears to cope well with HV channel variations. However, before declaring the ramping HV data as good for physics, a further check is performed to detect any non-Gaussian noise behaviour that could be induced by the ramping operations.

³The correction factors depend nonlinearly on the voltage and in this case are smaller than the relative voltage change.

All the 2011 collision data containing luminosity blocks affected by a HV trip or a ramp-up were considered for this study. A search for a potential noise excess was performed on the JetTauEtmiss stream data by considering the missing transverse momentum distributions computed in luminosity blocks with different HV conditions (trip, ramping up, stable). In figure 4(a), a clear noise excess is seen in the luminosity blocks when a trip occurred. The luminosity blocks with a ramping HV line exhibit behaviour very similar to that of the regular luminosity blocks. Figure 4(b) shows the same distributions after applying the “loose jet-cleaning procedure” applied routinely to ATLAS physics analyses [11, 23]. This cleaning procedure is based on a set of variables related to hadronic shower shapes, characteristics of ionization pulse shapes, etc. and is meant to remove fake jets due to calorimeter noise and out-of-time pile-up. The noise observed in the luminosity blocks (systematically rejected) where a trip occurred is largely reduced, whereas the other types of luminosity blocks still exhibit very similar behaviours.

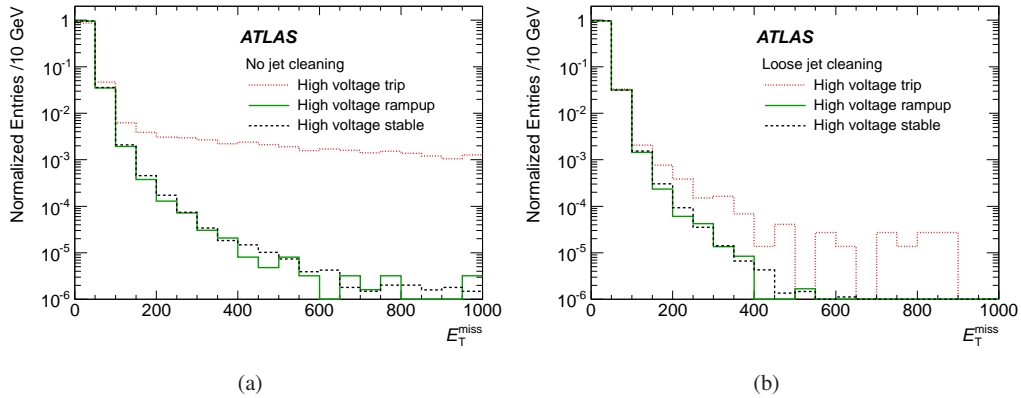


Figure 4: Distributions of missing transverse momentum, E_T^{miss} , measured in 2011 collision data in JetTauEtmiss stream for luminosity blocks with stable HV conditions (dashed line), a HV trip (dotted line) and a HV line ramping up (full line). Distributions are shown (a) without any jet-cleaning and (b) with a loose jet-cleaning procedure applied.

A complementary cross-check was performed by considering the rate of reconstructed jets in the same three types of luminosity blocks in the CosmicCalo stream where no collision is expected. Before any jet-cleaning procedure, it appears that the rate of jets in the luminosity blocks where a trip occurred is 1.6 times larger than in regular luminosity blocks. In the case of luminosity blocks with a ramping HV line, no difference from the regular luminosity blocks is observed within a statistical error of 10% on the ratio of the number of jets.

Hence, these studies confirm that the luminosity blocks with a ramping HV line can safely be kept for analysis. Those luminosity blocks are, however, marked with a tolerable defect, in order to keep track of this hardware feature and ease the extraction of the corresponding data for detailed studies.

3.4 Monitoring of coverage

The LAr calorimeter design nominally provides full hermeticity in azimuth and longitudinal cov-

erage up to $|\eta| = 4.9$. However, when hardware failures (though rare) occur, this coverage may be degraded. The inefficiencies can, for example, be due to a faulty HV sector where all HV lines are down. In this case, the resulting dead area is of typical size $\Delta\eta \times \Delta\phi = 0.2 \times 0.2$, and usually affects several calorimeter layers at the same time. Since such degraded coverage might significantly affect the physics performance, the corresponding data are systematically rejected by marking them with an intolerable coverage defect.

The detector coverage can also be degraded by a readout system defect. If the inactive region is limited to a single isolated FEB, the impact is usually restricted to a single layer in depth,⁴ and the data are not systematically rejected. An intolerable defect is set only when four or more FEBs are simultaneously affected. If an important readout problem cannot be immediately fixed and must remain present during a long data-taking period, the intolerable defect policy is not acceptable, since ATLAS cannot afford to reject all the data taken for an extended period. Instead, for such incidents the inactive region is included in the Monte Carlo simulation of the detector response to automatically account for the acceptance loss in physics analysis. Such a situation happened once in 2011: six FEBs remained inactive for several months due to a hardware problem that prevented the distribution of trigger and clock signals. The problem was traced to a blown fuse in the controller board housed in the same front-end crate as the affected FEBs. Given the impossibility of swapping out boards while the ATLAS detector is closed, the problem was remedied only during the 2011–2012 technical stop. However, a spare clock and trigger distribution board was installed in summer 2011, allowing the recovery of four FEBs out of six for the last months of 2011 data taking. Also, three FEBs had to be switched off for approximately two weeks in 2012 due to a problem with the cooling circuit.

3.5 Associated data rejection in 2012

Figure 5(a) shows the time evolution of the data rejection level due to HV trips in 2012. In this figure and in all the similar plots of the following sections, the varying bin widths reflect the varying integrated luminosities of the ten 2012 data-taking periods (see section 1). The remarkable reduction of the losses over the year is mainly due to two effects.

First, and for reasons not completely understood, the HV trips seemed to occur mainly when the LHC instantaneous luminosity was increasing significantly (typically doubled or tripled) over a few-day period. After a couple of days with stable peak luminosity, the occurrence of trips significantly decreased and then remained very low. When the collisions stopped or if the luminosity was very low for several weeks (machine development, long technical stops, etc.), this transient “training” period would recur briefly before a stable HV system was recovered.

Second, the rate of trips was reduced by installing new power supply modules shortly before the start of data taking period B. These new power supplies are able to temporarily switch to a “current mode”, delivering a user-programmed maximum current resulting in a brief voltage dip instead of a trip [24]. Only the most sensitive sectors of the electromagnetic endcap localized at large pseudorapidities (e.g. small radius) were equipped with these special power supplies. Additional modules of this type are planned to be installed in 2014 before the LHC restarts.

⁴Due to cabling reasons, this statement does not apply to the hadronic calorimeters.

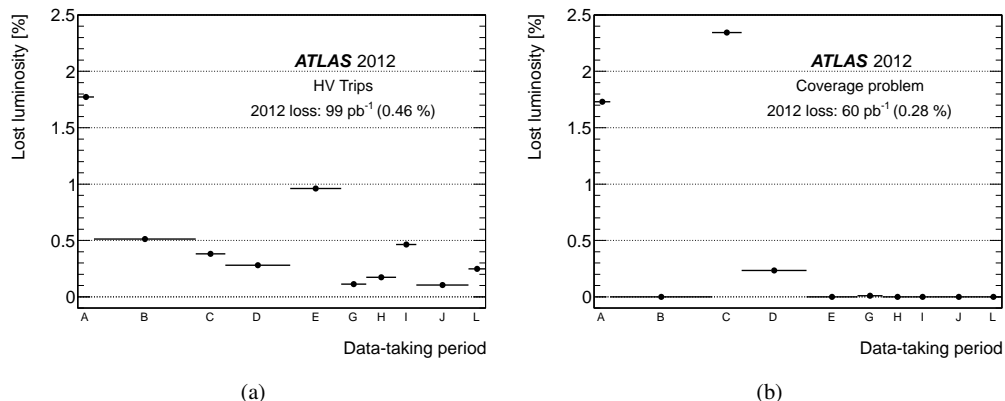


Figure 5: Lost luminosity due to (a) HV trips and (b) inefficient areas impacting detector coverage as a function of the data-taking period in 2012.

Figure 5(b) shows the time evolution of the 2012 data rejection level due to a large inefficient area of detector coverage. The highest inefficiency, observed during period C, comes from special collision runs with the toroidal magnet off, dedicated to the improvement of the relative alignment of the muon spectrometer. During this two-day period, expected to be rejected in any physics analysis, large regions of the HV system were intentionally switched off to investigate the source of noise bursts (see section 6). The two other sources of data loss in periods A and D are due to two faulty low-voltage power supplies in a front-end readout crate, equivalent to more than 25 missing FEBs or a coverage loss greater than 1%. These two problems were only transient, lasting less than a couple of hours, the time needed to replace the power supply.

4. Data integrity and online processing

Each one of the 1524 FEBs amplifies, shapes and digitizes the signals of up to 128 channels [5]. In order to achieve the required dynamic range, the amplification and shaping are performed in parallel with three different gains (of roughly 1, 9.9, and 93). When an event passes the first level of trigger, the signal is digitized. Only the signal with the optimal gain is digitized by a 12-bit analog to digital converter (ADC) at a sampling frequency of 40 MHz. After this treatment, five digitized samples⁵ are sent for each cell to the ROD system [6] via optical links. The ROD boards can either transparently transmit the digitized samples to the data-acquisition system (*transparent* mode), or compute the energy of the cell and transmit only one number, hence reducing the data size and the offline processing time (*results* mode). During calibration runs, the ROD can also work in a special mode, where several events are averaged to limit the data size and optimize processing time; however, this is not further considered in this article.

In results mode, the cell energy E , directly proportional to the pulse shape amplitude A , is computed with a Digital Signal Processing (DSP) chip mounted on the ROD boards, using an optimal filtering technique [25, 26] and transmitted to the central data-acquisition system. When

⁵In debugging/commissioning mode, up to 32 samples can be readout.

the energy is above a given threshold $T_{Q\tau}$, the peak time τ and a quality factor Q are also computed. These quantities can be expressed as:

$$E = \sum_{i=1}^5 a_i(s_i - ped) \quad E \times \tau = \sum_{i=1}^5 b_i(s_i - ped) \quad Q = \sum_{i=1}^5 (s_i - ped - A(g_i - \tau g'_i))^2$$

where s_i are the five digitized samples, ped is the electronics baseline value, and g_i and g'_i are respectively the normalized ionization pulse shape and its derivative with time. The optimal filtering weights, a_i and b_i are computed per cell and per gain from the predicted ionization pulse shape and the measured noise autocorrelation to minimize the noise and pile-up contributions to the amplitude A .

The quality factor that reflects how much the pulse shape looks like an argon ionization pulse shape, is lower than 4000 in more than 99% of argon ionization pulses. Because the quality factor is computed by the DSP chip in a 16-bit word, it is limited to $2^{16} - 1 = 65535$; the probability that this saturated value corresponds to a real energy deposit in the calorimeter is estimated negligible.

For cell energies above a second energy threshold T_{samples} (in absolute value), the five digitized samples are also transmitted to the central data-acquisition system. The two energy thresholds $T_{Q\tau}$ and T_{samples} are tuned such that approximately 1–2% of the cells are involved. This corresponds to an energy threshold of around 50 MeV–10 GeV depending on the layer/partition.

4.1 Basic data integrity

Since the FEB output is the basic detector information building block, careful data integrity monitoring at the earliest stages of the processing chain is mandatory. The input FPGA chip on the ROD board performs basic online checks of the FEB data: most importantly it checks for any error word sent by the different chips on each FEB and checks consistency of data (BCID, event identifier, etc.) defined for each channel which are expected to be uniform but not propagated individually to the data-acquisition system. Beyond these online consistency checks, a software algorithm running both online and offline performs additional checks which require: presence of all data blocks, unchanged data block length from the FEBs to the central data acquisition system, uniform data type and number of digitized samples among the 1524 FEBs. The most serious case of data corruption was observed in 2010 and consisted of a spurious loss of synchronization between the FEB clock and the central clock. The origin of this problem was identified in early 2011 as interference between the two redundant clock links available in each FEB: when only one was supplied with a signal, the inactive link could induce a desynchronization. The problem was fixed by permanently sending a fixed logic level to the inactive clock circuit.

An FEB integrity error indicates a fatal and irrecoverable data corruption. To ensure as uniform a readout coverage as possible within a run, any event containing a corrupted block is discarded. This event rejection is performed offline by applying the time-window veto procedure described in section 2.4. To limit the offline rejection when a permanent corruption error is observed during data taking, the run must be paused (or stopped and restarted) as promptly as possible to reconfigure the problematic FEBs. However, if the data corruption is limited to less than four FEBs, the ATLAS run coordinator may consider this loss as sustainable and keep the run going to maximize the data-taking efficiency. In this case, the problematic FEBs are masked offline (the data integrity issue

translates into a coverage inefficiency), and the data are not rejected but marked with a tolerable defect. This unwanted case happened only twice during 2012.

When the digitized samples are available, the yield of events with a null or saturated sample (i.e. an ADC value equal to 0 or 4095) is monitored. Several problems could induce a large yield of saturated or null samples: a malfunctioning ADC or gain selector, large out-of-time channel/FEB signal, data fragment loss, etc. The proportions of affected events per cell for the run 205071 are presented in figures 6(a) and 6(b). In the electromagnetic barrel and the hadronic endcaps, the proportions are close to zero. In the electromagnetic endcaps and forward calorimeter, the yield is slightly higher but still very low: around 0.01% of EMEC channels exhibit a saturated (null) sample in more than 10^{-5} ($0.8 \cdot 10^{-5}$) of events. Moreover, this observation is not due to a defect in the readout chain but simply to the out-of-time pile-up. For these events, the signal peak of the cell is shifted, and the gain selection based on the in-time signal is not appropriate. The endcaps are most affected because of a higher particle flux at large pseudorapidity. It is, however, less pronounced in the FCal than in EMEC due to the decision to allow only the medium and low gains in the FCal readout chain specifically for this reason. With a pile-up noise systematically greater than the medium gain electronics noise, this setting does not affect the overall performance. Neither does the very low occurrence of null/saturated samples measured in other partitions (EMB, EMEC and HEC).

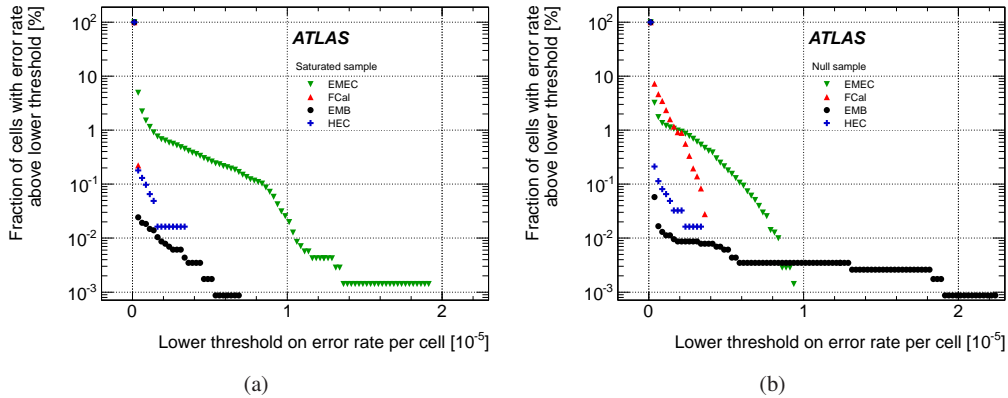


Figure 6: (a) Percentage of cells that exhibit a saturated sample in a certain proportion of events. (b) Percentage of cells that exhibit a null sample in a certain proportion of events. In both plots, the x -axis shows the lower threshold on the error rate per cell. The results are shown for the run 205071.

4.2 Online computation accuracy

In results mode, but only for cells where the digitized samples are available, the energy can be recomputed offline with the same optimal filter and compared to the online value to test the DSP computation reliability. Due to the intrinsic hardware limitations of the DSP chip, the precision of the energy computation varies from 1 MeV to 512 MeV, the least significant bit, depending on the energy range [4].

Figure 7(a) shows the distribution of the difference between the online and offline energy computations. A satisfactory agreement between the two calculations is found for the four partitions. Here again, the tails of the distributions are slightly more pronounced in the partitions most affected by out-of-time pile-up (EMEC, FCal). This can be explained by the limited size of the DSP registers (16 bits) that implies specific coefficients rounding rules optimized to deal with in-time signals. This explanation is supported by figure 7(b), which shows an increase in the computation-disagreement yield (normalized by the number of events and the number of channels in each partition) as a function of the instantaneous luminosity.

A similar analysis was also performed to check the correctness of the time and quality factor computed online, and similar accuracies were observed. Since the first LHC collisions, the DSP computation has proved to be fully accurate and never induced any data loss.

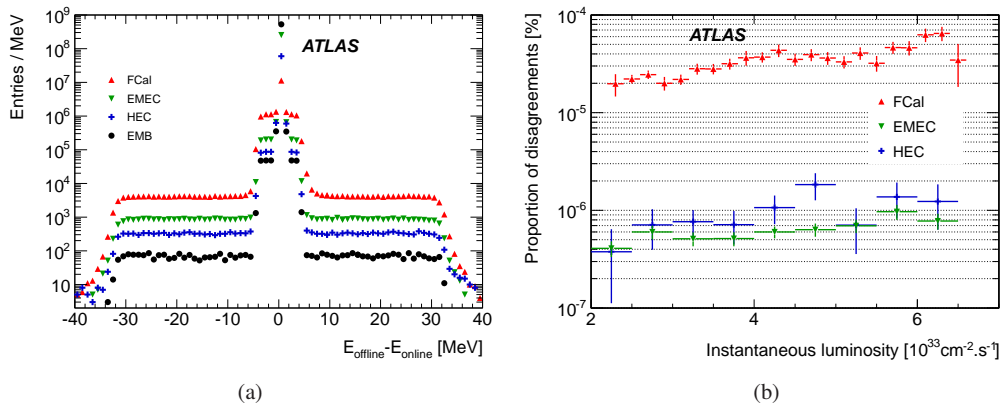


Figure 7: DSP energy computation accuracy in run 205071. (a) Distribution of the difference between the energy computed offline for the four different partitions and the energy computed online by the DSP. (b) Proportion of computation disagreements (i.e. when the online/offline energy difference lies outside the expected DSP accuracy range) per partition as a function of the instantaneous luminosity. The barrel proportion is not displayed, as only one single disagreement (one channel in one event) is observed.

4.3 Missing condition data

To limit the effect of out-of-time pile-up, the FEB shaping stage is bipolar (see figure 1(b)), allowing a global compensation between the signal due to the following collisions and the signal due to the previous ones. However, this remains inefficient for the collision events produced in the first (last) bunches of a train: the electronic baselines are then positively (negatively) biased. To correct this bias, the average energy shift is subtracted offline based on the position of the colliding bunches in the train. The pile-up correction makes use of the instantaneous luminosity per bunch provided by the ATLAS luminosity detectors. Due to hardware or software failures, the database information about the instantaneous luminosity may be missing. In that case, the reconstruction of the LAr calorimeter energy is considered non-optimal, and the data are rejected by assigning a dedicated intolerable defect associated with the luminosity detectors. Even if the origin of this

feature is not related to the LAr calorimeters, an additional intolerable defect associated with the LAr calorimeter is also assigned to keep track of the non-optimal reconstruction.

4.4 Associated data rejection in 2012

Figure 8 shows the time evolution of data corruption in 2012 in terms of lost luminosity. The rejection rate is computed from two complementary sources: (a) the time-window veto when the data corruption does not affect the whole luminosity block, and (b) the list of defects corresponding to a totally corrupted luminosity block. In both cases, the rejection rate remains very low throughout the year and below 0.02% on average.

Figure 9 shows the data rejection due to missing conditions data. It remains very low and affects mainly isolated luminosity blocks with corrupted instantaneous luminosity per bunch crossing.

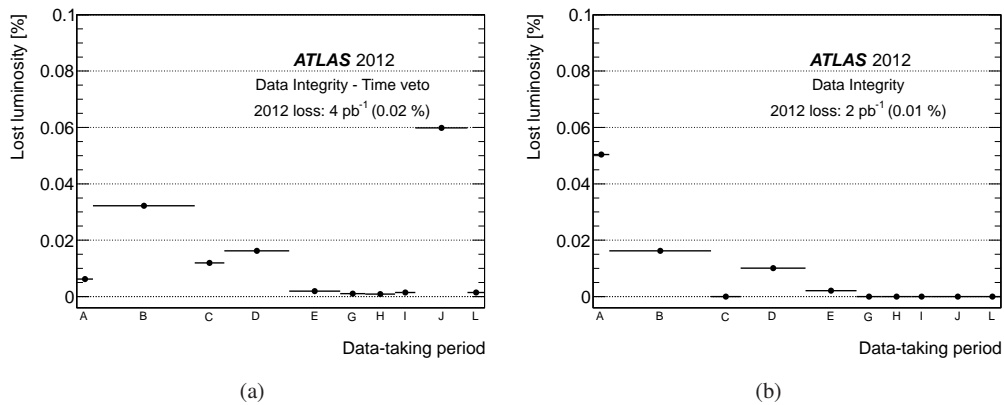


Figure 8: Lost luminosity due to data corruption as a function of the data-taking period in 2012. (a) Loss due to the time-window veto procedure. (b) Loss due to defect assignment.

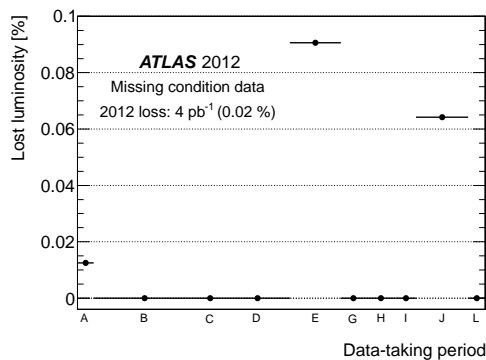


Figure 9: Lost luminosity due to missing conditions as a function of the data-taking period in 2012.

5. Calorimeter synchronization

A precise measurement of the time of the signal peak, derived from the optimal filter, is a valuable input to searches for exotic particles with a long lifetime or for very massive stable particles. Proper synchronization also contributes to improving the energy resolution. For these reasons, it is important to constantly monitor the calorimeter synchronization, both on a global scale and with finer granularity.

5.1 Global synchronization

A mean time is derived for each endcap by considering all cells of FCal (EMEC inner wheel⁶) above 1.2 GeV (250 MeV) and by averaging their signal peak time. At least two energetic cells are requested to limit the impact of noisy cells. When both are available, the average time of the two endcaps is derived to monitor the global synchronization, while the time difference allows a check of the beam spot's longitudinal position and the presence of beam halo. Since the two endcaps are electrically decoupled, the presence of simultaneous signals in both endcaps is very likely to be due to real energy deposits and not due to noise. The high particle flux observed at the considered pseudorapidities allows refined monitoring as a function of time (luminosity block).

Figure 10(a) shows the average value of the two endcaps' times for the run 205071. The distribution is centred around zero, indicating that the calorimeter (at least the FCal and EMEC inner wheel) is properly synchronized with the LHC clock, as is also shown in section 5.2.

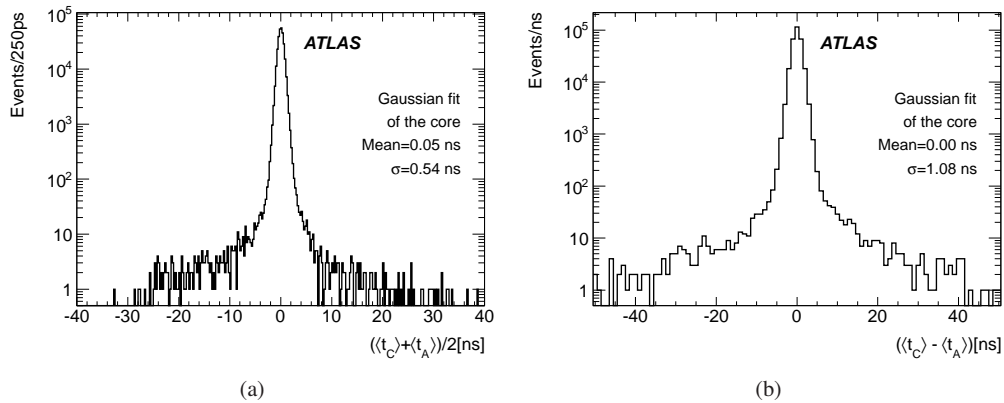


Figure 10: (a) Average and (b) difference of the two endcap mean times, as defined in the text. The results are shown for the run 205071.

Figure 10(b) shows the time difference between the two endcaps. The distribution is also centred around zero, indicating that the recorded events are mostly collisions well centred along the beam axis: the particles travel from the centre of the detector, and both endcaps send a signal synchronously. Some secondary peaks may arise due to beam halo, where particles cross the detector along the z -axis, from one endcap towards the other. Given the 9 m distance between the endcaps, and assuming that the particles travel at the speed of light, the difference between the

⁶The EMEC inner wheel covers $2.5 < |\eta| < 3.2$.

signal arrival times from the two endcaps should peak at 30 ns for beam halo. These peaks were observed mainly in 2010; just a tiny bump is observed in the negative tail in figure 10(b). The small continuous tails are due to out-of-time pile-up that may bias the average time of an endcap's signal.

5.2 Synchronization at front-end board level

The procedure detailed in section 5.1 is mainly meant to monitor online the global synchronization of the LAr calorimeter and its evolution throughout the luminosity blocks of a run. A refined analysis is also performed offline to monitor the time synchronization of each individual FEB and optimize the phase of the clock delivered to each FEB (adjustable in steps of 104 ps via hardware settings [5]). With loose trigger thresholds, the LArCells stream allows collecting enough signals to monitor the individual FEB synchronization in every single run with at least 100 pb^{-1} . After rejecting the events affected by a noise burst (see section 6) and masking all the channels flagged

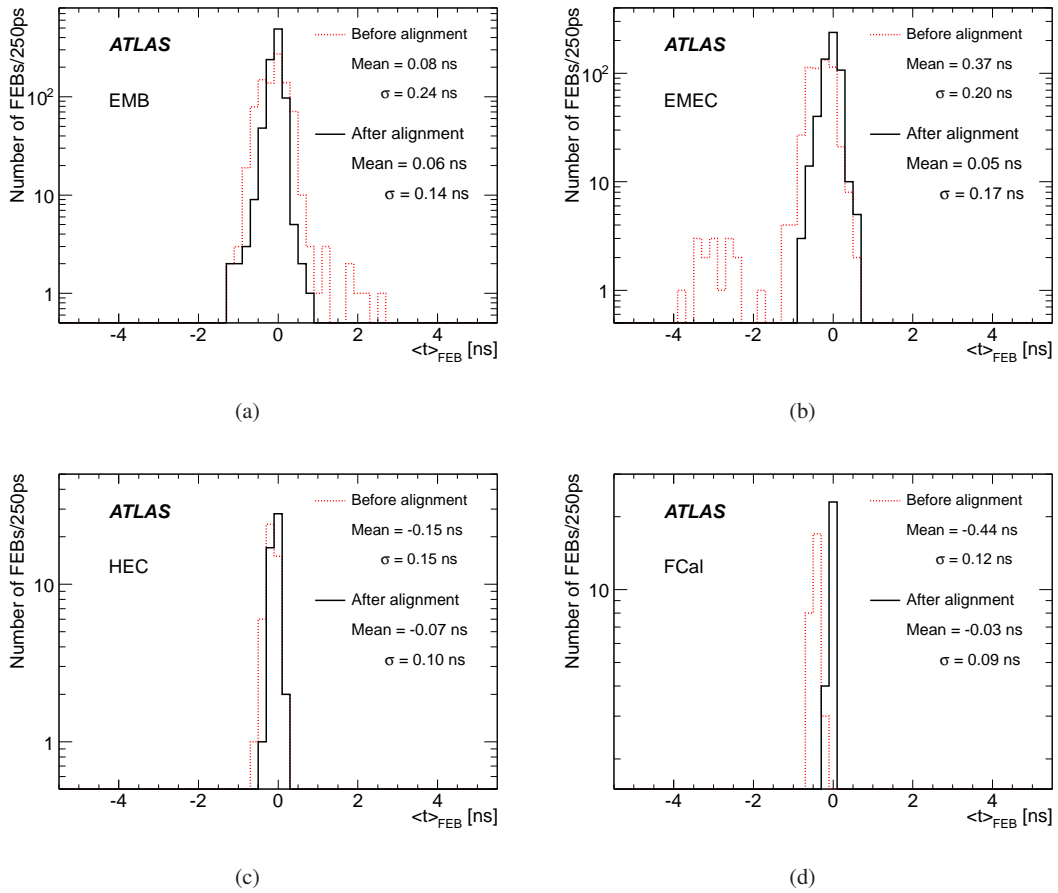


Figure 11: Distributions of the average FEB times in the four subdetectors: (a) EMB, (b) EMEC, (c) HEC, and (d) FCal. Distributions before and after spring 2012 timing alignment are superimposed, as described in the legend.

as problematic (see section 7), all cells above a certain energy threshold are selected. The energy thresholds vary between 1 GeV and 3.5 GeV (10 GeV in FCal) depending on the layer/partition and were optimized to lie well above the electronics noise without reducing the sample size too much. An energy-weighted distribution of the time of all cells of each FEB is built. The average time of each FEB is then derived from a two-step iterative procedure using a Gaussian fit of the distribution. In the rare cases of too few events or non-convergence of the fitting procedure, the median value of the distribution is used instead.

The average times of the 1524 FEBs were very accurately measured with the first 1.6 fb^{-1} of data accumulated in 2012 (period A and first runs of period B). The results are presented in figure 11: dispersions up to 240 ps were observed with some outliers. At this time, the clock delivery to each FEB was tuned individually, making use of the 104 ps adjustment facility provided by the timing system. The improvement associated with this alignment procedure is superimposed in figure 11. The dispersions, originally in the range 120–240 ps, were significantly reduced in each subdetector, and no outlier in the FEB average time distribution was observed above 1.5 ns.

With the large data sample accumulated during 2012, it was possible to routinely monitor the FEB synchronization during the year. An automated processing framework was set up on the CAF computing farm [17] to provide fast feedback to the signoff team. The evolution throughout 2012 of the average FEB time per subdetector is shown in figure 12. The effect of the first 2012 timing alignment previously mentioned is clearly visible at the beginning of the year. Shortly after this alignment, a system that automatically adjusts the ATLAS central clock to align with the LHC clock was commissioned. Originally tuned by hand, this adjustment compensates for the length variation of the optical fibres delivering the LHC clock to the ATLAS experiment due to temperature changes. With the level of synchronization achieved after the FEB synchronization, this automatic procedure became crucial. An illustration of this importance is given by the 200 ps

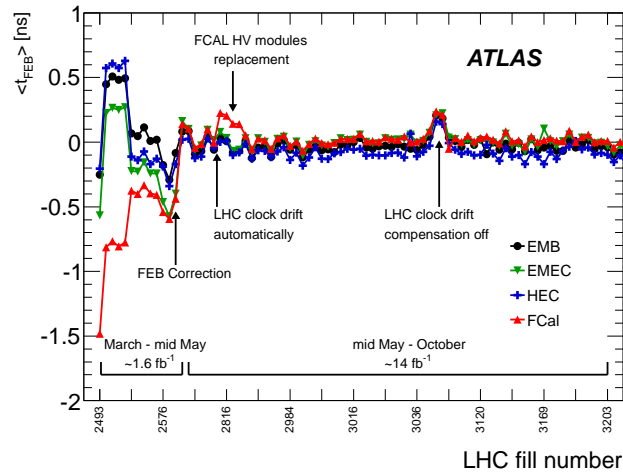


Figure 12: Average FEB time per subdetector as a function of the LHC fill number, during 2012 data taking. To improve readability, the period from October through December 2012, showing similar stability, is omitted.

bump observed in summer, when the automated compensation procedure was accidentally switched off (around LHC fill number 3050). Finally, another feature observed during summer 2012 was a ~ 300 ps time shift in the FCal FEBS around LHC fill number 2816. The origin of this problem was identified as the installation of two faulty HV modules that delivered a voltage lower than expected, hence impacting the electron drift time. As soon as the cause was identified, the faulty modules were replaced to recover the optimal synchronization. Beside this synchronization problem, these faulty modules also impacted the energy response. However, an offline correction was applied to recover an appropriate calibration. Except for these two minor incidents, which had negligible impact on data quality, figure 12 shows impressive global stability within 100 ps during the 2012 data taking.

A more refined synchronization at the cell level was implemented during a data reprocessing campaign. This should allow further improvement of the calorimeter timing accuracy that was measured in 2011 to around 190 ps for electrons and photons [27].

6. Treatment of large-scale coherent noise

When the instantaneous luminosity reaches $10^{32} \text{ cm}^{-2}\text{s}^{-1}$ and above, the LAr calorimeter is affected by large bursts of coherent noise, mainly located in the endcaps. Since the occurrence rate increases with instantaneous luminosity, a specific treatment had to be developed in summer 2011 to limit the data loss.

6.1 Description of the pathology

Between its installation inside the cavern in 2005 and the first collisions in 2009, the LAr calorimeter was extensively commissioned, and many detailed performance studies were pursued, with a special emphasis on the Gaussian coherent noise of the front-end boards. This Gaussian coherent noise was measured to be at a level lower than 10% of the total electronics noise per channel [4].

On a larger detector scale, the coherent noise can be estimated by considering the variable $Y_{3\sigma}$ for each partition, defined as the fraction of channels with a signal greater than three times the Gaussian electronics noise.⁷ Assuming a perfect, uncorrelated Gaussian noise behaviour in the entire calorimeter, the $Y_{3\sigma}$ variable is expected to peak around 0.13%. In the early days of commissioning, the $Y_{3\sigma}$ variable exhibited sizeable tails above 1% in randomly triggered events, characteristic of large coherent noise. Its source was identified as a major weakness of the high-voltage filter box supplying the presampler, which was fixed in 2007. After the fix, minor tails were still observed in the $Y_{3\sigma}$ variable distribution, but only within calorimeter self-triggered events (i.e. events triggered by a large signal in the LAr calorimeter).

Further studies were carried out before closing the detector in 2009, which led to the conclusion that the remaining coherent noise was likely to be introduced again inside the detector via the HV system: when all the HV power supplies were turned off, no noise was observed. Although some areas of the detector were obviously more affected than others, switching off only the specific HV lines powering the noisiest regions did not cure the problem. This indicated that the noise was most likely radiated by unshielded HV cables inside the cryostat, rather than directly injected. Imperfections or peculiarities of the cable routing inside the cryostat may explain why some regions

⁷The electronics noise is measured in calibration runs, using simple clock-generated trigger.

are more affected than others, but given the limited range of the problem and the difficult access to the hardware components, no further action was taken at that time.

During autumn 2010, the instantaneous luminosity reached $10^{32} \text{ cm}^{-2}\text{s}^{-1}$. At this time, pathological events with a very large signal (equivalent to several TeV) affecting a whole partition were observed in the empty bunches (CosmicCalo stream), when the LHC was in collision mode. The electromagnetic endcaps were especially affected. In the worst cases, some noise could be also observed in the hadronic endcap and the forward calorimeter at the same time as in the electromagnetic endcap. Figure 13 shows a typical event in the transverse plane of the electromagnetic endcap (A side) recorded at an instantaneous luminosity of $6 \times 10^{33} \text{ cm}^{-2}\text{s}^{-1}$: the total energy peaks around 2 TeV, and the $Y_{3\sigma}$ variable reaches 25%. Although the topologies and occurrence rates differ slightly, both endcaps are affected. They are treated in the same way and merged into the same distributions in all the following studies. The barrel distributions are also merged.

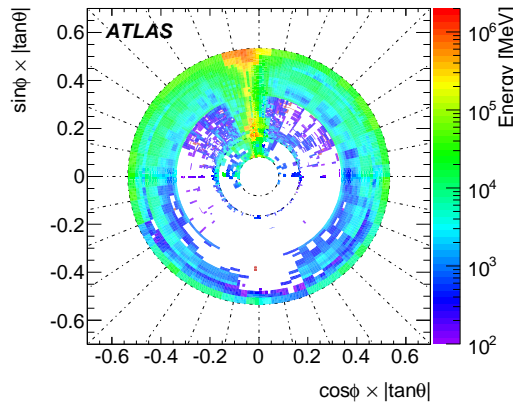


Figure 13: Example of a typical coherent noise event observed in the EMECA partition in run 205071 – CosmicCalo stream. The energies of the 3–4 layers were summed along a fixed value of pseudorapidity and partially along the azimuthal angle.

Figure 14(a) shows the $Y_{3\sigma}$ distribution, computed for the barrel and endcap partitions over a period of roughly 135 hours of data taking; during this period, 1.7 fb^{-1} of data were accumulated, with an instantaneous luminosity greater than $3 \times 10^{33} \text{ cm}^{-2}\text{s}^{-1}$. The distribution appears as expected in the barrel, with a sharp peak around 0.13% and negligible tails. But in the endcaps, the distribution exhibits very large tails, typical of coherent noise, with a very large fraction (up to 70% – not visible on this figure) of channels fluctuating coherently within a partition.

The noise burst topology shown in figure 13 is very similar to the one observed during the commissioning phase, but its amplitude is significantly larger. The very similar topologies at different times excluded the possibility that this pathology could be due to beam background or parasitic collisions. The HV lines were again suspected, the increased rates and amplitudes being explained by the larger drawn currents. This hypothesis was favoured because the endcaps are the most involved and their behaviour is almost Gaussian outside the LHC collision mode.

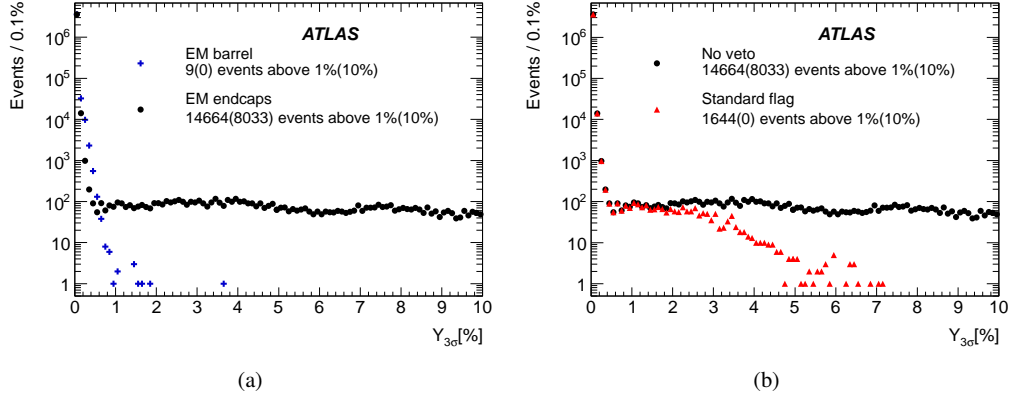


Figure 14: (a) $Y_{3\sigma}$ distributions for the four electromagnetic partitions (positive and negative pseudorapidities merged in a single distribution). (b) Effect of the *Standard* flag veto on the electromagnetic endcap $Y_{3\sigma}$ distribution. The event sample was acquired in the CosmicCalo stream during 135 hours corresponding to an integrated luminosity of 1.7 fb^{-1} .

6.2 Use of the quality factor for noise identification

In collision streams, the $Y_{3\sigma}$ variable is positively biased by the presence of energy deposits in the calorimeter due to collisions (typically peaking around 1–2% at high luminosity) and cannot be used to identify coherent noise. It is therefore crucial to define alternative ways to study this coherent noise in the presence of collisions. New Boolean variables, hereafter named *flags*, had to be introduced.

- The *Standard* flag requires strictly more than five FEBs containing more than 30 channels each with a quality factor greater than 4000.
- The *Saturated* flag requires more than 20 channels with an energy greater than 1 GeV and a saturated quality factor (i.e. equal to 65535).

The flag definitions are based on the observation of poor quality factors in the noisy events, indicative of abnormal pulse shapes and very unlikely to be due to argon ionization. The *Standard* flag is sensitive to phenomena largely spread over a partition. The *Saturated* flag, with a much higher constraint on the quality factor, is triggered in very atypical phenomena but possibly confined to a very reduced area. With this criterion, limited in terms of geometrical extent, the *Saturated* flag is less reliable than the *Standard* flag. However, it is useful for particular cases, described in the following. Figure 14(b) illustrates the *Standard* flag efficiency in reducing the tails of the $Y_{3\sigma}$ endcaps distribution. When vetoing on this flag, only 11% of events with $Y_{3\sigma}$ above 1% remain and no event remains with $Y_{3\sigma}$ above 10%.

6.3 Time duration of the pathology

To measure the time extent of the coherent noise, events with $Y_{3\sigma}$ greater than 1% and separated by less than one second are clustered, assuming that they belong to the same burst of noise. By this method, the time extent (defined as the difference between the first and last clustered events), was

measured to be around a few hundreds nanoseconds. However, this method is limited, since it relies on empty bunches: the empty bunch group is composed of a group of BCIDs of length 600–1000 ns between two trains of populated bunches of approximately 3.6–7.2 μs (see section 2.2). This method is therefore potentially biased by the empty bunch group’s timelength being comparable to the measured time extent.

To overcome this limitation, the same event clustering method can be applied by replacing the criterion for the $Y_{3\sigma}$ variable by a criterion for the Standard flag. To be conservative, events flagged by the Saturated method are also clustered with events flagged by the Standard method if they are separated by less than one second. Since the Saturated method was found to be less reliable, requesting the event to be close to an event flagged by the Standard flag limits the risk of considering fake noisy events. With this clustering definition independent of the $Y_{3\sigma}$ variable, it is possible to consider both the CosmicCalo and Express streams, and hence empty and filled bunches. The result is shown in figure 15. Virtually all pathologies are found to be shorter than 0.5 s (see figure 15(a)), and more than 90% of them are shorter than 5 μs (see figure 15(b)). Due to the short duration of the phenomenon, the pathologies are referred to as *noise bursts*. The very limited duration of the bursts, much shorter than the luminosity block length, also suggested the development of a dedicated offline treatment with a time-window veto procedure to limit the amount of data rejected.

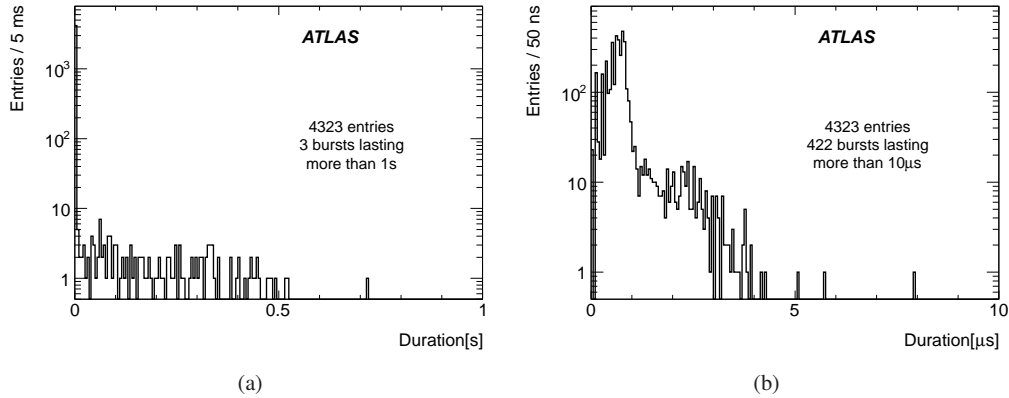


Figure 15: Distributions of the noise burst duration. Figure (b) zooms in on the shortest times of figure (a).

6.4 Time-window veto procedure

The scanning of a sample of noise bursts showed that most of them consist of a peak of *hard* events surrounded (before and after) by peripheral *soft* events: the hard events are characterized by a large $Y_{3\sigma}$ and are properly identified by the Standard flag, whereas the soft ones are characterized by a $Y_{3\sigma}$ variable around 2-3% (if recorded in empty bunches) and are not identified by the Standard flag. It was therefore proposed to apply a time-window veto procedure around the well-identified hard events to remove the soft ones.

Technically, the noise burst cleaning is achieved by storing a status word in the event header as explained in section 2.4. This requires the extraction of the noise burst’s peak timestamp with the express processing of the CosmicCalo and Express streams: a clustering procedure is performed on the same events as detailed in the previous section. The timestamps of the first and last flagged events are used to define a unique time interval. To veto the peripheral events of the noise burst, the time interval is extended by $\pm\delta t/2$, where δt is a parameter to be optimized. The computed time window is then stored in a dedicated conditions database during the calibration loop, and read back for the bulk reconstruction to fill the status word of all events falling inside the time-window veto.

Finally, it is important to emphasize that a noise burst candidate with a single flagged event in the peak is not vetoed. This is done deliberately, to avoid discarding unusual events where the decays of exotic particles deposit energy in the calorimeter at much later time than the bunch crossing (a delayed signal is very likely to have a poor quality factor). By requesting at least two events flagged within a short time, the risk of throwing away unexpected new physics events is considered negligible.

The improvement to the $Y_{3\sigma}$ distribution resulting from applying the time-window veto is shown in figure 16. The quantitative performance of the procedure is also summarized in table 3. In the two most sensitive partitions (the two electromagnetic endcaps), the time-window veto procedure reduces by a factor of four the number of events with a $Y_{3\sigma}$ greater than 1% remaining after having applied the Standard flagging method or by a factor of 35 when comparing with the uncleaned data sample. Several values of δt were tried, between 100 ms and 2 s, leading to the same

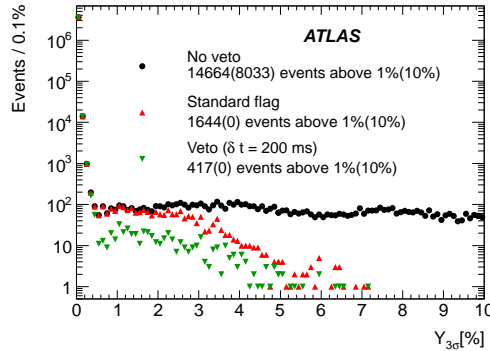


Figure 16: Effect of the time-window veto on the electromagnetic endcap $Y_{3\sigma}$ distribution for a value of $\delta t = 200$ ms. Same dataset as in figure 14.

efficiency as the one quoted in the table for a value of 200 ms. Compared to the measured time extent of the noise bursts, these numbers are very conservative, as confirmed by the stable efficiency. There is probably some room left for tuning this parameter, but given the very low associated data loss (see section 6.6), a conservative value of 200 ms (1 s) was applied in the 2012 (2011) data processing.

The number of affected events per hour ($Y_{3\sigma} > 1\%$) was originally around 108. With the time-window veto method, it decreased to only three events per hour.

Table 3: Number of events with a $Y_{3\sigma}$ greater than 1% after applying the simple Standard flagging and the time-window veto procedure. The efficiencies ε of each cleaning procedure are given in parentheses. Same dataset as in figure 14.

Partitions	No cleaning procedure	After applying the Standard flag method	After applying the time-window veto procedure ($\delta t = 200$ ms)
EM barrel	9	3 ($\varepsilon = 66.6\%$)	1 ($\varepsilon = 88.9\%$)
EM endcaps	14664	1644 ($\varepsilon = 88.8\%$)	417 ($\varepsilon = 97.2\%$)

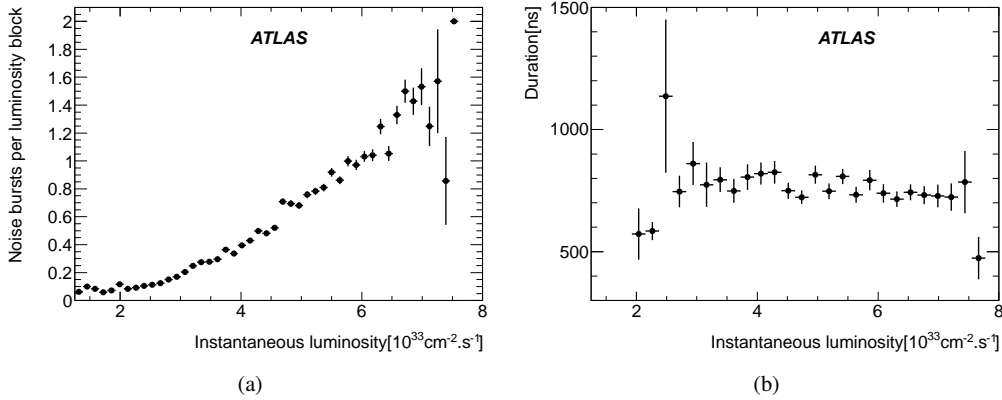


Figure 17: (a) Noise burst occurrence frequency per luminosity block and (b) luminosity dependence of the mean duration of the noise bursts as a function of instantaneous luminosity.

6.5 Luminosity dependence

In 2012, around 15% (40%) of the luminosity blocks contained a noise burst in the CosmicCalo (JetTauEtmis) streams. Figure 17(a) illustrates the number of noise bursts per luminosity block as a function of the instantaneous luminosity (in any stream). A steady dependence is observed. Parabolic extrapolations from this plot indicate that each luminosity block will contain around five noise bursts at the peak luminosity expected after 2015 ($1-2 \times 10^{34} \text{cm}^{-2} \text{s}^{-1}$). However, even if the rate evolves as a function of the instantaneous luminosity, the noise bursts' mean duration remains stable, as shown in figure 17(b). As the current choice of the δt parameter is very conservative with respect to the noise burst time extent, its reduction can be envisaged to fully compensate for the future increased occurrence yield.

6.6 Associated data rejection in 2012

The data loss associated with the time-window veto procedure as a function of the data-taking period is presented in figure 18(a). It amounts to 0.2%. The observed variation is explained by the differences in the instantaneous luminosity profiles impacting the noise burst rates, as explained in the previous section.

The efficiency of the time-window veto procedure is cross-checked in the JetTauEtmiss stream, by searching for remaining events flagged as noise bursts by the Standard method outside the defined time veto periods. Their treatment depends on whether such events are isolated in time or close to another one.

- If such an event is isolated in time, no action is taken, as it might be due to a delayed decay of exotic particles. In 2012, only 192 such events remain in the dataset considered for physics analysis. Furthermore, a complementary cleaning at the jet level is also available offline, to make sure that any remaining noise bursts do not bias physics analysis [11].
- If two or more events close in time remain, they are very likely to belong to a single noise burst not observed in the express processing streams. The only solution is to reject them by assigning an intolerable defect to the whole luminosity block. This induces a much larger data loss, not recoverable until the next full data reprocessing where the time-window veto procedure can be applied again using updated database information.

Consequently, the efficiency of the time-window veto procedure heavily relies on the ability to select the noise burst peak events in the Express and CosmicCalo streams in order to compute the veto interval periods before the start of the bulk processing. To achieve this, four dedicated trigger chains were designed to ensure efficient streaming. The trigger chains are seeded at the first-level trigger step from standard jet or E_T^{miss} triggers, and make use of quality factor (Q) information to design a pseudo-Standard-flag algorithm given as input to the higher trigger levels (second level and high level trigger).

Figure 18(b) summarises the 2012 data rejection due to noise bursts that were not identified in the express processing, hence not available for the definition of a time veto window. The overall inefficiency is found to be very low but for different reasons depending on the data-taking period. The low inefficiency observed in the data-taking periods A–G is due to the reprocessing campaign of autumn 2012 : the time windows for the veto were refined based on the original bulk processing output. The periods H–L did not benefit from this second update, and the low level of data rejection

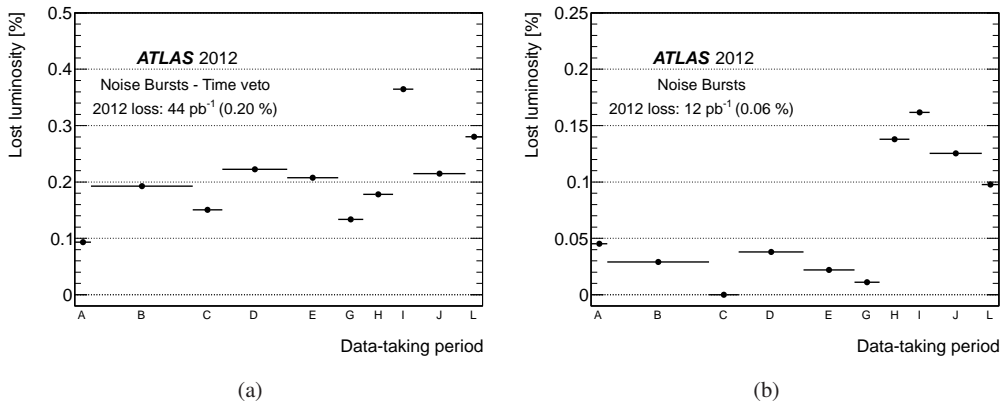


Figure 18: Lost luminosity due to noise bursts as a function of the data-taking period in 2012. (a) Loss due to the time-window veto procedure. (b) Loss due to defect assignment.

comes only from the noise burst identification in the calibration streams, showing a satisfactory trigger efficiency.

7. Treatment of per-channel noise

The regular calibration procedure [4] is the main input to identify problematic calorimeter channels. However, a specific source of non-Gaussian noise was found to occur only in the presence of LHC collisions. A reliable procedure to extract these channels had to be designed to treat them within the calibration loop.

7.1 Regular calibration procedure

The extraction of the electronic calibration constants requires three types of calibration runs: pedestal, ramp and delay. Pedestal runs allow the measurement of the baseline level and noise properties of the readout electronics, ramp runs allow the measurement of the readout gain, and delay runs allow the measurement of the pulse shape as a function of time. These special calibration runs are acquired between LHC fills, in absence of collisions, requiring only simple clock-generated triggers. Pedestal and ramp runs are taken several times a week, while the high stability of the calibration constants observed during the calorimeter commissioning [4] indicates that delay runs are needed only once a week. These calibration runs are also the primary input to identify and classify problematic channels in a dedicated database. The different pathologies imply different offline treatments. Three main treatments that are applied are listed below.

- When a cell is not operational (deteriorated signal routing in cryostat, dead readout channel, large noise, etc.), it is *unconditionally masked* offline. Its energy is then estimated from the average energy of the eight neighbouring channels in the same calorimeter layer. In this case, the peak time and quality factor are not available.
- A cell may be operational, but affected by large noise with very different characteristics compared to a real physics signal. The cell quality factor can be used to disentangle the signal due to a real energy deposit from the noise on an event-by-event basis. When the quality factor is lower than a fixed value (4000), the cell is considered as operational and no treatment is applied; when the quality factor is large, the cell energy is estimated from the eight neighbours of the same layer, as for an unconditionally masked cell. In this case, the cell is said to be *conditionally masked*.
- When a cell cannot be calibrated due to a faulty calibration line, its electronic calibration constants are estimated from those of similar cells in the same layer and at the same azimuthal position. In this case, the cell is *patched*.

At the beginning of 2012, less than 0.9% of the calorimeter channels were patched due to a faulty calibration line. The impact of this patching being almost negligible,⁸ it is not discussed further in the following. Table 4 summarises the proportion of cells unconditionally or conditionally masked at the beginning of 2012 that remained masked during the whole year. More than 99.9% of the channels were fully functional. The 119 pathological channels being widespread across all the

⁸The inaccuracy on the calibration was estimated about 3%.

calorimeter regions, no large inefficient area emerges, hence the impact on the performance is considered negligible. These pathological channels remain masked (conditionally or unconditionally) during the whole data-taking period, but in addition, some other channels exhibited transient pathologies to be treated on a per-run basis, as is explained in the following.

Table 4: Total number of channels unconditionally or conditionally masked at the beginning of 2012 in different partitions.

	Electromagnetic calorimeter	Hadronic endcap	Forward calorimeter	Global
Total number of channels	173312	5632	3524	182468
Channels unconditionally masked	76 (0.04%)	22 (0.39%)	8 (0.23%)	106 (0.06%)
Channels conditionally masked	8 ($5 \times 10^{-3}\%$)	5 (0.09%)	0	13 ($7 \times 10^{-3}\%$)

7.2 Monitoring of Gaussian noise during collision runs

Individual channel behaviour is also constantly monitored during collision runs. This monitoring largely relies on data streams with empty bunches (CosmicCalo and LArCellsEmpty streams), where no energy deposit is expected in the LAr calorimeter. The collision streams (Express, EGamma and JetTauEtmiss streams) are mainly used for data quality assessment in the reconstruction of higher-level objects (such as electron/photon, J/ψ candidates, etc.) beyond the scope of this article. However, these streams are especially useful in confirming non-operational or misbehaving channels spotted in calibration runs.

The Gaussian noise and electronics baseline, accurately characterized during the calibration runs, are cross-checked by looking at three distributions:

- mean energy and noise per cell;
- fraction of cells with energy above 3σ , where σ is the measured electronics noise.

If pathologies are observed in these distributions, the team responsible for the calibration is informed and they either inquire further and/or trigger urgently a new calibration procedure. No immediate systematic action is required by the signoff team. The 2012 experience showed that the Gaussian part of the electronics noise was very stable in the presence of collisions. But beside this reassuring statement, a sizeable non-Gaussian behaviour seriously complicated the data quality procedure.

7.3 Monitoring of non-Gaussian noise during collision runs

The non-Gaussian behaviours were identified in the CosmicCalo stream, where no large energy deposit is expected, from distributions showing the number of events with an energy far exceeding the expected electronics noise (typically $20\text{--}30\sigma$). At the express processing level, these distributions cannot be directly used, as they are polluted by noise bursts (the time-window veto cleaning procedure described in section 6 is applied only at the bulk processing stage). Such pollution can

be seen in figure 19(a): the large signal observed in the azimuthal ring at $\eta = 1.4$ is typical of noise bursts and can be also recognized in figure 13 (outer ring of the endcap).

To remove this pollution, the primary (temporary) Tier 0 monitoring outputs per luminosity block are merged, excluding the luminosity blocks affected by noise bursts. This procedure reduces the monitoring dataset by 15%, as explained in section 6.5, but is crucial to avoid masking channels that would look perfectly normal after the time-window veto is applied. An example of this custom merging procedure is shown in figure 19.

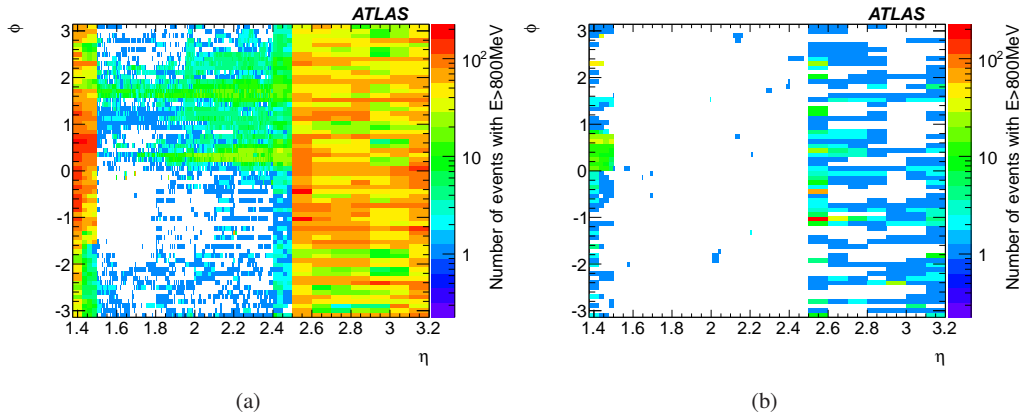


Figure 19: (η, ϕ) distributions of the number of events per cell with cell energy greater than 800 MeV in the first layer of EMECA (a) before and (b) after removal of luminosity blocks affected by a noise burst. The results are shown for the run 205071 (only CosmicCalo stream).

Beside the noise burst pollution, the CosmicCalo stream distributions were also found to be polluted by the LHC beam-induced background. This background – halo or beam-gas events – mainly originates far away from the interaction point (at more than 150 m [11]) and the trajectories are therefore almost parallel to the beam line. An example of such pollution is given in figure 20(a), where energy deposits above 800 MeV are observed in several contiguous cells at the same azimuthal position. As the radial coverage of the LAr calorimeters is very similar to the Cathode Strip Chamber (CSC) coverage of the muon spectrometer [28], it is possible to use the coincidence of signals registered in the CSC detectors to identify this background. The improvement due to this tagging method can be visualized by comparing figures 20(a) and 20(b). In the remainder of this section, the CSC tagging method is applied to all the monitoring distributions. Finally, given the trigger conditions (thresholds and prescales) and the typical energy deposit of the cosmic-ray muons [26], these distributions are not biased by the cosmic rays reaching the LAr calorimeter.

Despite the obvious improvement observed in figure 20(b) after vetoing the CSC tagged events in figure 20(a), a large accumulation of noisy cells remains, especially in the pseudorapidity region $-0.3 < \eta < 0$. This residual noise is mainly visible in the presampler, and is interpreted as a non-Gaussian noise source, originating from inside the cryostat. Further studies were carried on to characterize this noise.

- This noise is not visible in clock-generated triggered events.
- It is not constant over time, only appearing for a few to several minutes before disappearing.

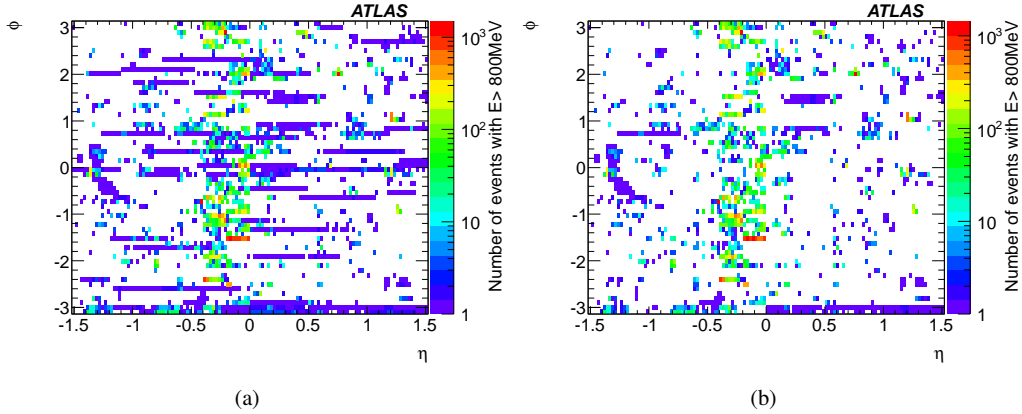


Figure 20: (η, ϕ) distributions of number of events per cell with cell energy greater than 800 MeV in the barrel presampler (a) before and (b) after the beam background removal with the CSC tagging method. The results are shown for the run 205071 (only CosmicCalo stream).

- The measured signal can reach up to 100 GeV in a single cell.
- This noise does not always affect the same cells from one run to another.
- Some regions are more affected than others, like the $-0.3 < \eta < 0$ region quoted above with no obvious correlation between the affected regions and any calorimeter components or integration conditions (electrode batches or vendors, assembly conditions, etc.).
- Lowering the HV settings in specific sectors reduces the noise amplitude in these sectors.
- No coherent behaviour is observed between the affected channels.

This phenomenon is very different from the noise bursts considered in section 6: the typical time scale is much longer and no coherent fluctuation is observed. The long time scale makes treatment with the time-window veto procedure impractical, as it would reject too much data. It was therefore decided to correct this noise by masking the affected channels. Given the non-permanent nature of this noise (usually named *sporadic*) and the large variations from one run to another, the list of affected channels has to be extracted per run and uploaded to the corresponding database during the calibration loop. As already explained in section 7.1, the masking choice – conditional or unconditional – depend on the noise shape, i.e. depend on the ability to distinguish between noise and real physics signal with the cell quality factor.

Figure 21 shows the fraction of high-energy events with a cell quality factor greater than 4000, i.e. the fraction of events where masking cells conditionally would be efficient. This distribution, convolved with the distribution shown in figure 20(b), provides the number of high-energy events per channel surviving a conditional masking. A conservative upper threshold of 80 events per cell per run was arbitrarily chosen to decide whether or not a channel should be conditionally masked. If more than 80 noisy events survive for a given channel, an unconditional masking has to be applied, more severely impacting the calorimeter performance.

The masking efficiency is double-checked on the same data streams after the bulk processing, where the database updates are included in the reconstruction. Figure 22(a), to be compared with

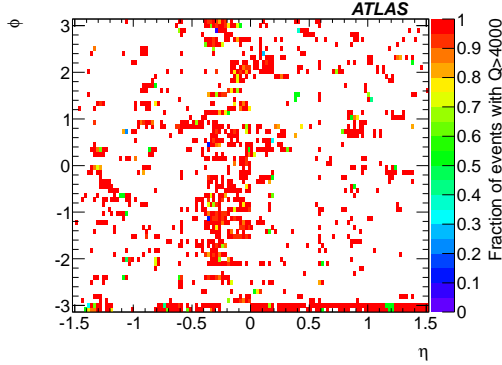


Figure 21: Fraction of events in which cells with cell energy greater than 800 MeV also have quality factor greater than 4000 in the barrel presampler. The results are shown for run 205071 (only CosmicCalo stream).

the original map in figure 20(b), illustrates the effect of masking the noisy cells. A large reduction of events with an energy above 800 MeV is observed. A final cross-check is performed by looking at the (η, ϕ) map of the clusters, the primary objects used in the electron/photon reconstruction, with a transverse energy greater than 10 GeV. This particular threshold was chosen as it corresponds to the minimal energy cut applied in most of the ATLAS analyses. The very limited number of clusters visible in figure 22(b) validates the satisfactory efficiency of the channel-masking procedure.

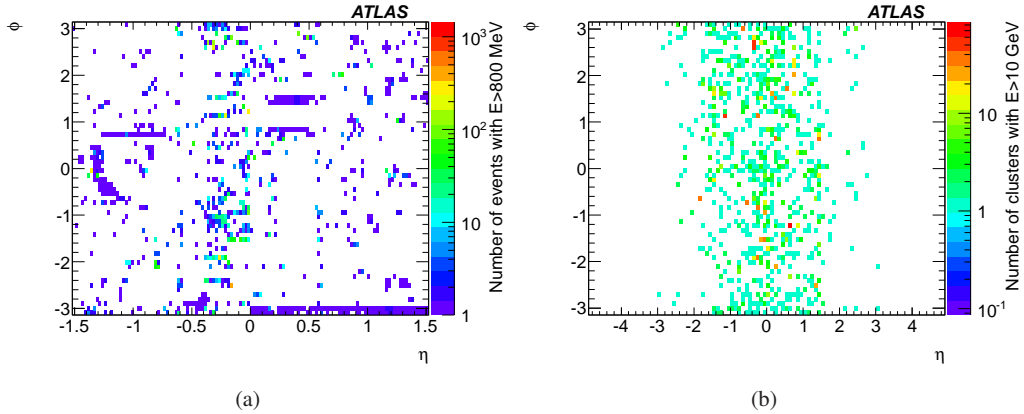


Figure 22: (η, ϕ) distributions produced after database updates with the same dataset as previously (run 205071 – CosmicCalo stream). (a) Number of events per cell with an energy greater than 800 MeV in the barrel presampler. (b) Number of clusters with a transverse energy greater than 10 GeV.

However, the masking procedure may sometimes fail. This happens in the very unfortunate cases where a cell is noisy only in luminosity blocks affected by a noise burst. The noisy luminosity blocks are excluded from the express processing output due to the custom merging procedure detailed in section 7.2, and the noisy cells are missed by the signoff team during the calibration

loop. During the bulk processing, the noise bursts are removed from the luminosity blocks with the time-window veto. The missing luminosity blocks are thus automatically re-included in the Tier 0 monitoring output of the bulk processing, and the sporadic noise emerges. Since it is too late to correct the data after the bulk processing, the offending luminosity block has to be discarded by assigning an intolerable defect. Still, the database is updated to include the additional noisy channels so that the masking can be applied during any future data reprocessing to recover the lost luminosity.

Given the large number of affected channels and their fluctuating nature, the whole procedure for the cell identification, masking proposal optimization, cluster matching, etc. is automatically performed within the dedicated LAr calorimeter data quality web infrastructure described in section 2.2.

7.4 Proportion of masked cells

Figure 23 shows the proportion of masked presampler channels as a function of the data-taking period in 2012; as a small dependence on integrated luminosity is observed for short runs, only the 95 runs with an integrated luminosity greater than 100 pb^{-1} recorded were considered. The proportion of unconditionally masked presampler cells remained below 0.2% for the whole LHC running period, while the proportion of conditionally masked presampler channels was greater than 7% during the first weeks of data taking. During the periods B–E, the HV settings of the most problematic lines were reduced from the original 1.6 kV to limit the sporadic noise, allowing reduction of the proportion of cells conditionally masked. Then, in September 2012 (middle of period G), it was decided to reduce globally the HV settings to 1.2 kV. This reduction gave a proportion of cells conditionally masked below 1%. The gain in electron and photon energy resolution due to the presampler is preserved despite a 10% increase in electronics noise.

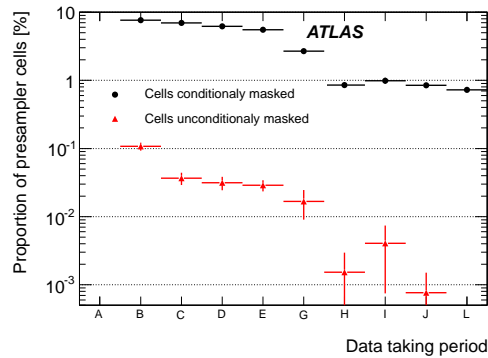


Figure 23: Proportion of presampler cells conditionally or unconditionally masked as a function of time, during the 2012 data-taking periods.

Figure 24 shows the proportion of channels masked in the same high-luminosity runs for all partitions except the presampler. The proportion of unconditionally masked channels remains very low in all the partitions: it is negligible in the electromagnetic calorimeter, and lower than 0.4% (0.2%) in the HEC (FCal) in 95% of the runs. The proportion of conditionally masked channels

is slightly larger, but the impact on performance is also negligible since only the subset of events with a high quality factor is effectively masked.

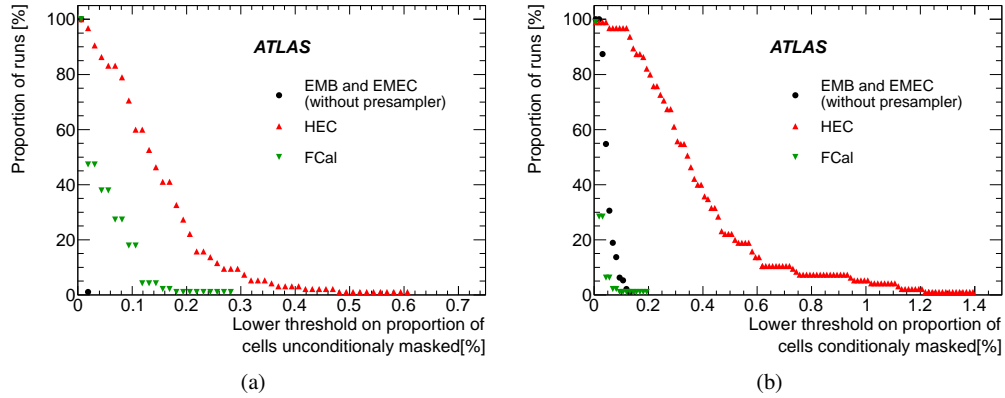


Figure 24: (a) Proportion of runs for which a proportion of unconditionally masked cells is above a given threshold. (b) Proportion of runs for which a proportion of conditionally masked cells is above a given threshold.

7.5 Associated data rejection in 2012

The data loss associated with a non-optimal treatment of the noisy channels (within the calibration loop) is shown in figure 25. This loss remains very low over the whole year, and it even goes to zero for the last 2012 data-taking periods, indicating that the latest version of the diagnostic algorithms was properly tuned and able to catch all the problematic channels within the calibration loop.

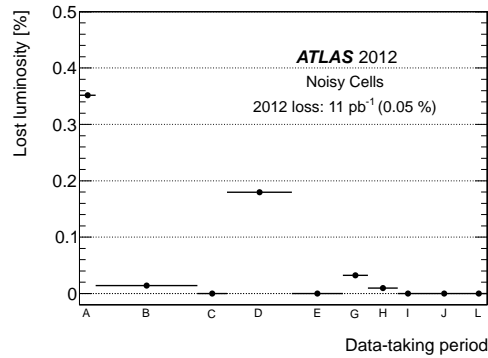


Figure 25: Lost luminosity due to noisy channels as a function of the data-taking period in 2012.

8. Achieved performance and outlook

8.1 Performance in proton–proton collision run (2011–2012)

Table 5 summarises the data rejection by defect assignment in the 2011 and 2012 datasets, corre-

sponding respectively to integrated recorded luminosities of 5.2 fb^{-1} and 21.3 fb^{-1} [7]. The 2011 performance is systematically worse than the 2012 performance described in detail in this article, and several reasons can be listed to explain this observation.

- The 2011 larger rejection due to HV trips is explained by luminosity conditions that were less stable in 2011 than in 2012 and by the replacement of several HV power supply modules with more sophisticated ones in 2012.
- The 2012 reduction of missed noise bursts is related to the implementation of a dedicated trigger chain in early 2012, which added more coherent noise events in the calibration streams and hence allowed a more efficient time-window veto procedure.
- The reduced data loss observed in 2012 for the other defects is due to the improved software robustness and automation in both the daily calorimeter operation and the data quality assessment.

Table 6 summarises the data rejection due to the time-window veto in 2011 and 2012. The rejection levels are very similar despite the much higher instantaneous luminosities recorded in 2012, which induced an enhanced yield of noise bursts. The higher noise burst rate in 2012 is counterbalanced by the choice of a narrower time window extension compared to 2011 ($\delta t = 200 \text{ ms}$ in 2012 vs $\delta t = 1 \text{ s}$ in 2011).

Table 5: Summary of data rejection by defect assignment for the 2011 and 2012 proton–proton collision datasets.

Year	Total	Data corruption	Missing condition data	HV trips	Coverage	Noise bursts	Noisy channels
2011	3.20%	0.04%	0.11%	0.96%	0.70%	1.24%	0.15%
2012	0.88%	0.01%	0.02%	0.46%	0.28%	0.06%	0.05%

Table 6: Summary of data rejection by the time-window veto procedure for the 2011 and 2012 proton–proton collision datasets.

Year	Total	Data corruption	Noise bursts
2011	0.28%	0.09%	0.20%
2012	0.22%	0.02%	0.20%

In 2011, as in 2012, the dataset was split into periods with similar data-taking conditions. The time evolution of the data rejection by defect assignment and time-window veto are displayed in figures 26 and 27 respectively using the datasets for proton–proton collisions collected in 2011 and 2012.

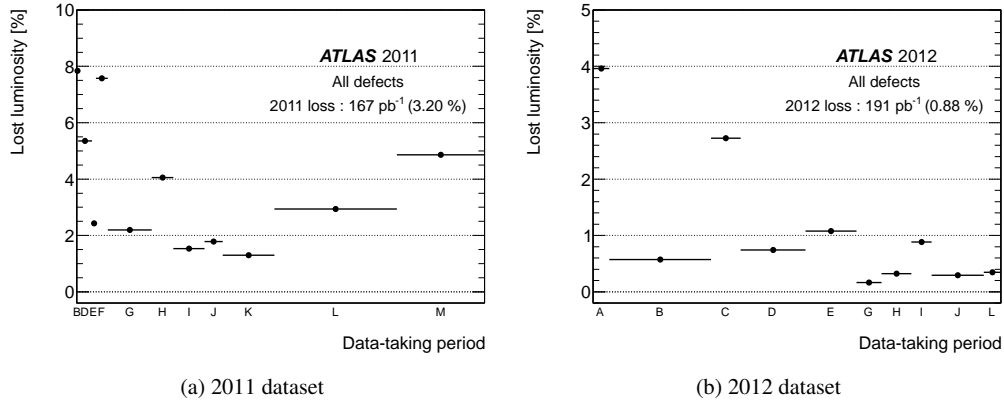


Figure 26: Lost luminosity associated to a defect assignment as a function of the data-taking period in 2012.

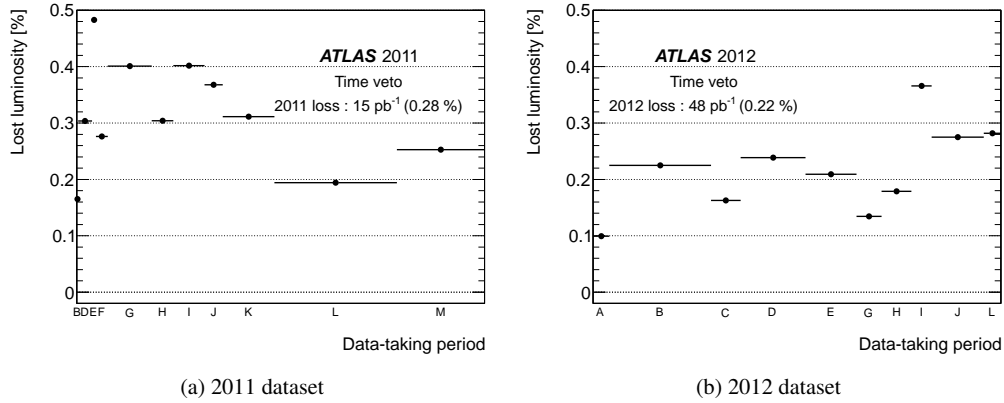


Figure 27: Lost luminosity associated to the time-window veto as a function of the data-taking period in 2012.

8.2 Performance in lead–lead and lead–proton collision run (2011–2013)

For completeness, the LAr calorimeter performance in the lead–lead and lead–proton collision runs is summarized in table 7. Given the much lower peak luminosity delivered during these runs ($5 \times 10^{26} \text{ cm}^{-2} \text{ s}^{-1}$ in 2011 and $10^{29} \text{ cm}^{-2} \text{ s}^{-1}$ in 2013), the impact of the phenomena correlated with the instantaneous luminosity (noise bursts and HV trips) was limited. The data rejection by the time-window veto procedure – not shown here – is also negligible. In 2013 a large data rejection was observed due to a single powering problem encountered in the hadronic endcap that lasted 90 minutes. Due to the shortness of the data taking period in 2013, this caused a data loss of 1.18%.

8.3 Outlook

The LHC is expected to restart in 2015 and to deliver collisions at the unprecedented energy and

Table 7: Summary of data rejection by defect assignment for the 2011 and 2013 lead–lead and lead–proton collision datasets.

Year	Total	Data corruption	Missing condition data	HV trips	Coverage	Noise bursts	Noisy channels
2011 (Pb–Pb)	0.19%	0.16%	-	0.03%	-	-	-
2013 (Pb–p)	1.50%	0.05%	-	0.22%	1.18%	0.04%	-

instantaneous peak luminosity of 13–14 TeV and $1\text{--}2 \times 10^{34} \text{ cm}^{-2}\text{s}^{-1}$ respectively.

As stated in section 3.5, the occurrence of HV trips, currently the main source of data loss, does not depend on the absolute instantaneous luminosity, but only on its evolution over a long timescale. When the LHC running conditions are stable, the data loss remains under control. In addition, many more of the upgraded power supplies are expected to be installed on the detector before the LHC restart to further reduce this loss.

The second largest source of data loss comes from large inefficient areas. However, out of the 0.28% yield observed in 2012, 0.15% were due to special runs that would have been rejected anyway. The remaining 0.13% originating from the LAr calorimeter arose from two defects of the low-voltage power supply system.

Considering the full data rejection by both defect assignment and the time-window veto, the loss due to noise bursts reaches 0.26% (0.20%+0.06%) in 2012. As explained in section 6.5, this yield should remain under control despite the regular increase in the frequency of noise bursts as a function of instantaneous luminosity. A parabolic extrapolation of the dependence curve of figure 17(a) indicates that the noise-burst rate could be in 2015 10–15 times higher than in 2012. However, there is still a lot of safety margin in the choice of the time window width to mitigate this rate increase.

The remaining sources of data losses measured in 2012 contribute less than 0.1%, and there is no indication of any luminosity dependence that could worsen the situation.

Therefore, the increased instantaneous luminosity of the LHC in 2015 is not expected to seriously degrade the data quality performance. However, two unknowns remain. First, the evolution of the sporadic noise with the instantaneous luminosity is still poorly known as is the robustness of the adopted solution (HV settings tuning). Second, it cannot be excluded that the almost doubled centre-of-mass energy may induce new problems or affect the magnitude of the already known ones. If these two risks are properly addressed, a similar efficiency around 98–99% can be considered as a realistic objective for the LHC restart in 2015.

Acknowledgments

We thank CERN for the very successful operation of the LHC, as well as the support staff from our institutions without whom ATLAS could not be operated efficiently.

We acknowledge the support of ANPCyT, Argentina; YerPhI, Armenia; ARC, Australia; BMWF and FWF, Austria; ANAS, Azerbaijan; SSTC, Belarus; CNPq and FAPESP, Brazil; NSERC,

NRC and CFI, Canada; CERN; CONICYT, Chile; CAS, MOST and NSFC, China; COLCIENCIAS, Colombia; MSMT CR, MPO CR and VSC CR, Czech Republic; D NRF, DNSRC and Lundbeck Foundation, Denmark; EPLANET, ERC and NSRF, European Union; IN2P3-CNRS, CEA-DSM/IRFU, France; GNSF, Georgia; BMBF, DFG, HGF, MPG and AvH Foundation, Germany; GSRT and NSRF, Greece; ISF, MINERVA, GIF, I-CORE and Benozziyo Center, Israel; INFN, Italy; MEXT and JSPS, Japan; CNRST, Morocco; FOM and NWO, Netherlands; BRF and RCN, Norway; MNiSW and NCN, Poland; GRICES and FCT, Portugal; MNE/IFA, Romania; MES of Russia and ROSATOM, Russian Federation; JINR; MSTD, Serbia; MSSR, Slovakia; ARRS and MIZŠ, Slovenia; DST/NRF, South Africa; MINECO, Spain; SRC and Wallenberg Foundation, Sweden; SER, SNSF and Cantons of Bern and Geneva, Switzerland; NSC, Taiwan; TAEK, Turkey; STFC, the Royal Society and Leverhulme Trust, United Kingdom; DOE and NSF, United States of America.

The crucial computing support from all WLCG partners is acknowledged gratefully, in particular from CERN and the ATLAS Tier-1 facilities at TRIUMF (Canada), NDGF (Denmark, Norway, Sweden), CC-IN2P3 (France), KIT/GridKA (Germany), INFN-CNAF (Italy), NL-T1 (Netherlands), PIC (Spain), ASGC (Taiwan), RAL (UK) and BNL (USA) and in the Tier-2 facilities worldwide.

References

- [1] ATLAS Collaboration, *Observation of a new particle in the search for the Standard Model Higgs boson with the ATLAS detector at the LHC*, *Phys. Lett. B* **716** (2012) 1–29, [arXiv:1207.7214].
- [2] ATLAS Collaboration, *The ATLAS Experiment at the CERN Large Hadron Collider*, 2008 *JINST* **3** S08003.
- [3] ATLAS Collaboration, *Liquid Argon Calorimeter Technical Design Report*. LHCC 96-041. CERN, 1996.
- [4] H. Abreu et al., *Performance of the electronic readout of the ATLAS liquid argon calorimeters*, 2010 *JINST* **5** P09003.
- [5] N. Buchanan et al., *Design and implementation of the Front End Board for the readout of the ATLAS liquid argon calorimeters*, 2008 *JINST* **3** P03004.
- [6] A. Bazan et al., *ATLAS liquid argon calorimeter back end electronics (RODs)*, 2007 *JINST* **2** P06002.
- [7] ATLAS Collaboration, *Improved luminosity determination in pp collisions at $\sqrt{s} = 7$ TeV using the ATLAS detector at the LHC*, *Eur. Phys. J. C* **73** (2013) 2518, [arXiv:1302.4393].
- [8] A. Corso-Radu et al., *Data quality monitoring framework for the ATLAS experiment: performance achieved with colliding beams at the LHC*, *J. Phys.: Conf. Ser.* **331** (2011) 022027.
- [9] A. Corso-Radu et al., *The electronic logbook for the information storage of ATLAS experiment at LHC (ELISA)*, *J. Phys.: Conf. Ser.* **396** (2012) 012014.
- [10] L. Evans and P. Bryant eds., *LHC machine*, 2008 *JINST* **3** S08001.
- [11] ATLAS Collaboration, *Characterisation and mitigation of beam-induced backgrounds observed in the ATLAS detector during the 2011 proton-proton run*, 2013 *JINST* **8** P07004, [arXiv:1303.0223].
- [12] ATLAS Collaboration, *Level 1 Trigger Technical Design Report*. LHCC 98-014. CERN, 1996.

- [13] ATLAS Collaboration, *High-Level Trigger, Data Acquisition and Controls Technical Design Report*. LHCC 03-022. CERN, 2003.
- [14] ATLAS Collaboration, *Performance of the ATLAS Trigger System in 2010*, *Eur. Phys. J. C* **72** (2012) 1849, [arXiv:1110.1530].
- [15] K. Korda et al., *ATLAS high level trigger infrastructure, ROI collection and event building*, in *Proceedings of the Computing in High Energy and Nuclear Physics Conference*, (Mumbai, India), 2006.
- [16] ATLAS Collaboration, *Computing Technical Design Report*. LHCC 05-022. CERN, 2005.
- [17] S. Campana et al., *Commissioning of a CERN production and analysis facility based on xrootd*, *J. Phys.: Conf. Ser.* **331** (2011) 7.
- [18] J. Adelman et al., *ATLAS offline data quality monitoring*, *J. Phys.: Conf. Ser.* **219** (2010) 042018.
- [19] R. Trentadue et al., *LCG persistency framework (CORAL, COOL, POOL): status and outlook in 2012*, *J. Phys.: Conf. Ser.* **396** (2012) 052067.
- [20] T. Golling et al., *The ATLAS data quality defect database system*, *Eur. Phys. J. C* **72** (2012) 1960, [arXiv:1110.6119].
- [21] A. Barriuso Poy et al., *The detector control system of the ATLAS experiment*, 2008 *JINST* **3** P05006.
- [22] ATLAS Collaboration, *Data quality from the detector control system at the ATLAS experiment*, *J. Phys.: Conf. Ser.* **219** (2010) 022037.
- [23] ATLAS Collaboration, *Data-quality requirements and event cleaning for jets and missing transverse energy reconstruction with the ATLAS detector in proton-proton collisions at a center-of-mass energy of $\sqrt{s} = 7$ TeV*. ATLAS-CONF-2010-038. CERN, 2010.
- [24] V. Grassi et al., *The ATLAS liquid argon calorimeter at the CERN Large Hadron Collider : general performance and latest developments of the high voltage system*, in *Proceedings of the IEEE Nuclear Science Symposium*, (Seoul, Korea), 2013.
- [25] W. Cleland et al., *Signal processing considerations for liquid ionization calorimeter in a high rate environment*, *Nucl. Instrum. Methods A* **338** (1994) 467.
- [26] ATLAS Collaboration, *Readiness of the ATLAS Liquid Argon Calorimeter for LHC Collisions*, *Eur. Phys. J. C* **70** (2010) 723, [arXiv:0912.2642].
- [27] ATLAS Collaboration, *Search for non-pointing photons in the diphoton and E_{miss}^T final state in $\sqrt{s} = 7$ TeV proton-proton collisions using the ATLAS detector*, *Phys. Rev. D* **88** (2013) 012001, [arXiv:1304.6310].
- [28] ATLAS Collaboration, *ATLAS Muon Spectrometer Technical Design Report*. LHCC 97-022. CERN, 1997.

Readiness of the ATLAS Liquid Argon Calorimeter for LHC Collisions

Received: date / Revised version: date

Abstract. The ATLAS liquid argon calorimeter has been operating continuously since August 2006. At this time, only part of the calorimeter was readout, but since the beginning of 2008, all calorimeter cells have been connected to the ATLAS readout system in preparation for LHC collisions. This paper gives an overview of the liquid argon calorimeter performance measured in situ with random triggers, calibration data, cosmic muons, and LHC beam splash events. Results on the detector operation, timing performance, electronics noise, and gain stability are presented. High energy deposits from radiative cosmic muons and beam splash events allow to check the intrinsic constant term of the energy resolution. The uniformity of the electromagnetic barrel calorimeter response along η (averaged over ϕ) is measured at the percent level using minimum ionizing cosmic muons. Finally, studies of electromagnetic showers from radiative muons have been used to cross-check the Monte Carlo simulation. The performance results obtained using the ATLAS readout, data acquisition, and reconstruction software indicate that the liquid argon calorimeter is well-prepared for collisions at the dawn of the LHC era.

1 Introduction

Installation of the liquid argon (LAr) calorimeter in the ATLAS [\[1\]](#) experimental hall was completed in early 2008. Until recently, the expected performance of the LAr calorimeter was extrapolated from intensive testing of a few modules with electron and pion beams from 1998 to 2003 (Ref. [\[2,3,4,5,6,7,8,9,10\]](#)), and in 2004 of a complete ATLAS detector slice [\[11,12,13\]](#). The 20 months separating the completion of the installation from the first LHC collisions have been used to commission the LAr calorimeter. This paper reviews the first in situ measurements of the electronics stability, the quality of the energy re-

construction, the calorimeter response uniformity and the agreement between data and the Monte Carlo simulation of electromagnetic shower shapes. The measurements are performed using calibration triggers, cosmic muons, and the first LHC beam events collected during this 20 months period. The results and the experience gained in the operation of the LAr calorimeter provide the foundation for a more rapid understanding of the experimental signatures of the first LHC collisions, involving electrons, photons, missing transverse energy (E_T^{miss}), jets, and τ s where the LAr calorimeter plays a central role.

This paper is organized as follows. Section 2 gives the present hardware status of the LAr calorimeter. Section 3 details the level of understanding of the ingredients entering the cell energy reconstruction: pedestals, noise, electronic gains, timing, and the quality of the signal pulse shape predictions. The current understanding of the first level trigger energy computation is also discussed. Section 4 describes the in situ performance of the electromagnetic LAr calorimeter using ionizing and radiating cosmic muons. Lastly, Section 5 draws the conclusions.

2 LAr calorimeter hardware status and data taking conditions

The LAr calorimeter is composed of electromagnetic and hadronic sub-detectors of which the main characteristics are described in Section 2.1. During the detector and electronics construction and installation, regular and stringent quality tests were performed, resulting in a fully functional LAr calorimeter. The operational stability of the cryostats since March 2008 is discussed in Section 2.2. The current status of the high voltage and the cell readout are discussed in Sections 2.3 and 2.4 respectively. Finally, the general data taking conditions are given in Section 2.5. In ATLAS, the positive x -axis is defined as pointing from the interaction point to the center of the LHC ring, the positive y -axis is defined as pointing upwards, and the positive z -axis corresponds to protons running anti-clockwise. The polar angle θ is measured from the beam axis (z -axis), the azimuthal angle ϕ is measured in the transverse (xy)-plane, and the pseudorapidity is defined as $\eta = -\ln \tan(\theta/2)$.

2.1 Main characteristics of the LAr calorimeter

The LAr calorimeter [1], shown in Figure 1, is composed of sampling detectors with full azimuthal symmetry, housed in one barrel and two endcap cryostats. More specifically, a highly granular electromagnetic (EM) calorimeter with accordion-shaped electrodes and lead absorbers in liquid argon covers the pseudorapidity range $|\eta| < 3.2$, and contains a barrel part (EMB [14], $|\eta| < 1.475$) and an endcap part (EMEC [15], $1.375 < |\eta| < 3.2$). For $|\eta| < 1.8$, a presampler (PS [16,15]), consisting of an active LAr layer and installed directly in front of the EM calorimeters, provides a measurement of the energy lost upstream. Located behind the EMEC is a copper-liquid argon hadronic endcap calorimeter (HEC [17], $1.5 < |\eta| < 3.2$), and a copper/tungsten-liquid argon forward calorimeter (FCal [18]) covers the region closest to the beam at $3.1 < |\eta| < 4.9$. An hadronic Tile calorimeter ($|\eta| < 1.7$) surrounding the LAr cryostats completes the ATLAS calorimetry.

All the LAr detectors are segmented transversally and divided in three or four layers in depth, and correspond to a total of 182,468 readout cells, i.e. 97.2% of the full ATLAS calorimeter readout.

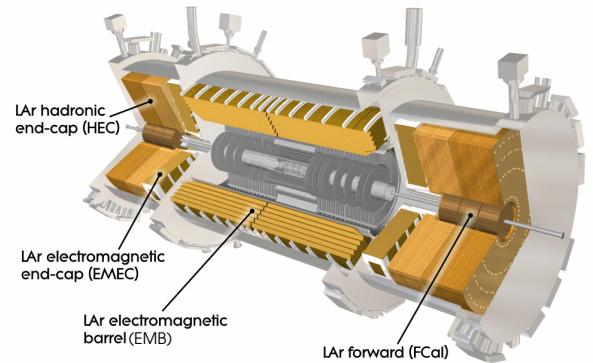


Fig. 1. Cut-away view of the LAr calorimeter, 17 m long (barrel + endcaps) and 4 m of diameter.

The relative energy resolution of the LAr calorimeter is usually parameterized by:

$$\frac{\sigma_E}{E} = \frac{a}{\sqrt{E}} \oplus \frac{b}{E} \oplus c, \quad (1)$$

where (a) is the stochastic term, (b) the noise term and (c) the constant term. The target values for these terms are respectively $a \simeq 10\%$, $b \simeq 170$ MeV (without pile-up) and $c = 0.7\%$.

2.2 Cryostat operation

Variations of the liquid argon temperature have a direct impact on the readout signal, and consequently on the energy scale, partly through the effect on the argon density, but mostly through the effect on the ionization electron drift velocity in the LAr. Overall, a $-2\%/K$ signal variation is expected [19]. The need to keep the corresponding contribution to the constant term of the energy resolution (Eq. 1) negligible (i.e. well below 0.2%) imposes a temperature uniformity requirement of better than 100 mK in each cryostat. In the liquid, ~ 500 temperature probes (PT100 platinum resistors) are fixed on the LAr detector components and read out every minute. In 2008-2009, installation activities in the ATLAS cavern prevented a stable cryostat temperature. A quiet period of ten days around the 2008 Christmas break, representative of what is expected during LHC collisions, allowed a check of the temperature stability in the absence of these external factors. The average dispersion (RMS) of the measurements of each temperature probe over this period is 1.6 mK (5 mK maximum), showing that no significant local temperature variation in time is observed in the three cryostats. Over this period, the temperature uniformity (RMS of all probes per cryostat) is illustrated for the barrel in Figure 2 and gives 59 mK. Results for the two endcap cryostats are also in the range 50-70 mK, below the required level of 100 mK. The average cryostat temperatures are slightly

different for the barrel (88.49 K) and the two endcaps (88.67 and 88.45 K) because they are independently regulated. An energy scale correction per cryostat will therefore be applied.

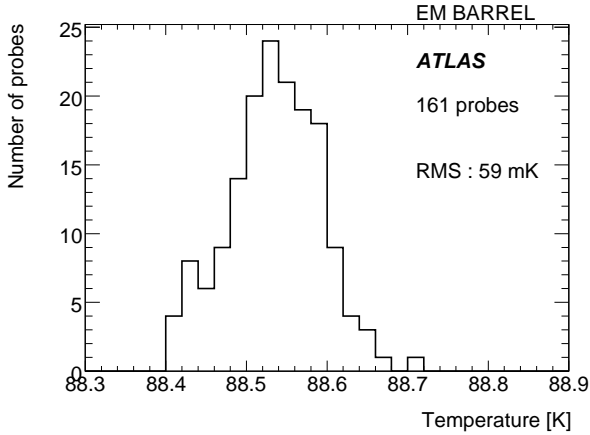


Fig. 2. Distribution of barrel cryostat probe temperatures averaged over a period of ten days.

To measure the effects of possible out-gassing of calorimeter materials under irradiation, which has been minimized by careful screening of components, 30 purity monitors measuring the energy deposition of radioactive sources in the LAr are installed in each cryostat and read every 15 minutes. The contribution to the constant term of the energy resolution is negligible for a level of electronegative impurities below 1000 ppb O_2 equivalent. All argon purity measurements over a period of two years are stable, in the range 200 ± 100 ppb O_2 equivalent, well below this requirement.

In summary, measurements of the liquid argon temperature and purity demonstrate that the stability of the operation of the three LAr cryostats is in the absence of proton beams within the required limits ensuring a negligible contribution to the energy resolution constant term.

2.3 High voltage status

The electron/ion drift speed in the LAr gap depends on the electric field, typically 1 kV/mm. Sub-detector-specific high voltage (HV) settings are applied. In the EM barrel, the high voltage is constant along η , while in the EMEC, where the gap varies continuously with radius, it is adjusted in steps along η . The HV supply granularity is typically in sectors of $\Delta\eta \times \Delta\phi = 0.2 \times 0.2$. For redundancy, each side of an EM electrode, which is in the middle of the LAr gap, is powered separately. In the HEC, each sub-gap is serviced by one of four different HV lines, while for the FCal each of the four electrode groups forming a normal readout channel is served by an independent HV line.

For HV sectors with non-optimal behavior, solutions were implemented in order to recover the corresponding

region. For example, in the EM calorimeter, faulty electrodes were connected to separate HV lines during the assembly phase at room temperature while, if the defect was identified during cryostat cold testing, the high voltage sector was divided into two in ϕ , each connected separately. The effect of zero voltage on one side of an electrode was studied in beam tests proving that with offline corrections the energy can still be measured, with only a small loss in accuracy. Finally, for HV sectors with a permanent short-circuit, high voltage modules permitting large DC current draws of up to 3 mA (more than three orders of magnitude above the nominal limit) are used in order to operate the faulty sector at 1000 V or above.

As a result, 93.9% of readout cells are operating under nominal conditions and the rest sees a reduced high voltage. However, even with a reduced high voltage, signals can be well reconstructed by using a correction scale factor. Figure 3 shows the distribution of all HV correction factors for the EM, HEC and FCal cells as of the end of September 2009. Since the beginning of 2008, no changes have been observed. The largest correction occurs if one side of an EM electrode is not powered, and only half of the signal is collected. For the faulty cells, this correction factor is applied online at the energy reconstruction level. A similar correction is currently being implemented at the first level (L1) trigger.

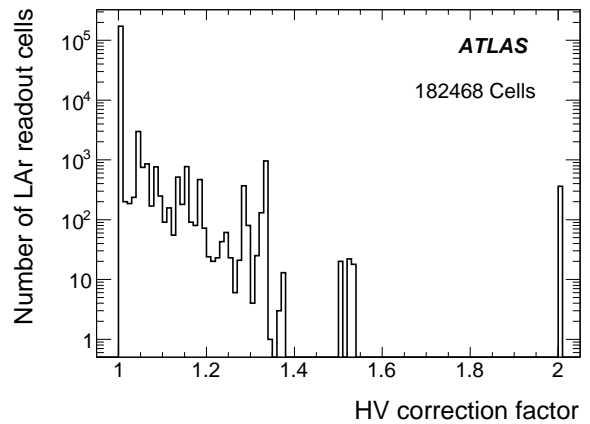


Fig. 3. High voltage correction factors for all LAr cells at the end of September 2009.

In conclusion, since the beginning of 2008, all 182,468 readout cells are powered with high voltage, and no dead region exists. Signals from regions with non-nominal high voltage are easily corrected and their impact on physics is negligible.

2.4 Readout cell status

The cell signals are read out through 1524 Front-End Boards (FEBs [20,21]) with 128 channels each, which sit inside front-end crates that are located around the periphery of the cryostats. The FEBs perform analog processing

(amplification and shaping - except for the HEC where the amplification is done inside the cryostat), store the signal while waiting for the L1 trigger decision, and digitize the accepted signals. The FEBs also perform fast analog summing of cell signals in predefined projective “towers” for the L1 trigger.

The digitized signals are transmitted via optical fibers to the Readout Drivers (RODs) [22] located in the counting room 70 m away. The cell energy is reconstructed on-line in the ROD modules up to a nominal maximum L1 rate of 75 kHz. The cell and trigger tower energy reconstruction is described in detail in Section 3.

The response of the 182,468 readout cells is regularly monitored using 122 calibration boards [23] located in the front-end crates. These boards inject calibrated current pulses through high-precision resistors to simulate energy deposits in the calorimeters. At the end of September 2009, 1.3% of cells have problems. The majority of them, i.e. 1.2% of the total number of cells, are not read-out because they are connected to 17 non-functioning FEBs. On these FEBs, the active part (VCSEL) of the optical transmitter to the ROD has failed. This failure, occurring at a rate of two or three devices per month, is under intensive investigation and are expected to be fixed during the next LHC shutdown. The remaining 0.1% of cells with problems can be split in three sub-types: incurable cells, i.e. cells not responding to the input pulse (0.02%), or which are permanently (0.03%) or sporadically (0.07%) very noisy. The first two types are always masked in the event reconstruction (121 cells), while the sporadically very noisy cells, not yet well understood, are masked on an event by event basis. For cells which do not receive calibration signals (0.3%) average calibration constants computed among neighboring cells are used. For cells with non-nominal high voltage (6.1%) a software correction factor is applied. Both have very limited impact on the energy reconstruction.

In total, 180,128 cells, representing 98.7% of the total number of cells in the LAr calorimeter, are used for event reconstruction at the end of September 2009. The number of inactive cells (1.3%) is dominated by the cells lost due to faulty optical drivers (1.2%): apart from these, the number of inactive cells has been stable in time.

2.5 Data taking conditions

The results presented here focus on the period starting in September 2008 when all the ATLAS sub-detectors were completed and integrated into the data acquisition. Apart from regular electronics calibration runs, two interesting types of data are used to commission the LAr calorimeter: the beam splash events and the cosmic muons. The first type corresponds to LHC events of September 10th 2008 when the first LHC beam hit the collimators located 200 m upstream of the ATLAS interaction point. A cascade of pions and muons parallel to the beam axis fired the beam related trigger, illuminated the whole ATLAS detector and deposited several PeV per event in the LAr calorimeter. The second type corresponds to long cosmic

muon runs acquired on September-October 2008 and on June-July 2009 where more than 300 million events were recorded, corresponding to more than 500 TB of data.

For the LAr commissioning, L1 calorimeter triggers are used to record radiative energy losses from cosmic muons while the first level muon spectrometer and second level inner detector triggers are used to study pseudo-projective minimum ionizing muons. In most of the runs analyzed, the toroidal and solenoidal magnetic fields were at the nominal value.

3 Electronic performance and quality of cell energy reconstruction

The robustness of the LAr calorimeter energy reconstruction has been studied in detail using calibration and randomly triggered events, cosmic muons and beam splash events. Section 3.1 briefly describes the energy reconstruction method in the trigger towers and in the cells, as well as a validation study of the trigger. The time stability of the electronics is discussed in Section 3.2. The status of the electronics timing for the first LHC collisions is presented in Section 3.3, and the quality of the LAr calorimeter energy reconstruction is assessed in Section 3.4.

3.1 Energy reconstruction in the LAr calorimeter

When charged particles cross the LAr gap between electrodes and absorbers, they ionize the liquid argon. Under the influence of the electric field, the ionization electrons drift towards the electrode inducing a current. The initial current is proportional to the energy deposited in the liquid argon. The calorimeter signals are then used to compute the energy per trigger tower or per cell as discussed in this section.

3.1.1 Energy reconstruction at the first level calorimeter trigger

The timing requirements for the L1 trigger latency can only be met with fast analogue summing in coarse granularity. In the EM part, the pre-summation of analog signals per layer on the FEBs serves as input to tower builder boards where the final trigger tower signal sum and shaping is performed. In the HEC and FCal, the summation is performed on the FEBs and transmitted to tower driver boards where only shaping is done. The tower sizes are $\Delta\eta \times \Delta\phi = 0.1 \times 0.1$ for $|\eta| < 2.5$ and go up to $\Delta\eta \times \Delta\phi = 0.4 \times 0.4$ for $3.1 < |\eta| < 4.9$. The analog trigger sum signals are sent to receiver modules in the service cavern. The main function of these modules is to compensate for the differences in energy calibration and signal attenuation over the long cables using programmable amplifier gains (g_R). The outputs are sent to L1 trigger pre-processor boards which perform the sampling at 40 MHz and the digitization of five samples. At this stage, both

the transverse energy and bunch crossing are determined using a finite impulse response filter, in order to maximize the signal-to-noise ratio and bunch crossing identification efficiency. During ATLAS operation, the output $g_R A^{L1}$ of the filter, which uses optimal filtering, is passed to a look-up table where pedestal (P in ADC counts) subtraction, noise suppression and the conversion from ADC counts to transverse energy in GeV ($F_{\text{ADC} \rightarrow \text{GeV}}^{L1}$) is performed in order to extract the final transverse energy value (E_T^{L1}) for each trigger tower:

$$E_T^{L1} = F_{\text{ADC} \rightarrow \text{GeV}}^{L1} (g_R A^{L1} - g_R P). \quad (2)$$

Arrays (in η - ϕ) of these E_T^{L1} energies, merged with similar information coming from the Tile calorimeter, are subsequently used to trigger on electrons, photons, jets, τ s and events with large missing transverse energy.

3.1.2 Energy reconstruction at cell level

At the cell level, the treatment of the analog signal is also performed in the front-end electronics. After shaping, the signal is sampled at 40 MHz and digitized if the event was selected by the L1 trigger. The reconstruction of the cell energy, performed in the ROD, is based on an optimal filtering algorithm applied to the samples s_j [24]. The amplitude A , in ADC counts, is computed as:

$$A = \sum_{j=1}^{N_{\text{samples}}} a_j (s_j - p), \quad (3)$$

where p is the ADC pedestal (Section 3.2.1). The Optimal Filtering Coefficients (OFCs) a_j are computed per cell from the predicted ionization pulse shape and the measured noise autocorrelation to minimize the noise and pile-up contributions to A . For cells with sufficient signal, the difference (Δt in ns) between the digitization time and the chosen phase is obtained from:

$$\Delta t = \frac{1}{A} \sum_{j=1}^{N_{\text{samples}}} b_j (s_j - p), \quad (4)$$

where b_j are time-OFCs. For a perfectly timed detector and in-time particles $|\Delta t|$ must be close to zero, while larger values indicate the need for better timing or the presence of out-of-time particles in the event.

The default number of samples used for A and Δt computation is $N_{\text{samples}} = 5$, but for some specific analyses more samples, up to a maximum of 32, are recorded. Finally, including the relevant electronic calibration constants, the deposited energy (in MeV) is extracted with:

$$E_{\text{cell}} = F_{\mu A \rightarrow \text{MeV}} \times F_{\text{DAC} \rightarrow \mu A} \times \frac{1}{\frac{M_{\text{phys}}}{M_{\text{cali}}}} \times G \times A, \quad (5)$$

where the various constants are linked to the calibration system: the cell gain G (to cover energies ranging from a maximum of 3 TeV down to noise level, three linear gains

are used: low, medium and high with ratios $\sim 1/10/100$) is computed by injecting a known calibration signal and reconstructing the corresponding cell response; the factor $1/\frac{M_{\text{phys}}}{M_{\text{cali}}}$ quantifies the ratio of response to a calibration pulse and an ionization pulse corresponding to the same input current; the factor $F_{\text{DAC} \rightarrow \mu A}$ converts digital-to-analog converter (DAC) counts set on the calibration board to μA ; finally, the factor $F_{\mu A \rightarrow \text{MeV}}$ is estimated from simulations and beam test results, and includes high voltage corrections for non-nominal settings (see Sec 2.3). Note that the crosstalk bias in the finely segmented first layer of the electromagnetic calorimeter is corrected for in the gain G [4].

3.1.3 Check of the first level tower trigger energy computation

The trigger decision is of utmost importance for ATLAS during LHC collisions since the data-taking rate is at maximum 200 Hz because of bandwidth limitations, i.e. a factor 2×10^5 smaller than the 40 MHz LHC clock. It is therefore important to check that no systematic bias is introduced in the computation of the L1 trigger energy and that the trigger energy resolution is not too degraded with respect to the offline reconstruction. In the following, this check is performed with the most granular part of the LAr calorimeter, the barrel part of the EM calorimeter, where 60 cell signals are summed per trigger tower.

Since cosmic muon events occur asynchronously with respect to the LHC clock, and the electronics for both the trigger and the standard readout is loaded with one set of filtering coefficients (corresponding to beam crossing), the reconstructed energy is biased by up to 10%, depending on the phase. For the study presented here, A^{L1} is recomputed offline by fitting a second-order polynomial to the three highest samples transmitted through the processors. The most critical part in the trigger energy computation is then to calibrate the individual receiver gains g_R . For that purpose, a common linearly increasing calibration pulse is sent to both the L1 trigger and the normal cell circuits: the inverse receiver gain $1/g_R$ is obtained by fitting the correlation between the L1 calorimeter transverse energy (E_T^{L1}) and the sum of cell transverse energies in the same trigger tower, later called *offline* trigger tower (E_T^{LAr}). In cosmic muon runs, receiver gains are set to 1.0 and are recomputed offline with dedicated calibration runs. As a cross check, the gain was also extracted using LHC beam splash event data which covers the full detector. In both cases, the L1 transverse energy is computed as in Eq. 2.

In the EM calorimeter, radiating cosmic muons may produce a local energy deposit of a few GeV, and fire the EM calorimeter trigger condition EM3 that requires a transverse energy greater than 3 GeV in a sum of four adjacent EM trigger towers. To mimic an electron coming from the interaction point, only those events that contain a track reconstructed with strict projectivity cuts are considered. Here, the L1 calorimeter transverse energy is computed using the gains determined with calibration runs. Figure 4 shows the correlation between E_T^{L1} and E_T^{LAr} .

Computing the ratio of E_T^{L1} and E_T^{LAr} gives a Gaussian distribution with a mean of 1.015 ± 0.002 , showing the very good correspondence between these two quantities, especially at low energy. This also shows that the trigger energy is well calibrated and almost unbiased with respect to the LAr readout.

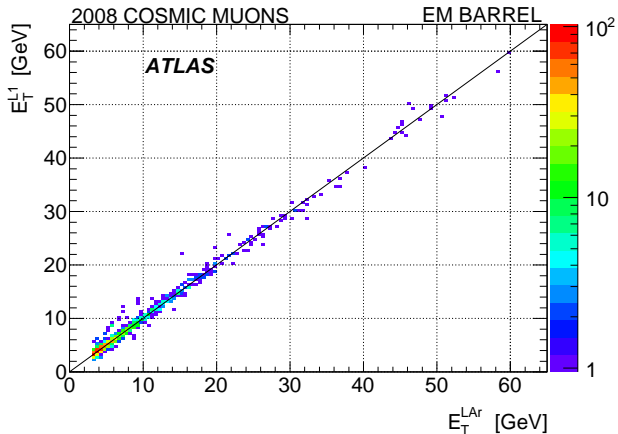


Fig. 4. $L1$ transverse energy (E_T^{L1}) computed with the receiver gains extracted from calibration runs versus the sum of cell transverse energies in the same trigger tower (E_T^{LAr}).

Figure 5 shows the corresponding resolution computed as the relative difference of E_T^{L1} and E_T^{LAr} . At low energy, the difference is dominated by electronic noise since the two readout paths have only part of their electronics in common. The ATLAS specification of 5% of $L1$ transverse energy resolution is reached for energies greater than 10 GeV. The $L1$ transverse energy resolution reaches around 3% at high energy.

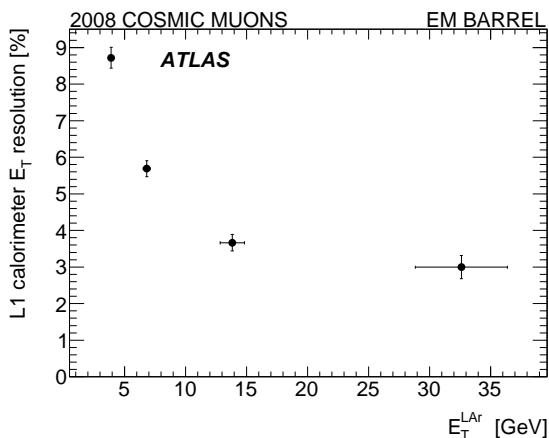


Fig. 5. Relative difference of E_T^{L1} and E_T^{LAr} ($L1$ Calorimeter E_T resolution) as a function of E_T^{LAr} . Strict projectivity cuts for the track pointing to the EM shower are applied. Horizontal error bars reflect the RMS of E_T^{LAr} in each bin.

As a crosscheck, a similar study was performed with gains computed from the beam splash events, without the projectivity cut. A slight degradation of the resolution is observed at high energy, but not at low energy where the noise dominates. Taking advantage of the higher statistics, it is possible to compute the 5 GeV “turn-on curve”, i.e. the relative efficiency for an offline trigger tower to meet the requirement $E_T^{L1} \geq 5$ GeV as a function of E_T^{LAr} . This is not the absolute efficiency as the calorimeter trigger condition EM3 is used to trigger the events. The efficiency is shown in Figure 6, where a sharp variation around a $E_T^{L1} = 5$ GeV energy threshold is observed.

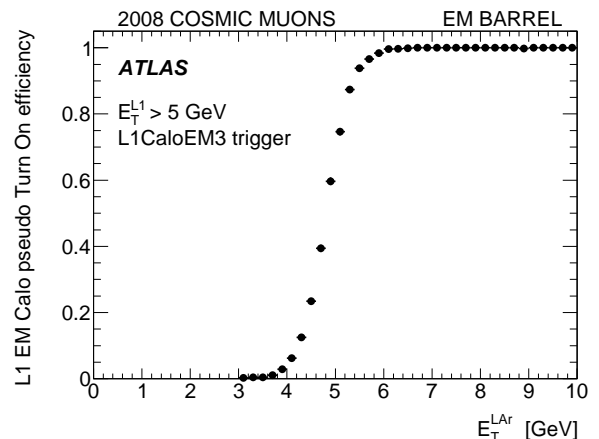


Fig. 6. Turn-on curve efficiency for $E_T^{L1} > 5$ GeV requirement obtained with events triggered by the EM3 $L1$ Calorimeter trigger.

These results give confidence that EM showers (electrons and photons) will be triggered efficiently in LHC events. After this study, the gains g_R were extracted from dedicated calibration runs and loaded into the receivers to be used for the first LHC collisions.

3.2 Electronic stability

Hundreds of millions of randomly triggered and calibration events can be used for a study of the stability of the properties of each readout channel, such as the pedestal, noise and gain. The first two quantities are computed for each cell as the mean (pedestal) of the signal samples s_j in ADC counts, and the width (noise) of the energy distribution. The gain is extracted by fitting the output pulse amplitudes against calibration pulses with increasing amplitudes.

3.2.1 Pedestal

The stability of the pedestals is monitored by measuring variations with respect to a reference pedestal value for each cell. For each FEB, an average over the 128 channels is computed.

As an example, Figure 7 illustrates the results for the 48 HEC FEBs over a period of six months in 2009. A slight drift of the pedestal with time, uncorrelated with the FEB temperature and/or magnetic field configurations, is observed. Overall, the FEB pedestal variations follow a Gaussian distribution with a standard deviation of 0.02 ADC counts, i.e. below 2 MeV. The same checks have been performed on all other FEBs, and give typical variations of around 1 (0.1) MeV and 10 (1) MeV in the EM and FCal calorimeters respectively, in medium (high) gain. These variations are much lower for the EM and HEC or at the same level for the FCal than the numerical precision of the energy computation, which is 8 (1) MeV in medium (high) gain.

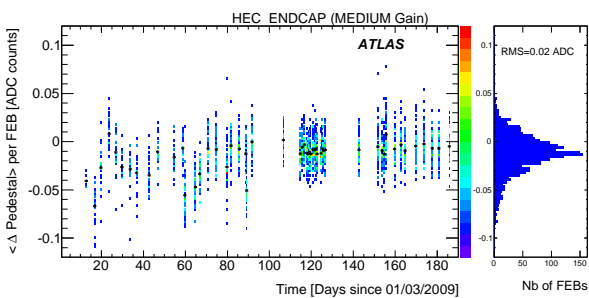


Fig. 7. Average FEB pedestal variations in ADC counts, in medium gain, for the HEC during 6 months of data taking in 2009. The crosses indicate the mean value for each time slice.

During the LHC running, it is foreseen to acquire pedestal and calibration runs between fills, thus it will be possible to correct for any small time dependence such as observed in Figure 7. In the same spirit, random triggers collected during physics runs can be used to track any pedestal variations during an LHC fill.

3.2.2 Noise

Figure 8 shows the noise measured in randomly triggered events at the cell level as a function of η for all layers of the LAr calorimeters. In all layers, a good agreement with the expected noise [1] is observed. Noise values are symmetric with respect to $\eta = 0$ and uniformly in ϕ within few percents. In the EM calorimeters, the noise ranges from 10 to 50 MeV, while it is typically a factor of 10 greater in the hadronic endcap and forward calorimeters where the granularity is 20 times coarser and the sampling fractions are lower. It should be noted that these results are obtained using five samples in Eq. (3) and (5), i.e. the noise is reduced by a factor varying from 1.5 to 1.8, depending on η , with respect to the single-sample noise value.

The coherent noise over the many cells used to measure electron and photon energies in the EM calorimeters should be kept below 5% [25] of the incoherent noise (i.e. the quadratic sum of all channel noise). For the second layer of the EM calorimeter, the contribution from the

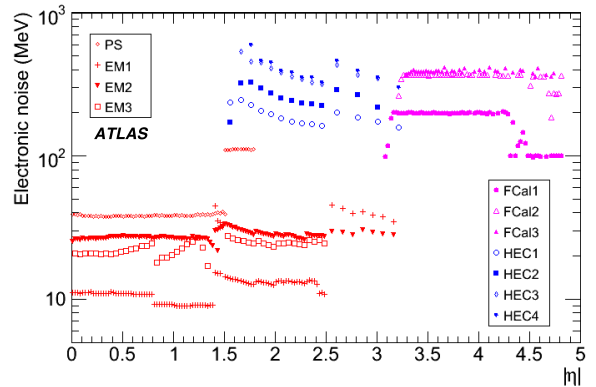


Fig. 8. Electronic noise (σ_{noise}) in randomly triggered events at the EM scale in individual cells for each layer of the calorimeter as a function of $|\eta|$. Results are averaged over ϕ .

coherent noise has been estimated to 2%, by studying simultaneous increase of noise in a group of channels.

Systematic studies of noise stability have been pursued: all noise variations are typically within ± 1 keV, 0.1 MeV and 1 MeV for EM, HEC and FCal, respectively. No correlations with the FEB temperature and/or changes of magnetic field conditions have been observed.

3.2.3 Gain

The calibration pulse is an exponential signal (controlled by two parameters, f_{step} and τ_{cali}) which emulates the triangular ionization signal. It is injected on the detector as close as possible to the electrodes, except for the FCal where it is applied at the base-plane of the front-end crates [18]. Thus, the analog cell response is treated by the FEBs in the same way as an ionization signal, but it is typically averaged over 100 triggers in the RODs and transmitted offline where the average signal peak height is computed. The cell gain is extracted as the inverse ratio of the response signal in ADC counts to the injected calibration signal in DAC counts.

The stability of the cell gain is monitored by looking at the relative gain difference averaged over 128 FEB channels. This is illustrated in Figure 9 for the 1448 FEBs of the EM calorimeter, in high gain. All variations are within $\pm 0.3\%$ and similar results are obtained for medium and low gains. An effect of 0.2% on the gains has recently been identified as coming from a particular setting of the FEBs. The two populations are most probably coming from this effect. Regular update of calibration database take account of the variations. Similar results are obtained for the HEC, and variations within $\pm 0.1\%$ are measured for the FCal.

In conclusion, results presented for the pedestals, noise, and gains illustrate the stability of the LAr electronics over several months of data taking. Values are stored in the ATLAS calibration database and are used for online and offline reconstruction.

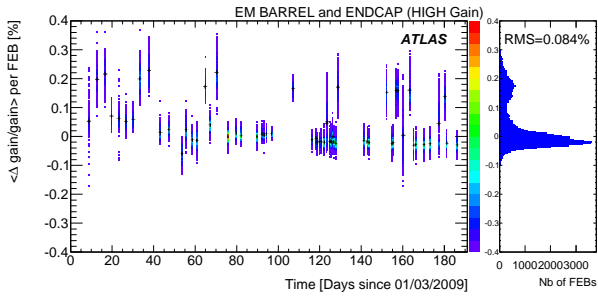


Fig. 9. Average FEB (high) gain variations during 6 months of 2009 data taking, in the EM part of the calorimeter. The crosses indicate the mean value for each time slice.

3.2.4 Global check with E_T^{miss} variable

Another way to investigate the level of understanding of pedestals and noise in the LAr calorimeter is to compute global quantities in randomly triggered events with the calorimeter, such as the vector sum of transverse cell energies. The calorimetric missing transverse energy E_T^{miss} is defined as:

$$\begin{aligned} E_x^{\text{miss}} &= -\sum_{i=1}^{N_{\text{cell}}} E_i \sin \theta_i \cos \phi_i, \\ E_y^{\text{miss}} &= -\sum_{i=1}^{N_{\text{cell}}} E_i \sin \theta_i \sin \phi_i, \\ E_T^{\text{miss}} &= \sqrt{(E_x^{\text{miss}})^2 + (E_y^{\text{miss}})^2}, \end{aligned} \quad (6)$$

where E_i is the cell energy, θ_i its polar angle and ϕ_i its azimuthal angle. Because of the high granularity of the LAr calorimeter, it is crucial to suppress noise contributions to E_T^{miss} , i.e. limit the number of cells, N_{cell} , used in the sum. In ATLAS, this is done with two methods: *i*) a cell-based method in which only cells above a noise threshold of two standard deviations ($|E_i| > 2\sigma_{\text{noise}}$) are kept; *ii*) a cluster-based method which uses only cells belonging to three-dimensional topological clusters [26]. These clusters are built around $|E_i| > 4\sigma_{\text{noise}}$ seeds by iteratively gathering neighboring cells with $|E_i| > 2\sigma_{\text{noise}}$ and, in a final step, adding all direct neighbors of these accumulated secondary cells (Topocluster 4/2/0). In randomly triggered events, about 8500 and 500 LAr cells, respectively, are selected with these two noise-suppression methods.

The distributions of E_x^{miss} and E_y^{miss} should be Gaussian and centered on zero in randomly triggered events. The measurements are compared with a Gaussian noise model, where no pedestal shift or coherent noise is present, obtained by randomizing the cell energy according to a Gaussian model for the cell noise. For this E_T^{miss} computation, cells with very high noise (see Section 2.4) are removed from the computation.

Figure 10 shows the E_T^{miss} distributions for a randomly triggered data sample acquired in 15 hours. The two noise suppression methods are compared to the corresponding Gaussian noise model. For the cell-based method, a good agreement is observed between the data and the simple model. Because of the lower number of cells kept in the cluster-based method, a smaller noise contribution to E_T^{miss} is observed. The agreement between the data and the

model is not as good as for the cell-based method, reflecting the higher sensitivity of the cluster-based method to the noise description. In both cases, no E_T^{miss} tails are present, reflecting the absence of large systematic pedestal shifts or abnormal noise.

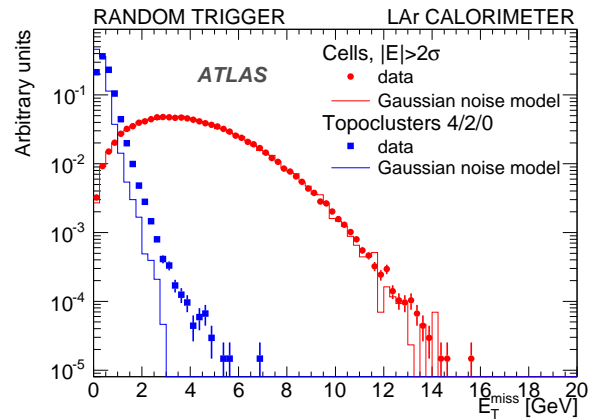


Fig. 10. E_T^{miss} distribution with LAr calorimeter cells for 135,000 randomly triggered events in June 2009. The dots (squares) show the cell-based (cluster-based) methods in the data, and the histograms show the equivalent distributions for the Gaussian noise model (see text).

Using E_T^{miss} it was possible to spot, in 2008, a high coherent noise due to the defective grounding of a barrel presampler HV cable and sporadic noise in a few preamplifiers. These two problems were repaired prior to the 2009 runs. The time stability of E_T^{miss} is regularly monitored using randomly triggered events by observing the mean and width of the E_x^{miss} and E_y^{miss} distributions. With the cluster-based method, the variation of all quantities was measured to be ± 0.1 GeV over 1.5 months. This variation is small compared to the expected E_T^{miss} resolution ($\simeq 5$ GeV for $W \rightarrow e\nu$ events) and can be controlled further by more frequent updates of the calibration constants.

A similar analysis was performed with L1 calorimeter triggered events, corresponding to radiative energy losses from cosmic muons, from the same run as used above. The L1 calorimeter trigger (L1calo) triggers events when either the sum of adjacent trigger tower transverse energies is above 3 GeV in the EM calorimeter (EM3) or 5 GeV when summing EM and hadronic towers [27]. The results are illustrated in Figure 11 for the cell-based noise suppression method. Most of these events are triggered by energy losses in the Tile calorimeter that do not spill in the LAr calorimeter, which therefore mainly records noise, leading to a E_T^{miss} distribution similar to the one obtained with random triggers. However, in few cases, events are triggered by the LAr calorimeter such as the EM3 trigger. The peak at 3 GeV is then shifted upwards to 6 GeV and the proportion of events with E_T^{miss} above 15 GeV is greatly enhanced.

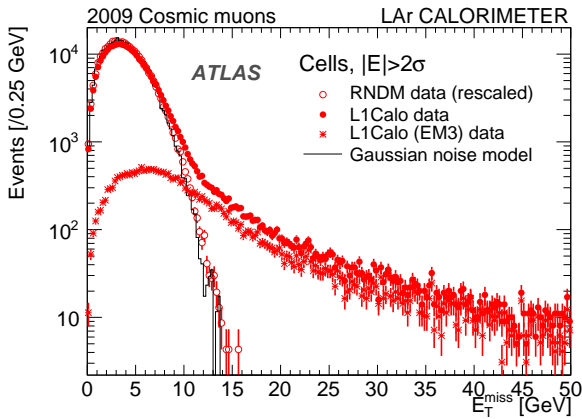


Fig. 11. E_T^{miss} distribution with LAr calorimeter cells for 300,000 L1 calorimeter (L1Calo) triggers reconstructed with the cell-based method. Results for EM3 trigger conditions (Section 3.1.3) from the same run are superimposed on the same plot and the results from randomly triggered events are again overlaid (open symbols and histogram).

3.3 LAr calorimeter timing

The energy reconstruction in each cell relies on the fact that in the standard (five samples) physics data acquisition mode, the third sample is located close to the signal maximum: this implies an alignment of the timing of all calorimeter cells to within a few ns.

Several parameters determine each cell timing: the first contribution comes from FEB internal delays which induce a cell timing variation of ± 2 ns within each FEB. This is accounted for when computing the optimal filtering coefficients. The second contribution concerns FEB to FEB variations due to different cable lengths to reach a given FEB: this relative FEB timing can vary by up to ± 10 ns and can be corrected for by setting an adjustable delay on each FEB.

The study presented here aims at predicting (using calibration data and additional hardware inputs) and measuring (using cosmic muons and beam splash data) this relative FEB timing in order to derive timing alignment delays for each FEB.

3.3.1 Timing prediction

The time of the signal maximum is different in a calibration run (t_{calib}) and in a physics run (t_{phys}). The main contribution to this time is the delay T_0 before the pulse starts to rise (the difference between the calibration and physics pulse widths is much smaller than this T_0 delay variation). This delay is driven by cable lengths which are different in these two configurations and additional delays in physics runs because of the particle time of flight, and the Timing, Trigger and Control (TTC) system configurations.

In a calibration run, a signal is injected from the calibration board through the calibration cables, and is then

read out through the physics signal cables. The value of the delay T_0^{calib} with respect to the signal injection can thus be computed for each FEB using the various cable lengths (L_{calib} , L_{physics}) and signal propagation speeds (v_{calib} , v_{physics}):

$$T_0^{\text{calib}} = \frac{L_{\text{calib}}}{v_{\text{calib}}} + \frac{L_{\text{physics}}}{v_{\text{physics}}}. \quad (7)$$

The above prediction is compared with the measured value in calibration runs. The measurement corresponds to the time at which the calibration pulse exceeds three standard deviations above the noise; it is found to agree with the prediction to within ± 2 ns, ignoring the variations within each FEB.

The time of the signal maximum t_{calib} is obtained by fitting the peak of the pulse of cells in a given FEB with a third order polynomial. As the cable length is a function of the cell position along the beam axis (z , η), the cell times are averaged per FEBs in a given layer (except for the HEC where layers are mixed inside a FEB) and a given η -bin in order to align the FEBs in time.

The time of the ionization pulse in each cell can then be predicted from the calibration time using the following formula:

$$t_{\text{phys}} = t_{\text{calib}} - \frac{L_{\text{calib}}}{v_{\text{calib}}} + t_{\text{flight}} + \Delta t_{\text{TTC}}, \quad (8)$$

where t_{calib} was defined in the previous paragraph; t_{flight} is the time of flight of an incident particle from the interaction point to the cell, which varies from 5 ns for a presampler cell at $\eta = 0$, to 19 ns for a back cell in the HEC; and Δt_{TTC} is a global correction for the six partitions due to the cabling of the TTC system which is needed to align all FEBs at the crate level. This predicted ionization pulse time is compared with the corresponding measurement in the next section.

3.3.2 Timing measurement

The ionization pulse time has been measured in beam splash and cosmic muon events. The time is reconstructed using optimal filtering coefficients. Since the arrival time of the particle is not known, one does not know in advance to which samples the time OFCs b_i should be applied (since these OFCs were computed for a particular set of samples around the pulse maximum). Therefore, an iterative procedure is used until the obtained Δt (see Eq. 4) is less than 3 ns.

The time is then corrected for two effects: first, the time-of-flight difference between the beam splash or cosmic muon configurations and the collision configuration, and second, the asynchronicity of the beam splash and cosmic muon events, where arrival times vary with respect to the TTC clock.

The comparison between the measured and the predicted (Eq. 8) ionization pulse time is shown in Figure 12 for the C-side ($\eta < 0$) of each LAr sub-detector.

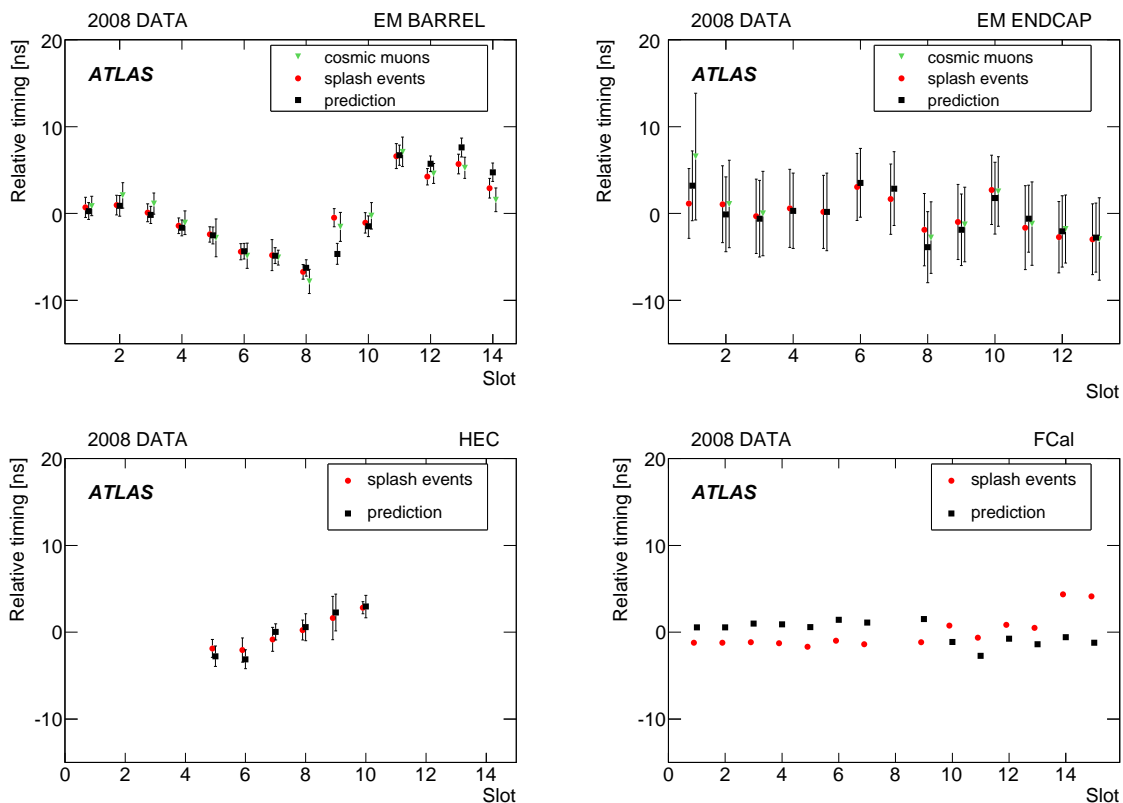


Fig. 12. Relative predicted and measured FEB times in the electromagnetic barrel (top left), electromagnetic endcap (top right), HEC (bottom left) and FCal (bottom right) calorimeters, for the C-side ($\eta < 0$). The x-axis (“Slot”) corresponds to a group of FEBs in a given layer (or a group of layers in the HEC) and η -range. The error bars show the width of the distributions in each slot.

This comparison is performed for each “slot” corresponding to a group of FEBs in a given layer and η -range, averaged over all calorimeter modules over ϕ . As mentioned in the introduction, the relative timing of each group of FEBs varies by ± 10 ns due to the different corresponding cable lengths.

On the plots, the error bars correspond to the RMS of values for all modules in a slot: in the FCal, there is only one module per slot, so no error bars are shown (also note that slot 8 is empty in the FCal). In some regions, the cosmic data statistics was not sufficient to extract the time: the corresponding bins are thus empty. The agreement between the prediction and the two measurements is within ± 2 ns (and at worst ± 5 ns for two slots of the FCal).

Finally, a set of FEB timing alignment delays is obtained from these well understood measured relative times. These delays will be used at the LHC startup and updated once the phase between the beam and the machine clock will be measured and shown to be stable. The desired precision of ± 1 ns should be reached then.

3.4 Signal reconstruction studies and impact on intrinsic global energy resolution constant term

The main ingredient for accurate energy and time reconstruction of signals from LHC collisions is the prediction of the ionization signal shape, from which the optimal filtering coefficients used in Eq. (3) are computed. After recalling the basics of the method used to predict the shape in Section 3.4.1, an estimate of the signal prediction quality with three samples in the EM calorimeter is presented in Section 3.4.2. The full 32 samples shape prediction is used to determine the ionization electron drift time needed for the OFC computation in the EM calorimeter (Section 3.4.3). Finally, from these two studies an estimate of the main contributions to the constant term in the global energy resolution of the EM calorimeter is given in Section 3.4.4.

3.4.1 Prediction of the ionization pulse shape

The standard ATLAS method for prediction of the ionization pulse shape in the EM and the HEC relies on the calibration system. A precisely known calibration signal is sent through the same path as seen by the ionization

pulses thus probing the actual electrical and readout properties of each calorimeter cell. In both the EM and the HEC, the calibration pulse properties are parameterized using two variables, f_{step} and τ_{cali} , which have been measured for all calibration boards [23] and are routinely extracted from calibration signals [28].

The predicted ionization shapes are calculated from the calibration pulses by modeling each readout cell as a resonant RLC circuit, where C is the cell capacitance, L the inductive path of ionization signal, and R the contact resistance between the cell electrode and the readout line. The effective LC and RC have been estimated from a frequency analysis of the output calibration pulse shape [28]. They were also measured with a network analyzer during the long validation period of the three cryostats [29,30,31]. For the HEC, calibration pulses are transformed into ionization signal predictions using a semi-analytical model of the readout electronics, with a functional form with zeros and poles accounting for the cable and pre-amplifier transfer functions [32,33]. The prediction of both the EM and HEC ionization pulses requires the knowledge of the electron drift time in liquid argon (T_{drift}), which can be inferred from the calorimeter properties or directly measured from data (see Section 3.4.3).

To illustrate the good quality of the pulse shape prediction, radiating cosmic muons depositing few GeV in a cell have been used. Figure 13 shows a typical 32-sample pulse recorded in the barrel (top left) and the endcap (top right) of the EM calorimeter, as well as in the HEC (bottom left). In each case, the pulse shape prediction, scaled to the measured cell energy, agrees at the few percent level with the measured pulse.

As already mentioned, in the FCal the calibration pulse is injected at the base-plane of the front-end crates, and therefore the response to a calibration signal differs significantly from the response to an ionization pulse, preventing the use of methods described above. Instead, seven sample pulse shapes recorded during the beam test campaign [9, 10] have been averaged to obtain a normalized reference pulse shape for each layer. Figure 13 (bottom right) shows a typical example where the agreement between the reference pulse shape and the data is at the 4% level.

3.4.2 Quality of signal reconstruction in the EM calorimeter

Several PeV were deposited in the full calorimeter in LHC beam splash events. As an example, Figure 14 shows the energy deposited in the second layer of the EM calorimeter. The structure in ϕ reflects the material encountered by the particle flux before hitting the calorimeter, such as the endcap toroid. In this layer, a total of 5×10^5 five sample signal shapes with at least 5 GeV of deposited energy were recorded. These events were used to estimate the quality of the pulse shape prediction for every cell.

For this purpose, a Q^2 -estimator is defined as :

$$Q^2 = \frac{1}{N_{\text{dof}}} \sum_{j=1}^{N_{\text{samples}}} \frac{(s_j - Ag_j^{\text{phys}})^2}{\sigma_{\text{noise}}^2 + (kA)^2}, \quad (9)$$

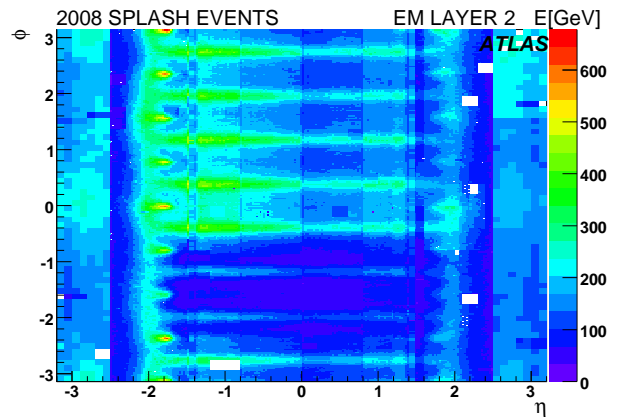


Fig. 14. Total energy deposited in the LHC beam splash events in every cell of the EM calorimeter second layer. Empty bins are due to non functioning electronics.

where the amplitude A (Eq. (3)) is computed with a number of samples $N_{\text{samples}} = 3$ (because the timing was not yet adjusted everywhere for the beam splash events, not all samples can be used), s_j is the amplitude of each sample j , in ADC counts, g_j^{phys} is the normalized predicted ionization shape and k is a factor quantifying the relative accuracy of the amplitude A . Assuming an accuracy of around 1%, with the 5 GeV energy cut applied one has $\sigma_{\text{noise}}^2 < (kA)^2$. In this regime, it is possible to fit a χ^2 function with 3 degree of freedom on the $Q^2 \times N_{\text{dof}}$ distribution over cells in the central region (where the Q^2 variation is small). Therefore, $N_{\text{dof}} = 3$. A given value of Q^2 can be interpreted as a precision on the amplitude at the level kQ .

Figure 15 shows the Q^2 -estimator in the second layer of the EM calorimeter averaged over ϕ , assuming $k = 1.5\%$ corresponding to $Q^2 \sim 1$ for $\eta \sim 0$. The accuracy is degraded by at most a factor of ~ 2 (i.e. $Q^2 \sim 4$) in some endcap regions. This shows that these data can be described with a reasonable precision.

3.4.3 Ionization electron drift time measurement in the EM calorimeter

During the 2008 cosmic runs, half a million pulses with 32 samples were recorded in the EM calorimeter from cells in which at least 1 GeV was reconstructed. Given the good accuracy of the predicted signal undershoot (see Figure 13), the drift time can be extracted from a fit to the measured signal [34].

Figure 16 shows the fitted drift time for all selected cells in the second layer using the standard pulse shape prediction method (Section 3.4.1). In the EMB, the drift time has also been measured with a method in which the shape is computed using a more analytical model and LC and RC extracted from network analyzer measurements [30]. The drift times extracted from the two methods are in excellent agreement, giving confidence in the

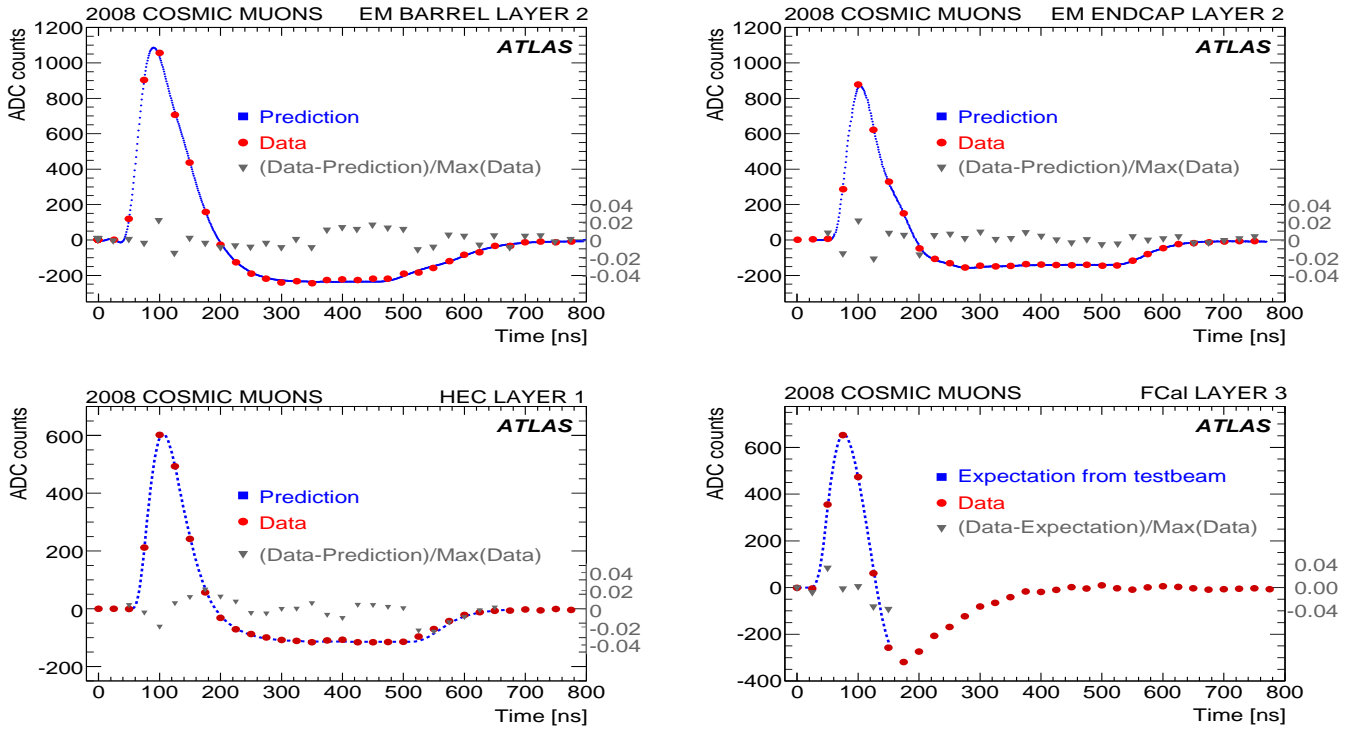


Fig. 13. Typical pulse shapes, recorded during the cosmic ray campaign, for a given cell in the second layer for the barrel (top left) and the endcap (top right) of the EM calorimeter, as well as in the first layer of the HEC (bottom left) and in the third layer of the FCal (bottom right). The relative difference between data and prediction is indicated by triangles on the right scale.

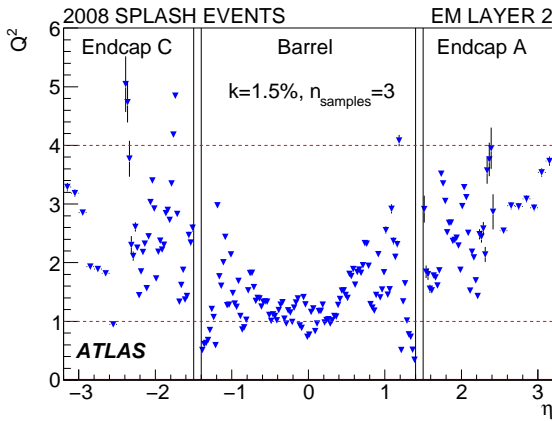


Fig. 15. Estimator Q^2 (defined in the text) as a function of η for 5×10^5 pulse shapes with $E > 5$ GeV in the EM calorimeter second layer cells. Q^2 is defined in Eq. (9) with $k = 1.5\%$.

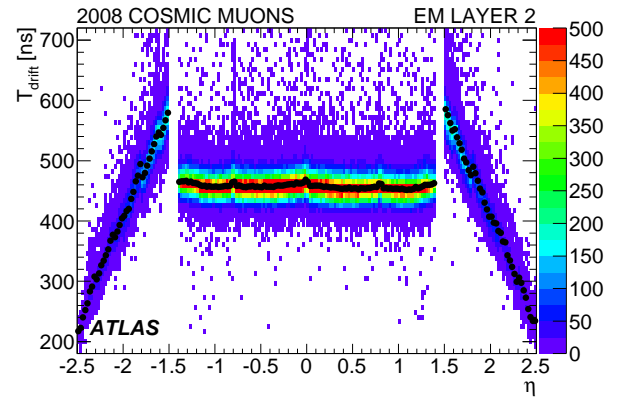


Fig. 16. Drift time measurement in the cells of the EM calorimeter second layer with $E > 1$ GeV for the 2008 cosmic muon run. The dots correspond to drift time values averaged in ϕ .

results: a constant value around the expected 460 ns is obtained, except near the electrode edges ($|\eta| = 0, 0.8$ and 1.4) where the electric field is lower. The decrease of the drift time in the EM endcap ($1.5 < |\eta| < 2.5$) reflects the decrease of the gap size with $|\eta|$. Similar results are obtained for the first and third layers of the EM calorimeters.

3.4.4 Impact on the global energy resolution constant term of the EM calorimeter

When five of the production EM calorimeter modules were tested individually in electron beams, the global constant term c of the energy resolution formula was measured to be $c \sim 0.5\%$ in the EM barrel and 0.7% in the EM end-

cap [4]. The main contributors are the signal reconstruction accuracy, the LAr gap uniformity, and the electronics calibration system. The first two contributions c_{SR} and c_{gap} can be investigated using results presented in Section 3.4.2 and 3.4.3, considering only the second layer of the EM calorimeter where most of the electromagnetic shower energy is deposited.

From Figure 15, one finds that $\langle Q^2 \rangle \sim 1.4$ in the EM barrel and 2.6 in endcap, and hence $\langle k \rangle = 1.8\%$ and 2.4% respectively. This corresponds to residuals between the predicted and measured pulses of 1 to 2% of the pulse amplitude (see Figure 13 for illustration), for samples around the signal maximum. Similar residuals were obtained in the electron beam test analysis [28]. At this time, the contribution of the signal reconstruction to the constant term was estimated to be $c_{SR} = 0.25\%$. Given the measured accuracy with beam splash events, the beam test result seems to be reachable with LHC collisions.

The drift time measured in Section 3.4.3 is a function of the gap thickness (w_{gap}) and the high voltage (V):

$$T_{drift} \sim \frac{w_{gap}^{\alpha+1}}{V^\alpha} \quad (10)$$

where $\alpha \simeq 0.3$ is empirically determined from measurements [19]. In the EM barrel, the electric field is constant, except in transition regions, and thus the drift time uniformly directly measures the LAr gap variations. To reduce statistical fluctuations, the measured drift time values are averaged over regions of $\Delta\eta \times \Delta\phi = 0.1 \times 0.1$. The distribution of the average drift time is shown in Figure 17 for the second layer of the EM barrel calorimeter.

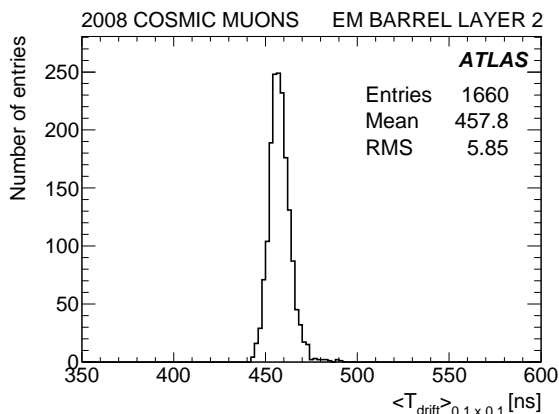


Fig. 17. Distribution of the local average drift time values in $\Delta\eta \times \Delta\phi = 0.1 \times 0.1$ bins, for the middle layer of the EM barrel.

The drift time uniformity, estimated as the ratio of the RMS of this distribution to its mean value, is $1.28 \pm 0.03\%$. Using the relation between the drift time and the gap from Eq. 10 and the fact that the signal amplitude is proportional to the initial ionization current ($I \simeq \frac{\rho \cdot w_{gap}}{T_{drift}} \simeq w_{gap}^{-\alpha}$ where ρ is the linear density of charge), one can relate the relative variation of the drift time to the one of the

amplitude applying a factor $\alpha/(1+\alpha)$ to the above result. Therefore, the drift time uniformity leads to a dispersion of response due to the barrel calorimeter gap variations of $(0.29_{-0.04}^{+0.05})\%$ where the systematic uncertainties are included. This represents an upper bound on the corresponding constant term c_{gap} .

For comparison, during the EM calorimeter barrel module construction, the LAr gap thickness was measured, yielding an estimate of the constant term due to gap size variations of $c_{gap} = 0.16\%$ [14]. The measurement of the gap size uniformity presented here takes into account further effects like deformations in the assembled wheels and possible systematic uncertainties from the in situ cosmic muon analysis.

4 In situ EM calorimeter performance with cosmic muons

In the previous sections, we demonstrated the good performance of the electronics operation and the good understanding of the energy reconstruction. The cosmic ray events can therefore now be used to validate the Monte Carlo simulation that will be used for the first collisions.

Two such analyses are presented in this section: the first study aims to investigate the electromagnetic barrel calorimeter uniformity using ionization signals from quasi-projective cosmic muons, and the second aims to reconstruct electromagnetic showers from radiative cosmic muons and to compare the measured shower shapes with simulation.

4.1 Monte Carlo simulation

The ATLAS Monte Carlo [35, 36] simulates the interaction of particles produced during LHC collisions or from cosmic muons within the ATLAS sub-detectors. It is based on the Geant4 toolkit [37] that provides the physics lists, geometry description and tracking tools. For cosmic muons, the material between the ground level and the ATLAS cavern is also simulated, i.e. the overburden and the two access shafts. The simulated cosmic ray spectrum corresponds to what was measured at sea level [38]. Air showers are not simulated but have a negligible effect on the analyses presented here. In order to save CPU time, the generated events are filtered before entering the full Geant4 simulation by requiring that the particles cross a specific detector volume (in the following analyses, typically inner detector volumes).

An important use of the simulation, amongst many others, is to validate the selection criteria on shower-shape for high-level trigger and offline algorithms, as well as to derive the electron and photon energy calibrations.

It is important to note that, thanks to the digitization step of the calorimeter simulation which emulates the behavior of the electronics, the standard energy reconstruction procedure can be applied to the simulated events. The special procedure used for asynchronous cosmic muon data, which uses an iterative determination of

the event time, is however not applied to the Monte Carlo data.

4.2 Uniformity of the electromagnetic barrel calorimeter

4.2.1 Goals and means of the analysis

Any non-uniformity in the response of the calorimeter has a direct impact on the constant term in the energy resolution (see Section 3.4.4); great care was taken during the construction to limit all sources of non-uniformity to the minimum achievable, aiming for a global constant term below 0.7%. The default ATLAS Monte Carlo simulation emulates the effect of the constant term, but for the present analysis, this emulation was turned off.

The uniformity of the calorimeter was measured for three barrel production modules using electrons during beam test campaigns [4]. Cosmic muons provide a unique opportunity to measure the calorimeter uniformity in situ over a larger number of modules, unfortunately limited to the barrel calorimeter due to both the topology of the cosmic muon events and the choice of triggers. The scope of this analysis is nevertheless quite different than in the beam test. First, muons behave very differently from electrons: in most events, they deposit only a minimum ionization energy in the liquid argon and they are much less sensitive to upstream material. The result can therefore not be easily extrapolated to the electron and photon response. Second, the cosmic run statistics are limited, so uniformity cannot be studied with cell-level granularity. The goal of this cosmic muon analysis is rather to quantify the agreement between data and Monte Carlo, and to exclude the presence of any significant non-uniformity in the calorimeter response.

A previous uniformity analysis using cosmic muons [39] from 2006 and 2007 relied on the hadronic Tile calorimeter to trigger events and to measure the muon sample purity. For the 2008 data discussed here, both the muon spectrometer and inner detector were operating and were used for triggering and event selection. The data sample consists of filtered events requiring a reconstructed track in the inner detector with at least one hit in the silicon tracker. The tracks are also selected to be reasonably projective by requiring that their transverse ($|d_0|$) and longitudinal ($|z_0|$) impact parameters, with respect to the center of the coordinate system be smaller than 300 mm.

4.2.2 Signal reconstruction

In the first step, a muon track is reconstructed in the inner detector. For that purpose, a dedicated algorithm looks for a single track crossing both the top and bottom hemispheres. This single track is then extrapolated both downward and upward into the calorimeter.

Around the two track impact positions in the calorimeter, a rectangle of cells (the cell road) is selected in the first and second layers (the signal to noise ratio for muons

is too low in the third layer). The cells of the first layer have a size of $\Delta\eta \times \Delta\phi = 0.003 \times 0.1$ and 12×3 such cells are kept. Similarly, the cells of the second layer have a size of $\Delta\eta \times \Delta\phi = 0.025 \times 0.025$, and 5×5 such cells are kept.

To reconstruct the energy of the selected cells, the muon timing is obtained via an iterative procedure that is usually only applied to cells with an ADC signal at least four times the noise level. Since most muons are minimum ionizing particles, the muon signal is small, typically 150 MeV is deposited in the most energetic cell in the second layer, only five times the noise, and many cells do not pass this threshold. Therefore, an alternative reconstruction is used in this analysis: in the first pass, the iteration threshold is lowered to zero so that the timing is computed for most of the cells. In the second pass, the timing of the most energetic cell determined in the first pass is applied to all the other cells of the road. The cell energy is reconstructed at the electron energy scale and thus does not represent the true energy loss of the muon. Finally, clusters are formed in each layer to reconstruct the muon energy loss. The criteria used to decide on the cluster size are described below.

4.2.3 Optimization of the uniformity measurement

In order to perform the most accurate evaluation of the calorimeter uniformity, the measurement granularity, the cluster size and the selection cuts have been optimized. The granularity chosen is a compromise between the need for high statistics (large binning) and the need for high precision. The cluster size optimizes the signal to noise ratio while the selection cuts reduce the biases while keeping high statistics.

The binning is determined by requiring a minimum of 500 events per unit. In the η direction, this corresponds to bins of 0.025 (equal to the second layer cell width) up to $|\eta| = 0.7$ and wider bins above.

In the first layer, the muon energy loss is measured using a $\Delta\eta \times \Delta\phi = 2 \times 1$ (in first layer cell unit) cluster, which contains most of the deposited energy. Adding an additional cell brings more noise than signal. In the second layer, a 1×3 (in second layer cell unit) cluster is used: it suffers less from noise than a 3×3 cluster, but requires the removal of non-projective events which leak outside the cluster along the η direction.

This projectivity cut is based on the centrality of the muon in the second layer cell: when the muon passes close to the edge of the cell, a very small non-projectivity induces a large energy leakage into the neighboring cell. Therefore, for each second layer cell, eight bins corresponding to the eight first layer cells located in front of it were defined, and in each bin a cut is applied on the beam impact parameter z_0 of the track, such that the muon is geometrically contained in the second layer cell. The remaining statistics after this projectivity cut is 76 k events in the data sample and 113 k events in the Monte Carlo sample. The events are mainly located under the cavern shafts leading to a coverage of around 20% of the full electromagnetic barrel calorimeter.

A comparison of the energy reconstructed in the first and second layers between data and Monte Carlo events is shown in Figure 18. Because the muon energy loss is mostly η -dependent, both distributions are shown for all events (top), showing a large width due to the variation of the energy response over η , and for a single η -bin (bottom).

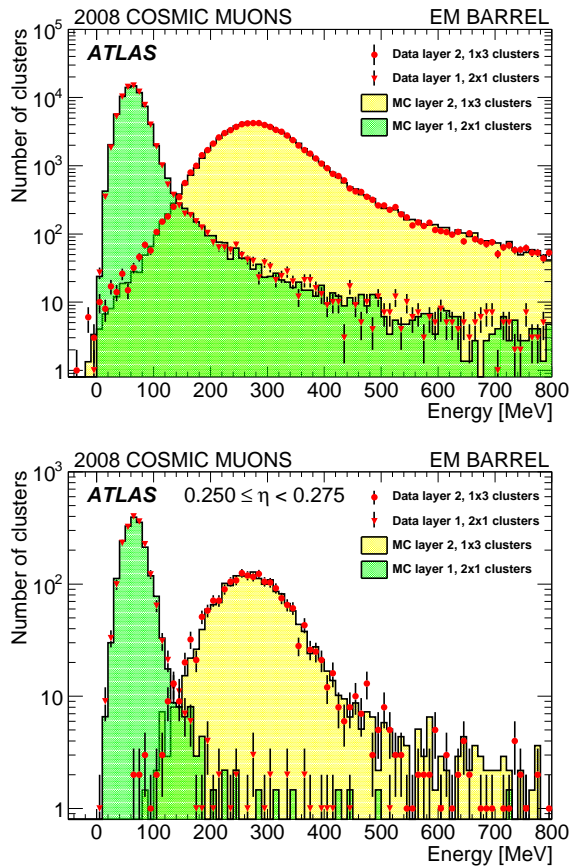


Fig. 18. Energy in a 2×1 cluster in the first layer (histogram for Monte Carlo and triangles for data) and in a 1×3 cluster in the second layer (histogram for Monte Carlo and full circles for data) for all events (top) and a single η -bin (bottom).

The agreement between the data and Monte Carlo distributions is very good, both for the shape and for the absolute energy scale which differs by only 2% in the front layer and 1% in the second layer. Part of the difference comes from the slight difference in acceptance for data and Monte Carlo, as well as from the difference in energy reconstruction. This overall energy scale difference is corrected for in the MC in the rest of the study.

4.2.4 Calorimeter uniformity along η

Given the limited statistics of the projective cosmic muon data, the uniformity of the response in η cannot be estimated at the cell level. A natural choice of cell combina-

tion is to integrate clusters in ϕ since the response should not vary along this direction due to the ϕ symmetry of the calorimeter. The response along the η direction for cosmic muons depends on the variation of the amount of liquid argon seen by the muon. In particular, a transition occurs at $|\eta| = 0.8$ where the lead thickness goes from 1.53 mm to 1.13 mm.

The estimation of the muon energy in each η -bin is done with a fit of the cluster energy distribution using a Landau function convoluted with a Gaussian. The Landau function accounts for fluctuations of the energy deposition in the ionization process and the Gaussian accounts for the electronic noise and possible remaining fluctuations. In particular, a 10% difference is observed between the width of the Gaussian expected from the electronic noise and the width of the fitted Gaussian. Mostly this bias comes from remaining cluster non-containment effects which are found to be η -independent and thus do not produce any artificial non-uniformity. The most probable value (MPV) of the Landau distribution estimates the energy deposition.

Distributions of data and Monte Carlo MPVs along the η direction for the first and second layers are shown in Figure 19.

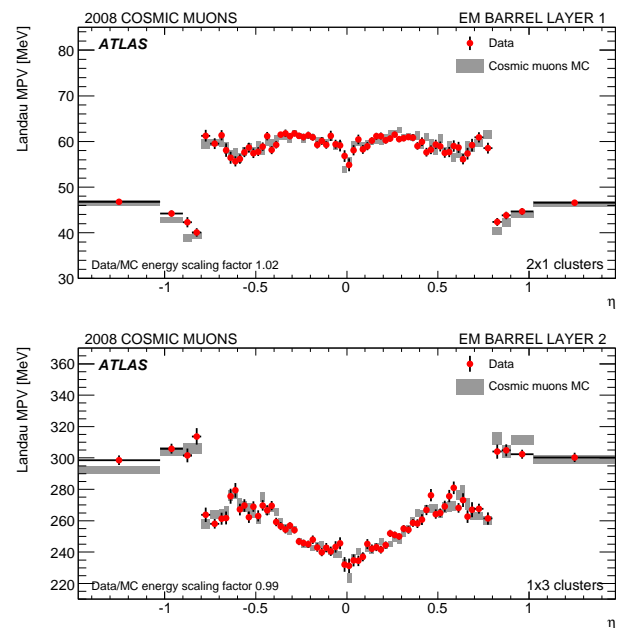


Fig. 19. Landau MPV as a function of η in the first (top) and second (bottom) layers for the data (red points) and Monte Carlo (grey bands).

In the first layer, the MPVs are roughly constant along η , except around $\eta = 0$ where some cells are physically missing in the detector, and around $|\eta| = 0.6$ where the cell depth is varying. In the second layer, the response follows a typical “V-shape” corresponding to the variation of the cell depth along η that rises up to $|\eta| = 0.6$. Again, the agreement between the data and Monte Carlo is very good, showing that the contribution of systematic

effects due to the energy reconstruction method or the non-projectivity of the tracks is small.

The response uniformity U_{meas} is given by the RMS of the normalized differences between the data and Monte Carlo MPVs in each η -bin :

$$U_{\text{meas}} = \sqrt{\frac{\sum_{i=1}^{N_b} (U_{i,\text{meas}} - \langle U_{i,\text{meas}} \rangle)^2}{N_b}}, \quad (11)$$

with:

$$U_{i,\text{meas}} = \frac{MPV_{i,\text{Data}} - MPV_{i,\text{MC}}}{MPV_{i,\text{Data}}}, \quad (12)$$

where $U_{i,\text{meas}}$ is averaged over ϕ , N_b is the number of bins in η , and $\langle U_{i,\text{meas}} \rangle = 0$ since the global energy scale difference was corrected by rescaling the MC.

The measured uniformity should be compared to the expected uniformity U_{exp} , which is obtained similarly to Eq. 11 with $U_{i,\text{exp}}$ given by:

$$U_{i,\text{exp}} = \frac{MPV_{i,\text{MC}}}{MPV_{i,\text{Data}}} \sqrt{U_{i,\text{Data}}^2 + U_{i,\text{MC}}^2} \quad (13)$$

with:

$$U_{i,\text{Data(MC)}} = \frac{\sigma(MPV_{i,\text{Data(MC)}})}{MPV_{i,\text{Data(MC)}}}, \quad (14)$$

where $\sigma(MPV_{i,\text{Data(MC)}})$ is the statistical uncertainty on the measured Landau MPV. This uncertainty is due to the finite statistics of the data and Monte Carlo samples in each bin, the Landau dispersion of the ionization, and the electronic noise.

The measured uniformity U_{meas} should agree with the expected uniformity U_{exp} if the Monte Carlo simulation reproduces the data well: the key ingredients are the acceptance, the muon spectrum, and the energy reconstruction method. A significant departure of the measured uniformity from the expected one would be a measurement of additional non-uniformities U_{Δ} ($U_{\Delta}^2 = U_{\text{meas}}^2 - U_{\text{exp}}^2$).

The measured and expected uniformities for the two EM layers are shown in Figure 20.

The fluctuations of the measured energies are large: the RMS of the corresponding distribution is $2.4 \pm 0.2\%$ in the first layer and $1.7 \pm 0.1\%$ in the second layer, showing that the statistical power of the analysis is limited given the available data and Monte Carlo statistics. The fluctuations mostly remain within the limits of the band representing the expected values. The RMS of the latter distribution is 2.2 % in the first layer and 1.6 % in the second layer. This demonstrates that no significant additional non-uniformity (U_{Δ}) is present in the data. An upper limit is derived and yields $U_{\Delta} < 1.7\%$ @ 95% CL in the first layer, and $U_{\Delta} < 1.1\%$ @ 95% CL in the second layer.

The calorimeter response uniformity along η (averaged over ϕ) is thus consistent at the percent level with the Monte Carlo simulation and shows no significant non-uniformity.

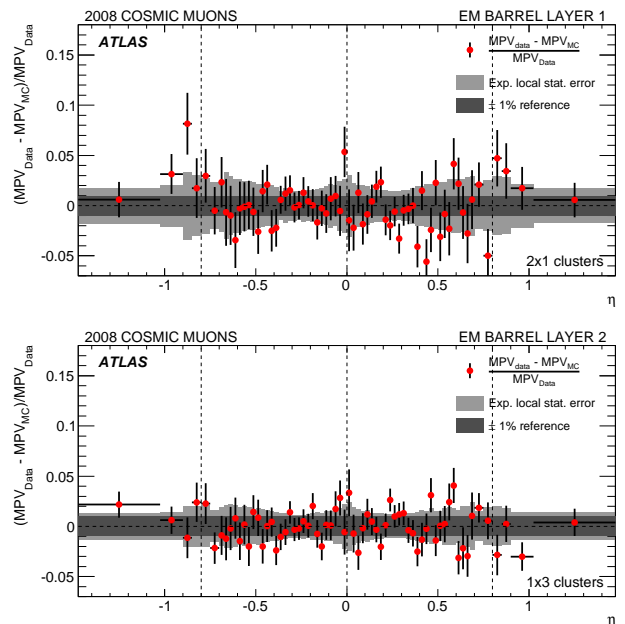


Fig. 20. Measured $U_{i,\text{meas}}$ (red points) and expected $U_{i,\text{exp}}$ (light grey band) cosmic muon energy dispersions as function of η for the first (top) and second (bottom) layers of the EM barrel. The dark grey band indicates a $\pm 1\%$ strip for reference.

4.3 Electromagnetic shower studies

The second analysis aims at validating the Monte Carlo simulation of the distribution of some key calorimeter variables used in the ATLAS electron/photon identification. This is done using radiative cosmic muons that can give rise to electromagnetic showers in the calorimeter through bremsstrahlung or pair conversions.

4.3.1 Selection of radiative muons

To increase the probability of the presence of a muon in the event, it is requested that at least one track has been reconstructed in the inner detector barrel with $|d_0| < 220$ mm and $p_T > 5$ GeV: these cuts ensure a similar acceptance for data and Monte Carlo.

A radiative energy loss is searched for in the electromagnetic barrel calorimeter by requiring a cluster with an energy greater than 5 GeV. Since the radiation can occur anywhere along the muon path, the corresponding shower is not always fully contained in the electromagnetic calorimeter: this is visible in Figure 21 which shows the fraction of the cluster energy deposited in the first layer for simulated single photons from interaction vertex and for electromagnetic showers from radiating cosmic muons. This shows that the longitudinal shower development of the radiative photons is well reproduced by the Monte Carlo simulation, and that most of the radiating muons deposit very little energy in the first layer. To select “collision-like” showers, this fraction is requested to be greater than 0.1. A total of 1200 candidates remain in

the data sample and 2161 in the Monte Carlo after this selection.

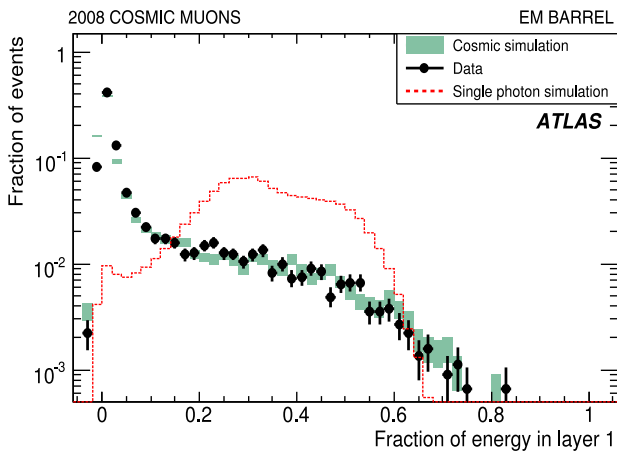


Fig. 21. Fraction of cluster energy deposited in the first layer of the electromagnetic barrel calorimeter for cosmic data (dots) and Monte Carlo (rectangles), as well as for simulated single photons of 5 GeV momentum from interaction vertex (red histogram).

4.3.2 Shower shape validation

Various shower shape distributions used for photon identification have been compared with the Monte Carlo simulation: Figures 22 and 23 show two distributions of variables related to lateral shower containment in the first and second layers of the electromagnetic calorimeter.

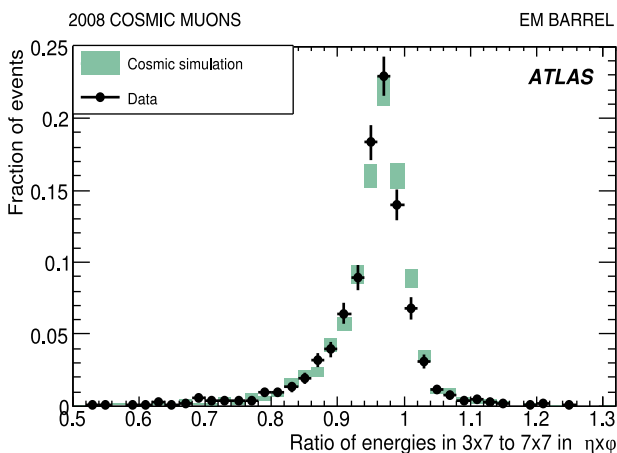


Fig. 22. Lateral shower containment in the second layer of the calorimeter given by the ratio of the energy deposited in a 3×7 cluster to a 7×7 cluster for radiative cosmic muon data (dots) and Monte Carlo simulation (rectangles).

Figure 22 shows the ratio of the energy deposited in a $\Delta\eta \times \Delta\phi = 3 \times 7$ (in second layer cell unit) cluster to that in a 7×7 cluster, in the second layer of the barrel calorimeter. In LHC collisions, this variable distinguishes electromagnetic showers, contained in 3 cells in η , from hadronic showers, leaking outside these 3 cells. The contribution from the noise explains that the ratio can be above 1.

Figure 23 shows the variable $F_{\text{side}} = (E_{\pm 3} - E_{\pm 1})/E_{\pm 1}$ computed as the ratio of energy within seven central cells in the first layer ($E_{\pm 3}$), outside a core of three central cells ($E_{\pm 1}$), over energy in the three central cells: in LHC collisions, this variable typically separates photons, where little energy is deposited outside the core region, from π^0 s, where the two photons produced by the π^0 deposit some energy outside the core region. The agreement between the Monte Carlo simulation and the cosmic ray data is very good in both the cases where the electromagnetic shower develops in the “collision-like” direction (in the bottom hemisphere) and the case where it develops in the backward direction (in the top hemisphere).

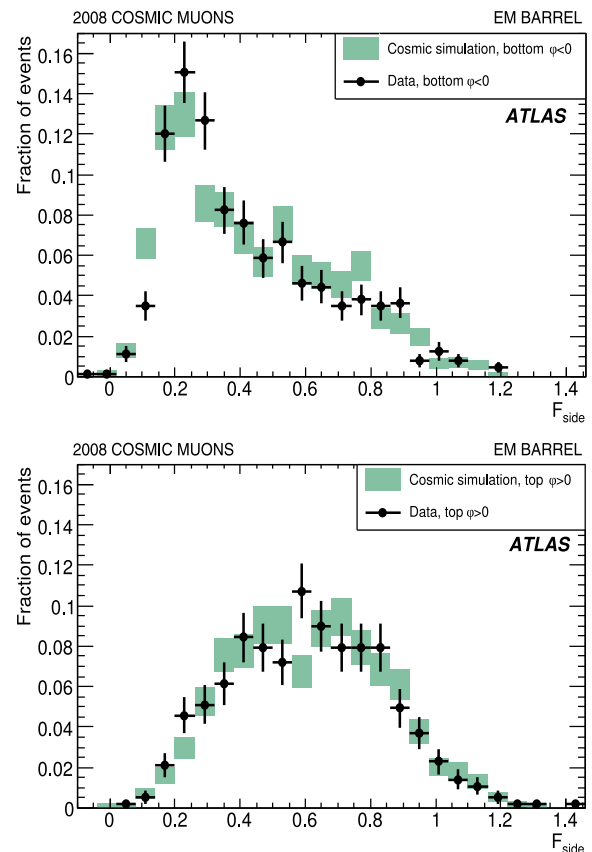


Fig. 23. Lateral shower containment in the first layer for “collision-like” (top panel) or “reverse” (bottom panel) electromagnetic showers for radiative cosmic muon data (dots) and Monte Carlo simulation (rectangles). The definition of the F_{side} is given in the text.

Within the statistics available from data, important calorimeter variables used in the electron/photon identification in ATLAS illustrate the good agreement between the Monte Carlo simulation and electromagnetic showers from radiative cosmic events in the calorimeter. These results, as well as the numerous comparisons done with beam test data [2,3,4,5,6], give confidence that robust photon and electron identification will be available for early data at the LHC.

5 Conclusions and Perspectives

The liquid argon calorimeter has been installed, connected and fully readout since the beginning of 2008. Since then, much experience has been gained in operating the system. Thanks to the very stable cryogenics and electronics operation over this period, first performance studies with the complete LAr calorimeter coverage have been done using several months of cosmic muon data and with LHC beam splash events from September 2008. These data provided a check of the first level trigger energy computation and the timing of the electronics. In the EM calorimeter, detailed studies of the signal shape predictions allow to check that, within the accuracy of the analysis, there is no extra contribution to the dominant contributions to the intrinsic constant term of the energy resolution. This indicates that the reach of a global constant term of 0.7% is achievable. The non-uniformity of the EM barrel calorimeter response to cosmic muons is consistent at the percent level with the simulated response. Finally, the electromagnetic shower profiles are in good agreement with the simulated ones, thus validating the Monte Carlo description. All these results allow for strong confidence in the readiness of the LAr calorimeter for the first LHC collisions.

The ultimate LAr calorimeter performance will be assessed with collision data: this is particularly true for the electromagnetic and hadronic energy scale computation in the ATLAS environment, which is needed for many ATLAS physics analyses.

6 Acknowledgements

We are greatly indebted to all CERN's departments and to the LHC project for their immense efforts not only in building the LHC, but also for their direct contributions to the construction and installation of the ATLAS detector and its infrastructure. We acknowledge equally warmly all our technical colleagues in the collaborating institutions without whom the ATLAS detector could not have been built. Furthermore we are grateful to all the funding agencies which supported generously the construction and the commissioning of the ATLAS detector and also provided the computing infrastructure.

The ATLAS detector design and construction has taken about fifteen years, and our thoughts are with all our colleagues who sadly could not see its final realisation.

We acknowledge the support of ANPCyT, Argentina; Yerevan Physics Institute, Armenia; ARC and DEST, Australia; Bundesministerium für Wissenschaft und Forschung, Austria; National Academy of Sciences of Azerbaijan; State Committee on Science & Technologies of the Republic of Belarus; CNPq and FINEP, Brazil; NSERC, NRC, and CFI, Canada; CERN; NSFC, China; Ministry of Education, Youth and Sports of the Czech Republic, Ministry of Industry and Trade of the Czech Republic, and Committee for Collaboration of the Czech Republic with CERN; Danish Natural Science Research Council; European Commission, through the ARTEMIS Research Training Network; IN2P3-CNRS and Dapnia-CEA, France; Georgian Academy of Sciences; BMBF, DESY, DFG and MPG, Germany; Ministry of Education and Religion, through the EPEAEK program PYTHAGORAS II and GSRT, Greece; ISF, MINERVA, GIF, DIP, and Benozziyo Center, Israel; INFN, Italy; MEXT, Japan; CNRST, Morocco; FOM and NWO, Netherlands; The Research Council of Norway; Ministry of Science and Higher Education, Poland; GRICES and FCT, Portugal; Ministry of Education and Research, Romania; Ministry of Education and Science of the Russian Federation, Russian Federal Agency of Science and Innovations, and Russian Federal Agency of Atomic Energy; JINR; Ministry of Science, Serbia; Department of International Science and Technology Cooperation, Ministry of Education of the Slovak Republic; Slovenian Research Agency, Ministry of Higher Education, Science and Technology, Slovenia; Ministerio de Educación y Ciencia, Spain; The Swedish Research Council, The Knut and Alice Wallenberg Foundation, Sweden; State Secretariat for Education and Science, Swiss National Science Foundation, and Cantons of Bern and Geneva, Switzerland; National Science Council, Taiwan; TAEK, Turkey; The Science and Technology Facilities Council and The Leverhulme Trust, United Kingdom; DOE and NSF, United States of America.

References

1. G. Aad *et al.*, *The ATLAS Experiment at the CERN Large Hadron Collider*, JINST **3** (2008) S08003.
2. J. Colas *et al.*, *Position resolution and particle identification with the ATLAS EM calorimeter*, Nucl. Inst. Meth. **A 550** (2005) 96.
3. M. Aharrouche *et al.*, *Energy linearity and resolution of the ATLAS electromagnetic barrel calorimeter in an electron test-beam*, Nucl. Inst. Meth. **A 568** (2006) 601.
4. M. Aharrouche *et al.*, *Response uniformity of the ATLAS liquid argon electromagnetic calorimeter*, Nucl. Inst. Meth. **A 582** (2007) 429.
5. M. Aharrouche *et al.*, *Time resolution of the ATLAS barrel liquid argon electromagnetic calorimeter*, Nucl. Inst. Meth. **A 597** (2008) 178.
6. M. Aharrouche *et al.*, *Study of the response of ATLAS electromagnetic liquid argon calorimeters to muons*, Nucl. Inst. Meth. **A 606** (2009) 419.
7. B. Dowler *et al.*, *Performance of the ATLAS hadronic end-cap calorimeter in beam tests*, Nucl. Inst. Meth. **A 482** (2002) 96.

8. A.E. Kiryunin *et al.*, *GEANT4 physics evaluation with testbeam data of the ATLAS hadronic end-cap calorimeter*, Nucl. Inst. Meth. **A 560** (2006) 278.
9. J.C. Armitage *et al.*, *Electron signals in the forward calorimeter prototype for ATLAS*, JINST **2** (2007) P11001.
10. J.P. Archambault *et al.*, *Energy calibration of the ATLAS liquid argon Forward Calorimeter*, JINST **3** (2008) P02002.
11. M. Aharrouche *et al.*, *Measurement of the Response of the ATLAS Liquid Argon Barrel Calorimeter to Electrons at the 2004 Combined Test-Beam*, Nucl. Inst. Meth. **A 614** (2010) 400.
12. C. Cojocaru *et al.*, *Hadronic calibration of the ATLAS liquid argon end-cap calorimeter in the pseudorapidity region $1.6 < \eta < 1.8$ in beam tests*, Nucl. Inst. Meth. **A 531** (2004) 481.
13. J. Pinfold *et al.*, *Performance of the ATLAS liquid argon endcap calorimeter in the pseudorapidity region $2.5 < \eta < 4.0$ in beam tests*, Nucl. Inst. Meth. **A 593** (2008) 324.
14. B. Aubert *et al.*, *Construction, assembly and tests of the ATLAS electromagnetic barrel calorimeter*, Nucl. Inst. Meth. **A 558** (2006) 388.
15. M. Aleksa *et al.*, *Construction, assembly and tests of the ATLAS electromagnetic end-cap calorimeter*, JINST **3** (2008) P06002.
16. M.L. Andrieux *et al.*, *Construction and test of the first two sectors of the ATLAS liquid argon presampler*, Nucl. Inst. Meth. **A 479** (2002) 316.
17. D.M. Gingrich *et al.*, *Construction, assembly and testing of the ATLAS hadronic end-cap calorimeter*, JINST **2** (2007) P05005.
18. A. Artamonov *et al.*, *The ATLAS forward calorimeters*, JINST **3** (2008) P02010.
19. C. de La Taille and L. Serin *Temperature dependence of the ATLAS electromagnetic calorimeter signal. Preliminary drift time measurement*, ATL-LARG-95-029.
20. N.J. Buchanan *et al.*, *Design and implementation of the front-end board for the readout of the ATLAS liquid argon calorimeters*, JINST **3** (2008) P03004.
21. N.J. Buchanan *et al.*, *ATLAS liquid argon calorimeter front end electronics system*, JINST **3** (2008) P09003.
22. A. Bazan *et al.*, *ATLAS liquid argon calorimeter back end electronics*, JINST **2** (2007) P06002.
23. J. Colas *et al.*, *Electronics calibration board for the ATLAS liquid argon calorimeters*, Nucl. Inst. Meth. **A 593** (2008) 269.
24. W.E. Cleland and E.G. Stern, *Signal processing considerations for liquid ionization calorimeter in a high rate environment*, Nucl. Inst. Meth. **A 338** (1994) 467.
25. ATLAS collaboration, *Liquid argon calorimeter technical design report*, CERN-LHCC-96-041, <http://cdsweb.cern.ch/record/331061>.
26. W. Lampl *et al.*, *Calorimeter clustering algorithms: Description and performance*, ATL-LARG-PUB-2008-002.
27. R. Achenbach *et al.*, *The ATLAS Level-1 calorimeter trigger*, JINST **3** (2008) P03001.
28. D. Banfi, M. Delmastro and M. Fanti, *Cell response equalization of the ATLAS electromagnetic calorimeter without the direct knowledge of the ionization signals*, JINST **1** (2006) P08001.
29. S. Baffioni *et al.*, *Electrical Measurements on the Atlas Electromagnetic Barrel Calorimeter*, ATL-LARG-PUB-2007-005.
30. C. Collard *et al.*, *Prediction of signal amplitude and shape for the ATLAS electromagnetic calorimeter*, ATL-LARG-PUB-2007-010.
31. C. Gabaldon Ruiz *et al.*, *Signal reconstruction in the EM end-cap calorimeter and check with cosmic data in the region $0 < \eta < 3.2$* , ATL-LARG-PUB-2008-001.
32. H. Brettel *et al.*, *Calibration of the ATLAS hadronic end-cap calorimeter*, Proceedings of the 6th Workshop on Electronics for LHC Experiments, Krakow (Poland, September 2000), p.218.
33. J. Ban *et al.*, *Cold electronics for the liquid argon hadronic end-cap calorimeter of ATLAS*, Nucl. Inst. Meth. **A 556** (2006) 158.
34. ATLAS Collaboration, *Drift Time Measurement in the ATLAS Liquid Argon Electromagnetic Calorimeter using Cosmic Muons Data*, to be published.
35. ATLAS Collaboration, *The ATLAS Monte Carlo project*, to be published.
36. J.P. Archambault *et al.*, *The Simulation of the ATLAS Liquid Argon Calorimetry*, ATL-LARG-PUB-2009-001
37. S. Agostinelli *et al.*, *GEANT4: A Simulation toolkit*, Nucl. Inst. Meth. **A 506** (2003) 250.
38. A. Dar, *Atmospheric neutrinos, astrophysical neutrons, and proton-decay experiments*, Phys.Rev.Lett. **51** (1983) 227-230.
39. M. Cooke *et al.*, *In situ commissioning of the ATLAS electromagnetic calorimeter with cosmic muons*, ATL-LARG-PUB-2007-013.

Measurement of isolated-photon pair production in pp collisions at $\sqrt{s} = 7$ TeV with the ATLAS detector



The ATLAS collaboration

E-mail: atlas.publications@cern.ch

ABSTRACT: The ATLAS experiment at the LHC has measured the production cross section of events with two isolated photons in the final state, in proton-proton collisions at $\sqrt{s} = 7$ TeV. The full data set collected in 2011, corresponding to an integrated luminosity of 4.9 fb^{-1} , is used. The amount of background, from hadronic jets and isolated electrons, is estimated with data-driven techniques and subtracted. The total cross section, for two isolated photons with transverse energies above 25 GeV and 22 GeV respectively, in the acceptance of the electromagnetic calorimeter ($|\eta| < 1.37$ and $1.52 < |\eta| < 2.37$) and with an angular separation $\Delta R > 0.4$, is $44.0^{+3.2}_{-4.2} \text{ pb}$. The differential cross sections as a function of the di-photon invariant mass, transverse momentum, azimuthal separation, and cosine of the polar angle of the largest transverse energy photon in the Collins-Soper di-photon rest frame are also measured. The results are compared to the prediction of leading-order parton-shower and next-to-leading-order and next-to-next-to-leading-order parton-level generators.

KEYWORDS: Hadron-Hadron Scattering

Contents

1	Introduction	1
2	The ATLAS detector	2
3	Data and Monte Carlo samples	3
4	Event selection	4
5	Signal yield extraction	5
5.1	Jet background subtraction	5
5.2	Electron background subtraction	9
6	Cross section measurement	10
6.1	Efficiency and unfolding	11
6.2	Trigger efficiency correction	12
6.3	Results	12
7	Comparison with theoretical predictions	13
8	Conclusion	15
A	Experimental differential cross section	17
	The ATLAS collaboration	26

1 Introduction

The measurement at the LHC of the production cross section, in pp collisions, of two isolated photons not originating from hadronic decays, $pp \rightarrow \gamma\gamma + X$, provides a tool to probe perturbative Quantum Chromodynamics (QCD) predictions and to understand the irreducible background to new physics processes involving photons in the final state. These processes include Higgs boson decays to photon pairs ($H \rightarrow \gamma\gamma$) or graviton decays predicted in some Universal Extra-Dimension models [1, 2].

Recent cross section measurements for di-photon production at hadron colliders were performed by the DØ [3] and CDF [4] collaborations at the $\sqrt{s} = 1.96$ TeV Tevatron $p\bar{p}$ collider, and by ATLAS [5] and CMS [6] using $\sqrt{s} = 7$ TeV pp collisions recorded at the LHC in 2010.

In this paper, the production cross section of two isolated photons with transverse energies (E_T) above 25 GeV and 22 GeV respectively, in the acceptance of the ATLAS electromagnetic calorimeter ($|\eta| < 1.37$ and $1.52 < |\eta| < 2.37$) and with an angular separation

$\Delta R > 0.4$, is measured. The results are obtained using the data collected by the ATLAS experiment in 2011, which corresponds to an integrated luminosity¹ of $(4.9 \pm 0.2) \text{ fb}^{-1}$, thus increasing the sample size by more than a factor of 100 compared to the previous measurement. The transverse energy thresholds for the two photons are higher than in the previous measurement (16 GeV).

The integrated di-photon production cross section is measured, as well as the differential cross sections as a function of four kinematic variables: the di-photon invariant mass ($m_{\gamma\gamma}$), the di-photon transverse momentum ($p_{T,\gamma\gamma}$), the azimuthal² separation between the photons in the laboratory frame ($\Delta\phi_{\gamma\gamma}$), and the cosine of the polar angle of the highest E_T photon in the Collins-Soper di-photon rest frame ($\cos\theta_{\gamma\gamma}^*$) [9]. The first distribution is of obvious interest for resonance searches; the second and the third provide important information in the study of higher-order QCD perturbative effects and fragmentation, especially in some specific regions such as the small $\Delta\phi_{\gamma\gamma}$ limit; the fourth can be used to investigate the spin of di-photon resonances. For this purpose, the Collins-Soper rest frame is preferred to other frame definitions because of its robustness with respect to initial state radiation. The results are compared to the predictions from: parton-shower Monte Carlo generators, PYTHIA [10] and SHERPA [11]; parton-level calculations with next-to-leading-order (NLO) QCD corrections using the DIPHOX [12] program complemented by GAMMA2MC [13]; and at next-to-next-to-leading-order (NNLO), using 2γ NNLO [14]. The contribution from the di-photon decays of the particle recently discovered by ATLAS [15] and CMS [16] in the search for the Standard Model Higgs boson is not included in the theoretical calculations. It is expected to contribute around 1% of the signal in the $120 < m_{\gamma\gamma} < 130 \text{ GeV}$ interval, and negligibly elsewhere.

2 The ATLAS detector

ATLAS [17] is a multipurpose detector with a forward-backward symmetric cylindrical geometry and nearly 4π coverage in solid angle. The most relevant subdetectors for the present analysis are the inner tracking detector (ID) and the calorimeters.

The ID consists of a silicon pixel detector and a silicon microstrip detector covering the pseudorapidity range $|\eta| < 2.5$, and a straw tube transition radiation tracker covering $|\eta| < 2.0$. It is immersed in a 2 T magnetic field provided by a superconducting solenoid. The ID allows efficient reconstruction of converted photons if the conversion occurs at a radius of up to $\approx 0.80 \text{ m}$.

The electromagnetic calorimeter (ECAL) is a lead/liquid-argon (LAr) sampling calorimeter providing coverage for $|\eta| < 3.2$. It consists of a barrel section ($|\eta| < 1.475$)

¹The 3.9% uncertainty in the integrated luminosity for the complete 2011 data set is based on the calibration described in refs. [7, 8] including an additional uncertainty for the extrapolation to the later data-taking period with higher instantaneous luminosity.

²ATLAS uses a right-handed coordinate system with its origin at the nominal interaction point (IP) in the centre of the detector and the z -axis coinciding with the axis of the beam pipe. The x -axis points from the IP to the centre of the LHC ring, and the y -axis points upward. Cylindrical coordinates (r, ϕ) are used in the transverse plane, ϕ being the azimuthal angle around the beam pipe. The pseudorapidity is defined in terms of the polar angle θ as $\eta = -\ln \tan(\theta/2)$.

and two end-caps ($1.375 < |\eta| < 3.2$). The central region ($|\eta| < 2.5$) is segmented into three longitudinal layers. The first (inner) layer, covering $|\eta| < 1.4$ in the barrel and $1.5 < |\eta| < 2.4$ in the end-caps, has high granularity in the η direction (between 0.003 and 0.006 depending on η), sufficient to provide event-by-event discrimination between single-photon showers and two overlapping showers from a π^0 decay. The second layer, which collects most of the energy deposited in the calorimeter by the photon shower, has a cell granularity of 0.025×0.025 in $\eta \times \phi$. The third layer is used to correct high energy showers for leakage beyond the ECAL. In front of the electromagnetic calorimeter a thin presampler layer, covering the pseudorapidity interval $|\eta| < 1.8$, is used to correct for energy loss before the ECAL.

The hadronic calorimeter (HCAL), surrounding the ECAL, consists of an iron/scintillator tile calorimeter in the range $|\eta| < 1.7$, and two copper/LAr calorimeters spanning $1.5 < |\eta| < 3.2$. The ECAL and HCAL acceptance is extended by two LAr forward calorimeters (using copper and tungsten as absorbers) up to $|\eta| < 4.9$.

Di-photon events are recorded using a three-level trigger system. The first level, implemented in hardware, is based on towers defined with a coarser granularity (0.1×0.1 in $\eta \times \phi$) than that of the ECAL. They are used to search for electromagnetic deposits in $\eta \times \phi$ regions of 2×1 and 1×2 towers, within a fixed window of size 2×2 and with a transverse energy above a programmable threshold. The second- and third-level triggers are implemented in software and exploit the full granularity and energy calibration of the calorimeter to refine the first-level trigger selection.

3 Data and Monte Carlo samples

The data set analysed consists of the 7 TeV proton-proton collisions recorded by the ATLAS detector in 2011. Only events where the beam conditions are stable and the trigger system, the tracking devices, and the calorimeters are operational, are considered.

Monte Carlo (MC) samples are produced using various generators as described below. Particle interactions with the detector material and the detector response are simulated with GEANT4 [18]. The events are reconstructed with the same algorithms used for collision data. More details of the event generation and simulation infrastructure are provided in ref. [19].

Simulated di-photon events are generated with both PYTHIA 6.4.21 and SHERPA 1.3.1. PYTHIA uses the modified leading-order MRST2007 [20] parton distribution functions (PDFs) while SHERPA uses the CTEQ6L1 [21] PDFs. The PYTHIA event-generator parameters are set according to the ATLAS AMBT2 [22] tune, while the SHERPA parameters are the default ones of the SHERPA 1.3.1 distribution. Photons originating from the hard scattering and quark bremsstrahlung are included in the analysis. The MC di-photon signal is generated with a photon E_T threshold of 20 GeV; one million events are produced both with PYTHIA and SHERPA. They are used to model the transverse isolation energy (see section 4) distribution of signal photons, to compute the reconstruction efficiency and to study the systematic uncertainties on the reconstructed quantities. Background γ -jet events are generated using ALPGEN [23] with the CTEQ6L1 PDF set.

4 Event selection

Events are collected using a di-photon trigger with a nominal transverse energy threshold of 20 GeV for both photon candidates. The photon trigger objects are required to pass a selection based on shower shape variables computed from the energy deposits in the second layer of the electromagnetic calorimeter and in the hadronic calorimeter. The requirements are looser than the photon identification criteria applied in the offline selection. In order to reduce non-collision backgrounds, events are required to have a reconstructed primary vertex with at least three associated tracks and consistent with the average beam spot position. The signal inefficiency of this requirement is negligible.

Photons are reconstructed from electromagnetic energy clusters in the calorimeter and tracking information provided by the ID as described in ref. [24]. Photons reconstructed near regions of the calorimeter affected by read-out or high-voltage failures are not considered.³ The cluster energies are corrected using an in-situ calibration based on the Z boson mass peak [25], and the determination of the pseudorapidities is optimized using the technique described in ref. [15]. In order to benefit from the fine segmentation of the first layer of the electromagnetic calorimeter to discriminate between genuine prompt photons and fake photons within jets, the photon candidate pseudorapidity must satisfy $|\eta| < 1.37$ or $1.52 < |\eta| < 2.37$. We retain photon candidates passing loose identification requirements, based on the same shower shape variables — computed with better granularity and resolution — and the same thresholds used at trigger level. The highest- E_T (“leading”) and second highest- E_T (“subleading”) photons within the acceptance and satisfying the loose identification criteria are required to have $E_{T,1} > 25$ GeV and $E_{T,2} > 22$ GeV, respectively. The fraction of events where the two selected photon candidates are not matched to the photon trigger objects is negligible. The angular separation between the two photons, $\Delta R = \sqrt{(\Delta\eta)^2 + (\Delta\phi)^2}$, is required to be larger than 0.4, in order to avoid one photon candidate depositing significant energy in the isolation cone of the other, as defined below.

Two further criteria are used to define the signal and background control regions. Firstly the tight photon selection [24] (abbreviated as **T** in the following) is designed to reject hadronic jet background, by imposing requirements on nine discriminating variables computed from the energy leaking into the HCAL and the lateral and longitudinal shower development in the ECAL. Secondly the transverse isolation energy E_T^{iso} is computed from the sum of the positive-energy topological clusters with reconstructed barycentres inside a cone of radius $\Delta R = 0.4$ around the photon candidate. The algorithm for constructing topological clusters suppresses noise by keeping only those cells with a significant energy deposit and their neighbouring cells. The cells within 0.125×0.175 in $\eta \times \phi$ around the photon are excluded from the calculation of E_T^{iso} . The mean value of the small leakage of the photon energy from this region into the isolation cone, evaluated as a function of the photon transverse energy, is subtracted from the measured value of E_T^{iso} (meaning that E_T^{iso} can be negative). The typical size of this correction is a few percent of the photon transverse energy. The measured value of E_T^{iso} is further corrected by subtracting the estimated

³This requirement leads to a typical loss of 0.8% to 1.4% on the photon reconstruction efficiency, depending on the data-taking period.

contributions from the underlying event and additional pp interactions. This correction is computed on an event-by-event basis, by calculating the transverse energy density from low-transverse-momentum jets, as suggested in refs. [26, 27]. The median transverse energy densities of the jets in two η regions, $|\eta| < 1.5$ and $1.5 < |\eta| < 3.0$, are computed separately, and the one for the region containing the photon candidate pseudorapidity is multiplied by the total area of all topological clusters used in the calculation of the isolation variable in order to estimate the correction. Signal photons are required to pass the tight selection (“tight photons”) and the isolation requirement **I**, $-4 < E_T^{\text{iso}} < 4 \text{ GeV}$. A total of 165 767 pairs of tight, isolated photons are selected. The fraction of events in which an additional photon pair passes all the selection criteria, except for the requirement on the two photons being the leading and subleading E_T candidates, is less than 1 per 100 000. The non-tight ($\tilde{\mathbf{T}}$) photon candidates are defined as those failing the tight criteria for at least one of the shower-shape variables that are computed from the energy deposits in a few cells of the first layer of the electromagnetic calorimeter adjacent to the cluster barycentre. Photon candidates with $4 < E_T^{\text{iso}} < 8 \text{ GeV}$ are considered non-isolated ($\tilde{\mathbf{I}}$).

5 Signal yield extraction

After the selection, the main background is due primarily to γ -jet and secondarily to di-jet (jj) final states, collectively called “jet background” in the following. Two methods, the two-dimensional sidebands and the two-dimensional fit, already exploited in ref. [5], are used to perform an in-situ statistical subtraction of the jet background from the selected photon candidate pairs, as described in section 5.1.

After the jet background contribution is subtracted, a small residual background contamination arises from events where isolated electrons are misidentified as photons. This contribution is estimated as described in section 5.2.

5.1 Jet background subtraction

Both the two-dimensional sidebands and the two-dimensional fit methods use the photon transverse isolation energy and the tight identification criteria to discriminate prompt photons from jets. They rely on the fact that the correlations between the isolation and the tight criteria in background events are small, and that the signal contamination in the non-tight or non-isolated control regions is low.

The two-dimensional sidebands method counts the numbers of photon candidate pairs where each of the candidates passes or fails the tight and the isolation criteria. Four categories are defined for each photon, resulting in 16 categories of events. The inputs to the method are the numbers of events in the categories and the signal efficiencies of the tight and isolation requirements. The correlation between these two requirements is assumed to be negligible for background events. The method allows the simultaneous extraction of the numbers of true di-photon signal, γj , $j\gamma$ ⁴ and jj background events, and the tight and isolation efficiencies for fake photon candidates from jets (“fake rates”). The

⁴Here and in the following, γj ($j\gamma$) denotes the events where the leading (subleading) candidate is a true photon, and the other candidate a true jet.

expected number of events in each category is written as a function of the parameters (yields, efficiencies, fake rates and correlation factors) and the system of 16 equations is solved with a χ^2 minimization procedure. This method is an extension of the one used in our previous di-photon analysis [5]. It allows the extraction of different isolation fake rates for jets in $j\gamma$ or jj events as well as a correlation factor for the isolation of jet pairs.

The two-dimensional fit method consists of an extended maximum likelihood template fit to the two-dimensional distribution of the transverse isolation energies $E_{T,1}^{\text{iso}}$ and $E_{T,2}^{\text{iso}}$ of the two photon candidates in events belonging to the **T-T** sample, i.e. where both photons satisfy the tight identification criteria. The fit is performed in the isolation range $-4 < E_{T,i}^{\text{iso}} < 8$ GeV ($i = 1, 2$). The correlations between the transverse isolation energies of the two candidates in di-photon, γj , and $j\gamma$ events are found to be negligible in MC samples, and the products of two one-dimensional templates for $E_{T,1}^{\text{iso}}$ and $E_{T,2}^{\text{iso}}$ are used for each of the three event species. For the jj component, large correlations are observed in data, and a two-dimensional template is used. The two-dimensional fit is described in detail in our previous paper [5]. There are two differences between the present and previous analyses: the use now of binned distributions instead of smooth parametric functions for the photon and jet templates, and the correction for signal leakage in the background templates, as described below.

The transverse isolation energy distributions of the signal photons and the corresponding efficiencies of the signal requirement $-4 < E_T^{\text{iso}} < 4$ GeV are obtained from the SHERPA di-photon sample, separately for the leading and the subleading candidates. In the two-dimensional fit method, the templates are shifted by +160 and +120 MeV respectively in order to maximize the likelihood, as determined from a scan as a function of the shifts. These values are also used to compute the signal efficiencies of the isolation requirement needed in the two-dimensional sidebands method. Shifts of similar size between ATLAS data and MC simulation have been observed in the transverse isolation energy distribution, computed with the same technique (based on topological clusters inside a cone of radius 0.4), of electron control samples selected from $Z \rightarrow ee$ decays with a tag-and-probe method. The E_T^{iso} distributions of prompt photons in γj and $j\gamma$ events are assumed to be identical to that of prompt photons in di-photon events, as found in simulated samples. The tight identification efficiencies for prompt photons, needed in the two-dimensional sidebands method and in the final cross section measurement, are estimated using the same di-photon MC sample. The shower shape variables are corrected for the observed differences between data and simulation in photon-enriched control samples. Residual differences between the efficiencies in the simulation and in data are corrected using scale factors determined from control samples of photons from radiative Z boson decays, electrons selected with a tag-and-probe technique from $Z \rightarrow ee$ decays, and photon-enriched control samples of known photon purity [28]. After applying these corrections, the photon identification efficiency in the simulation is estimated to reproduce the efficiency in data to within 2%. For the two-dimensional fit, the transverse isolation energy template of the leading (subleading) jet in $j\gamma$ (γj) events is extracted directly from data where one candidate passes the non-tight and the other passes both the tight identification and isolation (**TI**) requirements. For jj events, the two-dimensional template is obtained from data in which the two candidates

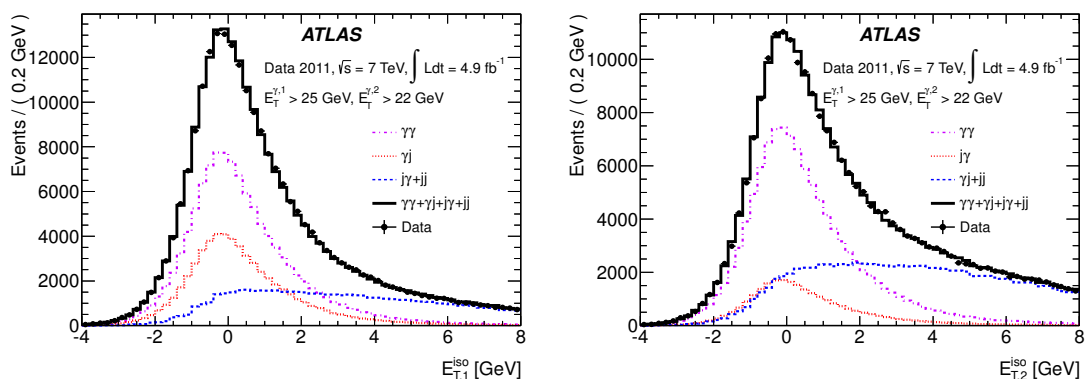


Figure 1. Projections of the two-dimensional fit to the transverse isolation energies of the two photon candidates: leading photon (left) and sub-leading photon (right). The photon templates from SHERPA are shifted by +160 MeV (+120 MeV) for the leading (subleading) photon. Solid circles represent the observed data. The (black) solid line is the fit result, the (violet) dash-dotted curve shows the $\gamma\gamma$ component. The (red) dotted line shows in the left (right) figure the contribution from γj ($j\gamma$) events. In both figures, the (blue) dashed line represents a broad background component in the photon candidates' sample: for the leading candidate this is due to $j\gamma$ and jj final states, whereas for the sub-leading candidate it comes from γj and jj final states.

Yield	two-dimensional sidebands results		two-dimensional fit results	
$N_{\gamma\gamma}$	113 200	± 600 (stat.) $+5000$ (syst.) -8000 (syst.)	111 700	± 500 (stat.) $+4500$ (syst.) -7600 (syst.)
$N_{\gamma j}$	31 500	± 400 (stat.) $+3900$ (syst.) -3100 (syst.)	31 500	± 300 (stat.) $+4800$ (syst.) -3600 (syst.)
$N_{j\gamma}$	13 000	± 300 (stat.) $+2500$ (syst.) -800 (syst.)	13 900	$+300$ (stat.) $+3400$ (syst.) -2100 (syst.)
N_{jj}	8 100	± 100 (stat.) $+1900$ (syst.) -1400 (syst.)	8 300	± 100 (stat.) $+300$ (syst.) -2100 (syst.)

Table 1. Total yields for two candidates satisfying the tight identification and the isolation requirement $-4 < E_T^{\text{iso}} < 4 \text{ GeV}$. Both statistical and total systematic uncertainties are listed.

are required to be non-tight. The correlation is found to be about 8%. The jet background templates are corrected for signal leakage in the control samples, estimated from the SHERPA sample.

Figure 1 shows the projections of the two-dimensional fit to the transverse isolation energies of the leading and subleading photon candidates. The yields for each of the four components extracted with the two-dimensional sidebands method and the two-dimensional fit are given in table 1. The di-photon purity is around 68% and the di-photon yields agree within 1.5% between the two methods.

To obtain the differential signal yields as a function of the di-photon kinematic variables, such as $m_{\gamma\gamma}$, $p_{T,\gamma\gamma}$, $\Delta\phi_{\gamma\gamma}$ and $\cos\theta_{\gamma\gamma}^*$, the above methods are applied in each bin of the variables. Figure 2 shows the differential spectra of the signal and background components obtained with the two-dimensional fit. In some regions of the di-photon spectra, discrepancies with the two-dimensional sidebands results are larger than those observed for the integrated yield. The results from the two-dimensional fit are used to extract the nominal cross sections, while differences between the results obtained with the two methods are included in the final systematic uncertainty.

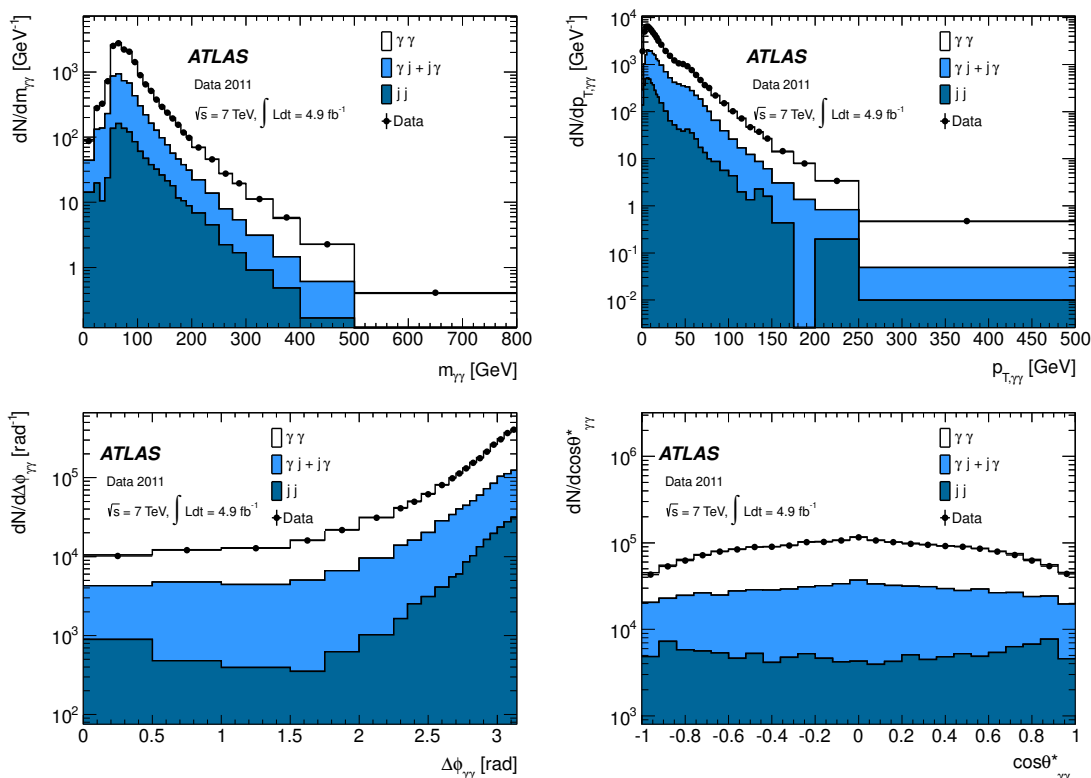


Figure 2. Differential spectra in data (solid circles) and from the two-dimensional fit, for the $\gamma\gamma$ (hollow histogram), $\gamma j + j\gamma$ (light solid histogram), and jj (dark solid histogram) contributions. The spectra are shown for the following di-photon variables: $m_{\gamma\gamma}$ (top left), $p_{T,\gamma\gamma}$ (top right), $\Delta\phi_{\gamma\gamma}$ (bottom left), $\cos\theta_{\gamma\gamma}^*$ (bottom right).

Several sources of systematic uncertainty on the signal yield, estimated after the jet background subtraction, are considered. The dominant uncertainty originates from the choice of the background control regions and accounts for both the uncertainty on the background transverse isolation energy distribution and its correlation with the identification criteria. It is first estimated by varying the number of relaxed criteria in the non-tight definition. For the integrated di-photon yield, the effect is found to be $^{+3}_{-6}\%$. In some bins of the $m_{\gamma\gamma}$ and $p_{T,\gamma\gamma}$ spectra where the size of the control samples is small, neighbouring bins are grouped together to extract the jet background templates. Since the background transverse isolation energies depend mildly on these kinematic variables, a systematic uncertainty is evaluated by repeating the yield extraction with jet templates from the adjacent groups of neighbouring bins. The uncertainty on the estimated signal yield is at most $\pm 9\%$.

In the nominal result, the photon isolation templates are taken from the SHERPA di-photon sample. A systematic uncertainty is evaluated by using alternative templates from the PYTHIA di-photon sample, and from data. The data-driven template for the leading (subleading) photon is obtained by selecting events where the requirement $E_T^{\text{iso}} < 8 \text{ GeV}$ is removed for the leading (subleading) photon candidate, and normalizing the leading (subleading) photon isolation distribution in $\tilde{\mathbf{T}}\text{-TI}$ ($\mathbf{TI}\text{-}\tilde{\mathbf{T}}$) events, where the leading

(subleading) candidate fails the tight identification while the other candidate passes tight identification and isolation criteria, to the isolation distribution of leading (subleading) candidates in **T-T** events in the $7 < E_T^{\text{iso}} < 17 \text{ GeV}$ region. The difference between the two distributions is used as an estimate of the photon distribution. The PYTHIA di-photon sample exhibits higher tails than SHERPA at large values of E_T^{iso} . The data-driven template, on the other hand, is characterized by smaller tails than the SHERPA template, since it is obtained by assuming that the isolation region above 7 GeV is fully populated by background. The corresponding uncertainty on the signal yield is estimated to be ${}_{-3}^{+2}\%$ of the integrated di-photon yield. It is rather uniform as a function of $m_{\gamma\gamma}$, $p_{T,\gamma\gamma}$, $\Delta\phi_{\gamma\gamma}$ and $\cos\theta_{\gamma\gamma}^*$ and always below 4%, except at very low $m_{\gamma\gamma}$ where it reaches $\pm 5\%$. The photon isolation template is, to a large extent, independent of the variables under study. Repeating the background subtraction procedure using photon isolation templates extracted in bins of the di-photon variable under study leads to variations of the estimated signal yield within ${}_{-4}^{+2}\%$.

Other systematic effects have been considered, and found to be smaller than those previously discussed. The bias created by neglecting the dependence of the identification and isolation efficiencies on η and E_T is estimated to be of +0.02% and -0.3% respectively. The effect of assuming identical templates for photons in di-photon and in γ -jet events is evaluated by using instead templates from ALPGEN γ -jet samples for photons in the γj and $j\gamma$ components. The uncertainty on the shifts applied to the MC photon templates ($\pm 10 \text{ MeV}$ for the leading photons and $\pm 5 \text{ MeV}$ for the subleading ones, as determined from the scan) is propagated to the di-photon yields. The impact of the identification efficiencies on the signal leakage correction is estimated by neglecting in the simulation the correction factors nominally applied to the shower shape variables to account for the observed differences between data and MC simulation. These effects produce systematic uncertainties of at most 0.5% on the differential spectra. Finally, no significant effect is observed due to the imperfect modelling of the material in front of the calorimeters.

5.2 Electron background subtraction

Isolated electrons from W or Z boson decays can be misidentified as photons, since the two particles (e and γ) generate similar electromagnetic showers in the ECAL. Usually a track is reconstructed in the inner detector pointing to the electron ECAL cluster, thus isolated electrons misidentified as photons are mostly classified as converted candidates. Pairs of misidentified, isolated electrons and positrons (ee) from processes such as Drell-Yan, $Z \rightarrow ee$, $WW \rightarrow e\nu e\nu$, or of photons and e^\pm from diboson production ($\gamma W \rightarrow \gamma e\nu$, $\gamma Z \rightarrow \gamma ee$), provide a background that cannot be distinguished from the di-photon signal based on the photon identification and isolation variables and must therefore be estimated in a separate way. The same procedure exploited in ref. [5], based on the number of γe ($N_{\gamma e}$) and ee (N_{ee}) events observed in data, is used to estimate their contributions to the di-photon yield $N_{\gamma\gamma}$ after jet background subtraction.

For a given bin i of the variable X ($X = m_{\gamma\gamma}$, $p_{T,\gamma\gamma}$, $\Delta\phi_{\gamma\gamma}$, or $\cos\theta_{\gamma\gamma}^*$), the signal component $N_{\gamma\gamma}^{\text{sig}}$ in the $N_{\gamma\gamma}$ sample can be evaluated:

$$N_{\gamma\gamma}^{\text{sig}} = \frac{N_{\gamma\gamma} - [f_{e\rightarrow\gamma}N_{\gamma e} - (f_{e\rightarrow\gamma})^2N_{ee}]}{(1 - f_{e\rightarrow\gamma}f_{\gamma\rightarrow e})^2} \quad (5.1)$$

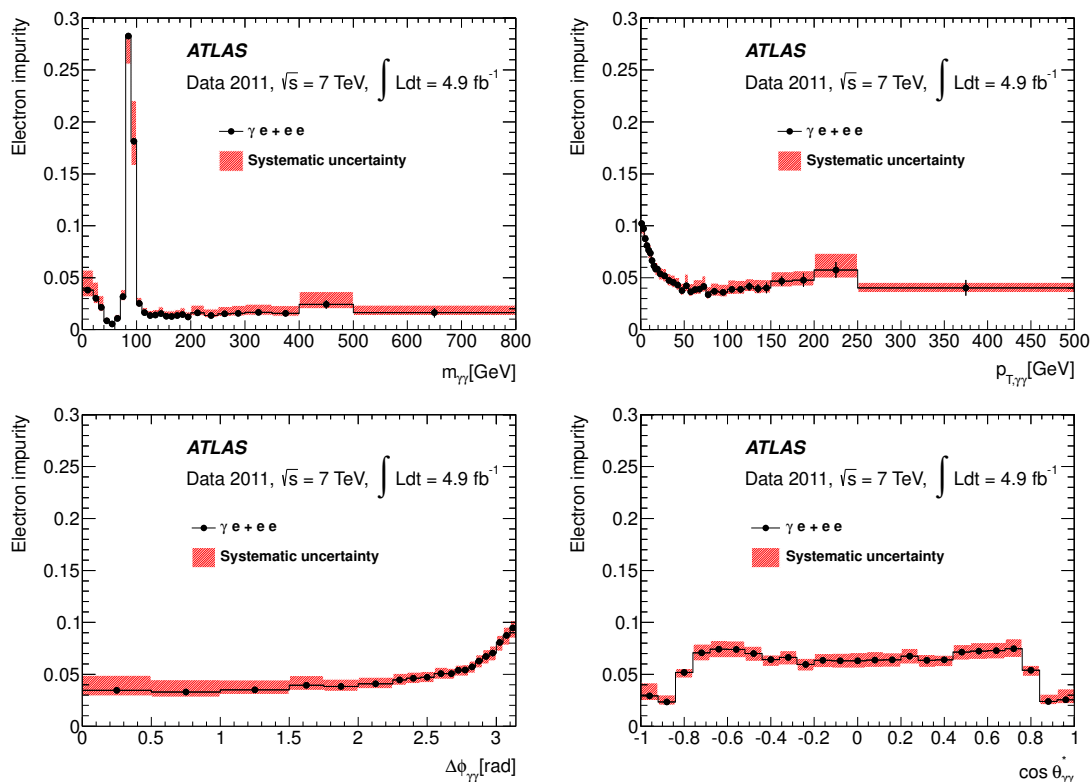


Figure 3. Fraction of electron background (impurity) as a function of $m_{\gamma\gamma}$, $p_{T,\gamma\gamma}$, $\Delta\phi_{\gamma\gamma}$, and $\cos\theta_{\gamma\gamma}^*$.

The fake rates $f_{e\rightarrow\gamma}$ and $f_{\gamma\rightarrow e}$ are measured using Z boson decays in data. $Z \rightarrow ee$ decays are used to estimate $f_{e\rightarrow\gamma}$ as $N_{\gamma e}^Z/(2N_{ee}^Z)$, where $N_{\gamma e}^Z$ and N_{ee}^Z are the numbers of γe and ee pairs with invariant mass within 1.5σ of the Z boson mass. $Z \rightarrow \gamma ee$ decays are similarly used to estimate $f_{\gamma\rightarrow e}$ as $N_{eee}^Z/N_{\gamma ee}^Z$. The numbers of continuum background events are estimated from the sidebands of the ee , γe , eee or γee invariant mass distributions (51 – 61 GeV and 121 – 131 GeV), and subtracted from N_{ee}^Z , $N_{\gamma e}^Z$, N_{eee}^Z and $N_{\gamma ee}^Z$, respectively. Electrons must satisfy identification criteria based on their shower shape in the electromagnetic calorimeter, quality criteria for the associated track in the ID, and an isolation requirement $E_T^{\text{iso}} < 4$ GeV. The measured fake rates, including statistical and systematic uncertainties, are $f_{e\rightarrow\gamma} = 0.062^{+0.040}_{-0.010}$ and $f_{\gamma\rightarrow e} = 0.038^{+0.024}_{-0.007}$, where the systematic uncertainty is dominated by the dependence on the transverse energy of the candidate photon. Other sources include the uncertainties on N_{ee}^Z , $N_{\gamma e}^Z$, N_{eee}^Z and $N_{\gamma ee}^Z$ which are evaluated by changing the definition of the Z boson mass window to $\pm 2\sigma$ and $\pm 1\sigma$, and shifting the sidebands by ± 5 GeV. The fraction of electron background as a function of $m_{\gamma\gamma}$, $p_{T,\gamma\gamma}$, $\Delta\phi_{\gamma\gamma}$, and $\cos\theta_{\gamma\gamma}^*$ is shown in figure 3. The enhancements at $m_{\gamma\gamma} \approx m_Z$, low $p_{T,\gamma\gamma}$ and $\Delta\phi_{\gamma\gamma} \approx \pi$ are due to the large Z boson production cross section.

6 Cross section measurement

This section describes the extraction of the final cross sections. The background-subtracted differential spectra are first unfolded to the generated-particle level, to take into account

reconstruction and selection efficiencies estimated from the simulation, and then divided by the integrated luminosity of the data sample and the trigger efficiency relative to the offline selection.

6.1 Efficiency and unfolding

The background-subtracted differential distributions obtained from the data are unfolded to obtain the particle-level spectra by dividing the signal yield in each bin of the di-photon observable under study by a “bin-by-bin” correction, which accounts for signal reconstruction and selection efficiencies and for finite resolution effects. The bin-by-bin nominal corrections are evaluated from the SHERPA di-photon simulated sample as the number of simulated di-photon events satisfying the selection criteria (excluding the trigger requirement) and for which the reconstructed value of the variable X under consideration is in bin i , divided by the number of simulated di-photon events satisfying the nominal acceptance criteria at generator-level and for which the generated value of X is in the same bin i . The generator-level photon transverse isolation energy is computed from the true four-momenta of the generated particles (excluding muons and neutrinos) inside a cone of radius 0.4 around the photon direction. The pile-up contribution is removed using an analogous method to the one for the experimental isolation variable, by subtracting the product of the area of the isolation cone and the median transverse energy density of the low-transverse-momentum truth-particle jets.

Alternative corrections are calculated with the PYTHIA di-photon sample or using a simulated di-photon sample which contains additional material upstream of the calorimeter. The variations induced on the measured cross sections by the alternative corrections are taken as systematic uncertainties, due to the uncertainty on the generated kinematic distributions, on the relative fraction of direct and fragmentation di-photon production, and on the amount of material in the ATLAS detector. The effect on the total cross section is within $\pm 2\%$ for $m_{\gamma\gamma}$, $\pm 3\%$ for $p_{T,\gamma\gamma}$, $\pm 3\%$ for $\Delta\phi_{\gamma\gamma}$ and $\pm 2\%$ for $\cos\theta_{\gamma\gamma}^*$.

The effect of the uncertainty on the efficiency of the photon identification criteria is estimated by varying the identification efficiency in the simulation by its uncertainty [28]. The uncertainties on the electromagnetic (photon) energy scale and resolution are also propagated to the final measurement by varying them within their uncertainties [25]. The effect on the differential cross section is typically $\pm 1\%$. Other uncertainties, related to the dependence on the average number of pile-up interactions of the efficiencies of the photon identification and transverse isolation energy requirements and to the observed data-MC shift in the photon transverse isolation energy distributions, are found to be negligible.

A closure test has been performed by unfolding the differential spectra of di-photon events selected in the PYTHIA signal sample with the bin-by-bin coefficients determined using the SHERPA sample, and comparing the unfolded spectra to the truth-level spectra in the same PYTHIA sample. Non-closure effects of at most 2% have been found and included in the final systematic uncertainty.

More sophisticated unfolding methods which account for migrations between bins, either based on the repeated (iterative) application of Bayes’ theorem [29] or on a least-square minimization followed by a regularization of the resulting spectra [30] have also been

investigated. The differences between the unfolded spectra obtained with these methods and the spectra extracted with the bin-by-bin corrections are negligible compared to the other uncertainties and therefore the bin-by-bin method was chosen for the final results.

6.2 Trigger efficiency correction

The unfolded spectra are then corrected for the event-level trigger efficiency, defined as the fraction of di-photon events — satisfying all the selection criteria — that pass the di-photon trigger used to collect the data. The trigger efficiency is measured in data using a bootstrap technique [31] from samples selected with fully efficient unbiased triggers with a lower threshold, and taking into account kinematic correlations between the photon candidates. The differences between the measured di-photon trigger efficiency and the efficiency estimated with simulated di-photon samples, or by applying the bootstrap technique to single-photon triggers and neglecting correlations between the two photon candidates, have been assigned as systematic uncertainties. The total trigger efficiency is then:

$$\varepsilon_{\text{trig}} = (97.8_{-1.5}^{+0.8}(\text{stat.}) \pm 0.8(\text{syst.})) \% \quad (6.1)$$

Using di-photon simulated samples, the trigger efficiency has been estimated to be constant, within the total uncertainties, as a function of the four di-photon observables under investigation.

6.3 Results

The differential cross sections as a function of $m_{\gamma\gamma}$, $p_{T,\gamma\gamma}$, $\Delta\phi_{\gamma\gamma}$, and $\cos\theta_{\gamma\gamma}^*$ are extracted following the unfolding procedure described in section 6.1 and using the trigger efficiency quoted in eq. (6.1). The numerical results are listed in appendix A.

The integrated cross section is measured by dividing the global $\gamma\gamma$ yield (obtained after subtracting the electron contribution from the two-dimensional fit result in table 1) by the product of the average event selection efficiency (from the simulation), trigger efficiency and integrated luminosity. The selection efficiency is defined as the number of reconstructed simulated di-photon events satisfying the detector-level selection criteria divided by the number of generated events satisfying the equivalent truth-level criteria, thus correcting for reconstructed events with true photons failing the acceptance cuts. It is computed from simulated di-photon events, reweighting the spectrum of one of the four di-photon variables under study in order to match the differential background-subtracted di-photon spectrum observed in data. Choosing different variables for the reweighting of the simulated events leads to slightly different but consistent efficiencies, with an average value of 49.6% and an RMS of 0.2%. Including systematic uncertainties on the photon reconstruction and identification efficiencies, from the same sources described in section 6.1, the event selection efficiency is estimated to be $49.6_{-1.7}^{+1.9}\%$. The dominant contributions to the efficiency uncertainty are from the photon identification efficiency uncertainty ($\pm 1.2\%$), the energy scale uncertainty ($_{-0.5}^{+1.2}\%$), and the choice of the MC generator and the detector simulation ($\pm 0.9\%$). Negligible uncertainties are found to arise from the energy resolution, the isolation requirement (evaluated by shifting the isolation variable by the observed data-MC

difference) and from the different pile-up dependence of the efficiency in data and MC simulation. With an integrated luminosity of $(4.9 \pm 0.2) \text{ fb}^{-1}$ at $\sqrt{s} = 7 \text{ TeV}$, we obtain an integrated cross section of $44.0_{-4.2}^{+3.2} \text{ pb}$, where the dominant uncertainties are the event selection efficiency and the jet subtraction systematic uncertainties. As a cross-check, the integrals of the one-dimensional differential cross sections are also computed. They are consistent with the measured integrated cross section quoted above.

7 Comparison with theoretical predictions

The results are compared both to fixed-order NLO and NNLO calculations, obtained with parton-level MC generators (DIPHOX+GAMMA2MC and 2γ NNLO), and to the generated-particle-level di-photon spectra predicted by leading-order (LO) parton-shower MC generators used in the ATLAS full simulation (PYTHIA and SHERPA). The contribution from the particle recently discovered by ATLAS and CMS in the search for the Standard Model Higgs boson is not included in the predictions: it is expected to be around 1% of the signal in the $120 < m_{\gamma\gamma} < 130 \text{ GeV}$ interval, and negligible elsewhere. The contribution from multiple parton interactions is also neglected: measurements by DØ [32] and ATLAS⁵ show that events with two jets (in γ +jets or W+jets) have a contamination between 5% and 10% from double parton interactions. In our data sample, the fraction of selected di-photon candidates with at least two additional jets not overlapping with the photons and not from pile-up is around 8%, thus the overall contribution to the signal from multiple parton interactions is estimated to be lower than 1%.

The main differences between the four predictions are the following:

- 2γ NNLO provides a NNLO calculation of the direct part of the di-photon production cross section, but neglects completely the contribution from the fragmentation component, where one or both photons are produced in the soft collinear fragmentation of coloured partons.
- DIPHOX provides a NLO calculation of both the direct and the fragmentation parts of the di-photon production cross section. It also includes the contribution from the box diagram ($gg \rightarrow \gamma\gamma$), which is in principle a term of the NNLO expansion in the strong coupling constant α_s , but — due to the large gluon luminosity at the LHC [33] — gives a contribution comparable to that of the LO terms. For these reasons, higher-order contributions to the box diagrams, technically at NNNLO but of size similar to that of NLO terms, are also included in our calculation by using GAMMA2MC.
- PYTHIA provides LO matrix elements for di-photon production and models the higher-order terms through γ -jet and di-jet production in combination with initial-state and/or final-state radiation. It also features parton showering and an underlying event model;

⁵Article in preparation.

- SHERPA has features similar to those of PYTHIA, and in addition includes the di-photon higher-order real-emission matrix elements. For this study, up to two additional QCD partons are generated.

The nominal factorization (μ_F), renormalization (μ_R), and — in the case of DIPHOX and GAMMA2MC — fragmentation (μ_f) scales are set in all cases to the di-photon invariant mass, $m_{\gamma\gamma}$. Different PDF sets are used by each program: CT10 NLO [34] for DIPHOX and GAMMA2MC, MSTW2008 NNLO [35] for 2γ NNLO, CTEQ6L1 for SHERPA and MRST2007 LO* for PYTHIA. The theoretical uncertainty error bands for PYTHIA and SHERPA include only statistical uncertainties. The theory uncertainty error bands for the NLO and NNLO predictions include in addition PDF and scale uncertainties. PDF uncertainties are estimated by varying each of the eigenvalues of the PDFs by $\pm 1\sigma$ and summing in quadrature separately positive and negative variations of the cross section. For DIPHOX and GAMMA2MC, scale uncertainties are evaluated by varying each scale to $m_{\gamma\gamma}/2$ and $2m_{\gamma\gamma}$, and the envelope of all variations is taken as a systematic error; the final uncertainty is dominated by the configurations in which the scales are varied incoherently. For 2γ NNLO, the scale uncertainty is evaluated by considering the variation of the predicted cross sections in the two cases $\mu_R = m_{\gamma\gamma}/2, \mu_F = 2m_{\gamma\gamma}$ and $\mu_R = 2m_{\gamma\gamma}, \mu_F = m_{\gamma\gamma}/2$.

Fixed-order predictions calculated at parton level do not include underlying event, pile-up or hadronization effects. While the ambient-energy density corrections to the photon isolation are expected to remove most of these effects from the photon isolation energy, it is not guaranteed that they correct the experimental isolation back to exactly the parton-level isolation computed from the elementary-process partons. To estimate these residual effects, PYTHIA and SHERPA di-photon samples are used to evaluate the ratio of generator-level cross sections with and without hadronization and the underlying event, and subsequently, the parton-level cross sections are multiplied bin-by-bin by this ratio. The central value of the envelope of the PYTHIA and SHERPA distributions is taken as the nominal correction and half of the difference between PYTHIA and SHERPA as the systematic uncertainty. The typical correction factor is around 0.95.

Both PYTHIA and SHERPA are expected to underestimate the total cross section, because of the missing NLO (and higher-order) contributions. At low $p_{T,\gamma\gamma}$ and for $\Delta\phi_{\gamma\gamma}$ near π where multiple soft gluon emission is important, PYTHIA and SHERPA are expected to better describe the shape of the differential distributions, thanks to the effective all-order resummation of the leading logs performed by the parton shower. On the other hand, in the same regions fixed-order calculations are expected to exhibit infrared divergences. Finally, 2γ NNLO is expected to underestimate the data in regions populated by the contribution from fragmentation (low $\Delta\phi_{\gamma\gamma}$ and $m_{\gamma\gamma}$, and $\cos\theta_{\gamma\gamma}^* \approx 1$).

The total cross section estimated by PYTHIA and SHERPA with the ATLAS simulation settings is 36 pb, and underestimates the measured cross section by 20%. The DIPHOX+GAMMA2MC total cross section is 39_{-6}^{+7} pb and the 2γ NNLO total cross section is 44_{-5}^{+6} pb, where the uncertainty is dominated by the choice of the nominal scales.

The comparisons between the experimental cross sections and the predictions by PYTHIA and SHERPA are shown in figure 4. In order to compare the shapes of the MC

differential distributions to the data, their cross sections are rescaled by a factor 1.2 to match the total cross section measured in data. PYTHIA misses higher order contributions, as clearly seen for low values of $\Delta\phi_{\gamma\gamma}$, but this is compensated by the parton shower for $\Delta\phi_{\gamma\gamma}$ near π and at low $p_{T,\gamma\gamma}$. It is worth noting that the shoulder expected (and observed) in the $p_{T,\gamma\gamma}$ cross section around the sum of the E_T thresholds of the two photons [36] is almost absent in PYTHIA, while SHERPA correctly reproduces the data in this region. This is interpreted as being due to the additional NLO contributions in SHERPA combined with differences in the parton showers. Overall, SHERPA reproduces the data rather well, except at large $m_{\gamma\gamma}$ and large $|\cos\theta_{\gamma\gamma}^*|$.

The comparisons between the data cross sections and the predictions by 2γ NNLO and DIPHOX+GAMMA2MC are shown in figure 5. In the $\Delta\phi_{\gamma\gamma} \simeq \pi$, low $p_{T,\gamma\gamma}$ region, DIPHOX+GAMMA2MC fails to match the data. This is expected because initial-state soft gluon radiation is divergent at NLO, without soft gluon resummation. Everywhere else DIPHOX+GAMMA2MC is missing NNLO contributions and clearly underestimates the data.

With higher order calculations included, 2γ NNLO is very close to the data within the uncertainties. However, the excess at $\Delta\phi_{\gamma\gamma} \simeq \pi$ and low $p_{T,\gamma\gamma}$ is still present, as expected for a fixed-order calculation. Since the fragmentation component is not calculated in 2γ NNLO, the data is slightly underestimated by 2γ NNLO in the regions where this component is larger: at low $\Delta\phi_{\gamma\gamma}$, low mass, intermediate $p_{T,\gamma\gamma}$ (between 20 GeV and 150 GeV) and large $|\cos\theta_{\gamma\gamma}^*|$.

8 Conclusion

A measurement of the production cross section of isolated-photon pairs in pp collisions at a centre-of-mass energy $\sqrt{s} = 7$ TeV is presented. The measurement uses an integrated luminosity of 4.9 fb^{-1} collected by the ATLAS detector at the LHC in 2011. The two photons are required to be isolated in the calorimeters, to be in the acceptance of the electromagnetic calorimeter ($|\eta| < 2.37$ with the exclusion of the barrel-endcap transition region $1.37 < |\eta| < 1.52$) and to have an angular separation $\Delta R > 0.4$ in the η, ϕ plane. Both photons have transverse energies $E_T > 22$ GeV, and at least one of them has $E_T > 25$ GeV.

The total cross section within the acceptance is $44.0^{+3.2}_{-4.2}$ pb. It is underestimated by SHERPA and PYTHIA, which both predict a value of 36 pb with the current ATLAS simulation tune. The central value of the cross section predicted by DIPHOX+GAMMA2MC, 39 pb, is lower than the data but it is consistent with data within the theoretical ($^{+7}_{-6}$ pb) and experimental errors. The NNLO calculation of 2γ NNLO ($\sigma_{\text{NNLO}} = 44^{+6}_{-5}$ pb) is in excellent agreement with the data.

The differential cross sections, as a function of the di-photon invariant mass, transverse momentum, azimuthal separation and of the cosine of the polar angle of the photon with largest transverse energy in the Collins-Soper di-photon rest frame, are also measured. Rather good agreement is found with Monte Carlo generators, after rescaling the PYTHIA and SHERPA distributions by a factor 1.2 in order to match the integrated cross section measured in data and fixed-order calculations, in the regions of phase space studied. All generators tend to underestimate the data at large $|\cos\theta_{\gamma\gamma}^*|$. SHERPA performs rather

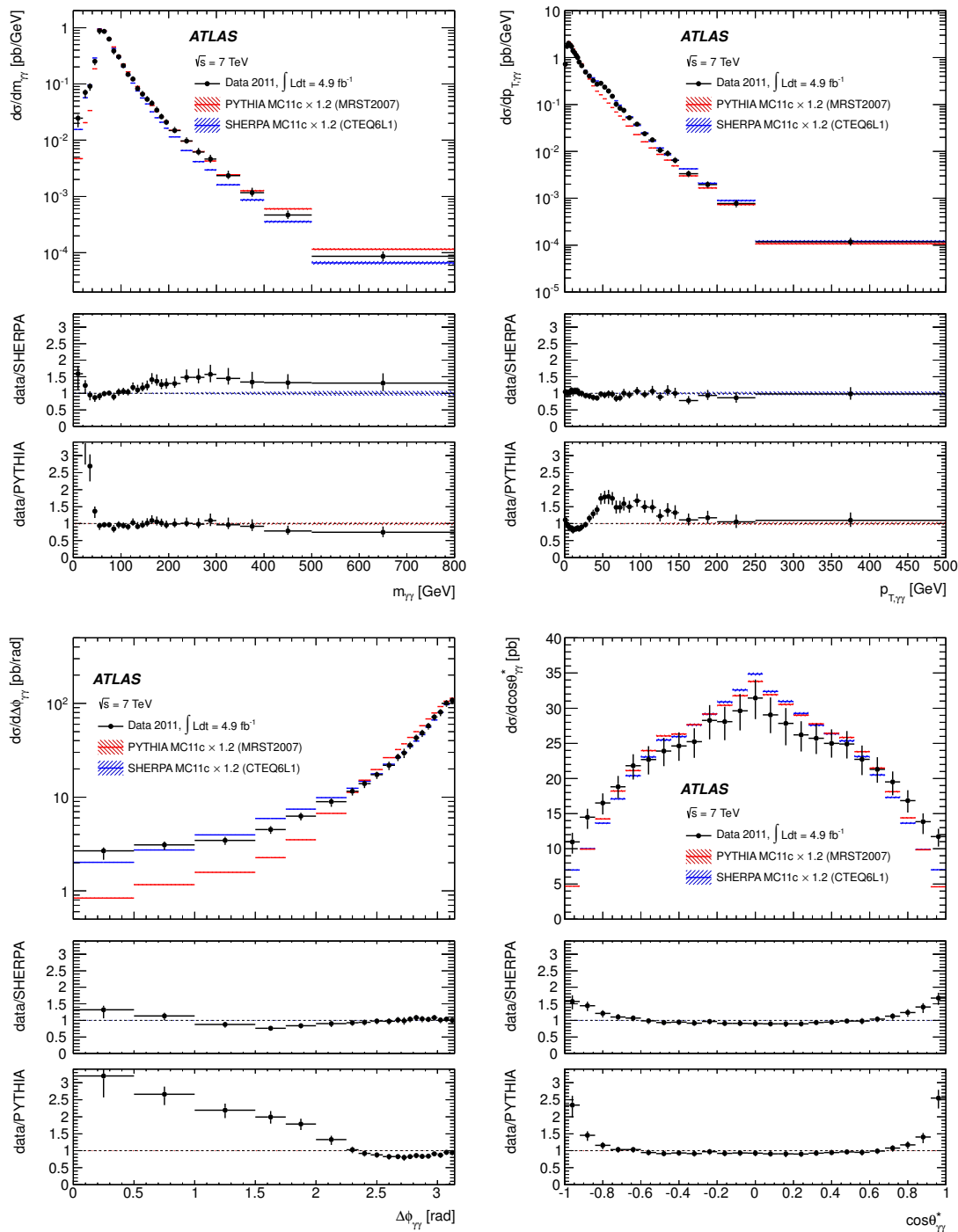


Figure 4. Comparison between the experimental cross sections and the predictions obtained with parton-shower LO simulations: $m_{\gamma\gamma}$ (top left), $p_{T,\gamma\gamma}$ (top right), $\Delta\phi_{\gamma\gamma}$ (bottom left), $\cos\theta_{\gamma\gamma}^*$ (bottom right). The LO cross sections have been scaled to the total data cross section, by a factor 1.2. Black dots correspond to data with error bars for their total uncertainties, which are dominated by the systematic component. The simulated cross sections include only statistical uncertainties.

well for most differential spectra, except for high $m_{\gamma\gamma}$. PYTHIA is missing higher order contributions, but this is compensated by the parton shower for $\Delta\phi_{\gamma\gamma}$ near π and at low $p_{T,\gamma\gamma}$. In these same regions the fixed-order calculations do not reproduce the data, due to the known infrared divergences from initial-state soft gluon radiation. Everywhere else DIPHOX+GAMMA2MC is missing NNLO contributions and clearly underestimates the data. On the other hand, with inclusion of NNLO terms, 2γ NNLO is able to match the data very closely within the uncertainties, except in limited regions where the fragmentation component — neglected in the 2γ NNLO calculation — is still significant after the photon isolation requirement.

Acknowledgments

We thank the 2γ NNLO authors for providing theoretical predictions of the NNLO di-photon cross section based on their code. We thank Leandro Cieri, Stefano Catani, Daniel De Florian, Michel Fontannaz, Jean-Philippe Guillet, Eric Pilon and Carl Schmidt, for fruitful discussions on the theoretical calculations and their uncertainties.

We thank CERN for the very successful operation of the LHC, as well as the support staff from our institutions without whom ATLAS could not be operated efficiently.

We acknowledge the support of ANPCyT, Argentina; YerPhI, Armenia; ARC, Australia; BMWF and FWF, Austria; ANAS, Azerbaijan; SSTC, Belarus; CNPq and FAPESP, Brazil; NSERC, NRC and CFI, Canada; CERN; CONICYT, Chile; CAS, MOST and NSFC, China; COLCIENCIAS, Colombia; MSMT CR, MPO CR and VSC CR, Czech Republic; DNRF, DNSRC and Lundbeck Foundation, Denmark; EPLANET, ERC and NSRF, European Union; IN2P3-CNRS, CEA-DSM/IRFU, France; GNSF, Georgia; BMBF, DFG, HGF, MPG and AvH Foundation, Germany; GSRT and NSRF, Greece; ISF, MINERVA, GIF, DIP and Benoziyo Center, Israel; INFN, Italy; MEXT and JSPS, Japan; CNRST, Morocco; FOM and NWO, Netherlands; BRF and RCN, Norway; MNiSW, Poland; GRICES and FCT, Portugal; MERYS (MECTS), Romania; MES of Russia and ROSATOM, Russian Federation; JINR; MSTB, Serbia; MSSR, Slovakia; ARRS and MVZT, Slovenia; DST/NRF, South Africa; MICINN, Spain; SRC and Wallenberg Foundation, Sweden; SER, SNSF and Cantons of Bern and Geneva, Switzerland; NSC, Taiwan; TAEK, Turkey; STFC, the Royal Society and Leverhulme Trust, United Kingdom; DOE and NSF, United States of America.

The crucial computing support from all WLCG partners is acknowledged gratefully, in particular from CERN and the ATLAS Tier-1 facilities at TRIUMF (Canada), NDGF (Denmark, Norway, Sweden), CC-IN2P3 (France), KIT/GridKA (Germany), INFN-CNAF (Italy), NL-T1 (Netherlands), PIC (Spain), ASGC (Taiwan), RAL (UK) and BNL (USA) and in the Tier-2 facilities worldwide.

A Experimental differential cross section

The numerical values of the differential cross sections displayed in figures 4 and 5 are quoted in tables 2–5. For each bin of the $m_{\gamma\gamma}$, $p_{T,\gamma\gamma}$, $\Delta\phi_{\gamma\gamma}$, and $\cos\theta_{\gamma\gamma}^*$ variables, the

cross section is given together with its statistical, systematic and total uncertainties. All values are divided by the bin width.

$m_{\gamma\gamma}$ [GeV]	$d\sigma/dm_{\gamma\gamma}$ [pb/GeV]	Statistical error		Systematic errors		Total error	
		high	low	high	low	high	low
[0, 20)	0.0247	+0.0015	-0.0015	+0.0032	-0.0076	+0.0036	-0.0077
[20, 30)	0.0704	+0.0032	-0.0032	+0.0087	-0.0140	+0.0093	-0.0144
[30, 40)	0.091	+0.004	-0.004	+0.011	-0.015	+0.012	-0.015
[40, 50)	0.252	+0.006	-0.006	+0.025	-0.037	+0.026	-0.037
[50, 60)	0.880	+0.012	-0.012	+0.073	-0.120	+0.074	-0.120
[60, 70)	0.857	+0.010	-0.010	+0.071	-0.068	+0.071	-0.068
[70, 80)	0.626	+0.008	-0.008	+0.051	-0.052	+0.051	-0.053
[80, 90)	0.384	+0.008	-0.008	+0.049	-0.048	+0.050	-0.049
[90, 100)	0.305	+0.006	-0.006	+0.031	-0.034	+0.032	-0.035
[100, 110)	0.212	+0.004	-0.004	+0.021	-0.021	+0.021	-0.021
[110, 120)	0.148	+0.004	-0.004	+0.015	-0.014	+0.015	-0.015
[120, 130)	0.122	+0.003	-0.003	+0.015	-0.010	+0.015	-0.011
[130, 140)	0.0829	+0.0025	-0.0025	+0.0112	-0.0073	+0.0115	-0.0077
[140, 150)	0.0656	+0.0022	-0.0022	+0.0088	-0.0057	+0.0091	-0.0061
[150, 160)	0.0535	+0.0019	-0.0019	+0.0072	-0.0051	+0.0075	-0.0054
[160, 170)	0.0451	+0.0017	-0.0017	+0.0063	-0.0038	+0.0065	-0.0042
[170, 180)	0.0343	+0.0015	-0.0015	+0.0050	-0.0031	+0.0052	-0.0035
[180, 190)	0.0262	+0.0013	-0.0013	+0.0032	-0.0024	+0.0035	-0.0027
[190, 200)	0.0209	+0.0011	-0.0011	+0.0025	-0.0019	+0.0028	-0.0022
[200, 225)	0.0149	+0.0006	-0.0006	+0.0023	-0.0014	+0.0024	-0.0015
[225, 250)	0.00970	+0.00049	-0.00049	+0.00150	-0.00086	+0.00158	-0.00099
[250, 275)	0.00616	+0.00039	-0.00039	+0.00104	-0.00064	+0.00111	-0.00075
[275, 300)	0.00464	+0.00036	-0.00036	+0.00080	-0.00059	+0.00087	-0.00069
[300, 350)	0.00235	+0.00017	-0.00017	+0.00048	-0.00026	+0.00051	-0.00031
[350, 400)	0.00116	+0.00011	-0.00011	+0.00024	-0.00013	+0.00026	-0.00017
[400, 500)	4.69e-04	+5.0e-05	-5.0e-05	+7.9e-05	-4.7e-05	+9.3e-05	-6.9e-05
[500, 800)	8.6e-05	+1.3e-05	-1.3e-05	+1.5e-05	-1.0e-05	+1.9e-05	-1.6e-05

Table 2. Experimental cross-section values per bin in pb/GeV for $m_{\gamma\gamma}$. The listed total errors are the quadratic sum of statistical and systematic uncertainties.

$p_{T,\gamma\gamma}$ [GeV]	$d\sigma/dp_{T,\gamma\gamma}$ [pb/GeV]	Statistical error		Systematic errors		Total error	
		high	low	high	low	high	low
[0, 2)	0.727	+0.022	-0.022	+0.057	-0.092	+0.061	-0.094
[2, 4)	1.75	+0.04	-0.04	+0.13	-0.23	+0.13	-0.23
[4, 6)	2.03	+0.04	-0.04	+0.15	-0.23	+0.15	-0.23
[6, 8)	1.88	+0.04	-0.04	+0.15	-0.21	+0.16	-0.21
[8, 10)	1.72	+0.03	-0.03	+0.13	-0.19	+0.14	-0.19
[10, 12)	1.40	+0.03	-0.03	+0.12	-0.16	+0.12	-0.16
[12, 14)	1.28	+0.03	-0.03	+0.10	-0.13	+0.11	-0.13
[14, 16)	1.122	+0.026	-0.026	+0.093	-0.114	+0.097	-0.117
[16, 18)	0.999	+0.024	-0.024	+0.086	-0.090	+0.090	-0.093
[18, 20)	0.810	+0.021	-0.021	+0.072	-0.076	+0.075	-0.079
[20, 25)	0.674	+0.012	-0.012	+0.056	-0.074	+0.058	-0.075
[25, 30)	0.492	+0.011	-0.011	+0.041	-0.045	+0.043	-0.047
[30, 35)	0.405	+0.009	-0.009	+0.034	-0.043	+0.035	-0.044
[35, 40)	0.325	+0.009	-0.009	+0.028	-0.034	+0.030	-0.035
[40, 45)	0.272	+0.008	-0.008	+0.024	-0.027	+0.026	-0.028
[45, 50)	0.282	+0.008	-0.008	+0.023	-0.027	+0.024	-0.028
[50, 55)	0.235	+0.007	-0.007	+0.023	-0.025	+0.025	-0.026
[55, 60)	0.194	+0.006	-0.006	+0.019	-0.024	+0.021	-0.024
[60, 65)	0.150	+0.006	-0.006	+0.015	-0.016	+0.016	-0.017
[65, 70)	0.102	+0.005	-0.005	+0.013	-0.012	+0.014	-0.013
[70, 75)	0.0836	+0.0041	-0.0041	+0.0103	-0.0087	+0.0111	-0.0096
[75, 80)	0.0748	+0.0036	-0.0036	+0.0087	-0.0086	+0.0094	-0.0093
[80, 90)	0.0521	+0.0021	-0.0021	+0.0059	-0.0056	+0.0063	-0.0059
[90, 100)	0.0381	+0.0017	-0.0017	+0.0043	-0.0036	+0.0047	-0.0040
[100, 110)	0.0239	+0.0013	-0.0013	+0.0028	-0.0023	+0.0031	-0.0026
[110, 120)	0.0175	+0.0011	-0.0011	+0.0024	-0.0016	+0.0027	-0.0019
[120, 130)	0.0106	+0.0009	-0.0009	+0.0015	-0.0011	+0.0017	-0.0014
[130, 140)	0.0090	+0.0008	-0.0008	+0.0012	-0.0008	+0.0015	-0.0012
[140, 150)	0.00646	+0.00064	-0.00064	+0.00089	-0.00063	+0.00110	-0.00090
[150, 175)	0.00333	+0.00031	-0.00031	+0.00047	-0.00039	+0.00056	-0.00049
[175, 200)	0.00195	+0.00023	-0.00023	+0.00025	-0.00017	+0.00034	-0.00028
[200, 250)	0.00077	+0.00010	-0.00010	+0.00012	-0.00008	+0.00016	-0.00013
[250, 500)	1.18e-04	+1.7e-05	-1.7e-05	+1.8e-05	-1.2e-05	+2.5e-05	-2.1e-05

Table 3. Experimental cross-section values per bin in pb/GeV for $p_{T,\gamma\gamma}$. The listed total errors are the quadratic sum of statistical and systematic uncertainties.

$\Delta\phi_{\gamma\gamma}$ [rad]	$d\sigma/d\Delta\phi_{\gamma\gamma}$ [pb/rad]	Statistical error		Systematic errors		Total error	
		high	low	high	low	high	low
[0.00, 0.50)	2.68	+0.08	-0.08	+0.22	-0.52	+0.24	-0.52
[0.50, 1.00)	3.10	+0.09	-0.09	+0.25	-0.36	+0.26	-0.37
[1.00, 1.50)	3.46	+0.09	-0.09	+0.29	-0.36	+0.31	-0.37
[1.50, 1.75)	4.51	+0.15	-0.15	+0.36	-0.42	+0.39	-0.44
[1.75, 2.00)	6.26	+0.17	-0.17	+0.53	-0.59	+0.55	-0.61
[2.00, 2.25)	8.93	+0.20	-0.20	+0.73	-1.02	+0.76	-1.04
[2.25, 2.35)	11.6	+0.4	-0.4	+0.9	-1.1	+1.0	-1.2
[2.35, 2.45)	13.9	+0.4	-0.4	+1.1	-1.3	+1.1	-1.4
[2.45, 2.55)	17.4	+0.4	-0.4	+1.3	-1.6	+1.4	-1.7
[2.55, 2.65)	21.8	+0.5	-0.5	+2.0	-2.2	+2.0	-2.3
[2.65, 2.70)	26.7	+0.8	-0.8	+2.1	-2.4	+2.3	-2.5
[2.70, 2.75)	29.6	+0.8	-0.8	+3.2	-3.4	+3.3	-3.5
[2.75, 2.80)	35.8	+0.9	-0.9	+2.8	-3.1	+3.0	-3.3
[2.80, 2.85)	42.9	+1.0	-1.0	+3.3	-3.8	+3.4	-3.9
[2.85, 2.90)	48.4	+1.1	-1.1	+3.8	-4.4	+3.9	-4.6
[2.90, 2.95)	57.4	+1.2	-1.2	+4.3	-4.6	+4.4	-4.7
[2.95, 3.00)	71.7	+1.3	-1.3	+5.4	-5.9	+5.6	-6.1
[3.00, 3.05)	80.8	+1.4	-1.4	+6.1	-7.4	+6.3	-7.6
[3.05, 3.10)	100.5	+1.6	-1.6	+7.3	-8.5	+7.4	-8.6
[3.10, 3.14)	107.6	+1.8	-1.8	+7.9	-9.6	+8.1	-9.8

Table 4. Experimental cross-section values per bin in pb/rad for $\Delta\phi_{\gamma\gamma}$. The listed total errors are the quadratic sum of statistical and systematic uncertainties.

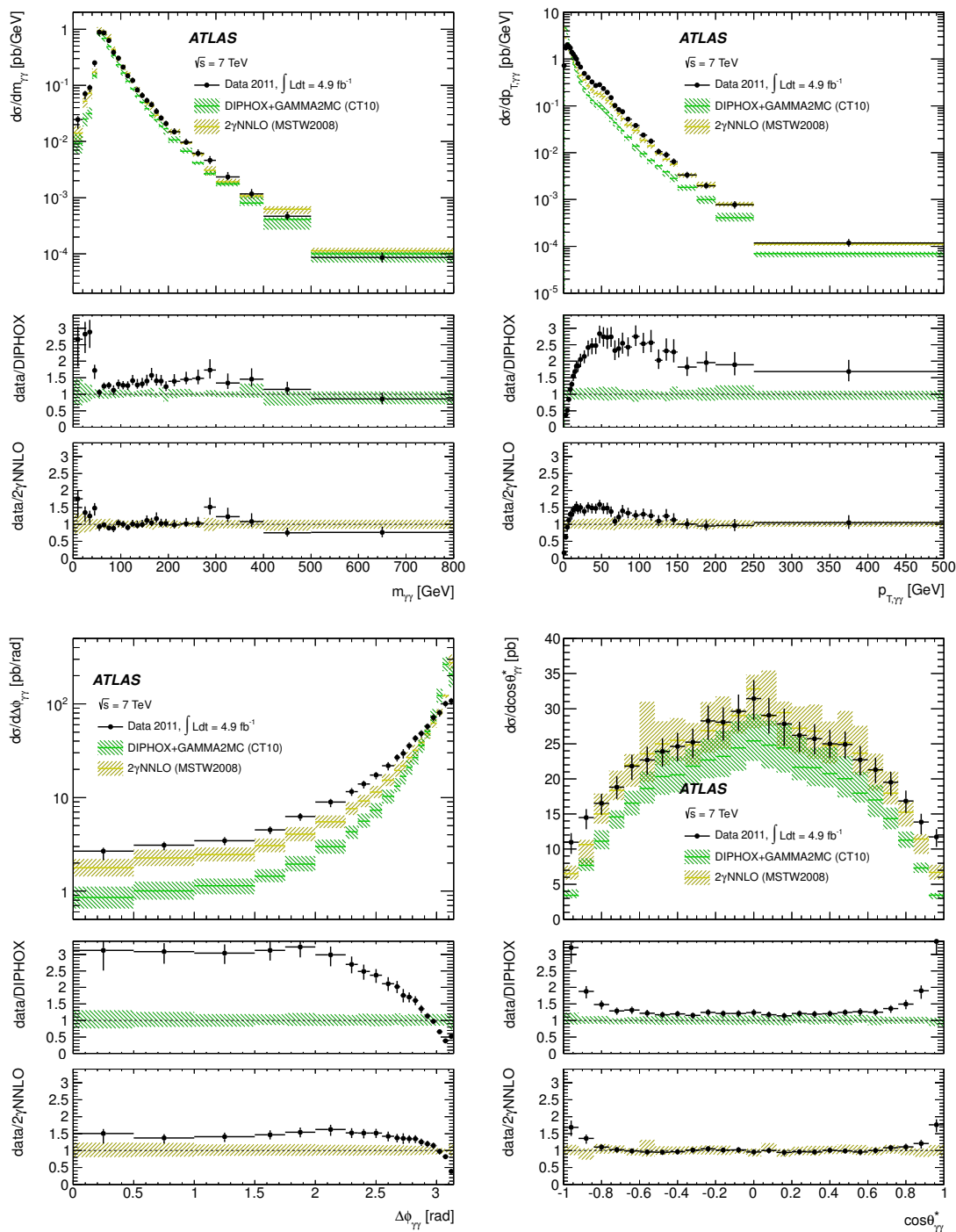


Figure 5. Comparison between the experimental cross sections and the predictions obtained with DIPHOX+GAMMA2MC (NLO) and 2γ NNLO (NNLO): $m_{\gamma\gamma}$ (top left), $p_{T,\gamma\gamma}$ (top right), $\Delta\phi_{\gamma\gamma}$ (bottom left), $\cos\theta_{\gamma\gamma}^*$ (bottom right). Black dots correspond to data with error bars for their total uncertainties, which are dominated by the systematic component. The theoretical uncertainties include contributions from the limited size of the simulated sample, from the scale choice and from uncertainties on the parton distribution functions and on the hadronization and underlying event corrections.

$\cos \theta_{\gamma\gamma}^*$	$d\sigma/d\cos \theta_{\gamma\gamma}^*$ [pb]	Statistical error		Systematic errors		Total error	
		high	low	high	low	high	low
[-1.00, -0.92)	11.0	+0.4	-0.4	+1.2	-1.6	+1.3	-1.7
[-0.92, -0.84)	14.5	+0.4	-0.4	+1.1	-1.6	+1.2	-1.6
[-0.84, -0.76)	16.5	+0.5	-0.5	+1.3	-1.6	+1.4	-1.6
[-0.76, -0.68)	18.8	+0.5	-0.5	+1.4	-1.6	+1.5	-1.7
[-0.68, -0.60)	21.8	+0.6	-0.6	+1.5	-1.9	+1.6	-1.9
[-0.60, -0.52)	22.7	+0.6	-0.6	+1.8	-2.0	+1.9	-2.1
[-0.52, -0.44)	23.9	+0.6	-0.6	+1.8	-2.1	+1.9	-2.1
[-0.44, -0.36)	24.6	+0.6	-0.6	+1.8	-2.0	+1.9	-2.1
[-0.36, -0.28)	25.2	+0.6	-0.6	+1.8	-2.2	+1.9	-2.3
[-0.28, -0.20)	28.3	+0.6	-0.6	+2.1	-2.6	+2.2	-2.7
[-0.20, -0.12)	28.1	+0.7	-0.7	+2.0	-2.6	+2.1	-2.6
[-0.12, -0.04)	29.6	+0.7	-0.7	+2.3	-2.7	+2.4	-2.8
[-0.04, 0.04)	31.4	+0.7	-0.7	+2.5	-2.9	+2.6	-3.0
[0.04, 0.12)	29.0	+0.7	-0.7	+2.4	-2.5	+2.5	-2.6
[0.12, 0.20)	27.8	+0.7	-0.7	+2.1	-3.0	+2.2	-3.1
[0.20, 0.28)	26.2	+0.6	-0.6	+1.8	-2.3	+2.0	-2.3
[0.28, 0.36)	25.7	+0.6	-0.6	+2.0	-2.1	+2.1	-2.2
[0.36, 0.44)	25.0	+0.6	-0.6	+1.9	-1.9	+2.0	-2.0
[0.44, 0.52)	24.9	+0.6	-0.6	+1.7	-2.0	+1.8	-2.1
[0.52, 0.60)	22.7	+0.6	-0.6	+1.9	-2.2	+2.0	-2.2
[0.60, 0.68)	21.3	+0.6	-0.6	+1.6	-1.8	+1.7	-1.9
[0.68, 0.76)	19.5	+0.5	-0.5	+1.4	-1.8	+1.5	-1.9
[0.76, 0.84)	16.9	+0.5	-0.5	+1.4	-1.6	+1.5	-1.7
[0.84, 0.92)	13.9	+0.4	-0.4	+1.1	-1.7	+1.2	-1.8
[0.92, 1.00)	11.7	+0.4	-0.4	+1.0	-1.4	+1.1	-1.4

Table 5. Experimental cross-section values per bin in pb for $\cos \theta_{\gamma\gamma}^*$. The listed total errors are the quadratic sum of statistical and systematic uncertainties.

Open Access. This article is distributed under the terms of the Creative Commons Attribution License which permits any use, distribution and reproduction in any medium, provided the original author(s) and source are credited.

References

- [1] L. Randall and R. Sundrum, *A Large mass hierarchy from a small extra dimension*, *Phys. Rev. Lett.* **83** (1999) 3370 [[hep-ph/9905221](#)] [[INSPIRE](#)].
- [2] N. Arkani-Hamed, S. Dimopoulos and G. Dvali, *The hierarchy problem and new dimensions at a millimeter*, *Phys. Lett. B* **429** (1998) 263 [[hep-ph/9803315](#)] [[INSPIRE](#)].
- [3] D0 collaboration, V. Abazov et al., *Measurement of direct photon pair production cross sections in $p\bar{p}$ collisions at $\sqrt{s} = 1.96$ TeV*, *Phys. Lett. B* **690** (2010) 108 [[arXiv:1002.4917](#)] [[INSPIRE](#)].
- [4] CDF collaboration, T. Aaltonen et al., *Measurement of the cross section for prompt isolated diphoton production in $p\bar{p}$ collisions at $\sqrt{s} = 1.96$ TeV*, *Phys. Rev. D* **84** (2011) 052006 [[arXiv:1106.5131](#)] [[INSPIRE](#)].
- [5] ATLAS collaboration, *Measurement of the isolated di-photon cross-section in pp collisions at $\sqrt{s} = 7$ TeV with the ATLAS detector*, *Phys. Rev. D* **85** (2012) 012003 [[arXiv:1107.0581](#)] [[INSPIRE](#)].
- [6] CMS collaboration, *Measurement of the production cross section for pairs of isolated photons in pp collisions at $\sqrt{s} = 7$ TeV*, *JHEP* **01** (2012) 133 [[arXiv:1110.6461](#)] [[INSPIRE](#)].
- [7] ATLAS collaboration, *Luminosity determination in pp collisions at $\sqrt{s} = 7$ TeV using the ATLAS detector at the LHC*, *Eur. Phys. J. C* **71** (2011) 1630 [[arXiv:1101.2185](#)] [[INSPIRE](#)].
- [8] ATLAS collaboration, *Luminosity determination in pp collisions at $\sqrt{s} = 7$ TeV using the ATLAS detector in 2011*, *ATLAS-CONF-2011-116* (2011).
- [9] J.C. Collins and D.E. Soper, *Angular distribution of dileptons in high-energy hadron collisions*, *Phys. Rev. D* **16** (1977) 2219 [[INSPIRE](#)].
- [10] T. Sjöstrand et al., *High-energy physics event generation with PYTHIA 6.1*, *Comput. Phys. Commun.* **135** (2001) 238 [[hep-ph/0010017](#)] [[INSPIRE](#)].
- [11] T. Gleisberg et al., *Event generation with SHERPA 1.1*, *JHEP* **02** (2009) 007 [[arXiv:0811.4622](#)] [[INSPIRE](#)].
- [12] T. Binoth, J. Guillet, E. Pilon and M. Werlen, *A full next-to-leading order study of direct photon pair production in hadronic collisions*, *Eur. Phys. J. C* **16** (2000) 311 [[hep-ph/9911340](#)] [[INSPIRE](#)].
- [13] Z. Bern, L.J. Dixon and C. Schmidt, *Isolating a light Higgs boson from the diphoton background at the CERN LHC*, *Phys. Rev. D* **66** (2002) 074018 [[hep-ph/0206194](#)] [[INSPIRE](#)].
- [14] S. Catani, L. Cieri, D. de Florian, G. Ferrera and M. Grazzini, *Diphoton production at hadron colliders: a fully-differential QCD calculation at NNLO*, *Phys. Rev. Lett.* **108** (2012) 072001 [[arXiv:1110.2375](#)] [[INSPIRE](#)].
- [15] ATLAS collaboration, *Observation of a new particle in the search for the standard model Higgs boson with the ATLAS detector at the LHC*, *Phys. Lett. B* **716** (2012) 1 [[arXiv:1207.7214](#)] [[INSPIRE](#)].

- [16] CMS collaboration, *Observation of a new boson at a mass of 125 GeV with the CMS experiment at the LHC*, *Phys. Lett. B* **716** (2012) 30 [[arXiv:1207.7235](#)] [[INSPIRE](#)].
- [17] ATLAS collaboration, *The ATLAS Experiment at the CERN Large Hadron Collider*, 2008 *JINST* **3** S08003 [[INSPIRE](#)].
- [18] GEANT4 collaboration, S. Agostinelli et al., *GEANT4: a simulation toolkit*, *Nucl. Instrum. Meth. A* **506** (2003) 250 [[INSPIRE](#)].
- [19] ATLAS collaboration, *The ATLAS simulation Infrastructure*, *Eur. Phys. J. C* **70** (2010) 823 [[arXiv:1005.4568](#)] [[INSPIRE](#)].
- [20] A. Sherstnev and R. Thorne, *Parton distributions for LO generators*, *Eur. Phys. J. C* **55** (2008) 553 [[arXiv:0711.2473](#)] [[INSPIRE](#)].
- [21] J. Pumplin et al., *New generation of parton distributions with uncertainties from global QCD analysis*, *JHEP* **07** (2002) 012 [[hep-ph/0201195](#)] [[INSPIRE](#)].
- [22] ATLAS collaboration, *ATLAS tunes of PYTHIA 6 and PYTHIA 8 for MC11*, [ATL-PHYS-PUB-2011-009](#) (2011).
- [23] M.L. Mangano, M. Moretti, F. Piccinini, R. Pittau and A.D. Polosa, *ALPGEN, a generator for hard multiparton processes in hadronic collisions*, *JHEP* **07** (2003) 001 [[hep-ph/0206293](#)] [[INSPIRE](#)].
- [24] ATLAS collaboration, *Measurement of the inclusive isolated prompt photon cross section in pp collisions at $\sqrt{s} = 7$ TeV with the ATLAS detector*, *Phys. Rev. D* **83** (2011) 052005 [[arXiv:1012.4389](#)] [[INSPIRE](#)].
- [25] ATLAS collaboration, *Electron performance measurements with the ATLAS detector using the 2010 LHC proton-proton collision data*, *Eur. Phys. J. C* **72** (2012) 1909 [[arXiv:1110.3174](#)] [[INSPIRE](#)].
- [26] M. Cacciari, G.P. Salam and G. Soyez, *The catchment area of jets*, *JHEP* **04** (2008) 005 [[arXiv:0802.1188](#)] [[INSPIRE](#)].
- [27] M. Cacciari, G.P. Salam and S. Sapeta, *On the characterisation of the underlying event*, *JHEP* **04** (2010) 065 [[arXiv:0912.4926](#)] [[INSPIRE](#)].
- [28] ATLAS collaboration, *Measurements of the photon identification efficiency with the ATLAS detector using 4.9 fb⁻¹ of pp collision data collected in 2011*, [ATLAS-CONF-2012-123](#) (2012).
- [29] G. D'Agostini, *A multidimensional unfolding method based on Bayes' theorem*, *Nucl. Instrum. Meth. A* **362** (1995) 487 [[INSPIRE](#)].
- [30] S. Schmitt, *TUnfold: an algorithm for correcting migration effects in high energy physics*, 2012 *JINST* **7** T10003 [[arXiv:1205.6201](#)] [[INSPIRE](#)].
- [31] ATLAS collaboration, *Performance of the ATLAS trigger system in 2010*, *Eur. Phys. J. C* **72** (2012) 1849 [[arXiv:1110.1530](#)] [[INSPIRE](#)].
- [32] D0 collaboration, V.M. Abazov et al., *Azimuthal decorrelations and multiple parton interactions in photon+2 jet and photon+3 jet events in p \bar{p} collisions at $\sqrt{s} = 1.96$ TeV*, *Phys. Rev. D* **83** (2011) 052008 [[arXiv:1101.1509](#)] [[INSPIRE](#)].
- [33] L. Ametller, E. Gava, N. Paver and D. Treleani, *Role of the QCD induced gluon-gluon coupling to gauge boson pairs in the multi-TeV region*, *Phys. Rev. D* **32** (1985) 1699 [[INSPIRE](#)].

Observation of a New Particle in the Search for the Standard Model Higgs Boson with the ATLAS Detector at the LHC

The ATLAS Collaboration

This paper is dedicated to the memory of our ATLAS colleagues who did not live to see the full impact and significance of their contributions to the experiment.

Abstract

A search for the Standard Model Higgs boson in proton-proton collisions with the ATLAS detector at the LHC is presented. The datasets used correspond to integrated luminosities of approximately 4.8 fb^{-1} collected at $\sqrt{s} = 7 \text{ TeV}$ in 2011 and 5.8 fb^{-1} at $\sqrt{s} = 8 \text{ TeV}$ in 2012. Individual searches in the channels $H \rightarrow ZZ^{(*)} \rightarrow 4\ell$, $H \rightarrow \gamma\gamma$ and $H \rightarrow WW^{(*)} \rightarrow e\nu\mu\nu$ in the 8 TeV data are combined with previously published results of searches for $H \rightarrow ZZ^{(*)}$, $WW^{(*)}$, $b\bar{b}$ and $\tau^+\tau^-$ in the 7 TeV data and results from improved analyses of the $H \rightarrow ZZ^{(*)} \rightarrow 4\ell$ and $H \rightarrow \gamma\gamma$ channels in the 7 TeV data. Clear evidence for the production of a neutral boson with a measured mass of $126.0 \pm 0.4 \text{ (stat)} \pm 0.4 \text{ (sys)} \text{ GeV}$ is presented. This observation, which has a significance of 5.9 standard deviations, corresponding to a background fluctuation probability of 1.7×10^{-9} , is compatible with the production and decay of the Standard Model Higgs boson.

1. Introduction

The Standard Model (SM) of particle physics [1–4] has been tested by many experiments over the last four decades and has been shown to successfully describe high energy particle interactions. However, the mechanism that breaks electroweak symmetry in the SM has not been verified experimentally. This mechanism [5–10], which gives mass to massive elementary particles, implies the existence of a scalar particle, the SM Higgs boson. The search for the Higgs boson, the only elementary particle in the SM that has not yet been observed, is one of the highlights of the Large Hadron Collider [11] (LHC) physics programme.

Indirect limits on the SM Higgs boson mass of $m_H < 158 \text{ GeV}$ at 95% confidence level (CL) have been set using global fits to precision electroweak results [12]. Direct searches at LEP [13], the Tevatron [14–16] and the LHC [17, 18] have previously excluded, at 95% CL, a SM Higgs boson with mass below 600 GeV, apart from some mass regions between 116 GeV and 127 GeV.

Both the ATLAS and CMS Collaborations reported excesses of events in their 2011 datasets of proton-proton (pp) collisions at centre-of-mass energy $\sqrt{s} = 7 \text{ TeV}$ at the LHC, which were compatible with SM Higgs boson production and decay in the mass region 124–126 GeV, with significances of 2.9 and 3.1 standard

deviations (σ), respectively [17, 18]. The CDF and DØ experiments at the Tevatron have also recently reported a broad excess in the mass region 120–135 GeV; using the existing LHC constraints, the observed local significances for $m_H = 125 \text{ GeV}$ are 2.7σ for CDF [14], 1.1σ for DØ [15] and 2.8σ for their combination [16].

The previous ATLAS searches in $4.6\text{--}4.8 \text{ fb}^{-1}$ of data at $\sqrt{s} = 7 \text{ TeV}$ are combined here with new searches for $H \rightarrow ZZ^{(*)} \rightarrow 4\ell^1$, $H \rightarrow \gamma\gamma$ and $H \rightarrow WW^{(*)} \rightarrow e\nu\mu\nu$ in the $5.8\text{--}5.9 \text{ fb}^{-1}$ of pp collision data taken at $\sqrt{s} = 8 \text{ TeV}$ between April and June 2012.

The data were recorded with instantaneous luminosities up to $6.8 \times 10^{33} \text{ cm}^{-2}\text{s}^{-1}$; they are therefore affected by multiple pp collisions occurring in the same or neighbouring bunch crossings (pile-up). In the 7 TeV data, the average number of interactions per bunch crossing was approximately 10; the average increased to approximately 20 in the 8 TeV data. The reconstruction, identification and isolation criteria used for electrons and photons in the 8 TeV data are improved, making the $H \rightarrow ZZ^{(*)} \rightarrow 4\ell$ and $H \rightarrow \gamma\gamma$ searches more robust against the increased pile-up. These analyses were re-optimised with simulation and frozen before looking at the 8 TeV data.

¹The symbol ℓ stands for electron or muon.

In the $H \rightarrow WW^{(*)} \rightarrow \ell\nu\ell\nu$ channel, the increased pile-up deteriorates the event missing transverse momentum, E_T^{miss} , resolution, which results in significantly larger Drell-Yan background in the same-flavour final states. Since the $e\mu$ channel provides most of the sensitivity of the search, only this final state is used in the analysis of the 8 TeV data. The kinematic region in which a SM Higgs boson with a mass between 110 GeV and 140 GeV is searched for was kept blinded during the analysis optimisation, until satisfactory agreement was found between the observed and predicted numbers of events in control samples dominated by the principal backgrounds.

This Letter is organised as follows. The ATLAS detector is briefly described in Section 2. The simulation samples and the signal predictions are presented in Section 3. The analyses of the $H \rightarrow ZZ^{(*)} \rightarrow 4\ell$, $H \rightarrow \gamma\gamma$ and $H \rightarrow WW^{(*)} \rightarrow e\nu\mu\nu$ channels are described in Sections 4–6, respectively. The statistical procedure used to analyse the results is summarised in Section 7. The systematic uncertainties which are correlated between datasets and search channels are described in Section 8. The results of the combination of all channels are reported in Section 9, while Section 10 provides the conclusions.

2. The ATLAS detector

The ATLAS detector [19–21] is a multipurpose particle physics apparatus with forward-backward symmetric cylindrical geometry. The inner tracking detector (ID) consists of a silicon pixel detector, a silicon microstrip detector (SCT), and a straw-tube transition radiation tracker (TRT). The ID is surrounded by a thin superconducting solenoid which provides a 2 T magnetic field, and by high-granularity liquid-argon (LAr) sampling electromagnetic calorimetry. The electromagnetic calorimeter is divided into a central barrel (pseudorapidity² $|\eta| < 1.475$) and end-cap regions on either end of the detector ($1.375 < |\eta| < 2.5$ for the outer wheel and $2.5 < |\eta| < 3.2$ for the inner wheel). In the region matched to the ID ($|\eta| < 2.5$), it is radially segmented into three layers. The first layer has a fine segmentation

²ATLAS uses a right-handed coordinate system with its origin at the nominal interaction point (IP) in the centre of the detector, and the z -axis along the beam line. The x -axis points from the IP to the centre of the LHC ring, and the y -axis points upwards. Cylindrical coordinates (r, ϕ) are used in the transverse plane, ϕ being the azimuthal angle around the beam line. Observables labelled “transverse” are projected into the $x - y$ plane. The pseudorapidity is defined in terms of the polar angle θ as $\eta = -\ln \tan(\theta/2)$.

in η to facilitate e/γ separation from π^0 and to improve the resolution of the shower position and direction measurements. In the region $|\eta| < 1.8$, the electromagnetic calorimeter is preceded by a presampler detector to correct for upstream energy losses. An iron-scintillator/tile calorimeter gives hadronic coverage in the central rapidity range ($|\eta| < 1.7$), while a LAr hadronic end-cap calorimeter provides coverage over $1.5 < |\eta| < 3.2$. The forward regions ($3.2 < |\eta| < 4.9$) are instrumented with LAr calorimeters for both electromagnetic and hadronic measurements. The muon spectrometer (MS) surrounds the calorimeters and consists of three large air-core superconducting magnets providing a toroidal field, each with eight coils, a system of precision tracking chambers, and fast detectors for triggering. The combination of all these systems provides charged particle measurements together with efficient and precise lepton and photon measurements in the pseudorapidity range $|\eta| < 2.5$. Jets and E_T^{miss} are reconstructed using energy deposits over the full coverage of the calorimeters, $|\eta| < 4.9$.

3. Signal and background simulation samples

The SM Higgs boson production processes considered in this analysis are the dominant gluon fusion ($gg \rightarrow H$, denoted ggF), vector-boson fusion ($qq' \rightarrow qq'H$, denoted VBF) and Higgs-strahlung ($qq' \rightarrow WH, ZH$, denoted WH/ZH). The small contribution from the associated production with a $t\bar{t}$ pair ($q\bar{q}/gg \rightarrow t\bar{t}H$, denoted $t\bar{t}H$) is taken into account only in the $H \rightarrow \gamma\gamma$ analysis.

For the ggF process, the signal cross section is computed at up to next-to-next-to-leading order (NNLO) in QCD [22–28]. Next-to-leading order (NLO) electroweak (EW) corrections are applied [29, 30], as well as QCD soft-gluon re-summations at up to next-to-next-to-leading logarithm (NNLL) [31]. These calculations, which are described in Refs. [32–35], assume factorisation between QCD and EW corrections. The transverse momentum, p_T , spectrum of the Higgs boson in the ggF process follows the HqT calculation [36], which includes QCD corrections at NLO and QCD soft-gluon re-summations up to NNLL; the effects of finite quark masses are also taken into account [37].

For the VBF process, full QCD and EW corrections up to NLO [38–41] and approximate NNLO QCD corrections [42] are used to calculate the cross section. Cross sections of the associated WH/ZH processes (VH) are calculated including QCD corrections up to NNLO [43–45] and EW corrections up to NLO [46].

The cross sections for the $t\bar{t}H$ process are estimated up to NLO QCD [47–51].

The total cross sections for SM Higgs boson production at the LHC with $m_H = 125$ GeV are predicted to be 17.5 pb for $\sqrt{s} = 7$ TeV and 22.3 pb for $\sqrt{s} = 8$ TeV [52, 53].

The branching ratios of the SM Higgs boson as a function of m_H , as well as their uncertainties, are calculated using the HDECAY [54] and PROPHECY4F [55, 56] programs and are taken from Refs. [52, 53]. The interference in the $H \rightarrow ZZ^{(*)} \rightarrow 4\ell$ final states with identical leptons is taken into account [53, 55, 56].

Table 1: Event generators used to model the signal and background processes. “PYTHIA” indicates that PYTHIA6 and PYTHIA8 are used for simulations of $\sqrt{s} = 7$ TeV and $\sqrt{s} = 8$ TeV data, respectively.

Process	Generator
ggF, VBF	POWHEG [57, 58]+PYTHIA
$WH, ZH, t\bar{t}H$	PYTHIA
W +jets, Z/γ^* +jets	ALPGEN [59]+HERWIG
$t\bar{t}, tW, tb$	MC@NLO [60]+HERWIG
tqb	AcerMC [61]+PYTHIA
$q\bar{q} \rightarrow WW$	MC@NLO+HERWIG
$gg \rightarrow WW$	gg2WW [62]+HERWIG
$q\bar{q} \rightarrow ZZ$	POWHEG [63]+PYTHIA
$gg \rightarrow ZZ$	gg2ZZ [64]+HERWIG
WZ	MadGraph+PYTHIA, HERWIG
$W\gamma$ +jets	ALPGEN+HERWIG
$W\gamma^*$ [65]	MadGraph+PYTHIA
$q\bar{q}/gg \rightarrow \gamma\gamma$	SHERPA

The event generators used to model signal and background processes in samples of Monte Carlo (MC) simulated events are listed in Table 1. The normalisations of the generated samples are obtained from the state of the art calculations described above. Several different programs are used to generate the hard-scattering processes. To generate parton showers and their hadronisation, and to simulate the underlying event [66–68], PYTHIA6 [69] (for 7 TeV samples and 8 TeV samples produced with MadGraph [70, 71] or AcerMC) or PYTHIA8 [72] (for other 8 TeV samples) are used. Alternatively, HERWIG [73] or SHERPA [74] are used to generate and hadronise parton showers, with the HERWIG underlying event simulation performed using JIMMY [75]. When PYTHIA6 or HERWIG are used, TAUOLA [76] and PHOTOS [77] are employed to describe tau lepton decays and additional photon radiation from charged leptons, respectively.

The following parton distribution function (PDF) sets are used: CT10 [78] for the POWHEG, MC@NLO, gg2WW and gg2ZZ samples; CTEQ6L1 [79] for the PYTHIA8, ALPGEN, AcerMC, MadGraph, HERWIG and SHERPA samples; and MRSTMCal [80] for the PYTHIA6 samples.

Acceptances and efficiencies are obtained mostly from full simulations of the ATLAS detector [81] using GEANT4 [82]. These simulations include a realistic modelling of the pile-up conditions observed in the data. Corrections obtained from measurements in data are applied to account for small differences between data and simulation (e.g. large samples of W, Z and J/ψ decays are used to derive scale factors for lepton reconstruction and identification efficiencies).

4. $H \rightarrow ZZ^{(*)} \rightarrow 4\ell$ channel

The search for the SM Higgs boson through the decay $H \rightarrow ZZ^{(*)} \rightarrow 4\ell$, where $\ell = e$ or μ , provides good sensitivity over a wide mass range (110–600 GeV), largely due to the excellent momentum resolution of the ATLAS detector. This analysis searches for Higgs boson candidates by selecting two pairs of isolated leptons, each of which is comprised of two leptons with the same flavour and opposite charge. The expected cross section times branching ratio for the process $H \rightarrow ZZ^{(*)} \rightarrow 4\ell$ with $m_H = 125$ GeV is 2.2 fb for $\sqrt{s} = 7$ TeV and 2.8 fb for $\sqrt{s} = 8$ TeV.

The largest background comes from continuum $(Z^{(*)}/\gamma^*)(Z^{(*)}/\gamma^*)$ production, referred to hereafter as $ZZ^{(*)}$. For low masses there are also important background contributions from Z + jets and $t\bar{t}$ production, where charged lepton candidates arise either from decays of hadrons with b - or c -quark content or from misidentification of jets.

The 7 TeV data have been re-analysed and combined with the 8 TeV data. The analysis is improved in several aspects with respect to Ref. [83] to enhance the sensitivity to a low-mass Higgs boson. In particular, the kinematic selections are revised, and the 8 TeV data analysis benefits from improvements in the electron reconstruction and identification. The expected signal significances for a Higgs boson with $m_H = 125$ GeV are 1.6σ for the 7 TeV data (to be compared with 1.25σ in Ref. [83]) and 2.1σ for the 8 TeV data.

4.1. Event selection

The data are selected using single-lepton or dilepton triggers. For the single-muon trigger, the p_T threshold is 18 GeV for the 7 TeV data and 24 GeV for the 8 TeV

data, while for the single-electron trigger the transverse energy, E_T , threshold varies from 20 GeV to 22 GeV for the 7 TeV data and is 24 GeV for the 8 TeV data. For the dielectron triggers, the thresholds are 12 GeV for both electrons. For the dimuon triggers, the thresholds for the 7 TeV data are 10 GeV for each muon, while for the 8 TeV data the thresholds are 13 GeV. An additional asymmetric dimuon trigger is used in the 8 TeV data with thresholds 18 GeV and 8 GeV for the leading and sub-leading muon, respectively.

Muon candidates are formed by matching reconstructed ID tracks with either a complete track or a track-segment reconstructed in the MS [84]. The muon acceptance is extended with respect to Ref. [83] using tracks reconstructed in the forward region of the MS ($2.5 < |\eta| < 2.7$), which is outside the ID coverage. If both an ID and a complete MS track are present, the two independent momentum measurements are combined; otherwise the information of the ID or the MS is used alone. Electron candidates must have a well-reconstructed ID track pointing to an electromagnetic calorimeter cluster and the cluster should satisfy a set of identification criteria [85] that require the longitudinal and transverse shower profiles to be consistent with those expected for electromagnetic showers. Tracks associated with electromagnetic clusters are fitted using a Gaussian-Sum Filter [86], which allows for bremsstrahlung energy losses to be taken into account.

Each electron (muon) must satisfy $p_T > 7$ GeV ($p_T > 6$ GeV) and be measured in the pseudorapidity range $|\eta| < 2.47$ ($|\eta| < 2.7$). All possible quadruplet combinations with same-flavour opposite-charge lepton pairs are then formed. The most energetic lepton in the quadruplet must satisfy $p_T > 20$ GeV, and the second (third) lepton in p_T order must satisfy $p_T > 15$ GeV ($p_T > 10$ GeV). At least one of the leptons must satisfy the single-lepton trigger or one pair must satisfy the dilepton trigger requirements. The leptons are required to be separated from each other by $\Delta R = \sqrt{(\Delta\eta)^2 + (\Delta\phi)^2} > 0.1$ if they are of the same flavour and by $\Delta R > 0.2$ otherwise. The longitudinal impact parameters of the leptons along the beam axis are required to be within 10 mm of the reconstructed primary vertex. The primary vertex used for the event is defined as the reconstructed vertex with the highest $\sum p_T^2$ of associated tracks and is required to have at least three tracks with $p_T > 0.4$ GeV. To reject cosmic rays, muon tracks are required to have a transverse impact parameter, defined as the distance of closest approach to the primary vertex in the transverse plane, of less than 1 mm.

The same-flavour and opposite-charge lepton pair

with an invariant mass closest to the Z boson mass (m_Z) in the quadruplet is referred to as the leading lepton pair. Its invariant mass, denoted by m_{12} , is required to be between 50 GeV and 106 GeV. The remaining same-flavour, opposite-charge lepton pair is the sub-leading lepton pair. Its invariant mass, m_{34} , is required to be in the range $m_{\min} < m_{34} < 115$ GeV, where the value of m_{\min} depends on the reconstructed four-lepton invariant mass, $m_{4\ell}$. The value of m_{\min} varies monotonically from 17.5 GeV at $m_{4\ell} = 120$ GeV to 50 GeV at $m_{4\ell} = 190$ GeV [87] and is constant above this value. All possible lepton pairs in the quadruplet that have the same flavour and opposite charge must satisfy $m_{\ell\ell} > 5$ GeV in order to reject backgrounds involving the production and decay of J/ψ mesons. If two or more quadruplets satisfy the above selection, the one with the highest value of m_{34} is selected. Four different analysis sub-channels, $4e$, $2e2\mu$, $2\mu2e$ and 4μ , arranged by the flavour of the leading lepton pair, are defined.

Non-prompt leptons from heavy flavour decays, electrons from photon conversions and jets mis-identified as electrons have broader transverse impact parameter distributions than prompt leptons from Z boson decays and/or are non-isolated. Thus, the Z +jets and $t\bar{t}$ background contributions are reduced by applying a cut on the transverse impact parameter significance, defined as the transverse impact parameter divided by its uncertainty, d_0/σ_{d_0} . This is required to be less than 3.5 (6.5) for muons (electrons). The electron impact parameter is affected by bremsstrahlung and thus has a broader distribution.

In addition, leptons must satisfy isolation requirements based on tracking and calorimetric information. The normalised track isolation discriminant is defined as the sum of the transverse momenta of tracks inside a cone of size $\Delta R = 0.2$ around the lepton direction, excluding the lepton track, divided by the lepton p_T . The tracks considered in the sum are those compatible with the lepton vertex and have $p_T > 0.4$ GeV ($p_T > 1$ GeV) in the case of electron (muon) candidates. Each lepton is required to have a normalised track isolation smaller than 0.15. The normalised calorimetric isolation for electrons is computed as the sum of the E_T of positive-energy topological clusters [88] with a reconstructed barycentre falling within a cone of size $\Delta R = 0.2$ around the candidate electron cluster, divided by the electron E_T . The algorithm for topological clustering suppresses noise by keeping cells with a significant energy deposit and their neighbours. The summed energy of the cells assigned to the electron cluster is excluded, while a correction is applied to account for the electron energy deposited outside the cluster. The ambient energy deposi-

tion in the event from pile-up and the underlying event is accounted for using a calculation of the median transverse energy density from low- p_T jets [89, 90]. The normalised calorimetric isolation for electrons is required to be less than 0.20. The normalised calorimetric isolation discriminant for muons is defined by the ratio to the p_T of the muon of the E_T sum of the calorimeter cells inside a cone of size $\Delta R = 0.2$ around the muon direction minus the energy deposited by the muon. Muons are required to have a normalised calorimetric isolation less than 0.30 (0.15 for muons without an associated ID track). For both the track- and calorimeter-based isolation, any contributions arising from other leptons of the quadruplet are subtracted.

The combined signal reconstruction and selection efficiencies for a SM Higgs with $m_H = 125$ GeV for the 7 TeV (8 TeV) data are 37% (36%) for the 4μ channel, 20% (22%) for the $2e2\mu/2\mu2e$ channels and 15% (20%) for the $4e$ channel.

The 4ℓ invariant mass resolution is improved by applying a Z -mass constrained kinematic fit to the leading lepton pair for $m_{4\ell} < 190$ GeV and to both lepton pairs for higher masses. The expected width of the reconstructed mass distribution is dominated by the experimental resolution for $m_H < 350$ GeV, and by the natural width of the Higgs boson for higher masses (30 GeV at $m_H = 400$ GeV). The typical mass resolutions for $m_H = 125$ GeV are 1.7 GeV, 1.7 GeV/2.2 GeV and 2.3 GeV for the 4μ , $2e2\mu/2\mu2e$ and $4e$ sub-channels, respectively.

4.2. Background estimation

The expected background yield and composition are estimated using the MC simulation normalised to the theoretical cross section for $ZZ^{(*)}$ production and by methods using control regions from data for the Z + jets and $t\bar{t}$ processes. Since the background composition depends on the flavour of the sub-leading lepton pair, different approaches are taken for the $\ell\ell + \mu\mu$ and the $\ell\ell + ee$ final states. The transfer factors needed to extrapolate the background yields from the control regions defined below to the signal region are obtained from the MC simulation. The MC description of the selection efficiencies for the different background components has been verified with data.

The reducible $\ell\ell + \mu\mu$ background is dominated by $t\bar{t}$ and Z + jets (mostly $Zb\bar{b}$) events. A control region is defined by removing the isolation requirement on the leptons in the sub-leading pair, and by requiring that at least one of the sub-leading muons fails the transverse impact parameter significance selection. These modifications remove $ZZ^{(*)}$ contributions, and allow both the $t\bar{t}$ and

Z + jets backgrounds to be estimated simultaneously using a fit to the m_{12} distribution. The $t\bar{t}$ background contribution is cross-checked by selecting a control sample of events with an opposite charge $e\mu$ pair with an invariant mass between 50 GeV and 106 GeV, accompanied by an opposite-charge muon pair. Events with a Z candidate decaying to a pair of electrons or muons in the aforementioned mass range are excluded. Isolation and transverse impact parameter significance requirements are applied only to the leptons of the $e\mu$ pair.

In order to estimate the reducible $\ell\ell + ee$ background, a control region is formed by relaxing the selection criteria for the electrons of the sub-leading pair. The different sources of electron background are then separated into categories consisting of non-prompt leptons from heavy flavour decays, electrons from photon conversions and jets mis-identified as electrons, using appropriate discriminating variables [91]. This method allows the sum of the Z + jets and $t\bar{t}$ background contributions to be estimated. As a cross-check, the same method is also applied to a similar control region containing same-charge sub-leading electron pairs. An additional cross-check of the $\ell\ell + ee$ background estimation is performed by using a control region with same-charge sub-leading electron pairs, where the three highest p_T leptons satisfy all the analysis criteria whereas the selection cuts are relaxed for the remaining electrons. All the cross-checks yield consistent results.

Table 2: Summary of the estimated numbers of Z + jets and $t\bar{t}$ background events, for the $\sqrt{s} = 7$ TeV and $\sqrt{s} = 8$ TeV data in the entire phase-space of the analysis after the kinematic selections described in the text. The backgrounds are combined for the $2\mu2e$ and $4e$ channels, as discussed in the text. The first uncertainty is statistical, while the second is systematic.

Background	Estimated numbers of events	
	$\sqrt{s} = 7$ TeV	$\sqrt{s} = 8$ TeV
4μ		
Z +jets	$0.3 \pm 0.1 \pm 0.1$	$0.5 \pm 0.1 \pm 0.2$
$t\bar{t}$	$0.02 \pm 0.02 \pm 0.01$	$0.04 \pm 0.02 \pm 0.02$
$2e2\mu$		
Z +jets	$0.2 \pm 0.1 \pm 0.1$	$0.4 \pm 0.1 \pm 0.1$
$t\bar{t}$	$0.02 \pm 0.01 \pm 0.01$	$0.04 \pm 0.01 \pm 0.01$
$2\mu2e$		
Z +jets, $t\bar{t}$	$2.6 \pm 0.4 \pm 0.4$	$4.9 \pm 0.8 \pm 0.7$
$4e$		
Z +jets, $t\bar{t}$	$3.1 \pm 0.6 \pm 0.5$	$3.9 \pm 0.7 \pm 0.8$

The data-driven background estimates are summarised in Table 2. The distribution of m_{34} , for events selected by the analysis except that the isolation and transverse impact parameter requirements for the sub-

leading lepton pair are removed, is presented in Fig. 1.

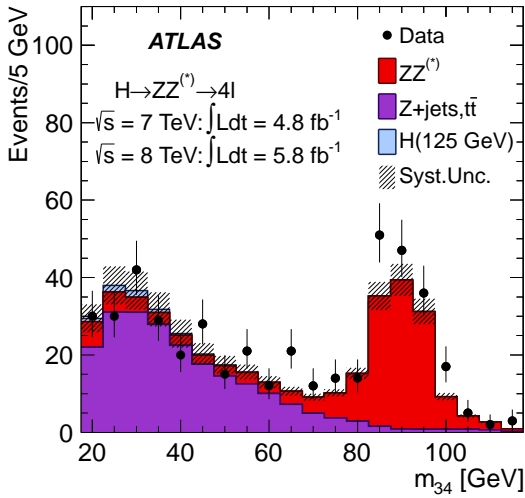


Figure 1: Invariant mass distribution of the sub-leading lepton pair (m_{34}) for a sample defined by the presence of a Z boson candidate and an additional same-flavour electron or muon pair, for the combination of $\sqrt{s} = 7$ TeV and $\sqrt{s} = 8$ TeV data in the entire phase-space of the analysis after the kinematic selections described in the text. Isolation and transverse impact parameter significance requirements are applied to the leading lepton pair only. The MC is normalised to the data-driven background estimations. The relatively small contribution of a SM Higgs with $m_H = 125$ GeV in this sample is also shown.

4.3. Systematic uncertainties

The uncertainties on the integrated luminosities are determined to be 1.8% for the 7 TeV data and 3.6% for the 8 TeV data using the techniques described in Ref. [92].

The uncertainties on the lepton reconstruction and identification efficiencies and on the momentum scale and resolution are determined using samples of W , Z and J/ψ decays [84, 85]. The relative uncertainty on the signal acceptance due to the uncertainty on the muon reconstruction and identification efficiency is $\pm 0.7\%$ ($\pm 0.5\%/\pm 0.5\%$) for the 4μ ($2e2\mu/2\mu2e$) channel for $m_{4\ell} = 600$ GeV and increases to $\pm 0.9\%$ ($\pm 0.8\%/\pm 0.5\%$) for $m_{4\ell} = 115$ GeV. Similarly, the relative uncertainty on the signal acceptance due to the uncertainty on the electron reconstruction and identification efficiency is $\pm 2.6\%$ ($\pm 1.7\%/\pm 1.8\%$) for the $4e$ ($2e2\mu/2\mu2e$) channel for $m_{4\ell} = 600$ GeV and reaches $\pm 8.0\%$ ($\pm 2.3\%/\pm 7.6\%$) for $m_{4\ell} = 115$ GeV. The uncertainty on the electron energy scale results in an uncertainty of $\pm 0.7\%$ ($\pm 0.5\%/\pm 0.2\%$) on the mass scale of the $m_{4\ell}$ distribution for the $4e$ ($2e2\mu/2\mu2e$) channel. The impact of the uncertainties on the electron energy

resolution and on the muon momentum resolution and scale are found to be negligible.

The theoretical uncertainties associated with the signal are described in detail in Section 8. For the SM $ZZ^{(*)}$ background, which is estimated from MC simulation, the uncertainty on the total yield due to the QCD scale uncertainty is $\pm 5\%$, while the effect of the PDF and α_s uncertainties is $\pm 4\%$ ($\pm 8\%$) for processes initiated by quarks (gluons) [53]. In addition, the dependence of these uncertainties on the four-lepton invariant mass spectrum has been taken into account as discussed in Ref. [53]. Though a small excess of events is observed for $m_{4\ell} > 160$ GeV, the measured $ZZ^{(*)} \rightarrow 4\ell$ cross section [93] is consistent with the SM theoretical prediction. The impact of not using the theoretical constraints on the $ZZ^{(*)}$ yield on the search for a Higgs boson with $m_H < 2m_Z$ has been studied in Ref. [87] and has been found to be negligible. The impact of the interference between a Higgs signal and the non-resonant $gg \rightarrow ZZ^{(*)}$ background is small and becomes negligible for $m_H < 2m_Z$ [94].

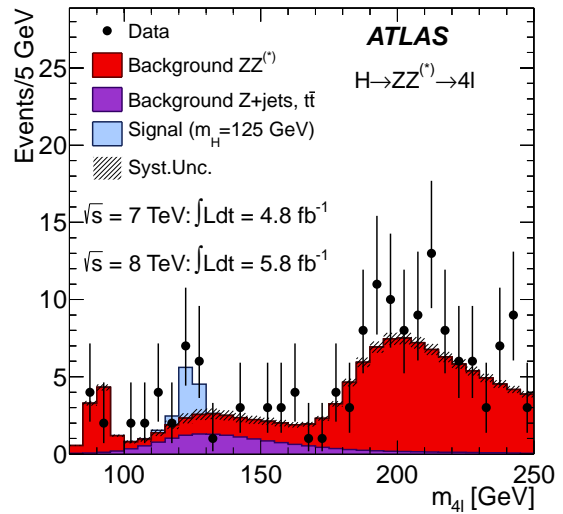


Figure 2: The distribution of the four-lepton invariant mass, $m_{4\ell}$, for the selected candidates, compared to the background expectation in the 80–250 GeV mass range, for the combination of the $\sqrt{s} = 7$ TeV and $\sqrt{s} = 8$ TeV data. The signal expectation for a SM Higgs with $m_H = 125$ GeV is also shown.

4.4. Results

The expected distributions of $m_{4\ell}$ for the background and for a Higgs boson signal with $m_H = 125$ GeV are compared to the data in Fig. 2. The numbers of observed and expected events in a window of ± 5 GeV around $m_H = 125$ GeV are presented for the combined

7 TeV and 8 TeV data in Table 3. The distribution of the m_{34} versus m_{12} invariant mass is shown in Fig. 3. The statistical interpretation of the excess of events near $m_{4\ell} = 125$ GeV in Fig. 2 is presented in Section 9.

Table 3: The numbers of expected signal ($m_H = 125$ GeV) and background events, together with the numbers of observed events in the data, in a window of size ± 5 GeV around 125 GeV, for the combined $\sqrt{s} = 7$ TeV and $\sqrt{s} = 8$ TeV data.

	Signal	$ZZ^{(*)}$	$Z + \text{jets}, t\bar{t}$	Observed
4μ	2.09 ± 0.30	1.12 ± 0.05	0.13 ± 0.04	6
$2e2\mu/2\mu2e$	2.29 ± 0.33	0.80 ± 0.05	1.27 ± 0.19	5
$4e$	0.90 ± 0.14	0.44 ± 0.04	1.09 ± 0.20	2

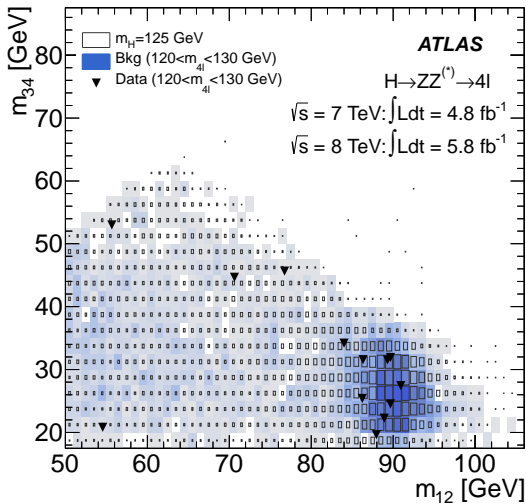


Figure 3: Distribution of the m_{34} versus the m_{12} invariant mass, before the application of the Z -mass constrained kinematic fit, for the selected candidates in the $m_{4\ell}$ range 120–130 GeV. The expected distributions for a SM Higgs with $m_H = 125$ GeV (the sizes of the boxes indicate the relative density) and for the total background (the intensity of the shading indicates the relative density) are also shown.

5. $H \rightarrow \gamma\gamma$ channel

The search for the SM Higgs boson through the decay $H \rightarrow \gamma\gamma$ is performed in the mass range between 110 GeV and 150 GeV. The dominant background is SM diphoton production ($\gamma\gamma$); contributions also come from γ +jet and jet+jet production with one or two jets mis-identified as photons (γj and $j j$) and from the Drell-Yan process. The 7 TeV data have been re-analysed and the results combined with those from the 8 TeV data. Among other changes to the analysis, a new category of events with two jets is introduced, which enhances

the sensitivity to the VBF process. Higgs boson events produced by the VBF process have two forward jets, originating from the two scattered quarks, and tend to be devoid of jets in the central region. Overall, the sensitivity of the analysis has been improved by about 20% with respect to that described in Ref. [95].

5.1. Event selection

The data used in this channel are selected using a diphoton trigger [96], which requires two clusters formed from energy depositions in the electromagnetic calorimeter. An E_T threshold of 20 GeV is applied to each cluster for the 7 TeV data, while for the 8 TeV data the thresholds are increased to 35 GeV on the leading (the highest E_T) cluster and to 25 GeV on the sub-leading (the next-highest E_T) cluster. In addition, loose criteria are applied to the shapes of the clusters to match the expectations for electromagnetic showers initiated by photons. The efficiency of the trigger is greater than 99% for events passing the final event selection.

Events are required to contain at least one reconstructed vertex with at least two associated tracks with $p_T > 0.4$ GeV, as well as two photon candidates. Photon candidates are reconstructed in the fiducial region $|\eta| < 2.37$, excluding the calorimeter barrel/end-cap transition region $1.37 \leq |\eta| < 1.52$. Photons that convert to electron-positron pairs in the ID material can have one or two reconstructed tracks matched to the clusters in the calorimeter. The photon reconstruction efficiency is about 97% for $E_T > 30$ GeV.

In order to account for energy losses upstream of the calorimeter and energy leakage outside of the cluster, MC simulation results are used to calibrate the energies of the photon candidates; there are separate calibrations for unconverted and converted candidates. The calibration is refined by applying η -dependent correction factors, which are of the order of $\pm 1\%$, determined from measured $Z \rightarrow e^+e^-$ events. The leading (sub-leading) photon candidate is required to have $E_T > 40$ GeV (30 GeV).

Photon candidates are required to pass identification criteria based on shower shapes in the electromagnetic calorimeter and on energy leakage into the hadronic calorimeter [97]. For the 7 TeV data, this information is combined in a neural network, tuned to achieve a similar jet rejection as the cut-based selection described in Ref. [95], but with higher photon efficiency. For the 8 TeV data, cut-based criteria are used to ensure reliable photon performance for recently-recorded data. This cut-based selection has been tuned to be robust against pile-up by relaxing requirements on shower shape criteria more susceptible to pile-up, and tightening others.

The photon identification efficiencies, averaged over η , range from 85% to above 95% for the E_T range under consideration.

To further suppress the jet background, an isolation requirement is applied. The isolation transverse energy is defined as the sum of the transverse energy of positive-energy topological clusters, as described in Section 4, within a cone of size $\Delta R = 0.4$ around the photon candidate, excluding the region within 0.125×0.175 in $\Delta\eta \times \Delta\phi$ around the photon barycentre. The distributions of the isolation transverse energy in data and simulation have been found to be in good agreement using electrons from $Z \rightarrow e^+e^-$ events and photons from $Z \rightarrow \ell^+\ell^-\gamma$ events. Remaining small differences are taken into account as a systematic uncertainty. Photon candidates are required to have an isolation transverse energy of less than 4 GeV.

5.2. Invariant mass reconstruction

The invariant mass of the two photons is evaluated using the photon energies measured in the calorimeter, the azimuthal angle ϕ between the photons as determined from the positions of the photons in the calorimeter, and the values of η calculated from the position of the identified primary vertex and the impact points of the photons in the calorimeter.

The primary vertex of the hard interaction is identified by combining the following information in a global likelihood: the directions of flight of the photons as determined using the longitudinal segmentation of the electromagnetic calorimeter (calorimeter pointing), the parameters of the beam spot, and the $\sum p_T^2$ of the tracks associated with each reconstructed vertex. In addition, for the 7 TeV data analysis, the reconstructed conversion vertex is used in the likelihood for converted photons with tracks containing hits in the silicon layers of the ID. The calorimeter pointing is sufficient to ensure that the contribution of the opening angle between the photons to the mass resolution is negligible. Using the calorimeter pointing alone, the resolution of the vertex z coordinate is ~ 15 mm, improving to ~ 6 mm for events with two reconstructed converted photons. The tracking information from the ID improves the identification of the vertex of the hard interaction, which is needed for the jet selection in the 2-jet category.

With the selection described in Section 5.1, in the diphoton invariant mass range between 100 GeV and 160 GeV, 23788 and 35251 diphoton candidates are observed in the 7 TeV and 8 TeV data samples, respectively.

Data-driven techniques [98] are used to estimate the numbers of $\gamma\gamma$, γj and jj events in the selected sam-

ple. The contribution from the Drell-Yan background is determined from a sample of $Z \rightarrow e^+e^-$ decays in data where either one or both electrons pass the photon selection. The measured composition of the selected sample is approximately 74%, 22%, 3% and 1% for the $\gamma\gamma$, γj , jj and Drell-Yan processes, respectively, demonstrating the dominance of the irreducible diphoton production. This decomposition is not directly used in the signal search; however, it is used to study the parameterisation of the background modelling.

5.3. Event categorisation

To increase the sensitivity to a Higgs boson signal, the events are separated into ten mutually exclusive categories having different mass resolutions and signal-to-background ratios. An exclusive category of events containing two jets improves the sensitivity to VBF. The other nine categories are defined by the presence or not of converted photons, η of the selected photons, and $p_{T\perp}$, the component³ of the diphoton p_T that is orthogonal to the axis defined by the difference between the two photon momenta [99, 100].

Jets are reconstructed [101] using the anti- k_r algorithm [102] with radius parameter $R = 0.4$. At least two jets with $|\eta| < 4.5$ and $p_T > 25$ GeV are required in the 2-jet selection. In the analysis of the 8 TeV data, the p_T threshold is raised to 30 GeV for jets with $2.5 < |\eta| < 4.5$. For jets in the ID acceptance ($|\eta| < 2.5$), the fraction of the sum of the p_T of tracks, associated with the jet and matched to the selected primary vertex, with respect to the sum of the p_T of tracks associated with the jet (jet vertex fraction, JVF) is required to be at least 0.75. This requirement on the JVF reduces the number of jets from proton-proton interactions not associated with the primary vertex. Motivated by the VBF topology, three additional cuts are applied in the 2-jet selection: the difference of the pseudorapidity between the leading and sub-leading jets (tag jets) is required to be larger than 2.8, the invariant mass of the tag jets has to be larger than 400 GeV, and the azimuthal angle difference between the diphoton system and the system of the tag jets has to be larger than 2.6. About 70% of the signal events in the 2-jet category come from the VBF process.

The other nine categories are defined as follows: events with two unconverted photons are separated into *unconverted central* ($|\eta| < 0.75$ for both candidates) and *unconverted rest* (all other events), events with at least

³ $p_{T\perp} = |(\mathbf{p}_T^{\gamma 1} + \mathbf{p}_T^{\gamma 2}) \times (\mathbf{p}_T^{\gamma 1} - \mathbf{p}_T^{\gamma 2})| / |\mathbf{p}_T^{\gamma 1} - \mathbf{p}_T^{\gamma 2}|$, where $\mathbf{p}_T^{\gamma 1}$ and $\mathbf{p}_T^{\gamma 2}$ are the transverse momenta of the two photons.

Table 4: Number of events in the data (N_D) and expected number of signal events (N_S) for $m_H = 126.5$ GeV from the $H \rightarrow \gamma\gamma$ analysis, for each category in the mass range 100–160 GeV. The mass resolution FWHM (see text) is also given for the 8 TeV data. The Higgs boson production cross section multiplied by the branching ratio into two photons ($\sigma \times B(H \rightarrow \gamma\gamma)$) is listed for $m_H = 126.5$ GeV. The statistical uncertainties on N_S and FWHM are less than 1%.

\sqrt{s}	7 TeV		8 TeV		FWHM [GeV]
$\sigma \times B(H \rightarrow \gamma\gamma)$ [fb]	39		50		
Category	N_D	N_S	N_D	N_S	
Unconv. central, low p_{T1}	2054	10.5	2945	14.2	3.4
Unconv. central, high p_{T1}	97	1.5	173	2.5	3.2
Unconv. rest, low p_{T1}	7129	21.6	12136	30.9	3.7
Unconv. rest, high p_{T1}	444	2.8	785	5.2	3.6
Conv. central, low p_{T1}	1493	6.7	2015	8.9	3.9
Conv. central, high p_{T1}	77	1.0	113	1.6	3.5
Conv. rest, low p_{T1}	8313	21.1	11099	26.9	4.5
Conv. rest, high p_{T1}	501	2.7	706	4.5	3.9
Conv. transition	3591	9.5	5140	12.8	6.1
2-jet	89	2.2	139	3.0	3.7
All categories (inclusive)	23788	79.6	35251	110.5	3.9

one converted photon are separated into *converted central* ($|\eta| < 0.75$ for both candidates), *converted transition* (at least one photon with $1.3 < |\eta| < 1.75$) and *converted rest* (all other events). Except for the *converted transition* category, each category is further divided by a cut at $p_{T1} = 60$ GeV into two categories, *low p_{T1}* and *high p_{T1}* . MC studies show that signal events, particularly those produced via VBF or associated production (WH/ZH and $t\bar{t}H$), have on average larger p_{T1} than background events. The number of data events in each category, as well as the sum of all the categories, which is denoted *inclusive*, are given in Table 4.

5.4. Signal modelling

The description of the Higgs boson signal is obtained from MC, as described in Section 3. The cross sections multiplied by the branching ratio into two photons are given in Table 4 for $m_H = 126.5$ GeV. The number of signal events produced via the ggF process is rescaled to take into account the expected destructive interference between the $gg \rightarrow \gamma\gamma$ continuum background and ggF [103], leading to a reduction of the production rate by 2–5% depending on m_H and the event category. For both the 7 TeV and 8 TeV MC samples, the fractions of ggF, VBF, WH , ZH and $t\bar{t}H$ production are approximately 88%, 7%, 3%, 2% and 0.5%, respectively, for $m_H = 126.5$ GeV.

In the simulation, the shower shape distributions are shifted slightly to improve the agreement with the data [97], and the photon energy resolution is broadened (by approximately 1% in the barrel calorimeter

and 1.2–2.1% in the end-cap regions) to account for small differences observed between $Z \rightarrow e^+e^-$ data and MC events. The signal yields expected for the 7 TeV and 8 TeV data samples are given in Table 4. The overall selection efficiency is about 40%.

The shape of the invariant mass of the signal in each category is modelled by the sum of a Crystal Ball function [104], describing the core of the distribution with a width σ_{CB} , and a Gaussian contribution describing the tails (amounting to <10%) of the mass distribution. The expected full-width-at-half-maximum (FWHM) is 3.9 GeV and σ_{CB} is 1.6 GeV for the inclusive sample. The resolution varies with event category (see Table 4); the FWHM is typically a factor 2.3 larger than σ_{CB} .

5.5. Background modelling

The background in each category is estimated from data by fitting the diphoton mass spectrum in the mass range 100–160 GeV with a selected model with free parameters of shape and normalisation. Different models are chosen for the different categories to achieve a good compromise between limiting the size of a potential bias while retaining good statistical power. A fourth-order Bernstein polynomial function [105] is used for the *unconverted rest (low p_{T1})*, *converted rest (low p_{T1})* and *inclusive* categories, an exponential function of a second-order polynomial for the *unconverted central (low p_{T1})*, *converted central (low p_{T1})* and *converted transition* categories, and an exponential function for all others.

Studies to determine the potential bias have been performed using large samples of simulated background events complemented by data-driven estimates. The background shapes in the simulation have been cross-checked using data from control regions. The potential bias for a given model is estimated, separately for each category, by performing a maximum likelihood fit to large samples of simulated background events in the mass range 100–160 GeV, of the sum of a signal plus the given background model. The signal shape is taken to follow the expectation for a SM Higgs boson; the signal yield is a free parameter of the fit. The potential bias is defined by the largest absolute signal yield obtained from the likelihood fit to the simulated background samples for hypothesised Higgs boson masses in the range 110–150 GeV. A pre-selection of background parameterisations is made by requiring that the potential bias, as defined above, is less than 20% of the statistical uncertainty on the fitted signal yield. The pre-selected parameterisation in each category with the best expected sensitivity for $m_H = 125$ GeV is selected as the background model.

The largest absolute signal yield as defined above is taken as the systematic uncertainty on the background model. It amounts to $\pm(0.2\text{--}4.6)$ and $\pm(0.3\text{--}6.8)$ events, depending on the category for the 7 TeV and 8 TeV data samples, respectively. In the final fit to the data (see Section 5.7) a signal-like term is included in the likelihood function for each category. This term incorporates the estimated potential bias, thus providing a conservative estimate of the uncertainty due to the background modelling.

5.6. Systematic uncertainties

Hereafter, in cases where two uncertainties are quoted, they refer to the 7 TeV and 8 TeV data, respectively. The dominant experimental uncertainty on the signal yield ($\pm 8\%$, $\pm 11\%$) comes from the photon reconstruction and identification efficiency, which is estimated with data using electrons from Z decays and photons from $Z \rightarrow \ell^+ \ell^- \gamma$ events. Pile-up modelling also affects the expected yields and contributes to the uncertainty ($\pm 4\%$). Further uncertainties on the signal yield are related to the trigger ($\pm 1\%$), photon isolation ($\pm 0.4\%$, $\pm 0.5\%$) and luminosity ($\pm 1.8\%$, $\pm 3.6\%$). Uncertainties due to the modelling of the underlying event are $\pm 6\%$ for VBF and $\pm 30\%$ for other production processes in the 2-jet category. Uncertainties on the predicted cross sections and branching ratio are summarised in Section 8.

The uncertainty on the expected fractions of signal events in each category is described in the following. The uncertainty on the knowledge of the material in front of the calorimeter is used to derive the amount of possible event migration between the converted and unconverted categories ($\pm 4\%$). The uncertainty from pile-up on the population of the converted and unconverted categories is $\pm 2\%$. The uncertainty from the jet energy scale (JES) amounts to up to $\pm 19\%$ for the 2-jet category, and up to $\pm 4\%$ for the other categories. Uncertainties from the JVF modelling are $\pm 12\%$ (for the 8 TeV data) for the 2-jet category, estimated from $Z+2$ -jets events by comparing data and MC. Different PDFs and scale variations in the HqT calculations are used to derive possible event migration among categories ($\pm 9\%$) due to the modelling of the Higgs boson kinematics.

The total uncertainty on the mass resolution is $\pm 14\%$. The dominant contribution ($\pm 12\%$) comes from the uncertainty on the energy resolution of the calorimeter, which is determined from $Z \rightarrow e^+ e^-$ events. Smaller contributions come from the imperfect knowledge of the material in front of the calorimeter, which affects the extrapolation of the calibration from electrons to photons ($\pm 6\%$), and from pile-up ($\pm 4\%$).

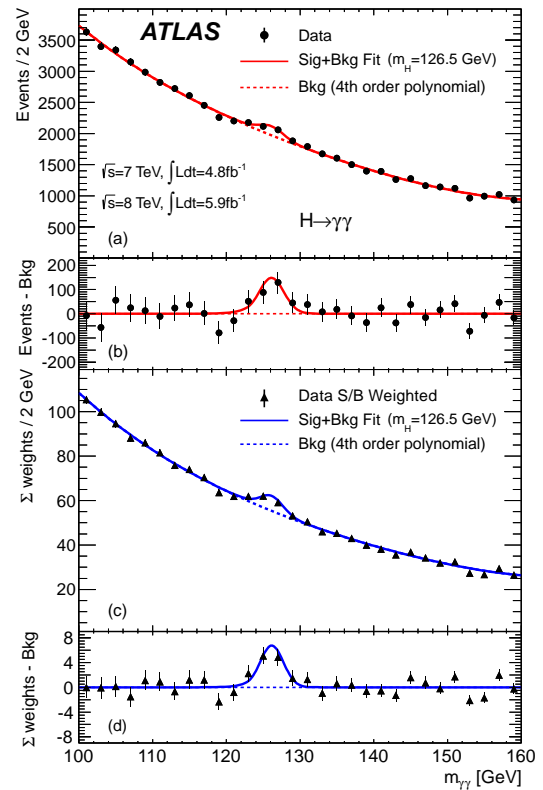


Figure 4: The distributions of the invariant mass of diphoton candidates after all selections for the combined 7 TeV and 8 TeV data sample. The inclusive sample is shown in (a) and a weighted version of the same sample in (c); the weights are explained in the text. The result of a fit to the data of the sum of a signal component fixed to $m_H = 126.5$ GeV and a background component described by a fourth-order Bernstein polynomial is superimposed. The residuals of the data and weighted data with respect to the respective fitted background component are displayed in (b) and (d).

5.7. Results

The distributions of the invariant mass, $m_{\gamma\gamma}$, of the diphoton events, summed over all categories, are shown in Fig. 4(a) and (b). The result of a fit including a signal component fixed to $m_H = 126.5$ GeV and a background component described by a fourth-order Bernstein polynomial is superimposed.

The statistical analysis of the data employs an unbinned likelihood function constructed from those of the ten categories of the 7 TeV and 8 TeV data samples. To demonstrate the sensitivity of this likelihood analysis, Fig. 4(c) and (d) also show the mass spectrum obtained after weighting events with category-dependent factors reflecting the signal-to-background ratios. The weight w_i for events in category $i \in [1, 10]$ for the 7 TeV and 8 TeV data samples is defined to be $\ln(1 + S_i/B_i)$,

where S_i is 90% of the expected signal for $m_H = 126.5$ GeV, and B_i is the integral, in a window containing S_i , of a background-only fit to the data. The values S_i/B_i have only a mild dependence on m_H .

The statistical interpretation of the excess of events near $m_{\gamma\gamma} = 126.5$ GeV in Fig. 4 is presented in Section 9.

6. $H \rightarrow WW^{(*)} \rightarrow e\nu\mu\nu$ channel

The signature for this channel is two opposite-charge leptons with large transverse momentum and a large momentum imbalance in the event due to the escaping neutrinos. The dominant backgrounds are non-resonant WW , $t\bar{t}$, and Wt production, all of which have real W pairs in the final state. Other important backgrounds include Drell-Yan events ($pp \rightarrow Z/\gamma^{(*)} \rightarrow \ell\ell$) with E_T^{miss} that may arise from mismeasurement, W +jets events in which a jet produces an object reconstructed as the second electron or muon, and $W\gamma$ events in which the photon undergoes a conversion. Boson pair production ($W\gamma^*/WZ^{(*)}$ and $ZZ^{(*)}$) can also produce opposite-charge lepton pairs with additional leptons that are not detected.

The analysis of the 8 TeV data presented here is focused on the mass range $110 < m_H < 200$ GeV. It follows the procedure used for the 7 TeV data, described in Ref. [106], except that more stringent criteria are applied to reduce the W +jets background and some selections have been modified to mitigate the impact of the higher instantaneous luminosity at the LHC in 2012. In particular, the higher luminosity results in a larger Drell-Yan background to the same-flavour final states, due to the deterioration of the missing transverse momentum resolution. For this reason, and the fact that the $e\mu$ final state provides more than 85% of the sensitivity of the search, the same-flavour final states have not been used in the analysis described here.

6.1. Event selection

For the 8 TeV $H \rightarrow WW^{(*)} \rightarrow e\nu\mu\nu$ search, the data are selected using inclusive single-muon and single-electron triggers. Both triggers require an isolated lepton with $p_T > 24$ GeV. Quality criteria are applied to suppress non-collision backgrounds such as cosmic-ray muons, beam-related backgrounds, and noise in the calorimeters. The primary vertex selection follows that described in Section 4. Candidates for the $H \rightarrow WW^{(*)} \rightarrow e\nu\mu\nu$ search are pre-selected by requiring exactly two opposite-charge leptons of different flavours, with p_T thresholds of 25 GeV for the leading

lepton and 15 GeV for the sub-leading lepton. Events are classified into two exclusive lepton channels depending on the flavour of the leading lepton, where $e\mu$ (μe) refers to events with a leading electron (muon). The dilepton invariant mass is required to be greater than 10 GeV.

The lepton selection and isolation have more stringent requirements than those used for the $H \rightarrow ZZ^{(*)} \rightarrow 4\ell$ analysis (see Section 4), to reduce the larger background from non-prompt leptons in the $\ell\nu\ell\nu$ final state. Electron candidates are selected using a combination of tracking and calorimetric information [85]; the criteria are optimised for background rejection, at the expense of some reduced efficiency. Muon candidates are restricted to those with matching MS and ID tracks [84], and therefore are reconstructed over $|\eta| < 2.5$. The isolation criteria require the scalar sums of the p_T of charged particles and of calorimeter topological clusters within $\Delta R = 0.3$ of the lepton direction (excluding the lepton itself) each to be less than 0.12-0.20 times the lepton p_T . The exact value differs between the criteria for tracks and calorimeter clusters, for both electrons and muons, and depends on the lepton p_T . Jet selections follow those described in Section 5.3, except that the JVF is required to be greater than 0.5.

Since two neutrinos are present in the signal final state, events are required to have large E_T^{miss} . $\mathbf{E}_T^{\text{miss}}$ is the negative vector sum of the transverse momenta of the reconstructed objects, including muons, electrons, photons, jets, and clusters of calorimeter cells not associated with these objects. The quantity $E_{T,\text{rel}}^{\text{miss}}$ used in this analysis is required to be greater than 25 GeV and is defined as: $E_{T,\text{rel}}^{\text{miss}} = E_T^{\text{miss}} \sin \Delta\phi_{\text{min}}$, where $\Delta\phi_{\text{min}}$ is $\min(\Delta\phi, \frac{\pi}{2})$, and E_T^{miss} is the magnitude of the vector $\mathbf{E}_T^{\text{miss}}$. Here, $\Delta\phi$ is the angle between $\mathbf{E}_T^{\text{miss}}$ and the transverse momentum of the nearest lepton or jet with $p_T > 25$ GeV. Compared to E_T^{miss} , $E_{T,\text{rel}}^{\text{miss}}$ has increased rejection power for events in which the E_T^{miss} is generated by a neutrino in a jet or the mismeasurement of an object, since in those events the $\mathbf{E}_T^{\text{miss}}$ tends to point in the direction of the object. After the lepton isolation and $E_{T,\text{rel}}^{\text{miss}}$ requirements that define the pre-selected sample, the multijet background is negligible and the Drell-Yan background is much reduced. The Drell-Yan contribution becomes very small after the topological selections, described below, are applied.

The background rate and composition depend significantly on the jet multiplicity, as does the signal topology. Without accompanying jets, the signal originates almost entirely from the ggF process and the background is dominated by WW events. In contrast, when

produced in association with two or more jets, the signal contains a much larger contribution from the VBF process compared to the ggF process, and the background is dominated by $t\bar{t}$ production. Therefore, to maximise the sensitivity to SM Higgs events, further selection criteria depending on the jet multiplicity are applied to the pre-selected sample. The data are subdivided into 0-jet, 1-jet and 2-jet search channels according to the number of jets in the final state, with the 2-jet channel also including higher jet multiplicities.

Owing to spin correlations in the $WW^{(*)}$ system arising from the spin-0 nature of the SM Higgs boson and the V-A structure of the W boson decay vertex, the charged leptons tend to emerge from the primary vertex pointing in the same direction [107]. This kinematic feature is exploited for all jet multiplicities by requiring that $|\Delta\phi_{\ell\ell}| < 1.8$, and the dilepton invariant mass, $m_{\ell\ell}$, be less than 50 GeV for the 0-jet and 1-jet channels. For the 2-jet channel, the $m_{\ell\ell}$ upper bound is increased to 80 GeV.

In the 0-jet channel, the magnitude $p_T^{\ell\ell}$ of the transverse momentum of the dilepton system, $\mathbf{p}_T^{\ell\ell} = \mathbf{p}_T^{\ell 1} + \mathbf{p}_T^{\ell 2}$, is required to be greater than 30 GeV. This improves the rejection of the Drell-Yan background.

In the 1-jet channel, backgrounds from top quark production are suppressed by rejecting events containing a b -tagged jet, as determined using a b -tagging algorithm that uses a neural network and exploits the topology of weak decays of b - and c -hadrons [108]. The total transverse momentum, p_T^{tot} , defined as the magnitude of the vector sum $\mathbf{p}_T^{\text{tot}} = \mathbf{p}_T^{\ell 1} + \mathbf{p}_T^{\ell 2} + \mathbf{p}_T^j + \mathbf{E}_T^{\text{miss}}$, is required to be smaller than 30 GeV to suppress top background events that have jets with p_T below the threshold defined for jet counting. In order to reject the background from $Z \rightarrow \tau\tau$, the $\tau\tau$ invariant mass, $m_{\tau\tau}$, is computed under the assumptions that the reconstructed leptons are τ lepton decay products. In addition the neutrinos produced in these decays are assumed to be the only source of E_T^{miss} and to be collinear with the leptons [109]. Events with $|m_{\tau\tau} - m_Z| < 25$ GeV are rejected if the collinear approximation yields a physical solution.

The 2-jet selection follows the 1-jet selection described above, with the p_T^{tot} definition modified to include all selected jets. Motivated by the VBF topology, several additional criteria are applied to the tag jets, defined as the two highest- p_T jets in the event. These are required to be separated in rapidity by a distance $|\Delta y_{jj}| > 3.8$ and to have an invariant mass, m_{jj} , larger than 500 GeV. Events with an additional jet with $p_T > 20$ GeV between the tag jets ($y_{j1} < y < y_{j2}$) are rejected.

A transverse mass variable, m_T [110], is used to test for the presence of a signal for all jet multiplicities. This variable is defined as:

$$m_T = \sqrt{(E_T^{\ell\ell} + E_T^{\text{miss}})^2 - |\mathbf{p}_T^{\ell\ell} + \mathbf{E}_T^{\text{miss}}|^2},$$

where $E_T^{\ell\ell} = \sqrt{|\mathbf{p}_T^{\ell\ell}|^2 + m_{\ell\ell}^2}$. The statistical analysis of the data uses a fit to the m_T distribution in the signal region after the $\Delta\phi_{\ell\ell}$ requirement (see Section 6.4), which results in increased sensitivity compared to the analysis described in Ref. [111].

For a SM Higgs boson with $m_H = 125$ GeV, the cross section times branching ratio to the $e\nu\mu\nu$ final state is 88 fb for $\sqrt{s} = 7$ TeV, increasing to 112 fb at $\sqrt{s} = 8$ TeV. The combined acceptance times efficiency of the 8 TeV 0-jet and 1-jet selection relative to the ggF production cross section times branching ratio is about 7.4%. The acceptance times efficiency of the 8 TeV 2-jet selection relative to the VBF production cross section times branching ratio is about 14%. Both of these figures are based on the number of events selected before the final m_T criterion is applied (as described in Section 6.4).

6.2. Background normalisation and control samples

The leading backgrounds from SM processes producing two isolated high- p_T leptons are WW and top (in this section, “top” background always includes both $t\bar{t}$ and single top, unless otherwise noted). These are estimated using partially data-driven techniques based on normalising the MC predictions to the data in control regions dominated by the relevant background source. The W +jets background is estimated from data for all jet multiplicities. Only the small backgrounds from Drell-Yan and diboson processes other than WW , as well as the WW background for the 2-jet analysis, are estimated using MC simulation.

The control and validation regions are defined by selections similar to those used for the signal region but with some criteria reversed or modified to obtain signal-depleted samples enriched in a particular background. The term “validation region” distinguishes these regions from the control regions that are used to directly normalise the backgrounds. Some control regions have significant contributions from backgrounds other than the targeted one, which introduces dependencies among the background estimates. These correlations are fully incorporated in the fit to the m_T distribution. In the following sections, each background estimate is described after any others on which it depends. Hence, the largest background (WW) is described last.

6.2.1. W +jets background estimation

The W +jets background contribution is estimated using a control sample of events where one of the two leptons satisfies the identification and isolation criteria described in Section 6.1, and the other lepton fails these criteria but satisfies a loosened selection (denoted “anti-identified”). Otherwise, events in this sample are required to pass all the signal selections. The dominant contribution to this sample comes from W +jets events in which a jet produces an object that is reconstructed as a lepton. This object may be either a true electron or muon from the decay of a heavy quark, or else a product of the fragmentation identified as a lepton candidate.

The contamination in the signal region is obtained by scaling the number of events in the data control sample by a transfer factor. The transfer factor is defined here as the ratio of the number of identified lepton candidates passing all selections to the number of anti-identified leptons. It is calculated as a function of the anti-identified lepton p_T using a data sample dominated by QCD jet production (dijet sample) after subtracting the residual contributions from leptons produced by leptonic W and Z decays, as estimated from data. The small remaining lepton contamination, which includes $W\gamma^{(*)}/WZ^{(*)}$ events, is subtracted using MC simulation.

The processes producing the majority of same-charge dilepton events, W +jets, $W\gamma^{(*)}/WZ^{(*)}$ and $Z^{(*)}Z^{(*)}$, are all backgrounds in the opposite-charge signal region. W +jets and $W\gamma^{(*)}$ backgrounds are particularly important in a search optimised for a low Higgs boson mass hypothesis. Therefore, the normalisation and kinematic features of same-charge dilepton events are used to validate the predictions of these backgrounds. The predicted number of same-charge events after the $E_{T,rel}^{miss}$ and zero-jet requirements is 216 ± 7 (stat) ± 42 (syst), while 182 events are observed in the data. Satisfactory agreement between data and simulation is observed in various kinematic distributions, including those of $\Delta\phi_{\ell\ell}$ (see Fig. 5(a)) and the transverse mass.

6.2.2. Top control sample

In the 0-jet channel, the top quark background prediction is first normalised using events satisfying the pre-selection criteria described in Section 6.1. This sample is selected without jet multiplicity or b -tagging requirements, and the majority of events contain top quarks. Non-top contributions are subtracted using predictions from simulation, except for W +jets, which is estimated using data. After this normalisation is performed, the fraction of events with zero jets that pass all selections is evaluated. This fraction is small (about 3%), since the top quark decay $t \rightarrow Wb$ has a branching ratio of nearly

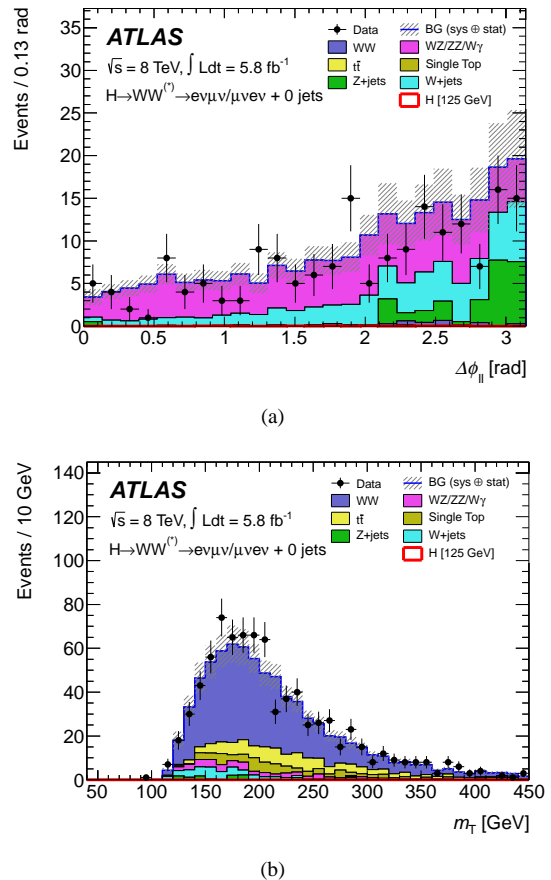


Figure 5: Validation and control distributions for the $H \rightarrow WW^{(*)} \rightarrow e\nu\mu\nu$ analysis. a) $\Delta\phi_{\ell\ell}$ distribution in the same-charge validation region after the $E_{T,rel}^{miss}$ and zero-jet requirements. b) m_T distribution in the WW control region for the 0-jet channel. The $e\mu$ and μe final states are combined. The hashed area indicates the total uncertainty on the background prediction. The expected signal for $m_H = 125$ GeV is negligible and therefore not visible.

1. Predictions of this fraction from MC simulation are sensitive to theoretical uncertainties such as the modelling of initial- and final-state radiation, as well as experimental uncertainties, especially that on the jet energy scale. To reduce the impact of these uncertainties, the top quark background determination uses data from a b -tagged control region in which the one-to-two jet ratio is compared to the MC simulation [112]. The resulting correction factor to a purely MC-based background estimate after all selections amounts to 1.11 ± 0.06 (stat).

In the 1-jet and 2-jet analyses, the top quark background predictions are normalised to the data using control samples defined by reversing the b -jet veto and removing the requirements on $\Delta\phi_{\ell\ell}$ and $m_{\ell\ell}$. The $|\Delta y_{jj}|$

and m_{jj} requirements are included in the definition of the 2-jet control region. The resulting samples are dominated by top quark events. The small contributions from other sources are taken into account using MC simulation and the data-driven W +jets estimate. Good agreement between data and MC simulation is observed for the total numbers of events and the shapes of the m_T distributions. The resulting normalisation factors are 1.11 ± 0.05 for the 1-jet control region and 1.01 ± 0.26 for the 2-jet control region. Only the statistical uncertainties are quoted.

6.2.3. WW control sample

The MC predictions of the WW background in the 0-jet and 1-jet analyses, summed over lepton flavours, are normalised using control regions defined with the same selections as for the signal region except that the $\Delta\phi_{\ell\ell}$ requirement is removed and the upper bound on $m_{\ell\ell}$ is replaced with a lower bound: $m_{\ell\ell} > 80$ GeV. The numbers of events and the shape of the m_T distribution in the control regions are in good agreement between data and MC, as shown in Fig. 5(b). WW production contributes about 70% of the events in the 0-jet control region and about 45% in the 1-jet region. Contaminations from sources other than WW are derived as for the signal region, including the data-driven W +jets and top estimates. The resulting normalisation factors with their associated statistical uncertainties are 1.06 ± 0.06 for the 0-jet control region and 0.99 ± 0.15 for the 1-jet control region.

6.3. Systematic uncertainties

The systematic uncertainties that have the largest impact on the sensitivity of the search are the theoretical uncertainties associated with the signal. These are described in Section 9. The main experimental uncertainties are associated with the JES, the jet energy resolution (JER), pile-up, E_T^{miss} , the b -tagging efficiency, the W +jets transfer factor, and the integrated luminosity. The largest uncertainties on the backgrounds include WW normalisation and modelling, top normalisation, and $W\gamma^{(*)}$ normalisation. The 2-jet systematic uncertainties are dominated by the statistical uncertainties in the data and the MC simulation, and are therefore not discussed further.

Variations of the jet energy scale within the systematic uncertainties can cause events to migrate between the jet bins. The uncertainty on the JES varies from $\pm 2\%$ to $\pm 9\%$ as a function of jet p_T and η for jets with $p_T > 25$ GeV and $|\eta| < 4.5$ [101]. The largest impact of this uncertainty on the total signal (background) yield

amounts to 7% (4%) in the 0-jet (1-jet) bin. The uncertainty on the JER is estimated from *in situ* measurements and it impacts mostly the 1-jet channel, where its effect on the total signal and background yields is 4% and 2%, respectively. An additional contribution to the JES uncertainty arises from pile-up, and is estimated to vary between $\pm 1\%$ and $\pm 5\%$ for multiple pp collisions in the same bunch crossing and up to $\pm 10\%$ for neighbouring bunch crossings. This uncertainty affects mainly the 1-jet channel, where its impact on the signal and background yields is 4% and 2%, respectively. JES and lepton momentum scale uncertainties are propagated to the E_T^{miss} measurement. Additional contributions to the E_T^{miss} uncertainties arise from jets with $p_T < 20$ GeV and from low-energy calorimeter deposits not associated with reconstructed physics objects [113]. The impact of the E_T^{miss} uncertainty on the total signal and background yields is $\sim 3\%$. The efficiency of the b -tagging algorithm is calibrated using samples containing muons reconstructed in the vicinity of jets [114]. The uncertainty on the b -jet tagging efficiency varies between $\pm 5\%$ and $\pm 18\%$ as a function of the jet p_T , and its impact on the total background yield is 10% for the 1-jet channel. The uncertainty in the W +jets transfer factor is dominated by differences in jet properties between dijet and W +jets events as observed in MC simulations. The total uncertainty on this background is approximately $\pm 40\%$, resulting in an uncertainty on the total background yield of 5%. The uncertainty on the integrated luminosity is $\pm 3.6\%$.

A fit to the distribution of m_T is performed in order to obtain the signal yield for each mass hypothesis (see Section 6.4). Most theoretical and experimental uncertainties do not produce statistically significant changes to the m_T distribution. The uncertainties that do produce significant changes of the distribution of m_T have no appreciable effect on the final results, with the exception of those associated with the WW background. In this case, an uncertainty is included to take into account differences in the distribution of m_T and normalisation observed between the MCFM [115], MC@NLO+HERWIG and POWHEG+PYTHIA generators. The potential impact of interference between resonant (Higgs-mediated) and non-resonant $gg \rightarrow WW$ diagrams [116] for $m_T > m_H$ was investigated and found to be negligible. The effect of the WW normalisation, modelling, and shape systematics on the total background yield is 9% for the 0-jet channel and 19% for the 1-jet channel. The uncertainty on the shape of the total background is dominated by the uncertainties on the normalisations of the individual backgrounds. The main uncertainties on the top background in the 0-jet

analysis include those associated with interference effects between $t\bar{t}$ and single top, initial state and final state radiation, b -tagging, and JER. The impact on the total background yield in the 0-jet bin is 3%. For the 1-jet analysis, the impact of the top background on the total yield is 14%. Theoretical uncertainties on the $W\gamma$ background normalisation are evaluated for each jet bin using the procedure described in Ref. [117]. They are $\pm 11\%$ for the 0-jet bin and $\pm 50\%$ for the 1-jet bin. For $W\gamma^*$ with $m_{\ell\ell} < 7$ GeV, a k-factor of 1.3 ± 0.3 is applied to the MadGraph LO prediction based on the comparison with the MCFM NLO calculation. The k-factor for $W\gamma^*/WZ^{(*)}$ with $m_{\ell\ell} > 7$ GeV is 1.5 ± 0.5 . These uncertainties affect mostly the 1-jet channel, where their impact on the total background yield is approximately 4%.

Table 5: The expected numbers of signal ($m_H = 125$ GeV) and background events after all selections, including a cut on the transverse mass of $0.75 m_H < m_T < m_H$ for $m_H = 125$ GeV. The observed numbers of events in data are also displayed. The $e\mu$ and μe channels are combined. The uncertainties shown are the combination of the statistical and all systematic uncertainties, taking into account the constraints from control samples. For the 2-jet analysis, backgrounds with fewer than 0.01 expected events are marked with ‘-’.

	0-jet	1-jet	2-jet
Signal	20 ± 4	5 ± 2	0.34 ± 0.07
WW	101 ± 13	12 ± 5	0.10 ± 0.14
$WZ^{(*)}/ZZ/W\gamma^{(*)}$	12 ± 3	1.9 ± 1.1	0.10 ± 0.10
$t\bar{t}$	8 ± 2	6 ± 2	0.15 ± 0.10
$tW/tb/tqb$	3.4 ± 1.5	3.7 ± 1.6	-
$Z/\gamma^* + \text{jets}$	1.9 ± 1.3	0.10 ± 0.10	-
W + jets	15 ± 7	2 ± 1	-
Total Background	142 ± 16	26 ± 6	0.35 ± 0.18
Observed	185	38	0

6.4. Results

Table 5 shows the numbers of events expected from a SM Higgs boson with $m_H = 125$ GeV and from the backgrounds, as well as the numbers of candidates observed in data, after application of all selection criteria plus an additional cut on m_T of $0.75 m_H < m_T < m_H$. The uncertainties shown in Table 5 include the systematic uncertainties discussed in Section 6.3, constrained by the use of the control regions discussed in Section 6.2. An excess of events relative to the background expectation is observed in the data.

Figure 6 shows the distribution of the transverse mass after all selection criteria in the 0-jet and 1-jet channels combined, and for both lepton channels together.

The statistical analysis of the data employs a binned likelihood function constructed as the product of Poisson probability terms for the $e\mu$ channel and the μe

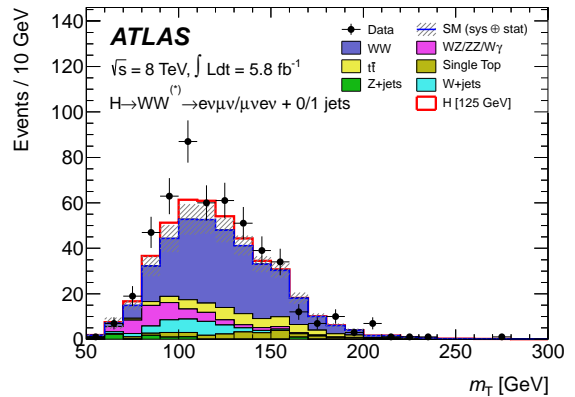


Figure 6: Distribution of the transverse mass, m_T , in the 0-jet and 1-jet analyses with both $e\mu$ and μe channels combined, for events satisfying all selection criteria. The expected signal for $m_H = 125$ GeV is shown stacked on top of the background prediction. The W+jets background is estimated from data, and WW and top background MC predictions are normalised to the data using control regions. The hashed area indicates the total uncertainty on the background prediction.

channel. The mass-dependent cuts on m_T described above are not used. Instead, the 0-jet (1-jet) signal regions are subdivided into five (three) m_T bins. For the 2-jet signal region, only the results integrated over m_T are used, due to the small number of events in the final sample. The statistical interpretation of the observed excess of events is presented in Section 9.

7. Statistical procedure

The statistical procedure used to interpret the data is described in Refs. [17, 118–121]. The parameter of interest is the global signal strength factor μ , which acts as a scale factor on the total number of events predicted by the Standard Model for the Higgs boson signal. This factor is defined such that $\mu = 0$ corresponds to the background-only hypothesis and $\mu = 1$ corresponds to the SM Higgs boson signal in addition to the background. Hypothesised values of μ are tested with a statistic $\lambda(\mu)$ based on the profile likelihood ratio [122]. This test statistic extracts the information on the signal strength from a full likelihood fit to the data. The likelihood function includes all the parameters that describe the systematic uncertainties and their correlations.

Exclusion limits are based on the CL_s prescription [123]; a value of μ is regarded as excluded at 95% CL when CL_s is less than 5%. A SM Higgs boson with mass m_H is considered excluded at 95% confidence level (CL) when $\mu = 1$ is excluded at that mass. The significance of an excess in the data is first quan-

tified with the local p_0 , the probability that the background can produce a fluctuation greater than or equal to the excess observed in data. The equivalent formulation in terms of number of standard deviations, Z_l , is referred to as the local significance. The global probability for the most significant excess to be observed anywhere in a given search region is estimated with the method described in Ref. [124]. The ratio of the global to the local probabilities, the trials factor used to correct for the "look elsewhere" effect, increases with the range of Higgs boson mass hypotheses considered, the mass resolutions of the channels involved in the combination, and the significance of the excess.

The statistical tests are performed in steps of values of the hypothesised Higgs boson mass m_H . The asymptotic approximation [122] upon which the results are based has been validated with the method described in Ref. [17].

The combination of individual search sub-channels for a specific Higgs boson decay, and the full combination of all search channels, are based on the global signal strength factor μ and on the identification of the nuisance parameters that correspond to the correlated sources of systematic uncertainty described in Section 8.

8. Correlated systematic uncertainties

The individual search channels that enter the combination are summarised in Table 6.

The main uncorrelated systematic uncertainties are described in Sections 4–6 for the $H \rightarrow ZZ^{(*)} \rightarrow 4\ell$, $H \rightarrow \gamma\gamma$ and $H \rightarrow WW^{(*)} \rightarrow \ell\nu\ell\nu$ channels and in Ref. [17] for the other channels. They include the background normalisations or background model parameters from control regions or sidebands, the Monte Carlo simulation statistical uncertainties and the theoretical uncertainties affecting the background processes.

The main sources of correlated systematic uncertainties are the following.

1. *Integrated luminosity:* The uncertainty on the integrated luminosity is considered as fully correlated among channels and amounts to $\pm 3.9\%$ for the 7 TeV data [132, 133], except for the $H \rightarrow ZZ^{(*)} \rightarrow 4\ell$ and $H \rightarrow \gamma\gamma$ channels which were re-analysed; the uncertainty is $\pm 1.8\%$ [92] for these channels. The uncertainty is $\pm 3.6\%$ for the 8 TeV data.

2. *Electron and photon trigger identification:* The uncertainties in the trigger and identification efficiencies are treated as fully correlated for electrons and photons.

3. *Electron and photon energy scales:* The electron and photon energy scales in the $H \rightarrow ZZ^{(*)} \rightarrow 4\ell$ and $H \rightarrow \gamma\gamma$ channels are described by five parameters, which provide a detailed account of the sources of systematic uncertainty. They are related to the calibration method, the presampler energy scale in the barrel and end-cap calorimeters, and the material description upstream of the calorimeters.

4. *Muon reconstruction:* The uncertainties affecting muons are separated into those related to the ID and MS, in order to obtain a better description of the correlated effects among channels using different muon identification criteria and different ranges of muon p_T .

5. *Jet energy scale and missing transverse energy:* The jet energy scale and jet energy resolution are affected by uncertainties which depend on the p_T , η , and flavour of the jet. A simplified scheme is used in which independent JES and JER nuisance parameters are associated with final states with significantly different kinematic selections and sensitivity to scattering processes with different kinematic distributions or flavour composition. This scheme includes a specific treatment for b -jets. The sensitivity of the results to various assumptions about the correlation between these sources of uncertainty has been found to be negligible. An uncorrelated component of the uncertainty on E_T^{miss} is included, in addition to the JES uncertainty, which is due to low energy jet activity not associated with reconstructed physics objects.

6. *Theory uncertainties:* Correlated theoretical uncertainties affect mostly the signal predictions. The QCD scale uncertainties for $m_H=125$ GeV amount to $^{+7\%}_{-8\%}$ for the ggF process, $\pm 1\%$ for the VBF and WH/ZH processes, and $^{+4\%}_{-9\%}$ for the $t\bar{t}H$ process [52, 53]; the small dependence of these uncertainties on m_H is taken into account. The uncertainties on the predicted branching ratios amount to $\pm 5\%$. The uncertainties related to the parton distribution functions amount to $\pm 8\%$ for the predominantly gluon-initiated ggF and $t\bar{t}H$ processes, and $\pm 4\%$ for the predominantly quark-initiated VBF and WH/ZH processes [78, 134–136]. The theoretical uncertainty associated with the exclusive Higgs boson production process with additional jets in the $H \rightarrow \gamma\gamma$, $H \rightarrow WW^{(*)} \rightarrow \ell\nu\ell\nu$ and $H \rightarrow \tau^+\tau^-$ channels is estimated using the prescription of Refs. [53, 117, 118], with the noticeable difference that an explicit calculation of the gluon-fusion process at NLO using MCFM [137] in the 2-jet category reduces the uncertainty on this non-negligible contribution to 25%. An additional theoretical uncertainty on the signal normalisation of $\pm 150\% \times (m_H/\text{TeV})^3$ (e.g. $\pm 4\%$ for $m_H = 300$ GeV) accounts for effects related to off-shell Higgs boson pro-

Table 6: Summary of the individual channels entering the combination. The transition points between separately optimised m_H regions are indicated where applicable. In channels sensitive to associated production of the Higgs boson, V indicates a W or Z boson. The symbols \otimes and \oplus represent direct products and sums over sets of selection requirements, respectively.

Higgs Boson Decay	Subsequent Decay	Sub-Channels	m_H Range [GeV]	$\int L dt$ [fb $^{-1}$]	Ref.
2011 $\sqrt{s}=7$ TeV					
$H \rightarrow ZZ^{(*)}$	4ℓ	$\{4e, 2e2\mu, 2\mu2e, 4\mu\}$	110–600	4.8	[87]
	$\ell\ell\nu\bar{\nu}$	$\{ee, \mu\mu\} \otimes \{\text{low, high pile-up}\}$	200–280–600	4.7	[125]
	$\ell\ell q\bar{q}$	$\{b\text{-tagged, untagged}\}$	200–300–600	4.7	[126]
$H \rightarrow \gamma\gamma$	–	10 categories $\{p_{T1} \otimes \eta_\gamma \otimes \text{conversion}\} \oplus \{2\text{-jet}\}$	110–150	4.8	[127]
$H \rightarrow WW^{(*)}$	$\ell\nu\ell\nu$	$\{ee, e\mu/\mu e, \mu\mu\} \otimes \{0\text{-jet, 1-jet, 2-jet}\} \otimes \{\text{low, high pile-up}\}$	110–200–300–600	4.7	[106]
	$\ell\nu qq'$	$\{e, \mu\} \otimes \{0\text{-jet, 1-jet, 2-jet}\}$	300–600	4.7	[128]
$H \rightarrow \tau\tau$	$\tau_{\text{lep}}\tau_{\text{lep}}$	$\{e\mu\} \otimes \{0\text{-jet}\} \oplus \{\ell\ell\} \otimes \{1\text{-jet, 2-jet, } VH\}$	110–150	4.7	[129]
	$\tau_{\text{lep}}\tau_{\text{had}}$	$\{e, \mu\} \otimes \{0\text{-jet}\} \otimes \{E_T^{\text{miss}} < 20 \text{ GeV}, E_T^{\text{miss}} \geq 20 \text{ GeV}\}$	110–150	4.7	
	$\tau_{\text{had}}\tau_{\text{had}}$	$\oplus \{e, \mu\} \otimes \{1\text{-jet}\} \oplus \{\ell\} \otimes \{2\text{-jet}\}$ $\{1\text{-jet}\}$	110–150	4.7	
$VH \rightarrow Vbb$	$Z \rightarrow \nu\nu$	$E_T^{\text{miss}} \in \{120 - 160, 160 - 200, \geq 200 \text{ GeV}\}$	110–130	4.6	[130]
	$W \rightarrow \ell\nu$	$p_{T1}^W \in \{< 50, 50 - 100, 100 - 200, \geq 200 \text{ GeV}\}$	110–130	4.7	
	$Z \rightarrow \ell\ell$	$p_{T1}^Z \in \{< 50, 50 - 100, 100 - 200, \geq 200 \text{ GeV}\}$	110–130	4.7	
2012 $\sqrt{s}=8$ TeV					
$H \rightarrow ZZ^{(*)}$	4ℓ	$\{4e, 2e2\mu, 2\mu2e, 4\mu\}$	110–600	5.8	[87]
$H \rightarrow \gamma\gamma$	–	10 categories $\{p_{T1} \otimes \eta_\gamma \otimes \text{conversion}\} \oplus \{2\text{-jet}\}$	110–150	5.9	[127]
$H \rightarrow WW^{(*)}$	$e\nu\mu\nu$	$\{e\mu, \mu e\} \otimes \{0\text{-jet, 1-jet, 2-jet}\}$	110–200	5.8	[131]

Table 7: Characterisation of the excess in the $H \rightarrow ZZ^{(*)} \rightarrow 4\ell$, $H \rightarrow \gamma\gamma$ and $H \rightarrow WW^{(*)} \rightarrow \ell\nu\ell\nu$ channels and the combination of all channels listed in Table 6. The mass value m_{max} for which the local significance is maximum, the maximum observed local significance Z_l and the expected local significance $E(Z_l)$ in the presence of a SM Higgs boson signal at m_{max} are given. The best fit value of the signal strength parameter $\hat{\mu}$ at $m_H = 126$ GeV is shown with the total uncertainty. The expected and observed mass ranges excluded at 95% CL (99% CL, indicated by a *) are also given, for the combined $\sqrt{s} = 7$ TeV and $\sqrt{s} = 8$ TeV data.

Search channel	Dataset	m_{max} [GeV]	Z_l [σ]	$E(Z_l)$ [σ]	$\hat{\mu}(m_H = 126 \text{ GeV})$	Expected exclusion [GeV]	Observed exclusion [GeV]
$H \rightarrow ZZ^{(*)} \rightarrow 4\ell$	7 TeV	125.0	2.5	1.6	1.4 ± 1.1		
	8 TeV	125.5	2.6	2.1	1.1 ± 0.8		
	7 & 8 TeV	125.0	3.6	2.7	1.2 ± 0.6	124–164, 176–500	131–162, 170–460
$H \rightarrow \gamma\gamma$	7 TeV	126.0	3.4	1.6	2.2 ± 0.7		
	8 TeV	127.0	3.2	1.9	1.5 ± 0.6		
	7 & 8 TeV	126.5	4.5	2.5	1.8 ± 0.5	110–140	112–123, 132–143
$H \rightarrow WW^{(*)} \rightarrow \ell\nu\ell\nu$	7 TeV	135.0	1.1	3.4	0.5 ± 0.6		
	8 TeV	120.0	3.3	1.0	1.9 ± 0.7		
	7 & 8 TeV	125.0	2.8	2.3	1.3 ± 0.5	124–233	137–261
Combined	7 TeV	126.5	3.6	3.2	1.2 ± 0.4		
	8 TeV	126.5	4.9	3.8	1.5 ± 0.4		
	7 & 8 TeV	126.5	6.0	4.9	1.4 ± 0.3	110–582 113–532 (*)	111–122, 131–559 113–114, 117–121, 132–527 (*)

duction and interference with other SM processes [53].

Sources of systematic uncertainty that affect both the 7 TeV and the 8 TeV data are taken as fully correlated. The uncertainties on background estimates based on control samples in the data are considered uncorrelated between the 7 TeV and 8 TeV data.

9. Results

The addition of the 8 TeV data for the $H \rightarrow ZZ^{(*)} \rightarrow 4\ell$, $H \rightarrow \gamma\gamma$ and $H \rightarrow WW^{(*)} \rightarrow e\nu\mu\nu$ channels, as well as the improvements to the analyses of the 7 TeV data in the

first two of these channels, bring a significant gain in sensitivity in the low-mass region with respect to the previous combined search [17].

9.1. Excluded mass regions

The combined 95% CL exclusion limits on the production of the SM Higgs boson, expressed in terms of the signal strength parameter μ , are shown in Fig. 7(a) as a function of m_H . The expected 95% CL exclusion region covers the m_H range from 110 GeV to 582 GeV. The observed 95% CL exclusion regions are 111–122 GeV and 131–559 GeV. Three mass regions

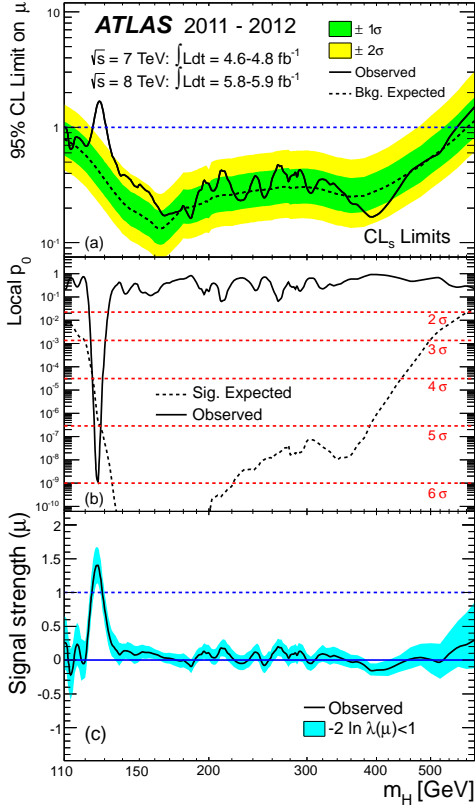


Figure 7: Combined search results: (a) The observed (solid) 95% CL limits on the signal strength as a function of m_H and the expectation (dashed) under the background-only hypothesis. The dark and light shaded bands show the $\pm 1\sigma$ and $\pm 2\sigma$ uncertainties on the background-only expectation. (b) The observed (solid) local p_0 as a function of m_H and the expectation (dashed) for a SM Higgs boson signal hypothesis ($\mu = 1$) at the given mass. (c) The best-fit signal strength $\hat{\mu}$ as a function of m_H . The band indicates the approximate 68% CL interval around the fitted value.

are excluded at 99% CL, 113–114, 117–121 and 132–527 GeV, while the expected exclusion range at 99% CL is 113–532 GeV.

9.2. Observation of an excess of events

An excess of events is observed near $m_H = 126$ GeV in the $H \rightarrow ZZ^{(*)} \rightarrow 4\ell$ and $H \rightarrow \gamma\gamma$ channels, both of which provide fully reconstructed candidates with high resolution in invariant mass, as shown in Figures 8(a) and 8(b). These excesses are confirmed by the highly sensitive but low-resolution $H \rightarrow WW^{(*)} \rightarrow \ell\nu\ell\nu$ channel, as shown in Fig. 8(c).

The observed local p_0 values from the combination of channels, using the asymptotic approximation, are shown as a function of m_H in Fig. 7(b) for the full mass range and in Fig. 9 for the low mass range.

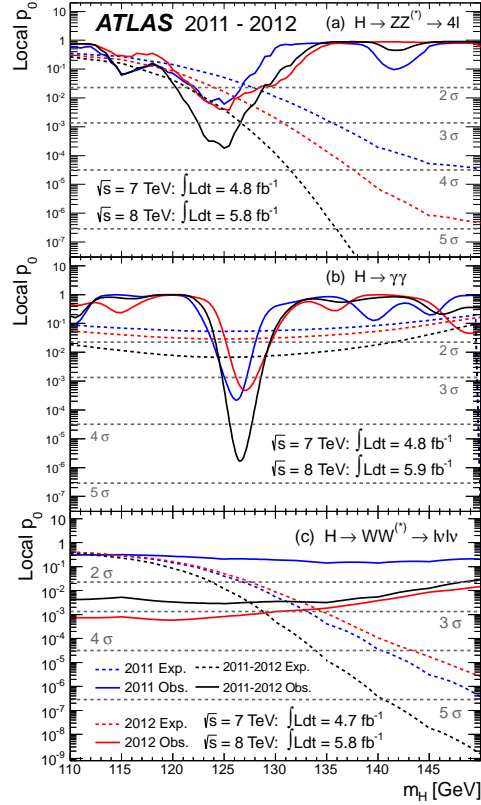


Figure 8: The observed local p_0 as a function of the hypothesised Higgs boson mass for the (a) $H \rightarrow ZZ^{(*)} \rightarrow 4\ell$, (b) $H \rightarrow \gamma\gamma$ and (c) $H \rightarrow WW^{(*)} \rightarrow \ell\nu\ell\nu$ channels. The dashed curves show the expected local p_0 under the hypothesis of a SM Higgs boson signal at that mass. Results are shown separately for the $\sqrt{s} = 7$ TeV data (dark, blue), the $\sqrt{s} = 8$ TeV data (light, red), and their combination (black).

The largest local significance for the combination of the 7 and 8 TeV data is found for a SM Higgs boson mass hypothesis of $m_H = 126.5$ GeV, where it reaches 6.0σ , with an expected value in the presence of a SM Higgs boson signal at that mass of 4.9σ (see also Table 7). For the 2012 data alone, the maximum local significance for the $H \rightarrow ZZ^{(*)} \rightarrow 4\ell$, $H \rightarrow \gamma\gamma$ and $H \rightarrow WW^{(*)} \rightarrow \ell\nu\ell\nu$ channels combined is 4.9σ , and occurs at $m_H = 126.5$ GeV (3.8σ expected).

The significance of the excess is mildly sensitive to uncertainties in the energy resolutions and energy scale systematic uncertainties for photons and electrons; the effect of the muon energy scale systematic uncertainties is negligible. The presence of these uncertainties, evaluated as described in Ref. [138], reduces the local significance to 5.9σ .

The global significance of a local 5.9σ excess anywhere in the mass range 110–600 GeV is estimated to be approximately 5.1σ , increasing to 5.3σ in the range

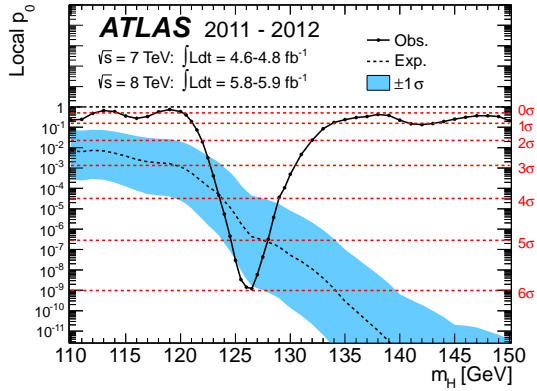


Figure 9: The observed (solid) local p_0 as a function of m_H in the low mass range. The dashed curve shows the expected local p_0 under the hypothesis of a SM Higgs boson signal at that mass with its $\pm 1\sigma$ band. The horizontal dashed lines indicate the p -values corresponding to significances of 1 to 6σ .

110–150 GeV, which is approximately the mass range not excluded at the 99% CL by the LHC combined SM Higgs boson search [139] and the indirect constraints from the global fit to precision electroweak measurements [12].

9.3. Characterising the excess

The mass of the observed new particle is estimated using the profile likelihood ratio $\lambda(m_H)$ for $H \rightarrow ZZ^{(*)} \rightarrow 4\ell$ and $H \rightarrow \gamma\gamma$, the two channels with the highest mass resolution. The signal strength is allowed to vary independently in the two channels, although the result is essentially unchanged when restricted to the SM hypothesis $\mu = 1$. The leading sources of systematic uncertainty come from the electron and photon energy scales and resolutions. The resulting estimate for the mass of the observed particle is 126.0 ± 0.4 (stat) ± 0.4 (sys) GeV.

The best-fit signal strength $\hat{\mu}$ is shown in Fig. 7(c) as a function of m_H . The observed excess corresponds to $\hat{\mu} = 1.4 \pm 0.3$ for $m_H = 126$ GeV, which is consistent with the SM Higgs boson hypothesis $\mu = 1$. A summary of the individual and combined best-fit values of the strength parameter for a SM Higgs boson mass hypothesis of 126 GeV is shown in Fig. 10, while more information about the three main channels is provided in Table 7.

In order to test which values of the strength and mass of a signal hypothesis are simultaneously consistent with the data, the profile likelihood ratio $\lambda(\mu, m_H)$ is used. In the presence of a strong signal, it will produce closed contours around the best-fit point $(\hat{\mu}, \hat{m}_H)$, while

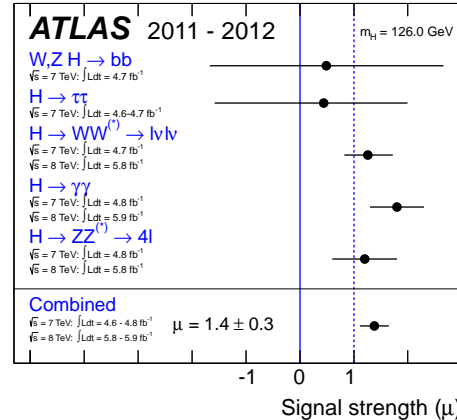


Figure 10: Measurements of the signal strength parameter μ for $m_H = 126$ GeV for the individual channels and their combination.

in the absence of a signal the contours will be upper limits on μ for all values of m_H .

Asymptotically, the test statistic $-2 \ln \lambda(\mu, m_H)$ is distributed as a χ^2 distribution with two degrees of freedom. The resulting 68% and 95% CL contours for the $H \rightarrow \gamma\gamma$ and $H \rightarrow WW^{(*)} \rightarrow \ell\nu\ell\nu$ channels are shown in Fig. 11, where the asymptotic approximations have been validated with ensembles of pseudo-experiments. Similar contours for the $H \rightarrow ZZ^{(*)} \rightarrow 4\ell$ channel are also shown in Fig. 11, although they are only approximate confidence intervals due to the smaller number of candidates in this channel. These contours in the (μ, m_H) plane take into account uncertainties in the energy scale and resolution.

The probability for a single Higgs boson-like particle to produce resonant mass peaks in the $H \rightarrow ZZ^{(*)} \rightarrow 4\ell$ and $H \rightarrow \gamma\gamma$ channels separated by more than the observed mass difference, allowing the signal strengths to vary independently, is about 8%.

The contributions from the different production modes in the $H \rightarrow \gamma\gamma$ channel have been studied in order to assess any tension between the data and the ratios of the production cross sections predicted in the Standard Model. A new signal strength parameter μ_i is introduced for each production mode, defined by $\mu_i = \sigma_i / \sigma_{i,SM}$. In order to determine the values of (μ_i, μ_j) that are simultaneously consistent with the data, the profile likelihood ratio $\lambda(\mu_i, \mu_j)$ is used with the measured mass treated as a nuisance parameter.

Since there are four Higgs boson production modes at the LHC, two-dimensional contours require either some μ_i to be fixed, or multiple μ_i to be related in some way. Here, μ_{ggF} and $\mu_{\bar{t}t}$ have been grouped together as they scale with the $t\bar{t}H$ coupling in the SM, and are denoted

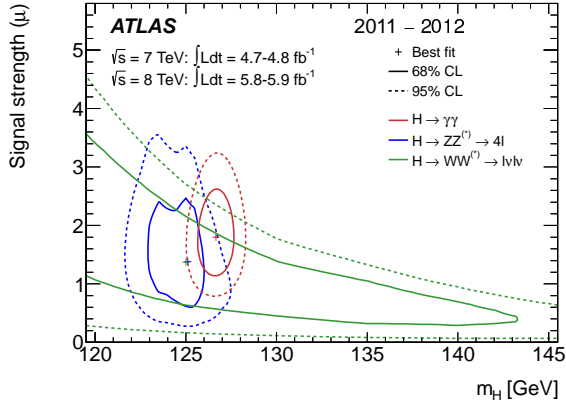


Figure 11: Confidence intervals in the (μ, m_H) plane for the $H \rightarrow ZZ^{(*)} \rightarrow 4\ell$, $H \rightarrow \gamma\gamma$, and $H \rightarrow WW^{(*)} \rightarrow \ell\nu\ell\nu$ channels, including all systematic uncertainties. The markers indicate the maximum likelihood estimates ($\hat{\mu}, \hat{m}_H$) in the corresponding channels (the maximum likelihood estimates for $H \rightarrow ZZ^{(*)} \rightarrow 4\ell$ and $H \rightarrow WW^{(*)} \rightarrow \ell\nu\ell\nu$ coincide).

by the common parameter $\mu_{\text{ggF}+\text{i}\bar{\text{i}}H}$. Similarly, μ_{VBF} and μ_{VH} have been grouped together as they scale with the WWH/ZZH coupling in the SM, and are denoted by the common parameter $\mu_{\text{VBF}+\text{VH}}$. Since the distribution of signal events among the 10 categories of the $H \rightarrow \gamma\gamma$ search is sensitive to these factors, constraints in the plane of $\mu_{\text{ggF}+\text{i}\bar{\text{i}}H} \times B/B_{\text{SM}}$ and $\mu_{\text{VBF}+\text{VH}} \times B/B_{\text{SM}}$, where B is the branching ratio for $H \rightarrow \gamma\gamma$, can be obtained (Fig. 12). Theoretical uncertainties are included so that the consistency with the SM expectation can be quantified. The data are compatible with the SM expectation at the 1.5σ level.

10. Conclusion

Searches for the Standard Model Higgs boson have been performed in the $H \rightarrow ZZ^{(*)} \rightarrow 4\ell$, $H \rightarrow \gamma\gamma$ and $H \rightarrow WW^{(*)} \rightarrow \ell\nu\ell\nu$ channels with the ATLAS experiment at the LHC using $5.8\text{--}5.9\text{ fb}^{-1}$ of pp collision data recorded during April to June 2012 at a centre-of-mass energy of 8 TeV. These results are combined with earlier results [17], which are based on an integrated luminosity of $4.6\text{--}4.8\text{ fb}^{-1}$ recorded in 2011 at a centre-of-mass energy of 7 TeV, except for the $H \rightarrow ZZ^{(*)} \rightarrow 4\ell$ and $H \rightarrow \gamma\gamma$ channels, which have been updated with the improved analyses presented here.

The Standard Model Higgs boson is excluded at 95% CL in the mass range $111\text{--}559\text{ GeV}$, except for the narrow region $122\text{--}131\text{ GeV}$. In this region, an excess of events with significance 5.9σ , corresponding to $p_0 = 1.7 \times 10^{-9}$, is observed. The excess is driven

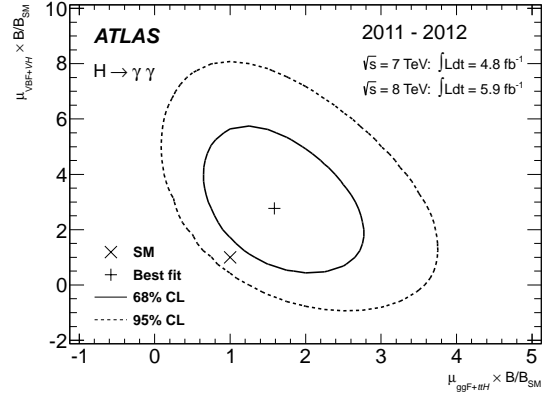


Figure 12: Likelihood contours for the $H \rightarrow \gamma\gamma$ channel in the $(\mu_{\text{ggF}+\text{i}\bar{\text{i}}H}, \mu_{\text{VBF}+\text{VH}})$ plane including the branching ratio factor B/B_{SM} . The quantity $\mu_{\text{ggF}+\text{i}\bar{\text{i}}H}$ ($\mu_{\text{VBF}+\text{VH}}$) is a common scale factor for the ggF and $\text{i}\bar{\text{i}}H$ (VBF and VH) production cross sections. The best fit to the data (+) and 68% (full) and 95% (dashed) CL contours are also indicated, as well as the SM expectation (\times).

by the two channels with the highest mass resolution, $H \rightarrow ZZ^{(*)} \rightarrow 4\ell$ and $H \rightarrow \gamma\gamma$, and the equally sensitive but low-resolution $H \rightarrow WW^{(*)} \rightarrow \ell\nu\ell\nu$ channel. Taking into account the entire mass range of the search, $110\text{--}600\text{ GeV}$, the global significance of the excess is 5.1σ , which corresponds to $p_0 = 1.7 \times 10^{-7}$.

These results provide conclusive evidence for the discovery of a new particle with mass 126.0 ± 0.4 (stat) ± 0.4 (sys) GeV. The signal strength parameter μ has the value 1.4 ± 0.3 at the fitted mass, which is consistent with the SM Higgs boson hypothesis $\mu = 1$. The decays to pairs of vector bosons whose net electric charge is zero identify the new particle as a neutral boson. The observation in the diphoton channel disfavors the spin-1 hypothesis [140, 141]. Although these results are compatible with the hypothesis that the new particle is the Standard Model Higgs boson, more data are needed to assess its nature in detail.

Acknowledgements

The results reported in this Letter would not have been possible without the outstanding performance of the LHC. We warmly thank CERN and the entire LHC exploitation team, including the operation, technical and infrastructure groups, and all the people who have contributed to the conception, design and construction of this superb accelerator. We thank also the support staff at our institutions without whose excellent contri-

butions ATLAS could not have been successfully constructed or operated so efficiently.

We acknowledge the support of ANPCyT, Argentina; YerPhI, Armenia; ARC, Australia; BMWF, Austria; ANAS, Azerbaijan; SSTC, Belarus; CNPq and FAPESP, Brazil; NSERC, NRC and CFI, Canada; CERN; CONICYT, Chile; CAS, MOST and NSFC, China; COLCIENCIAS, Colombia; MSMT CR, MPO CR and VSC CR, Czech Republic; DNRF, DNSRC and Lundbeck Foundation, Denmark; EPLANET and ERC, European Union; IN2P3-CNRS, CEA-DSM/IRFU, France; GNAS, Georgia; BMBF, DFG, HGF, MPG and AvH Foundation, Germany; GSRT, Greece; ISF, MINERVA, GIF, DIP and Benoziyo Center, Israel; INFN, Italy; MEXT and JSPS, Japan; CNRST, Morocco; FOM and NWO, Netherlands; RCN, Norway; MNiSW, Poland; GRICES and FCT, Portugal; MERYS (MECTS), Romania; MES of Russia and ROSATOM, Russian Federation; JINR; MSTD, Serbia; MSSR, Slovakia; ARRS and MVZT, Slovenia; DST/NRF, South Africa; MICINN, Spain; SRC and Wallenberg Foundation, Sweden; SER, SNSF and Cantons of Bern and Geneva, Switzerland; NSC, Taiwan; TAEK, Turkey; STFC, the Royal Society and Leverhulme Trust, United Kingdom; DOE and NSF, United States of America.

The crucial computing support from all WLCG partners is acknowledged gratefully, in particular from CERN and the ATLAS Tier-1 facilities at TRIUMF (Canada), NDGF (Denmark, Norway, Sweden), CC-IN2P3 (France), KIT/GridKA (Germany), INFN-CNAF (Italy), NL-T1 (Netherlands), PIC (Spain), ASGC (Taiwan), RAL (UK) and BNL (USA) and in the Tier-2 facilities worldwide.

References

- [1] S. L. Glashow, *Partial-symmetries of weak interactions*, Nucl. Phys. **22** no. 4, (1961) 579.
- [2] S. Weinberg, *A Model of Leptons*, Phys. Rev. Lett. **19** (1967) 1264.
- [3] A. Salam, “*Weak and electromagnetic interactions*”, in *Elementary particle theory: relativistic groups and analyticity*, N. Svartholm, ed., p. 367. Almqvist & Wiksell, 1968. Proceedings of the eighth Nobel symposium.
- [4] G. ’t Hooft and M. Veltman, *Regularization and Renormalization of Gauge Fields*, Nucl. Phys. **B44** (1972) 189.
- [5] F. Englert and R. Brout, *Broken symmetry and the mass of gauge vector mesons*, Phys. Rev. Lett. **13** (1964) 321.
- [6] P. W. Higgs, *Broken symmetries, massless particles and gauge fields*, Phys. Lett. **12** (1964) 132.
- [7] P. W. Higgs, *Broken symmetries and the masses of gauge bosons*, Phys. Rev. Lett. **13** (1964) 508.
- [8] G. S. Guralnik, C. R. Hagen, and T. W. B. Kibble, *Global conservation laws and massless particles*, Phys. Rev. Lett. **13** (1964) 585.
- [9] P. W. Higgs, *Spontaneous symmetry breakdown without massless bosons*, Phys. Rev. **145** (1966) 1156.
- [10] T. W. B. Kibble, *Symmetry breaking in non-Abelian gauge theories*, Phys. Rev. **155** (1967) 1554.
- [11] L. Evans and P. Bryant (Eds.), *LHC Machine*, JINST **3** (2008) S08001.
- [12] ALEPH, CDF, DØ, DELPHI, L3, OPAL, SLD Collaborations, the LEP Electroweak Working Group, the Tevatron Electroweak Working Group, and the SLD electroweak and heavy flavour groups, *Precision Electroweak Measurements and Constraints on the Standard Model*, CERN-PH-EP-2010-095 (2010), arXiv:1012.2367 [hep-ex].
- [13] ALEPH, DELPHI, L3 and OPAL Collaborations, The LEP Working Group for Higgs boson searches, *Search for the standard model Higgs boson at LEP*, Phys. Lett. **B 565** (2003) 61.
- [14] CDF Collaboration, T. Aaltonen et al., *Combined search for the standard model Higgs boson decaying to a $b\bar{b}$ pair using the full CDF data set*, accepted by Phys. Rev. Lett. (2012), arXiv:1207.1707 [hep-ex].
- [15] DØ Collaboration, V. M. Abazov et al., *Combined search for the standard model Higgs boson decaying to $b\bar{b}$ using the DØ Run II data set*, submitted to Phys. Rev. Lett. (2012), arXiv:1207.6631 [hep-ex].
- [16] CDF Collaboration, DØ Collaboration, *Evidence for a particle produced in association with weak bosons and decaying to a bottom-antibottom quark pair in Higgs boson searches at the Tevatron*, submitted to Phys. Rev. Lett. (2012), arXiv:1207.6436 [hep-ex].
- [17] ATLAS Collaboration, *Combined search for the Standard Model Higgs boson in pp collisions at $\sqrt{s}=7$ TeV with the ATLAS detector*, Phys. Rev. **D86** (2012) 032003.
- [18] CMS Collaboration, *Combined results of searches for the standard model Higgs boson in pp collisions at $\sqrt{s} = 7$ TeV*, Phys. Lett. **B 710** (2012) 26.
- [19] ATLAS Collaboration, *ATLAS: letter of intent for a general-purpose pp experiment at the large hadron collider at CERN*, CERN-LHCC-92-004 (1992).
- [20] ATLAS Collaboration, *ATLAS Technical Proposal for a General-Purpose pp Experiment at the Large Hadron Collider at CERN*, CERN-LHCC-94-43 (1994).
- [21] ATLAS Collaboration, *The ATLAS Experiment at the CERN Large Hadron Collider*, JINST **3** (2008) S08003.
- [22] H. M. Georgi, S. L. Glashow, M. E. Machacek, and D. V. Nanopoulos, *Higgs bosons from two gluon-annihilation in proton-proton collisions*, Phys. Rev. Lett. **40** (1978) 692.
- [23] A. Djouadi, M. Spira, and P. M. Zerwas, *Production of Higgs bosons in proton colliders: QCD corrections*, Phys. Lett. **B 264** (1991) 440.
- [24] S. Dawson, *Radiative corrections to Higgs boson production*, Nucl. Phys. **B359** (1991) 283.
- [25] M. Spira, A. Djouadi, D. Graudenz, and P. M. Zerwas, *Higgs boson production at the LHC*, Nucl. Phys. **B453** (1995) 17.
- [26] R. V. Harlander and W. B. Kilgore, *Next-to-next-to-leading order Higgs production at hadron colliders*, Phys. Rev. Lett. **88** (2002) 201801.
- [27] C. Anastasiou and K. Melnikov, *Higgs boson production at hadron colliders in NNLO QCD*, Nucl. Phys. **B646** (2002) 220.
- [28] V. Ravindran, J. Smith, and W. L. van Neerven, *NNLO corrections to the total cross section for Higgs boson production in hadron-hadron collisions*, Nucl. Phys. **B665** (2003) 325.
- [29] U. Aglietti, R. Bonciani, G. Degrossi, and A. Vicini, *Two-loop*

- light fermion contribution to Higgs production and decays, Phys. Lett. **B 595** (2004) 432.
- [30] S. Actis, G. Passarino, C. Sturm, and S. Uccirati, *NLO electroweak corrections to Higgs boson production at hadron colliders*, Phys. Lett. **B 670** (2008) 12.
- [31] S. Catani, D. de Florian, M. Grazzini, and P. Nason, *Soft-gluon resummation for Higgs boson production at hadron colliders*, JHEP **0307** (2003) 028.
- [32] C. Anastasiou, R. Boughezal, and F. Petriello, *Mixed QCD-electroweak corrections to Higgs boson production in gluon fusion*, JHEP **0904** (2009) 003.
- [33] D. de Florian and M. Grazzini, *Higgs production at the LHC: updated cross sections at $\sqrt{s} = 8$ TeV*, arXiv:1206.4133 [hep-ph].
- [34] C. Anastasiou, S. Buehler, F. Herzog, and A. Lazopoulos, *Inclusive Higgs boson cross-section for the LHC at 8 TeV*, JHEP **1204** (2012) 004.
- [35] J. Baglio and A. Djouadi, *Higgs production at the LHC*, JHEP **1103** (2011) 055.
- [36] D. de Florian, G. Ferrera, M. Grazzini, and D. Tommasini, *Transverse-momentum resummation: Higgs boson production at the Tevatron and the LHC*, JHEP **1111** (2011) 064.
- [37] E. Bagnaschi, G. Degrassi and A. Vicini, *Higgs production via gluon fusion in the POWHEG approach in the SM and in the MSSM*, JHEP **1202** (2012) 88.
- [38] R. N. Cahn and S. Dawson, *Production of very massive Higgs bosons*, Phys. Lett. **B 136** (1984) 196, Erratum–ibid. **B 138** (1984) 464.
- [39] M. Ciccolini, A. Denner, and S. Dittmaier, *Strong and electroweak corrections to the production of Higgs + 2 jets via weak interactions at the Large Hadron Collider*, Phys. Rev. Lett. **99** (2007) 161803.
- [40] M. Ciccolini, A. Denner, and S. Dittmaier, *Electroweak and QCD corrections to Higgs production via vector-boson fusion at the Large Hadron Collider*, Phys. Rev. **D77** (2008) 013002.
- [41] K. Arnold et al., *VBFNLO: A parton level Monte Carlo for processes with electroweak bosons*, Comput. Phys. Commun. **180** (2009) 1661.
- [42] P. Bolzoni, F. Maltoni, S.-O. Moch, and M. Zaro, *Higgs boson production via vector-boson fusion at next-to-next-to-leading order in QCD*, Phys. Rev. Lett. **105** (2010) 011801.
- [43] S. L. Glashow, D. V. Nanopoulos, and A. Yildiz, *Associated production of Higgs bosons and Z particles*, Phys. Rev. **D18** (1978) 1724.
- [44] T. Han and S. Willenbrock, *QCD correction to the $pp \rightarrow WH$ and ZH total cross sections*, Phys. Lett. **B 273** (1991) 167.
- [45] O. Brein, A. Djouadi, and R. Harlander, *NNLO QCD corrections to the Higgs-strahlung processes at hadron colliders*, Phys. Lett. **B 579** (2004) 149.
- [46] M. L. Ciccolini, S. Dittmaier, and M. Krämer, *Electroweak radiative corrections to associated WH and ZH production at hadron colliders*, Phys. Rev. **D68** (2003) 073003.
- [47] Z. Kunszt, *Associated production of heavy Higgs boson with top quarks*, Nucl. Phys. **B247** (1984) 339.
- [48] W. Beenakker et al., *Higgs Radiation Off Top Quarks at the Tevatron and the LHC*, Phys. Rev. Lett. **87** (2001) 201805.
- [49] W. Beenakker et al., *NLO QCD corrections to $t\bar{t}H$ production in hadron collisions*, Nucl. Phys. **B653** (2003) 151.
- [50] S. Dawson, L. H. Orr, L. Reina, and D. Wackerth, *Next-to-leading order QCD corrections to $pp \rightarrow t\bar{t}H$ at the CERN Large Hadron Collider*, Phys. Rev. **D67** (2003) 071503.
- [51] S. Dawson, C. Jackson, L. H. Orr, L. Reina, and D. Wackerth, *Associated Higgs boson production with top quarks at the CERN Large Hadron Collider: NLO QCD corrections*, Phys. Rev. **D68** (2003) 034022.
- [52] LHC Higgs Cross Section Working Group, S. Dittmaier, C. Mariotti, G. Passarino, and R. Tanaka (Eds.), *Handbook of LHC Higgs Cross Sections: 1. Inclusive Observables*, CERN-2011-002 (2011), arXiv:1101.0593 [hep-ph].
- [53] LHC Higgs Cross Section Working Group, S. Dittmaier, C. Mariotti, G. Passarino, and R. Tanaka (Eds.), *Handbook of LHC Higgs Cross Sections: 2. Differential Distributions*, CERN-2012-002 (2012), arXiv:1201.3084 [hep-ph].
- [54] A. Djouadi, J. Kalinowski, and M. Spira, *HDECAY: A program for Higgs boson decays in the standard model and its supersymmetric extension*, Comput. Phys. Commun. **108** (1998) 56.
- [55] A. Bredenstein, A. Denner, S. Dittmaier, and M. M. Weber, *Precise predictions for the Higgs-boson decay $H \rightarrow WW/ZZ \rightarrow 4$ leptons*, Phys. Rev. **D74** (2006) 013004.
- [56] A. Bredenstein, A. Denner, S. Dittmaier, and M. M. Weber, *Radiative corrections to the semileptonic and hadronic Higgs-boson decays $H \rightarrow WW/ZZ \rightarrow 4$ fermions*, JHEP **0702** (2007) 080.
- [57] S. Alioli, P. Nason, C. Oleari, and E. Re, *NLO Higgs boson production via gluon fusion matched with shower in POWHEG*, JHEP **0904** (2009) 002.
- [58] P. Nason and C. Oleari, *NLO Higgs boson production via vector-boson fusion matched with shower in POWHEG*, JHEP **1002** (2010) 037.
- [59] M. L. Mangano et al., *ALPGEN, a generator for hard multiparton processes in hadronic collisions*, JHEP **0307** (2003) 001.
- [60] S. Frixione and B. R. Webber, *Matching NLO QCD computations and parton shower simulations*, JHEP **0206** (2002) 029; S. Frixione, P. Nason, and B. R. Webber, *Matching NLO QCD and parton showers in heavy flavour production*, JHEP **0308** (2003) 007; S. Frixione, E. Laenen, P. Motylinski, and B. R. Webber, *Single-top production in MC@NLO*, JHEP **0603** (2006) 092; S. Frixione, E. Laenen, P. Motylinski, C. White, and B. R. Webber, *Single-top hadroproduction in association with a W boson*, JHEP **0807** (2008) 029; S. Frixione, F. Stoeckli, P. Torrielli, and B. R. Webber, *NLO QCD corrections in Herwig++ with MC@NLO*, JHEP **1101** (2011) 053.
- [61] B. P. Kersevan and E. Richter-Was, *The Monte Carlo event generator AcerMC version 2.0 with interfaces to PYTHIA 6.2 and HERWIG 6.5*, arXiv:hep-ph/0405247.
- [62] T. Binoth, M. Ciccolini, N. Kauer and M. Krämer, *Gluon-induced W-boson pair production at the LHC*, JHEP **0612** (2006) 046.
- [63] T. Melia, P. Nason, R. Röntsch, and G. Zanderighi, *W^+W^- , WZ and ZZ production in the POWHEG BOX*, JHEP **1111** (2011) 078.
- [64] T. Binoth, N. Kauer and P. Mertsch, *Gluon-induced QCD Corrections to $pp \rightarrow ZZ \rightarrow \ell\bar{\ell}'\ell'$* , arXiv:0807.0024 [hep-ph].
- [65] R. C. Gray, C. Kilic, M. Park, S. Somalwar, and S. Thomas, *Backgrounds to Higgs Boson Searches from $W\gamma^* \rightarrow l\nu(l)$ Asymmetric Internal Conversion*, arXiv:1110.1368 [hep-ph].
- [66] ATLAS Collaboration, *New ATLAS event generator tunes to 2010 data*, ATL-PHYS-PUB-2011-008 (2011). <http://cdsweb.cern.ch/record/1345343>.
- [67] ATLAS Collaboration, *ATLAS tunes of PYTHIA 6 and Pythia 8 for MC11*, ATL-PHYS-PUB-2011-009 (2011). <http://cdsweb.cern.ch/record/1363300>.

- [68] ATLAS Collaboration, *Further ATLAS tunes of PYTHIA6 and Pythia 8*, ATL-PHYS-PUB-2011-014 (2011). <http://cdsweb.cern.ch/record/1400677>.
- [69] T. Sjöstrand, S. Mrenna, and P. Skands, *PYTHIA 6.4 physics and manual*, JHEP **0605** (2006) 026.
- [70] J. Alwall et al., *MadGraph/MadEvent v4: The New Web Generation*, JHEP **0709** (2007) 028.
- [71] J. Alwall, M. Herquet, F. Maltoni, O. Mattelaer, and T. Stelzer, *MadGraph 5 : Going Beyond*, JHEP **1106** (2011) 128.
- [72] T. Sjöstrand, S. Mrenna, and P. Skands, *A Brief Introduction to PYTHIA 8.1*, Comput. Phys. Commun. **178** (2008) 852.
- [73] G. Corcella, I. Knowles, G. Marchesini, S. Moretti, K. Odagiri, et al., *HERWIG 6: An Event generator for hadron emission reactions with interfering gluons (including supersymmetric processes)*, JHEP **0101** (2001) 010.
- [74] T. Gleisberg et al., *Event generation with SHERPA 1.1*, JHEP **0902** (2009) 007.
- [75] J. M. Butterworth, J. R. Forshaw, and M. H. Seymour, *Multiparton interactions in photoproduction at HERA*, Z. Phys. **C72** (1996) 637.
- [76] S. Jadach, Z. Was, R. Decker, and J. H. Kuhn, *The tau decay library TAUOLA: Version 2.4*, Comput. Phys. Commun. **76** (1993) 361.
- [77] P. Golonka and Z. Was, *PHOTOS Monte Carlo: A Precision tool for QED corrections in Z and W decays*, Eur.Phys.J. **C45** (2006) 97.
- [78] H.-L. Lai et al., *New parton distributions for collider physics*, Phys. Rev. **D82** (2010) 074024.
- [79] P. M. Nadolsky et al., *Implications of CTEQ global analysis for collider observables*, Phys. Rev. **D78** (2008) 013004.
- [80] A. Sherstnev and R. S. Thorne, *Parton distributions for LO Generators*, Eur. Phys. J **C55** (2008) 553.
- [81] ATLAS Collaboration, *The ATLAS Simulation Infrastructure*, Eur. Phys. J. **C70** (2010) 823.
- [82] S. Agostinelli et al., *GEANT4, a simulation toolkit*, Nucl. Instrum. Meth. **A506** (2003) 250.
- [83] ATLAS Collaboration, *Search for the Standard Model Higgs boson in the decay channel $H \rightarrow ZZ^{(*)} \rightarrow 4\ell$ with 4.8 fb^{-1} of pp collision data at $\sqrt{s} = 7 \text{ TeV}$ with ATLAS*, Phys. Lett. **B 710** (2012) 383.
- [84] ATLAS Collaboration, *Muon reconstruction efficiency in reprocessed 2010 LHC proton-proton collision data recorded with the ATLAS detector*, ATLAS-CONF-2011-063 (2011). <http://cdsweb.cern.ch/record/1345743>.
- [85] ATLAS Collaboration, *Electron performance measurements with the ATLAS detector using the 2010 LHC proton-proton collision data*, Eur. Phys. J. **C72** (2012) 1909.
- [86] ATLAS Collaboration, *Improved electron reconstruction in ATLAS using the Gaussian Sum Filter-based model for bremsstrahlung*. <http://cdsweb.cern.ch/record/1449796>.
- [87] ATLAS Collaboration, *Observation of an excess of events in the search for the Standard Model Higgs boson in the $H \rightarrow ZZ^{(*)} \rightarrow 4\ell$ channel with the ATLAS detector*, ATLAS-CONF-2012-092 (2012). <http://cdsweb.cern.ch/record/1460411>.
- [88] W. Lampl, S. Laplace, D. Lelas, P. Loch, H. Ma, S. Menke, S. Rajagopalan, D. Rousseau, S. Snyder, and G. Unal, *Calorimeter Clustering Algorithms: Description and Performance*, ATL-LARG-PUB-2008-002 (2008). <http://cdsweb.cern.ch/record/1099735>.
- [89] M. Cacciari and G. P. Salam, *Pileup subtraction using jet areas*, Phys. Lett. **B 659** (2008) 119.
- [90] M. Cacciari, G. P. Salam, and G. Soyez, *FastJet user manual*, Eur. Phys. J. **C72** (2012) 1896.
- [91] ATLAS Collaboration, *Measurements of the electron and muon inclusive cross-sections in proton-proton collisions at $\sqrt{s} = 7 \text{ TeV}$ with the ATLAS detector*, Phys. Lett. **B 707** (2012) 438.
- [92] ATLAS Collaboration, *Improved Luminosity Determination in pp Collisions at $\sqrt{s} = 7 \text{ TeV}$ using the ATLAS Detector at the LHC*, ATLAS-CONF-2012-080 (2012). <http://cdsweb.cern.ch/record/1460392>.
- [93] ATLAS Collaboration, *Measurement of the total ZZ production cross section in the four-lepton channel using 5.8 fb^{-1} of ATLAS data at $\sqrt{s} = 8 \text{ TeV}$* , ATLAS-CONF-2012-090 (2012). <http://cdsweb.cern.ch/record/1460409>.
- [94] N. Kauer and G. Passarino, *Inadequacy of zero-width approximation for a light Higgs boson signal*, arXiv:1206.4803 [hep-ph].
- [95] ATLAS Collaboration, *Search for the Standard Model Higgs boson in the diphoton decay channel with 4.9 fb^{-1} of pp collision data at $\sqrt{s} = 7 \text{ TeV}$ with ATLAS*, Phys. Rev. Lett. **108** (2012) 111803.
- [96] ATLAS Collaboration, *Performance of the ATLAS Trigger System in 2010*, Eur. Phys. J. **C72** (2012) 1849.
- [97] ATLAS Collaboration, *Measurement of the inclusive isolated prompt photon cross section in pp collisions at $\sqrt{s} = 7 \text{ TeV}$ with the ATLAS detector*, Phys. Rev. **D83** (2011) 052005.
- [98] ATLAS Collaboration, *Search for the Standard Model Higgs boson in the two photon decay channel with the ATLAS detector at the LHC*, Phys. Lett. **B 705** (2011) 452.
- [99] OPAL Collaboration, K. Ackerstaff et al., *Search for anomalous production of dilepton events with missing transverse momentum in e^+e^- collisions at $\sqrt{s} = 161 \text{ GeV}$ and 172 GeV* , Eur. Phys. J. **C4** (1998) 47, arXiv:hep-ex/9710010 [hep-ex].
- [100] M. Vesterinen and T. R. Wyatt, *A Novel Technique for Studying the Z Boson Transverse Momentum Distribution at Hadron Colliders*, Nucl. Instrum. Meth. **A602** (2009) 432.
- [101] ATLAS Collaboration, *Jet energy measurement with the ATLAS detector in proton-proton collisions at $\sqrt{s} = 7 \text{ TeV}$* , submitted to Eur. Phys. J. C (2011), arXiv:1112.6426 [hep-ex].
- [102] M. Cacciari, G. P. Salam, and G. Soyez, *The anti-k_t jet clustering algorithm*, JHEP **0804** (2008) 063.
- [103] L. J. Dixon and M. S. Siu, *Resonance continuum interference in the diphoton Higgs signal at the LHC*, Phys. Rev. Lett. **90** (2003) 252001.
- [104] J. Gaiser, *Charmonium spectroscopy from radiative decays of the J/Ψ and Ψ'* , Ph.D. Thesis No. SLAC-R-255, (1982).
- [105] S. N. Bernstein, *Démonstration du théorème de Weierstrass fondée sur le calcul des probabilités*, Comm. Soc. Math. Kharkov **13** (1912) 1.
- [106] ATLAS Collaboration, *Search for the Standard Model Higgs boson in the $H \rightarrow WW^{(*)} \rightarrow \ell\nu\ell\nu$ decay mode with 4.7 fb^{-1} of ATLAS data at $\sqrt{s} = 7 \text{ TeV}$* , Phys. Lett. **B 716** (2012) 62.
- [107] M. Dittmar and H. Dreiner, *How to find a Higgs boson with a mass between 155 and 180 GeV at the CERN LHC*, Phys. Rev. **D55** (1997) 167.
- [108] ATLAS Collaboration, *Commissioning of the ATLAS high-performance b-tagging algorithms in the 7 TeV collision data*, ATLAS-CONF-2011-102 (2011). <http://cdsweb.cern.ch/record/1369219>.
- [109] R.K. Ellis et al., *Higgs decay to $\tau^+\tau^-$: A possible signature of intermediate mass Higgs bosons at the SSC*, Nucl. Phys. **B297** (1988) 221.
- [110] A. J. Barr, B. Gripaios, and C. G. Lester, *Measuring the Higgs boson mass in dileptonic W-boson decays at hadron colliders*, JHEP **0907** (2009) 072.

- [111] ATLAS Collaboration, *Search for the Higgs boson in the $H \rightarrow WW^{(*)} \rightarrow \ell\nu\ell\nu$ decay channel in pp collisions at $\sqrt{s} = 7$ TeV with the ATLAS detector*, Phys. Rev. Lett. **108** (2012) 111802.
- [112] ATLAS Collaboration, *Limits on the production of the Standard Model Higgs Boson in pp collisions at $\sqrt{s} = 7$ TeV with the ATLAS detector*, Eur. Phys. J. **C 71** (2011) 1728.
- [113] ATLAS Collaboration, *Performance of missing transverse momentum reconstruction in proton-proton collisions at 7 TeV with ATLAS*, Eur. Phys. J. **C72** (2012) 1844.
- [114] ATLAS Collaboration, *Measurement of the b -tag Efficiency in a Sample of Jets Containing Muons with 5 fb^{-1} of Data from the ATLAS Detector*, ATLAS-CONF-2012-043 (2012). <http://cdsweb.cern.ch/record/1435197>.
- [115] J. M. Campbell, R. K. Ellis, and C. Williams, *Vector boson pair production at the LHC*, JHEP **1107** (2011) 018.
- [116] J. Campbell, R. Ellis, and C. Williams, *Gluon-gluon contributions to W^+W^- production and Higgs interference effects*, JHEP **1110** (2011) 005.
- [117] I. Stewart and F. Tackmann, *Theory uncertainties for Higgs mass and other searches using jet bins*, Phys. Rev. **D85** (2012) 034011.
- [118] ATLAS and CMS Collaborations, *Procedure for the LHC Higgs boson search combination in Summer 2011*, ATL-PHYS-PUB-2011-011, CERN-CMS-NOTE-2011-005 (2011). <http://cdsweb.cern.ch/record/1375842>.
- [119] L. Moneta, K. Belasco, K. S. Cranmer, S. Kreiss, A. Lazzaro, et al., *The RooStats Project*, PoS **ACAT2010** (2010) 057, arXiv:1009.1003 [physics.data-an].
- [120] K. Cranmer, G. Lewis, L. Moneta, A. Shibata, and W. Verkerke, *HistFactory: A tool for creating statistical models for use with RooFit and RooStats*, CERN-OPEN-2012-016 (2012). <http://cdsweb.cern.ch/record/1456844>.
- [121] W. Verkerke and D. Kirkby, *The RooFit toolkit for data modeling*, Tech. Rep. physics/0306116, SLAC, Stanford, CA, Jun, 2003. arXiv:physics/0306116 [physics.data-an].
- [122] G. Cowan, K. Cranmer, E. Gross, and O. Vitells, *Asymptotic formulae for likelihood-based tests of new physics*, Eur. Phys. J. **C71** (2011) 1554.
- [123] A. L. Read, *Presentation of search results: The CL_s technique*, J. Phys. **G28** (2002) 2693.
- [124] E. Gross and O. Vitells, *Trial factors for the look elsewhere effect in high energy physics*, Eur. Phys. J. **C 70** (2010) 525.
- [125] ATLAS Collaboration, *Search for a Standard Model Higgs boson in the $H \rightarrow ZZ \rightarrow ll\nu\nu$ decay channel using 4.7 fb^{-1} of $\sqrt{s} = 7$ TeV data with the ATLAS detector*, submitted to Phys. Lett. **B** (2012), arXiv:1205.6744 [hep-ex].
- [126] ATLAS Collaboration, *Search for a Standard Model Higgs boson in the mass range 200-600 GeV in the $H \rightarrow ZZ \rightarrow llqq$ decay channel*, submitted to Phys. Lett. **B** (2012), arXiv:1206.2443 [hep-ex].
- [127] ATLAS Collaboration, *Observation of an excess of events in the search for the Standard Model Higgs boson in the gamma-gamma channel with the ATLAS detector*, ATLAS-CONF-2012-091 (2012). <http://cdsweb.cern.ch/record/1460410>.
- [128] ATLAS Collaboration, *Search for the Higgs boson in the $H \rightarrow WW \rightarrow l\nu jj$ decay channel at $\sqrt{s} = 7$ TeV with the ATLAS detector*, submitted to Phys. Lett. **B** (2012), arXiv:1206.6074 [hep-ex].
- [129] ATLAS Collaboration, *Search for the Standard Model Higgs boson in the $H \rightarrow \tau^+\tau^-$ decay mode in $\sqrt{s} = 7$ TeV pp collisions with ATLAS*, accepted by JHEP (2012), arXiv:1206.5971 [hep-ex].
- [130] ATLAS Collaboration, *Search for the Standard Model Higgs boson produced in association with a vector boson and decaying to a b -quark pair with the ATLAS detector*, submitted to Phys. Lett. **B** (2012), arXiv:1207.0210 [hep-ex].
- [131] ATLAS Collaboration, *Observation of an Excess of Events in the Search for the Standard Model Higgs Boson in the $H \rightarrow WW^{(*)} \rightarrow \ell\nu\ell\nu$ Channel with the ATLAS Detector*, ATLAS-CONF-2012-098 (2012). <http://cdsweb.cern.ch/record/1462530>.
- [132] ATLAS Collaboration, *Luminosity Determination in pp Collisions at $\sqrt{s} = 7$ TeV Using the ATLAS Detector at the LHC*, Eur. Phys. J. **C 71** (2011) 1630.
- [133] ATLAS Collaboration, *Luminosity Determination in pp Collisions at $\sqrt{s} = 7$ TeV using the ATLAS Detector in 2011*, ATLAS-CONF-2011-116 (2011). <http://cdsweb.cern.ch/record/1376384>.
- [134] M. Botje, J. Butterworth, A. Cooper-Sarkar, A. de Roeck, J. Feltesse, et al., *The PDF4LHC Working Group Interim Recommendations*, arXiv:1101.0538 [hep-ph].
- [135] A. Martin, W. Stirling, R. Thorne, and G. Watt, *Parton distributions for the LHC*, Eur. Phys. J. **C63** (2009) 189.
- [136] R. D. Ball et al., *Impact of heavy quark masses on parton distributions and LHC phenomenology*, Nucl. Phys. **B 849** (2011) 296.
- [137] J. M. Campbell, R. K. Ellis, and G. Zanderighi, *Next-to-Leading order Higgs + 2 jet production via gluon fusion*, JHEP **0610** (2006) 028.
- [138] ATLAS Collaboration, *Observation of an Excess of Events in the Search for the Standard Model Higgs boson with the ATLAS detector at the LHC*, ATLAS-CONF-2012-093 (2012). <http://cdsweb.cern.ch/record/1460439>.
- [139] ATLAS and CMS Collaborations, *Combined Standard Model Higgs boson searches with up to 2.3 fb^{-1} of pp collisions at $\sqrt{s}=7$ TeV at the LHC*, ATLAS-CONF-2011-157, CMS-PAS-HIG-11-023 (2011). <http://cdsweb.cern.ch/record/1399599>.
- [140] L. D. Landau, *The moment of a 2-photon system*, Dokl. Akad. Nauk. **USSR 60** (1948) 207.
- [141] C. N. Yang, *Selection Rules for the Dematerialization of a Particle Into Two Photons*, Phys. Rev. **77** (1950) 242.

Measurements of Higgs boson production and couplings in diboson final states with the ATLAS detector at the LHC

Abstract

Measurements are presented of production properties and couplings of the recently discovered Higgs boson using the decays into boson pairs, $H \rightarrow \gamma\gamma$, $H \rightarrow ZZ^* \rightarrow 4\ell$ and $H \rightarrow WW^* \rightarrow \ell\nu\ell\nu$. The results are based on the complete pp collision data sample recorded by the ATLAS experiment at the CERN Large Hadron Collider at centre-of-mass energies of $\sqrt{s}=7$ TeV and $\sqrt{s}=8$ TeV, corresponding to an integrated luminosity of about 25 fb^{-1} . Evidence for Higgs boson production through vector-boson fusion is reported. Results of combined fits probing Higgs boson couplings to fermions and bosons, as well as anomalous contributions to loop-induced production and decay modes, are presented. All measurements are consistent with expectations for the Standard Model Higgs boson.

1. Introduction

The discovery of a new particle of mass about 125 GeV in the search for the Standard Model (SM) Higgs boson at the CERN Large Hadron Collider (LHC) [1], reported in July 2012 by the ATLAS [2] and CMS [3] Collaborations, is a milestone in the quest to understand the origin of electroweak symmetry breaking [4–9].

This paper presents measurements of several properties of the newly observed particle, including its mass, production strengths and couplings to fermions and bosons, using diboson final states:¹ $H \rightarrow \gamma\gamma$, $H \rightarrow ZZ^* \rightarrow 4\ell$, and $H \rightarrow WW^* \rightarrow \ell\nu\ell\nu$. Spin studies are reported elsewhere [10]. Due to the outstanding performance of the LHC accelerator throughout 2012, the present data sample is a factor of ~ 2.5 larger than that used in Ref. [2]. With these additional data, many aspects of the ATLAS studies have been improved: several experimental uncertainties have been reduced and new exclusive analyses have been included. In particular, event categories targeting specific production modes have been introduced, providing enhanced sensitivity to different Higgs boson couplings.

The results reported here are based on the data samples recorded with the ATLAS detector [11] in 2011 (at $\sqrt{s} = 7$ TeV) and 2012 (at $\sqrt{s} = 8$ TeV), corresponding to integrated luminosities of about 4.7 fb^{-1} and 20.7 fb^{-1} , respectively. Similar studies, including

also fermionic decays, have been reported recently by the CMS Collaboration using a smaller dataset [12].

This paper is organised as follows. Section 2 describes the data sample and the event reconstruction. Section 3 summarises the Monte Carlo (MC) samples used to model signal and background processes. The analyses of the three decay channels are presented in Sections 4–6. Measurements of the Higgs boson mass, production properties and couplings are discussed in Section 7. Section 8 is devoted to the conclusions.

2. Data sample and event reconstruction

After data quality requirements, the integrated luminosities of the samples used for the studies reported here are about 4.7 fb^{-1} in 2011 and 20.7 fb^{-1} in 2012, with uncertainties given in Table 1 (determined as described in Ref. [13]). Because of the high LHC peak luminosity (up to $7.7 \times 10^{33} \text{ cm}^{-2} \text{ s}^{-1}$ in 2012) and the 50 ns bunch spacing, the number of proton–proton interactions occurring in the same bunch crossing is large (on average 20.7, up to about 40). This “pile-up” of events requires the use of dedicated algorithms and corrections to mitigate its impact on the reconstruction of *e.g.* leptons, photons and jets.

For the $H \rightarrow ZZ^* \rightarrow 4\ell$ and $H \rightarrow WW^* \rightarrow \ell\nu\ell\nu$ channels, the primary vertex of the event is defined as the reconstructed vertex with the highest $\sum p_{\text{T}}^2$, where p_{T} is the magnitude of the transverse momentum² of each

¹Throughout this paper, the symbol ℓ stands for electron or muon.

²ATLAS uses a right-handed coordinate system with its origin at

Table 1: Main sources of experimental uncertainty, and of theoretical uncertainty on the signal yield, common to the three channels considered in this study. Theoretical uncertainties are given for a SM Higgs boson of mass $m_H = 125$ GeV and are taken from Refs. [14–16]. “QCD scale” indicates (here and throughout this paper) QCD renormalisation and factorisation scales and “PDFs” indicates parton distribution functions. The ranges for the experimental uncertainties cover the variations with p_T and η .

Source (experimental)	Uncertainty (%)
Luminosity	± 1.8 (2011), ± 3.6 (2012)
Electron efficiency	± 2 – 5
Jet energy scale	± 1 – 5
Jet energy resolution	± 2 – 40
Source (theory)	Uncertainty (%)
QCD scale	± 8 (ggF), ± 1 (VBF, VH), $^{+4}_{-9}$ (ttH)
PDFs + α_s	± 8 (ggF, ttH), ± 4 (VBF, VH)

associated track; it is required to have at least three associated tracks with $p_T > 0.4$ GeV. For the $H \rightarrow \gamma\gamma$ analysis a different primary vertex definition is used, as described in Section 4.

Muon candidates [17] are formed by matching reconstructed tracks in the inner detector (ID) with either complete tracks or track segments reconstructed in the muon spectrometer (MS). The muon acceptance is extended to the region $2.5 < |\eta| < 2.7$, which is outside the ID coverage, using tracks reconstructed in the forward part of the MS.

Electron candidates [18] must have a well-reconstructed ID track pointing to a cluster of cells with energy depositions in the electromagnetic calorimeter. The cluster should satisfy a set of identification criteria requiring the longitudinal and transverse shower profiles to be consistent with those expected for electromagnetic showers. Tracks associated with electromagnetic clusters are fitted using a Gaussian Sum Filter [19], which allows bremsstrahlung energy losses to be taken into account. The identification criteria described in Ref. [18] have been modified with time to maintain optimal performance as a function of pile-up, in particular for low- p_T electrons.

The reconstruction, identification and trigger efficiencies for electrons and muons, as well as their energy and momentum scales and resolutions, are determined us-

the nominal interaction point (IP) in the centre of the detector, and the z -axis along the beam line. The x -axis points from the IP to the centre of the LHC ring, and the y -axis points upwards. Cylindrical coordinates (r, ϕ) are used in the transverse plane, ϕ being the azimuthal angle around the beam line. Observables labelled “transverse” are projected into the $x - y$ plane. The pseudorapidity is defined in terms of the polar angle θ as $\eta = -\ln \tan(\theta/2)$.

ing large samples of $Z \rightarrow \ell\ell$, $W \rightarrow \ell\nu$ and $J/\psi \rightarrow \ell\ell$ events [18, 20]. The resulting uncertainties are smaller than $\pm 1\%$ in most cases, one exception being the uncertainty on the electron selection efficiency which varies between $\pm 2\%$ and $\pm 5\%$ as a function of p_T and η .

Photon candidates [21] are reconstructed and identified using shower shapes in the electromagnetic calorimeter, with or without associated conversion tracks, as described in Section 4.

Jets [22, 23] are built from topological clusters [24] using the anti- k_t algorithm [25] with a distance parameter $R = 0.4$. They are typically required to have transverse energies greater than 25 GeV (30 GeV) for $|\eta| < 2.4$ ($2.4 \leq |\eta| < 4.5$), where the higher threshold in the forward region reduces the contribution from jet candidates produced by pile-up. To reduce this contribution further, jets within the ID acceptance ($|\eta| < 2.47$) are required to have more than 25–75% (depending on the pile-up conditions and Higgs boson decay mode) of the summed scalar p_T of their associated tracks coming from tracks originating from the event primary vertex. Pile-up corrections based on the average event transverse energy density in the jet area [26] and the number of reconstructed vertices in the data are also applied.

Jets originating from b -quarks [27–29] are identified (“ b -tagged”) by combining information from algorithms exploiting the impact parameter of tracks (defined as the distance of closest approach to the primary vertex in the transverse plane), the presence of a displaced vertex, and the reconstruction of D - and B -hadron decays.

The missing transverse momentum, E_T^{miss} [30], is the magnitude of the negative vector sum of the p_T of muons, electrons, photons, jets and clusters of calorimeter cells with $|\eta| < 4.9$ not associated with these objects. The uncertainty on the E_T^{miss} energy scale is obtained from the propagation of the uncertainties on the contributing components and thus depends on the considered final state. A track-based missing transverse momentum, $\mathbf{p}_T^{\text{miss}}$, is calculated as the negative vector sum of the transverse momenta of tracks associated with the primary vertex.

The main sources of experimental uncertainty common to all the channels considered in this study are summarised in the top part of Table 1.

3. Signal and background simulation

The SM Higgs boson production processes considered in these studies are gluon fusion ($gg \rightarrow H$, denoted ggF), vector-boson fusion ($qq' \rightarrow qq'H$, denoted

VBF), and Higgs-strahlung ($q\bar{q}' \rightarrow WH, ZH$, denoted WH/ZH or jointly VH). The small contribution from the associated production with a $t\bar{t}$ pair ($gg/q\bar{q} \rightarrow t\bar{t}H$, denoted $t\bar{t}H$) is taken into account in the $H \rightarrow \gamma\gamma$ and $H \rightarrow ZZ^*$ analyses. Samples of MC-simulated events

Table 2: Event generators used to model the signal and the main background processes. ‘‘PYTHIA’’ indicates that PYTHIA6 [31] and PYTHIA8 [32] are used for the simulations of 7 TeV and 8 TeV data, respectively.

Process	Generator
ggF, VBF	POWHEG [33, 34]+PYTHIA
$WH, ZH, t\bar{t}H$	PYTHIA
$H \rightarrow ZZ^* \rightarrow 4\ell$ decay	PROPHECY4f [35, 36]
W +jets, Z/γ^* +jets	ALPGEN [37]+HERWIG [38], POWHEG+PYTHIA, SHERPA [39]
$t\bar{t}, tW, tb$	MC@NLO [40]+HERWIG
tqb	AcerMC [41]+PYTHIA6
$q\bar{q} \rightarrow WW$	POWHEG+PYTHIA6
$gg \rightarrow WW$	gg2WW [42, 43]+HERWIG
$q\bar{q} \rightarrow ZZ^*$	POWHEG [44]+PYTHIA
$gg \rightarrow ZZ^*$	gg2ZZ [43, 45]+HERWIG
WZ	MadGraph [46, 47]+PYTHIA6, HERWIG
$W\gamma$ +jets	ALPGEN+HERWIG
$W\gamma^*$	MadGraph [48]+PYTHIA6 for $m_{\gamma^*} < 7$ GeV POWHEG+PYTHIA for $m_{\gamma^*} > 7$ GeV
$q\bar{q}/gg \rightarrow \gamma\gamma$	SHERPA

are employed to model Higgs boson production and compute signal selection efficiencies. The event generators are listed in Table 2. Cross-section normalisations and other corrections (*e.g.* Higgs boson p_T spectrum) are obtained from up-to-date calculations as described in Refs. [2, 14–16, 49–77]. Table 3 shows the production cross sections and the branching ratios for the final states considered in this study for a Higgs boson with mass $m_H = 125$ GeV, while Table 1 summarises the theoretical uncertainties on the expected signal common to all channels.

Backgrounds are determined using data alone or a combination of data and MC simulation, as discussed in Sections 4–6. The generators employed in most cases are also listed in Table 2. To generate parton showers and their hadronisation, and to simulate the underlying event [78–80], PYTHIA6 (for 7 TeV samples as well as for 8 TeV samples produced with MadGraph or AcerMC) or PYTHIA8 (for other 8 TeV samples) are used. Alternatively, HERWIG is employed, combined with the underlying event simulation provided by JIMMY [81]. When PYTHIA6 or HERWIG are used, PHOTOS [82, 83] is employed to describe additional photon radiation from charged leptons. The small contributions from $Z^{(*)}$ and $W^{(*)}$ decays to electrons and muons through intermediate τ -leptons are included in

the signal and background generation.

The following parton distribution function (PDF) sets are used in most cases: CT10 [84] for the POWHEG, MC@NLO, gg2WW and gg2ZZ samples; CTEQ6L1 [85] for the PYTHIA8, ALPGEN, AcerMC, MadGraph, HERWIG and SHERPA samples; and MRSTMCal [86] for the PYTHIA6 samples. In most cases, the generated MC samples are processed through a full simulation [87] of the ATLAS detector based on GEANT4 [88]. Corrections obtained from measurements in the data are applied to the simulation to account for small differences between data and simulation in *e.g.* the reconstruction of leptons, photons and jets. The simulation also includes realistic modelling (tuned to the data) of the event pile-up from the same and nearby bunch crossings.

Table 3: SM Higgs boson cross sections (in pb) at $\sqrt{s}=8$ (7) TeV for $m_H = 125$ GeV. The total values as well as the contributions from the individual production modes are listed. The branching ratios to the final-state channels considered in this paper are also given (where ℓ stands for electron or muon), together with their relative uncertainty. Up-to-date theoretical calculations are used [14–16, 35, 36, 89].

Cross section (pb) at $\sqrt{s}=8$ (7) TeV	Branching ratio (relative uncertainty)	
ggF	19.52 (15.32)	$H \rightarrow WW^* \rightarrow \ell\nu\ell\nu$ 0.010 ($\pm 5\%$)
VBF	1.58 (1.22)	$H \rightarrow \gamma\gamma$ 2.28×10^{-3} ($\pm 5\%$)
WH	0.70 (0.57)	$H \rightarrow ZZ^* \rightarrow 4\ell$ 1.25×10^{-4} ($\pm 5\%$)
ZH	0.39 (0.31)	
$t\bar{t}H$	0.13 (0.09)	
Total	22.32 (17.51)	

4. The $H \rightarrow \gamma\gamma$ channel

This channel is particularly sensitive to physics beyond the Standard Model since the decay proceeds via loops (which in the SM are dominated by W -boson exchange).

Events are required to have two high- p_T photons with invariant mass in the range 100–160 GeV. The main background is continuum $\gamma\gamma$ production, with smaller contributions from γ -jet and dijet processes. Compared to the previously published results [2], additional categories of events are introduced in the analysis of the 8 TeV data to increase the sensitivity to production through VBF or in association with a W or Z boson.

4.1. Event selection

The data used in this channel are selected using a diphoton trigger [90] requiring two clusters formed from energy depositions in the electromagnetic

calorimeter, with shapes compatible with electromagnetic showers. An E_T threshold of 20 GeV is applied to each cluster for the 7 TeV data, while at 8 TeV the thresholds are increased to 35 GeV on the leading (highest E_T) and 25 GeV on the sub-leading (next-highest E_T) cluster. The trigger efficiency is larger than 99% for events passing the final event selection.

In the offline analysis, photon candidates are required to have $E_T > 40$ GeV and 30 GeV for the leading and sub-leading photon, respectively. Both photons must be reconstructed in the fiducial region $|\eta| < 2.37$, excluding the calorimeter barrel/end-cap transition region $1.37 \leq |\eta| < 1.56$.

Photon candidates are required to pass tight identification criteria based mainly on shower shapes in the electromagnetic calorimeter [2]. They are classified as converted if they are associated with two tracks consistent with a $\gamma \rightarrow e^+e^-$ conversion process or a single track leaving no hit in the innermost layer of the inner detector, and as unconverted otherwise [91]. Identification efficiencies, averaged over η , range from 85% to above 95% for the E_T range under consideration. Jets misidentified as photons are further rejected by applying calorimeter and track isolation requirements to the photon candidates. The calorimeter isolation is defined as the sum of the transverse energies of positive-energy topological clusters within a cone of size $\Delta R = \sqrt{\Delta\phi^2 + \Delta\eta^2} = 0.4$ around the photon candidates, excluding the core of the showers. It is required to be smaller than 4 GeV and 6 GeV for the 7 TeV and 8 TeV data, respectively. The pile-up contribution is corrected on an event-by-event basis [92]. The track isolation, applied to the 8 TeV data only, is defined as the scalar sum of the transverse momenta of all tracks with $p_T > 1$ GeV associated with the diphoton production vertex (defined below) and lying within a cone of size $\Delta R = 0.2$ around the photon candidate; it is required to be smaller than 2.6 GeV. Conversion tracks associated with either photon candidate are excluded.

For the precise measurement of the diphoton invariant mass ($m_{\gamma\gamma}$), as well as for the computation of track-based quantities (*e.g.* track isolation, selection of jets associated with the hard interaction), the diphoton production vertex should be known precisely. The determination of the vertex position along the beam axis is based on so-called ‘‘photon pointing’’, where the directions of the two photons, measured using the longitudinal and lateral segmentation of the electromagnetic calorimeter, are combined with a constraint from the average beam-spot position. For converted photons the position of the conversion vertex is also used. This technique alone is

sufficient to ensure that the contribution of angular measurement uncertainties to the diphoton invariant mass resolution is negligible. For a more precise identification of the primary vertex, needed for the computation of track-based quantities, this pointing information is combined with tracking information from each reconstructed vertex: the Σp_T^2 for the tracks associated with a given vertex and, for the 8 TeV data, the Σp_T of the tracks and the azimuthal angle between the transverse momentum of the diphoton system and that of the vector sum of the track \mathbf{p}_T . A Neural Network (likelihood) discriminant is used for the 8 TeV (7 TeV) data. The performance of this algorithm is studied using $Z \rightarrow ee$ decays, ignoring the tracks associated with the electrons and weighting the events so that the p_T and rapidity distributions of the Z boson match those expected from the Higgs boson signal. The probability of finding a vertex within 0.3 mm of the one computed from the electron tracks is larger than 75%.

The photon energy calibration is obtained from a detailed simulation of the detector geometry and response, independently for converted and unconverted photons. The calibration is refined by applying η -dependent correction factors determined from studies of $Z \rightarrow ee$ events in data [18]: they range from $\pm 0.5\%$ to $\pm 1.5\%$ depending on the pseudorapidity of the photon. Samples of radiative $Z \rightarrow \ell\ell\gamma$ decays are used to verify the photon energy scale. The energy response of the calorimeter shows a stability of better than $\pm 0.1\%$ with time and various pile-up conditions.

The signal efficiency of the above selections at 8 TeV is estimated to be 37.5% for a Higgs boson with $m_H = 125$ GeV.

The number of events in the diphoton mass region 100–160 GeV passing this inclusive selection is 23788 in the 7 TeV data and 118893 in the 8 TeV data. The fraction of genuine $\gamma\gamma$ events, as estimated from data [93], is $(75^{+3}_{-4})\%$.

4.2. Event categorisation

To increase the sensitivity to the overall Higgs boson signal, as well as to the specific VBF and VH production modes, the selected events are separated into 14 mutually exclusive categories for further analysis, following the order of preference listed below.

Lepton category (8 TeV data only): This category targets mainly VH events where the W or Z bosons decay to charged leptons. An isolated electron ($E_T > 15$ GeV) or muon ($p_T > 10$ GeV) candidate is required. To remove contamination from $Z\gamma$ production with $Z \rightarrow ee$, electrons forming an invariant mass with either photon

in the range $84 \text{ GeV} < m_{e\gamma} < 94 \text{ GeV}$ are not considered.

E_T^{miss} category (8 TeV data only): This category targets mainly VH events with $W \rightarrow \ell\nu$ or $Z \rightarrow \nu\nu$. An E_T^{miss} significance (defined as $E_T^{\text{miss}}/\sigma_{E_T^{\text{miss}}}$, where in this case $\sigma_{E_T^{\text{miss}}} = 0.67 \text{ GeV}^{1/2} \sqrt{\Sigma E_T}$ with ΣE_T being the event total transverse energy) greater than five is required, corresponding to $E_T^{\text{miss}} > 70 - 100 \text{ GeV}$ depending on ΣE_T .

Low-mass two-jet category (8 TeV data only): To select VH events where the W or Z boson decays hadronically, a pair of jets with invariant mass in the range $60 \text{ GeV} < m_{jj} < 110 \text{ GeV}$ is required. To reduce the ggF contamination, the pseudorapidity difference between the dijet and diphoton systems is required to be $|\Delta\eta_{\gamma\gamma,jj}| < 1$, and the component of the diphoton transverse momentum orthogonal to the diphoton thrust axis in the transverse plane³ [94, 95] is required to satisfy $p_{T\perp} > 70 \text{ GeV}$.

High-mass two-jet categories: These categories are designed to select events produced through the VBF process, which is characterised by the presence of two forward jets with little hadronic activity in the central part of the detector. Jets are reconstructed as described in Section 2. The selection for the 8 TeV data is based on a multivariate technique using a Boosted Decision Tree (BDT), whose input quantities are: the pseudorapidities of the two jets (η_{j1}, η_{j2}) and their separation in η ; the invariant mass of the dijet system; the difference $\eta^* = \eta_{\gamma\gamma} - (\eta_{j1} + \eta_{j2})/2$, where $\eta_{\gamma\gamma}$ is the pseudorapidity of the diphoton system; the minimal radial distance ($\Delta R = \sqrt{\Delta\phi^2 + \Delta\eta^2}$) of any jet–photon pair; and the difference $\Delta\phi_{\gamma\gamma,jj}$ between the azimuthal angles of the diphoton and dijet momenta. The BDT training is performed using a signal sample, as well as a background sample composed of simulated $\gamma\gamma$ events combined with γj and jj components obtained from data. The BDT response distributions for data and simulation are shown in Fig. 1. The BDT output is used to define two high-mass two-jet categories: a “tight” category corresponding to $\text{BDT} \geq 0.74$, and a “loose” category for $0.44 \leq \text{BDT} < 0.74$. For the 7 TeV data, the same cut-based selection as described in Ref. [2] is applied, namely $m_{jj} > 400 \text{ GeV}$, $|\Delta\eta_{jj}| > 2.8$ and $|\Delta\phi_{\gamma\gamma,jj}| > 2.8$.

Untagged categories: Events not selected in any of the above categories (corresponding to more than 90% of the expected signal, dominated by ggF production)

³ $p_{T\perp} = |(\mathbf{p}_T^{\gamma 1} + \mathbf{p}_T^{\gamma 2}) \times \hat{\mathbf{t}}|$, where $\hat{\mathbf{t}} = \frac{\mathbf{p}_T^{\gamma 1} - \mathbf{p}_T^{\gamma 2}}{|\mathbf{p}_T^{\gamma 1} - \mathbf{p}_T^{\gamma 2}|}$ denotes the thrust axis in the transverse plane, and $\mathbf{p}_T^{\gamma 1}, \mathbf{p}_T^{\gamma 2}$ are the transverse momenta of the two photons.

are classified in nine additional categories according to

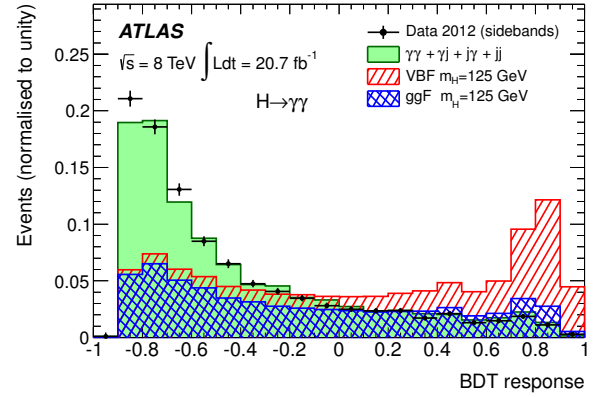


Figure 1: Distribution of the VBF BDT response after applying the selection of the inclusive analysis and requiring in addition the presence of two jets with $|\Delta\eta_{jj}| > 2$ and $|\eta^*| < 5$. The data in the signal sidebands (*i.e.* excluding the $m_{\gamma\gamma}$ region 120–130 GeV), the expected background, and the expected signal from VBF and ggF production are shown. They are all normalised to unity except ggF, which is normalised to the ratio between the numbers of ggF and VBF events passing the selection described above.

the properties of their diphoton system. Events with both photons unconverted are classified into *unconverted central* if $|\eta| < 0.75$ for both photons, and *unconverted rest* otherwise. Events with at least one converted photon are similarly separated into *converted central* if $|\eta| < 0.75$ for both photons, *converted transition* if $1.3 < |\eta| < 1.75$ for either photon, and *converted rest* otherwise. Finally, all untagged categories except *converted transition* are split into *low* $p_{T\perp}$ and *high* $p_{T\perp}$ subcategories by a cut at $p_{T\perp} = 60 \text{ GeV}$. This classification is motivated by differences in mass resolution and signal-to-background ratio for the various categories.

The use of the 14 categories improves the sensitivity of the analysis by about 40% compared to the inclusive analysis.

4.3. Background estimation

The background is obtained from fits to the diphoton mass spectrum in the data over the range 100–160 GeV after the full selection. The procedure, the choice of the analytical forms for the background and the determination of the corresponding uncertainties follow the method described in Ref. [2]. Depending on the category, the analytical form is either a fourth-order Bernstein polynomial [96] (used also for the inclusive sample), an exponential of a second-order polynomial, or a single exponential. In these fits, the Higgs boson signal

is described by the sum of a Crystal Ball function [97] for the core of the distribution and a Gaussian function for the tails.

4.4. Systematic uncertainties

Systematic uncertainties can affect the signal yield, the signal fractions in the various categories (with possible migrations between them), the signal mass resolution and the mass measurement. The main sources specific to the $H \rightarrow \gamma\gamma$ channel are listed in Table 4, while sources in common with other decay channels are summarised in Section 2 and Table 1. The uncertainties described below are those affecting the 8 TeV analysis (see Ref. [2] for the 7 TeV analysis).

Table 4: For $m_H = 125$ GeV and the 8 TeV data analysis, the impact of the main sources of systematic uncertainty specific to the $H \rightarrow \gamma\gamma$ channel on the signal yield, event migration between categories and mass measurement and resolution. Uncertainties common to all channels are listed in Table 1. The \pm and \mp signs indicate anticorrelations between categories.

Source	Uncertainty (%)
	on signal yield
Photon identification	± 2.4
Trigger	± 0.5
Isolation	± 1.0
Photon energy scale	± 0.25
ggF (theory), tight high-mass two-jet cat.	± 48
ggF (theory), loose high-mass two-jet cat.	± 28
ggF (theory), low-mass two-jet cat.	± 30
Impact of background modelling	$\pm(2-14)$, cat.-dependent
	on category population (migration)
Material modelling	-4 (unconv), $+3.5$ (conv)
p_T modelling	± 1 (low- p_T), $\mp(9-12)$ (high- p_T , jets), $\pm(2-4)$ (lepton, E_T^{miss})
$\Delta\phi_{\gamma\gamma, jj}$, η^* modelling in ggF	$\pm(9-12)$, $\pm(6-8)$
Jet energy scale and resolution	$\pm(7-12)$ (jets), $\mp(0-1)$ (others)
Underlying event two-jet cat.	± 4 (high-mass tight), ± 8 (high-mass loose), ± 12 (low-mass)
E_T^{miss}	± 4 (E_T^{miss} category)
	on mass scale and resolution
Mass measurement	± 0.6 , cat.-dependent
Signal mass resolution	$\pm(14-23)$, cat.-dependent

Signal yield: Relevant experimental uncertainties on the signal yield come from the knowledge of the luminosity (Table 1) and the photon identification efficiency. The latter is estimated by comparing the efficiencies obtained using MC simulations and several data-driven methods: $Z \rightarrow ee$ events with a simulation-based extrapolation from electrons to photons, an isolation sideband technique using an inclusive photon sample, and photons from $Z \rightarrow \ell\ell\gamma$ radiative decays. Owing to several analysis improvements and the large size of the

8 TeV data sample, the resulting uncertainty is significantly reduced compared to that reported in Ref. [2] and amounts to $\pm 2.4\%$. Smaller experimental uncertainties come from the knowledge of the trigger efficiency, the impact of the photon isolation requirement and the photon energy scale. In addition to the theoretical uncertainties on inclusive Higgs boson production listed in Table 1, the ggF contribution to the two-jet categories is subject to large uncertainties (Table 4) due to missing higher-order corrections; they are estimated using the method described in Ref. [98] and the MCFM [99] generator calculations. Finally, the background modelling contributes an uncertainty between $\pm 2\%$ and $\pm 14\%$ depending on the category.

Event migration: Mis-modelling of the detector material could cause event migration between the unconverted and converted photon categories in the simulation. The uncertainty is obtained from MC samples produced with variations of the material description. The uncertainty in the population of the p_T categories due to the description of the Higgs boson p_T spectrum is determined by varying the QCD scales and PDFs used in the HqT program [62]. Uncertainties on the modelling of two-jet variables for the ggF process, in particular $\Delta\phi_{\gamma\gamma, jj}$ and η^* , affect the contribution of ggF events to the high-mass two-jet categories. They are estimated by comparing the baseline POWHEG generator with SHERPA and MCFM. Uncertainties on the jet energy scale and resolution affect the selection of jets used in some category definitions, thereby causing migration between jet-based and other categories. The uncertainty due to the modelling of the underlying event is estimated by comparing simulations with and without multi-parton interactions. Uncertainties on the E_T^{miss} reconstruction are assessed by varying the transverse energies of its components (photons, electrons, jets, soft energy deposits) within their respective uncertainties.

Mass measurement and mass resolution: The measurement of the Higgs boson mass in the $H \rightarrow \gamma\gamma$ channel is discussed in Section 7.2. Uncertainties on the diphoton mass scale come from the following sources: the calibration of the electron energy scale (obtained from $Z \rightarrow ee$ events); the uncertainty on its extrapolation to the energy scale of photons, dominated by the description of the detector material; and the knowledge of the energy scale of the presampler detector located in front of the electromagnetic calorimeter. The total uncertainty amounts to $\pm 0.55\%$ (corresponding to ± 0.7 GeV). The mass resolution, obtained from the Crystal Ball function used in the fits described in Section 4.3, ranges from 1.4 GeV to 2.5 GeV depending on the category. The main uncertainties come from the

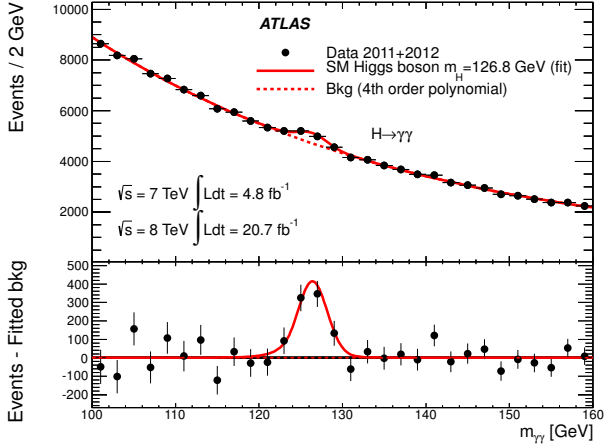


Figure 2: Invariant mass distribution of diphoton candidates after all selections of the inclusive analysis for the combined 7 TeV and 8 TeV data. The result of a fit to the data with the sum of a SM Higgs boson signal (with $m_H = 126.8$ GeV and free signal strength) and background is superimposed. The residuals of the data with respect to the fitted background are displayed in the lower panel.

calorimeter energy scale and the extrapolation from the electron to the photon response. Smaller contributions arise from pile-up and the primary vertex selection.

4.5. Results

The diphoton invariant mass distribution after selections for the full data sample is shown in Fig. 2. The data are fit by categories, using background shapes (see Section 4.3), as well as parameters for the Crystal Ball and Gaussian functions describing the signal, specific to each category. At the maximum deviation from the background-only expectation, which occurs for $m_H \sim 126.5$ GeV, the significance of the observed peak is 7.4σ for the combined 7 TeV and 8 TeV data (compared with 4.3σ expected from SM Higgs boson production at this mass), which establishes a discovery-level signal in the $\gamma\gamma$ channel alone. Table 5 lists the observed number of events in the main categories, the estimated background from fits to the data (described in Section 4.3), and the predicted signal contributions from the various production processes.

Additional interpretation of these results is presented in Section 7.

5. The $H \rightarrow ZZ^* \rightarrow 4\ell$ channel

Despite the small branching ratio, this channel provides good sensitivity to Higgs boson studies, *e.g.* to

Table 5: For the $H \rightarrow \gamma\gamma$ analysis of the $\sqrt{s} = 8$ TeV data, the numbers of events observed in the data (N_D), the numbers of background events (N_B) estimated from fits to the data, and the expected SM Higgs boson signal (N_S) for $m_H = 126.8$ GeV, split by category. All numbers are given in a mass window centred at $m_H = 126.8$ GeV and containing 90% of the expected signal (the size of this window changes from category to category and for the inclusive sample). The predicted numbers of signal events in each of the ggF, VBF, WH , ZH and $t\bar{t}H$ processes are also given.

Category	N_D	N_B	N_S	ggF	VBF	WH	ZH	$t\bar{t}H$
Untagged	14248	13582	350	320	19	7.0	4.2	1.0
Loose high-mass two-jet	41	28	5.0	2.3	2.7	< 0.1	< 0.1	< 0.1
Tight high-mass two-jet	23	13	7.7	1.8	5.9	< 0.1	< 0.1	< 0.1
Low-mass two-jet	19	21	3.1	1.5	< 0.1	0.92	0.54	< 0.1
E_T^{miss} significance	8	4	1.2	< 0.1	< 0.1	0.43	0.57	0.14
Lepton	20	12	2.7	< 0.1	< 0.1	1.7	0.41	0.50
All categories (inclusive)	13931	13205	370	330	27	10	5.8	1.7

the coupling to Z bosons, mainly because of the large signal-to-background ratio.

Events are required to have two pairs of same-flavour, opposite-charge, isolated leptons: $4e$, $2e2\mu$, $2\mu2e$, 4μ (where final states with two electrons and two muons are ordered by the flavour of the dilepton pair with mass closest to the Z -boson mass). The largest background comes from continuum $(Z^*/\gamma^*)(Z^*/\gamma^*)$ production, referred to hereafter as ZZ^* . Important contributions arise also from Z + jets and $t\bar{t}$ production, where two of the charged lepton candidates can come from decays of hadrons with b - or c -quark content, misidentification of light-quark jets, and photon conversions.

The analysis presented here is largely the same as that described in Ref. [100] with only minor changes. The electron identification is tightened in the 8 TeV data to improve the background rejection for final states with a pair of electrons forming the lower-mass Z^* boson. The mass measurement uses a constrained fit to the Z mass to improve the resolution. The lepton pairing is modified to reduce the mis-pairing in the 4μ and $4e$ final states, and the minimum requirement on the mass of the second Z^* boson is relaxed. Final-state radiation (FSR) is included in the reconstruction of the first $Z^{(*)}$ in events containing muons. Finally, a classification which separates Higgs boson candidate events into ggF-like, VBF-like and VH-like categories is introduced.

5.1. Event selection

The data are selected using single-lepton or dilepton triggers. The p_T threshold of the single-muon trigger is 24 GeV (18 GeV) in 2012 (2011) and the E_T threshold of the single-electron trigger is 24 GeV (20–22 GeV). The dielectron trigger threshold is $E_T = 12$ GeV and the dimuon trigger threshold is $p_T = 13$ GeV (10 GeV

in 2011) for both leptons. In addition, an asymmetric dimuon trigger and electron–muon triggers are used as described in Ref. [100]. The efficiency for events passing the offline analysis cuts to be selected by at least one of the above triggers is between 97% and 100%.

Muon and electron candidates are reconstructed as described in Section 2. In the region $|\eta| < 0.1$, which has limited MS coverage, ID tracks with $p_T > 15$ GeV are identified as muons if their calorimetric energy deposits are consistent with a minimum ionising particle. Only one muon per event is allowed to be reconstructed either in the MS alone or without MS information. For the 2012 data, the electron requirements are tightened in the transition region between the barrel and end-cap calorimeters ($1.37 < |\eta| < 1.52$), and the pixel-hit requirements are stricter to improve the rejection of photon conversions.

Each electron (muon) must satisfy $E_T > 7$ GeV ($p_T > 6$ GeV) and be measured in the pseudorapidity range $|\eta| < 2.47$ ($|\eta| < 2.7$). The highest- p_T lepton in the quadruplet must satisfy $p_T > 20$ GeV, and the second (third) lepton must satisfy $p_T > 15$ GeV ($p_T > 10$ GeV). To reject cosmic rays, muon tracks are required to have a transverse impact parameter of less than 1 mm.

Multiple quadruplets within a single event are possible. For each quadruplet, the same-flavour, opposite-charge lepton pair with invariant mass closest to the Z -boson mass (m_Z) is referred to as the leading lepton pair. Its invariant mass, denoted by m_{12} , is required to be between 50 GeV and 106 GeV. The invariant mass of the other (sub-leading) lepton pair, m_{34} , is required to be in the range $m_{\min} < m_{34} < 115$ GeV. The value of m_{\min} is 12 GeV for a reconstructed four-lepton mass $m_{4\ell} < 140$ GeV, rises linearly to 50 GeV at $m_{4\ell} = 190$ GeV, and remains constant for higher masses. If two or more quadruplets satisfy the above requirements, the one with m_{34} closest to the Z -boson mass is selected. For further analysis, events are classified in four sub-channels, $4e$, $2e2\mu$, $2\mu2e$, 4μ .

The Z +jets and $t\bar{t}$ background contributions are reduced by applying requirements on the lepton transverse impact parameter divided by its uncertainty, $|d_0|/\sigma_{d_0}$. This ratio must be smaller than 3.5 for muons and smaller than 6.5 for electrons (the electron impact parameter is affected by bremsstrahlung and thus its distribution has longer tails). In addition, leptons must satisfy isolation requirements based on tracking and calorimetric information, similar to those described in Section 4.1, as discussed in Ref. [2].

The impact of FSR photon emission on the reconstructed invariant mass is modelled using the MC simulation (PHOTOS), which reproduces the rate of

collinear photons with $E_T > 1.3$ GeV in $Z \rightarrow \mu\mu$ decays in data to $\pm 5\%$ [101]. Leading muon pairs with $66 \text{ GeV} < m_{12} < 89 \text{ GeV}$ are corrected for FSR by including any reconstructed photon with E_T above 1 GeV lying close (typically within $\Delta R < 0.15$) to the muon tracks, provided that the corrected m_{12} satisfies $m_{12} < 100$ GeV. The MC simulation predicts that about 4% of all $H \rightarrow ZZ^* \rightarrow 4\mu$ candidate events should have this correction.

For the 8 TeV data, the signal reconstruction and selection efficiency for a SM Higgs boson with $m_H = 125$ GeV is 39% for the 4μ sub-channel, 26% for the $2e2\mu/2\mu2e$ sub-channels and 19% for the $4e$ sub-channel.

The final discriminating variable in this analysis is the 4ℓ invariant mass. Its resolution, which is improved by typically 15% by applying a Z -mass constrained kinematic fit to the leading lepton pair, is about 1.6 GeV, 1.9 GeV and 2.4 GeV for the 4μ , $2e2\mu/2\mu2e$ and $4e$ sub-channels, respectively, and for $m_H = 125$ GeV.

5.2. Event categorisation

To enhance the sensitivity to the individual production modes, events passing the above selection are assigned to one of three categories, named VBF-like, VH-like, and ggF-like. Events are VBF-like if the two highest p_T jets are separated by more than three units in pseudorapidity and have an invariant mass greater than 350 GeV. Events that do not qualify as VBF-like are considered for the VH-like category. They are accepted in this category if they contain an additional lepton (e or μ) with $p_T > 8$ GeV, satisfying the same requirements as the four leading leptons. The remaining events are assigned to the ggF-like category. No classification based on the 4ℓ flavour is made in the VBF-like and VH-like categories. Higgs boson production through VBF and VH is expected to account for about 60% and 70% of the total signal events in the VBF-like and VH-like categories, respectively. The signal-to-background ratio in the signal peak region is about five for the VBF-like category, about three for the VH-like category, and about 1.5 for the inclusive analysis.

5.3. Background estimation

The expected background yield and composition are estimated using the MC simulation for ZZ^* production, and methods based on control regions (CRs) from data for the Z +jets and $t\bar{t}$ processes [2]. The transfer factors used to extrapolate the background yields from the CRs to the signal region are obtained from the MC simulation and cross-checked with data. Since the background

composition depends on the flavour of the sub-leading lepton pair, different approaches are followed for the $\ell\ell + \mu\mu$ and the $\ell\ell + ee$ final states.

The reducible $\ell\ell + \mu\mu$ background is dominated by $t\bar{t}$ and $Z + \text{jets}$ (mostly $Zb\bar{b}$) events. A CR is defined by removing the isolation requirement for the muons of the sub-leading pair, and by requiring that at least one of them fails the transverse impact parameter selection. This procedure allows the $t\bar{t}$ and $Z + \text{jets}$ backgrounds to be estimated simultaneously from a fit to the m_{12} distribution.

To determine the reducible $\ell\ell + ee$ background, a CR is formed by relaxing the selection criteria for the electrons of the sub-leading pair: each of these electrons is then classified as “electron-like” or “fake-like” based on requirements on appropriate discriminating variables [102]. The numbers of events with different combinations of “electron-like” or “fake-like” objects are then used to estimate the true composition of the CR (in terms of isolated electrons, non-prompt electrons from heavy-flavour decays, electrons from photon conversions and jets misidentified as electrons), from which the expected yields in the signal region can be obtained using transfer factors from the MC simulation.

Similar techniques are used to determine the backgrounds for the VBF-like and VH-like categories.

5.4. Systematic uncertainties

The dominant sources of systematic uncertainty affecting the $H \rightarrow ZZ^*$ 8 TeV analysis are listed in Table 6 (see Ref. [2] for the 7 TeV analysis). Lepton reconstruction

Table 6: For $m_H = 125$ GeV and the 8 TeV data analysis, the impact of the main sources of systematic uncertainty specific to the $H \rightarrow ZZ^*$ channel on the signal yield, estimated reducible background, event migration between categories and mass measurement. Uncertainties common to all channels are listed in Table 1.

Source	Uncertainty (%)			
Signal yield	4μ	$2\mu 2e$	$2e 2\mu$	$4e$
Muon reconstruction and identification	± 0.8	± 0.4	± 0.4	-
Electron reconstruction and identification	-	± 8.7	± 2.4	± 9.4
Reducible background (inclusive analysis)	± 24	± 10	± 23	± 13
Migration between categories				
ggF/VBF/VH contributions to VBF-like cat.	$\pm 32/11/11$			
ZZ^* contribution to VBF-like cat.	± 36			
ggF/VBF/VH contributions to VH-like cat.	$\pm 15/5/6$			
ZZ^* contribution to VH-like cat.	± 30			
Mass measurement	4μ	$2\mu 2e$	$2e 2\mu$	$4e$
Lepton energy and momentum scale	± 0.2	± 0.2	± 0.3	± 0.4

tion, identification and selection efficiencies, as well as energy and momentum resolutions and scales, are determined using large control samples from the data, as described in Section 2. Only the electron uncertainty

contributes significantly to the uncertainty on the signal yield.

The background uncertainty is dominated by the uncertainty on the transfer factors from the CRs to the signal region and the available number of events in the control regions.

The uncertainty on the population of the various categories (migration) comes mainly from the knowledge of the theoretical cross sections for the various production processes, the modelling of the underlying event and the knowledge of the jet energy scale.

The $H \rightarrow ZZ^* \rightarrow 4\ell$ mass measurement is discussed in Section 7.2. The main sources contributing to the electron energy scale uncertainty are described in Section 4.4; the largest impact ($\pm 0.4\%$) is on the $4e$ final state. Systematic uncertainties from the knowledge of the muon momentum scale (discussed in detail in Ref. [100]) are smaller. Mass scale uncertainties related to FSR and background contamination are below $\pm 0.1\%$.

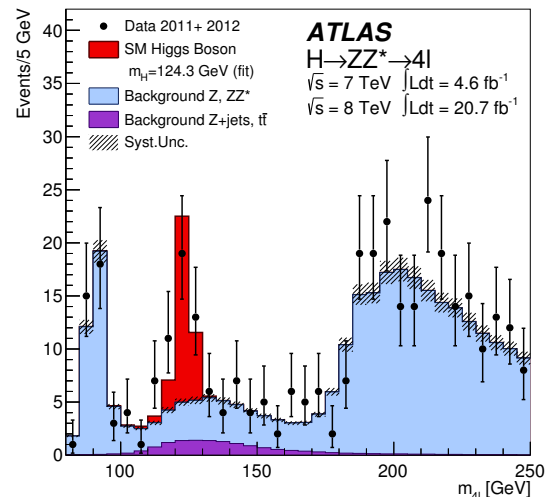


Figure 3: The distribution of the four-lepton invariant mass, $m_{4\ell}$, for the selected candidates in the data. The estimated background, as well as the expected SM Higgs boson signal for $m_H = 124.3$ GeV (scaled by the signal strength obtained from fits to the data), are also shown. The single-resonant peak at $m_{4\ell} \sim 90$ GeV includes contributions from s -channel Z/γ^* and t -channel $(Z^*/\gamma^*)(Z^*/\gamma^*)$ production.

5.5. Results

The reconstructed four-lepton mass spectrum after all selections of the inclusive analysis is shown in Fig. 3. The data are compared to the (scaled) expected Higgs boson signal for $m_H = 124.3$ GeV and

to the estimated backgrounds. At the maximum deviation from the background-only expectation (occurring at $m_H = 124.3$ GeV), the significance of the observed peak is 6.6σ for the combined 7 TeV and 8 TeV data, to be compared with 4.4σ expected from SM Higgs boson production at this mass. This result establishes a discovery-level signal in the 4ℓ channel alone.

Table 7 presents the numbers of observed and expected events in the peak region. Out of a total of 32 events selected in the data, one and zero candidates are found in the VBF-like and VH-like categories, respectively, compared with an expectation of 0.7 and 0.1 events from the signal and 0.14 and 0.04 events from the background.

Additional interpretation of these results is presented in Section 7.

Table 7: For the $H \rightarrow ZZ^* \rightarrow 4\ell$ inclusive analysis, the number of expected signal ($m_H = 125$ GeV) and background events, together with the number of events observed in the data, in a window of size ± 5 GeV around $m_{4\ell} = 125$ GeV, for the combined $\sqrt{s} = 7$ TeV and $\sqrt{s} = 8$ TeV data.

	Signal	ZZ^*	Z + jets, $t\bar{t}$	Observed
4μ	6.3 ± 0.8	2.8 ± 0.1	0.55 ± 0.15	13
$2e2\mu/2\mu2e$	7.0 ± 0.6	3.5 ± 0.1	2.11 ± 0.37	13
$4e$	2.6 ± 0.4	1.2 ± 0.1	1.11 ± 0.28	6

6. The $H \rightarrow WW^* \rightarrow \ell\nu\ell\nu$ channel

This decay mode provides direct access to the Higgs boson couplings to W bosons. Its rate is large, but a narrow mass peak cannot be reconstructed due to the presence of two neutrinos in the final state. The reconstructed topology consists of two opposite-charge leptons and a large momentum imbalance from the neutrinos. The dominant SM backgrounds are WW (which includes WW^*), $t\bar{t}$ and Wt , all of which produce two W bosons. The classification of events by jet multiplicity (N_{jet}) allows the control of the background from top quarks, which contains b -quark jets, as well as the extraction of the signal strengths for the ggF and VBF production processes. For the hypothesis of a SM Higgs boson, the spin-zero initial state and the $V-A$ structure of the W -boson decays imply a correlation between the directions of the charged leptons, which can be exploited to reject the WW background. These correlations lead to the use of quantities such as the dilepton invariant mass $m_{\ell\ell}$ and angular separation $\Delta\phi_{\ell\ell}$ in the selection criteria described below. Drell-Yan (DY) events ($pp \rightarrow Z/\gamma^* \rightarrow \ell\ell$) may be reconstructed with significant missing transverse momentum because of leptonic

τ decays or the degradation of the $E_{\text{T}}^{\text{miss}}$ measurement in the high pile-up environment of the 2012 run. Finally, W +jets production in which a jet is reconstructed as a lepton, and the diboson processes $W\gamma^{(*)}$, WZ , and ZZ^* , are also significant backgrounds after all event selection.

The studies presented here are a significant update of those reported in Ref. [2]. The signal regions considered include ee , $e\mu$, and $\mu\mu$ final states with zero, one, or at least two reconstructed jets. The $N_{\text{jet}} \geq 2$ analysis has been re-optimised to increase the sensitivity to Higgs boson production through VBF for $m_H = 125$ GeV. Improved DY rejection and estimation techniques have allowed the inclusion of ee and $\mu\mu$ events from the 8 TeV data. The analysis of the 7 TeV data, most recently documented in Ref. [103], has been updated to apply improvements from the 8 TeV analysis, including more stringent lepton isolation requirements, which reduce the W +jets background by 40%.

6.1. Event selection

Events are required to have two opposite-charge leptons (e or μ) and to pass the same single-lepton triggers as described in Section 5 for the $H \rightarrow ZZ^*$ channel. The leading lepton must satisfy $p_{\text{T}} > 25$ GeV and the sub-leading lepton $p_{\text{T}} > 15$ GeV. Electron and muon identification and isolation requirements (see Ref. [2]) are more restrictive than those used in the $H \rightarrow ZZ^*$ analysis in order to suppress the W +jets background.

In the $ee/\mu\mu$ channels, $Z \rightarrow \ell\ell$ and low-mass $\gamma^* \rightarrow \ell\ell$ events, including J/ψ and Υ production, are rejected by requiring $|m_{\ell\ell} - m_Z| > 15$ GeV and $m_{\ell\ell} > 12$ GeV, respectively. In the $e\mu$ channels, low-mass $\gamma^* \rightarrow \tau\tau \rightarrow e\nu\mu\nu\nu$ production is rejected by imposing $m_{\ell\ell} > 10$ GeV.

Drell-Yan and multi-jet backgrounds are suppressed by requiring large missing transverse momentum. For $N_{\text{jet}} \leq 1$, a requirement is made on $E_{\text{T,rel}}^{\text{miss}} = E_{\text{T}}^{\text{miss}} \cdot \sin|\Delta\phi_{\text{closest}}|$, where $\Delta\phi_{\text{closest}}$ is the smallest azimuthal angle between the $\mathbf{E}_{\text{T}}^{\text{miss}}$ vector and any jet or high- p_{T} charged lepton in the event; if $|\Delta\phi_{\text{closest}}| > \pi/2$, then $E_{\text{T,rel}}^{\text{miss}} = E_{\text{T}}^{\text{miss}}$ is taken. For additional rejection of the DY background in the $ee/\mu\mu$ channels with $N_{\text{jet}} \leq 1$, the track-based $\mathbf{p}_{\text{T}}^{\text{miss}}$ described in Section 2 is used, modified to $p_{\text{T,rel}}^{\text{miss}}$ in a similar way as $E_{\text{T,rel}}^{\text{miss}}$. For these channels, requirements are also made on f_{recoil} , an estimate of the magnitude of the soft hadronic recoil opposite to the system consisting of the leptons and any accompanying jet, normalised to the momentum of the system itself. The f_{recoil} value in DY events is on average larger than that of non-DY events,

where the high- p_T system is balanced at least in part by recoiling neutrinos.

The $N_{\text{jet}} \geq 2$ analysis uses $E_{T, \text{rel}}^{\text{miss}}$ instead of $E_{T, \text{rel}}^{\text{miss}}$ because the larger number of jets in the final states reduces the signal efficiency of the $E_{T, \text{rel}}^{\text{miss}}$ criterion. For the $ee/\mu\mu$ channels with $N_{\text{jet}} \geq 2$, an $E_{T, \text{rel}}^{\text{miss}}$ variant called “ $E_{T, \text{STVF}}^{\text{miss}}$ ” is also employed. In the calculation of $E_{T, \text{STVF}}^{\text{miss}}$, the energies of (soft) calorimeter deposits unassociated with high- p_T leptons, photons, or jets are scaled by the ratio of the summed scalar p_T of tracks from the primary vertex unmatched with such objects to the summed scalar p_T of all tracks from any vertex in the event which are also unmatched with objects [104].

For all jet multiplicities, selections exploiting the kinematic features of $H \rightarrow WW^* \rightarrow \ell\nu\ell\nu$ events are applied. The dilepton invariant mass is required to be small, $m_{\ell\ell} < 50$ GeV for $N_{\text{jet}} \leq 1$ and $m_{\ell\ell} < 60$ GeV for $N_{\text{jet}} \geq 2$; the azimuthal separation of the leptons is also required to be small, $\Delta\phi_{\ell\ell} < 1.8$.

6.2. Event categorisation

The analysis is divided into categories with $N_{\text{jet}} = 0$, $N_{\text{jet}} = 1$, and $N_{\text{jet}} \geq 2$. In the $N_{\text{jet}} = 0$ analysis, $E_{T, \text{rel}}^{\text{miss}} > 25$ GeV ($E_{T, \text{rel}}^{\text{miss}} > 45$ GeV and $p_{T, \text{rel}}^{\text{miss}} > 45$ GeV) is required for $e\mu$ ($ee/\mu\mu$) final states. The transverse momentum of the dilepton system is required to be large, $p_T^{\ell\ell} > 30$ GeV. For $ee/\mu\mu$ events, the hadronic recoil is required to be typical of events with neutrinos in the final state, $f_{\text{recoil}} < 0.05$. Finally, the azimuthal separation between the $\mathbf{p}_T^{\ell\ell}$ and $\mathbf{E}_T^{\text{miss}}$ vectors must satisfy $|\Delta\phi_{\ell\ell, E_T^{\text{miss}}}| > \pi/2$, in order to remove potentially poorly reconstructed events.

In the $N_{\text{jet}} = 1$ analysis, the $E_{T, \text{rel}}^{\text{miss}}$ and $p_{T, \text{rel}}^{\text{miss}}$ requirements are the same as for $N_{\text{jet}} = 0$, but the hadronic recoil threshold is looser, $f_{\text{recoil}} < 0.2$. The top-quark background is suppressed by rejecting events with a b -tagged jet. The b -tagging algorithm described in Section 2 is used, at an operating point with 85% efficiency for b -quark jets and a mis-tag rate of 11% for light-quark and gluon jets, as measured in a sample of simulated $t\bar{t}$ events. The $Z \rightarrow \tau\tau$ background in $e\mu$ final states is suppressed using an invariant mass $m_{\tau\tau}$ computed assuming that the neutrinos from τ decays are collinear with the charged leptons [105] and that they are the only source of E_T^{miss} . The requirement $|m_{\tau\tau} - m_Z| \geq 25$ GeV is applied.

The $N_{\text{jet}} \geq 2$ analysis is optimised for the selection of the VBF production process. The two leading jets, referred to as “tagging jets”, are required to have a large rapidity separation, $|\Delta y_{jj}| > 2.8$, and a high invariant mass, $m_{jj} > 500$ GeV. To reduce the contribution

from ggF, events containing any jet with $p_T > 20$ GeV in the rapidity gap between the two tagging jets are rejected. Both leptons are required to be in the rapidity gap. The DY background is suppressed by imposing $E_T^{\text{miss}} > 20$ GeV for $e\mu$, and $E_T^{\text{miss}} > 45$ GeV and $E_{T, \text{STVF}}^{\text{miss}} > 35$ GeV for $ee/\mu\mu$. The same $Z \rightarrow \tau\tau$ veto and b -jet veto are applied as in the $N_{\text{jet}} = 1$ analysis. The $t\bar{t}$ background is further reduced by requiring a small total transverse momentum, $|\mathbf{p}_T^{\text{tot}}| < 45$ GeV, where $\mathbf{p}_T^{\text{tot}} = \mathbf{p}_T^{\ell\ell} + \mathbf{p}_T^{\text{jets}} + \mathbf{E}_T^{\text{miss}}$, and $\mathbf{p}_T^{\text{jets}}$ is the vectorial sum of all jets in the event with $p_T > 25$ GeV.

The total signal selection efficiency for $H \rightarrow WW^* \rightarrow \ell\nu\ell\nu$ events produced with $\ell = e, \mu$, including all the final state topologies considered, is about 5.3% at 8 TeV for a Higgs boson mass of 125 GeV.

The dilepton transverse mass m_T is the discriminating variable used in the fit to the data to extract the signal strength. It is defined as $m_T = ((E_T^{\ell\ell} + E_T^{\text{miss}})^2 - |\mathbf{p}_T^{\ell\ell} + \mathbf{E}_T^{\text{miss}}|^2)^{1/2}$ with $E_T^{\ell\ell} = (|\mathbf{p}_T^{\ell\ell}|^2 + m_{\ell\ell}^2)^{1/2}$. For the $e\mu$ channels with $N_{\text{jet}} \leq 1$, the fit is performed separately for events with $10 \text{ GeV} < m_{\ell\ell} < 30 \text{ GeV}$ and events with $30 \text{ GeV} < m_{\ell\ell} < 50 \text{ GeV}$, since the signal-to-background ratio varies across the $m_{\ell\ell}$ distribution, as shown in Fig. 4.

6.3. Background estimation

The leading SM processes producing two isolated high- p_T leptons and large values of E_T^{miss} are WW and top-quark production, where the latter includes (here and in the following) both $t\bar{t}$ and single top-quark processes (tW , tb and tqb). These backgrounds, as well as $Z \rightarrow \tau\tau$, are normalised to the data in control regions defined by selections similar to those used for the signal region, but with some criteria reversed or modified to obtain signal-depleted samples enriched in particular backgrounds. The event yield in the CR (after subtracting contributions from processes other than the targeted one) is extrapolated to the signal region using transfer factors obtained from MC simulation.

Additional significant backgrounds arise from W +jets and Z/γ^* , which are dissimilar to the signal but have large cross sections. A small fraction of these pass the event selection through rare final-state configurations and/or mis-measurements. This type of background is difficult to model reliably with the simulation and is therefore estimated mainly from data.

A third category of background consists of diboson processes with smaller cross sections, including $W\gamma^{(*)}$, WZ , and ZZ^* (inclusively indicated in the following

as *Other VV*), and the WW background in the $N_{\text{jet}} \geq 2$ analysis. These processes are estimated using the MC simulation normalised to the NLO cross sections from MCFM [106], except for the $N_{\text{jet}} \geq 2$ WW background, for which the cross section from the relevant MC generators (see Table 2) is used. The *Other VV* processes all produce same-charge and opposite-charge lepton pairs, as does W +jets. The number and kinematic features of same-charge events which would otherwise pass the full event selection are compared to the above-mentioned predictions for these backgrounds, and good agreement is observed.

6.3.1. W +jets

The W +jets background is estimated using a CR in the data in which one of the two leptons satisfies the identification and isolation criteria, and the other lepton (denoted here as “anti-identified”) fails these criteria but satisfies looser requirements. All other analysis selections are applied. The contribution to the signal region is then obtained by scaling the number of events in the CR by transfer factors, defined as the ratio of the number of fully identified lepton candidates passing all selections to the number of anti-identified leptons. The transfer factors are obtained from a dijet sample as a function of the p_T and η of the anti-identified lepton.

6.3.2. Z/γ^*

The Z/γ^* yield in the $ee/\mu\mu$ channels for $N_{\text{jet}} \leq 1$ is estimated using the f_{recoil} requirement efficiency in data for DY and non-DY processes. The former is measured in $ee/\mu\mu$ events in the Z -boson peak region. The latter is measured in the $e\mu$ signal region, taking advantage of the fact that the f_{recoil} distribution is nearly identical for all non-DY processes including the signal, as well as for $e\mu$ and $ee/\mu\mu$ final states. The DY normalisation in the $ee/\mu\mu$ signal region can then be extracted, given the two measured efficiencies and the total number of events in the $ee/\mu\mu$ signal region before and after the f_{recoil} requirement. For the $ee/\mu\mu$ channels with $N_{\text{jet}} \geq 2$, the two-dimensional distribution ($E_{\text{T}}^{\text{miss}}, m_{\ell\ell}$) in the data is used to estimate the total Z/γ^* yield, as in Ref. [103].

The $Z \rightarrow \tau\tau$ background is normalised to the data using an $e\mu$ CR defined by the back-to-back configuration of the leptons, $\Delta\phi_{\ell\ell} > 2.8$. For the corresponding CR with $N_{\text{jet}} \geq 2$, no b -tagged jets are allowed, and $|\mathbf{p}_{\text{T}}^{\text{lo}}| < 45$ GeV is required in addition, in order to reduce the contamination from top-quark production. A separate CR in the $Z \rightarrow \ell\ell$ peak region is used to correct the modelling of the VBF-related event selection.

6.3.3. $t\bar{t}$ and single top-quark

The top-quark background for the $N_{\text{jet}} = 0$ category is estimated using the procedure described in Ref. [2], namely from the number of events in data with any number of reconstructed jets passing the $E_{\text{T,rel}}^{\text{miss}}$ requirement (a sample dominated by top-quark production), multiplied by the fraction of top-quark events with no reconstructed jets obtained from simulation. This estimate is corrected using a CR containing b -tagged jets. The top-quark background in the $N_{\text{jet}} \geq 1$ channels is normalised to the data in a CR defined by requiring exactly one b -tagged jet and all other signal selections except for the requirements on $\Delta\phi_{\ell\ell}$ and $m_{\ell\ell}$.

6.3.4. WW

The WW background for $N_{\text{jet}} \leq 1$ is normalised using CRs in data defined with the same selection as the signal region except that the $\Delta\phi_{\ell\ell}$ requirement is removed and the $m_{\ell\ell}$ bound is modified: for $N_{\text{jet}} = 0$ $50 \text{ GeV} \leq m_{\ell\ell} < 100 \text{ GeV}$ is required, while for $N_{\text{jet}} = 1$ $m_{\ell\ell} > 80 \text{ GeV}$ is used to define the CR. Figure 4 shows the $m_{\ell\ell}$ distribution of $e\mu$ events with $N_{\text{jet}} = 0$ in the 8 TeV data. The level of agreement between the predicted background and the data for $m_{\ell\ell} > 100 \text{ GeV}$, a region with negligible signal contribution, validates the WW background normalisation and the extrapolation procedure based on the simulation. The $N_{\text{jet}} \geq 2$ prediction is taken from simulation because of the difficulty of isolating a kinematic region with enough events and small contamination from the top-quark background.

6.4. Systematic uncertainties

The systematic uncertainties affecting this analysis are summarized here and described in detail in Ref. [107]. The leading sources, i.e., those resulting in at least 4% uncertainty on the total signal or background yield in at least one N_{jet} category, are reported in Table 8.

Theoretical uncertainties on the inclusive signal production cross sections are given in Section 2. Additional, larger uncertainties from the QCD renormalisation and factorisation scales affect the predicted distribution of the ggF signal among the exclusive jet bins and can produce migration between categories. These uncertainties are estimated using the HNNLO program [108, 109] and the method reported in Ref. [110]. Their impact on the signal yield is summarised in Table 8, in addition to other non-negligible contributions (parton shower and underlying event modelling, as well as acceptance uncertainties due to QCD scale variations).

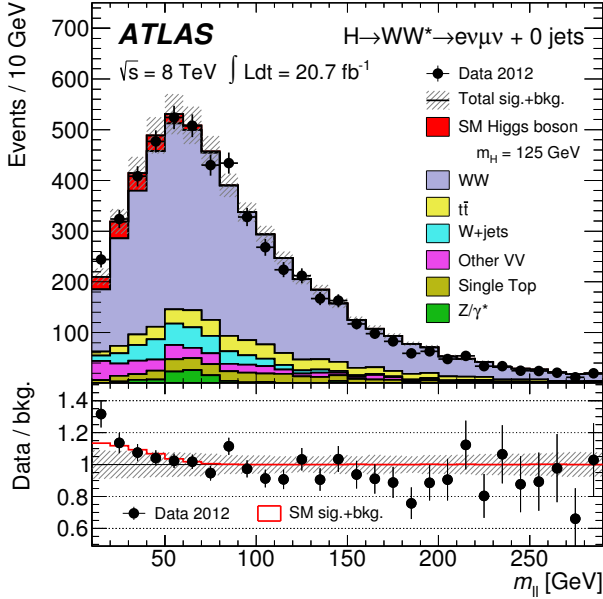


Figure 4: The $m_{\ell\ell}$ distribution of $e\mu$ events with $N_{\text{jet}} = 0$ for the 8 TeV $H \rightarrow WW^* \rightarrow \ell\nu\ell\nu$ analysis. The events with $m_{\ell\ell} < 50$ GeV correspond to the signal region except that the $\Delta\phi_{\ell\ell} < 1.8$ requirement is not applied here, and the events with $50 \text{ GeV} < m_{\ell\ell} < 100$ GeV correspond to the $N_{\text{jet}} = 0$ WW control region. The signal is stacked on top of the background. The hatched area represents the total uncertainty on the sum of the signal and background yields from statistical, experimental, and theoretical sources. The lower part of the figure shows the ratio of the data to the predicted background. For comparison, the expected ratio of the signal plus background to the background alone is also shown.

The experimental uncertainties affecting the expected signal and background yields are associated primarily with the reconstruction and identification efficiency, and with the energy and momentum scale and resolution, of the final-state objects (leptons, jets, and E_T^{miss}), as described in Section 2. The largest impact on the signal expectation comes from the knowledge of the jet energy scale and resolution (up to 6% in the $N_{\text{jet}} \geq 2$ channel).

For the backgrounds normalised using control regions, uncertainties come from the numbers of events in the CR and the contributions of other processes, as well as the transfer factors to the signal region.

For the WW background in the $N_{\text{jet}} \leq 1$ final states, the theoretical uncertainties on the transfer factors (evaluated according to the prescription of Ref. [15]) include the impact of missing higher-order QCD corrections, PDF variations, and MC modelling choices. They amount to $\pm 2\%$ and $\pm 4\text{--}6\%$ relative to the predicted WW background in the $N_{\text{jet}} = 0$ and $N_{\text{jet}} = 1$ final states, respectively. For the WW yield in the $N_{\text{jet}} \geq 2$ chan-

Table 8: For $m_H = 125$ GeV, the leading systematic uncertainties on the total signal and background yields for the 8 TeV $H \rightarrow WW^* \rightarrow \ell\nu\ell\nu$ analysis. All numbers are summed over lepton flavours. Sources contributing less than 4% are omitted, and individual entries below 1% are indicated with a ‘-’. Relative signs indicate correlation and anticorrelation (migration) between the N_{jet} categories represented by adjacent columns, and a \pm indicates an uncorrelated uncertainty. The exception is the jet energy scale and resolution, which includes multiple sources of uncertainty treated as correlated across categories but uncorrelated with each other. All rows are uncorrelated.

Source	$N_{\text{jet}} = 0$	$N_{\text{jet}} = 1$	$N_{\text{jet}} \geq 2$
Theoretical uncertainties on total signal yield (%)			
QCD scale for ggF, $N_{\text{jet}} \geq 0$	+13	-	-
QCD scale for ggF, $N_{\text{jet}} \geq 1$	+10	-27	-
QCD scale for ggF, $N_{\text{jet}} \geq 2$	-	-15	+4
QCD scale for ggF, $N_{\text{jet}} \geq 3$	-	-	+4
Parton shower and underlying event	+3	-10	± 5
QCD scale (acceptance)	+4	+4	± 3
Experimental uncertainties on total signal yield (%)			
Jet energy scale and resolution	5	2	6
Uncertainties on total background yield (%)			
Jet energy scale and resolution	2	3	7
WW transfer factors (theory)	± 1	± 2	± 4
b -tagging efficiency	-	+7	+2
f_{recoil} efficiency	± 4	± 2	-

nel, which is obtained from simulation, the total uncertainty is 42% for QCD production with gluon emission, and 11% for the smaller but non-negligible contribution from purely electroweak processes; the latter includes the size of possible interference with Higgs boson production through VBF. The resulting uncertainties on the total background yield for all N_{jet} are quoted in Table 8.

The leading uncertainties on the top-quark background are experimental. The b -tagging efficiency is the most important of these, and it appears in Table 8 primarily through its effect on this background. Theoretical uncertainties on the top-quark background have the greatest relative importance, $\pm 2\%$ on the total background yield, for $N_{\text{jet}} \geq 2$, and therefore do not appear in Table 8.

The W +jets transfer factor uncertainty ($\pm(40\text{--}45)\%$) is dominated by differences in the jet composition between dijet and W +jets samples as observed in the MC simulation. The uncertainties on the muon and electron transfer factors are treated as correlated among the N_{jet} categories but uncorrelated with each other. The impact on the total background uncertainty is at most $\pm 2.5\%$. The main uncertainty on the DY contribution in the $N_{\text{jet}} \leq 1$ channels comes from the use of the f_{recoil} efficiency evaluated at the peak of the Z -boson mass distribution for the estimation of the DY contamination in the low- $m_{\ell\ell}$ region.

Table 9: For the $H \rightarrow WW^* \rightarrow \ell\nu\ell\nu$ analysis of the 8 TeV data, the numbers of events observed in the data and expected from signal ($m_H = 125.5$ GeV) and backgrounds inside the transverse mass regions $0.75 m_H < m_T < m_H$ for $N_{\text{jet}} \leq 1$ and $m_T < 1.2 m_H$ for $N_{\text{jet}} \geq 2$. All lepton flavours are combined. The total background as well as its main components are shown. The quoted uncertainties include the statistical and systematic contributions, and account for anticorrelations between the background predictions.

	$N_{\text{jet}} = 0$	$N_{\text{jet}} = 1$	$N_{\text{jet}} \geq 2$
Observed	831	309	55
Signal	100 ± 21	41 ± 14	10.9 ± 1.4
Total background	739 ± 39	261 ± 28	36 ± 4
WW	551 ± 41	108 ± 40	4.1 ± 1.5
Other VV	58 ± 8	27 ± 6	1.9 ± 0.4
Top-quark	39 ± 5	95 ± 28	5.4 ± 2.1
Z+jets	30 ± 10	12 ± 6	22 ± 3
W+jets	61 ± 21	20 ± 5	0.7 ± 0.2

The uncertainty on the m_T shape for the total background, which is used in the fit to extract the signal yield, is dominated by the uncertainties on the normalisations of the individual components. The only explicit m_T shape uncertainty is applied to the WW background, and is determined by comparing several generators and showering algorithms.

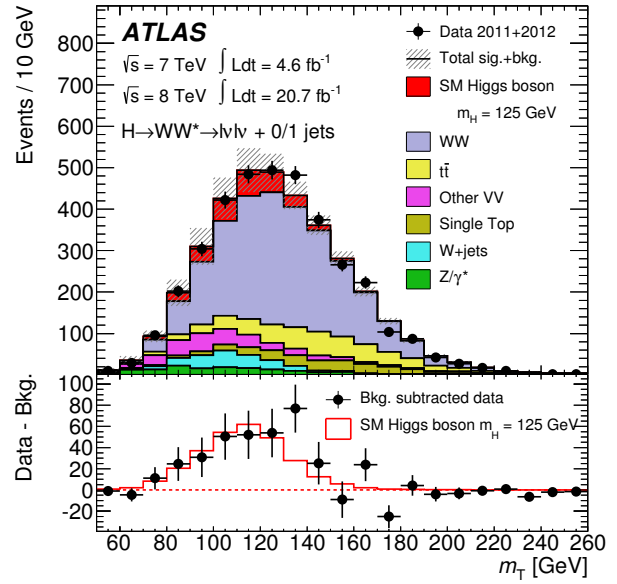
The estimated background contributions with their uncertainties are listed in Table 9.

6.5. Results

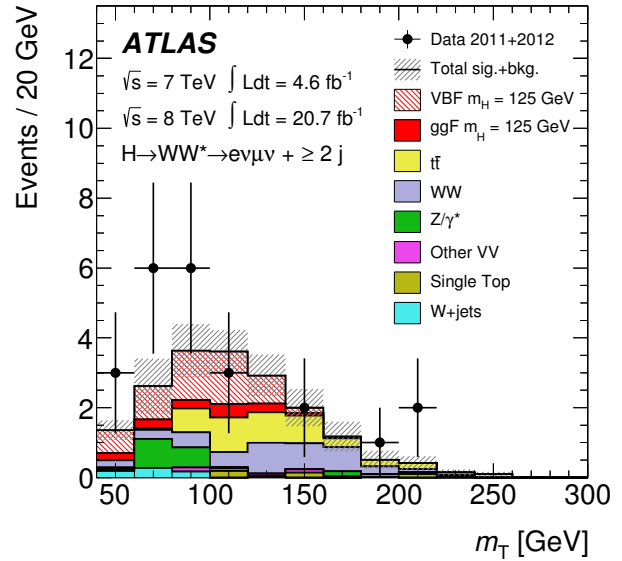
Figure 5 shows the transverse mass distributions after the full selection for $N_{\text{jet}} \leq 1$ and $N_{\text{jet}} \geq 2$ final states. The regions with $m_T > 150$ GeV are depleted of signal contribution; the level of agreement of the data with the expectation in these regions, which are different from those used to normalise the backgrounds, illustrates the quality of the background estimates. The expected numbers of signal and background events at 8 TeV are presented in Table 9. The VBF process contributes 2%, 12% and 81% of the predicted signal in the $N_{\text{jet}} = 0, 1$, and ≥ 2 final states, respectively. The total number of observed events in the same m_T windows as in Table 9 is 218 in the 7 TeV data and 1195 in the 8 TeV data.

An excess of events relative to the background-only expectation is observed in the data, with the maximum deviation (4.1σ) occurring at $m_H = 140$ GeV. For $m_H = 125.5$ GeV, a significance of 3.8σ is observed, compared with an expected value of 3.8σ for a SM Higgs boson.

Additional interpretation of these results is presented in Section 7.



(a)



(b)

Figure 5: The transverse mass distributions for events passing the full selection of the $H \rightarrow WW^* \rightarrow \ell\nu\ell\nu$ analysis: (a) summed over all lepton flavours for final states with $N_{\text{jet}} \leq 1$; (b) different-flavour final states with $N_{\text{jet}} \geq 2$. The signal is stacked on top of the background, and in (b) is shown separately for the ggF and VBF production processes. The hatched area represents the total uncertainty on the sum of the signal and background yields from statistical, experimental, and theoretical sources. In the lower part of (a), the residuals of the data with respect to the estimated background are shown, compared to the expected m_T distribution of a SM Higgs boson.

7. Higgs boson property measurements

The results from the individual channels described in the previous sections are combined here to extract information about the Higgs boson mass, production properties and couplings.

7.1. Statistical method

The statistical treatment of the data is described in Refs. [111–115]. Hypothesis testing and confidence intervals are based on the profile likelihood ratio [116] $\Lambda(\alpha)$. The latter depends on one or more parameters of interest α , such as the Higgs boson production strength μ normalised to the SM expectation (so that $\mu = 1$ corresponds to the SM Higgs boson hypothesis and $\mu = 0$ to the background-only hypothesis), mass m_H , coupling strengths κ , ratios of coupling strengths λ , as well as on nuisance parameters θ :

$$\Lambda(\alpha) = \frac{L(\alpha, \hat{\theta}(\alpha))}{L(\hat{\alpha}, \hat{\theta})} \quad (1)$$

The likelihood functions in the numerator and denominator of the above equation are built using sums of signal and background probability density functions (pdfs) in the discriminating variables (chosen to be the $\gamma\gamma$ and 4ℓ mass spectra for $H \rightarrow \gamma\gamma$ and $H \rightarrow ZZ^* \rightarrow 4\ell$, respectively, and the m_T distribution for the $H \rightarrow WW^* \rightarrow \ell\nu\ell\nu$ channel). The pdfs are derived from MC simulation for the signal and from both data and simulation for the background, as described in Sections 4–6. Likelihood fits to the observed data are done for the parameters of interest. The single circumflex in Eq. (1) denotes the unconditional maximum likelihood estimate of a parameter and the double circumflex denotes the conditional maximum likelihood estimate for given fixed values of the parameters of interest α . Systematic uncertainties and their correlations [111] are modelled by introducing nuisance parameters θ described by likelihood functions associated with the estimate of the corresponding effect. The choice of the parameters of interest depends on the test under consideration, with the remaining parameters being “profiled”, *i.e.*, similarly to nuisance parameters they are set to the values that maximise the likelihood function for the given fixed values of the parameters of interest.

7.2. Mass and production strength

The mass of the new particle is measured from the data using the two channels with the best mass resolution, $H \rightarrow \gamma\gamma$ and $H \rightarrow ZZ^* \rightarrow 4\ell$. In the two cases, $m_H = 126.8 \pm 0.2$ (stat) ± 0.7 (sys) GeV and $m_H =$

$124.3^{+0.6}_{-0.5}$ (stat) $^{+0.5}_{-0.3}$ (sys) GeV are obtained from fits to the mass spectra.

To derive a combined mass measurement, the profile likelihood ratio $\Lambda(m_H)$ is used; the signal production strengths $\mu^{\gamma\gamma}$ and $\mu^{4\ell}$, giving the signal yields measured in the two individual channels normalised to the SM expectation, are treated as independent nuisance parameters in order to allow for the possibility of different deviations from the SM prediction in the two decays modes. The ratios of the cross sections for the various production modes for each channel are fixed to the SM values. It was verified that this restriction does not cause any bias in the results. The combined mass is measured to be:

$$m_H = 125.5 \pm 0.2$$
 (stat) $^{+0.5}_{-0.6}$ (sys) GeV (2)

As discussed in Sections 4.4 and 5.4, the main sources of systematic uncertainty are the photon and lepton energy and momentum scales. In the combination, the consistency between the muon and electron final states in the $H \rightarrow ZZ^* \rightarrow 4\ell$ channel causes a $\sim 0.8\sigma$ adjustment of the overall e/γ energy scale, which translates into a ~ 350 MeV downward shift of the fitted $m_H^{\gamma\gamma}$ value with respect to the value measured from the $H \rightarrow \gamma\gamma$ channel alone.

To quantify the consistency between the fitted $m_H^{\gamma\gamma}$ and $m_H^{4\ell}$ masses, the data are fitted with the profile likelihood ratio $\Lambda(\Delta m_H)$, where the parameter of interest is the mass difference $\Delta m_H = m_H^{\gamma\gamma} - m_H^{4\ell}$. The average mass m_H and the signal strengths $\mu^{\gamma\gamma}$ and $\mu^{4\ell}$ are treated as independent nuisance parameters. The result is:

$$\Delta m_H = 2.3^{+0.6}_{-0.7}$$
 (stat) ± 0.6 (sys) GeV (3)

where the uncertainties are 68% confidence intervals computed with the asymptotic approximation [116]. From the value of the likelihood at $\Delta m_H = 0$, the probability for a single Higgs boson to give a value of $\Lambda(\Delta m_H)$ disfavouring the $\Delta m_H = 0$ hypothesis more strongly than observed in the data is found to be at the level of 1.2% (2.5σ) using the asymptotic approximation, and 1.5% (2.4σ) using Monte Carlo ensemble tests. In order to test the effect of a possible non-Gaussian behaviour of the three principal sources contributing to the electron and photon energy scale systematic uncertainty (the $Z \rightarrow ee$ calibration procedure, the knowledge of the material upstream of the electromagnetic calorimeter and the energy scale of the presampler detector) the consistency between the two mass measurements is also evaluated by considering $\pm 1\sigma$ values for these uncertainties. With this treatment, the consistency increases to up to 8%.

To measure the Higgs boson production strength, the parameter μ is determined from a fit to the data using the profile likelihood ratio $\Lambda(\mu)$ for a fixed mass hypothesis corresponding to the measured value $m_H = 125.5$ GeV. The results are shown in Fig. 6, where the production strengths measured in the three channels and in their main analysis categories are presented. The signal production strength normalised to the SM expectation, obtained by combining the three channels, is:

$$\mu = 1.33 \pm 0.14 (\text{stat}) \pm 0.15 (\text{sys}) \quad (4)$$

where the systematic uncertainty receives similar contributions from the theoretical uncertainty on the signal cross section (ggF QCD scale and PDF, see Table 1) and all other, mainly experimental, sources. The uncertainty on the mass measurement reported in Eq. (2) produces a $\pm 3\%$ variation of μ . The consistency between this measurement and the SM Higgs boson expectation ($\mu = 1$) is about 7%; the use of a flat likelihood for the ggF QCD scale systematic uncertainty in the quoted $\pm 1\sigma$ interval yields a similar level of consistency with the $\mu = 1$ hypothesis. The overall compatibility between the signal strengths measured in the three final states and the SM predictions is about 14%, with the largest deviation ($\sim 1.9\sigma$) observed in the $H \rightarrow \gamma\gamma$ channel. Good consistency between the measured and expected signal strengths is also found for the various categories of the $H \rightarrow \gamma\gamma$, $H \rightarrow ZZ^* \rightarrow 4\ell$ and $H \rightarrow WW^* \rightarrow \ell\nu\ell\nu$ analyses, which are the primary experimental inputs to the fit discussed in this section. If the preliminary $H \rightarrow \tau\tau$ [117] and $H \rightarrow b\bar{b}$ [118] results, for which only part of the 8 TeV dataset is used (13 fb^{-1}), were included, the combined signal strength would be $\mu = 1.23 \pm 0.18$.

7.3. Evidence for production via vector-boson fusion

The measurements of the signal strengths described in the previous section do not give direct information on the relative contributions of the different production mechanisms. Furthermore, fixing the ratios of the production cross sections for the various processes to the values predicted by the Standard Model may conceal tensions between the data and the theory. Therefore, in addition to the signal strengths for different decay modes, the signal strengths of different production processes contributing to the same decay mode⁴ are determined, exploiting the sensitivity offered by the use of event categories in the analyses of the three channels.

⁴Such an approach avoids model assumptions needed for a consistent parameterisation of production and decay modes in terms of Higgs boson couplings.

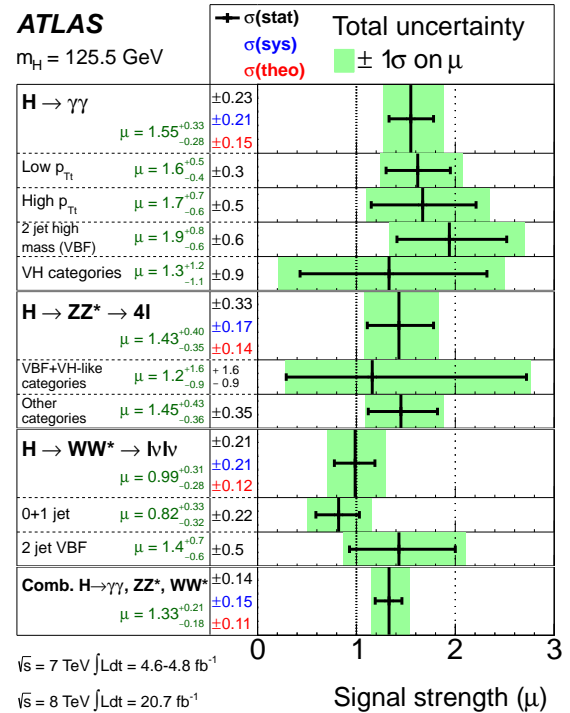


Figure 6: The measured production strengths for a Higgs boson of mass $m_H = 125.5$ GeV, normalised to the SM expectations, for the individual diboson final states and their combination. Results are also given for the main categories of each analysis (described in Sections 4.2, 5.2 and 6.2). The best-fit values are shown by the solid vertical lines, with the total $\pm 1\sigma$ uncertainty indicated by the shaded band, and the statistical uncertainty by the superimposed horizontal error bars. The numbers in the second column specify the contributions of the (symmetrised) statistical uncertainty (top), the total (experimental and theoretical) systematic uncertainty (middle), and the theory uncertainty in the signal cross section (from QCD scale, PDF, and branching ratios) alone; for the individual categories only the statistical uncertainty is given.

The data are fitted separating vector-boson-mediated processes, VBF and VH , from gluon-mediated processes, ggF and $t\bar{t}H$, involving fermion (mainly top-quark) loops or legs.⁵ Two signal strength parameters, $\mu_{\text{ggF}+t\bar{t}H}^f = \mu_{\text{ggF}}^f = \mu_{t\bar{t}H}^f$ and $\mu_{\text{VBF}+VH}^f = \mu_{\text{VBF}}^f = \mu_{VH}^f$, which scale the SM-predicted rates to those observed, are introduced for each of the considered final states ($f = H \rightarrow \gamma\gamma, H \rightarrow ZZ^* \rightarrow 4\ell, H \rightarrow WW^* \rightarrow \ell\nu\ell\nu$). The results are shown in Fig. 7. The 95% CL contours of the measurements are consistent with the SM expectation. A combination of all channels would provide a higher-sensitivity test of the theory. This can be done in

⁵Such a separation is possible under the assumption that the kinematic properties of these production modes agree with the SM predictions within uncertainties.

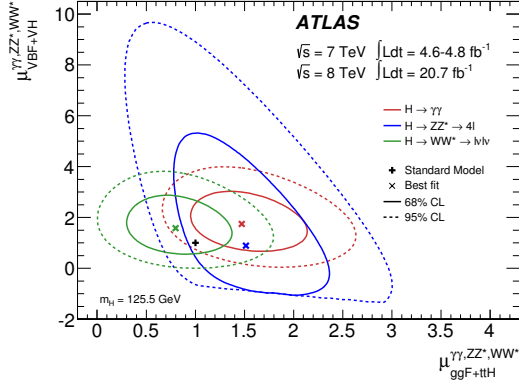


Figure 7: Likelihood contours in the $(\mu_{\text{ggF}+t\bar{t}H}^f, \mu_{\text{VBF}+VH}^f)$ plane for the final states $f=H \rightarrow \gamma\gamma$, $H \rightarrow ZZ^* \rightarrow 4\ell$, $H \rightarrow WW^* \rightarrow \ell\nu\ell\nu$ and a Higgs boson mass $m_H = 125.5$ GeV. The sharp lower edge of the $H \rightarrow ZZ^* \rightarrow 4\ell$ contours is due to the small number of events in this channel and the requirement of a positive pdf. The best fits to the data (x) and the 68% (full) and 95% (dashed) CL contours are indicated, as well as the SM expectation (+).

a model-independent way (*i.e.* without assumptions on the Higgs boson branching ratios) by measuring the ratios $\mu_{\text{VBF}+VH}/\mu_{\text{ggF}+t\bar{t}H}$ for the individual final states and their combination. The results of the fit to the data with the likelihood $\Lambda(\mu_{\text{VBF}+VH}/\mu_{\text{ggF}+t\bar{t}H})$ are shown in Fig. 8. Good agreement with the SM expectation is observed for the individual final states and their combination.

To test the sensitivity to VBF production alone, the data are also fitted with the ratio $\mu_{\text{VBF}}/\mu_{\text{ggF}+t\bar{t}H}$. A value

$$\mu_{\text{VBF}}/\mu_{\text{ggF}+t\bar{t}H} = 1.4^{+0.6}_{-0.5} (\text{stat})^{+0.5}_{-0.3} (\text{sys}) \quad (5)$$

is obtained from the combination of the three channels (Fig. 9), where the main components of the systematic uncertainty come from the theoretical predictions for the ggF contributions to the various categories and jet multiplicities and the knowledge of the jet energy scale and resolution. This result provides evidence at the 3.3σ level that a fraction of Higgs boson production occurs through VBF (as Fig. 9 shows, the probability for a vanishing value of $\mu_{\text{VBF}}/\mu_{\text{ggF}+t\bar{t}H}$, given the observation in the data, is 0.04%). The inclusion of preliminary $H \rightarrow \tau\tau$ results [117], which also provide some sensitivity to this ratio, would give a significance of 3.1σ .

7.4. Couplings measurements

Following the approach and benchmarks recommended in Refs. [119], measurements of couplings are implemented using a leading-order tree-level motivated framework. This framework is based on the following assumptions:

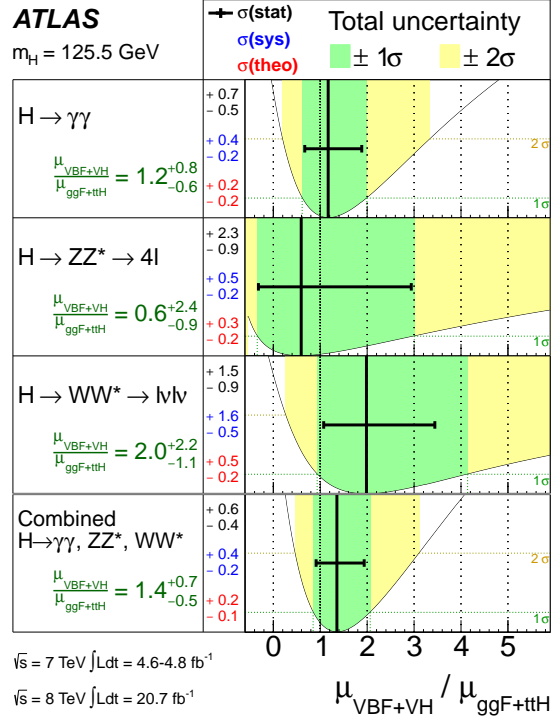


Figure 8: Measurements of the $\mu_{\text{VBF}+VH}/\mu_{\text{ggF}+t\bar{t}H}$ ratios for the individual diboson final states and their combination, for a Higgs boson mass $m_H = 125.5$ GeV. The best-fit values are represented by the solid vertical lines, with the total $\pm 1\sigma$ and $\pm 2\sigma$ uncertainties indicated by the dark- and light-shaded band, respectively, and the statistical uncertainties by the superimposed horizontal error bars. The numbers in the second column specify the contributions of the statistical uncertainty (top), the total (experimental and theoretical) systematic uncertainty (middle), and the theoretical uncertainty (bottom) on the signal cross section (from QCD scale, PDF, and branching ratios) alone. For a more complete illustration, the distributions of the likelihood ratios from which the total uncertainties are extracted are overlaid.

- The signals observed in the different search channels originate from a single resonance. A mass of 125.5 GeV is assumed here; the impact of the uncertainty reported in Eq. (2) on the results discussed in this section is negligible.
- The width of the Higgs boson is narrow, justifying the use of the zero-width approximation. Hence the predicted rate for a given channel can be decomposed in the following way:

$$\sigma \cdot B(i \rightarrow H \rightarrow f) = \frac{\sigma_i \cdot \Gamma_f}{\Gamma_H} \quad (6)$$

where σ_i is the production cross section through the initial state i , B and Γ_f are the branching ratio and partial decay width into the final state f ,

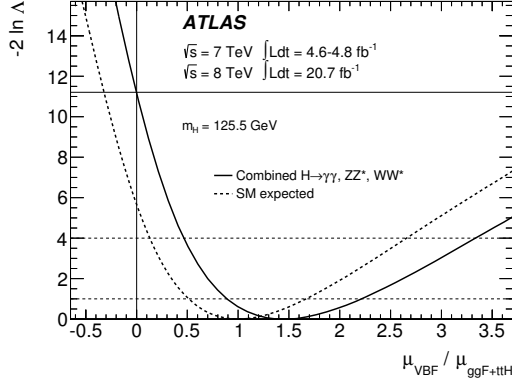


Figure 9: Likelihood curve for the ratio $\mu_{\text{VBF}}/\mu_{\text{ggF}+\text{ttH}}$ for the combination of the $H \rightarrow \gamma\gamma$, $H \rightarrow ZZ^* \rightarrow 4\ell$ and $H \rightarrow WW^* \rightarrow \ell\nu\ell\nu$ channels and a Higgs boson mass $m_H = 125.5$ GeV. The parameter $\mu_{\text{VH}}/\mu_{\text{ggF}+\text{ttH}}$ is profiled in the fit. The dashed curve shows the SM expectation. The horizontal dashed lines indicate the 68% and 95% CL.

respectively, and Γ_H the total width of the Higgs boson.

- Only modifications of coupling strengths are considered, while the tensor structure of the Lagrangian is assumed to be the same as in the Standard Model. This implies in particular that the observed state is a CP-even scalar.⁶

The coupling scale factors κ_j are defined in such a way that the cross sections σ_j and the partial decay widths Γ_j associated with the SM particle j scale with κ_j^2 compared to the SM prediction [119]. With this notation, and with κ_H^2 being the scale factor for the total Higgs boson width Γ_H , the cross section for the $gg \rightarrow H \rightarrow \gamma\gamma$ process, for example, can be expressed as:

$$\frac{\sigma \cdot B(gg \rightarrow H \rightarrow \gamma\gamma)}{\sigma_{\text{SM}}(gg \rightarrow H) \cdot B_{\text{SM}}(H \rightarrow \gamma\gamma)} = \frac{\kappa_g^2 \cdot \kappa_\gamma^2}{\kappa_H^2} \quad (7)$$

In some of the fits, κ_H and the effective scale factors κ_γ and κ_g for the loop-induced $H \rightarrow \gamma\gamma$ and $gg \rightarrow H$ processes are expressed as a function of the more fundamental factors $\kappa_W, \kappa_Z, \kappa_t, \kappa_b$ and κ_τ (only the dominant fermion contributions are indicated here for simplicity). The relevant relationships are:

$$\kappa_g^2(\kappa_b, \kappa_t) = \frac{\kappa_t^2 \cdot \sigma_{ggH}^{tt} + \kappa_b^2 \cdot \sigma_{ggH}^{bb} + \kappa_t \kappa_b \cdot \sigma_{ggH}^{tb}}{\sigma_{ggH}^{tt} + \sigma_{ggH}^{bb} + \sigma_{ggH}^{tb}}$$

⁶The spin-CP hypothesis is addressed in Ref. [10].

$$\kappa_\gamma^2(\kappa_b, \kappa_t, \kappa_\tau, \kappa_W) = \frac{\sum_{i,j} \kappa_i \kappa_j \cdot \Gamma_{\gamma\gamma}^{ij}}{\sum_{i,j} \Gamma_{\gamma\gamma}^{ij}} \quad (8)$$

$$\kappa_H^2 = \sum_{\substack{jj=WW^*, ZZ^*, b\bar{b}, \tau^-\tau^+, \\ \gamma\gamma, Z\gamma, gg, t\bar{t}, c\bar{c}, s\bar{s}, \mu^-\mu^+}} \frac{\kappa_j^2 \Gamma_{jj}^{\text{SM}}}{\Gamma_H^{\text{SM}}}$$

where σ_{ggH}^{ij} , $\Gamma_{\gamma\gamma}^{ij}$ and Γ_{ff}^{SM} are obtained from theory [14, 119].

Results are extracted from fits to the data using the profile likelihood ratio $\Lambda(\kappa)$, where the κ_j couplings are treated either as parameters of interest or as nuisance parameters, depending on the measurement.

The assumptions made for the various measurements are summarised in Table 10 and discussed in the next sections together with the results.

7.4.1. Couplings to fermions and bosons

The first benchmark considered here (indicated as model 1 in Table 10) assumes one coupling scale factor for fermions, κ_F , and one for bosons, κ_V ; in this scenario, the $H \rightarrow \gamma\gamma$ and $gg \rightarrow H$ loops and the total Higgs boson width depend only on κ_F and κ_V , with no contributions from physics beyond the Standard Model (BSM). The strongest constraint on κ_F comes indirectly from the $gg \rightarrow H$ production loop.

Figure 10 shows the results of the fit to the data for the three channels and their combination. Since only the relative sign of κ_F and κ_V is physical, in the following $\kappa_V > 0$ is assumed. Some sensitivity to this relative sign is provided by the negative interference between the W -boson loop and t -quark loop in the $H \rightarrow \gamma\gamma$ decay. The data prefer the minimum with positive relative sign, which is consistent with the SM prediction, but the local minimum with negative sign is also compatible with the observation (at the $\sim 2\sigma$ level). The two-dimensional compatibility of the SM prediction with the best-fit value is 12%. The 68% CL intervals of κ_F and κ_V , obtained by profiling over the other parameter, are:

$$\kappa_F \in [0.76, 1.18] \quad (9)$$

$$\kappa_V \in [1.05, 1.22] \quad (10)$$

with similar contributions from the statistical and systematic uncertainties.

In this benchmark model, the assumption of no contributions from new particles to the Higgs boson width provides strong constraints on the fermion coupling κ_F ,

Table 10: Summary of the coupling benchmark models discussed in this paper, where $\lambda_{ij} = \kappa_i/\kappa_j$, $\kappa_{ii} = \kappa_i\kappa_i/\kappa_H$, and the functional dependence assumptions are: $\kappa_V = \kappa_W = \kappa_Z$, $\kappa_F = \kappa_t = \kappa_b = \kappa_\tau$ (and similarly for the other fermions), $\kappa_g = \kappa_g(\kappa_b, \kappa_t)$, $\kappa_\gamma = \kappa_\gamma(\kappa_b, \kappa_t, \kappa_\tau, \kappa_W)$, and $\kappa_H = \kappa_H(\kappa_i)$. The tick marks indicate which assumptions are made in each case. The last column shows, as an example, the relative couplings involved in the $gg \rightarrow H \rightarrow \gamma\gamma$ process, see Eq. (7), and their functional dependence in the various benchmark models.

Model	Probed couplings	Parameters of interest	Functional assumptions					Example: $gg \rightarrow H \rightarrow \gamma\gamma$
			κ_V	κ_F	κ_g	κ_γ	κ_H	
1	Couplings to fermions and bosons	κ_V, κ_F	√	√	√	√	√	$\kappa_F^2 \cdot \kappa_V^2(\kappa_F, \kappa_V)/\kappa_H^2(\kappa_F, \kappa_V)$
2		$\lambda_{FV}, \kappa_{VV}$	√	√	√	√	-	$\kappa_{VV}^2 \cdot \lambda_{FV}^2 \cdot \kappa_V^2(\lambda_{FV}, \lambda_{FV}, \lambda_{FV}, 1)$
3	Custodial symmetry	$\lambda_{WZ}, \lambda_{FZ}, \kappa_{ZZ}$	-	√	√	√	-	$\kappa_{ZZ}^2 \cdot \lambda_{FZ}^2 \cdot \kappa_V^2(\lambda_{FZ}, \lambda_{FZ}, \lambda_{FZ}, \lambda_{WZ})$
4		$\lambda_{WZ}, \lambda_{FZ}, \lambda_{\gamma Z}, \kappa_{ZZ}$	-	√	√	-	-	$\kappa_{ZZ}^2 \cdot \lambda_{FZ}^2 \cdot \lambda_{\gamma Z}^2$
5	Vertex loops	κ_g, κ_γ	=1	=1	-	-	√	$\kappa_g^2 \cdot \kappa_\gamma^2/\kappa_H^2(\kappa_g, \kappa_\gamma)$

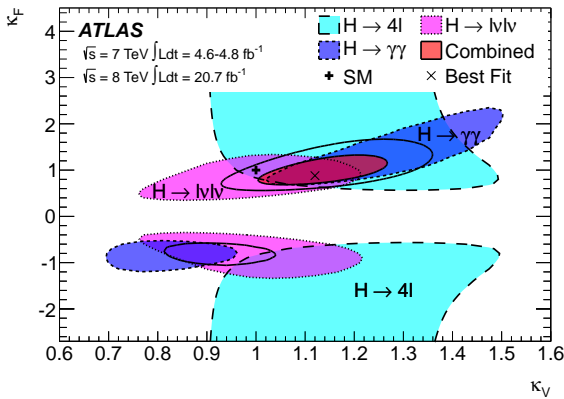


Figure 10: Likelihood contours (68% CL) of the coupling scale factors κ_F and κ_V for fermions and bosons (benchmark model 1 in Table 10), as obtained from fits to the three individual channels and their combination (for the latter, the 95% CL contour is also shown). The best-fit result (x) and the SM expectation (+) are also indicated.

as about 75% of the total SM width comes from decays to fermions or involving fermions. If this assumption is relaxed, only the ratio $\lambda_{FV} = \kappa_F/\kappa_V$ can be measured (benchmark model 2 in Table 10), which still provides useful information on the relationship between Yukawa and gauge couplings. Fits to the data give the following 68% CL intervals for λ_{FV} and $\kappa_{VV} = \kappa_V\kappa_V/\kappa_H$ (when profiling over the other parameter):

$$\lambda_{FV} \in [0.70, 1.01] \quad (11)$$

$$\kappa_{VV} \in [1.13, 1.45] \quad (12)$$

The two-dimensional compatibility of the SM prediction with the best-fit value is 12%. These results also exclude vanishing couplings of the Higgs boson to fermions (indirectly, mainly through the $gg \rightarrow H$ production loop) by more than 5σ .

7.4.2. Ratio of couplings to the W and Z bosons

In the Standard Model, custodial symmetry imposes the constraint that the W and Z bosons have related couplings to the Higgs boson, $g_{HVV} \sim m_V^2/v$ (where v is the vacuum expectation value of the Higgs field), and that $\rho = m_W^2/(m_Z^2 \cdot \cos^2 \theta_W)$ (where θ_W is the weak Weinberg angle) is equal to unity (as measured at LEP [120]). The former constraint is tested here by measuring the ratio $\lambda_{WZ} = \kappa_W/\kappa_Z$.

The simplest and most model-independent approach is to extract the ratio of branching ratios normalised to their SM expectation, $\lambda_{WZ}^2 = \mathcal{B}(H \rightarrow WW^*)/\mathcal{B}(H \rightarrow ZZ^*) \cdot \mathcal{B}_{\text{SM}}(H \rightarrow ZZ^*)/\mathcal{B}_{\text{SM}}(H \rightarrow WW^*)$, from the measured inclusive rates of the $H \rightarrow WW^*$ and $H \rightarrow ZZ^*$ channels. A fit to the data with the likelihood $\Lambda(\lambda_{WZ})$, where $\mu_{\text{ggF}+tH} \times \mathcal{B}(H \rightarrow ZZ^*)/\mathcal{B}_{\text{SM}}(H \rightarrow ZZ^*)$ and $\mu_{\text{VBF}+VH}/\mu_{\text{ggF}+tH}$ are profiled, gives $\lambda_{WZ} = 0.81^{+0.16}_{-0.15}$.

A more sensitive measurement can be obtained by also using information from WH and ZH production, from the VBF process (which in the SM is roughly 75% W-fusion and 25% Z-fusion mediated) and from the $H \rightarrow \gamma\gamma$ decay mode. A fit to the data using benchmark model 3 in Table 10 gives the likelihood curve shown in Fig. 11, with $\lambda_{WZ} \in [0.61, 1.04]$ at the 68% CL, dominated by the statistical uncertainty; the other parameters, λ_{FZ} and κ_{ZZ} , are profiled. The three-dimensional compatibility of the SM prediction with the best-fit value is 19%.

Potential contributions from BSM physics affecting the $H \rightarrow \gamma\gamma$ channel could produce apparent deviations of the ratio λ_{WZ} from unity even if custodial symmetry is not broken. It is therefore desirable to decouple the observed $H \rightarrow \gamma\gamma$ event rate from the measurement of λ_{WZ} . This is done with an extended fit for the ratio λ_{WZ} , where one extra degree of freedom ($\lambda_{\gamma Z} = \kappa_\gamma/\kappa_Z$) absorbs possible BSM effects in the $H \rightarrow \gamma\gamma$ channel (benchmark model 4 in Table 10). This measurement

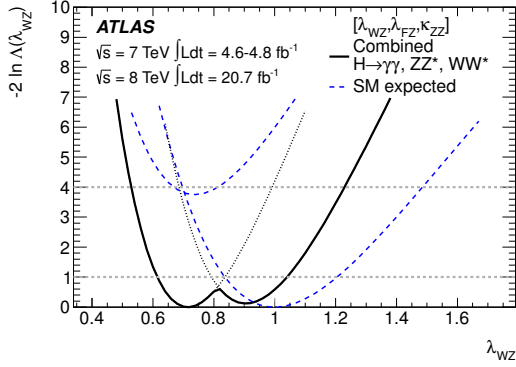


Figure 11: Likelihood curve for the coupling scale factor λ_{WZ} (benchmark model 3 in Table 10). The thin dotted lines indicate the continuation of the likelihood curve when restricting λ_{FZ} to be either positive or negative. The dashed curves show the SM expectation with the right (left) minimum indicating λ_{FZ} positive (negative).

yields:

$$\lambda_{WZ} = 0.82 \pm 0.15 \quad (13)$$

and a four-dimensional compatibility of the SM prediction with the best-fit value of 20%.

7.4.3. Constraints on production and decay loops

Many BSM physics scenarios predict the existence of new heavy particles, which can contribute to loop-induced processes such as $gg \rightarrow H$ production and $H \rightarrow \gamma\gamma$ decay. In the approach used here (benchmark model 5 in Table 10), it is assumed that the new particles do not contribute to the Higgs boson width and that the couplings of the known particles to the Higgs boson have SM strength (*i.e.* $\kappa_i=1$). Effective scale factors κ_g and κ_γ are introduced to parameterise the $gg \rightarrow H$ and $H \rightarrow \gamma\gamma$ loops. The results of their measurements from a fit to the data are shown in Fig. 12. The best-fit values when profiling over the other parameters are:

$$\kappa_g = 1.04 \pm 0.14 \quad (14)$$

$$\kappa_\gamma = 1.20 \pm 0.15 \quad (15)$$

The two-dimensional compatibility of the SM prediction with the best-fit value is 14%.

7.4.4. Summary

The results of the measurements of the coupling scale factors discussed in the previous sections, obtained under the assumptions detailed in Section 7.4 and Table 10, are summarised in Fig. 13. The measurements

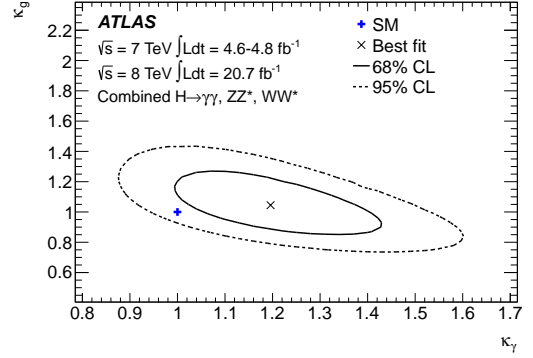


Figure 12: Likelihood contours for the coupling scale factors κ_γ and κ_g probing BSM contributions to the $H \rightarrow \gamma\gamma$ and $gg \rightarrow H$ loops, assuming no BSM contributions to the total Higgs boson width (benchmark model 5 in Table 10). The best-fit result (\times) and the SM expectation ($+$) are also indicated.

in the various benchmark models are strongly correlated, as they are obtained from fits to the same experimental data. A simple χ^2 -like compatibility test with the SM is therefore not meaningful.

The coupling of the new particle to gauge bosons κ_V is constrained by several channels, directly and indirectly, at the $\pm 10\%$ level. Couplings to fermions with a significance larger than 5σ are indirectly observed mainly through the gluon-fusion production process, assuming the loop is dominated by fermion exchange. The ratio of the relative couplings of the Higgs boson to the W and Z bosons, κ_W/κ_Z , is measured to be consistent with unity, as predicted by custodial symmetry. Under the hypothesis that all couplings of the Higgs boson to the known particles are fixed to their SM values, and assuming no BSM contributions to the Higgs boson width, no significant anomalous contributions to the $gg \rightarrow H$ and $H \rightarrow \gamma\gamma$ loops are observed.

8. Conclusions

Data recorded by the ATLAS experiment at the CERN Large Hadron Collider in 2011 and 2012, corresponding to an integrated luminosity of up to 25 fb^{-1} at $\sqrt{s} = 7 \text{ TeV}$ and $\sqrt{s} = 8 \text{ TeV}$, have been analysed to determine several properties of the recently discovered Higgs boson using the $H \rightarrow \gamma\gamma$, $H \rightarrow ZZ^* \rightarrow 4\ell$ and $H \rightarrow WW^* \rightarrow \ell\nu\ell\nu$ decay modes. The reported results include measurements of the mass and signal strength, evidence for production through vector-boson fusion, and constraints on couplings to bosons and fermions as well as on anomalous contributions to loop-induced processes. The precision exceeds previously published results in several cases. All measurements are consistent

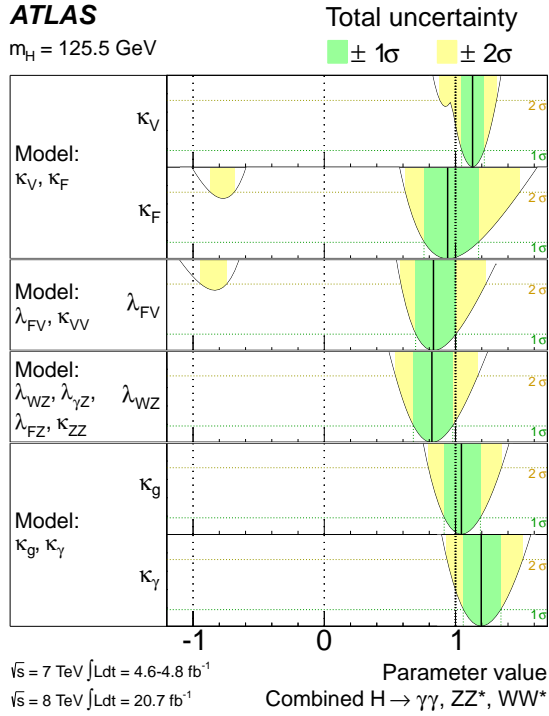


Figure 13: Summary of the measurements of the coupling scale factors for a Higgs boson with mass $m_H = 125.5$ GeV. The best-fit values are represented by the solid vertical lines, with the $\pm 1\sigma$ and $\pm 2\sigma$ uncertainties given by the dark- and light-shaded band, respectively. For a more complete illustration, the distributions of the likelihood ratios from which the total uncertainties are extracted are overlaid. The measurements in the various benchmark models, separated by double horizontal lines, are strongly correlated.

with expectations for the Standard Model Higgs boson.

9. Acknowledgements

We thank CERN for the very successful operation of the LHC, as well as the support staff from our institutions without whom ATLAS could not be operated efficiently.

We acknowledge the support of ANPCyT, Argentina; YerPhI, Armenia; ARC, Australia; BMWF and FWF, Austria; ANAS, Azerbaijan; SSTC, Belarus; CNPq and FAPESP, Brazil; NSERC, NRC and CFI, Canada; CERN; CONICYT, Chile; CAS, MOST and NSFC, China; COLCIENCIAS, Colombia; MSMT CR, MPO CR and VSC CR, Czech Republic; DNRF, DNSRC and Lundbeck Foundation, Denmark; EPLANET, ERC and NSRF, European Union; IN2P3-CNRS, CEA-DSM/IRFU, France; GNSF, Georgia; BMBF, DFG, HGF, MPG and AvH Foundation, Germany; GSRT and NSRF, Greece; ISF, MINERVA, GIF, DIP and Benoziyo

Center, Israel; INFN, Italy; MEXT and JSPS, Japan; CNRST, Morocco; FOM and NWO, Netherlands; BRF and RCN, Norway; MNiSW, Poland; GRICES and FCT, Portugal; MERYYS (MECTS), Romania; MES of Russia and ROSATOM, Russian Federation; JINR; MSTD, Serbia; MSSR, Slovakia; ARRS and MIZŠ, Slovenia; DST/NRF, South Africa; MICINN, Spain; SRC and Wallenberg Foundation, Sweden; SER, SNSF and Cantons of Bern and Geneva, Switzerland; NSC, Taiwan; TAEK, Turkey; STFC, the Royal Society and Leverhulme Trust, United Kingdom; DOE and NSF, United States of America.

The crucial computing support from all WLCG partners is acknowledged gratefully, in particular from CERN and the ATLAS Tier-1 facilities at TRIUMF (Canada), NDGF (Denmark, Norway, Sweden), CC-IN2P3 (France), KIT/GridKA (Germany), INFN-CNAF (Italy), NL-T1 (Netherlands), PIC (Spain), ASGC (Taiwan), RAL (UK) and BNL (USA) and in the Tier-2 facilities worldwide.

References

- [1] L. Evans and P. Bryant, *LHC Machine*, JINST **3** (2008) S08001.
- [2] ATLAS Collaboration, *Observation of a new particle in the search for the Standard Model Higgs boson with the ATLAS detector at the LHC*, Phys. Lett. **B 716** (2012) 1, arXiv:1207.7214 [hep-ex].
- [3] CMS Collaboration, *Observation of a new boson at a mass of 125 GeV with the CMS experiment at the LHC*, Phys. Lett. **B 716** (2012) 30, arXiv:1207.7235 [hep-ex].
- [4] F. Englert and R. Brout, *Broken symmetry and the mass of gauge vector mesons*, Phys. Rev. Lett. **13** (1964) 321.
- [5] P. W. Higgs, *Broken symmetries, massless particles and gauge fields*, Phys. Lett. **12** (1964) 132.
- [6] P. W. Higgs, *Broken symmetries and the masses of gauge bosons*, Phys. Rev. Lett. **13** (1964) 508.
- [7] G. S. Guralnik, C. R. Hagen, and T. W. B. Kibble, *Global conservation laws and massless particles*, Phys. Rev. Lett. **13** (1964) 585.
- [8] P. W. Higgs, *Spontaneous symmetry breakdown without massless bosons*, Phys. Rev. **145** (1966) 1156.
- [9] T. W. B. Kibble, *Symmetry breaking in non-Abelian gauge theories*, Phys. Rev. **155** (1967) 1554.
- [10] ATLAS Collaboration, *Evidence for the spin-zero nature of the Higgs boson using ATLAS data*, submitted to Phys. Lett. B.
- [11] ATLAS Collaboration, *The ATLAS experiment at the CERN Large Hadron Collider*, JINST **3** (2008) S08003.
- [12] CMS Collaboration, *Observation of a new boson with mass near 125 GeV in pp collisions at $\sqrt{s} = 7$ and 8 TeV*, submitted to JHEP, arXiv:1303.4571 [hep-ex].
- [13] ATLAS Collaboration, *Improved luminosity determination in pp Collisions at $\sqrt{s} = 7$ TeV using the ATLAS detector at the LHC*, submitted to Eur. Phys. J., arXiv:1302.4393 [hep-ex].
- [14] LHC Higgs Cross Section Working Group, S. Dittmaier, C. Mariotti, G. Passarino, and R. Tanaka (Eds.), *Handbook of LHC Higgs cross sections: 1. Inclusive observables*,

- CERN-2011-002 (CERN, Geneva, 2011), arXiv:1101.0593 [hep-ph].
- [15] LHC Higgs Cross Section Working Group, S. Dittmaier, C. Mariotti, G. Passarino, and R. Tanaka (Eds.), *Handbook of LHC Higgs Cross Sections: 2. Differential distributions*, CERN-2012-002 (CERN, Geneva, 2012), arXiv:1201.3084 [hep-ph].
- [16] The Higgs Cross Section Working Group web page. <https://twiki.cern.ch/twiki/bin/view/LHCPhysics/CrossSections>, 2012.
- [17] ATLAS Collaboration, *Measurement of the $W \rightarrow l\nu$ and $Z/\gamma \rightarrow ll$ production cross sections in proton-proton collisions at $\sqrt{s} = 7$ TeV with the ATLAS detector*, JHEP **1012** (2010) 060, arXiv:1010.2130 [hep-ex].
- [18] ATLAS Collaboration, *Electron performance measurements with the ATLAS detector using the 2010 LHC proton-proton collision data*, Eur. Phys. J. C **72** (2012) 1909, arXiv:1110.3174 [hep-ex].
- [19] ATLAS Collaboration, *Improved electron reconstruction in ATLAS using the Gaussian Sum Filter-based model for bremsstrahlung*, ATLAS-CONF-2012-047 (2012). <http://cdsweb.cern.ch/record/1449796>.
- [20] ATLAS Collaboration, *Muon reconstruction efficiency in reprocessed 2010 LHC proton-proton collision data recorded with the ATLAS detector*, ATLAS-CONF-2011-063 (2011). <http://cdsweb.cern.ch/record/1345743>.
- [21] ATLAS Collaboration, *Measurement of the inclusive isolated prompt photon cross section in pp collisions at $\sqrt{s} = 7$ TeV with the ATLAS detector*, Phys. Rev. **D83** (2011) 052005.
- [22] ATLAS Collaboration, *Jet energy measurement with the ATLAS detector in proton-proton collisions at $\sqrt{s} = 7$ TeV*, Eur. Phys. J. C **73** (2013) 2304, arXiv:1112.6426 [hep-ex].
- [23] ATLAS Collaboration, *Jet energy scale and its systematic uncertainty in proton-proton collisions at $\sqrt{s}=7$ TeV with ATLAS 2011 data*, ATLAS-CONF-2013-004 (2013). <https://cds.cern.ch/record/1509552>.
- [24] W. Lampl, S. Laplace, D. Lelas, P. Loch, H. Ma, S. Menke, S. Rajagopalan, D. Rousseau, S. Snyder, and G. Unal, *Calorimeter Clustering Algorithms: Description and Performance*, ATL-LARG-PUB-2008-002 (2008). <http://cdsweb.cern.ch/record/1099735>.
- [25] M. Cacciari, G. P. Salam, and G. Soyez, *The anti- k_t jet clustering algorithm*, JHEP **0804** (2008) 063.
- [26] ATLAS Collaboration, *Pile-up corrections for jets from proton-proton collisions at $\sqrt{s} = 7$ TeV in ATLAS in 2011*, ATLAS-CONF-2012-064 (2012). <https://cds.cern.ch/record/1459529>.
- [27] ATLAS Collaboration, *Measurement of the Mistag Rate with 5 fb^{-1} of Data Collected by the ATLAS Detector*, ATLAS-CONF-2012-040 (2012). <https://cdsweb.cern.ch/record/1435194>.
- [28] ATLAS Collaboration, *Measurement of the b -tag Efficiency in a Sample of Jets Containing Muons with 5 fb^{-1} of Data from the ATLAS Detector*, ATLAS-CONF-2012-043 (2012). <https://cdsweb.cern.ch/record/1435197>.
- [29] ATLAS Collaboration, *Commissioning of the ATLAS high-performance b -tagging algorithms in the 7 TeV collision data*, ATLAS-CONF-2011-102 (2011). <http://cds.cern.ch/record/1369219>.
- [30] ATLAS Collaboration, *Performance of Missing Transverse Momentum Reconstruction in Proton-Proton Collisions at $\sqrt{s} = 7$ TeV with ATLAS*, Eur. Phys. J. C **72** (2012) 1844, arXiv:1108.5602 [hep-ex].
- [31] T. Sjostrand, S. Mrenna, and P. Z. Skands, *PYTHIA 6.4 physics and manual*, JHEP **0605** (2006) 026.
- [32] T. Sjostrand, S. Mrenna, and P. Z. Skands, *A Brief Introduction to PYTHIA 8.1*, Comput. Phys. Commun. **178** (2008) 852.
- [33] S. Alioli, P. Nason, C. Oleari, and E. Re, *NLO Higgs boson production via gluon fusion matched with shower in POWHEG*, JHEP **0904** (2009) 002.
- [34] P. Nason and C. Oleari, *NLO Higgs boson production via vector-boson fusion matched with shower in POWHEG*, JHEP **1002** (2010) 037.
- [35] A. Bredenstein, A. Denner, S. Dittmaier, and M. M. Weber, *Precise predictions for the Higgs-boson decay $H \rightarrow WW/ZZ \rightarrow 4$ leptons*, Phys. Rev. **D74** (2006) 013004, arXiv:hep-ph/0604011.
- [36] A. Bredenstein, A. Denner, S. Dittmaier, and M. M. Weber, *Radiative corrections to the semileptonic and hadronic Higgs-boson decays $H \rightarrow WW/ZZ \rightarrow 4$ fermions*, JHEP **0702** (2007) 080.
- [37] M. L. Mangano et al., *ALPGEN, a generator for hard multiparton processes in hadronic collisions*, JHEP **0307** (2003) 001.
- [38] G. Corcella, I. Knowles, G. Marchesini, S. Moretti, K. Odagiri, et al., *HERWIG 6: An Event generator for hadron emission reactions with interfering gluons (including supersymmetric processes)*, JHEP **0101** (2001) 010.
- [39] T. Gleisberg et al., *Event generation with SHERPA 1.1*, JHEP **0902** (2009) 007.
- [40] S. Frixione and B. R. Webber, *Matching NLO QCD computations and parton shower simulations*, JHEP **0206** (2002) 029.
- [41] B. P. Kersevan and E. Richter-Was, *The Monte Carlo event generator AcerMC version 2.0 with interfaces to PYTHIA 6.2 and HERWIG 6.5*, arXiv:hep-ph/0405247.
- [42] T. Binoth, M. Ciccolini, N. Kauer and M. Krämer, *Gluon-induced W -boson pair production at the LHC*, JHEP **0612** (2006) 046.
- [43] N. Kauer and G. Passarino, *Inadequacy of zero-width approximation for a light Higgs boson signal*, JHEP **1208** (2012) 116, arXiv:1206.4803 [hep-ph].
- [44] T. Melia, P. Nason, R. Rontsch, and G. Zanderighi, *W^+W^- , WZ and ZZ production in the POWHEG BOX*, JHEP **1111** (2011) 078.
- [45] T. Binoth, N. Kauer and P. Mertsch, *Gluon-induced QCD Corrections to $pp \rightarrow ZZ \rightarrow \ell\ell'\ell'$* , arXiv:0807.0024 [hep-ph].
- [46] J. Alwall et al., *MadGraph/MadEvent v4: The New Web Generation*, JHEP **0709** (2007) 028.
- [47] J. Alwall, M. Herquet, F. Maltoni, O. Mattelaer, and T. Stelzer, *MadGraph 5: Going Beyond*, JHEP **1106** (2011) 128.
- [48] R. C. Gray, C. Kilic, M. Park, S. Somalwar, and S. Thomas, *Backgrounds to Higgs Boson Searches from $W\gamma^* \rightarrow l\nu(l)$ Asymmetric Internal Conversion*, arXiv:1110.1368 [hep-ph].
- [49] H. Georgi, S. Glashow, M. Machacek, and D. V. Nanopoulos, *Higgs bosons from two gluon annihilation in proton proton collisions*, Phys. Rev. Lett. **40** (1978) 692.
- [50] A. Djouadi, M. Spira, and P. M. Zerwas, *Production of Higgs bosons in proton colliders: QCD corrections*, Phys. Lett. **B 264** (1991) 440.
- [51] S. Dawson, *Radiative corrections to Higgs boson production*, Nucl. Phys. **B359** (1991) 283.
- [52] M. Spira, A. Djouadi, D. Graudenz, and P. M. Zerwas, *Higgs boson production at the LHC*, Nucl. Phys. **B453** (1995) 17.
- [53] R. Harlander and W. B. Kilgore, *Next-to-next-to-leading order Higgs production at hadron colliders*, Phys. Rev. Lett. **88**

- (2002) 201801.
- [54] C. Anastasiou and K. Melnikov, *Higgs boson production at hadron colliders in NNLO QCD*, Nucl. Phys. **B646** (2002) 220.
- [55] V. Ravindran, J. Smith, and W. L. van Neerven, *NNLO corrections to the total cross section for Higgs boson production in hadron hadron collisions*, Nucl. Phys. **B665** (2003) 325.
- [56] U. Aglietti, R. Bonciani, G. Degrossi, and A. Vicini, *Two-loop light fermion contribution to Higgs production and decays*, Phys. Lett. **B 595** (2004) 432.
- [57] S. Actis, G. Passarino, C. Sturm, and S. Uccirati, *NLO electroweak corrections to Higgs boson production at hadron colliders*, Phys. Lett. **B 670** (2008) 12.
- [58] S. Catani, D. de Florian, M. Grazzini, and P. Nason, *Soft-gluon re-summation for Higgs boson production at hadron colliders*, JHEP **0307** (2003) 028.
- [59] D. de Florian and M. Grazzini, *Higgs production at the LHC: updated cross sections at $\sqrt{s} = 8$ TeV*, arXiv:1206.4133 [hep-ph].
- [60] C. Anastasiou, S. Buehler, F. Herzog, and A. Lazopoulos, *Inclusive Higgs boson cross-section for the LHC at 8 TeV*, JHEP **1204** (2012) 004.
- [61] J. Baglio and A. Djouadi, *Higgs production at the LHC*, JHEP **1103** (2011) 055.
- [62] D. de Florian, G. Ferrera, M. Grazzini, and D. Tommasini, *Transverse-momentum resummation: Higgs boson production at the Tevatron and the LHC*, JHEP **1111** (2011) 064.
- [63] E. Bagnaschi, G. Degrossi, P. Slavich, and A. Vicini, *Higgs production via gluon fusion in the POWHEG approach in the SM and in the MSSM*, JHEP **1202** (2012) 88.
- [64] R. Cahn and S. Dawson, *Production of very massive Higgs bosons*, Phys. Lett. **B 136** (1984) 196, Erratum–ibid. **B 138** (1984) 464.
- [65] M. Ciccolini, A. Denner, and S. Dittmaier, *Strong and electroweak corrections to the production of Higgs+2jets via weak interactions at the LHC*, Phys. Rev. Lett. **99** (2007) 161803.
- [66] M. Ciccolini, A. Denner, and S. Dittmaier, *Electroweak and QCD corrections to Higgs production via vector-boson fusion at the LHC*, Phys. Rev. **D 77** (2008) 013002.
- [67] K. Arnold, M. Bahr, G. Bozzi, F. Campanario, C. Englert, et al., *VBFNLO: A parton level Monte Carlo for processes with electroweak bosons*, Comput. Phys. Commun. **180** (2009) 1661.
- [68] P. Bolzoni, F. Maltoni, S.-O. Moch, and M. Zaro, *Higgs production via vector-boson fusion at NNLO in QCD*, Phys. Rev. Lett. **105** (2010) 011801.
- [69] S. Glashow, D. V. Nanopoulos, and A. Yildiz, *Associated production of Higgs bosons and Z particles*, Phys. Rev. **D 18** (1978) 1724.
- [70] T. Han and S. Willenbrock, *QCD correction to the $pp \rightarrow WH$ and ZH total cross sections*, Phys. Lett. **B 273** (1991) 167.
- [71] O. Brein, A. Djouadi, and R. Harlander, *NNLO QCD corrections to the Higgs-strahlung processes at hadron colliders*, Phys. Lett. **B 579** (2004) 149.
- [72] M. L. Ciccolini, S. Dittmaier, and M. Kramer, *Electroweak radiative corrections to associated WH and ZH production at hadron colliders*, Phys. Rev. **D 68** (2003) 073003.
- [73] Z. Kunszt, *Associated production of heavy Higgs boson with top quarks*, Nucl. Phys. **B 247** (1984) 339.
- [74] W. Beenakker et al., *Higgs Radiation Off Top Quarks at the Tevatron and the LHC*, Phys. Rev. Lett. **87** (2001) 201805.
- [75] W. Beenakker et al., *NLO QCD corrections to $t\bar{t}H$ production in hadron collisions*, Nucl. Phys. **B 653** (2003) 151.
- [76] S. Dawson, L. H. Orr, L. Reina, and D. Wackerroth, *Next-to-leading order QCD corrections to $pp \rightarrow t\bar{t}H$ at the CERN Large Hadron Collider*, Phys. Rev. **D 67** (2003) 071503.
- [77] S. Dawson, C. Jackson, L. H. Orr, L. Reina, and D. Wackerroth, *Associated Higgs production with top quarks at the Large Hadron Collider: NLO QCD corrections*, Phys. Rev. **D 68** (2003) 034022.
- [78] ATLAS Collaboration, *New ATLAS event generator tunes to 2010 data*, ATL-PHYS-PUB-2011-008 (2011). <http://cdsweb.cern.ch/record/1345343>.
- [79] ATLAS Collaboration, *ATLAS tunes of PYTHIA 6 and Pythia 8 for MC11*, ATL-PHYS-PUB-2011-009 (2011). <http://cdsweb.cern.ch/record/1363300>.
- [80] ATLAS Collaboration, *Further ATLAS tunes of PYTHIA6 and Pythia 8*, ATL-PHYS-PUB-2011-014 (2011). <http://cdsweb.cern.ch/record/1400677>.
- [81] J. M. Butterworth, J. R. Forshaw, and M. H. Seymour, *Multiparton interactions in photoproduction at HERA*, Z. Phys. **C 72** (1996) 637.
- [82] P. Golonka and Z. Was, *PHOTOS Monte Carlo: A Precision tool for QED corrections in Z and W decays*, Eur. Phys. J. **C 45** (2006) 97.
- [83] N. Davidson, T. Przedzinski, and Z. Was, *PHOTOS interface in C++: technical and physics documentation*, arXiv:1011.0937 [hep-ph].
- [84] H.-L. Lai et al., *New parton distributions for collider physics*, Phys. Rev. **D 82** (2010) 074024.
- [85] P. M. Nadolsky et al., *Implications of CTEQ global analysis for collider observables*, Phys. Rev. **D 78** (2008) 013004.
- [86] A. Sherstnev and R. S. Thorne, *Parton distributions for the LHC*, Eur. Phys. J. **C 55** (2009) 553, arXiv:0711.2473 [hep-ph].
- [87] ATLAS Collaboration, *The ATLAS simulation infrastructure*, Eur. Phys. J. **C 70** (2010) 823, arXiv:1005.4568 [physics.ins-det].
- [88] S. Agostinelli et al., *GEANT4, a simulation toolkit*, Nucl. Instrum. Meth. **A 506** (2003) 250.
- [89] A. Djouadi, J. Kalinowski, and M. Spira, *HDECAY: A program for Higgs boson decays in the standard model and its supersymmetric extension*, Comput. Phys. Commun. **108** (1998) 56.
- [90] ATLAS Collaboration, *Performance of the ATLAS Trigger System in 2010*, Eur. Phys. J. **C 72** (2012) 1849, arXiv:1110.1530 [hep-ex].
- [91] ATLAS Collaboration, *Expected photon performance in the ATLAS experiment*, ATL-PHYS-PUB-2011-007 (2011). <http://cds.cern.ch/record/1345329>.
- [92] M. Cacciari and G. P. Salam, *Pileup subtraction using jet areas*, Phys. Lett. **B 659** (2008) 119.
- [93] ATLAS Collaboration, *Search for the Standard Model Higgs boson in the two photon decay channel with the ATLAS detector at the LHC*, Phys. Lett. **B 705** (2011) 452.
- [94] OPAL Collaboration, K. Ackerstaff et al., *Search for anomalous production of dilepton events with missing transverse momentum in e^+e^- collisions at $\sqrt{s} = 161$ GeV and 172 GeV*, Eur. Phys. J. **C 4** (1998) 47, arXiv:hep-ex/9710010 [hep-ex].
- [95] M. Vesterinen and T. R. Wyatt, *A Novel Technique for Studying the Z Boson Transverse Momentum Distribution at Hadron Colliders*, Nucl. Instrum. Meth. **A 602** (2009) 432.
- [96] S. N. Bernstein, *Démonstration du théorème de Weierstrass fondée sur le calcul des probabilités*, Comm. Soc. Math. Kharkov **13** (1912) 1.
- [97] M. J. Oreglia, *A study of reactions $\psi' \rightarrow \gamma\gamma\psi$* , Ph.D. thesis,

- SLAC-R-0236 (1980) Appendix D.
- [98] S. Gangal and F. J. Tackmann, *NLO Uncertainties in Higgs + 2 jets from Gluon Fusion*, arXiv:1302.5437 [hep-ph].
- [99] J. M. Campbell and R. K. Ellis, *MCFM for the Tevatron and the LHC*, Nucl. Phys. Proc. Suppl. **205-206** (2010) 10.
- [100] ATLAS Collaboration, *Updated results and measurements of properties of the new Higgs-like particle in the four-lepton decay channel with the ATLAS detector*, ATLAS-CONF-2012-169 (2012). <http://cds.cern.ch/record/1499628>.
- [101] ATLAS Collaboration, *Reconstruction of collinear final-state radiation photons in Z decays to muons in $\sqrt{s} = 7$ TeV proton-proton collisions*, ATLAS-CONF-2012-143 (2012). <https://cds.cern.ch/record/1491697>.
- [102] ATLAS Collaboration, *Measurements of the electron and muon inclusive cross-sections in proton-proton collisions at $\sqrt{s} = 7$ TeV with the ATLAS detector*, Phys. Lett. **B 707** (2012) 438, arXiv:1109.0525 [hep-ex].
- [103] ATLAS Collaboration, *Search for the Standard Model Higgs boson in the $H \rightarrow WW^{(*)} \rightarrow \ell\nu\ell\nu$ decay mode with 4.7 fb^{-1} of ATLAS data at $\sqrt{s} = 7$ TeV*, Phys. Lett. **B 716** (2012) 62, arXiv:1206.0756 [hep-ex].
- [104] ATLAS Collaboration, *Performance of missing transverse momentum reconstruction in ATLAS with 2011 proton-proton collisions at $\sqrt{s} = 7$ TeV*, ATLAS-CONF-2012-101 (2012). <http://cds.cern.ch/record/1463915>.
- [105] R.K. Ellis et al., *Higgs decay to $\tau^+\tau^-$: A possible signature of intermediate mass Higgs bosons at the SSC*, Nucl. Phys. **B 297** (1988) 221.
- [106] J. M. Campbell and R. K. Ellis, *An update on vector boson pair production at hadron colliders*, Phys. Rev. **D60** (1999) 113006.
- [107] ATLAS Collaboration, *Measurements of the properties of the Higgs-like boson in the $WW^{(*)} \rightarrow \ell\nu\ell\nu$ decay channel with the ATLAS detector using 25 fb^{-1} of proton-proton collision data*, ATLAS-CONF-2013-030 (2013). <http://cds.cern.ch/record/1527126>.
- [108] S. Catani and M. Grazzini, *An NNLO subtraction formalism in hadron collisions and its application to Higgs boson production at the LHC*, Phys. Rev. Lett. **98** (2007) 222002, arXiv:hep-ph/0703012.
- [109] M. Grazzini, *NNLO predictions for the Higgs boson signal in the $H \rightarrow WW \rightarrow \ell\nu\ell\nu$ and $H \rightarrow ZZ \rightarrow 4\ell$ decay channels*, JHEP **0802** (2008) 043, arxiv:0801.3232 [hep-ph].
- [110] I. Stewart and F. Tackmann, *Theory uncertainties for Higgs mass and other searches using jet bins*, Phys. Rev. **D 85** (2012) 034011.
- [111] ATLAS Collaboration, *Combined search for the Standard Model Higgs boson in pp collisions at $\sqrt{s}=7$ TeV with the ATLAS detector*, Phys. Rev. **D 86** (2012) 032003, arXiv:1207.0319 [hep-ex].
- [112] ATLAS and CMS Collaborations, *Procedure for the LHC Higgs boson search combination in Summer 2011*, ATL-PHYS-PUB-2011-011, CERN-CMS-NOTE-2011-005 (2011). <http://cdsweb.cern.ch/record/1375842>.
- [113] L. Moneta, K. Belasco, K. S. Cranmer, S. Kreiss, A. Lazzaro, et al., *The RooStats Project*, PoS **ACAT2010** (2010) 057, arXiv:1009.1003 [physics.data-an].
- [114] K. Cranmer, G. Lewis, L. Moneta, A. Shibata, and W. Verkerke, *HistFactory: A tool for creating statistical models for use with RooFit and RooStats*, CERN-OPEN-2012-016 (2012). <http://cdsweb.cern.ch/record/1456844>.
- [115] W. Verkerke and D. Kirkby, *The RooFit toolkit for data modelling*, Tech. Rep. physics/0306116, SLAC, Stanford, CA, Jun, 2003. arXiv:physics/0306116v1 [physics.data-an].
- [116] G. Cowan, K. Cranmer, E. Gross, and O. Vitells, *Asymptotic formulae for likelihood-based tests of new physics*, Eur. Phys. J. **C 71** (2011) 1554.
- [117] ATLAS Collaboration, *Search for the Standard Model Higgs boson in $H \rightarrow \tau^+\tau^-$ decays in proton-proton collisions with the ATLAS detector*, ATLAS-CONF-2012-160 (2012). <http://cds.cern.ch/record/1493624>.
- [118] ATLAS Collaboration, *Search for the Standard Model Higgs boson produced in association with a vector boson and decaying to bottom quarks with the ATLAS detector*, ATLAS-CONF-2012-161 (2012). <http://cds.cern.ch/record/1493625>.
- [119] LHC Higgs Cross Section Working Group, S. Heinemeyer, C. Mariotti, G. Passarino, and R. Tanaka (Eds.), *Handbook of LHC Higgs Cross Sections: 3. Higgs Properties*, arXiv:1307.1347 [hep-ph].
- [120] ALEPH, DELPHI, L3, OPAL and SLD Collaborations, LEP Electroweak Working Group, SLD electroweak heavy flavour groups, *Precision Electroweak Measurements on the Z resonance*, Phys. Rep. **427** (2006) 257, arXiv:hep-ex/0509008v3.

Search for Scalar Diphoton Resonances in the Mass Range 65–600 GeV with the ATLAS Detector in pp Collision Data at $\sqrt{s} = 8$ TeV

ATLAS Collaboration

A search for scalar particles decaying via narrow resonances into two photons in the mass range 65–600 GeV is performed using 20.3 fb^{-1} of $\sqrt{s} = 8$ TeV pp collision data collected with the ATLAS detector at the Large Hadron Collider. The recently discovered Higgs boson is treated as a background. No significant evidence for an additional signal is observed. The results are presented as limits at the 95% confidence level on the production cross-section of a scalar boson times branching ratio into two photons, in a fiducial volume where the reconstruction efficiency is approximately independent of the event topology. The upper limits set extend over a considerably wider mass range than previous searches.

PACS numbers: 13.85.Qk,14.70.Bh,14.80.Da,14.80.Ec

In July 2012, the ATLAS and CMS collaborations reported the discovery of a new particle [1, 2] whose measured couplings and properties are compatible with the Standard Model Higgs boson (H) [3–6]. However, several extensions to the Standard Model, in particular models featuring an extended Higgs sector [7–13], predict new scalar resonances below or above the H mass which may be narrow when their branching ratio to two photons is non-negligible.

This Letter presents a search for a scalar particle X of mass m_X decaying via narrow resonances into two photons. It extends the method developed for the measurement of the H couplings in the $H \rightarrow \gamma\gamma$ channel [3] to the range $65 < m_X < 600$ GeV. Analytical descriptions of the signal and background distributions are fitted to the measured diphoton invariant mass spectrum $m_{\gamma\gamma}$ to determine the signal and background yields. The result is presented as a limit on the production cross-section times the branching ratio $BR(X \rightarrow \gamma\gamma)$, restricted to a fiducial volume where the reconstruction efficiency is approximately independent of the event topology. The resonance with mass m_X is considered narrow when its intrinsic width is smaller than $0.09 \text{ GeV} + 0.01 \cdot m_X$. This upper limit is defined such that the bias in the number of fitted signal events is kept below 10%, and ensures that the diphoton invariant mass width is dominated by the experimental resolution in the ATLAS detector. Model-dependent interference effects between the resonance and the continuum diphoton background are not considered.

The ATLAS detector [14] at the LHC [15] covers the pseudorapidity [16] range $|\eta| < 4.9$ and the full azimuthal angle ϕ . It consists of an inner tracking detector covering the pseudorapidity range $|\eta| < 2.5$, surrounded by electromagnetic and hadronic calorimeters and an external muon spectrometer.

The search is carried out using the $\sqrt{s} = 8$ TeV pp collision dataset collected in 2012, with stable beam conditions and all ATLAS subsystems operational, which corresponds to an integrated luminosity of $\mathcal{L} = 20.3 \pm 0.6 \text{ fb}^{-1}$ [17]. The data were recorded using a

diphoton trigger that required two electromagnetic clusters with transverse energies E_T above 20 GeV, both fulfilling identification criteria based on shower shapes in the electromagnetic calorimeter. The efficiency of the diphoton trigger [18] is $(98.7 \pm 0.5)\%$ for signal events passing the analysis selection.

The event selection requires at least one reconstructed primary vertex with two or more tracks with transverse momenta $p_T > 0.4$ GeV, and at least two photon candidates with $E_T > 22$ GeV and $|\eta| < 2.37$, excluding the barrel/endcap transition region of the calorimeter, $1.37 < |\eta| < 1.56$.

Photon reconstruction is seeded by clusters of electromagnetic calorimeter cells. Clusters without matching tracks are classified as unconverted photons. Clusters with matched tracks are considered as electron candidates, but are classified as converted photons if they are associated with two tracks consistent with a $\gamma \rightarrow e^+e^-$ conversion process, or a single track leaving no hit in the innermost layer of the inner tracking detector. The photon energy calibration procedure is the same as in Ref. [3].

Photon candidates are required to fulfill identification criteria based on shower shapes in the electromagnetic calorimeter, and on energy leakage into the hadronic calorimeter [19]. Identification efficiencies, averaged over η , range from 70% to above 99% for the E_T range under consideration. To further reduce the background from jets, the calorimeter isolation transverse energy E_T^{iso} is required to be smaller than 6 GeV, where E_T^{iso} is defined as the sum of transverse energies of the positive-energy topological clusters [20] within a cone of size $\Delta R = \sqrt{(\Delta\phi)^2 + (\Delta\eta)^2} = 0.4$ around the photon candidate. The core of the photon shower is excluded, and E_T^{iso} is corrected for the leakage of the photon shower into the isolation cone. The contributions from the underlying event and pile-up are subtracted using the technique proposed in Ref. [21] and implemented as described in Ref. [22]. In addition, the track isolation, defined as the scalar sum of the p_T of the primary vertex tracks with

$p_T > 1$ GeV in a $\Delta R = 0.2$ cone around the photon candidate, excluding the conversion tracks, is required to be smaller than 2.6 GeV.

The $m_{\gamma\gamma}$ invariant mass is evaluated using the leading photon (γ_1) and subleading photon (γ_2) energies measured in the calorimeter, the azimuthal angle $\Delta\phi$ and the pseudorapidity $\Delta\eta$ separations between the photons determined from their positions in the calorimeter and the position of the reconstructed diphoton vertex [3].

After selection, the data sample consists of a continuum background with dominantly $\gamma\gamma$, γ -jet, jet-jet events and Drell-Yan (DY) production of electron pairs where both electrons are misidentified as photons. Two peaking backgrounds arise from the Z boson component of the DY and from $H \rightarrow \gamma\gamma$.

To increase the sensitivity, the search is split into two analyses: a categorized low-mass analysis covering the range $65 < m_X < 110$ GeV, and an inclusive high-mass analysis covering $110 < m_X < 600$ GeV. To provide sidebands on both sides of the tested mass point m_X , the $m_{\gamma\gamma}$ ranges are wider than the m_X ranges probed and overlap at the transition between the two analyses.

The low-mass analysis requires a precise modeling of the DY background, dominated by the Z boson resonance, where both electrons are misidentified as photons, mostly classified as converted photons. The loss of signal sensitivity is mitigated by separating the events into three categories with different signal-to-background ratios, according to the conversion status of the photon pair: two unconverted (UU), one converted and one unconverted (CU) or two converted photons (CC). Table I shows the fractions of signal and DY events expected in each category.

TABLE I. Number of diphoton events in data (N_{data}), number of expected Drell-Yan events (N_{DY}), fractions of expected signal (f_X) and Drell-Yan (f_{DY}) in each conversion category for the low-mass analysis. The signal fraction is given for $m_X = 90$ GeV but the mass-dependence is negligible.

$\gamma\gamma$ category	UU	CU	CC
N_{data}	272184	253804	63224
N_{DY}	1080 ± 260	3400 ± 600	2700 ± 250
f_{DY}	15.0%	47.3%	37.7%
f_X	48.7%	42.5%	8.8%

In each category, the Z resonance shape is described by a double-sided Crystal Ball function [23]. Due to the limited size of the fully simulated $Z \rightarrow ee$ sample [24, 25] where both electrons are misidentified as photons, the shape parameters are determined by a fit to a dielectron data sample, where both electrons are required to fulfill shower shape identification criteria and the same E_T thresholds as the photons.

Since most of the electrons misidentified as photons underwent large bremsstrahlung, the invariant mass distribution of the Z boson reconstructed as a photon pair

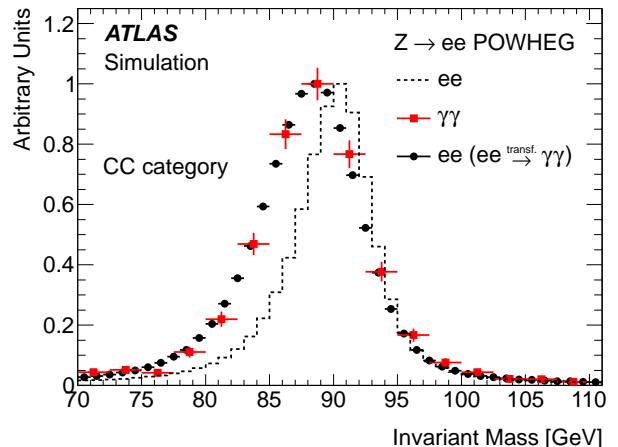


FIG. 1. Invariant mass distributions in the CC category for fully simulated $Z \rightarrow ee$ events reconstructed as ee (dotted-lines), reconstructed as $\gamma\gamma$ (squares), and reconstructed as ee after transforming the electrons to match the kinematics of the electrons misidentified as converted photons (circles).

is wider and shifted to lower masses by up to 2 GeV with respect to the Z boson mass reconstructed as an electron pair. The $Z \rightarrow ee$ invariant mass distributions extracted from data in each category are transformed by applying E_T -dependent shifts and smearing factors to the electron E_T and ϕ , to match the kinematics of the electrons misidentified as photons. Two sets of transformations are derived for γ_1 and γ_2 depending on their conversion status, using a $Z \rightarrow ee$ sample generated with POWHEG [26, 27] interfaced with PYTHIA8 [28] for showering and hadronization. Figure 1 illustrates the effect of the electrons' transformations on the invariant mass shapes in the fully simulated $Z \rightarrow ee$ sample. Systematic uncertainties on the template shapes and the Z peak position are evaluated by varying the parameters of the electrons' transformations by $\pm 1\sigma$.

The DY normalization is computed from the $e \rightarrow \gamma$ fake rates, defined as the ratios of $e\gamma$ to ee pairs measured in $Z \rightarrow ee$ data, separately for γ_1 and γ_2 and each conversion status. A correction factor obtained from fully simulated $Z \rightarrow ee$ events is applied to account for additional effects, mainly the differences in isolation efficiencies and vertex reconstruction efficiency between $\gamma\gamma$ and ee events. The associated uncertainties (9 to 25%) are dominated by the subtraction of the continuum background and the detector material description.

The determination of the analytical form of the continuum background and the corresponding uncertainties follow the method detailed in Ref. [1]. The sum of a Landau distribution and an exponential distribution is used over the full $m_{\gamma\gamma}$ range. The bias on the signal yield induced by the analytical shape function is required to be lower than 20% of the statistical uncertainty on the fitted sig-

nal yield for the background-only spectrum. This bias is measured from a large sample generated from a parameterized detector response, and is accounted for by a mass-dependent uncertainty. Figure 2 shows background-only fits to the data in the low-mass analysis for the three conversion categories.

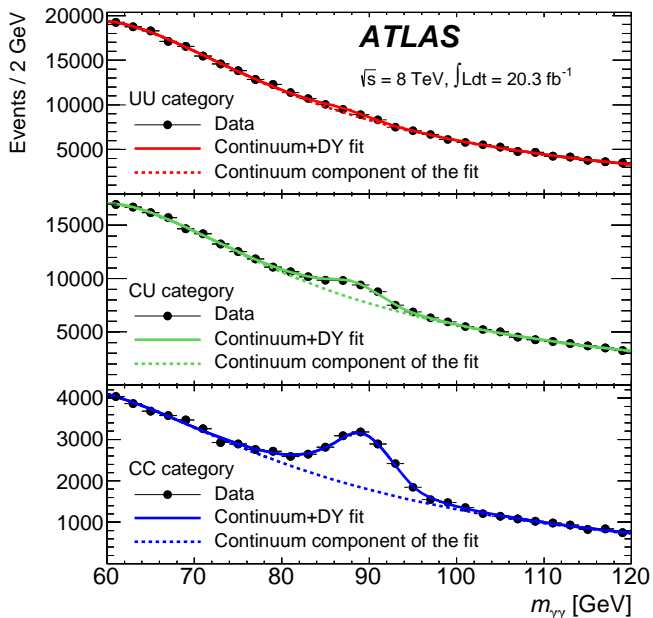


FIG. 2. Background-only fits to the data (black dots) as functions of the diphoton invariant mass $m_{\gamma\gamma}$ for the three conversion categories in the low-mass range. The solid lines show the sum of the Drell–Yan and the continuum background components. The dashed lines show the continuum background component only.

In the high-mass analysis, relative cuts $E_T^{\gamma 1}/m_{\gamma\gamma} > 0.4$ and $E_T^{\gamma 2}/m_{\gamma\gamma} > 0.3$ are added to the selection requirements to reduce the continuum backgrounds and thereby increase the signal sensitivity. In total, 108654 events with $100 < m_{\gamma\gamma} < 800$ GeV are selected.

To determine the continuum background shape over this large mass range, an exponential of a second-order polynomial is fitted inside a sliding $m_{\gamma\gamma}$ window of width $80 \cdot (m_X - 110 \text{ GeV})/110 + 20 \text{ GeV}$, centered on the mass point m_X . The analytical shape and the fit window width are chosen to fulfill the signal yield bias criterion, as defined for the low-mass analysis, to minimize the statistical uncertainty on the background.

The H background shape is modeled by a double-sided Crystal Ball function, and normalized for $m_H = 125.9 \text{ GeV}$ [29][30] using the most up-to-date Standard Model cross-section calculations and corrections [31] of the five main production modes: gluon fusion (ggF), vector-boson fusion (VBF), Higgs-strahlung (WH, ZH), and associated production with a top quark pair ($t\bar{t}H$). The ggF and VBF samples [3] are simulated with the POWHEG generator interfaced with PYTHIA8. The $WH,$

ZH and $t\bar{t}H$ samples [3] are simulated with PYTHIA8. Figure 3 shows background-only fits to the data in the high-mass analysis.

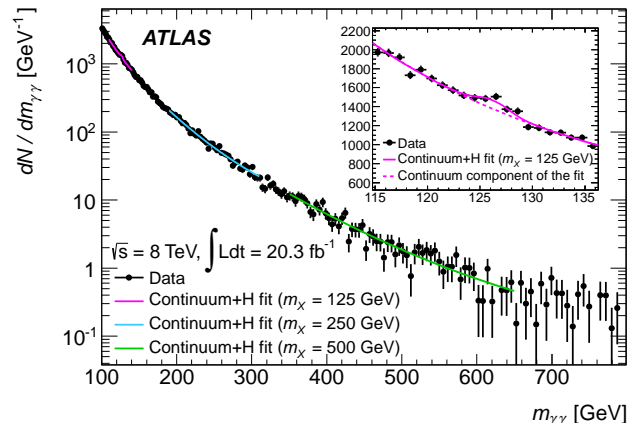


FIG. 3. Background-only fits to the data (black dots) as functions of the diphoton invariant mass $m_{\gamma\gamma}$ for the inclusive high-mass analysis. The solid line shows the sum of the Higgs boson and the continuum background components. The dashed line shows the continuum background component only.

The expected invariant mass distribution of the narrow resonance signal X is also modeled with a double-sided Crystal Ball function in the mass range $65 \leq m_X \leq 600 \text{ GeV}$, using fully simulated ggF(X) samples generated as for H , where H is replaced by a scalar boson with a constant width of 4 MeV. Polynomial parameterizations of the signal shape parameters as a function of m_X are obtained from a simultaneous fit to all the generated mass points m_X , separately for the high-mass analysis and the three low-mass analysis categories. The signal shape parameters extracted from ggF(X) are compared to the other production modes VBF(X), WX, ZX and $t\bar{t}X$; the bias on the signal yield due to the choice of ggF(X) shape is negligible. The systematic uncertainty on the signal shape due to the photon energy resolution uncertainty ranges from 10% to 40% as a function of m_X [3]. The systematic uncertainty on the X peak position due to the photon energy scale uncertainty is 0.6% [3].

The fiducial cross-section $\sigma_{\text{fid}} \cdot BR(X \rightarrow \gamma\gamma)$ includes an efficiency correction factor C_X through

$$\sigma_{\text{fid}} \cdot BR(X \rightarrow \gamma\gamma) = \frac{N_{\text{data}}}{C_X \cdot \mathcal{L}} \quad \text{with} \quad C_X = \frac{N_{\text{MC}}^{\text{reco}}}{N_{\text{MC}}^{\text{fid}}},$$

where N_{data} is the number of fitted signal events in data, $N_{\text{MC}}^{\text{reco}}$ the number of simulated signal events passing the selection criteria and $N_{\text{MC}}^{\text{fid}}$ the number of simulated signal events generated within the fiducial volume. The fiducial volume, defined from geometrical and kinematical constraints at the generated particle level, is optimized to reduce the model-dependence of C_X using fully simulated samples of the five X production modes to cover

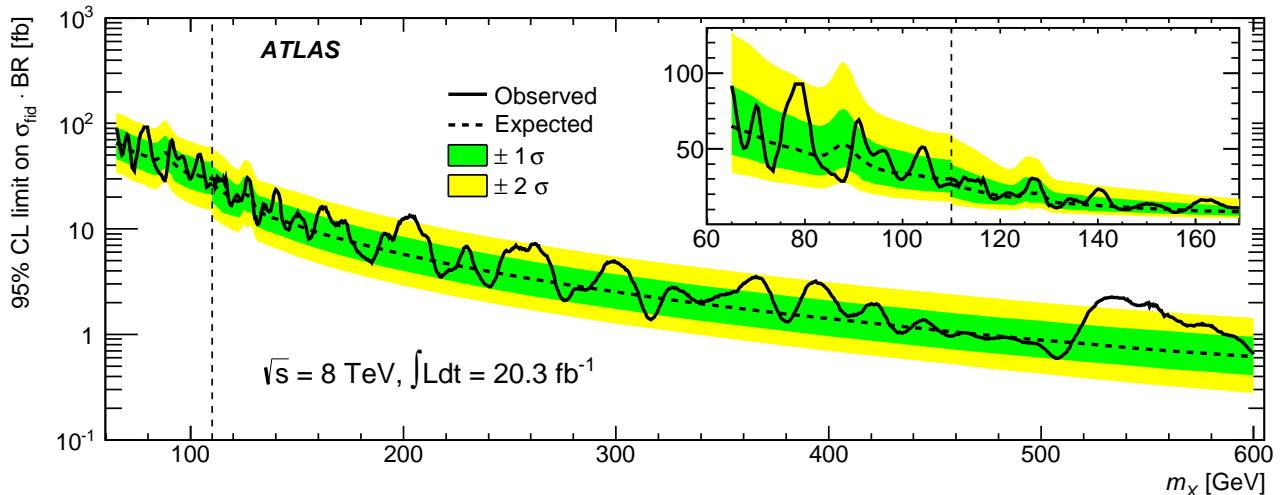


FIG. 4. Observed and expected 95% CL limit on the fiducial cross-section times branching ratio $BR(X \rightarrow \gamma\gamma)$ as a function of m_X in the range $65 < m_X < 600$ GeV. The discontinuity in the limit at $m_X = 110$ GeV (vertical dashed line) is due to the transition between the low-mass and high-mass analyses. The green and yellow bands show the $\pm 1\sigma$ and $\pm 2\sigma$ uncertainties on the expected limit. The inset shows a zoom around the transition point.

a large variety of topologies. The photon selection at generation level is similar to the selection applied to the data: two photons with $E_T > 22$ GeV and $|\eta| < 2.37$ are required; for m_X greater than 110 GeV, the relative cuts $E_T^{\gamma 1}/m_{\gamma\gamma} > 0.4$ and $E_T^{\gamma 2}/m_{\gamma\gamma} > 0.3$ are imposed. The particle isolation, defined as the scalar sum of p_T of all the stable particles (except neutrinos) found within a $\Delta R = 0.4$ cone around the photon direction, is required to be less than 12 GeV. The C_X factor is parameterized from the $ggF(X)$ samples, and ranges from 0.56 to 0.71 as a function of m_X . Systematic uncertainties include the maximum difference between the C_X of the five production modes, the effect of the underlying event (U.E.) and pile-up.

The statistical analysis of the data uses unbinned maximum likelihood fits. The DY and H shapes and normalizations are allowed to float within the uncertainties. In the low-mass analysis, a simultaneous fit to the three conversion categories is performed. Only two excesses with 2.1σ and 2.2σ local significances above the background are observed over the full mass range 65–600 GeV, for $m_X=201$ GeV and $m_X=530$ GeV respectively. This corresponds to a deviation of less than 0.5σ from the background-only hypothesis. Consequently, a 95% limit on $\sigma_{\text{fid}} \cdot BR(X \rightarrow \gamma\gamma)$ is computed using the procedure of Ref. [1]. The systematic uncertainties listed in Table II are accounted for by nuisance parameters in the likelihood function. In the low-mass analysis, the dominant uncertainties are the DY normalization and the residual topology dependence of C_X . In the high-mass analysis, the largest uncertainties arise from the energy resolution and the theoretical uncertainty on the production rate of the Standard Model Higgs boson around 126 GeV.

TABLE II. Summary of the systematic uncertainties

<i>Signal and Higgs boson yield</i>		<i>Z component of Drell-Yan</i>	
Luminosity	2.8%	Normalization ^b	9–25%
Trigger	0.5%	Peak position ^b	1.5–3.5%
γ identification ^a	1.6–2.7%	Template shape ^b	1.5–3%
γ isolation ^a	1–6%	<i>Higgs boson background</i>	
Energy resolution ^{ab}	10–40%	Cross-section ^c	9.6%
<i>Signal and Higgs boson peak position</i>		Branching ratio	4.8%
Energy scale	0.6%	<i>C_X factor</i>	
Continuum $\gamma\gamma$, γj , jj , DY		Topology ^a	3–15%
Signal bias ^a	1–67 events	Pile-up & U. E. ^a	1.4–3.2%

^a mass-dependent.

^b category-dependent.

^c factorization scale + PDF uncertainties [31].

The observed and expected limits, shown in Fig. 4, are in good agreement, consistent with the absence of a signal. The limits on $\sigma_{\text{fid}} \cdot BR(X \rightarrow \gamma\gamma)$ for an additional scalar resonance range from 90 fb for $m_X=65$ GeV to 1 fb for $m_X=600$ GeV. These results extend over a considerably wider mass range than the previous searches by the ATLAS and CMS collaborations [1, 35], are complementary to spin-2 particles searches [36, 37], and are the first such limits independent of the event topology.

We thank CERN for the very successful operation of the LHC, as well as the support staff from our institutions without whom ATLAS could not be operated efficiently.

We acknowledge the support of ANPCyT, Argentina; YerPhI, Armenia; ARC, Australia; BMWF and FWF, Austria; ANAS, Azerbaijan; SSTC, Belarus; CNPq and FAPESP, Brazil; NSERC, NRC and CFI, Canada; CERN; CONICYT, Chile; CAS, MOST and NSFC,

China; COLCIENCIAS, Colombia; MSMT CR, MPO CR and VSC CR, Czech Republic; DNRF, DNSRC and Lundbeck Foundation, Denmark; EPLANET, ERC and NSRF, European Union; IN2P3-CNRS, CEA-DSM/IRFU, France; GNSF, Georgia; BMBF, DFG, HGF, MPG and AvH Foundation, Germany; GSRT and NSRF, Greece; ISF, MINERVA, GIF, I-CORE and Benozziyo Center, Israel; INFN, Italy; MEXT and JSPS, Japan; CNRST, Morocco; FOM and NWO, Netherlands; BRF and RCN, Norway; MNiSW and NCN, Poland; GRICES and FCT, Portugal; MNE/IFA, Romania; MES of Russia and ROSATOM, Russian Federation; JINR; MSTD, Serbia; MSSR, Slovakia; ARRS and MIZŠ, Slovenia; DST/NRF, South Africa; MINECO, Spain; SRC and Wallenberg Foundation, Sweden; SER, SNSF and Cantons of Bern and Geneva, Switzerland; NSC, Taiwan; TAEK, Turkey; STFC, the Royal Society and Leverhulme Trust, United Kingdom; DOE and NSF, United States of America.

The crucial computing support from all WLCG partners is acknowledged gratefully, in particular from CERN and the ATLAS Tier-1 facilities at TRIUMF (Canada), NDGF (Denmark, Norway, Sweden), CC-IN2P3 (France), KIT/GridKA (Germany), INFN-CNAF (Italy), NL-T1 (Netherlands), PIC (Spain), ASGC (Taiwan), RAL (UK) and BNL (USA) and in the Tier-2 facilities worldwide.

-
- [1] ATLAS Collaboration, *Phys. Lett. B* **716** (2012) 1, [arXiv:1207.7214 \[hep-ex\]](#).
- [2] CMS Collaboration, *Phys. Lett. B* **716** (2012) 30, [arXiv:1207.7235 \[hep-ex\]](#).
- [3] ATLAS Collaboration, *Phys. Lett. B* **726** (2013) 88, [arXiv:1307.1427 \[hep-ex\]](#).
- [4] CMS Collaboration, *J. High Energy Phys.* **06** (2013) 081, [arXiv:1303.4571 \[hep-ex\]](#).
- [5] ATLAS Collaboration, *Phys. Lett. B* **726** (2013) 120, [arXiv:1307.1432 \[hep-ex\]](#).
- [6] CMS Collaboration, *Phys. Rev. Lett.* **110** (2013) 081, [arXiv:1212.6639 \[hep-ex\]](#).
- [7] A. Hill and J. van der Bij, *Phys. Rev. D* **36** (1987) 3463.
- [8] M. Veltman and F. Yndurain, *Nucl. Phys. B* **325** (1989) 1.
- [9] T. Binoth and J. van der Bij, *Z. Phys. C* **75** (1997) 17, [arXiv:hep-ph/9608245 \[hep-ph\]](#).
- [10] R. Schabinger and J. D. Wells, *Phys. Rev. D* **72** (2005) 093007, [arXiv:hep-ph/0509209 \[hep-ph\]](#).
- [11] B. Patt and F. Wilczek, [arXiv:hep-ph/0605188 \[hep-ph\]](#).
- [12] G. M. Pruna and T. Robens, *Phys. Rev. D* **88** (2013) 115012, [arXiv:1303.1150 \[hep-ph\]](#).
- [13] T. D. Lee, *Phys. Rev. D* **8** (1973) 1226.
- [14] ATLAS Collaboration, *JINST* **3** (2008) S08003.
- [15] L. Evans and P. Bryant, *JINST* **3** (2008) S08001.
- [16] ATLAS uses a right-handed coordinate system with its origin at the nominal interaction point (IP) in the center of the detector, and the z -axis along the beam line. The x -axis points from the IP to the center of the LHC ring, and the y -axis points upwards. Cylindrical coordinates (r, ϕ) are used in the transverse plane, ϕ being the azimuthal angle around the beam line. Observables labeled transverse are projected into the x - y plane. The pseudorapidity is defined in terms of the polar angle θ as $\eta = -\ln[\tan(\theta/2)]$.
- [17] ATLAS Collaboration, *Eur. Phys. J. C* **73** (2013) 2518, [arXiv:1302.4393 \[hep-ex\]](#).
- [18] ATLAS Collaboration, ATLAS-CONF-2012-048. <http://cds.cern.ch/record/1450089>.
- [19] ATLAS Collaboration, ATLAS-PHYS-PUB-2011-007. <https://cdsweb.cern.ch/record/1345329>.
- [20] ATLAS Collaboration, *Phys. Rev. D* **83** (2011) 052005, [arXiv:1012.4389 \[hep-ex\]](#).
- [21] M. Cacciari, G. P. Salam, and S. Sapeta, *J. High Energy Phys.* **04** (2010) 065, [arXiv:0912.4926 \[hep-ph\]](#).
- [22] ATLAS Collaboration, *Phys. Rev. D* **85** (2012) 012003, [arXiv:1107.0581 \[hep-ex\]](#).
- [23] A double-sided Crystal Ball function is composed of a Gaussian distribution at the core, connected with two power-law distributions describing the lower and upper tails [32].
- [24] GEANT4 Collaboration, S. Agostinelli et al., *Nucl. Instrum. Meth. A* **506** (2003) 250.
- [25] ATLAS Collaboration, *Eur. Phys. J. C* **70** (2010) 823, [arXiv:1005.4568 \[physics.ins-det\]](#).
- [26] S. Alioli, P. Nason, C. Oleari, and E. Re, *J. High Energy Phys.* **04** (2009) 002, [arXiv:0812.0578 \[hep-ph\]](#).
- [27] P. Nason and C. Oleari, *J. High Energy Phys.* **02** (2010) 037, [arXiv:0911.5299 \[hep-ph\]](#).
- [28] T. Sjostrand, S. Mrenna, and P. Z. Skands, *J. High Energy Phys.* **05** (2006) 026, [arXiv:hep-ph/0603175 \[hep-ph\]](#).
- [29] Particle Data Group, J. Beringer, et al., *Phys. Rev. D* **86** (2012) 010001. And 2013 partial update for the 2014 edition.
- [30] Differences between this choice of reference mass and the new mass measurements [33, 34] are covered by the energy scale uncertainties listed in Table II.
- [31] LHC Higgs Cross Section Working Group, S. Heinemeyer (Ed.), et al., CERN-2013-004 (2013), [arXiv:1307.1347 \[hep-ph\]](#).
- [32] M. Oreglia, SLAC-R-0236 (1980) Appendix D. PhD thesis, Univ. Stanford.
- [33] ATLAS Collaboration, [arXiv:1406.3827 \[hep-ph\]](#).
- [34] CMS Collaboration, CMS-PAS-HIG-14-009. <http://cds.cern.ch/record/1728249?ln=en>.
- [35] CMS Collaboration, [arXiv:1407.0558 \[hep-ph\]](#).
- [36] ATLAS Collaboration, *New J. Phys.* **15** (2013) 043007, [arXiv:1112.2194 \[hep-ph\]](#).
- [37] CMS Collaboration, *Phys. Rev. Lett.* **108** (2012) 111801, [arXiv:1112.0688 \[hep-ph\]](#).